NASA-CR-183413

CSC/TM-80/6176

ONBOARD ORBIT DETERMINATION WITH TRACKING AND DATA RELAY SATELLITE SYSTEM (TDRSS) DATA

VOLUME I. EXTENDED KALMAN FILTER EVALUATION

Prepared for

GODDARD SPACE FLIGHT CENTER

By

COMPUTER SCIENCES CORPORATION

Under

Contract NAS 5-24300
Task Assignment 977

Prepared by:

A. C. Long — Date 10/30/80

for P. S. Gural — Date 10/30/80

Reviewed by:

J. B. Dunham, Section Manager — Date 10/30/80

Approved by:

R. D. Headrick, Department Manager — Date

(NASA-CR-183413) ONBOARD ORBIT DETERMINATION WITH TRACKING AND DATA RELAY SATELLITE SYSTEM (TDRSS) DATA. VOLUME 1: EXTENDED KALMAN FILTER EVALUATION (Computer Sciences Corp.) 437 p

N89-70061

Unclas
00/13 0169538

PREFACE

Three estimation algorithms have been studied to determine their suitability for onboard use with Tracking and Data Relay Satellite System (TDRSS) data: the extended Kalman filter (EKF), the sliding batch differential corrector (SBDC), and the consider Kalman and extended Kalman filters. This volume of Onboard Orbit Determination With Tracking and Data Relay Satellite System (TDRSS) Data presents the results of the EKF study. The SBDC and consider filter study results are described in Volumes II and III, respectively.

ACKNOWLEDGMENT

The authors wish to acknowledge the support of J. Teles and R. Pajerski of Goddard Space Flight Center in the direction of the analysis documented in this memorandum and the assistance of E. Fang of Computer Sciences Corporation in the generation of many of the computer runs.

ABSTRACT

This document presents the results of an evaluation of Landsat-D and Gamma Ray Observatory (GRO) orbit determination accuracies achievable using Tracking and Data Relay Satellite System (TDRSS) data in the extended Kalman filter (EKF). The evaluation used the Research and Development Goddard Trajectory Determination System (R&D GTDS) to analyze the effects of parameters such as data contact frequency, data type, data simulation errors, and EKF options. The result is a recommendation on the feasibility of using the EKF as an onboard orbit estimator in future spaceflight missions.

TABLE OF CONTENTS

Section 1 - Introduction 1-1

1.1 Summary 1-1
1.2 Conclusions and Recommendations 1-2

Section 2 - Measurement Models for TDRSS Data. 2-1

2.1 Range and Delta-Range Measurements. 2-4

2.1.1 TDRSS Pseudo-Range Measurement 2-4
2.1.2 TDRSS Pseudo Delta-Range Measurement . . 2-5

2.2 TDRSS Tracking Schedules. 2-7

Section 3 - Evaluation Procedure 3-1

3.1 Test Cases. 3-1
3.2 Measurement Error Models. 3-4

3.2.1 Measurement Biases 3-4
3.2.2 Random Measurement Errors. 3-4
3.2.3 TDRS Ephemeris Error 3-6
3.2.4 User-Clock Errors. 3-6

3.3 Dynamic Modeling Errors 3-8

3.3.1 Geopotential Model 3-8
3.3.2 Drag Parameters. 3-10
3.3.3 Solar Radiation Parameters 3-10

3.4 Baseline EKF Processing Parameters. 3-10

Section 4 - Evaluation Results for Landsat-D 4-1

4.1 Two-Way Range and Delta-Range Data. 4-1

4.1.1 Baseline Runs. 4-6
4.1.2 Variation of Contact Frequency 4-6
4.1.3 Variation of TDRS Ephemeris Errors . . . 4-7
4.1.4 Contacts With Only a Single TDRS 4-9

4.2 Two-Way Delta-Range Data. 4-9
4.3 One-Way Delta-Range Data. 4-12

4.3.1 Baseline Run With Accurate Onboard Clock. 4-12
4.3.2 Variation of Contact Frequency 4-15

TABLE OF CONTENTS

Section 4 (Cont'd)

4.3.3 Variation of TDRS Ephemeris Errors . . . 4-15
4.3.4 Baseline Runs With NASA Standard Transponder Model 4-16

4.4 Anomalous Data Cases. 4-18

Section 5 - Evaluation Results for GRO 5-1

5.1 Two-Way Range and Delta-Range Data. 5-1

5.1.1 Baseline Runs. 5-1
5.1.2 Variation of Contact Frequency 5-8
5.1.3 Variation of TDRS Ephemeris Errors . . . 5-8

5.2 Two-Way Delta-Range Data. 5-9

5.2.1 Baseline Runs. 5-9
5.2.2 Variation of Contact Frequency 5-11
5.2.3 Variation of TDRS Ephemeris Errors . . . 5-12

5.3 One-Way Delta-Range Data. 5-12

5.3.1 Baseline Runs. 5-12
5.3.2 Variation of Contact Frequency 5-14
5.3.3 Baseline Runs With NASA Standard Transponder Model 5-14

5.4 Anomalous Data Cases. 5-16

Section 6 - Conclusions. 6-1

6.1 Landsat-D Estimation. 6-1
6.2 GRO Estimation. 6-4

Appendix A - Landsat-D Error Plots

Appendix B - GRO Error Plots

Appendix C - Accuracy of EKF Baseline Ephemeris

Appendix D - Computation of Measurement Standard Deviation Arising From TDRS Ephemeris Errors

Appendix E - Sample Deck Setup

References

LIST OF ILLUSTRATIONS

Figure

2-1 One-Way Tracking Signal Geometry. 2-2
2-2 Two-Way Tracking Signal Geometry. 2-3
3-1 Evaluation Procedure for TDRSS Study. 3-2
3-2 TDRS-E Ephemeris Errors 3-7
4-1 TDRSS Tracking Contacts for Landsat-D for One-Revolution Contact Frequency. 4-2
4-2 TDRSS Tracking Contacts for Landsat-D for Two-Revolution Contact Frequency. 4-3
4-3 TDRSS Tracking Contacts for Landsat-D for Three-Revolution Contact Frequency. 4-4
5-1 TDRSS Tracking Contacts for GRO for One-Revolution Contact Frequency. 5-2
5-2 TDRSS Tracking Contacts for GRO for Two-Revolution Contact Frequency. 5-3
5-3 TDRSS Tracking Contacts for GRO for Three-Revolution Contact Frequency. 5-4

LIST OF TABLES

Table

3-1 Landsat-D, GRO, TDRS-E, and TDRS-W Orbital Elements, Area, and Mass. 3-3
3-2 Data Simulation Measurement Errors. 3-5
3-3 Data Simulation TDRS Ephemeris Error Model. . 3-5
3-4 Data Simulation Quadratic User-Clock Error Model 3-5
3-5 Dynamic Models. 3-9
3-6 Options Used in EKF 3-11
3-7 A Priori Values and Measurement Standard Deviations in EKF 3-11
4-1 Landsat-D Estimation Using Two-Way Range and Delta-Range Data (Runs A1 Through D6) . . . 4-5
4-2 Landsat-D Estimation Using Two-Way Range and Delta-Range Data (Runs E1 Through F3) . . . 4-8
4-3 Landsat-D Estimation Using Two-Way Delta-Range Data (Runs G1 Through J4) 4-10
4-4 Landsat-D Estimation Using Two-Way Delta-Range Data (Runs K2 Through L4) 4-11
4-5 Landsat-D Estimation Using One-Way Delta-Range Data for Accurate Clock Model 4-13
4-6 Landsat-D Estimation Using One-Way Delta-Range Data With NASA Standard Transponder Model . 4-17
4-7 Landsat-D Estimation Using Anomalous Data Sets. 4-19
4-8 Anomalous Data Sets for Landsat-D 4-20
4-9 Landsat-D Estimation Using One-Way Data With Sinusoidal Error Model. 4-22
5-1 GRO Estimation Using Two-Way Range and Delta-Range Data. 5-6
5-2 GRO Estimation Using Two-Way Delta-Range Data. 5-10
5-3 GRO Estimation Using One-Way Delta-Range Data. 5-13
5-4 GRO Estimation Using One-Way Delta-Range Data With NASA Transponder Model. 5-15
5-5 Anomalous Data Sets for GRO 5-17
5-6 GRO Estimation Using Anomalous Data Sets. . . 5-18
5-7 GRO Estimation Using One-Way Data With Sinusoidal Error Model. 5-20
6-1 Best Landsat-D Estimate After 24 Hours of Processing. 6-2
6-2 Best GRO Estimate After 24 Hours of Processing. 6-5

SECTION 1 - INTRODUCTION

The National Aeronautics and Space Administration's Goddard Space Flight Center (NASA/GSFC) is currently investigating the feasibility of autonomous spacecraft navigation. As part of that study, an onboard orbit determination algorithm must be selected that will provide both reliability and accuracy. One candidate for this role is the extended Kalman filter (EKF), which updates the spacecraft orbital parameters with each successive observation. This sequential processing capability is particularly advantageous for onboard orbit estimation.

This document presents the results of an evaluation of the feasibility of using the EKF with Tracking and Data Relay Satellite (TDRS) System (TDRSS) data. The use of TDRSS data for onboard estimation has the advantage that NASA will already be using TDRSS for ground-based satellite tracking and the relay of command and telemetry data. Therefore, TDRSS interfaces will already exist, and NASA spacecraft will be equipped with TDRSS transponders. However, the major constraint in the use of TDRSS is that only a limited number of users may use the forward link at a given time, which limits the frequency of tracking contacts.

1.1 SUMMARY

The performance of the EKF was evaluated for estimating the orbital parameters of the Landsat-D and Gamma Ray Observatory (GRO) missions using either two-way or one-way TDRSS tracking data. The evaluation was performed using the capabilities of the Research and Development Goddard Trajectory Determination System (R&D GTDS) available at the time of the study (References 1 and 2).

A nominal tracking schedule of one 10-minute tracking contact per revolution was used. The effect on the EKF's performance of the following factors was investigated: (1) the processing of range and Doppler data or Doppler data only, (2) the reduction of the tracking schedule to once every two or three revolutions, (3) the presence of large errors in the TDRSS positions used in the computation of the observations, (4) the accuracy of the onboard frequency standard used in extraction of one-way Doppler data, and (5) the presence of passes of data with anomalously high measurement errors.

Section 2 of this document discusses the TDRSS measurement models used in the evaluation. Section 3 discusses the evaluation procedure (i.e., comparing truth models to EKF estimated solutions) and describes the baseline data simulation and estimation parameters. Section 4 analyzes the orbital parameter accuracies achievable for the Landsat-D satellite using TDRSS data and the EKF. Section 5 discusses a parallel analysis performed for GRO. Section 6 summarizes the conclusions reached as to the feasibility of using the EKF and TDRSS data for onboard orbit determination.

1.2 CONCLUSIONS AND RECOMMENDATIONS

Based on the simulations described in this document, the following general conclusions can be drawn:

- Using an EKF with a tracking schedule of one contact per revolution yields Landsat-D equilibrium solutions accurate to 50 meters in root-mean-square (rms) and 80 meters in maximum deviation for both two-way data cases. The corresponding performance for GRO is 60 to 90 meters in rms and 90 to 150 meters in maximum deviation.

- The accuracy of the equilibrium solution is more significantly affected by reductions in data when

additional solve-for parameters are added, e.g., atmospheric drag parameter for GRO and frequency bias parameters for one-way data.

- In general, TDRS ephemeris errors with amplitudes as large as 280 meters in the radial and cross-track directions and 320 meters in the along-track direction produced little increase in the error in the equilibrium solution. An along-track rate of 1 kilometer per day resulted in a biased estimate in the case of one-way data for Landsat-D and all data cases for GRO. This effect may result from the correlation of the along-track rate with clock parameters and the atmospheric drag parameter.

- When anomalous data passes were introduced, no significant increase in error was obtained when the data were edited. However, when the data were processed, significant increases occurred at the time of processing; these diminished as more data were processed.

- Processing of one-way data simulated with the NASA standard transponder model produced a tenfold increase in the error in the solution. This increase was essentially eliminated by estimating both terms in the clock model.

- The presence of sinusoidal variations in the clock bias as large as 2×10^{-6} seconds produced a tenfold increase in the Landsat-D errors but did not significantly increase the GRO errors. This is probably due to the absorption of the effects of this timing error in the estimate obtained for the atmospheric drag coefficient in the GRO case.

Based on the results presented in this report, the following recommendations are made:

- The use of two-way range and Doppler data or two-way Doppler data is recommended to achieve accuracies

on the order of 100 meters in rms No conclusive result was obtained as to whether inclusion of range data is beneficial.

- If one-way Doppler data are used, the accuracy of the resulting solution is highly dependent on the accuracy of the model used for the reference frequency standard. Choice of an appropriate model will require extensive calibration of candidate models against realistic oscillator performance data.

- In general, performance was not significantly degraded when data passes were deleted. Therefore, data editing algorithms should be further investigated for use in the presence of anomalous data

SECTION 2 - MEASUREMENT MODELS FOR TDRSS DATA

TDRSS is a system of three tracking and data relay satellites to be maintained in circular, near-equatorial, geosynchronous orbits. Two operational satellites, TDRS East (TDRS-E) and TDRS West (TDRS-W), will be spaced approximately 130 degrees apart at 41 degrees and 171 degrees west longitude, respectively. The third, TDRS Spare, to be situated between the other two, will be used primarily in the event of a failure in one of the operational satellites. TDRSS is discussed in detail in Reference 3.

In the current study, both one- and two-way TDRSS tracking data were investigated for use in onboard orbit determination. One-way TDRSS data are Doppler measurements that are extracted on board the user satellite from tracking signals originating on the ground, relayed through a TDRS, and received by the user spacecraft. TDRSS ephemeris data are uplinked to the user spacecraft via the TDRSS command stream. The accuracy of the one-way measurements is degraded by any timing errors in the onboard user clock that is used to extract the tracking signals.

Two-way TDRSS data are extracted on the ground from a round-trip propagation of the tracking signals; the resulting range and/or Doppler measurements are relayed back to the user spacecraft. For onboard orbit determination applications, the two-way data would be transmitted to the user spacecraft via the TDRS command stream. In addition, the TDRS ephemeris data would also be uplinked. Figures 2-1 and 2-2 illustrate the geometry of the one-way and two-way measurements, respectively.

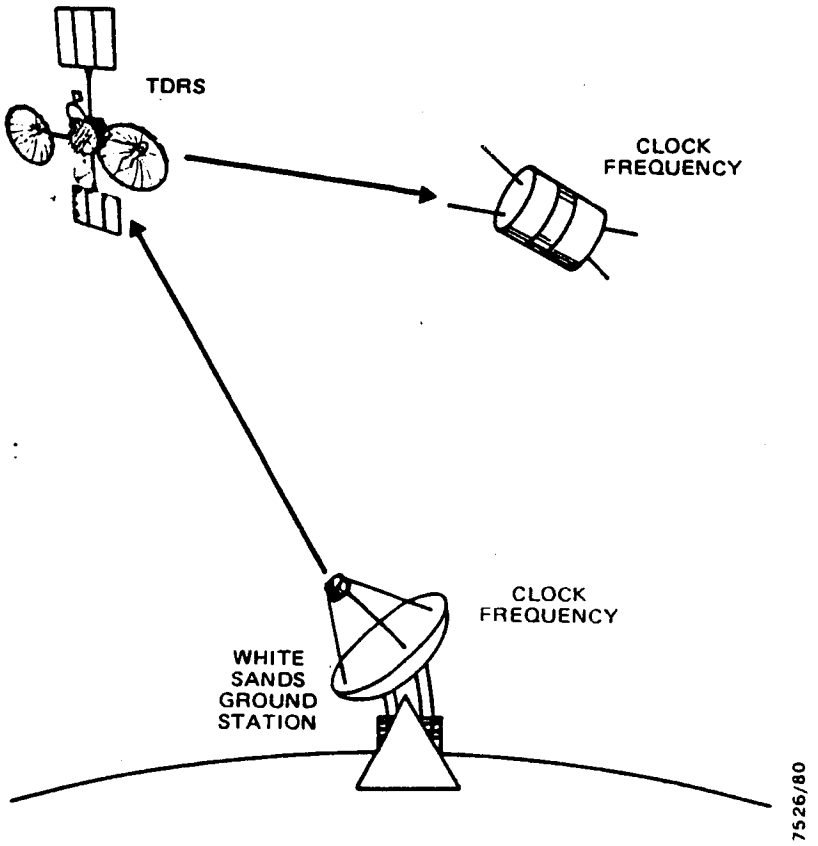

Figure 2-1. One-Way Tracking Signal Geometry

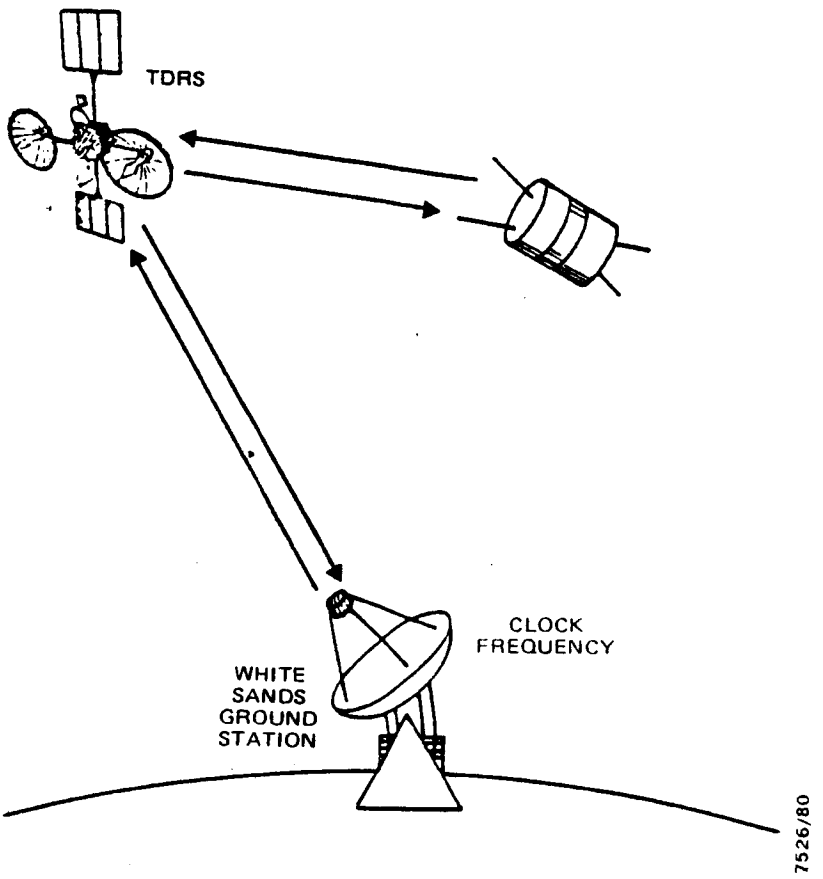

Figure 2-2. Two-Way Tracking Signal Geometry

2.1 RANGE AND DELTA-RANGE MEASUREMENTS

The one- and two-way TDRSS tracking measurements were simulated and processed using the pseudo-TDRSS data capabilities in the Data Simulation (DATASIM) program and FILTER program of R&D GTDS. (A discussion of the derivation of these measurements can be found in Reference 2.) To be able to use these existing R&D GTDS data simulation and EKF capabilities, the Doppler measurements were simulated and processed using a delta-range measurement model. The TDRSS range and delta-range models that were used are summarized in the following subsections.

2.1.1 TDRSS PSEUDO-RANGE MEASUREMENT

The TDRSS pseudo-range measurement, R, is the difference between the measured signal receive time, $t_R + \Delta t_R$, and the measured signal transmit time, $t_T + \Delta t_T$, multiplied by the speed of light plus measurement biases and random noise:

$$R(t_R + \Delta t_R) = c[(t_R + \Delta t_R) - (t_T + \Delta t_T)] + R_b + \sigma_R \qquad (2\text{-}1)$$

where t_R = true signal receive time
Δt_R = timing bias error in the receive time
t_T = true signal transmit time
Δt_T = timing bias error in the transmit time
c = speed of light
R_b = range bias
σ_R = random measurement error

The difference between the true receive and transmit times is given by

$$t_R - t_T = \frac{\rho(t_R)}{c} + \Delta RC + \Delta\tau \qquad (2\text{-}2)$$

where $\rho(t_R)$ = total distance along the signal propagation path at time t_R

ΔRC = refraction correction effects

$\Delta\tau$ = total transponder delay

In the pseudo-TDRSS implementation, refraction correction and transponder delays are absorbed into the range bias term such that Equation (2-1) reduces to

$$R(t_R + \Delta t_R) = \rho(t_R) + c(\Delta t_R - \Delta t_T) + R_b + \sigma_R \qquad (2\text{-}3)$$

In the case of two-way data, the receive and transmit times are measured by the same clock such that

$$\Delta t_R - \Delta t_T \simeq 0$$

In the pseudo-TDRSS implementation, only the range from the TDRSS to the user is computed, such that

$$\rho(t_R) = |\vec{r}_{TDRS}(t_T) - \vec{r}_{USER}(t_R)| \qquad (2\text{-}4)$$

where $\vec{r}_{TDRS}$ = TDRS position vector

$\vec{r}_{USER}$ = user spacecraft position vector

The TDRS position vector at each measurement time is input to the EKF in addition to the measurements and the measurement time tags.

2.1.2 TDRSS PSEUDO DELTA-RANGE MEASUREMENT

The TDRSS pseudo delta-range measurement, ΔR, is modeled as the difference of two ranges measured at closely spaced times, ΔT:

$$\Delta R(t_R + \Delta t_R) = R(t_R + \Delta t_R) - R(t_R + \Delta t_R - \Delta T) + \Delta R_b + \sigma_{\Delta R} \qquad (2\text{-}5)$$

where R is computed according to Equation (2-3) (without the addition of σ_R and R_b).

The delta-range measurement is physically independent of the range measurement, since it is measured directly by the receiver and is not measured as the difference of two ranges. Therefore, the bias, ΔR_b, and noise, $\sigma_{\Delta R}$, which are associated with the delta-range measurement, are independent of the range bias, R_b, and the noise, σ_R.

For one-way data, the receive time is measured by an onboard clock that may not be as accurate as the ground terminal clocks. To model the effect of this clock error, a quadratic clock error model is used:

$$\Delta t_R = b + \dot{b}(t_R - t_0) + \frac{\ddot{b}}{2}(t_R - t_0)^2 \qquad (2\text{-}6)$$

where b = constant clock bias determined at the epoch of the polynomial

$\dot{b}$ = clock drift arising from a bias in the reference frequency

$\ddot{b}$ = clock drift rate arising from a drift in the reference frequency

t_0 = epoch time of the model

Substituting Equations (2-3) and (2-6) into Equation (2-5) yields

$$\begin{aligned}\Delta R(t_R + \Delta t_R) &= \rho(t_R) - \rho(t_R - \Delta T) \\ &\quad + c\left[\dot{b}\Delta T + \ddot{b}\Delta T\left(t_R - t_0 - \frac{\Delta T}{2}\right)\right] \qquad (2\text{-}7) \\ &\quad + \Delta R_b + \sigma_{\Delta R}\end{aligned}$$

where ρ is given by Equation (2-4).

For the two-way data, the terms $\dot{b}$ and $\ddot{b}$ are zero.

A sinusoidal plus quadratic clock error model is also available. In this case

$$\Delta t_R = b + a_1 \sin \omega(t_R - t_0) + a_2 \cos \omega(t_R - t_0) + \dot{b}(t_R - t_0) + \frac{\ddot{b}}{2}\left(t_R - t_0\right)^2 \tag{2-8}$$

where a_1, a_2 = amplitudes measured in seconds
ω = input frequency nominally equal to 2π divided by the period of the spacecraft

The sinusoidal terms produce an additional bias in the delta-range measurement equal to

$$c\omega\Delta T\left[a_1 \cos \omega(t_R - t_0) - a_2 \sin \omega(t_R - t_0)\right] \tag{2-9}$$

2.2 TDRSS TRACKING SCHEDULES

In all cases, it was assumed that the user satellite was in contact with a single TDRS for 10 minutes for each tracking contact. The time between range and delta-range measurements and the delta-range computation interval were set at 10 seconds, which yields 30 delta-range measurements for every complete tracking contact. (For both measurement types combined, there are 30 range and 30 delta-range measurements.)

In the computation of the potential tracking contact times, the single-access TDRS antenna configuration (with a half-cone angle of 22.5 degrees) was used. The user-satellite antenna model was a cone aligned with the satellite's radius vector with a half-cone angle of 100 degrees. TDRS-to-user-satellite signals that passed within 650 kilometers of the Earth's surface were edited.

The time span of line-of-sight contact between Landsat-D or GRO and any single TDRS ranges from 40 to 60 minutes. A 10-minute contact can occur at any time within that visibility interval. During the early phases of the feasibility study, several models were run to investigate the dependence of the prediction accuracy on the time from the first or last possible contact with a TDRS. It was determined that tracking measurements made consistently at the beginning or end of a visibility interval (edge-justified data) yield better estimation accuracy than those centered in the visibility arc (center-justified data). This is due to the better geometry available for delta-range observations when the user satellite is moving directly along the line of sight to the TDRS. However, this investigation did not include the effect of refraction correction errors. Since neither data set represents a realistic case, a more random distribution of tracking contacts was selected for use in the remainder of the study. These contact times are defined in Sections 4 and 5 for Landsat-D and GRO, respectively.

SECTION 3 - EVALUATION PROCEDURE

Several programs available in R&D GTDS were used in the evaluation of the orbit determination accuracy. Figure 3-1 illustrates the evaluation procedure by which the ephemeris of a "truth" model for the user satellite was compared with the ephemeris produced by the EKF estimator. Deviations between the two ephemerides provide a measurement of the accuracy obtained by the EKF for a particular test case. The simulated data used by the EKF is supplied by the DATASIM program, which has the capability to corrupt the range and delta-range measurements with measurement errors and random measurement noise. A sample R&D GTDS deck setup is given in Appendix D.

The analysis procedure used in comparing the ephemerides involved examining (1) the solve-for parameter report, (2) the rms and the maximum deviations of the position and velocity errors, and (3) the radial, along-track, and cross-track ephemeris comparison plots of the position and velocity errors for the full estimation time span. These statistics were recorded for all runs along with pass frequency, number of TDRSs observed, and measurement and modeling errors applied.

3.1 TEST CASES

The Landsat-D and GRO spacecraft were selected as the sample test cases for onboard orbit estimation. Landsat-D has a near-polar inclination and a medium altitude. GRO has a lower altitude and a less-inclined orbit.

For each satellite, baseline runs were generated representing each of the three data types (one-way delta-range data, two-way delta-range data, and two-way range and delta-range data). Table 3-1 lists the orbital elements

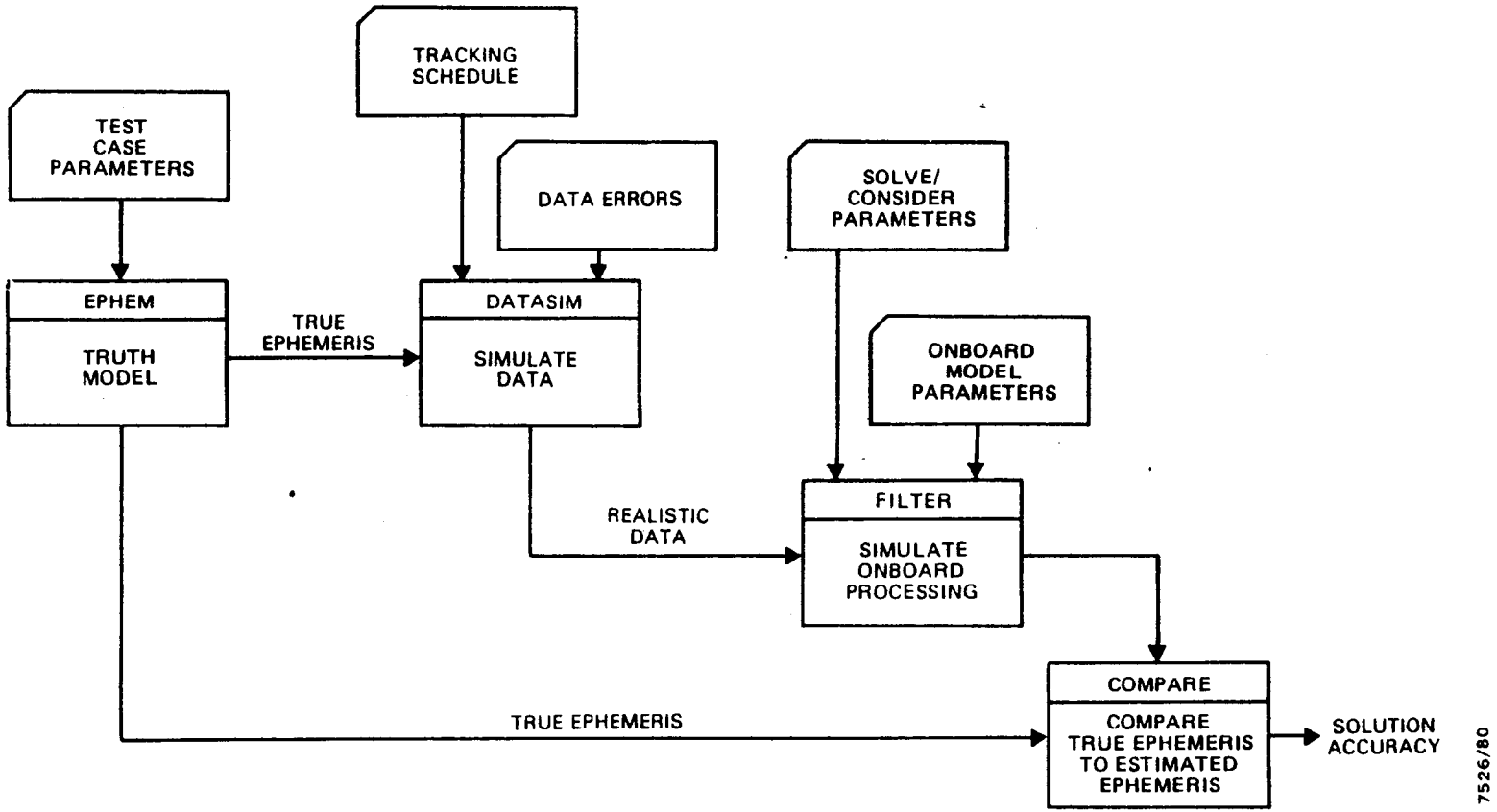

Figure 3-1. Evaluation Procedure for TDRSS Study

Table 3-1. Landsat-D, GRO, TDRS-E, and TDRS-W Orbital Elements, Area, and Mass

PARAMETER	LANDSAT-D	GRO	TDRS-E	TDRS-W
EPOCH	OCTOBER 1, 1980	OCTOBER 1, 1980	OCTOBER 1, 1980	OCTOBER 1, 1980
COORDINATE SYSTEM	TRUE OF DATE	TRUE OF DATE	TRUE OF DATE	TRUE OF DATE
SEMIMAJOR AXIS (km)	7086.901	6778.140	42,166.75	42,166.75
ECCENTRICITY	0.001	0.0017	0.0004	0.0004
INCLINATION (deg)	98.181	28.0	5.0	5.0
PERIOD (min)	98.956	92.56	1436.2	1436.2
AREA (m^2)	20.0	20.0	–	–
MASS (kg)	1700.0	1700.0	–	–

7526/80

and spacecraft parameters of Landsat-D and GRO and the orbital elements of TDRS-E and TDRS-W.

3.2 MEASUREMENT ERROR MODELS

The TDRSS observation data set is generated in the DATASIM program. The observation data set consists of the TDRSS range and/or delta-range measurements, the measurement time tags, and the coordinates of the TDRS at the measurement time. The format of this data set is given in Appendix C of Reference 4. The measurement biases and random measurement errors are applied to the measurement. The TDRS ephemeris errors are applied to the TDRS coordinates. The user-clock errors affect the measurements and the time tags. Tables 3-2, 3-3, and 3-4 list the nominal values for these error sources. Measurement errors arising from refraction correction errors were not included.

3.2.1 MEASUREMENT BIASES

The range measurement bias used in all runs has a standard deviation of 7 meters. In the cases run, the TDRS-E range measurement bias is -18 meters, and the TDRS-W range measurement bias is -2 meters. In the nominal two-way cases, a delta-range measurement bias was not added. In the one-way case, the error in the clock drift (or reference frequency) gives rise to the delta-range bias given in Equation (3-1).

3.2.2 RANDOM MEASUREMENT ERRORS

The two-way data were simulated using a standard deviation of 1 meter for range measurements and 1 centimeter for delta-range measurements. The one-way delta-range data were simulated with a standard deviation of 10 centimeters to simulate the expected performance of an onboard receiver.

Table 3-2. Data Simulation Measurement Errors

PARAMETER	BASELINE STANDARD DEVIATION	
	ONE-WAY DATA	TWO-WAY DATA
RANDOM RANGE ERROR (m)	–	1
RANDOM DELTA-RANGE ERROR (cm)	10	1
RANGE MEASUREMENT BIAS (m)	–	7
DELTA-RANGE MEASUREMENT BIAS (m)	EQUATION (3–1)	–

7526/80

Table 3-3. Data Simulation TDRS Ephemeris Error Model

PARAMETER	VALUE
PERIOD OF SINUSOID[1] (hr)	24
RADIAL AMPLITUDE (H) (m)	35
CROSS-TRACK AMPLITUDE (C) (m)	35
ALONG-TRACK AMPLITUDE (L) (m)	80
ALONG-TRACK GROWTH RATE ($\dot{L}$) (m/day)	250

7526/80

[1]SINUSOIDAL PERIOD FOR RADIAL, CROSS-TRACK, AND ALONG-TRACK TDRS EPHEMERIS ERRORS.

Table 3-4. Data Simulation Quadratic User-Clock Error Model

COEFFICIENT	ONE-WAY DATA		TWO-WAY DATA
	NASA STANDARD TRANSPONDER	ACCURATE ONBOARD CLOCK	PERFECT CLOCK
USER-CLOCK BIAS (b) (sec)	0	0	0
USER-CLOCK DRIFT ($\dot{b}$) (sec/sec)	1×10^{-6}	2×10^{-7}	0
USER-CLOCK DRIFT RATE ($\ddot{b}$) (sec/sec/day)	2×10^{-7}	2×10^{-9}	0
USER-CLOCK SINUSOIDAL BIAS AMPLITUDES (sec)	0	0	0

7526/80

3.2.3 TDRS EPHEMERIS ERROR

The TDRS ephemeris errors are added to the TDRS coordinates that are generated for each measurement. These coordinates are used in the FILTER program to compute the range and delta-range measurements. Therefore, the TDRS ephemeris errors affect the computed measurements, not the simulated measurements.

The TDRS ephemeris errors were modeled as a sinusoidal term for the radial (H), cross-track (C), and along-track (L) errors with an additional linear along-track rate included. The sinusoidal errors H, C, and L are all in phase, starting with a value of zero at epoch for TDRS-E. The TDRS-W errors are 180 degrees out of phase with the TDRS-E errors. The period is equal to the period of the TDRS satellite, i.e., 24 hours. The baseline amplitude for H and C is 35 meters; for L, 80 meters. The along-track rate is 250 meters per day. Figure 3-2 illustrates the time variation of the TDRS-E ephemeris errors for the baseline case.

Changes in the ephemeris errors were made to determine their influence on prediction accuracy. In some cases the errors were increased by nearly an order of magnitude over their initial baseline values.

3.2.4 USER-CLOCK ERRORS

One-way delta-range data were simulated with user-clock errors to account for errors introduced by the onboard clock, which is used as a frequency standard in the measurement extraction process. Two levels of onboard user-clock errors were generated using the quadratic clock model given in Equation (2-6). The values of the coefficients for user-clock bias (b), drift ($\dot{b}$), and drift rate ($\ddot{b}$) were based on (1) the NASA standard transponder and (2) an "accurate" onboard clock. For the case of one-way

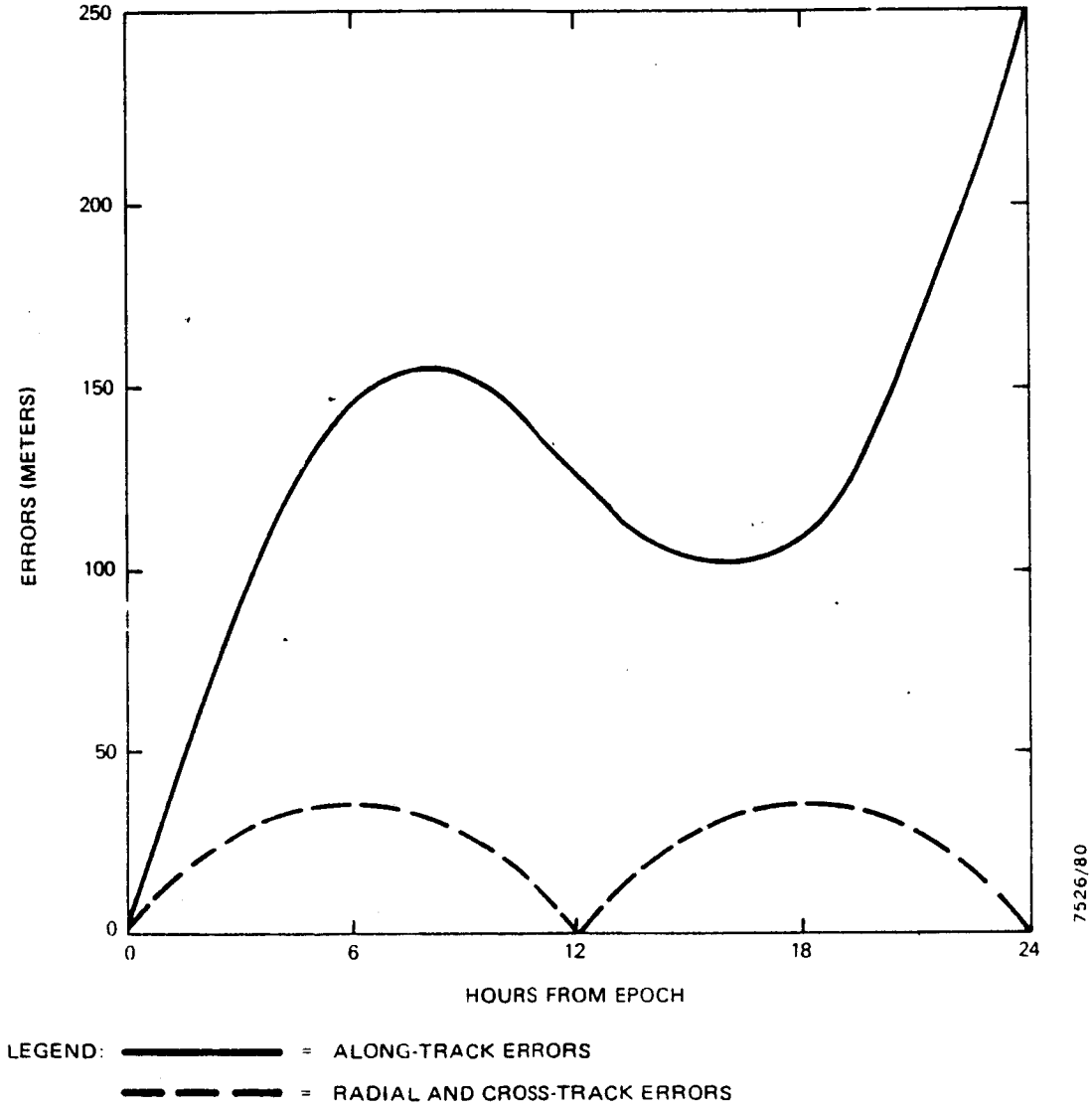

Figure 3-2. TDRS-E Ephemeris Errors

data, the user-clock drift ($\dot{b}$) was an additional solve-for parameter in the FILTER program.

The user-clock errors are added to the measurement time tag. In addition (and more importantly), the accumulated relative frequency error produces a bias on the delta-range measurement. This bias is equal to

$$c\Delta T\left[\dot{b} + \ddot{b}(t - t_0) + a_1\omega \cos \omega(t - t_0) - a_2\omega \sin \omega(t - t_0)\right] \tag{3-1}$$

The nominal values given in Table 3-4 produce a delta-range bias of $[3 + 0.6(t - t_0)]$ kilometers for the NASA transponder and $[0.6 + 0.006(t - t_0)]$ kilometers for the accurate clock, where $t - t_0$ is the elapsed time from epoch measured in days.

3.3 DYNAMIC MODELING ERRORS

Dynamic modeling errors are simulated by mismatching the spacecraft acceleration and clock models that are used in the data simulation and the EKF processing. Physically, these errors arise from the lack of precise models for the accelerations acting on the spacecraft and the behavior of onboard clocks. The dynamic modeling errors affect the accuracy of the propagation of the orbital state vectors. Appendix C discusses the Landsat-D and GRO prediction errors that result from the mismatched models that are listed in Table 3-5.

3.3.1 GEOPOTENTIAL MODEL

A 15-by-15 Goddard Earth Model-9 (GEM-9) geopotential was used in the R&D GTDS DATASIM program, and an 8-by-8 GEM-1 geopotential was used in the R&D GTDS FILTER program. The purpose of this mismatch is to simulate errors in the

Table 3-5. Dynamic Models

PARAMETER	DATA SIMULATION VALUE	EKF VALUE
GEOPOTENTIAL	15 x 15, GEM-9[a]	8 x 8, GEM-1
SOLAR FLUX	150×10^{-22} watt/m^2/Hz	200×10^{-22} watt/m^2/Hz
AERODYNAMIC DRAG COEFFICIENT	2.0	2.2
SUN AND MOON	YES	YES
SOLAR RADIATION PRESSURE	NO	NO
INTEGRATOR	COWELL 12TH-ORDER	RUNGE-KUTTA 3(4+1)
RESONANCE (GRO ONLY)	YES	NO

7526/80

knowledge of the Earth's geopotential field when using the FILTER program. Higher order resonant terms were included for GRO only.

3.3.2 DRAG PARAMETERS

The aerodynamic drag coefficient, C_D, was taken to be a constant of 2.0 for data simulation and 2.2 in the FILTER program. Additional drag modeling errors were simulated by using a solar flux value of 150×10^{-22} watts per square meter per hertz in the data simulation and 200×10^{-22} watts per square meter per hertz in the FILTER program.

3.3.3 SOLAR RADIATION PARAMETERS

Solar radiation pressure was not included in either the data simulation or estimation models because of its small effect at the altitudes of the spacecraft under study.

3.4 BASELINE EKF PROCESSING PARAMETERS

Table 3-6 lists the parameters that were estimated and the process noise terms that were included in the EKF processing. Table 3-7 lists the a priori values or offsets and a priori covariances associated with the estimated parameters and the measurement standard deviations that were used in the baseline runs.

In the case of one-way data, the clock drift term, $\dot{b}$, is estimated in addition to the orbital state vector. For GRO, the atmospheric drag parameter, ρ_1, is also estimated.

The state, clock, and drag covariance process noise rates were modeled using the linear model

$$Q(t_k) = \dot{Q} \cdot (t_k - t_{k-1})$$

Table 3-6. Options Used in EKF

OPTION	ONE-WAY DATA	TWO-WAY DATA
ESTIMATED PARAMETERS		
LANDSAT-D	$x, y, z, \dot{x}, \dot{y}, \dot{z}, \dot{b}$	$x, y, z, \dot{x}, \dot{y}, \dot{z}$
GRO	$x, y, z, \dot{x}, \dot{y}, \dot{z}, \dot{b}, \rho_1$	$x, y, z, \dot{x}, \dot{y}, \dot{z}, \rho_1$
PROCESS NOISE TERMS		
LANDSAT-D	$\dot{x}, \dot{y}, \dot{z}, \dot{b}$	$\dot{x}, \dot{y}, \dot{z}$
GRO	$\dot{x}, \dot{y}, \dot{z}, \dot{b}, \rho_1$	$\dot{x}, \dot{y}, \dot{z}, \rho_1$

7526/80

Table 3-7. A Priori Values and Measurement Standard Deviations in EKF

PARAMETER	BASELINE INPUT VALUE	
	ONE-WAY DATA	TWO-WAY DATA
A PRIORI STATE OFFSETS		
x, y, z	100 m	100 m
$\dot{x}, \dot{y}, \dot{z}$	30 cm/sec	30 cm/sec
A PRIORI USER CLOCK PARAMETERS		
b (BIAS)	0 sec	–
$\dot{b}$ (DRIFT)		
NASA STANDARD TRANSPONDER	1.1×10^{-6} sec/sec	–
ACCURATE ONBOARD CLOCK	2.2×10^{-7} sec/sec	–
$\ddot{b}$ (DRIFT RATE)	0 sec/sec/day	–
A PRIORI ρ_1	0.0	0.0
A PRIORI COVARIANCES		
x, y, z	0.1 km^2	0.1 km^2
$\dot{x}, \dot{y}, \dot{z}$	1.0 m^2/sec^2	1.0 m^2/sec^2
$\dot{b}$	1×10^{-6} sec/sec	–
ρ_1 (GRO ONLY)	1.0	1.0
STANDARD DEVIATION OF MEASUREMENT ERROR		
RANGE	–	40 m
DELTA-RANGE	10 cm	1 cm

7526/80

where $Q(t_k)$ = process noise

$\dot{Q}$ = diagonal matrix of constants that are the assumed noise variance rates of change for the solve-for parameter set

t_k = measurement time

t_{k-1} = measurement time of previous observation

The state covariance is augmented by $Q(t_k)$ at each measurement time, t_k. In the current study, nonzero process noise rates of change were used for the velocity, clock drift, and drag (GRO only) terms.

SECTION 4 - EVALUATION RESULTS FOR LANDSAT-D

This section presents the results of evaluating the EKF for determination of the Landsat-D orbit from TDRSS tracking data. Table 3-1 (Section 3) specifies the nominal Landsat-D orbital elements. Figures 4-1 through 4-3 illustrate the periods of potential contact of Landsat-D with TDRS-E and TDRS-W and the 10-minute time spans that were selected for the nominal one-, two-, and three-revolution contact frequencies, respectively.

Sections 4.1 through 4.3 discuss the performance of the EKF using two-way range and delta-range data, two-way delta-range data, and one-way delta-range data, respectively. Section 4.4 discusses the performance of the EKF in the presence of anomalous data passes. Radial, cross-track, and along-track plots of the position errors for several representative runs are given in Appendix A. The complete set of difference plots is contained in Reference 5.

4.1 TWO-WAY RANGE AND DELTA-RANGE DATA

This section presents the results of evaluating the EKF performance using two-way range and delta-range data. Table 4-1 is representative of the format used throughout this document to present the performance statistics. The table contains the following information:

- Run identification number
- Contact frequency
- Process noise covariance rate input for all three velocity components
- TDRS ephemeris errors--The baseline values are specified in Table 3-3. A notation such as 8H signifies eight times the baseline radial error.

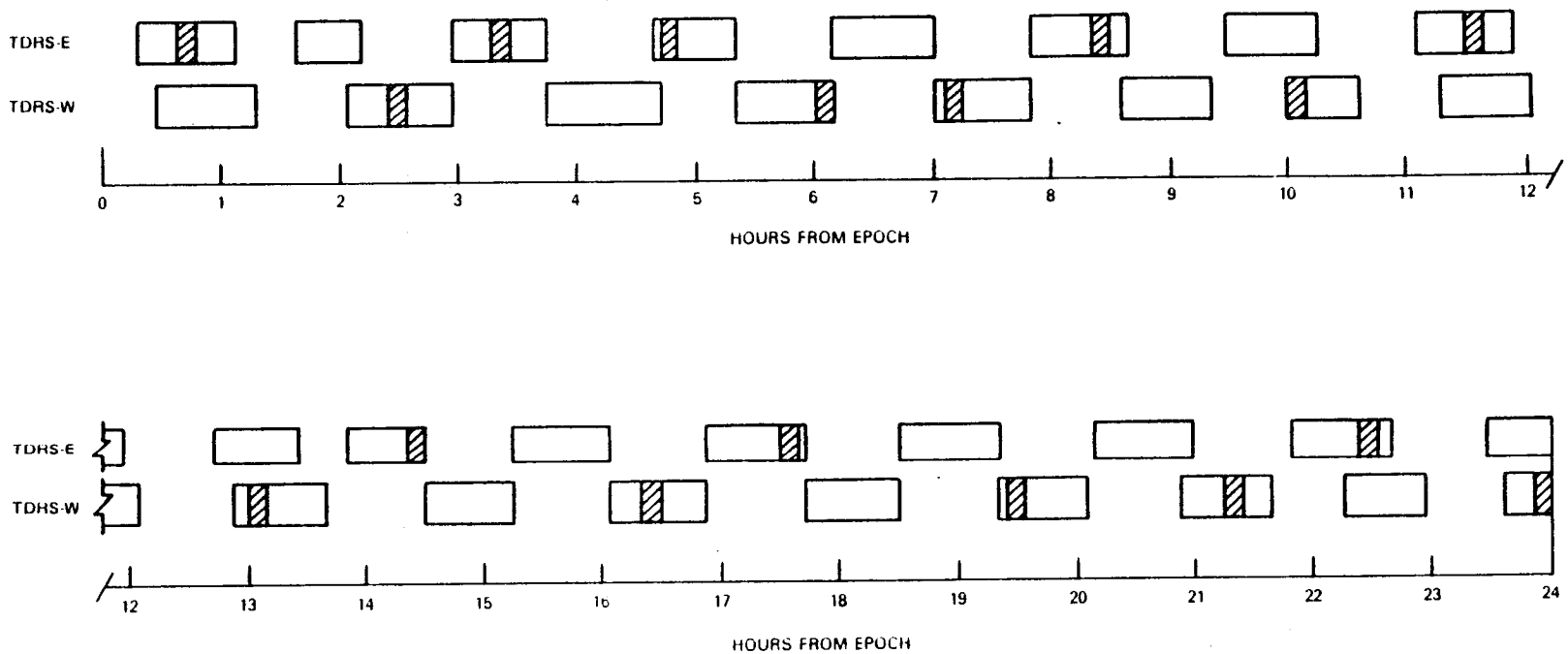

NOTES: 1. EPOCH OCTOBER 1, 1980.

2. SHADED AREAS CORRESPOND TO ONE CONTACT PER REVOLUTION DATA SET

Figure 4-1. TDRSS Tracking Contacts for Landsat-D for One-Revolution Contact Frequency

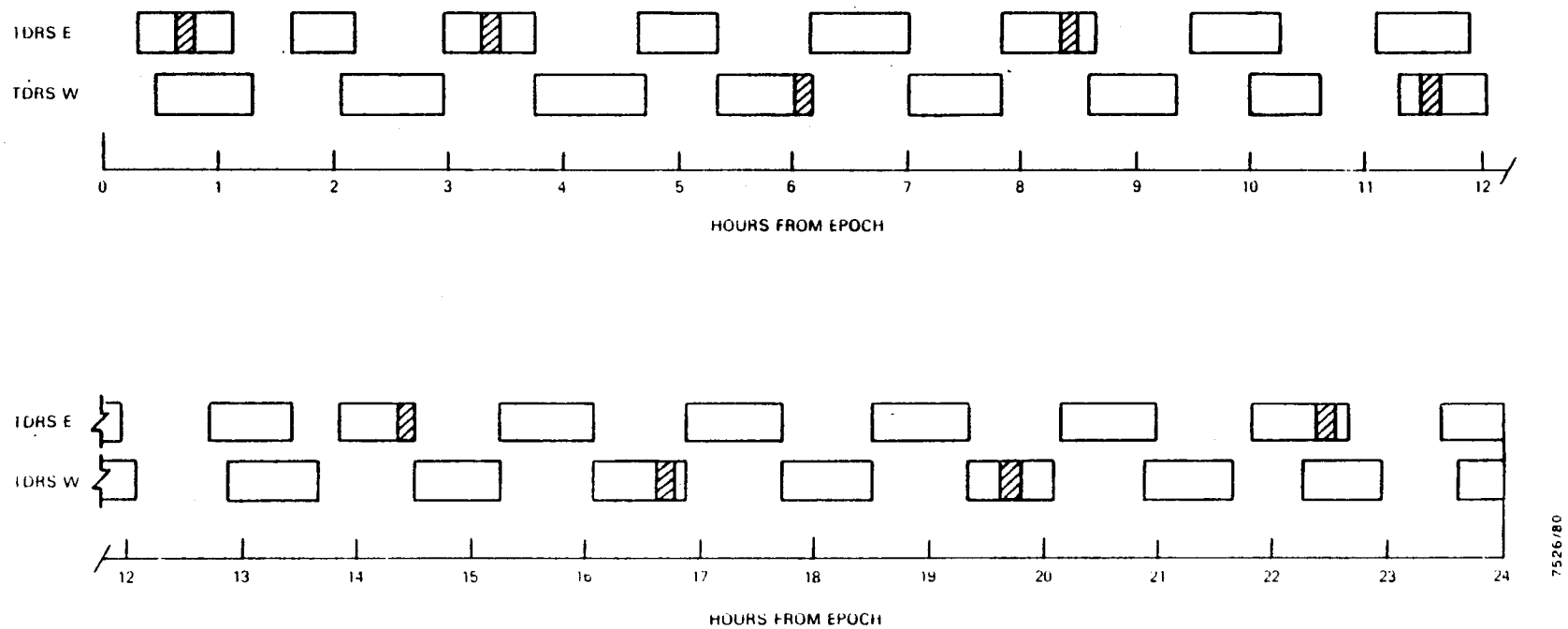

NOTES 1. EPOCH OCTOBER 1, 1980

2. SHADED AREAS CORRESPOND TO ONE CONTACT PER TWO REVOLUTIONS DATA SET.

Figure 4-2. TDRSS Tracking Contacts for Landsat-D for Two-Revolution Contact Frequency

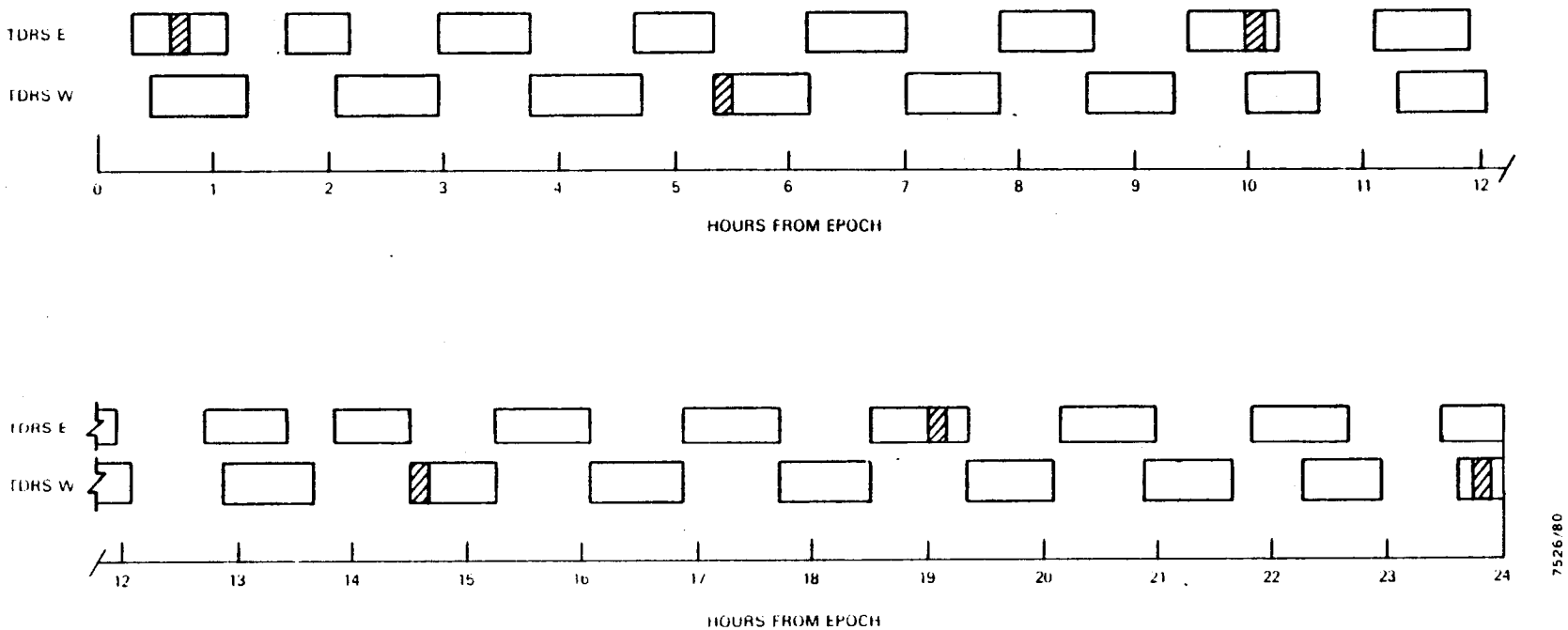

NOTES 1. EPOCH OCTOBER 1, 1980

2. SHADED AREAS CORRESPOND TO ONE CONTACT PER THREE REVOLUTIONS DATA SET.

Figure 4-3. TDRSS Tracking Contacts for Landsat-D for Three-Revolution Contact Frequency

Table 4-1. Landsat-D Estimation Using Two-Way Range and Delta-Range Data (Runs A1 Through D6)

RUN	CONTACT FREQUENCY (2 TDRSs)	STATE PROCESS NOISE (km^2/sec^3)	TDRS EPHEMERIS ERRORS	σ_R FILTER ERRORS[1] (m)	rms POSITION DIFFERENCE (m)				MAXIMUM POSITION DIFFERENCE (m)				FIGURE NUMBER (A-)
					0^h-12^h	0^h-24^h	9^h-12^h	21^h-24^h	0^h-12^h	0^h-24^h	9^h-12^h	21^h-24^h	
A1	ALL[2]	10^{-14}	BASELINE	40	164		23		945		72		1, 2, 3
B1	1 REV	10^{-12}	BASELINE	40	486	366	257	99	2549	2549	666	156	
B2		10^{-14}			461	338	46	120	2549	2549	80	219	4, 5, 6
B3		10^{-16}			769	547	139	92	2549	2549	235	135	
B4		10^{-18}			774	549	78	48	2549	2549	105	115	
B5		10^{-20}			774	550	78	41	2549	2549	130	65	7, 8, 9
B6		10^{-22}			774	550	91	60	2549	2549	145	115	
C1	2 REVs	10^{-14}	BASELINE	40	649		198		2549		337		
C2		10^{-16}			1238	877	62	148	4256	4256	100	244	
C3		10^{-18}			1251	886	51	91	4304	4304	78	117	
C4		10^{-20}			1251	886	67	68	4304	4304	99	111	
C5		10^{-22}				886	69	39	4304	4304	99	55	10, 11, 12
C6		10^{-24}				842	70	39	4106	4106	102	58	
D1	3 REVs	10^{-14}	BASELINE	40		898	546	747		2931	1081	1133	
D2		10^{-16}				1790	83	73		6517	162	119	13, 14, 15
D3		10^{-18}				1811	100	106		6560	182	164	
D4		10^{-20}				1811	101	102		6591	182	154	
D5		10^{-22}				1811	101	99		6591	182	152	
D6		10^{-24}				1811	101	99		6591	182	152	

7526/80

[1] σ_R - ESTIMATED MEASUREMENT ERROR.

[2] INCLUDES ALL POSSIBLE CONTACT TIMES WITH EITHER TDRS-E OR TDRS-W.

- Range standard deviation used in the EKF--All other input values are as described in Section 3.
- Root-mean-square and maximum position vector differences obtained by comparison with the "true" ephemeris over the time intervals listed
- Reference figure numbers--The numbers of the appropriate error plots in Appendix A are specified.

4.1.1 BASELINE RUNS

Runs B1 through B6 in Table 4-1 summarize the effect of varying the state process noise for the baseline run of one tracking contact every revolution for two-way range and delta-range observations. The optimum value for the process noise is approximately 10^{-20} kilometers squared per second cubed (km^2/sec^3) (run B5) with a resulting rms positional error of 41 meters during the last 3 hours. Comparison of Figures A-4 through A-6 with Figures A-7 through A-9 shows that the value of 10^{-14} km^2/sec^3 permits rapid convergence to the solution, as indicated by the low error in the 9-hours-to-12-hours range. However, the value of 10^{-20} km^2/sec^3 produces more stable behavior, which results in the most accurate solution after 24 hours of processing. Inspection of Figures A-7 through A-9 indicates that initial transients essentially disappear after processing about 3 hours or two contacts of data.

4.1.2 VARIATION OF CONTACT FREQUENCY

The remainder of Table 4-1 indicates the effect of varying contact frequency on the optimum state process noise value and the position accuracy. The optimum value for the state process noise appears to be in the range of 10^{-16} km^2/sec^3 to 10^{-22} km^2/sec^3. If one value for state

process noise were to be selected, 10^{-20} km^2/sec^3 would be the most appropriate for all three contact frequency cases.

Comparing runs B5, C5, and D2 and their representative plots (Figures A-7 through A-15), the initial transients in position determination increase in amplitude with longer data gaps. However, most large-scale transients have disappeared after the second 10-minute contact in all data frequency cases. The steady-state solutions for all three contact frequencies are of essentially equivalent accuracy.

4.1.3 VARIATION OF TDRS EPHEMERIS ERRORS

The TDRS ephemeris errors primarily degrade the range measurements. The standard deviations of the range and delta-range measurement errors arising from the ephemeris errors are derived in Appendix D. The measurement standard deviations were adjusted in each EKF run accordingly, resulting in a considerable downweighting of the range measurements.

Table 4-2 shows that changes in the baseline values of the TDRS ephemeris errors had varying influence on the results. Changes in radial (H) and cross-track (C) errors by factors of up to eight times the baseline values yielded virtually no change in the position accuracy. Quadrupling the along-track sinusoidal amplitude (L) or linear rate coefficient ($\dot{L}$) produced a small increase in the errors after 12 hours of processing. The cross-track plots for the 8H, 8C, and 4$\dot{L}$ cases show initial position differences that are larger than the standard model by 30 meters, decreasing to the error levels of the baseline run after 6 hours of processing (see Figures A-17 and A-20).

Table 4-2. Landsat-D Estimation Using Two-Way Range and Delta-Range Data (Runs E1 Through F3)

RUN	CONTACT FREQUENCY (2 TDRSs)	STATE PROCESS NOISE (km^2/sec^3)	TDRS EPHEMERIS ERRORS	σ_R FILTER ERRORS (m)	rms POSITION DIFFERENCE (m)		MAXIMUM POSITION DIFFERENCE (m)		FIGURE NUMBER (A-)
					0^h-12^h	9^h-12^h	0^h-12^h	9^h-12^h	
B2	1 REV	10^{-14}	BASELINE	40	461	46	2549	80	4, 5, 6
E2			2H, 2C	50	461	52	2549	107	
E3			4H, 4C	100	467	43	2549	72	
E4			8H, 8C	200	485	41	2549	85	16, 17, 18
E5			4L	65	461	60	2549	95	19, 20, 21
E6			2L	40	462	52	2549	81	
E7			4L	40	465	71	2549	105	22, 23, 24
F1	1 REV, TDRS E ONLY	10^{-14}	BASELINE	40	238	95	945	199	25, 26, 27
F2		10^{-16}		40	274	61	945	123	
F3		10^{-18}		40	294	64	945	120	

7526/80

4.1.4 CONTACTS WITH ONLY A SINGLE TDRS

Runs F1 through F3 (Table 4-2) are those in which only one TDRS was observed during the entire time span. The results from these runs are somewhat worse than those obtained when two TDRSs are alternately observed. This can be explained by the larger range measurement bias on TDRS-E and possibly the better geometry available to the user when sighting two tracking satellites rather than just one.

4.2 TWO-WAY DELTA-RANGE DATA

Tables 4-3 and 4-4 present the results from processing two-way delta-range data. Baseline run H3 with one pass of data every revolution obtained the best rms position accuracy of 49 meters over the last 3 hours for a process noise value of 10^{-18} km^2/sec^3. For this case, there is essentially no degradation in the position accuracy of the steady-state solution when the range observations were removed as compared to the range and delta-range results discussed earlier. For contact frequencies of two and three revolutions (I6 and J3), the maximum initial errors are considerably smaller than when the range data were included; however, the three-revolution contact frequency appears to require more processing time (three contacts) to achieve a steady-state solution. An optimum value of process noise for all pass frequency cases appears to be in the range of 10^{-18} km^2/sec^3 to 10^{-20} km^2/sec^3.

As can be seen in Table 4-4, the effects of changing the along-track errors to 4L and 8L are significant after 12 hours of processing but disappear after 21 hours of processing. However, increases in the radial and cross-track errors or along-track error rate result in negligible changes in positional accuracies. For observations every third revolution, the effect on the positional

Table 4-3. Landsat-D Estimation Using Two-Way Delta-Range Data (Runs G1 Through J4)

RUN	CONTACT FREQUENCY (2 TDRSs)	STATE PROCESS NOISE (km^2/sec^3)	TDRS EPHEMERIS ERRORS	rms POSITION DIFFERENCE (m)				MAXIMUM POSITION DIFFERENCE (m)				FIGURE NUMBER (A–)
				0^h–12^h	0^h–24^h	9^h–12^h	21^h–24^h	0^h–12^h	0^h–24^h	9^h–12^h	21^h–24^h	
G1	ALL[1]	10^{-14}	BASELINE	245		26		1996		64		28, 29, 30
H1	1 REV	10^{-14}	BASELINE	578		124		2549		219		
H2		10^{-16}		452	355	97	75	2549	2549	136	108	
H3		10^{-18}		448	353	66	49	2549	2549	95	82	31, 32, 33
H4		10^{-20}		449	353	93	50	2549	2549	146	99	
H5		0		449		94		2549		147		
I1	2 REVs	10^{-10}	BASELINE	554		116		2549		196		
I2		10^{-12}		425		32		2549		51		
I3		10^{-14}		983		35		3389		55		
I4		10^{-16}		701	499	45	98	2549	2549	66	126	
I5		10^{-18}		699	577	74	70	2720	2720	114	105	
I6		10^{-20}		699	578	78	39	2720	2720	117	58	34, 35, 36
I7		10^{-22}			578	78	39		2720	117	63	
J1	3 REVs	10^{-16}	BASELINE		930	327	122		3306	670	179	
J2		10^{-18}			922	327	91		3280	671	137	
J3		10^{-20}			922	327	84		3280	671	126	37, 38, 39
J4		10^{-22}			922	327	84		3280	671	126	

[1] INCLUDES ALL POSSIBLE CONTACT TIMES WITH EITHER TDRS-E OR TDRS-W.

7526/80

Table 4-4. Landsat-D Estimation Using Two-Way Delta-Range Data (Runs K2 Through L4)

RUN	CONTACT FREQUENCY (2 TDRSs)	STATE PROCESS NOISE (km^2/sec^3)	TDRS EPHEMERIS ERRORS	rms POSITION DIFFERENCE (m)				MAXIMUM POSITION DIFFERENCE (m)				FIGURE NUMBER (A–)
				0^h-12^h	0^h-24^h	9^h-12^h	21^h-24^h	0^h-12^h	0^h-24^h	9^h-12^h	21^h-24^h	
H4	1 REV	10^{-20}	BASELINE	449	340	93	50	2549	2549	146	99	
K2			8H, 8C	455		89		2549		130		40, 41, 42
K3			4L	446		85		2549		128		43, 44, 45
K4			1.5L	448		99		2549		155		
K5			2L	448		106		2549		170		
K6			4L	447	351	140	42	2549	2549	231	73	46, 47, 48
K7			8L	451		214		2549		361		
J3	3 REVs	10^{-20}	BASELINE		922	327	84		3280	671	126	37, 38, 39
L2			8H, 8C		945	321	71		3337	667	126	
L3			4L		910	293	91		3248	605	135	
L4			4L		908	382	78		3217	780	117	44, 50, 57

7526/80

accuracy of increasing the along-track ephemeris error is significant after 12 hours of processing but disappears after 21 hours of processing.

4.3 ONE-WAY DELTA-RANGE DATA

One-way delta-range data differ from two-way delta-range data because of the additional errors introduced by the onboard clock timing and frequency errors (see Table 3-4) and the higher random measurement noise level. To account for the timing errors, the clock drift term is estimated in the one-way case, and clock process noise covariance terms are included. Determination of appropriate process noise levels thus becomes a two-dimensional problem.

4.3.1 BASELINE RUN WITH ACCURATE ONBOARD CLOCK

Runs M1 through M30 in Table 4-5 were made to determine appropriate process noise levels for the baseline case using one-way delta-range data simulated with an accurate clock model at contact frequencies of one, two, and three revolutions. In addition to the data presented in previous tables, Table 4-5 lists the error in the estimated value for the clock drift, $\Delta\dot{b}$, after 12 or 24 hours of processing. At 24 hours the correct value for the clock drift is 2.02×10^{-7} seconds per second.

For the one-revolution contact frequency, a state process noise level of 10^{-12} (km^2/sec^3) is too large, and 10^{-14} through 10^{-20} yield identical results. For the clock process noise, a value of 10^{-19} seconds squared per second cubed (sec^2/sec^3) yields large initial transients, 10^{-20} yields the best results, and 10^{-21} yields poorer results over the last 3 hours. The steady-state solution given in run M4 is equivalent to results obtained using two-way data.

Table 4-5. Landsat-D Estimation Using One-Way Delta-Range Data for Accurate Clock Model (1 of 2)

RUN	CONTACT FREQUENCY (2 TDRSs)	PROCESS NOISE		TDRS EPHEMERIS ERRORS	rms POSITION DIFFERENCE (m)				MAXIMUM POSITION DIFFERENCE (m)				$\Delta\dot{b}$ (10^{-9}) (sec/sec)[1]		FIGURE NUMBER (A)
		STATE (km^2/sec^3)	CLOCK DRIFT (sec^2/sec^3)		0^h 12^h	0^h - 24^h	9^h 12^h	21^h - 24^h	0^h - 12^h	0^h - 24^h	9^h 12^h	21^h 24^h	12^h	24^h	
M1	1 REV	10^{-12}	10^{-19}	BASELINE		1960	122	197		9444	198	321		0.21	
M2		10^{-12}	10^{-21}			394	273	331		2549	406	679		0.09	
M3		10^{-14}	10^{-19}			1956	123	97		9444	214	156		0.09	52, 53, 54
M4		10^{-14}	10^{-20}			401	282	87		2549	418	169		0.16	55, 56, 57
M5		10^{-14}	10^{-21}			382	307	153		2549	474	257		0.16	58, 59, 60
M6		10^{-16}	10^{-19}			1956	124	98		9444	215	160		0.07	
M7		10^{-16}	10^{-20}			403	283	87		2549	419	169		0.16	
M8		10^{-18}	10^{-20}		540	403	283	87	2549	2549	419	169	0.20	0.16	
M9		10^{-18}	10^{-22}		469		316		2549		492		0.20		
M10		10^{-20}	10^{-20}			404	283	87		2549	419	169		0.16	
M11	2 REVs	10^{-12}	10^{-23}	BASELINE		418	259	256		2549	424	443		0.35	
M12		10^{-14}	10^{-20}			684	214	314		3063	316	634		0.02	
M13		10^{-14}	10^{-22}			388	252	200		2549	373	367		0.04	
M14		10^{-14}	10^{-23}			416	296	146		2549	466	240		0.05	61, 62, 63

[1] $\Delta\dot{b}$ - CLOCK DRIFT ERROR

7526/80

Table 4-5. Landsat-D Estimation Using One-Way Delta-Range Data for Accurate Clock Model (2 of 2)

RUN	CONTACT FREQUENCY (2 TDRSs)	PROCESS NOISE		TDRS EPHEMERIS ERRORS	rms POSITION DIFFERENCE (m)				MAXIMUM POSITION DIFFERENCE (m)				$\Delta\dot{u}$ (10^{-9}) (sec/sec)[1]		FIGURE NUMBER (A-)
		STATE (km^2/sec^3)	CLOCK DRIFT (sec^2/sec^3)		0^h-12^h	0^h-24^h	9^h-12^h	21^h-24^h	0^h-12^h	0^h-24^h	9^h-12^h	21^h-24^h	12^h	24^h	
M15		10^{-14}	10^{-24}	BASELINE		627	300	234		2,549	487	427		0.25	
M16		10^{-16}	10^{-18}			5126	544	1429		23,062	880	2086		1.1	
M17		10^{-16}	10^{-22}			392	252	243		2,549	369	488		0.06	
M18		10^{-16}	10^{-23}			402	301	178		2,549	465	338		0.12	
M19		10^{-18}	10^{-20}			686	214	330		3,063	315	650		0.001	
M20		10^{-20}	10^{-18}			5126	544	1430		23,062	880	2086		1.1	
M21	3 REVs	10^{-12}	10^{-19}	BASELINE		7623	1879	2082		24,427	3101	2749		0.4	
M22		10^{-12}	10^{-20}			1277	520	524		4,471	997	683		1.0	
M23		10^{-14}	10^{-20}			1279	523	546		4,464	997	695		1.3	
M24		10^{-14}	10^{-21}			685	306	476		2,549	431	621		1.5	
M25		10^{-14}	10^{-22}			527	234	410		2,549	330	550		1.4	
M26		10^{-14}	10^{-23}			603	290	311		2,549	389	439		1.3	64, 65, 66
M27		10^{-14}	10^{-24}			1101	390	324		3,578	637	443		1.3	
M28		10^{-16}	10^{-21}			686	306	495		2,549	431	625		1.5	
M29		10^{-16}	10^{-23}			620	288	403		2,549	384	502		1.3	
M30		10^{-18}	10^{-21}			686	306	485		2,549	431	625		1.5	
M31	1 REV	10^{-16}	10^{-20}	8H, 8C		409	275	56		2,549	423	105		0.08	
M32		10^{-16}	10^{-20}	4L		423	348	66		2,549	525	144		0.18	
M33		10^{-16}	10^{-20}	4L		409	273	150		2,549	399	225		0.4	67, 68, 69

[1] $\Delta\dot{u}$ - CLOCK DRIFT ERROR

7526/80

4.3.2 VARIATION OF CONTACT FREQUENCY

For the case of a two-revolution contact frequency, a state process noise level of 10^{-12} (km^2/sec^3) is too large and 10^{-14} through 10^{-20} appear to yield nearly identical results. Values of 10^{-18} through 10^{-20} (sec^2/sec^3) for the clock drift process noise covariance are too large; values of 10^{-22} and 10^{-23} yield the best results, and 10^{-24} appears to be too small. The best results for this case (M14) demonstrate a 50-percent increase in the error in the steady-state solution as compared with the baseline case.

Similar results were obtained for the three-revolution contact frequency cases. For the state process noise level, values of 10^{-12} through 10^{-20} produced comparable accuracies. For the clock drift noise, values of 10^{-19} and 10^{-22} were too large, and 10^{-23} produced the best results. In this case the steady-state errors are about three time larger than in the one-revolution case.

4.3.3 VARIATION OF TDRS EPHEMERIS ERRORS

Runs M31 through M33 illustrate the effect of TDRS ephemeris errors when using one-way delta-range data. Comparison with run M7 indicates that errors as large as 280 meters in the radial and cross-track directions or 320 meters in the along-track direction do not significantly degrade the estimated position after 24 hours of processing. However, the increased along-track error does produce a 60-meter increase after only 12 hours of processing, and an along-track rate of 1 kilometer per day produces an increase in error of about 30 meters at the end of 24 hours, probably due to the larger error in the clock drift estimate.

4.3.4 BASELINE RUNS WITH NASA STANDARD TRANSPONDER MODEL

Table 4-6 summarizes the runs that were made to determine appropriate process noise levels for the baseline case using one-way delta-range data simulated with the NASA standard transponder model parameters given in Table 3-4. As in the case with the accurate clock, comparison of the statistics indicates that values for the state process noise of 10^{-14} through 10^{-20} (km^2/sec^3) yield comparable results. A value of 10^{-12} appears to be somewhat less optimal. The accuracy of the solution is more sensitive to the value of the process noise covariance rate for the clock drift term. A value of 10^{-14} for the clock drift noise is too large; 10^{-22} is too small; and 10^{-17} and 10^{-18} produce the best results over the first 12 hours. The value 10^{-16} produces the best results for both the drift term and the spacecraft position over the last 12 hours.

The accuracy of the estimation process using data simulated with the NASA standard transponder model parameters is limited by the inadequacy of estimating and predicting the linearly varying clock drift term using a constant model. In this case, the clock drift rate is 100 times larger than in the case of the accurate clock model. Similarly, the optimum value for the clock drift process noise rate is 10^4 times larger to compensate for the larger clock drift rate. Comparison of the along-track position difference plots for cases M4 and N6 (Figures A-57 and A-72, respectively) illustrates that the prediction errors in the case of the poorer clock are about 10 times larger.

Table 4-6. Landsat-D Estimation Using One-Way Delta-Range Data With NASA Standard Transponder Model

RUN	CONTACT FREQUENCY (2 TDRSs)	PROCESS NOISE		TDRS EPHEMERIS ERRORS	rms POSITION DIFFERENCE (m)				MAXIMUM POSITION DIFFERENCE (m)				$\Delta\dot{b}$ (10^{-9}) (sec/sec)		FIGURE NUMBER (A-)
		STATE (km^2/sec^3)	CLOCK DRIFT (sec^2/sec^3)		0^h-12^h	0^h-24^h	9^h-24^h	21^h-24^h	0^h-12^h	0^h-24^h	9^h-12^h	21^h-24^h	12^h	24^h	
N1	1 HEV	10^{-12}	10^{-14}	BASELINE	32,888		40,100		46,260		46,260		50.0		
N2		10^{-12}	10^{-16}		7,533		4,685	1223	14,378	14,378	7,864	2063		5.0	
N3		10^{-14}	10^{-16}		7,532	5485	4,688	1136	14,378	14,378	7,668	1987		5.0	
N4		10^{-14}	10^{-18}		6,839	5325	4,374	2466	14,025	14,025	6,558	4985		10.0	
N5		10^{-16}	10^{-14}		32,900		40,109		46,275		46,275		50.0		
N6		10^{-16}	10^{-16}		7,532	5485	4,688	1136	14,378	14,378	7,666	1986		5.0	70, 71, 72
N7		10^{-16}	10^{-17}		6,589	4902	4,168	1476	14,345	14,345	6,747	2762		7.4	
N8		10^{-16}	10^{-18}		6,838	5325	4,372	2432	14,025	14,025	6,556	4935		10.0	
N9		10^{-18}	10^{-16}		7,532		4,688		14,378		7,668		8.3		
N10		10^{-18}	10^{-17}		6,589	4902	4,168	1476	14,345	14,345	6,747	2762		7.4	
N11		10^{-18}	10^{-18}		6,838		4,371		14,025		6,556		6.6		
N12		10^{-18}	10^{-22}		9,751	9817	15,600	4118	24,417	30,528	24,417	9083		10.0	
N13		10^{-20}	10^{-17}		6,589		4,168		14,345		6,747		7.6		
N14		10^{-18}	0		701	501	110	47	2,772	2,772	190	92		0.016	73, 74, 75

7526/80

To determine whether a more accurate model for the NASA standard transponder would improve the solution accuracy, run N14 was made in which the clock drift rate, $\ddot{b}$, was estimated using no clock process noise. Results from this run show improvement to the level of accuracy achieved in the two-way cases.

4.4 ANOMALOUS DATA CASES

Several simulations were made to investigate the EKF's performance in the presence of anomalous variations in the baseline data sets. The results from these simulations are discussed below.

To assess the impact on the EKF's performance of processing a pass of data with large time-varying range and delta-range measurement errors, data set 1 in Table 4-7 was substituted for the TDRS-E data that occur at 4 hours and 45 minutes in the baseline data set with a one-revolution contact frequency. This pass occurs 1 hour before the maximum in the sinusoidal ephemeris error model for TDRS-E, resulting in an approximate range error of 7 kilometers and a delta-range error of 300 centimeters. In addition, the last two passes in the baseline one-revolution data set were deleted (see Figure 4-1). The statistics from this simultaton using two-way range and delta-range data and delta-range data only are listed as runs O1 and O2 in Table 4-8. A 500-sigma edit test was used for both runs. Comparison with baseline simulations B4 and H3 shows an approximate doubling of the errors after both 12 and 24 hours of processing. Inspection of Figures A-76 through A-81 shows significant along-track errors at the time the data are processed.

Simulations were also performed in which the effect of one pass of data with a large delta-range measurement bias was

Table 4-7. Landsat-D Estimation Using Anomalous Data Sets

PARAMETER	VALUE			
	DATA SET 1	DATA SET 2	DATA SET 3	DATA SET 4
TIME OF ANOMALOUS DATA	$4^h45^m - 4^h55^m$	$13^h0^m - 13^h10^m$	$0^h - 24^h$	
TDRS EPHEMERIS ERRORS				
H	6.6 km	180 m	8H	
C	6.6 km	180 m	8C	
L	25.6 km	3.12 km	4L, 4$\dot{L}$ (UPDATE EPOCH AT 14^h)	
RANGE BIAS (m)				
TDRS-E	−360		−18	
TDRS-W		−40	−2	
DELTA-RANGE BIAS (cm)	0	60,000 OR 200	0	
RANDOM RANGE ERROR (m)	10	10	1	
RANDOM DELTA-RANGE ERROR (cm)	10	10	1	
DELETED DATA PASSES	$22^h20^m - 22^h30^m$ $23^h50^m - 24^h$	$22^h20^m - 22^h30^m$ $23^h50^m - 24^h$		$4^h45^m - 4^h55^m$ $10^h - 10^h10^m$ $16^h20^m - 16^h30^m$

7526/80

Table 4-8. Anomalous Data Sets for Landsat-D

RUN	DATA TYPE[1]	CONTACT FREQUENCY (2 TDRSs)	STATE PROCESS NOISE (km^2/sec^3)	ANOMALOUS DATA SET	rms POSITION DIFFERENCE (m)			ANOMALOUS DATA EDITED	MAXIMUM POSITION DIFFERENCE (m)			FIGURE NUMBER (A-)
					0^h-24^h	9^h-12^h	21^h-24^h		0^h-24^h	9^h-12^h	21^h-24^h	
01	TWO-WAY R AND ΔR	1 REV	10^{-18}	1	629	145	76	19 ΔR	2549	224	127	76, 77, 78
02	TWO-WAY ΔR	1 REV	10^{-18}	1	424	149	139	19 ΔR	2549	255	240	79, 80, 81
03	TWO-WAY ΔR	1 REV	10^{-18}	2 (ΔR BIAS = 60000 cm)	319	66	51	30 ΔR	2549	95	86	82, 83, 84
04	TWO-WAY ΔR	1 REV	10^{-18}	2 (ΔR BIAS = 200 cm)	386	66	140	0	2549	95	228	85, 86, 87
05	TWO-WAY R AND ΔR	1 REV	10^{-18}	3	733	173	163		3254	267	330	88, 89, 90
06	TWO WAY ΔR	1 REV	10^{-18}	3	357	165	160		2549	244	292	91, 92, 93
07	TWO-WAY R AND ΔR	1 REV	10^{-18}	4	319	76	37	NA[2]	2549	119	61	94, 95, 96
08	TWO-WAY ΔR	1 REV	10^{-18}	4	314	76	55	NA	2549	118	100	97, 98, 99

7526/80

[1]R - RANGE; ΔR - DELTA-RANGE

[2]NA - NOT APPLICABLE.

studied. In run O3, data set 2 with a delta-range bias of 600 meters was substituted from a nominal pass of data. All of these data were edited, resulting in essentially no degradation in accuracy as compared to baseline case H3. In run O4, data set 2 with a delta-range bias of 200 centimeters was substituted. These data were not edited, resulting in a doubling of the error after 24 hours of processing.

Simulations were made with data set 3 to investigate the effect of receiving updated TDRS ephemerides during the processing. In both cases O5 and O6, this update produced little effect on the final solutions.

The effect of losing or deleting a pass of data was also studied. This case is represented by runs O7 and O8, which use data set 4 in which the 4th, 8th, and 12th passes were deleted from the baseline 1-revolution case. Comparison of cases O7 and O8 with case B5 and H3 indicates that no degradation results using two-way data with an appropriate value for the process noise covariance rate.

Several runs were also made processing one-way data that was simulated using the accurate quadratic clock model with the addition of sinusoidal clock bias errors, as given by Equation (2-8). The sinusoidal clock bias errors also produce a sinusoidal bias in the delta-range data that is given by Equation (2-9). The frequency of the errors was equal to the orbital frequency of Landsat-D. The amplitudes were chosen such that a_1 ranges from 2×10^{-7} to 2×10^{-6} seconds and a_2 is zero. These values produce an amplitude in the delta-range bias of between 60 and 600 centimeters. Table 4-9 summarizes the results from these runs.

Table 4-9. Landsat-D Estimation Using One-Way Data With Sinusoidal Error Model

RUN	CLOCK MODEL	SINUSOIDAL DELTA RANGE BIAS AMPLITUDE (cm)	$\sigma_{\Delta R}$ IN FILTER (cm)	CONTACT FREQUENCY	PROCESS NOISE		rms POSITION DIFFERENCE (m)			MAXIMUM POSITION DIFFERENCE (m)			$\Delta\dot{b}$ (10^{-9}) (sec/sec)	FIGURE NUMBER (A–)
					STATE (km^2/sec^3)	CLOCK DRIFT (sec^2 sec^3)	0^h-24^h	9^h-12^h	21^h-24^h	0^h-24^h	9^h-12^h	21^h-24^h		
09	ACCURATE	60	10	1 REV	10^{-14}	10^{-20}	399	336	160	2549	454	261	0.15	
010	ACCURATE	300	10	1 REV	10^{-14}	10^{-20}	609	657	550	2549	1115	879	0.10	100, 101, 102
011	ACCURATE	600	10	1 REV	10^{-14}	10^{-20}	1061	1116	1053	2549	1950	1680	0.14	103, 104, 105
012	ACCURATE	300	200	1 REV	10^{-14}	10^{-20}	594	644	503	2549	1080	871	0.82	

7526/80

Comparison with run M4 indicates that an amplitude of 60 centimeters, which is 0.1 percent of the bias produced by the clock drift term ($\dot{b}$), produces about a 75-percent increase in the solution error after 21 hours of processing. Run O11 indicates that an amplitude of 600 centimeters produces a tenfold increase in the error in the solution after 21 hours of processing. In run O12 the measurement standard deviation was increased to account for the oscillating bias caused by the sinusoidal clock bias errors. This did not produce any significant improvement.

SECTION 5 - EVALUATION RESULTS FOR GRO

This section presents the results of evaluating the EKF for determination of the GRO orbit from TDRSS tracking data. Table 3-1 (Section 3.1) specifies the nominal GRO orbital elements. Figures 5-1 through 5-3 illustrate the periods of potential contact of GRO with TDRS-E and TDRS-W and the 10-minute time spans that were selected for the nominal one-, two-, and three-revolution contact frequencies, respectively.

Sections 5.1 through 5.3 discuss the performance of the EKF using two-way range and delta-range data, two-way delta-range data, and one-way delta-range data, respectively. Section 5.4 discusses the EKF performance on anomalous data sets. Radial, cross-track, and along-track plots of the position errors for several representative cases are provided in Appendix B. The complete set of plots is available in Reference 5.

5.1 TWO-WAY RANGE AND DELTA-RANGE DATA

This section presents the results of evaluating the EKF performance using two-way range and delta-range data. Tables 3-2, 3-3, and 3-5 (Section 3) specify the nominal measurement error levels and dynamic modeling errors. Tables 3-6 and 3-7 (Section 3) summarize the baseline EKF processing options and a priori values.

5.1.1 BASELINE RUNS

The GRO orbit, which has an altitude of 400 kilometers, is strongly perturbed by atmospheric drag effects. Atmospheric density modeling errors, which are simulated by a mismatch of the atmospheric drag coefficients and the density models, produce large prediction errors, as described in Appendix C. To reduce the effect of these modeling

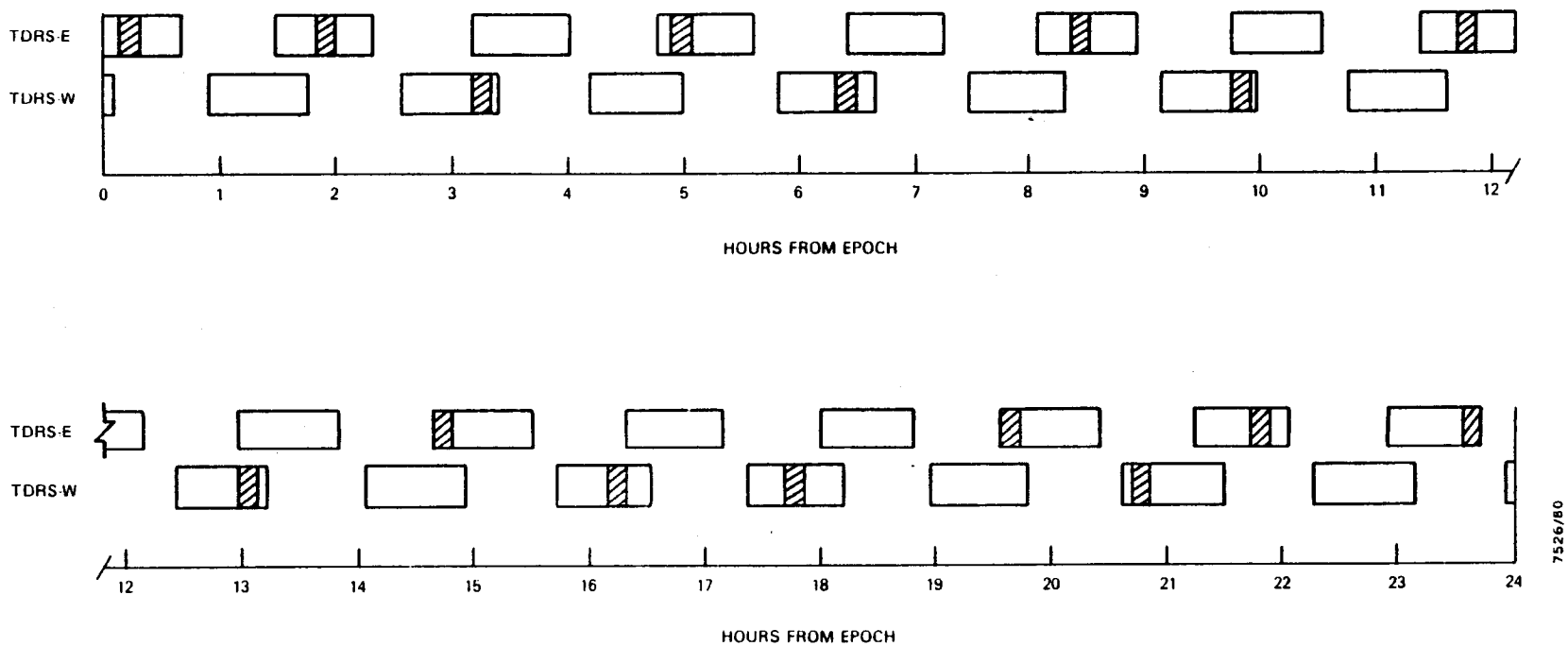

NOTES: 1. EPOCH = OCTOBER 1, 1980.

2. SHADED AREAS CORRESPOND TO ONE PASS PER REVOLUTION DATA SET

Figure 5-1. TDRSS Tracking Contacts for GRO for One-Revolution Contact Frequency

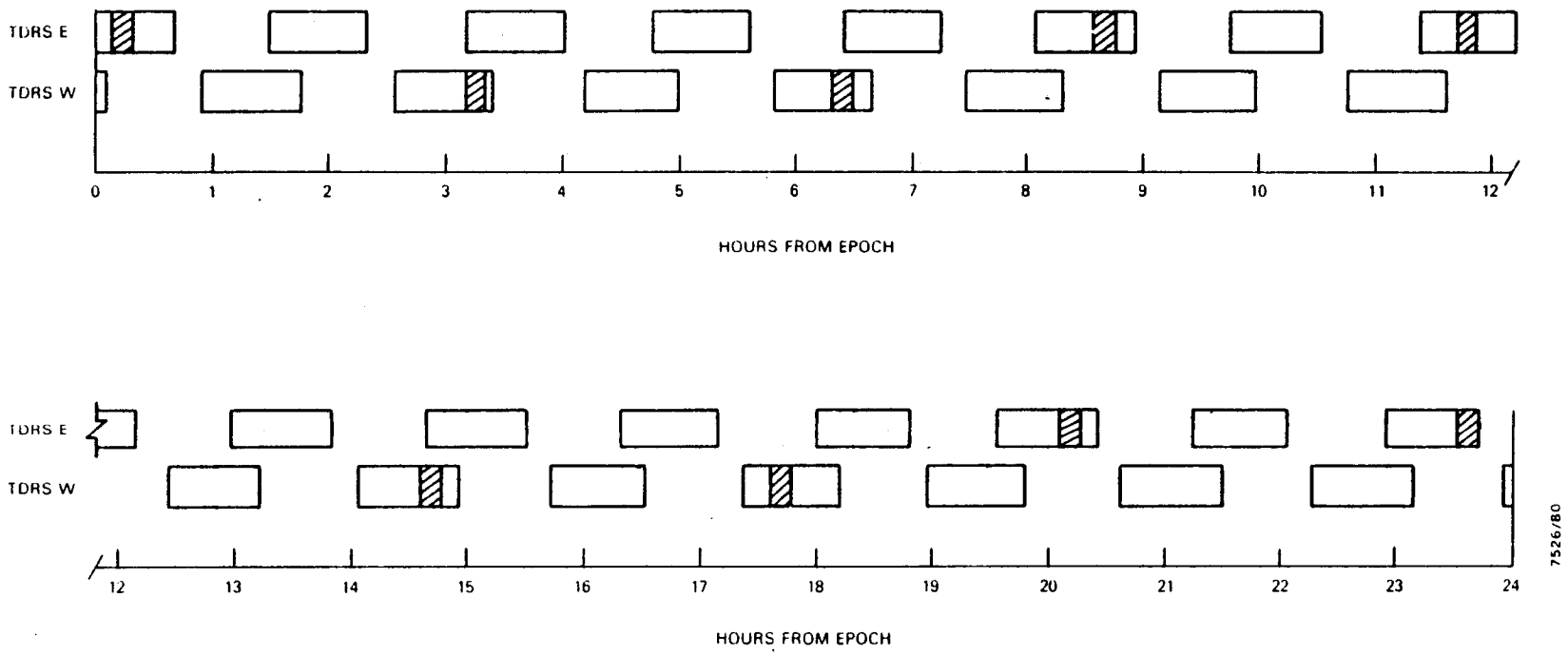

NOTES. 1. EPOCH OCTOBER 1, 1980.

2. SHADED AREAS CORRESPOND TO ONE PASS PER TWO REVOLUTIONS DATA SET.

Figure 5-2. TDRSS Tracking Contacts for GRO for Two-Revolution Contact Frequency

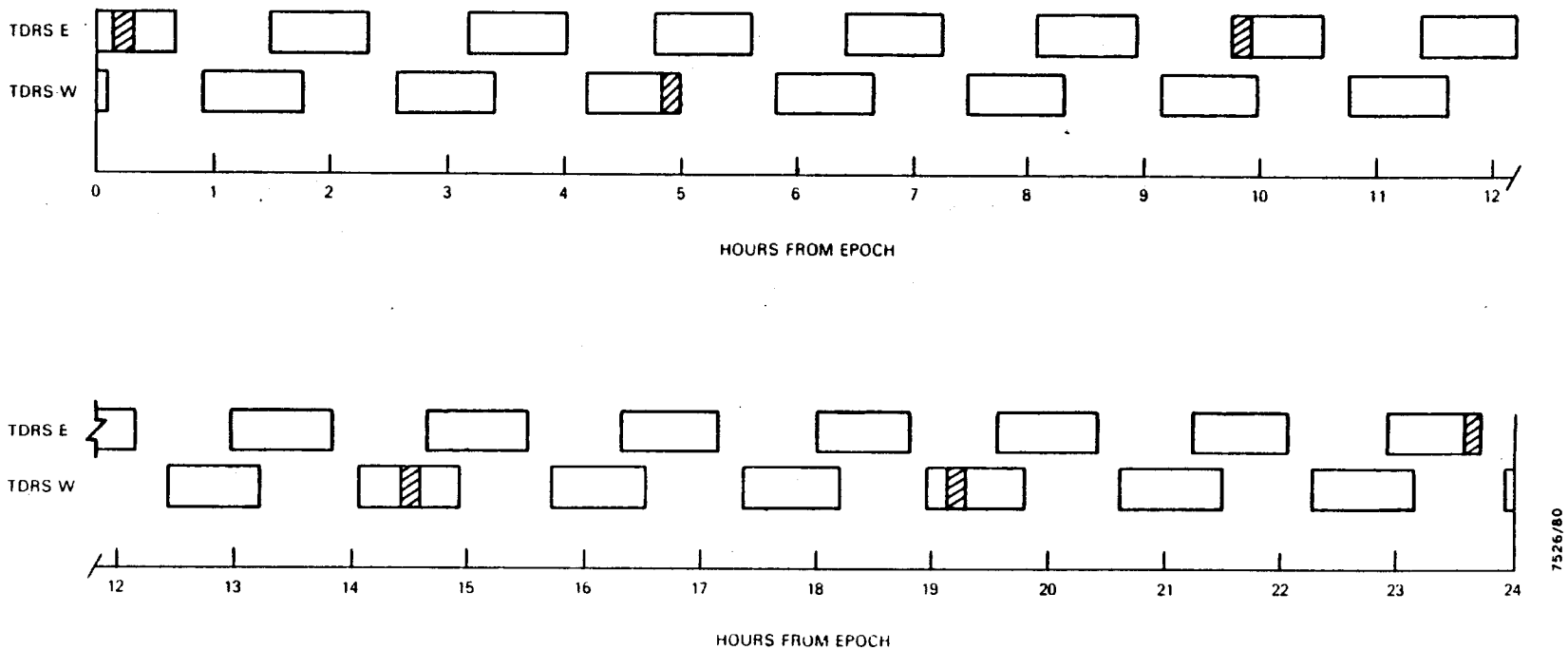

NOTES: 1. EPOCH OCTOBER 1, 1980

2. SHADED AREAS CORRESPOND TO ONE PASS PER THREE REVOLUTIONS DATA SET.

Figure 5-3. TDRSS Tracking Contacts for GRO for Three-Revolution Contact Frequency

errors, estimation of the drag parameter, ρ_1, in the Harris-Priester density model was investigated for the baseline case. Estimation of this parameter also requires the adjustment of the associated process noise covariance rate.

Runs P1 through P16 in Table 5-1 illustrate the performance obtained for several values of the state and drag process noise with and without estimation of ρ_1. The estimated value for ρ_1 is also tabulated. The atmospheric density mismodeling cannot be exactly corrected through selection of a constant ρ_1. However, a value for ρ_1 in the range of -0.43 to -0.55 produces drag accelerations approximately equal to the truth model values at the 400-kilometer altitude.

Inspection of the cases in which ρ_1 is not estimated (P3, P5, P9, P14, and P16) indicates that state processing noise values on the order of 10^{-10} km^2/sec^3 and 10^{-12} km^2/sec^3 produce the best results. However, these results are not as good as those obtained when ρ_1 is estimated and the state and drag process noise rates are properly chosen.

The optimum value for the state process noise appears to be about 10^{-18} km^2/sec^3. The solution is considerably less sensitive to the value of the drag covariance rate; however, a value in the range of 10^{-12} to 10^{-14} per second produces better results does than a value of 10^{-10} per second. Comparison of Figures B-1 through B-3 with Figures B-4 through B-6 shows that the estimator's behavior is more stable when ρ_1 is estimated. Based on this result, in all further GRO simulations the parameter ρ_1 is estimated.

Table 5-1. GRO Estimation Using Two-Way Range and Delta-Range Data (1 of 2)

RUN	CONTACT FREQUENCY (2 TDRSs)	PROCESS NOISE		TDRS EPHEMERIS ERRORS	rms POSITION DIFFERENCE (m)				MAXIMUM POSITION DIFFERENCE (m)				ρ_1	FIGURE NUMBER (B-)
		STATE (km^2/sec^3)	DRAG (sec^2/sec^3)		0^h-12^h	0^h-24^h	9^h-12^h	21^h-24^h	0^h-12^h	0^h-24^h	9^h-12^h	21^h-24^h		
P1	1 REV	10^{-10}	10^{-12}	BASELINE		375	102	239	1677	1677	159	480	−0.066	
P2		10^{-10}	10^{-14}		498		102		1677		159		−0.065	
P3		10^{-10}			516	390	102	254	1770	1770	169	517	NE[1]	1, 2, 3
P4		10^{-12}	10^{-14}		338		132		846		294		−0.358	
P5		10^{-12}			450	352	121	258	1436	1436	257	533	NE	
P6		10^{-14}	10^{-10}			251	147	105	1108	1108	272	203	−0.338	
P7		10^{-14}	10^{-12}		316		147		1108		272		−0.306	
P8		10^{-14}	10^{-14}		316		147		1108		273		−0.305	
P9		10^{-14}			375		223		1108		480		NE	
P10		10^{-16}	10^{-12}			315	153	68	1457	1457	245	149	−0.394	
P11		10^{-18}	10^{-10}			295	141	68	1463	1463	233	103	−0.455	
P12		10^{-18}	10^{-12}			295	141	60	1463	1463	234	88	−0.473	4, 5, 6
P13		10^{-18}	10^{-14}			295	141	60	1463	1463	234	89	−0.473	
P14		10^{-18}			450		227		1463		418		NE	
P15		10^{-20}	10^{-12}			308	170	113	1463	1463	256	214	−0.473	
P16		10^{-20}			882		1216		1875		1875		NE	
P17	2 REVs	10^{-12}	10^{-12}	BASELINE		1093	536	1463		2470	1035	2470	−0.521	
P18		10^{-14}	10^{-12}			721	590	503		2070	1132	798	−0.529	
P19		10^{-16}	10^{-12}			647	146	410		2765	286	697	−0.645	
P20		10^{-18}	10^{-12}			635	331	168		2776	565	304	−0.483	
P21		10^{-20}	10^{-12}			636	364	127		2777	631	189	−0.461	7, 8, 9
P22		10^{-22}	10^{-12}			638	364	162		2777	632	212	−0.459	

[1] NE = NOT ESTIMATED.

7526/80

Table 5-1. GRO Estimation Using Two-Way Range and Delta-Range Data (2 of 2)

RUN	CONTACT FREQUENCY (2 TDRSs)	PROCESS NOISE		TDRS EPHEMERIS ERRORS	rms POSITION DIFFERENCE (m)			MAXIMUM POSITION DIFFERENCE (m)			ρ_1	FIGURE NUMBER (B-)
		STATE (km^2/sec^3)	DRAG (sec^2/sec^3)		0^h-24^h	9^h-12^h	21^h-24^h	0^h-24^h	9^h-12^h	21^h-24^h		
P23	3 REVs	10^{-14}	10^{-12}	BASELINE	2167	3384	2436	6089	6089	3922	−0.319	
P24		10^{-16}	10^{-12}		1175	1090	102	3769	2048	157	−0.444	10, 11, 12
P25		10^{-16}	10^{-14}		1175	1090	102	3769	2048	157	−0.444	
P26		10^{-18}	10^{-12}		1157	996	162	3786	1892	262	−0.429	
P27		10^{-18}	10^{-14}		1157	996	162	3786	1892	262	−0.429	
P28		10^{-18}	10^{-16}		1157	996	162	3786	1892	262	−0.429	
P29		10^{-20}	10^{-12}		1157	994	187	3786	1890	289	−0.453	
P30	1 REV	10^{-18}	10^{-12}	8H, 8C	304	145	83	1523	237	115	−0.470	
P31		10^{-18}	10^{-12}	4L	305	187	76	1436	303	115	−0.492	
P32		10^{-18}	10^{-12}	4L*	309	175	128	1450	286	163	−0.466	13, 14, 15
P33	3 REVs	10^{-16}	10^{-12}	4H, 4C	1461	1704	97	3855	3429	144	−0.433	
P34		10^{-16}	10^{-12}	8H, 8C	1936	2564	102	5300	5300	159	−0.417	16, 17, 18
P35		10^{-16}	10^{-12}	4L	1153	1060	101	3689	1973	158	−0.437	
P36		10^{-16}	10^{-12}	8L	1126	1023	108	3584	1876	165	−0.428	
P37		10^{-16}	10^{-12}	4L*	1177	1115	137	3729	2085	200	−0.426	19, 20, 21

7526/80

5.1.2 VARIATION OF CONTACT FREQUENCY

Runs P17 through P22 in Table 5-1 illustrate the EKF's performance for the two-revolution contact frequency case. For this case the optimum value for the state process noise covariance rate is approximately 10^{-20} km^2/sec^3. This value produces slower but more uniform convergence than does the value 10^{-16} km^2/sec^3. The error in the steady-state solution for the two-revolution contact frequency is about twice the error obtained using a one-revolution contact frequency.

Runs P23 through P29 demonstrate the EKF's performance for the three-revolution contact frequency case. The optimum value for the state process noise is approximately 10^{-16} km^2/sec^3. As in the one-revolution case, comparison of runs P26 through P28 indicates that the solution accuracy is not highly sensitive to the value of the drag process noise rate.

The values of 10^{-18} km^2/sec^3 for the state process noise covariance rate and 10^{-12} per second for the drag process noise rate appear to be the best single choices for processing all three contact frequencies.

5.1.3 VARIATION OF TDRS EPHEMERIS ERRORS

Runs P30 through P32 and P33 through P37 demonstrate the effect on the EKF's performance of increasing the TDRS ephemeris errors for the one- and three-revolution cases, respectively. For both frequencies, TDRS ephemeris errors as large as 280 meters in the radial and cross-track directions or 320 meters in the along-track direction do not produce significantly larger errors in the steady-state solution.

For the one-revolution contact frequency, inspection of Figure B-15 indicates that the increase in the along-track

rate produces the largest effect, an along-track bias of about 100 meters in the maximum error over the last 3 hours of processing. The 320-meter along-track error produces a 70-meter increase in the maximum error after 9 hours of processing; however, this decreases to 25 meters during the last 3 hours.

For the three-revolution contact frequency, the 280-meter radial and cross-track errors significantly increase the errors during the first 12 hours of processing; however, this effect disappears during the last 3 hours of processing. Along-track errors as large as 640 meters do not produce a significant increase in the solution error. The increased along-track rate produces a biased along-track error of about 50 meters in the steady-state solution.

The biased solution resulting from the presence of the along-track rate error in the TDRS ephemerides is probably an indication of difficulty in decoupling this error from the ρ_1 estimate.

5.2 TWO-WAY DELTA-RANGE DATA

This section discusses the performance of the EKF using only two-way delta-range data. The data that were used are a subset of the two-way range and delta-range data sets defined in Section 5.1. The baseline EKF processing options and a priori values are identical to those used in the processing of two-way range and delta-range data. Table 5-2 summarizes the results.

5.2.1 BASELINE RUNS

Runs Q1 through Q7 in Table 5-2 show the effect of varying the state and drag process noise levels for the baseline case of one-revolution contact frequency. As was the case with the two-way range and delta-range data, nearly

Table 5-2. GRO Estimation Using Two-Way Delta-Range Data

RUN	CONTACT FREQUENCY (2 TDRSs)	PROCESS NOISE		TDRS EPHEMERIS ERRORS	rms POSITION DIFFERENCE (m)			MAXIMUM POSITION DIFFERENCE (m)			ρ_1	FIGURE NUMBER (B-)
		STATE (km^2/sec^3)	DRAG (sec^2/sec^3)		0^h-24^h	9^h-12^h	21^h-24^h	0^h-24^h	9^h-12^h	21^h-24^h		
Q1	1 REV	10^{-14}	10^{-12}	BASELINE	378	191	214	1457	314	303	−0.928	
Q2		10^{-14}	10^{-14}		424	216	456	1481	343	653	−0.928	
Q3		10^{-16}	10^{-12}		372	147	67	1699	261	91	−0.590	22, 23, 24
Q4		10^{-16}	10^{-14}		372	147	67	1699	261	91	−0.591	
Q5		10^{-18}	10^{-12}		363	160	89	1702	243	154	−0.472	25, 26, 27
Q6		10^{-18}	10^{-14}		363	160	89	1702	243	154	−0.472	
Q7		10^{-20}	10^{-12}		367	168	123	1702	255	238	−0.472	
Q8	2 REVs	10^{-16}	10^{-12}	BASELINE	1032	1171	568	3730	1953	1020	−0.936	
Q9		10^{-18}	10^{-12}		952	1302	98	3737	2214	167	−0.485	28, 29, 30
Q10		10^{-20}	10^{-12}		954	1318	146	3737	2239	190	−0.459	
Q11	3 REVs	10^{-16}	10^{-12}	BASELINE	1737	1942	957	5365	3883	1652	−0.795	
Q12		10^{-18}	10^{-12}		1894	2422	450	5368	4522	753	−0.494	
Q13		10^{-20}	10^{-12}		1894	2429	378	5368	4530	577	−0.468	31, 32, 33
Q14		10^{-22}	10^{-12}		1894	2429	377	5368	4530	575	−0.468	
Q15	1 REV	10^{-16}	10^{-12}	8H, 8C	380	150	99	1749	262	131	−0.584	
Q16		10^{-16}	10^{-12}	4L	387	179	82	1673	264	147	−0.621	
Q17		10^{-16}	10^{-12}	4L*	376	173	109	1686	315	194	−0.583	34, 35, 36
Q18	3 REVs	10^{-20}	10^{-12}	8H, 8C	1892	2359	437	5524	4524	656	−0.472	
Q19		10^{-20}	10^{-12}	4L	1932	2556	397	5312	4794	592	−0.470	
Q20		10^{-20}	10^{-12}	4L*	1882	2423	361	5340	4557	557	−0.469	37, 38, 39

7526/80

identical results were obtained using drag process noise levels of 10^{-12} per second and 10^{-14} per second when the state process noise level was properly adjusted. The optimum value for the state process noise is on the order of 10^{-16} to 10^{-18} km^2/sec^3. The value of 10^{-16} km^2/sec^3 (Q3) produces the smallest errors after 21 hours of processing; the value of 10^{-18} km^2/sec^3 (Q5) produces the best estimate for the parameter ρ_1. Comparison of Figures B-24 and B-27 indicates that run Q5 produces a smoother along-track error history than does run Q3.

5.2.2 VARIATION OF CONTACT FREQUENCY

Runs Q8 through Q10 and Q11 through Q14 illustrate the EKF's performance for the two- and three-revolution contact frequency cases, respectively. A state process noise value of 10^{-18} km^2/sec^2 produces the smallest error for the two-revolution case. After 9 hours of processing, these errors are about 10 times larger than in the 1-revolution case. However, after 12 hours of processing, the steady-state solution error reduces to approximately the level achieved in the one-revolution case (see Figures B-25 through B-30).

For the three-revolution contact frequency, a state process noise value of 10^{-20} km^2/sec^2 produces the best steady-state solution. After 9 hours of processing, the errors are 30 times larger than those in the 1-revolution case. After 21 hours of processing, the errors decrease to five times the errors obtained in the one-revolution case. This error level is more than three times larger than the steady-state error level obtained when both two-way range and delta-range data are processed with a three-revolution contact frequency.

5.2.3 VARIATION OF TDRS EPHERMIS ERRORS

Runs Q15 through Q17 and Q18 through Q20 demonstrate the effect of increasing the TDRS ephemeris errors for the case of one and three contacts per revolution, respectively. Radial and cross-track amplitudes of 280 meters or an along-track amplitude of 320 meters does not significantly increase the error in the solution as compared to the baseline case. The increase in the along-track amplitude primarily affects the estimate for the parameter ρ_1. However, an increase in the along-track rate produces a biased solution for the one-revolution contact frequency, as in the range and delta-range case (see Figure B-36).

5.3 ONE-WAY DELTA-RANGE DATA

This section discusses the performance of the EKF using one-way delta-range data. The data occur at the same times as do the two-way delta-range data; however, the one-way data are simulated with a larger measurement noise standard deviation, 10 centimeters, and the two levels of user-clock errors defined in Table 3-4 (Section 3). The baseline EKF processing options and a priori values are identical to those used in the processing of two-way data except for the larger delta-range standard deviation and the addition of clock drift, $\dot{b}$, as an estimated parameter. Table 5-3 summarizes the results.

5.3.1 BASELINE RUNS

Runs R1 through R9 demonstrate the effect of varying the process noise parameters for the baseline one-revolution case, simulated with an accurate clock model. The solution is most sensitive to the value chosen for the clock drift process noise. State process noise values of 10^{-16} km^2/sec^3 and 10^{-18} km^2/sec^3 produce identical

Table 5-3. GRO Estimation Using One-Way Delta-Range Data

RUN	CONTACT FREQUENCY (2 TDRS)	CLOCK MODEL	PROCESS NOISE			TDRS EPHEMERIS ERRORS	rms POSITION DIFFERENCE (m)			MAXIMUM POSITION DIFFERENCE (m)			$\Delta\dot{b}$ (10^{-9}) (sec/sec)	ρ_1	FIGURE NUMBER (B –)
			STATE (km^2/sec^3)	CLOCK DRIFT (sec^2/sec^3)	DRAG (sec^{-1})		0^h-24^h	9^h–12^h	21^h–24^h	0^h–24^h	9^h–12^h	21^h–24^h	24^h		
R1	1 REV	ACCURATE	10^{-16}	10^{-20}	10^{-12}	BASELINE	578	460	186	1514	726	330	0.30	−0.481	
R2			10^{-18}	10^{-19}	10^{-12}		646	480	202	2145	776	331	0.38	−0.472	
R3			10^{-18}	10^{-20}	10^{-12}		578	460	186	1514	726	329	0.35	−0.481	
R4			10^{-18}	10^{-21}	10^{-12}		512	488	189	1264	749	336	0.30	−0.482	
R5			10^{-18}	10^{-22}	10^{-12}		476	418	174	1449	629	319	0.30	−0.478	
R6			10^{-18}	10^{-23}	10^{-12}		441	333	147	1830	496	271	0.23	−0.476	
R7			10^{-18}	10^{-23}	10^{-14}		441	333	147	1830	496	271	0.23	−0.476	
R8			10^{-18}	10^{-24}	10^{-12}		462	306	129	2144	453	235	0.12	−0.477	40, 41, 42
R9			10^{-18}	10^{-25}	10^{-12}		470	313	145	2195	458	242	0.16	−0.475	
R10	2 REVs	ACCURATE	10^{-18}	10^{-18}	10^{-12}	BASELINE	1375	1159	1406	3260	1619	1850	0.01	−0.483	
R11			10^{-18}	10^{-19}	10^{-12}		1556	1427	880	4388	2227	1121	0.18	−0.487	43, 44, 45
R12			10^{-18}	10^{-20}	10^{-12}		1982	1926	1087	4932	3125	1322	0.50	−0.472	
R13			10^{-18}	10^{-21}	10^{-12}		2178	2201	1180	5713	3537	1506	1.00	−0.446	
R14			10^{-20}	10^{-20}	10^{-12}		1982	1926	1087	4932	3125	1322	0.50	−0.472	
R15	3 REVs	ACCURATE	10^{-20}	10^{-17}	10^{-12}	BASELINE	2190	1241	3482	4861	2043	4494	0.30	−0.327	46, 47, 48
R16			10^{-20}	10^{-18}	10^{-12}		2213	1245	3272	5399	2082	4426	0.80	−0.356	
R17			10^{-20}	10^{-19}	10^{-12}		2680	1260	3973	7024	1997	5213	1.10	−0.324	
R18			10^{-20}	10^{-20}	10^{-12}		3126	1574	5177	6483	2095	6483	1.40	−0.269	
R19			10^{-20}	10^{-21}	10^{-12}		3582	2039	5864	7183	2571	7183	1.50	−0.148	

7526/80

results. Similarly, drag process noise values of 10^{-12} per second and 10^{-14} per second produce identical results. A clock drift process noise rate of 10^{-24} sec^2/sec^3 produced the smallest errors, which were about 50 percent larger than those in the two-way delta-range case. In addition, a longer processing time, i.e., about 15 hours, was required to achieve a steady-state solution than was required in the two-way cases.

5.3.2 VARIATION OF CONTACT FREQUENCY

Runs R10 through R14 and R15 through R19 were run with contact frequencies of two and three revolutions, respectively. In the two-revolution case, a clock drift process noise covariance rate of 10^{-19} sec^2/sec^3 produced the smallest error, which was about 5 times larger than that in the 1-revolution 1-way case and 10 times larger than that in the 2-revolution 2-way case. Inspection of the corresponding along-track error graph (Figure B-45) indicates a bias of about 700 meters in the steady-state solution. In the 3-revolution case, a clock drift process noise rate of 10^{-17} to 10^{-18} sec^2/sec^3 produces the best solution, with errors 15 times larger than those in the 1-revolution case. In addition, significantly larger errors in the clock drift and ρ_1 estimates were obtained. Inspection of the corresponding along-track error graph (Figure B-48) indicates that the EKF may not have reached a steady-state solution in this case. This result may indicate that more tracking data are required to achieve a reasonable level of accuracy.

5.3.3 BASELINE RUNS WITH NASA STANDARD TRANSPONDER MODEL

Table 5-4 summarizes the runs that were made to investigate the EKF's performance using the NASA transponder model as a frequency standard. The best solution was

Table 5-4. GRO Estimation Using One-Way Delta-Range Data With NASA Transponder Model

RUN	CONTACT FREQUENCY (2 TDRSs)	CLOCK MODEL	PROCESS NOISE			rms POSITION DIFFERENCE (m)			MAXIMUM POSITION DIFFERENCE (m)			$\Delta\dot{b}$ (10^{-9}) (sec/sec)	ρ_1	FIGURE NUMBER (B-)
			STATE (km^2/sec^3)	CLOCK DRIFT (sec^2/sec^3)	DRAG (sec^{-1})	0^h-24^h	9^h-12^h	21^h-24^h	0^h-24^h	9^h-12^h	21^h-24^h	24^h		
S1	1 REV	NASA TRANSPONDER	10^{-18}	10^{-14}	10^{-12}	8029	11,272	3833	12,479	12,479	4708	0.4	-0.02	
S2			10^{-18}	10^{-16}	10^{-10}	7289	8,701	1062	14,820	12,343	2530	0.4	-0.087	
S3			10^{-18}	10^{-16}	10^{-12}	7289	8,701	1062	14,820	12,343	2530	0.4	-0.087	49, 50, 51
S4			10^{-18}	10^{-16}	10^{-14}	7289	8,701	1062	14,820	12,343	2530	0.4	-0.087	
S5			10^{-18}	10^{-18}	10^{-12}	7729	8,855	2943	17,402	12,452	5078	0.3	-0.417	

7526/80

obtained using a state process noise of 10^{-18} km^2/sec^2 and a clock drift process noise of 10^{-16} sec^2/sec^3. The solutions did not appear to be sensitive to the value for the drag process noise. The best solution has an error after 21 hours of processing that is about six times larger than that obtained using data simulated with the accurate clock model. Inspection of the corresponding error plots indicates that the EKF may not have converged to a steady-state solution after 24 hours of processing.

5.4 ANOMALOUS DATA CASES

To assess the impact on the EKF's performance of processing a pass of data with large time-varying range and delta-range measurement errors, data set 1 in Table 5-5 was substituted for the TDRS-W data that occur at 13 hours in the baseline one-revolution data set (see Figure 5-1). This pass occurs 1 hour after the minimum in the sinusoidal ephemeris error model for TDRS-W, resulting in an approximate range error of 5 kilometers. The delta-range error of 500 centimeters is due primarily to the along-track rate. Runs T1 and T2 in Table 5-6 correspond to performing this simulation using two-way range and delta-range and two-way delta-range, respectively. A 500-sigma edit test was used for both cases. Comparison with the baseline simulations P12 and Q5 shows essentially no increase in the error in the steady-state solution. Inspection of Figures B-52 through B-57 shows some increase in error at 13 hours, when the anomalous data are processed.

Run T3 corresponds to a simulation in which the effect of one pass of data with a large delta-range measurement bias was studied. Data set 2 with a delta-range bias of 200 centimeters was substituted for a nominal pass of

Table 5-5. Anomalous Data Sets for GRO

PARAMETER	VALUE		
	DATA SET 1	DATA SET 2	DATA SET 3
TIME OF DATA	$13^h - 13^h10^m$	$13^h - 13^h10^m$	
TDRS EPHEMERIS ERRORS			
H	1.8 km	180 m	
C	1.8 km	180 m	
L	31.2 km	3.12 km	
RANGE BIAS (m)			
TDRS-W	−40	−40	
DELTA-RANGE BIAS (cm)	0	200	
RANDOM RANGE ERROR (m)	10	10	
RANDOM DELTA-RANGE ERROR (cm)	10	10	
DELETED DATA PASSES			$4^h55^m - 5^h5m$ $11^h40^m - 11^h50^m$ $17^h40^m - 17^h50^m$

7526/80

Table 5-6. GRO Estimation Using Anomalous Data Sets

RUN	DATA TYPE	CONTACT FREQUENCY (2 TDRSs)	PROCESS NOISE		ANOMALOUS DATA SET	ANOMALOUS DATA EDITED	rms POSITION DIFFERENCE (m)			MAXIMUM POSITION DIFFERENCE (m)			μ_1	FIGURE NUMBER (8–)
			STATE (km^2/sec^3)	DRAG (sec^2/sec^3)			0^h-24^h	9^h-12^h	21^h-24^h	0^h-24^h	9^h-12^h	21^h-24^h		
T1	TWO-WAY R AND ΔR	1 REV	10^{-18}	10^{-12}	1	27 Δμ	335	141	70	1492	235	118	-0.502	52, 53, 54
T2	TWO-WAY ΔR	1 REV	10^{-18}	10^{-12}	1	30 Δμ	333	162	120	1583	248	202	-0.470	55, 56, 57
T3	TWO-WAY ΔR	1 REV	10^{-18}	10^{-12}	2	7 Δμ	392	162	226	1583	248	379	-0.474	58, 59, 60
T4	TWO-WAY R AND ΔR	1 REV	10^{-18}	10^{-12}	3		367	151	53	1492	276	94	-0.475	61, 62, 63
T5	TWO-WAY ΔR	1 REV	10^{-18}	10^{-12}	3		360	124	45	1583	203	76	-0.478	64, 65, 66

7526/80

data. This data set was not edited and resulted in a significant increase in the solution error 7 hours later.

The effect of losing or deleting a pass of data was simulated in runs T4 and T5. Data set 3, in which the 4th, 8th, and 16th passes were deleted from the baseline 1-revolution case, was used. These results do not indicate any significant increase in the error in the solution.

Several runs were also made processing one-way data that was simulated with sinusoidal clock bias errors in addition to the accurate quadratic clock model (see Equation (2-8)). The sinusoidal clock bias errors also produce a sinusoidal bias in the delta-range data that is given by Equation (2-9). The frequency of the errors was equal to the orbital frequency of GRO. The amplitudes were chosen such that a_1 ranges from 2×10^{-7} to 2×10^{-6} seconds and a_2 is zero. These values produce an amplitude in the delta-range bias of between 60 and 600 centimeters. Table 5-7 summarizes the results from these runs.

Comparison with run R8 indicates that a 60-centimeter bias amplitude, which is equal to 0.1 percent of the bias caused by the clock drift ($\dot{b}$), does not produce any degradation. An amplitude as large as 600 centimeters produces about a 100-percent increase in the solution error after 21 hours of processing. In run T9, the measurement standard deviation was increased to 200 centimeters to account for the sinusoidal measurement bias produced by the clock error. In run T10 the clock drift process noise covariance rate was increased to 10^{-22} sec^2/sec^3. Comparison of run T10 with run R8 indicates that after 21 hours of processing, the effect of the sinsuoidal clock error is essentially eliminated. Run T11 also demonstrates a significant improvement in the overall solution

Table 5-7. GRO Estimation Using One-Way Data With Sinusoidal Error Model

RUN	CLOCK MODEL	SINUSOIDAL DELTA-RANGE BIAS AMPLITUDE (cm)	$\sigma_{\Delta R}$ IN FILTER (cm)	CONTACT FREQUENCY (2 TDRSs)	PROCESS NOISE		DRAG (sec^{-1})	rms POSITION DIFFERENCE (m)			MAXIMUM POSITION DIFFERENCE (m)			$\Delta\dot{\nu}$ (10^{-9}) (sec/sec)	ρ_1	FIGURE NUMBER (B-)
					STATE (km^2/sec^3)	CLOCK DRIFT (sec^2/sec^3)		0^h-24^h	9^h-12^h	21^h-24^h	0^h-24^h	9^h-12^h	21^h-24^h			
T6	ACCURATE	60	10	1 REV	10^{-18}	10^{-24}	10^{-12}	526	187	109	2589	354	170	0.04	0.475	
T7	ACCURATE	300	10	1 REV	10^{-18}	10^{-24}	10^{-12}	921	584	110	4367	1118	187	0.7	0.464	67, 68, 69
T8	ACCURATE	600	10	1 REV	10^{-18}	10^{-24}	10^{-12}	1513	1383	237	6639	2560	511	0.5	0.448	
T9	ACCURATE	300	200	1 REV	10^{-18}	10^{-24}	10^{-12}	447	490	304	1105	969	474	1.0	0.444	
T10	ACCURATE	300	200	1 REV	10^{-18}	10^{-22}	10^{-12}	429	511	97	1065	967	105	0.6	0.461	70, 71, 72
T11	ACCURATE	600	400	1 REV	10^{-18}	10^{-22}	10^{-12}	730	1032	210	1683	1610	350	1.0	0.438	73, 74, 75

7526/80

accuracy using the larger measurement standard deviation and clock drift process noise covariance rate.

SECTION 6 - CONCLUSIONS

This section discusses conclusions resulting from comparison of the EKF's performance characteristics when processing two-way range and delta-range data, two-way delta-range data, and one-way delta-range data for estimation of the orbits of Landsat-D and GRO. Comparisons are made with respect to (1) accuracy in the baseline one-contact-per-revolution case, (2) effect of varying contact frequency, (3) effect of increased TDRS ephemeris errors, and (4) accuracy in the presence of anomalous or deleted data set cases.

6.1 LANDSAT-D ESTIMATION

Table 6-1 summarizes the simultations that produced the most accurate Landsat-D orbital estimates after 24 hours of processing. Comparison of these results yields the following general conclusions:

- Baseline performance--For the baseline one-contact-per-revolution case, both two-way data sets (B5 and H3) yield comparable solutions with rms differences of 50 meters and maximum differences of 100 meters during the last 3 hours of processing. Using the one-way data simulated with an accurate clock model requires about 15 hours to achieve a steady-state solution with rms differences of 90 meters and maximum differences of 170 meters as compared to about two contacts or 3 hours for the two-way data cases. This longer processing time probably indicates that additional processing is required to decouple the state corrections from clock drift corrections.

- Performance with reduced tracking--Comparison of tne two- and three-contact-per-revolution cases indicates that in the case of two-way data, accuracies comparable to

Table 6-1. Best Landsat-D Estimate After 24 Hours of Processing

RUN	DATA TYPE	CONTACT FREQUENCY (2 TDRSs)	USER-CLOCK MODEL	PROCESS NOISE		rms POSITION DIFFERENCE (m)			MAXIMUM POSITION DIFFERENCE (m)			CLOCK DRIFT ERROR (10^{-9}) (sec/sec)	FIGURE NUMBER (A-)
				STATE (km^2/sec^3)	CLOCK DRIFT (sec^2/sec^3)	0^h-24^h	9^h-12^h	21^h-24^h	0^h-24^h	9^h-12^h	21^h-24^h	24^h	
B5	TWO-WAY R AND ΔR	1 REV	NO ERROR	10^{-20}		549	78	41	2,549	130	65		7, 8, 9
C5		2 REVs		10^{-22}		886	69	39	4,304	99	55		10, 11, 12
D2		3 REVs		10^{-16}		1790	83	73	6,517	162	119		13, 14, 15
H3	TWO-WAY ΔR	1 REV	NO ERROR	10^{-18}		353	66	49	2,549	95	82		31, 32, 33
I6		2 REVs		10^{-20}		578	78	39	2,549	117	58		34, 35, 36
J3		3 REVs		10^{-20}		922	327	84	3,280	671	126		37, 38, 39
M4	ONE-WAY ΔR	1 REV	ACCURATE	10^{-14}	10^{-20}	401	282	87	2,549	418	169	0.16	55, 56, 57
M14		2 REVs	ACCURATE	10^{-14}	10^{-23}	416	296	146	2,549	466	240	0.05	61, 62, 63
M26		3 REVs	ACCURATE	10^{-14}	10^{-23}	603	290	311	2,549	389	439	1.3	64, 65, 66
N6	ONE-WAY ΔR	1 REV	NASA TRANSPONDER	10^{-16}	10^{-16}	5485	4688	1136	14,378	7666	1986	5.0	70, 71, 72
N14		1 REV	NASA TRANSPONDER (b ESTIMATED)	10^{-18}	0	501	110	47	2,772	190	92	0.016	73, 74, 75

7526/80

those achieved in the one-revolution case are achieved for both the two- and three-contact-per-revolution cases (C4, D2, I6, and J3). For two-way delta-range data, the initial transients have smaller amplitudes than those in the comparable range and delta-range case, but the three-revolution case requires more processing (i.e., three contacts) to achieve a steady-state solution. In the one-way cases simulated with an accurate clock (M14 and M24), the solutions demonstrate comparable performance to the two-way delta-range cases in processing the first contact but do not achieve as accurate a steady-state solution as is achieved in the one-revolution contact frequency cases.

- TDRS ephemeris errors--Examination of the results presented previously for simulations in which the TDRS ephemeris errors were increased indicates that ephemeris errors with radial and cross-track amplitude of 280 meters (E4, K2, and M31) did not significantly increase the errors obtained in the steady-state solution as compared with the baseline one-revolution cases. Along-track error amplitude of 320 meters (E7, K6, and M32) produce significant increases in the transient deviations for the delta-range-only cases (e.g., 50 to 60 meters at 12 hours); however, these increases essentially disappear after 24 hours of processing. An increase in the along-track error rate to 1000 meters per day did not significantly increase the errors obtained when processing two-way data (E5 and K3); however, in the one-way data case (M33), the error in the steady-state solution was increased by about 30 meters. This increase may result from the high correlation between a user-clock drift rate and an along-track TDRS ephemeris error.

- User-clock errors--Inspection of the results obtained from simulations using the accurate user-clock model (M4) with those using the NASA standard transponder model (N6) shows that the NASA standard transponder produces more than a tenfold increase in the solution errors even after 24 hours of procesing. Estimation of the clock drift rate of the NASA standard transponder model (N14) yields a solution as accurate as that obtained in the two-way data simulations. This demonstrates that it is the inadequacy of the linear clock model rather than the magnitude of the clock drift term that limits the accuracy of the solutions for the poorer clock. Sinusoidal bias errors with amplitudes of 2×10^{-7} seconds (which produce a 60-centimeter oscillation in the delta-range bias), in addition to the accurate quadratic model, approximately doubled the error as compared to the errors obtained using only the quadratic model. An amplitude of 2×10^{-6} seconds produced an approximately tenfold increase in the error.

- Performance with anomalous data--Inspection of the results presented in Table 4-9 (Section 4) indicates that processing one pass of data with anomalously large measurement errors significantly increases the errors during the time of processing the anomalous data. In addition, the errors in the solution as much as 16 hours later remain somewhat larger. Cases in which the data pass was edited (O3) or deleted (O7 and O8) snow no significant degradation in the accuracy of the solution. This result indicates that editing as much as 20 percent of the data is preferable to processing data with large errors. Thus, appropriate EKF editing algorithms should be given further attention.

6.2 GRO ESTIMATION

Table 6-2 summarizes the simulations that produced the most accurate GRO orbital estimates after 24 hours of processing. Comparison of these results yields the following general conclusions:

- Baseline performance--Estimation of an atmospheric drag parameter, ρ_1, was found to significantly increase accuracies obtained in the baseline case. For the one-contact-per-revolution cases, both two-way data sets, P12 and Q5, produced solutions of comparable accuracy with an rms difference of about 80 meters and a maximum difference of 90 and 150 meters, respectively. Using one-way data produced solutions with about twice the error obtained in the two-way cases. All these cases required a longer processing span to achieve an equilibrium solution than was required in the Landsat-D cases.

- Performance with reduced tracking--Comparison of the two- and three-revolution contact frequency simulations indicates that final solutions of accuracies comparable to those achieved in the one-revolution case are achieved with two-way range and delta-range data for both frequencies and with two-way delta-range data only for the two-revolution frequency. Significantly larger errors are obtained in the one-way cases. All cases, except the two-way range and delta-range two-revolution case, still have large errors after 9 hours of processing. These results indicate that these cases require more tracking data to achieve a good solution.

- TDRS ephemeris errors--Inspection of the results presented previously indicate that radial and cross-track TDRS ephemeris errors as large as 280 meters or along-track errors as large as 320 meters do not produce significantly larger errors in the solution using two-way data

Table 6-2. Best GRO Estimate After 24 Hours of Processing

RUN	DATA TYPE	CONTACT FREQUENCY (2 TDRSs)	USER CLOCK MODEL	PROCESS NOISE			rms POSITION DIFFERENCE (m)			MAXIMUM POSITION DIFFERENCE (m)			CLOCK DRIFT ERROR (10^{-9}) (sec/sec)	ρ_1	FIGURE NUMBER (B)
				STATE ($km^2 \cdot sec^3$)	DRAG ($sec^2 \cdot sec^3$)	CLOCK DRIFT (sec^{-1})	0^h - 24^h	9^h - 12^h	21^h - 24^h	0^h - 24^h	9^h - 12^h	21^h - 24^h	24^h		
P12	TWO-WAY R AND ΔR	1 REV	NO ERROR	10^{-18}	10^{-12}		295	141	60	1,463	234	88		0.473	4, 5, 6
P21		2 REVs		10^{-20}	10^{-12}		636	364	127	2,777	631	189		-0.461	7, 8, 9
P24		3 REVs		10^{-16}	10^{-12}		1175	1090	102	3,769	2,048	157		0.444	10, 11, 12
Q5	TWO-WAY ΔR	1 REV	NO ERROR	10^{-18}	10^{-12}		363	160	89	1,702	243	154		-0.472	25, 26, 27
Q9		2 REVs		10^{-18}	10^{-12}		952	1302	98	3,737	2,214	167		-0.485	28, 29, 30
Q13		3 REVs		10^{-20}	10^{-12}		1894	2429	378	5,368	4,530	575		0.468	31, 32, 33
R8	ONE-WAY ΔR	1 REV	ACCURATE	10^{-18}	10^{-12}	10^{-24}	462	306	129	2,144	453	235	0.12	-0.477	40, 41, 42
R11		2 REVs	ACCURATE	10^{-18}	10^{-12}	10^{-19}	1556	1427	680	4,388	2,227	1121	0.18	-0.487	43, 44, 45
R15		3 REVs	ACCURATE	10^{-20}	10^{-12}	10^{-17}	2190	1241	3482	4,861	2,043	4492	0.30	0.327	46, 47, 48
S3	ONE-WAY ΔR	1 REV	NASA TRANSPONDER	10^{-18}	10^{-12}	10^{-17}	7289	8701	1062	14,820	12,343	2530	0.40	0.087	49, 50, 51

7526/81

at a one-revolution contact frequency (P30, P31, Q15, and Q16). However, an increase in the along-track rate to 1 kilometer per day produces solutions biased by about 100 meters. In the three-revolution cases, the increased radial and cross-track errors produce significant increases in the transient errors, but these increases disappear after 21 hours of processing. The increased along-track amplitude does not have a significant effect; the increased along-track rate produces a 50-meter bias in the final solution.

- User-clock errors--The best solutions obtained using one-way data simulated with an accurate clock produced errors that were about 50 percent larger than those in the two-way delta-range case. Using data simulated with the NASA standard transponder model produced a six-fold increase in the error in the solution as compared to that produced using the accurate clock. Sinusoidal bias errors with amplitudes of 2×10^{-7} seconds (which produce a 60-centimeter oscillation in the delta-range bias), in addition to accurate clock timing errors, did not produce any degradation in accuracy. An amplitude of 2×10^{-6} seconds doubled the solution error after 21 hours of processing.

- Performance with anomalous data--Cases in which data were deleted or the anomalous data were edited resulted in essentially no increase in the error in solution. Processing of anomalous data produced large transient errors that decreased as more data were processed.

APPENDIX A - LANDSAT-D ERROR PLOTS

This appendix contains plots of the radial, cross-track, and along-track position differences that were obtained by differencing the "truth" and EKF estimated ephemerides. Table A-1 is an index to this appendix; the run identification numbers are identical to those defined in Section 4 in the tables listed.

Table A-1. Appendix A Index

RUN NUMBER	TABLE REFERENCE	DATA PLOTTED[1]	TIME SPAN	FIGURE NUMBERS (A–)
A1	4–1	ΔR, ΔC, ΔL	0^h–12^h	1, 2, 3
B2	4–1	ΔR, ΔC, ΔL	0^h–24^h	4, 5, 6
B5	4–1	ΔR, ΔC, ΔL	0^h–24^h	7, 8, 9
C5	4–1	ΔR, ΔC, ΔL	0^h–24^h	10, 11, 12
D2	4–1	ΔR, ΔC, ΔL	0^h–24^h	13, 14, 15
E4	4–2	ΔR, ΔC, ΔL	0^h–12^h	16, 17, 18
E5	4–2	ΔR, ΔC, ΔL	0^h–12^h	19, 20, 21
E7	4–2	ΔR, ΔC, ΔL	0^h–12^h	22, 23, 24
F1	4–2	ΔR, ΔC, ΔL	0^h–12^h	25, 26, 27
G1	4–3	ΔR, ΔC, ΔL	0^h–12^h	28, 29, 30
H3	4–3	ΔR, ΔC, ΔL	0^h–24^h	31, 32, 33
I6	4–3	ΔR, ΔC, ΔL	0^h–24^h	34, 35, 36
J3	4–3	ΔR, ΔC, ΔL	0^h–24^h	37, 38, 39
K2	4–4	ΔR, ΔC, ΔL	0^h–12^h	40, 41, 42
K3	4–4	ΔR, ΔC, ΔL	0^h–12^h	43, 44, 45
K6	4–4	ΔR, ΔC, ΔL	0^h–24^h	46, 47, 48
L4	4–4	ΔR, ΔC, ΔL	0^h–24^h	49, 50, 51
M3	4–5	ΔR, ΔC, ΔL	0^h–24^h	52, 53, 54
M4	4–5	ΔR, ΔC, ΔL	0^h–24^h	55, 56, 57
M5	4–5	ΔR, ΔC, ΔL	0^h–24^h	58, 59, 60
M14	4–5	ΔR, ΔC, ΔL	0^h–24^h	61, 62, 63
M26	4–5	ΔR, ΔC, ΔL	0^h–24^h	64, 65, 66
M33	4–5	ΔR, ΔC, ΔL	0^h–24^h	67, 68, 69
N6	4–6	ΔR, ΔC, ΔL	0^h–24^h	70, 71, 72
N14	4–6	ΔR, ΔC, ΔL	0^h–24^h	73, 74, 75
O1	4–9	ΔR, ΔC, ΔL	0^h–24^h	76, 77, 78
O2	4–9	ΔR, ΔC, ΔL	0^h–24^h	79, 80, 81
O3	4–9	ΔR, ΔC, ΔL	0^h–24^h	82, 83, 84
O4	4–9	ΔR, ΔC, ΔL	0^h–24^h	85, 86, 87
O5	4–9	ΔR, ΔC, ΔL	0^h–24^h	88, 89, 90
O6	4–9	ΔR, ΔC, ΔL	0^h–24^h	91, 92, 93
O7	4–9	ΔR, ΔC, ΔL	0^h–24^h	94, 95, 96
O8	4–9	ΔR, ΔC, ΔL	0^h–24^h	97, 98, 99
O10	4–10	ΔR, ΔC, ΔL	0^h–24^h	100, 101, 102
O11	4–10	ΔR, ΔC, ΔL	0^h–24^h	103, 104, 105

7526/80

[1] ΔR = RADIAL POSITION DIFFERENCE; ΔC = CROSS-TRACK POSITION DIFFERENCE; ΔL = ALONG-TRACK POSITION DIFFERENCE.

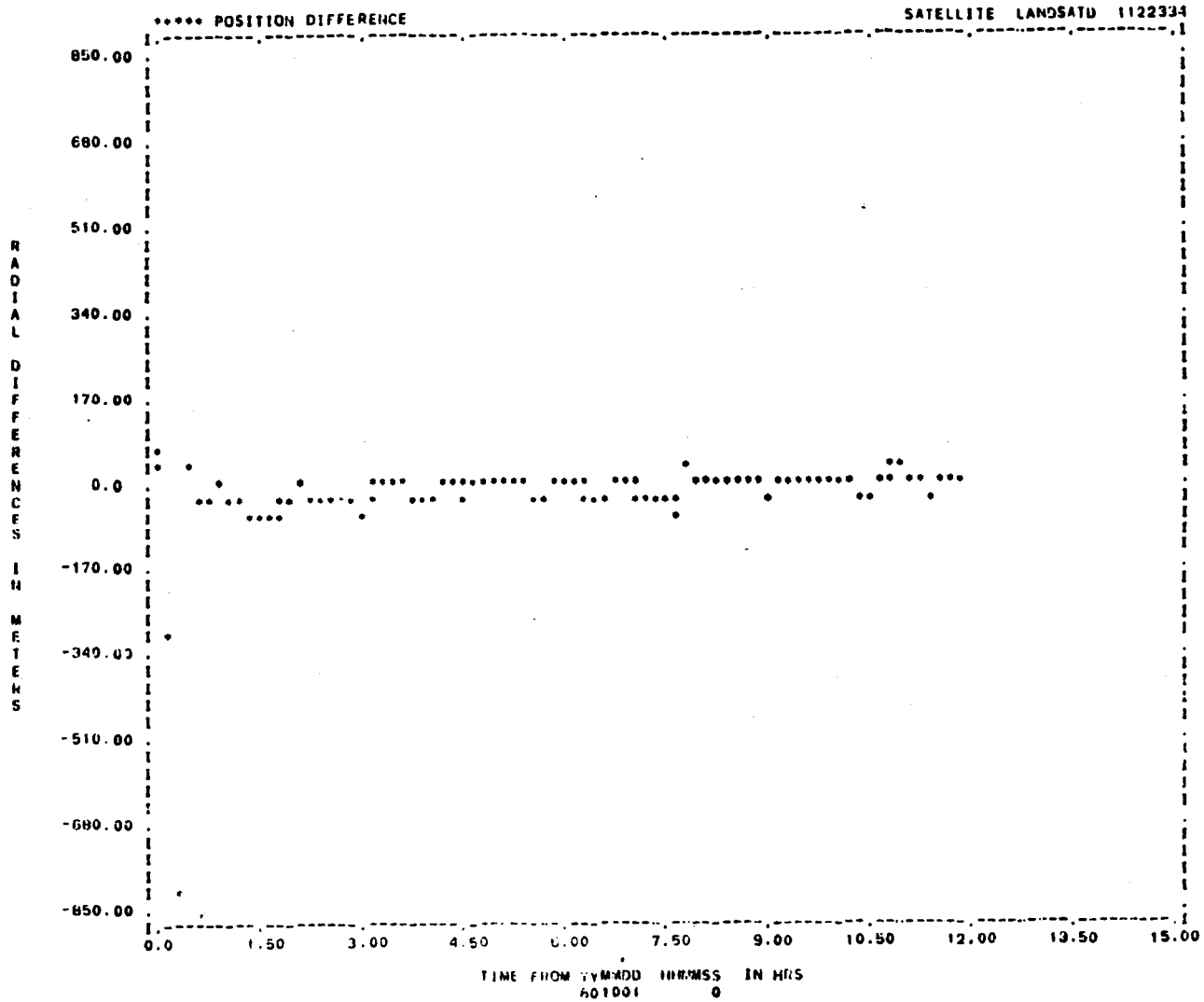

Figure A-1. Radial Differences for Run A1

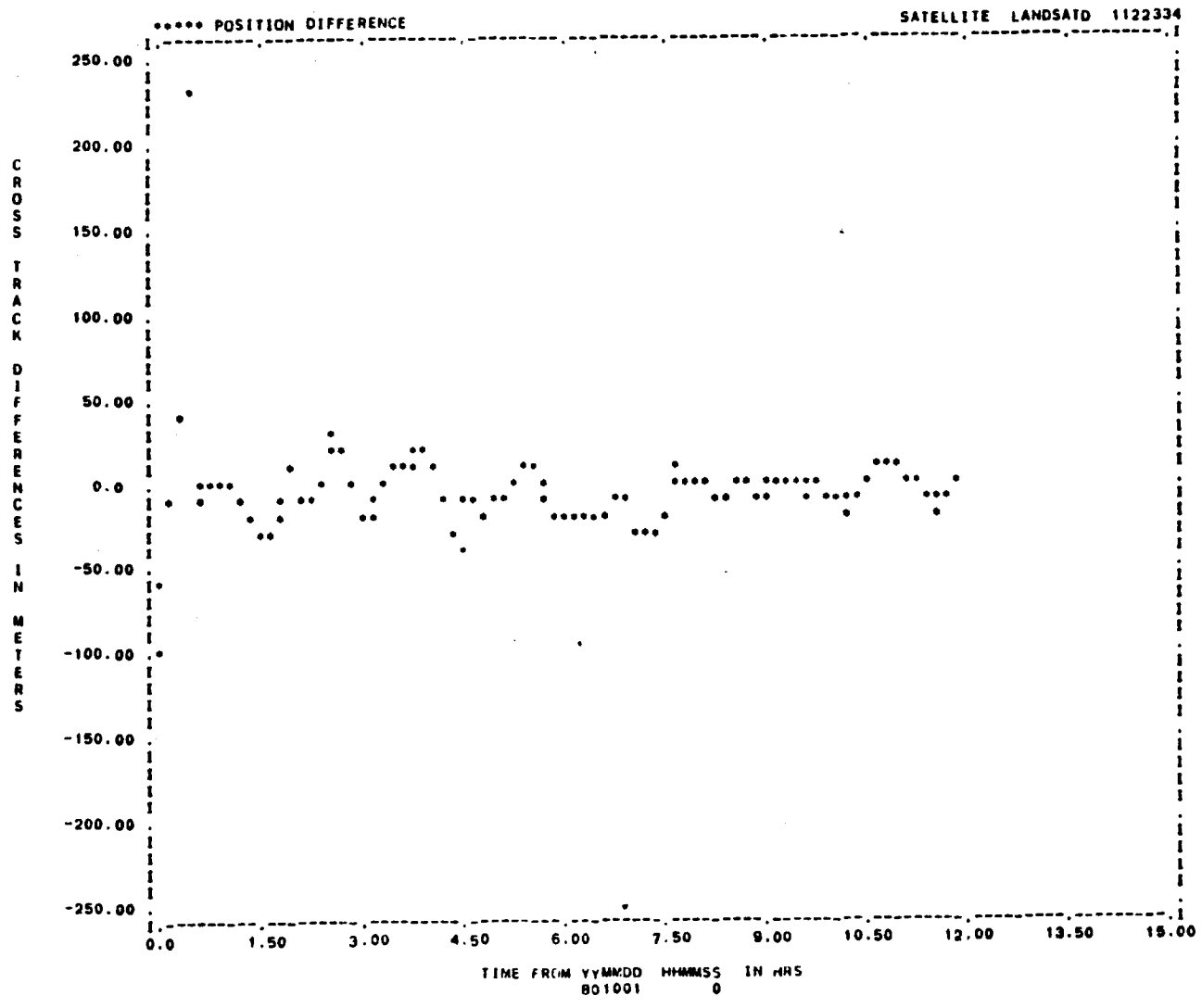

Figure A-2. Cross-Track Differences for Run A1

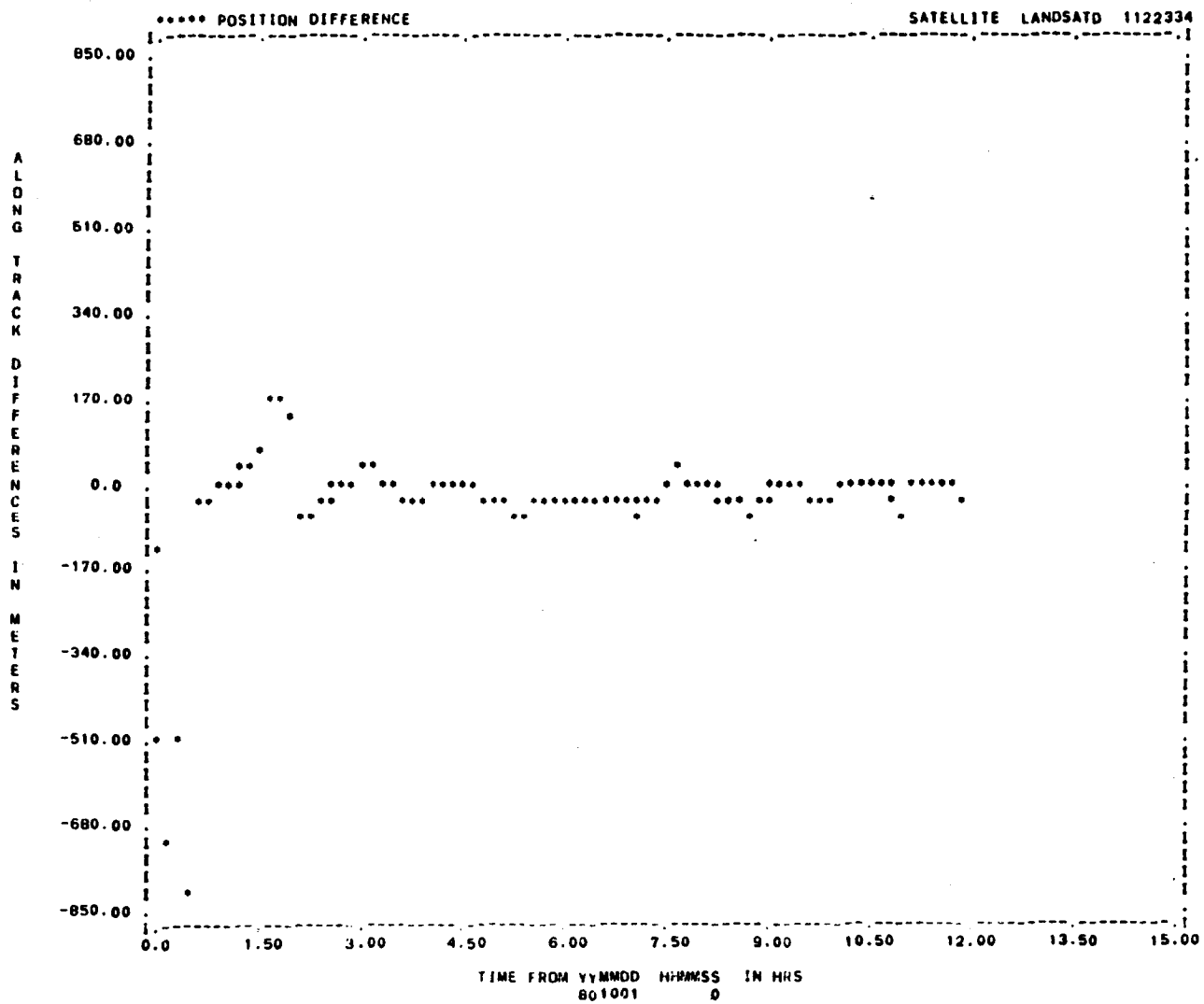

Figure A-3. Along-Track Differences for Run A1

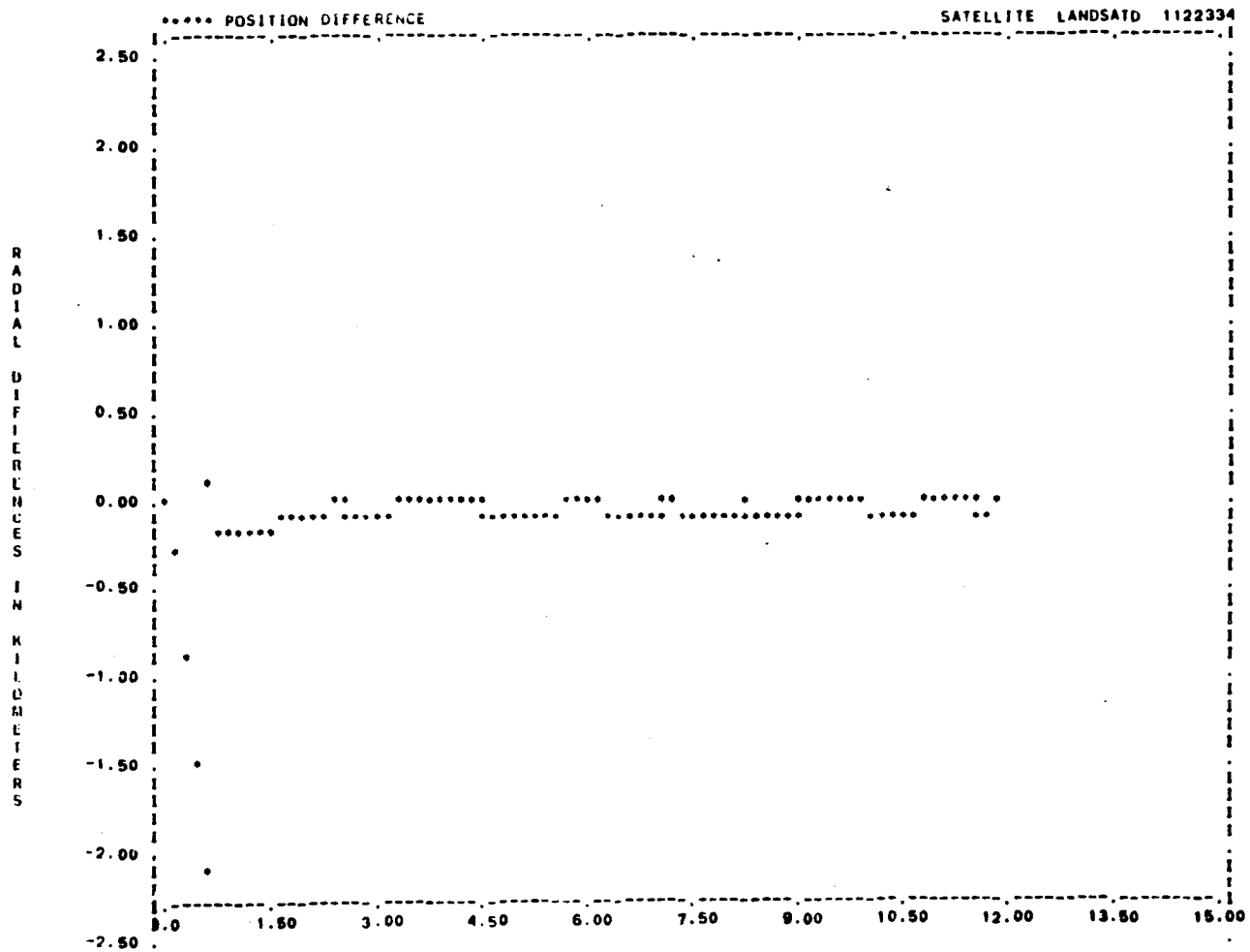

Figure A-4. Radial Differences for Run B2 (1 of 2)

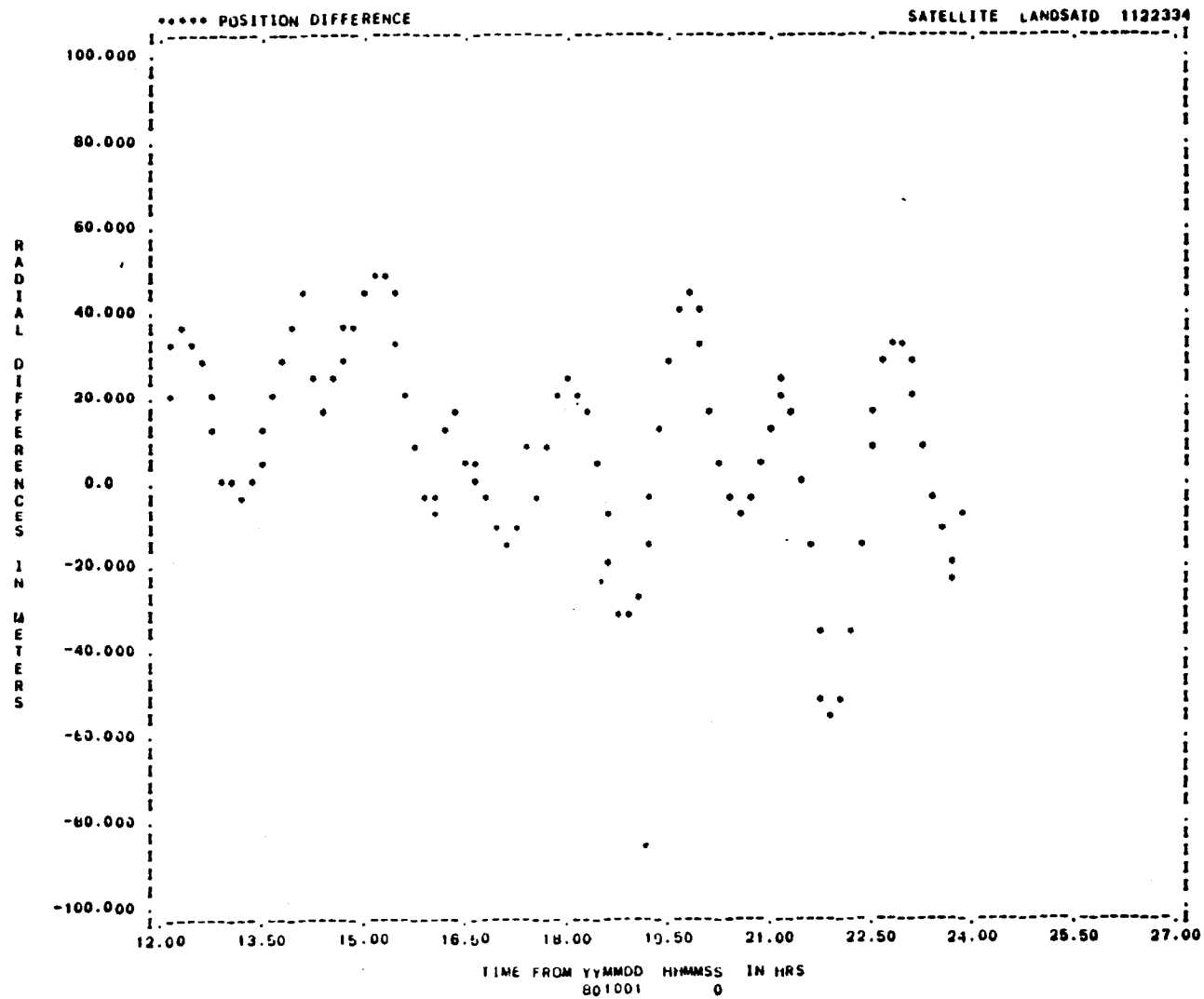

Figure A-4. Radial Differences for Run B2 (2 of 2)

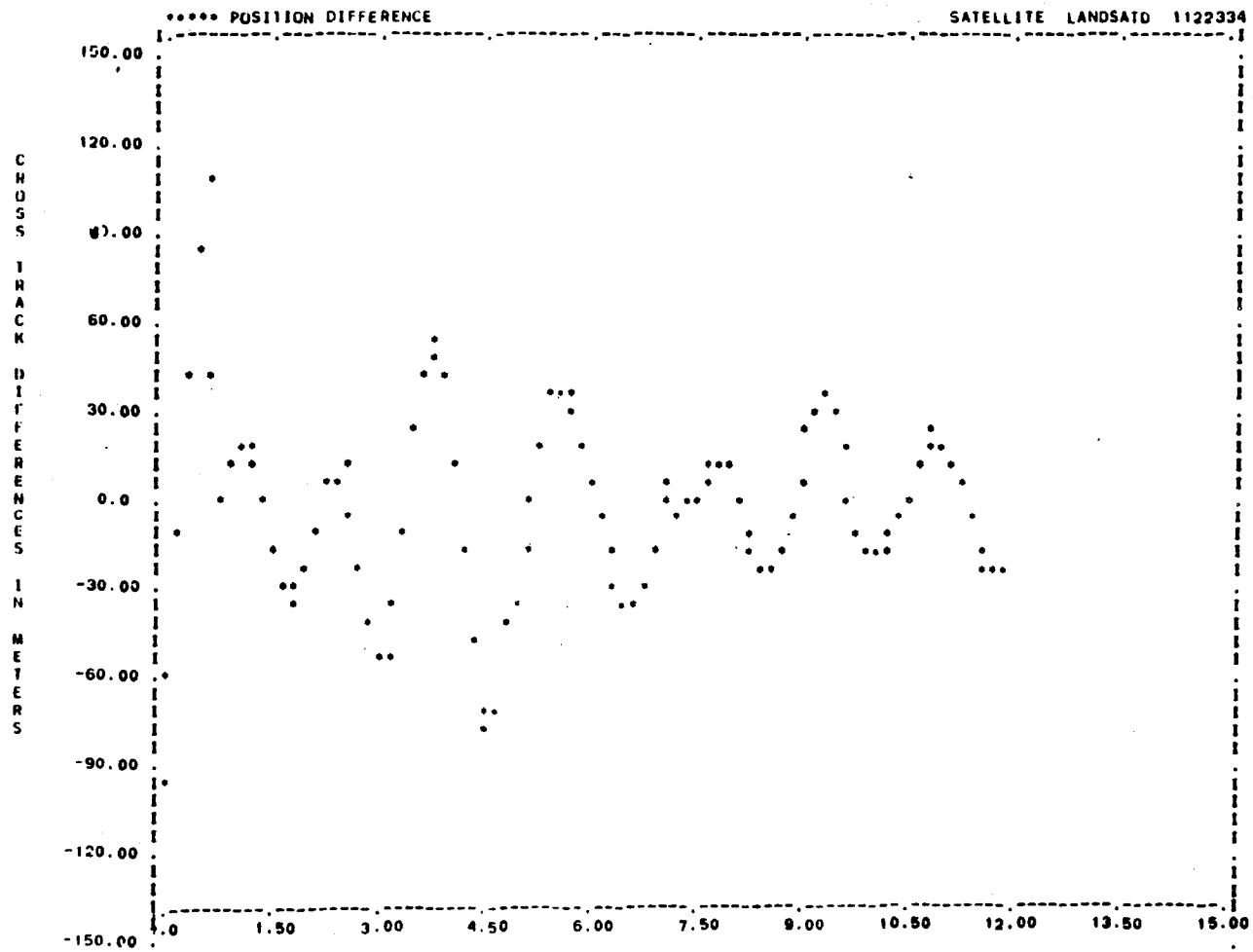

Figure A-5. Cross-Track Differences for Run B2 (1 of 2)

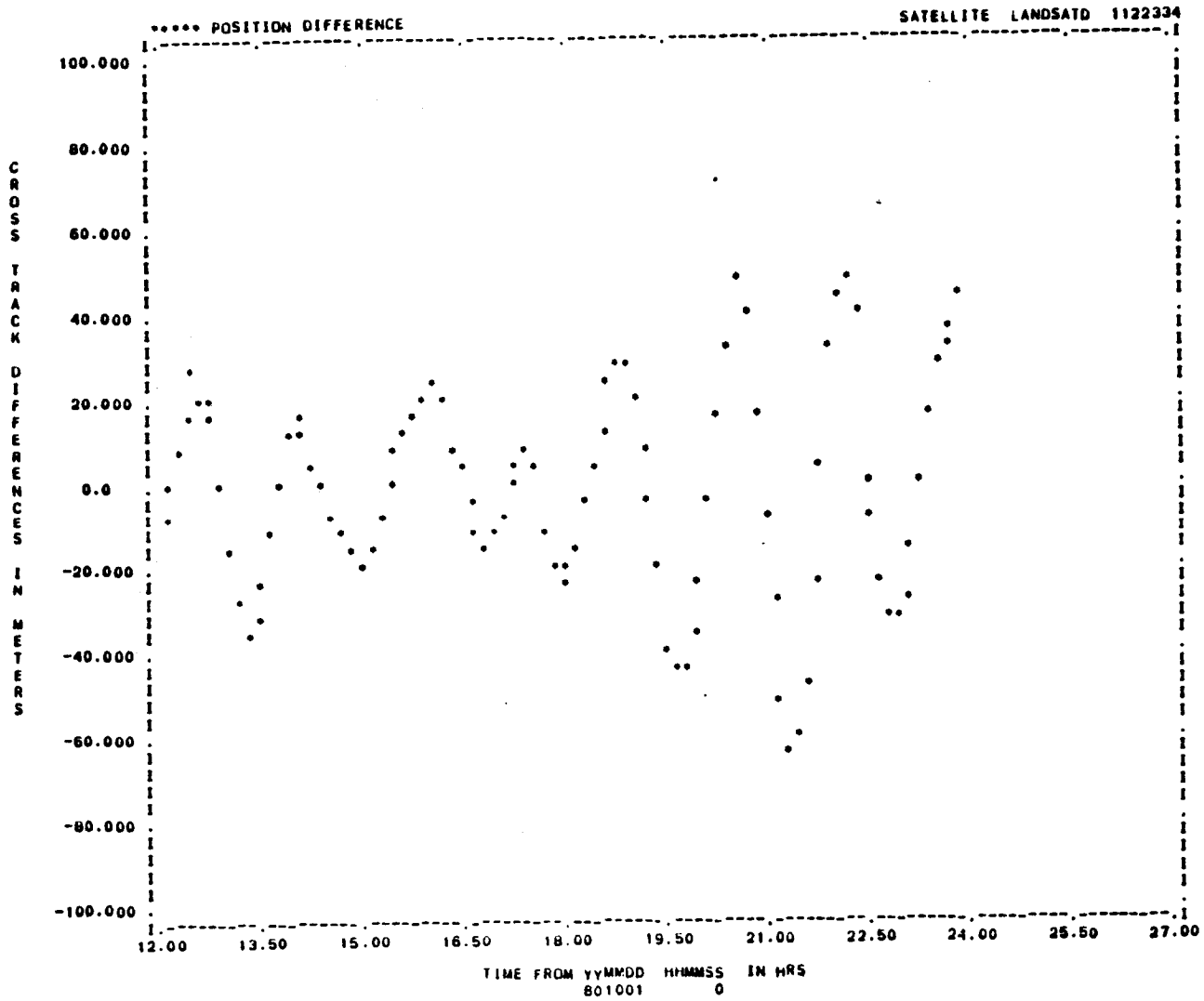

Figure A-5. Cross-Track Differences for Run B2 (2 of 2)

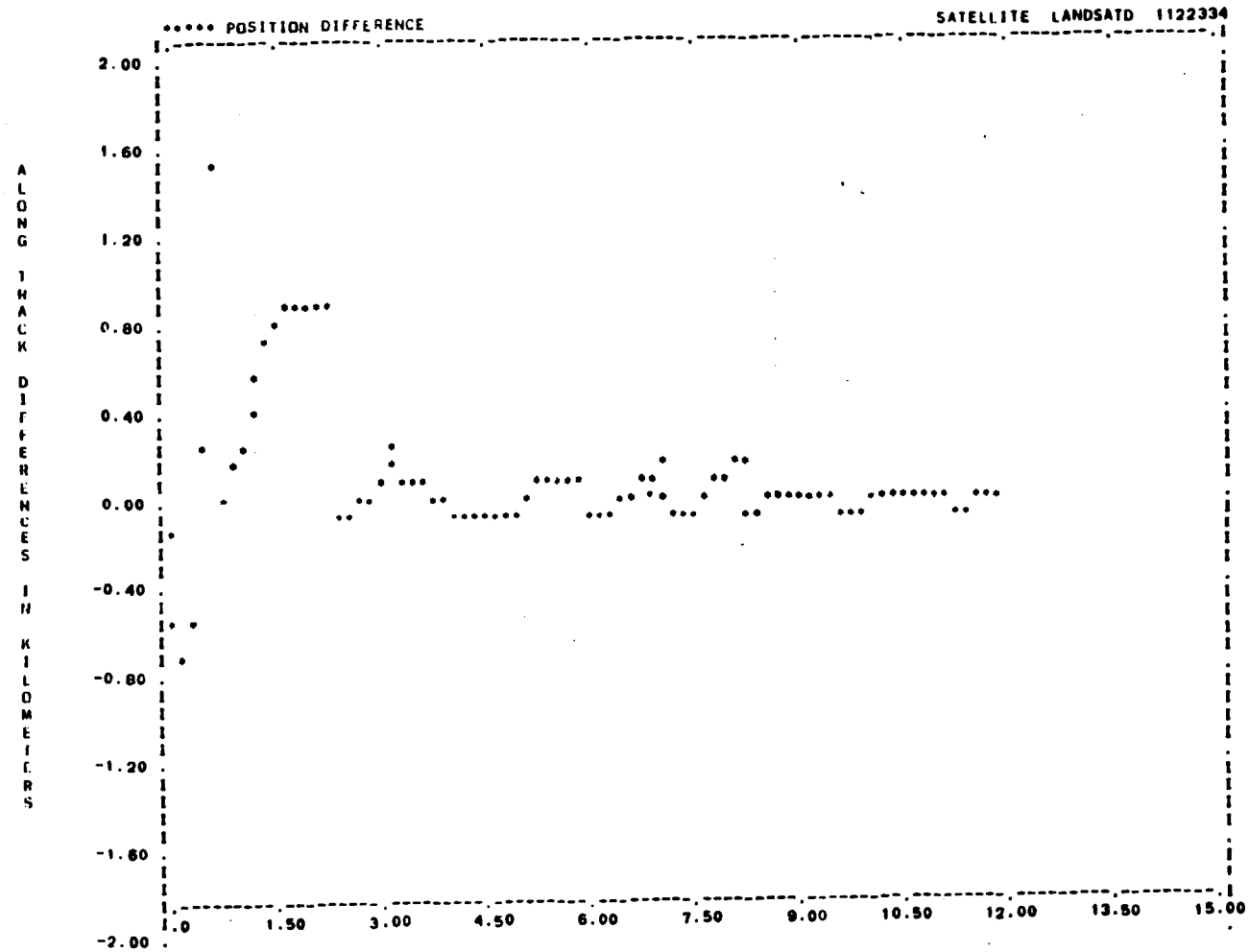

Figure A-6. Along-Track Differences for Run B2 (1 of 2)

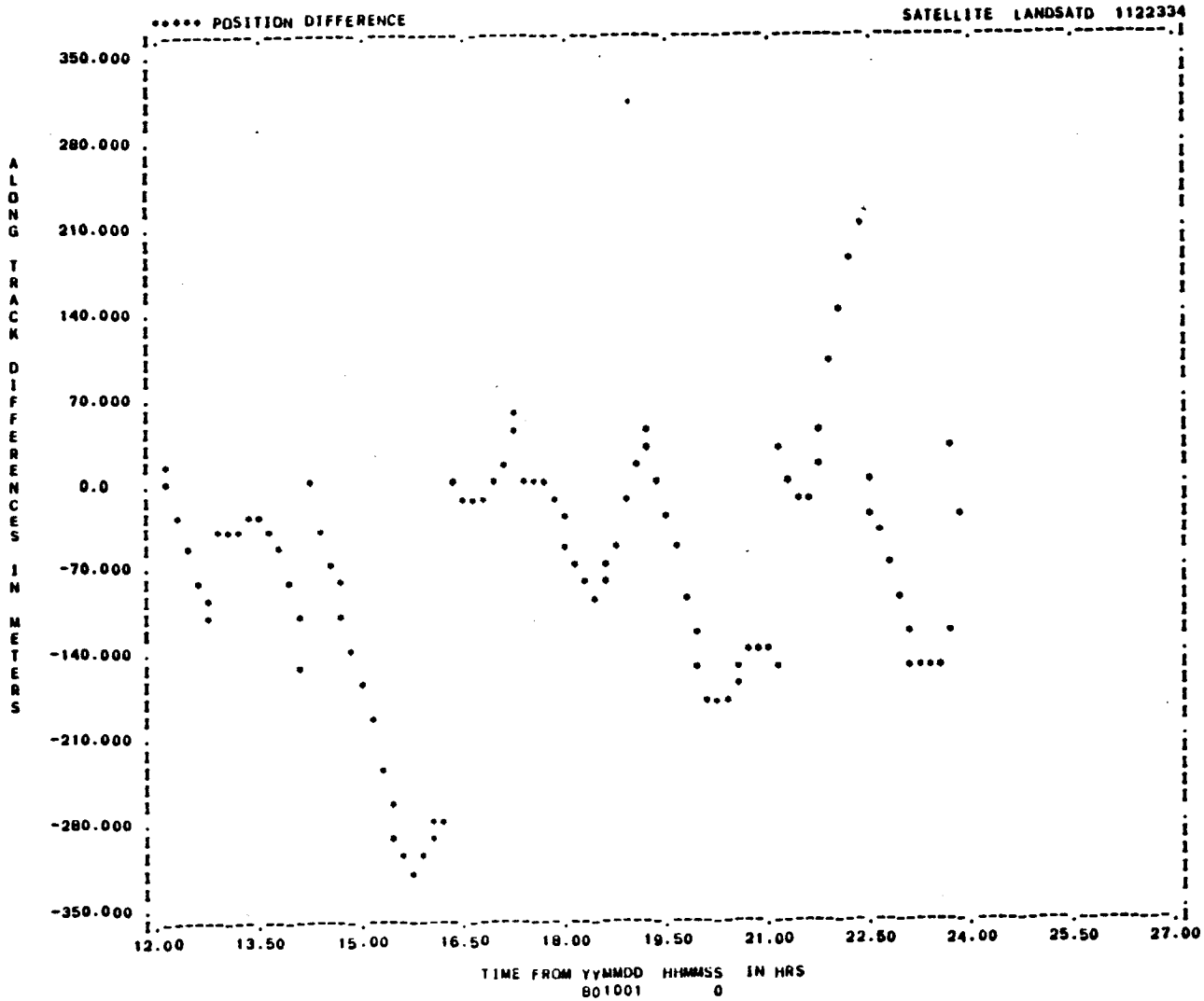

Figure A-6. Along-Track Differences for Run B2 (2 of 2)

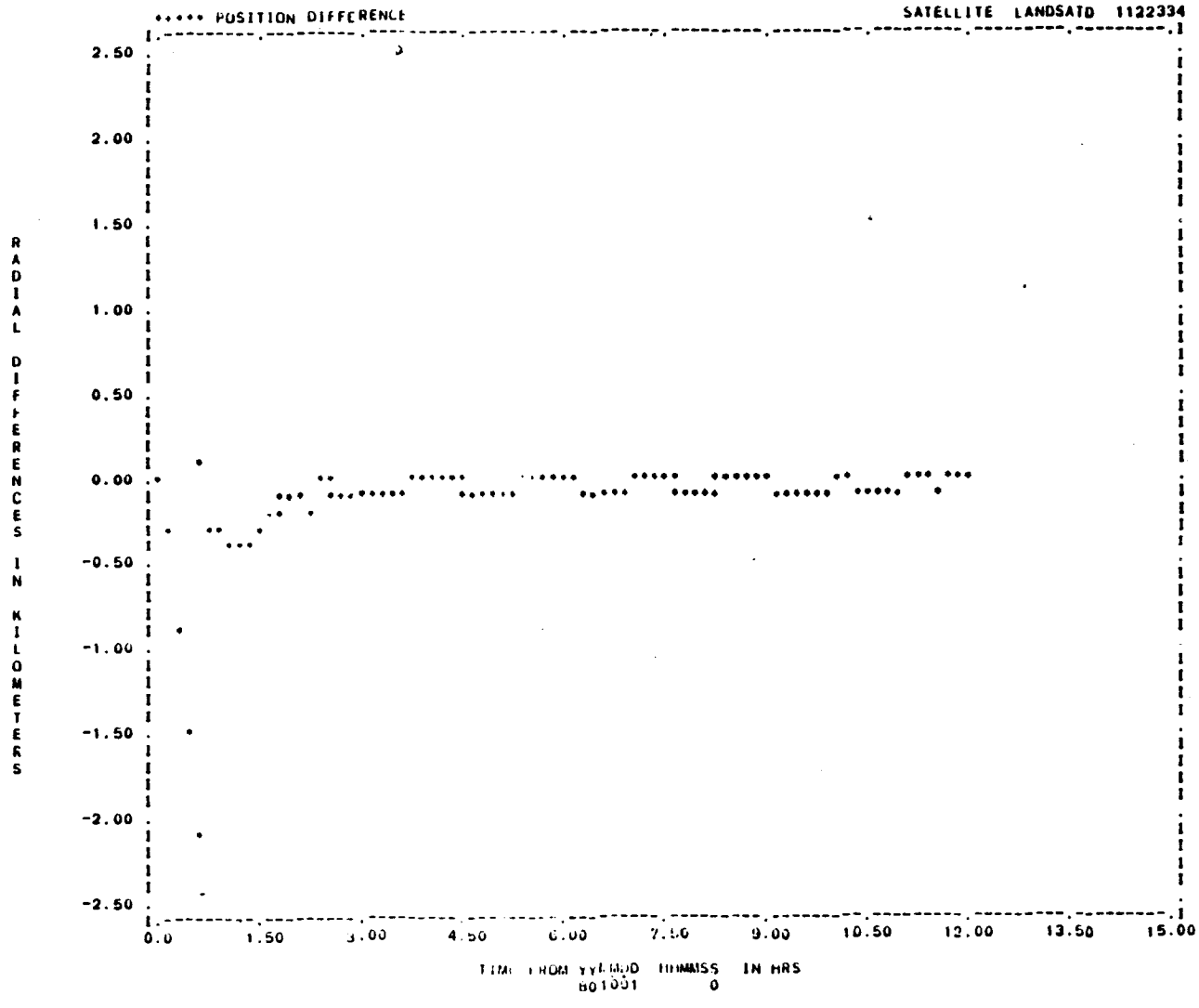

Figure A-7. Radial Differences for Run B5 (1 of 2)

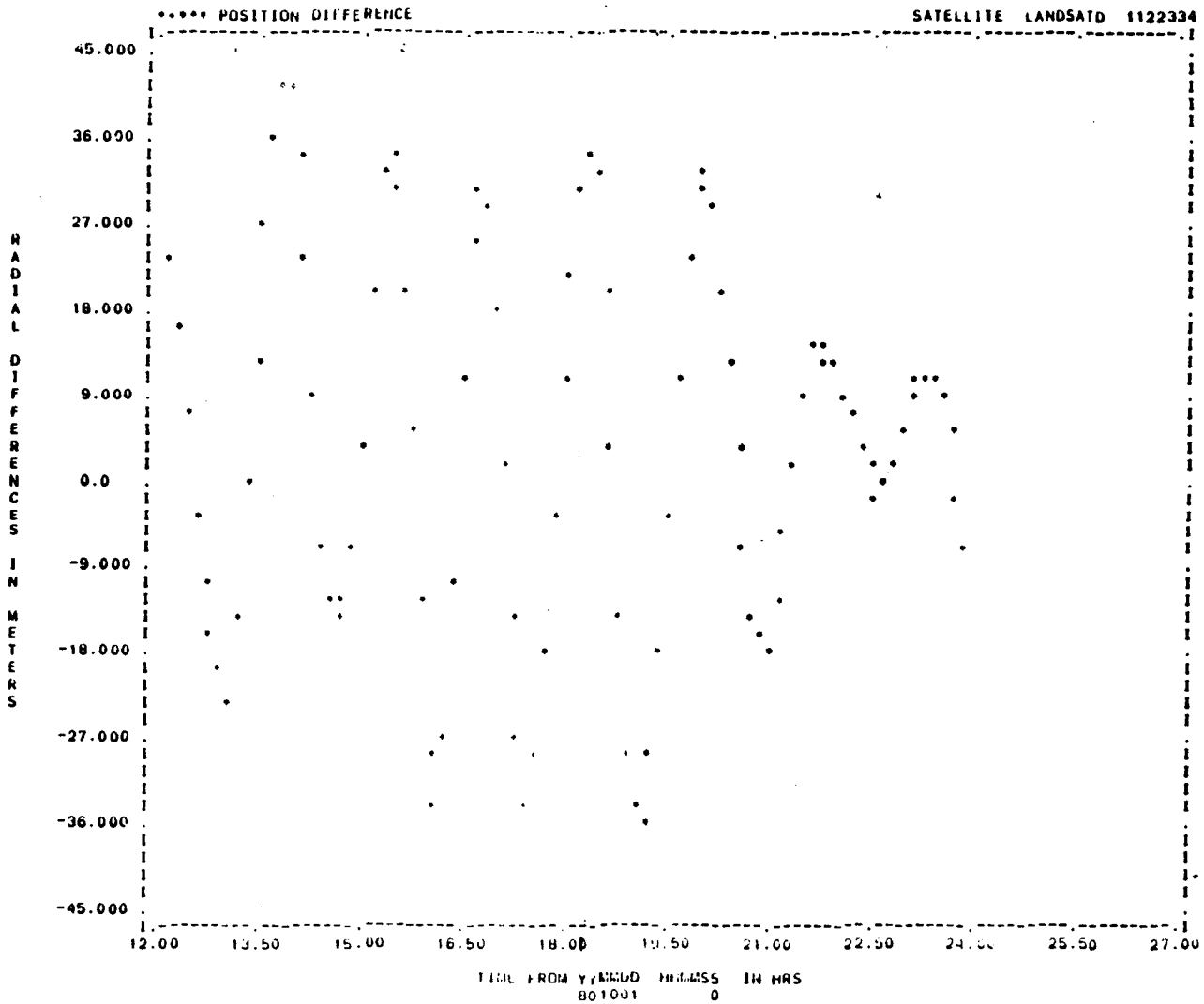

Figure A-7. Radial Differences for Run B5 (2 of 2)

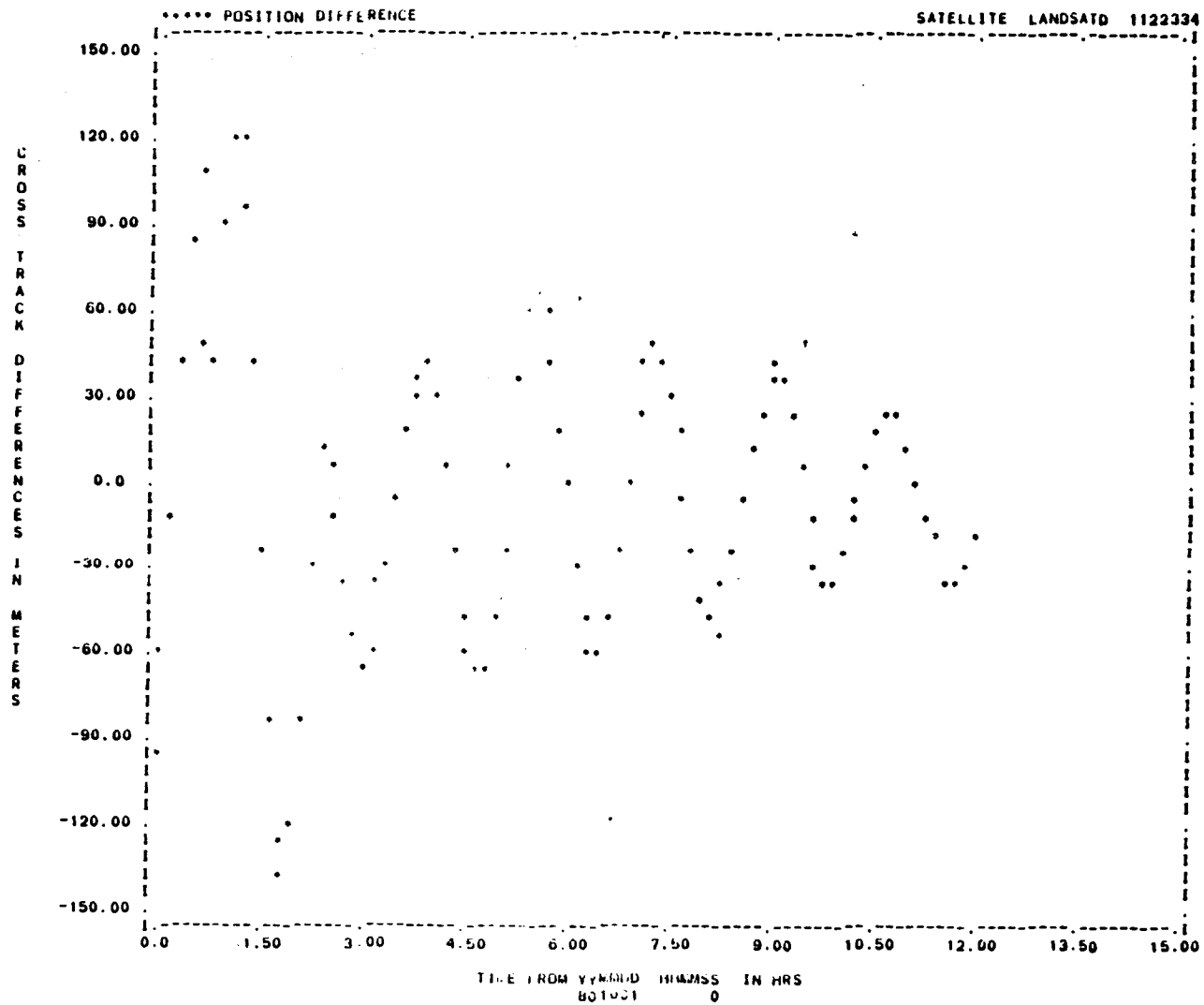

Figure A-8. Cross-Track Differences for Run B5 (1 of 2)

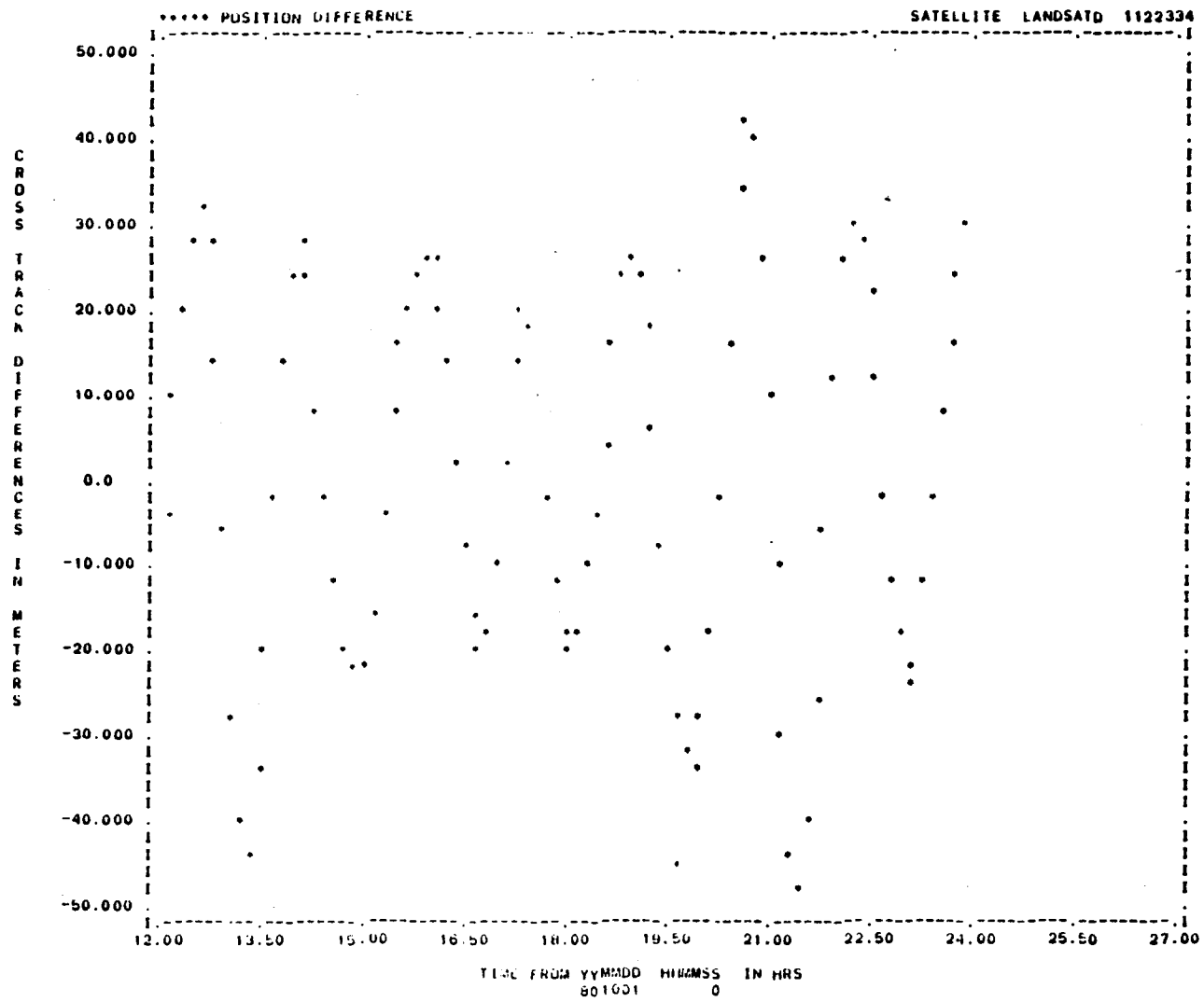

Figure A-8. Cross-Track Differences for Run B5 (2 of 2)

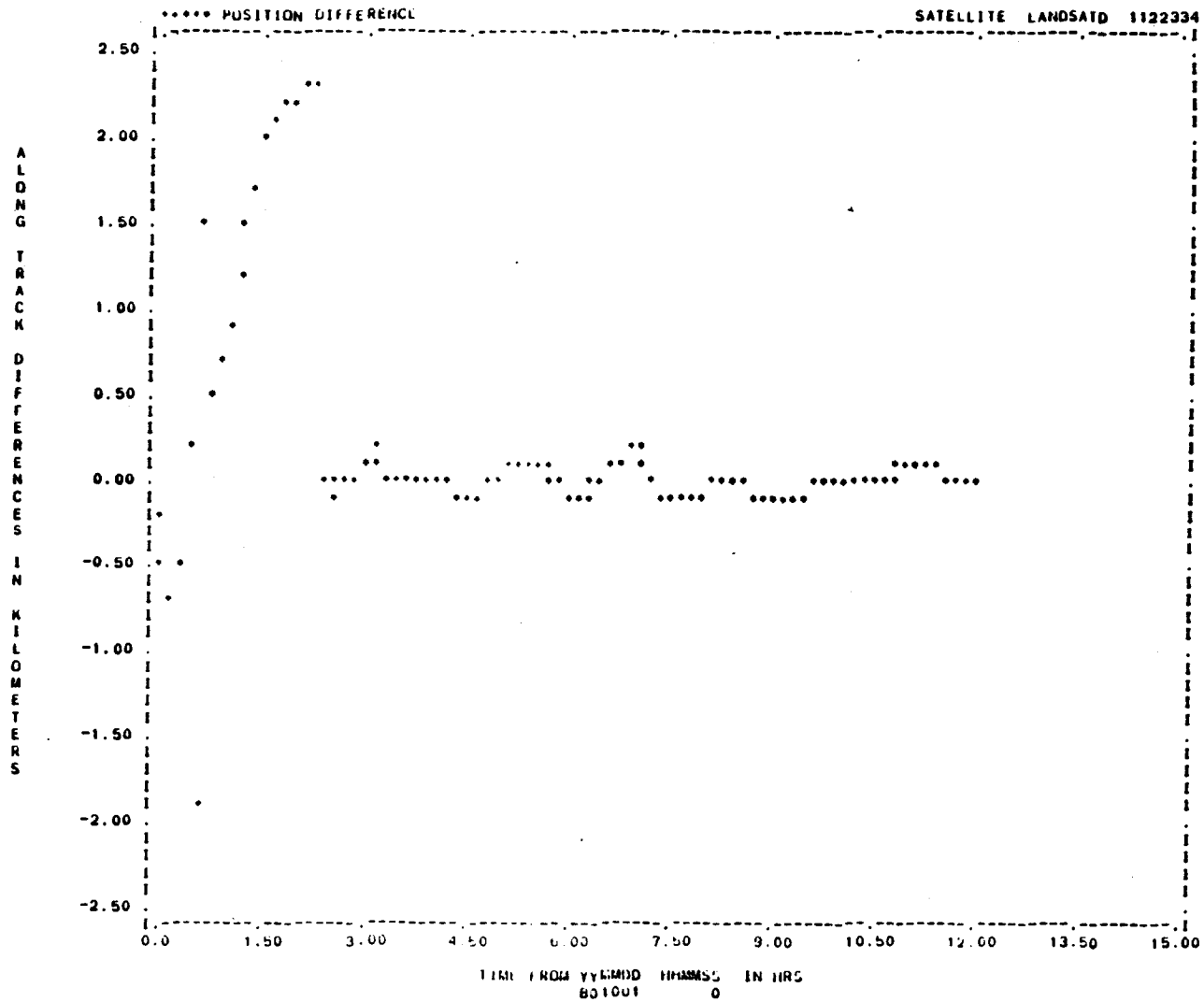

Figure A-9. Along-Track Differences for Run B5 (1 of 2)

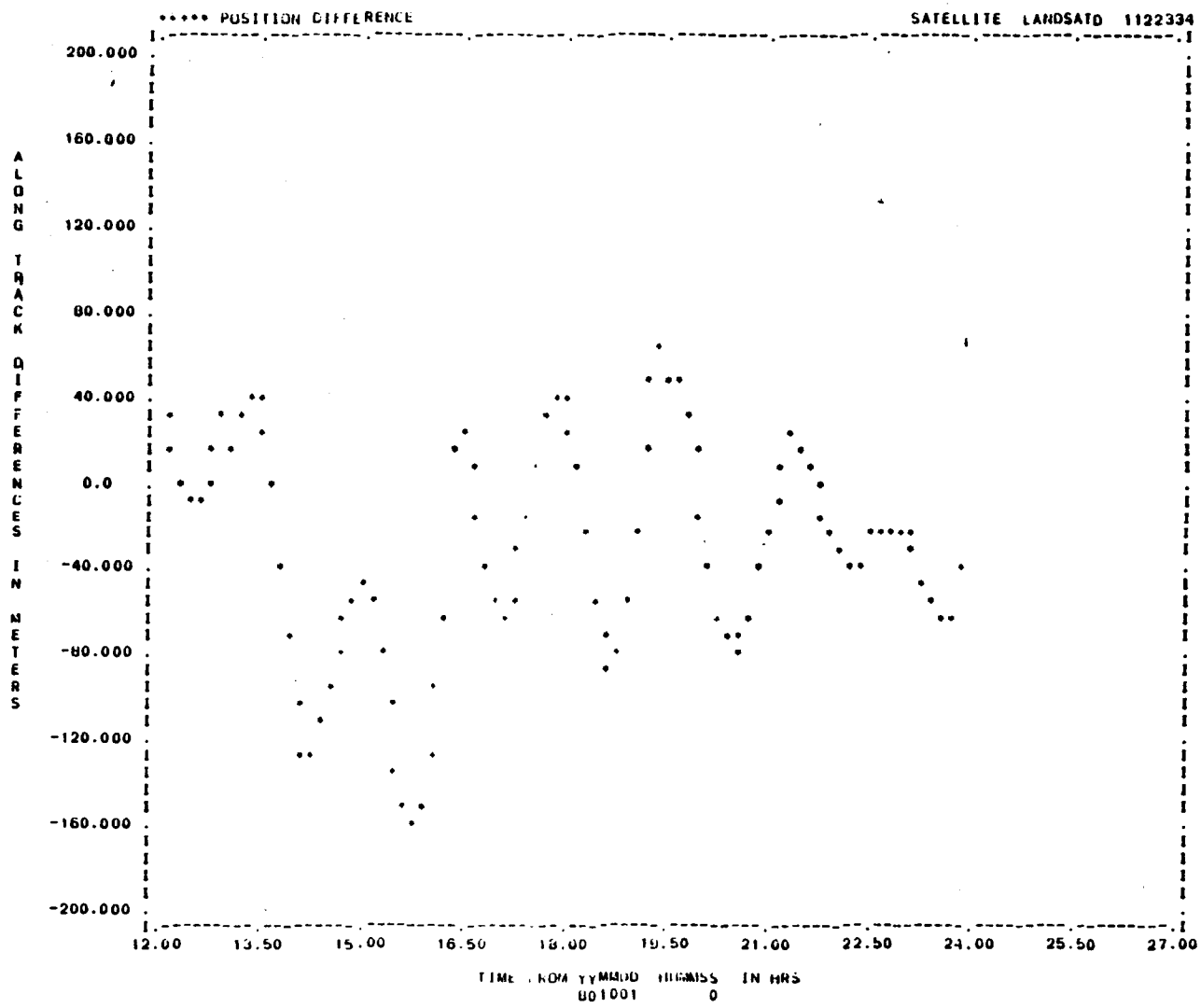

Figure A-9. Along-Track Differences for Run B5 (2 of 2)

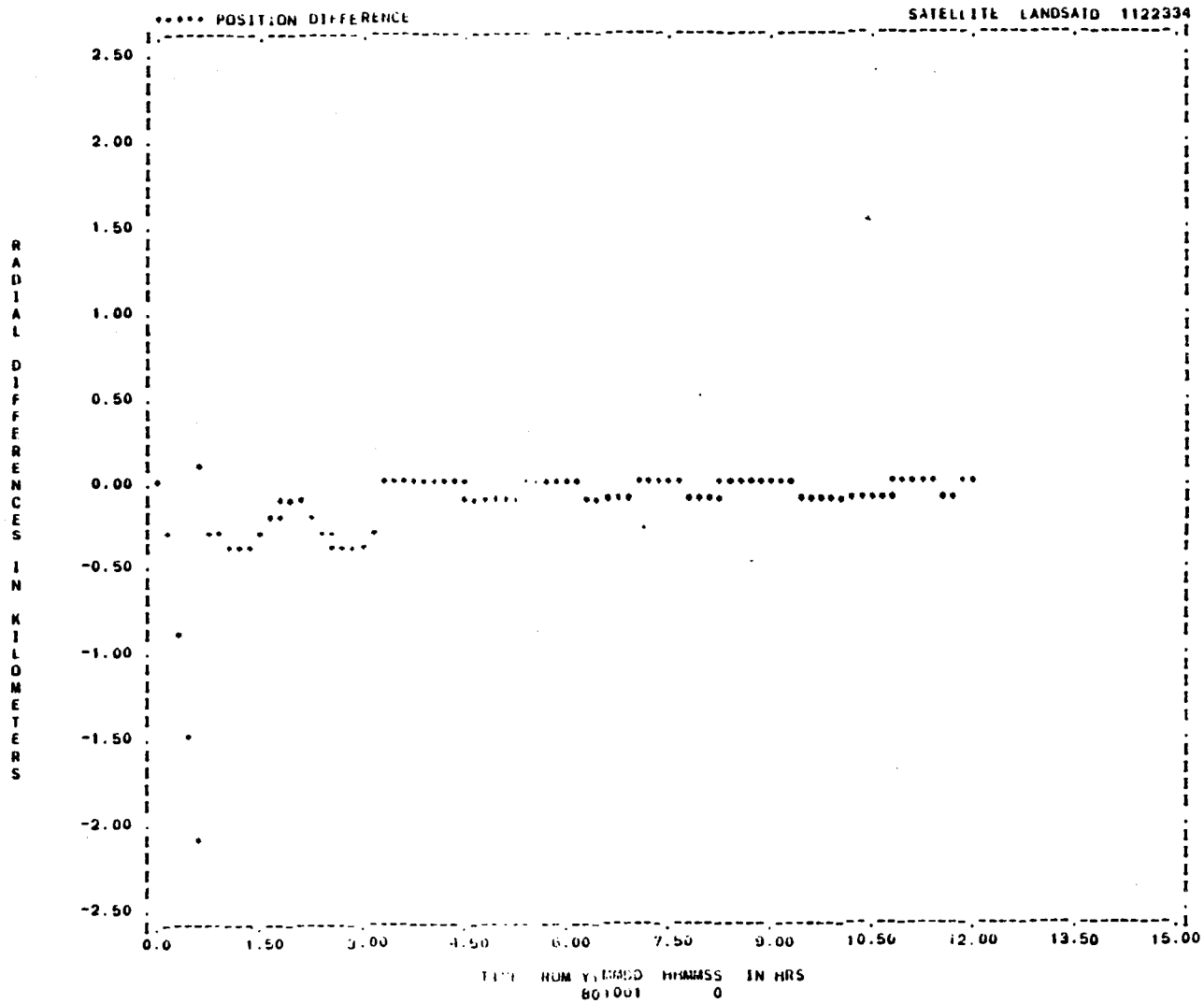

Figure A-10. Radial Differences for Run C5 (1 of 2)

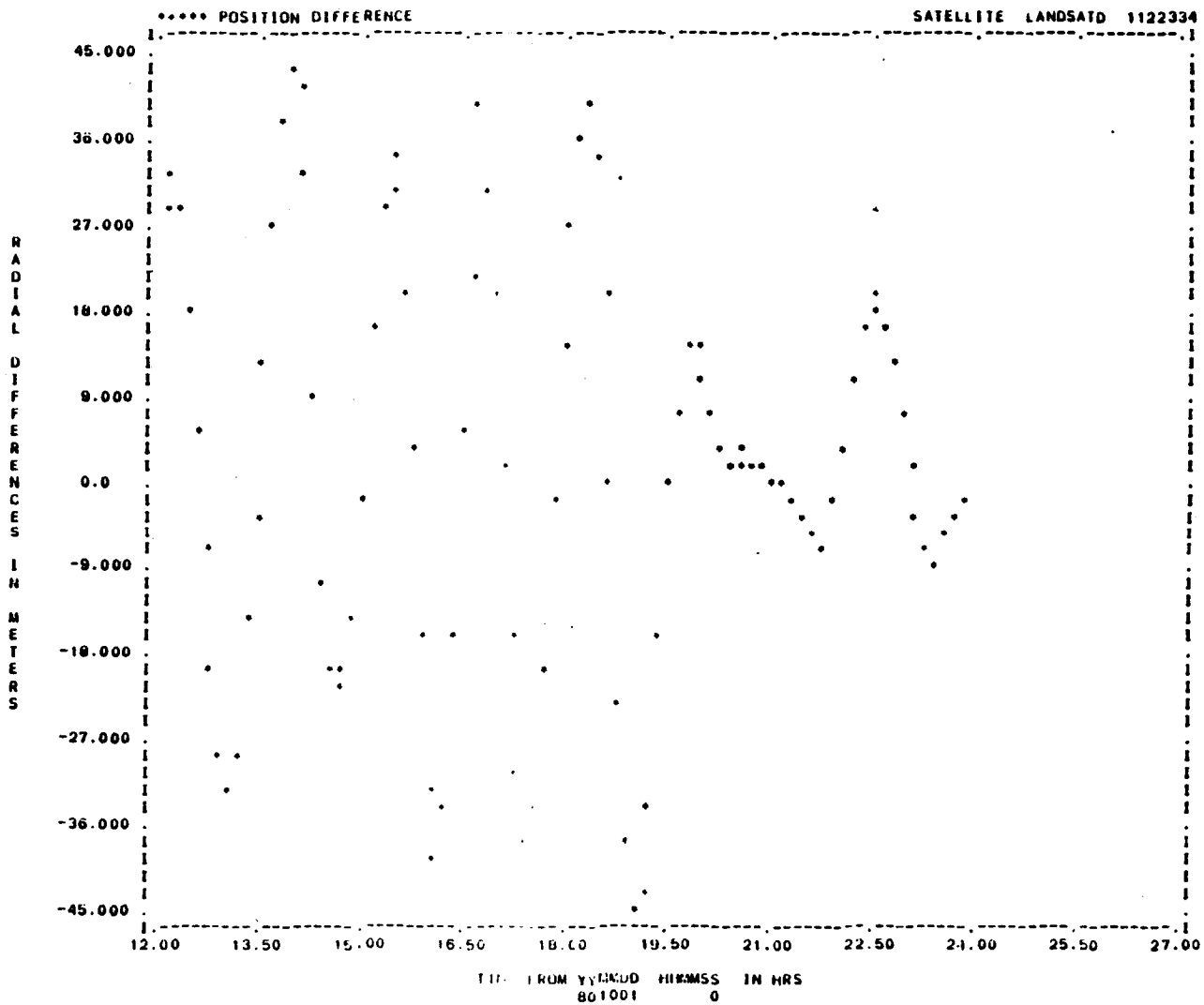

Figure A-10. Radial Differences for Run C5 (2 of 2)

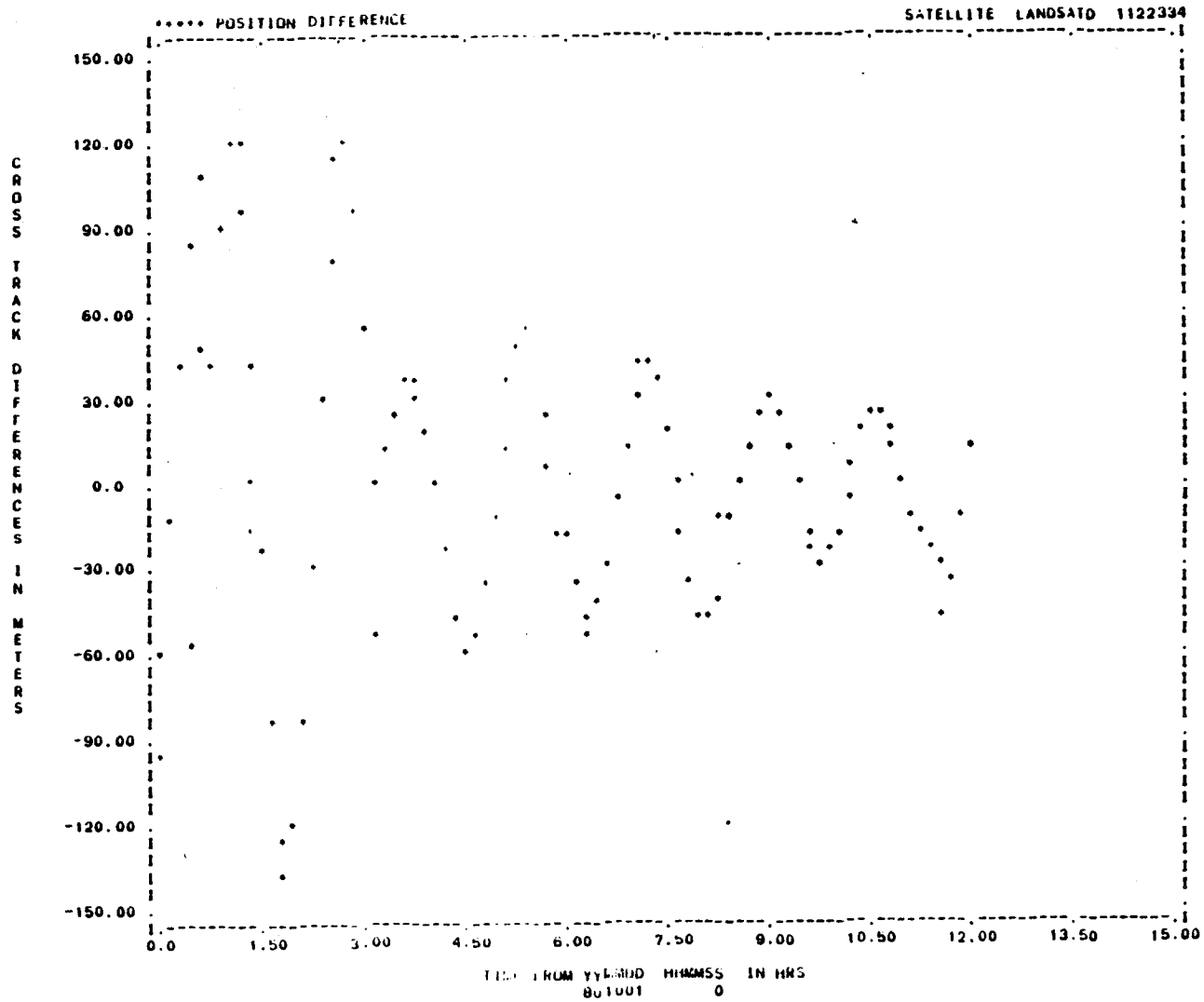

Figure A-11. Cross-Track Differences for Run C5 (1 of 2)

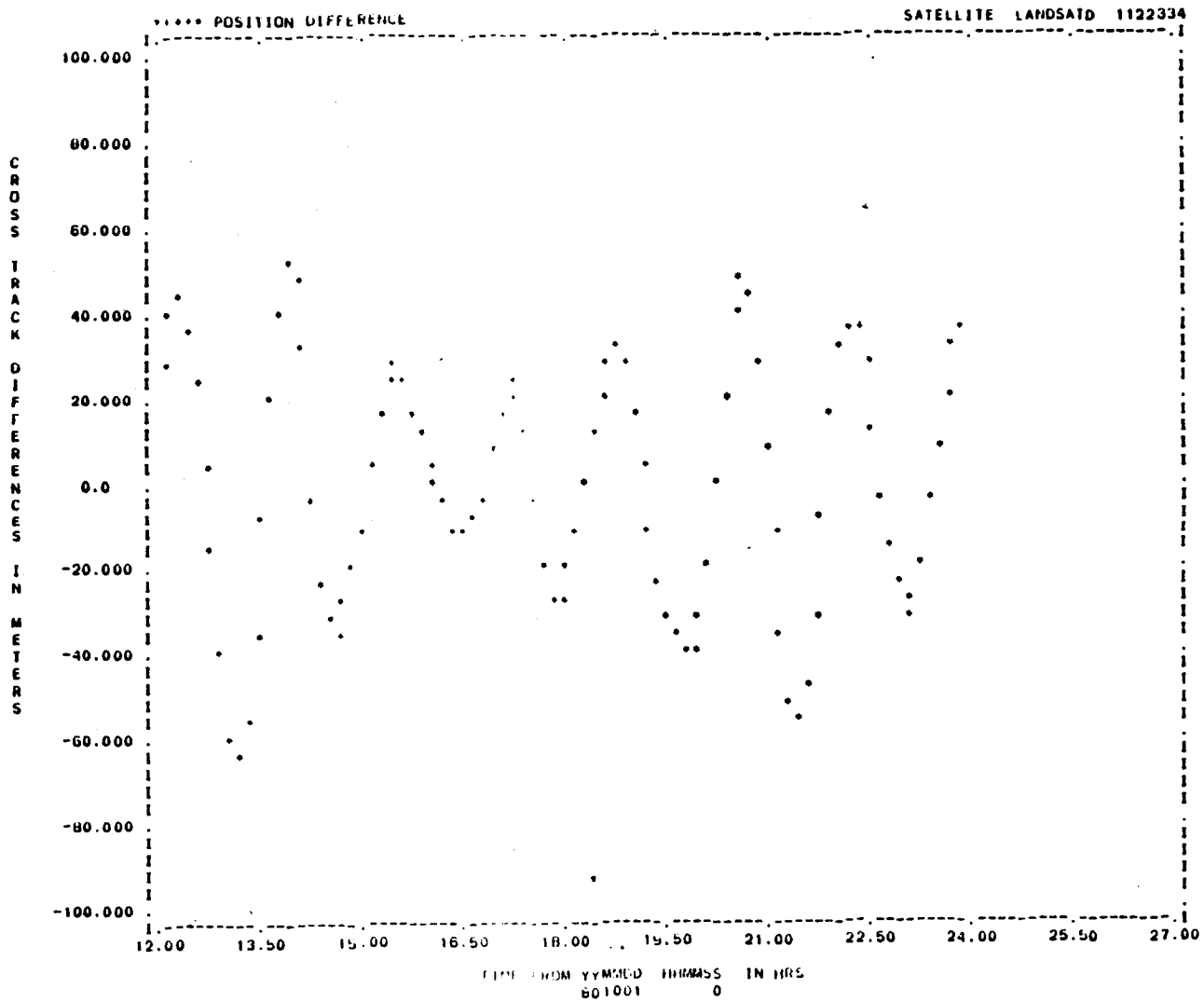

Figure A-11. Cross-Track Differences for Run C5 (2 of 2)

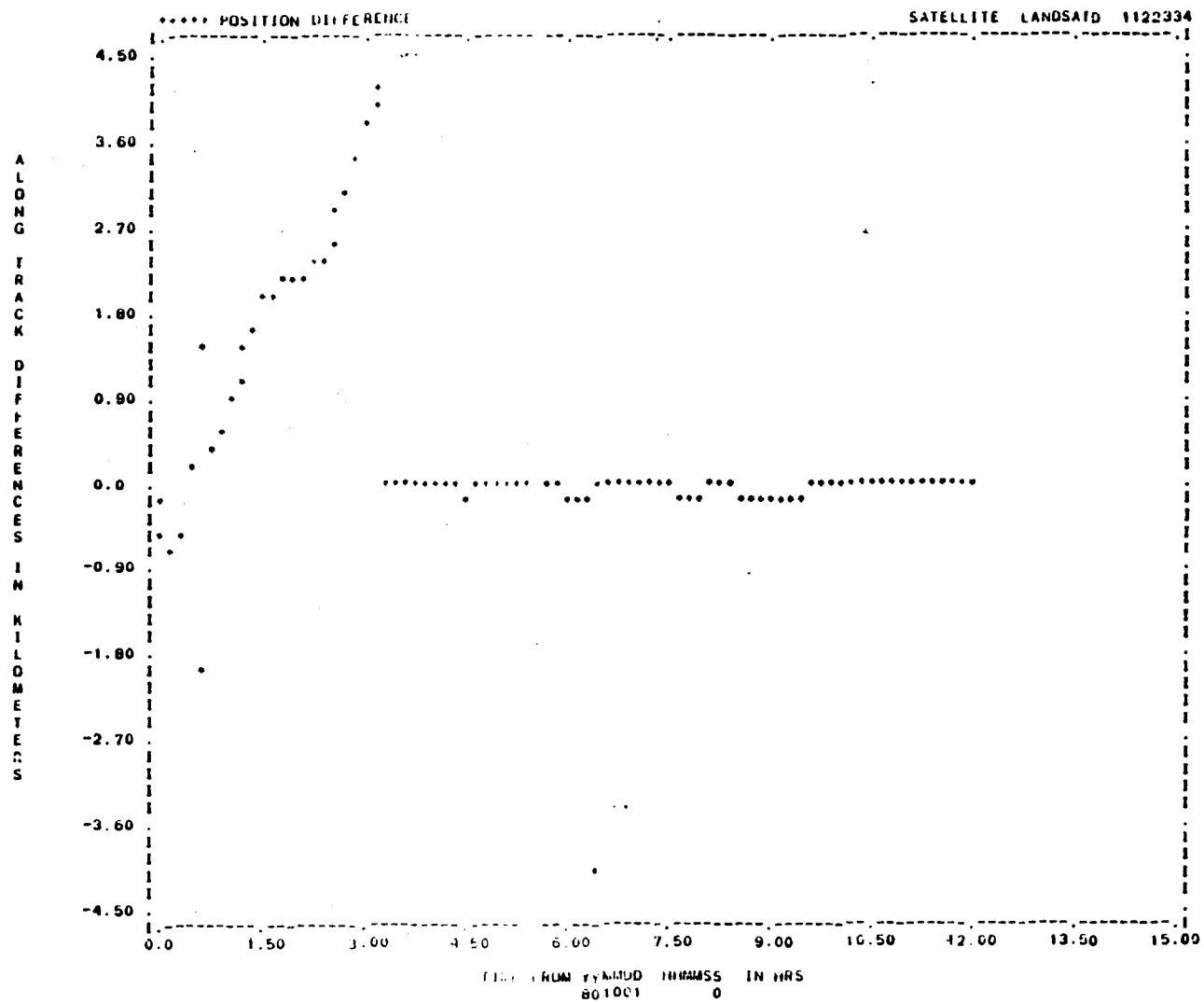

Figure A-12. Along-Track Differences for Run C5 (1 of 2)

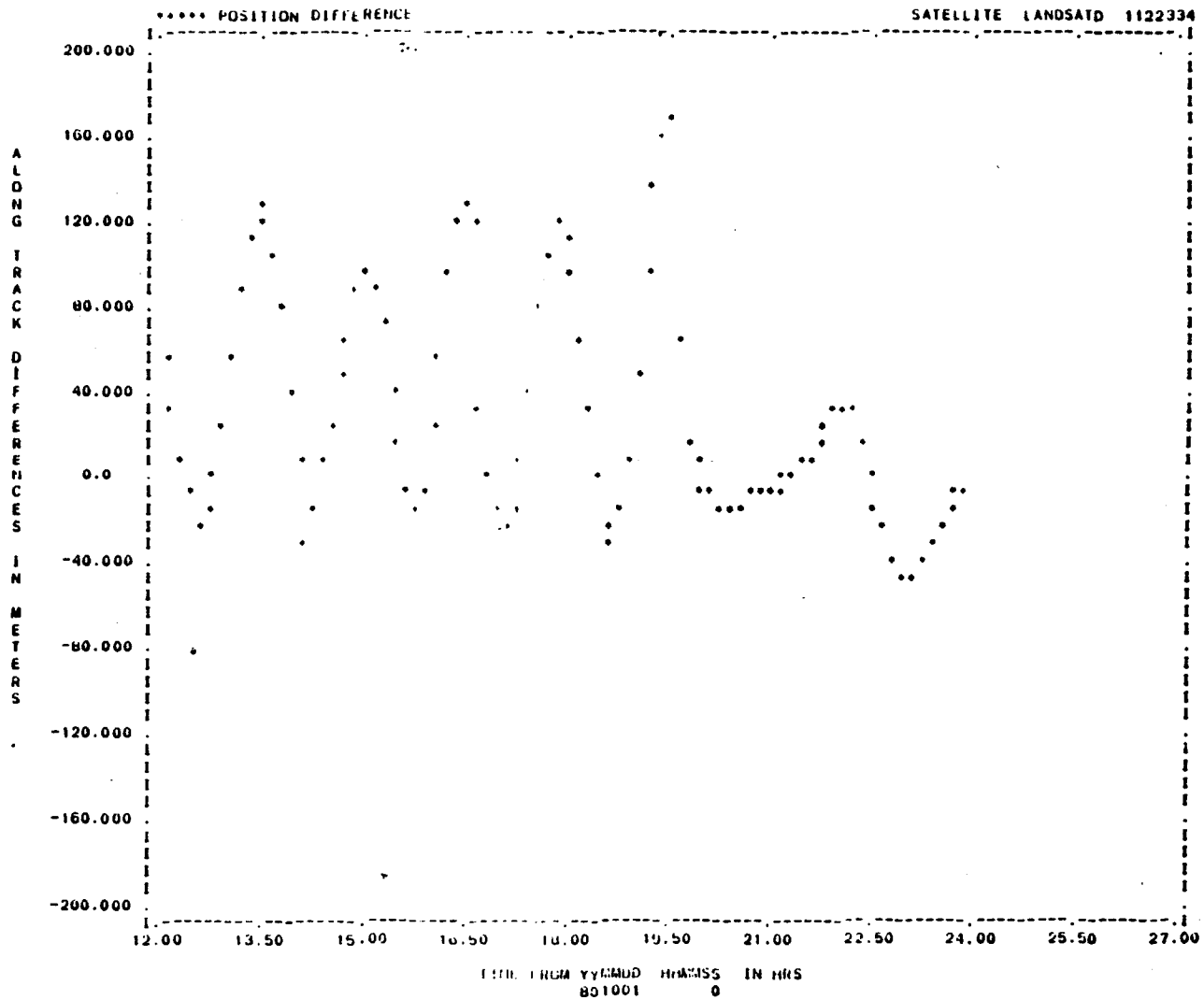

Figure A-12. Along-Track Differences for Run C5 (2 of 2)

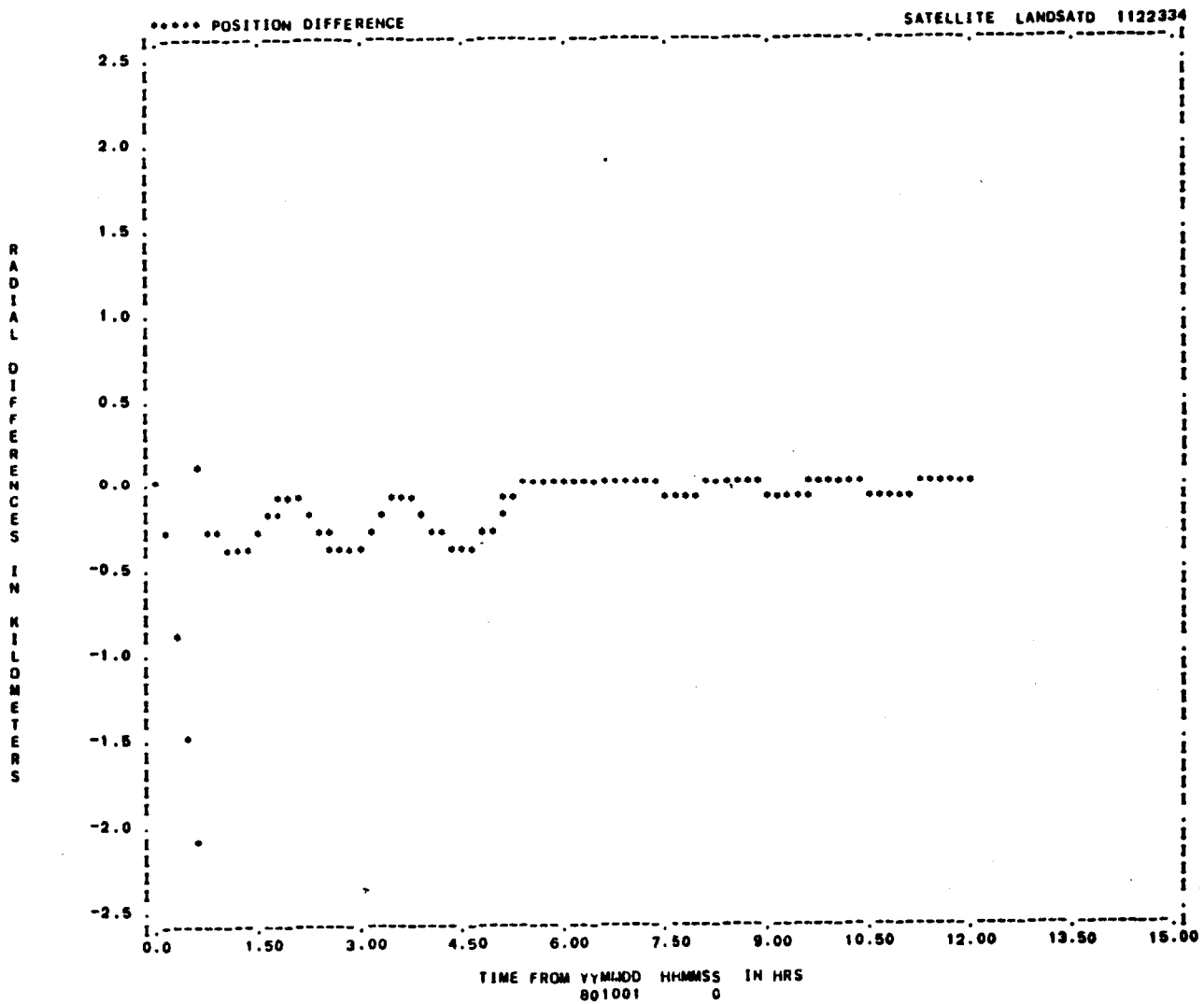

Figure A-13. Radial Differences for Run D2 (1 of 2)

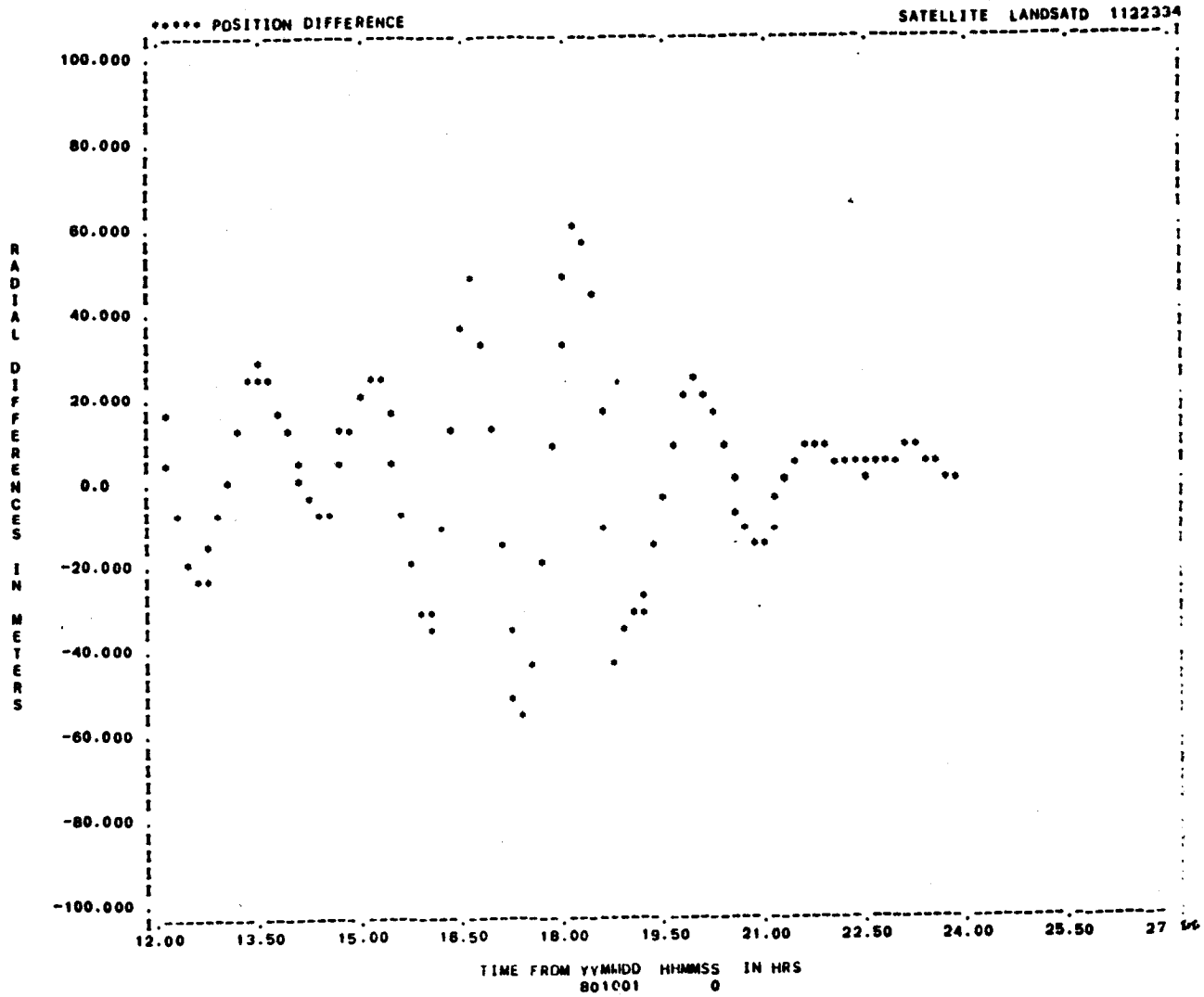

Figure A-13. Radial Differences for Run D2 (2 of 2)

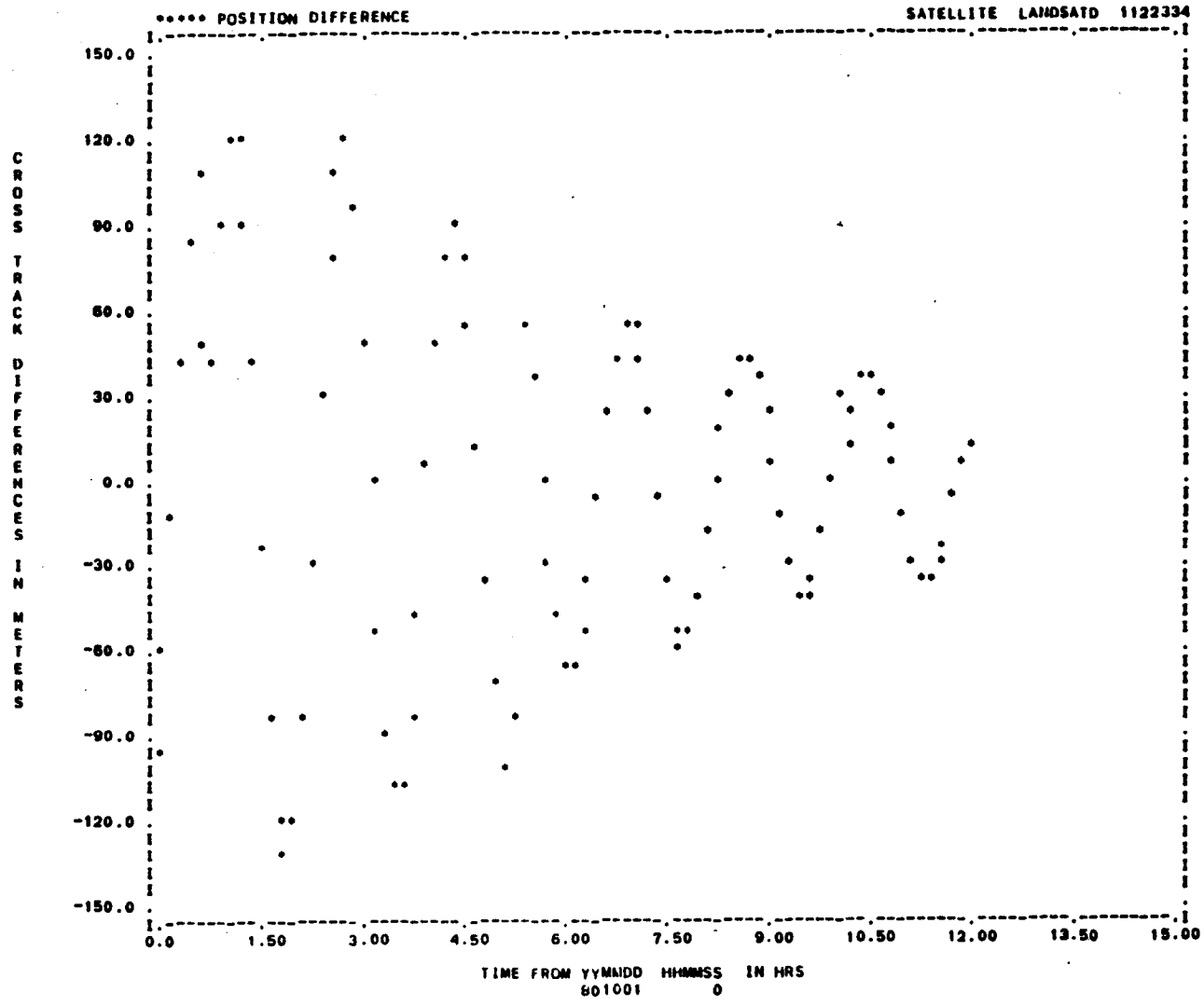

Figure A-14. Cross-Track Differences for Run D2 (1 of 2)

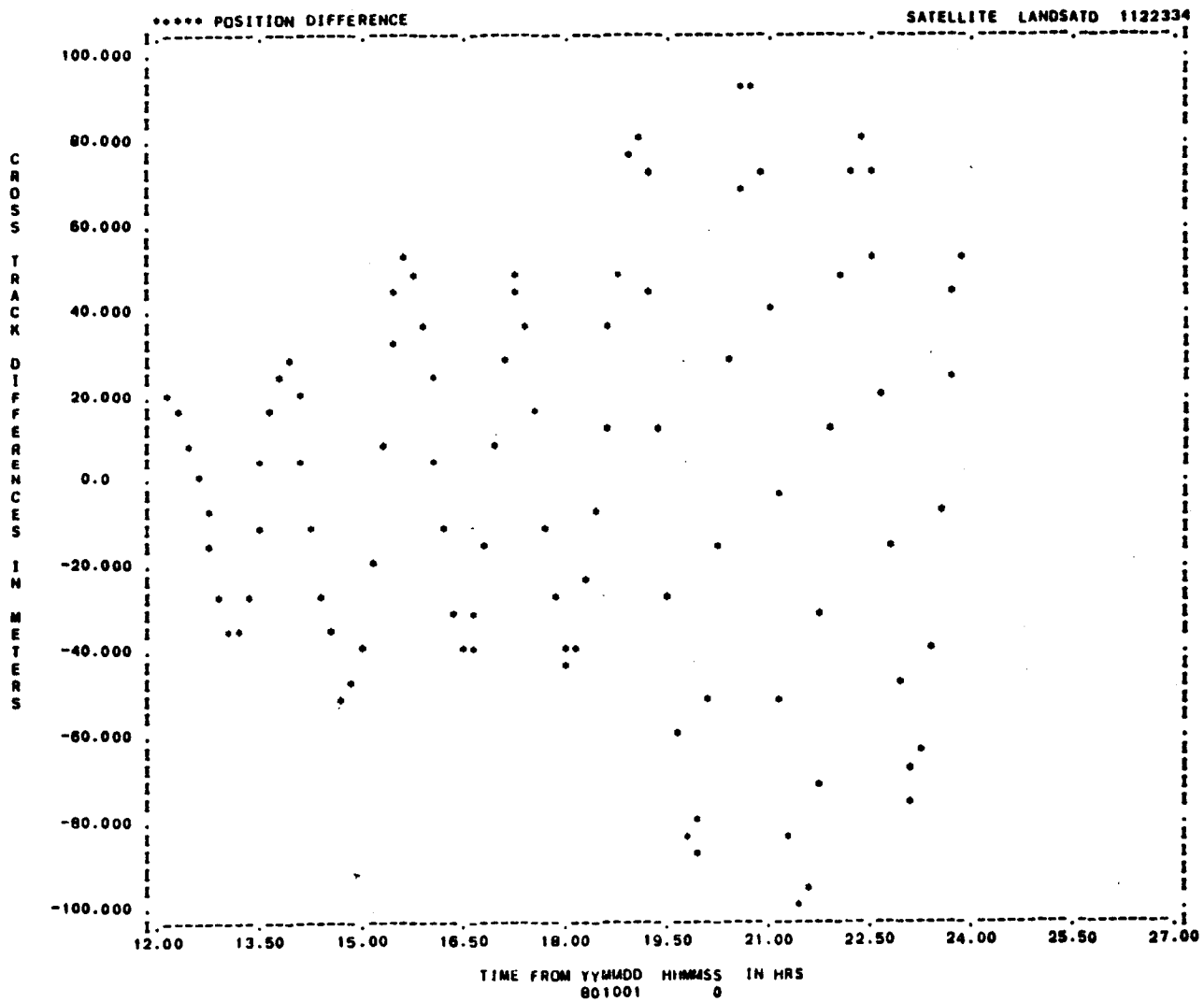

Figure A-14. Cross-Track Differences for Run D2 (2 of 2)

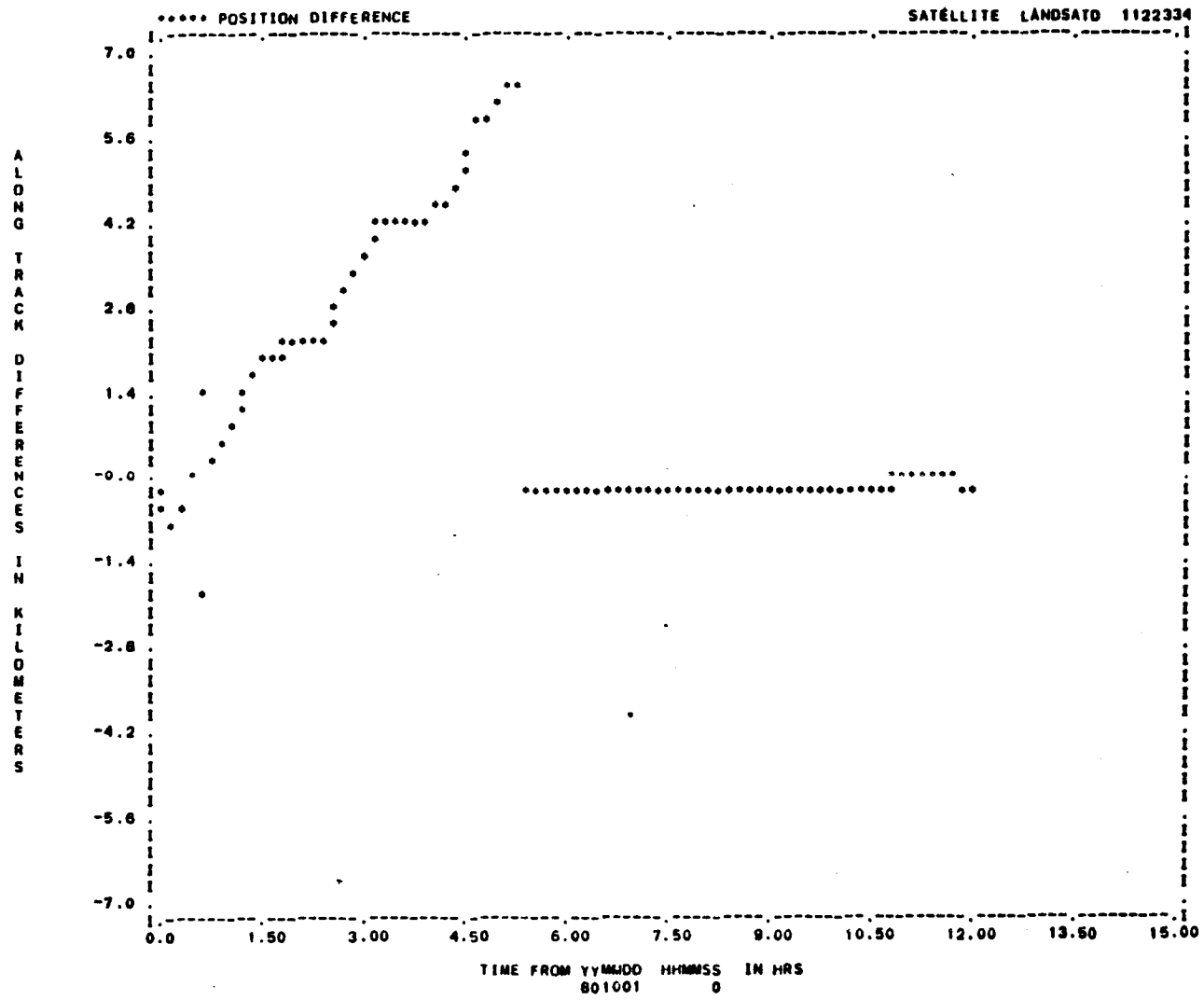

Figure A-15. Along-Track Differences for Run D2 (1 of 2)

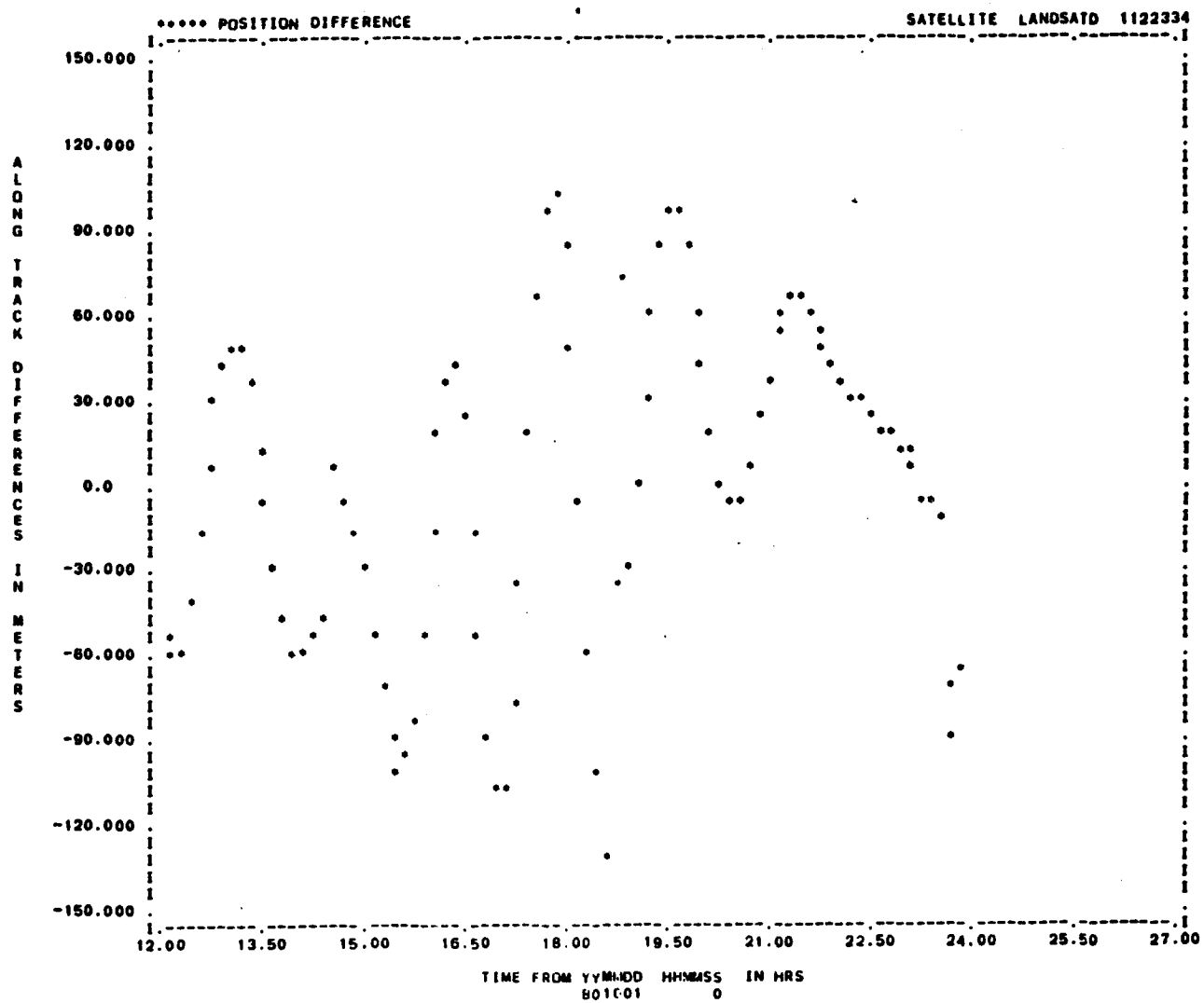

Figure A-15. Along-Track Differences for Run D2 (2 of 2)

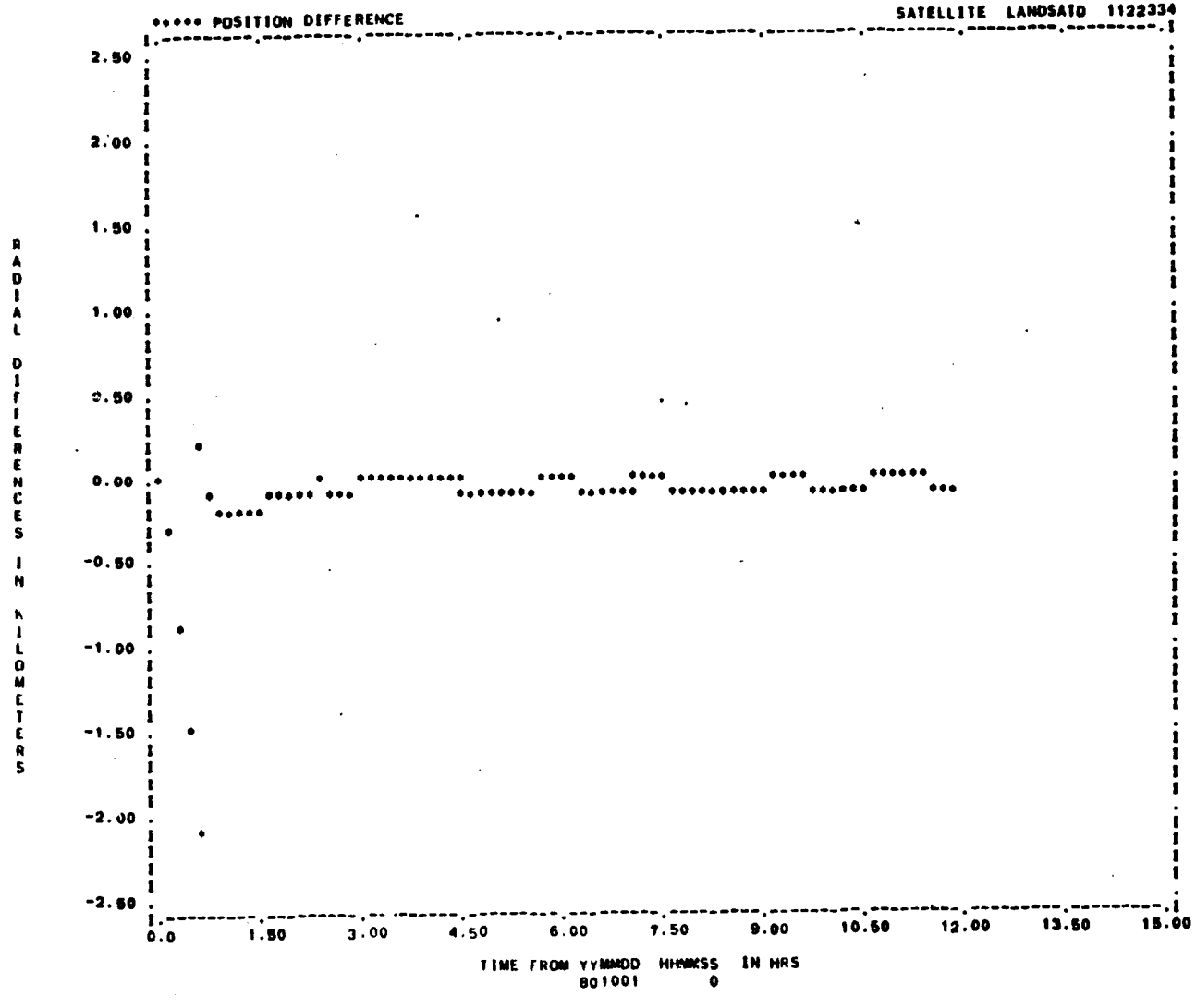

Figure A-16. Radial Differences for Run E4

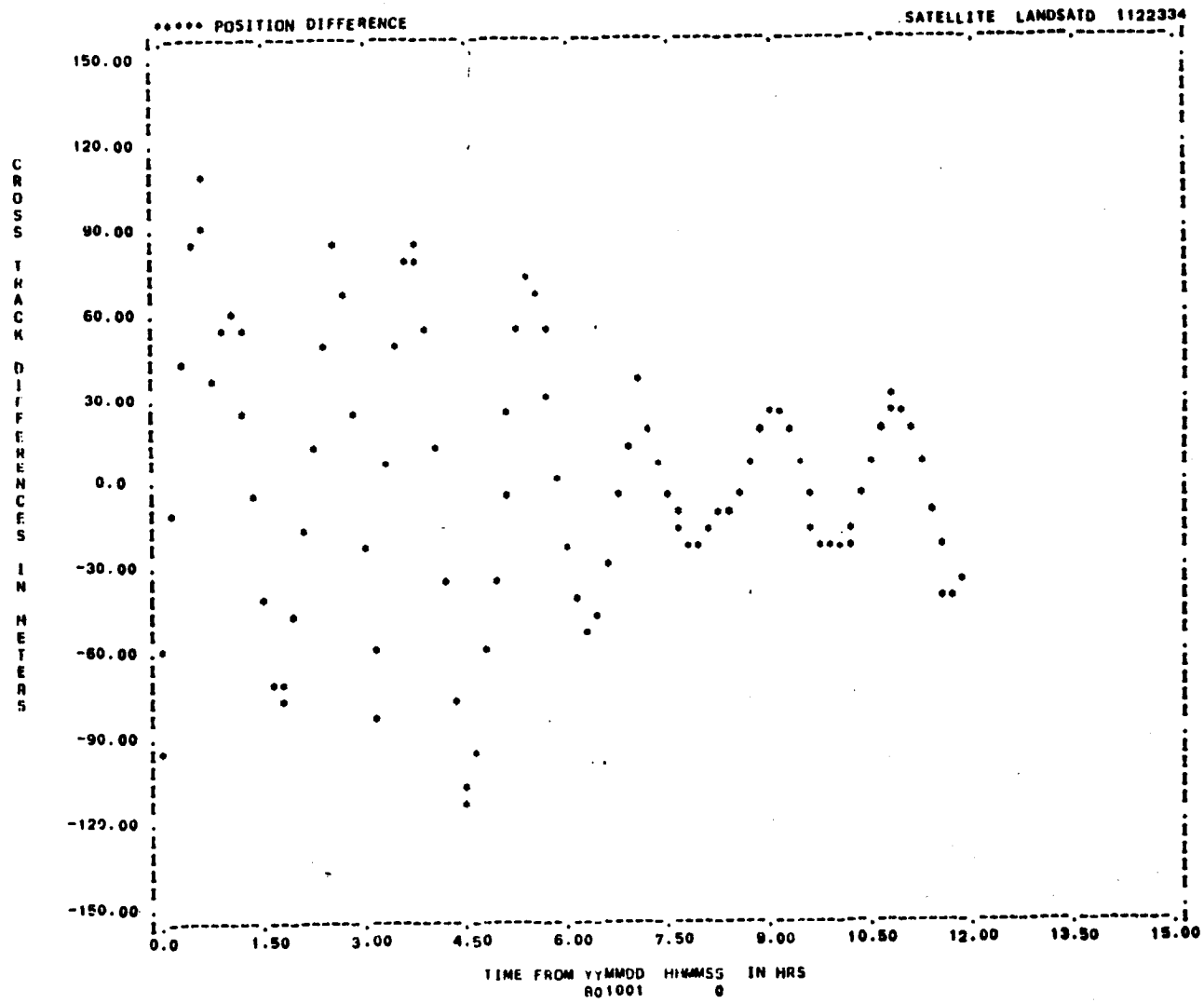

Figure A-17. Cross-Track Differences for Run E4

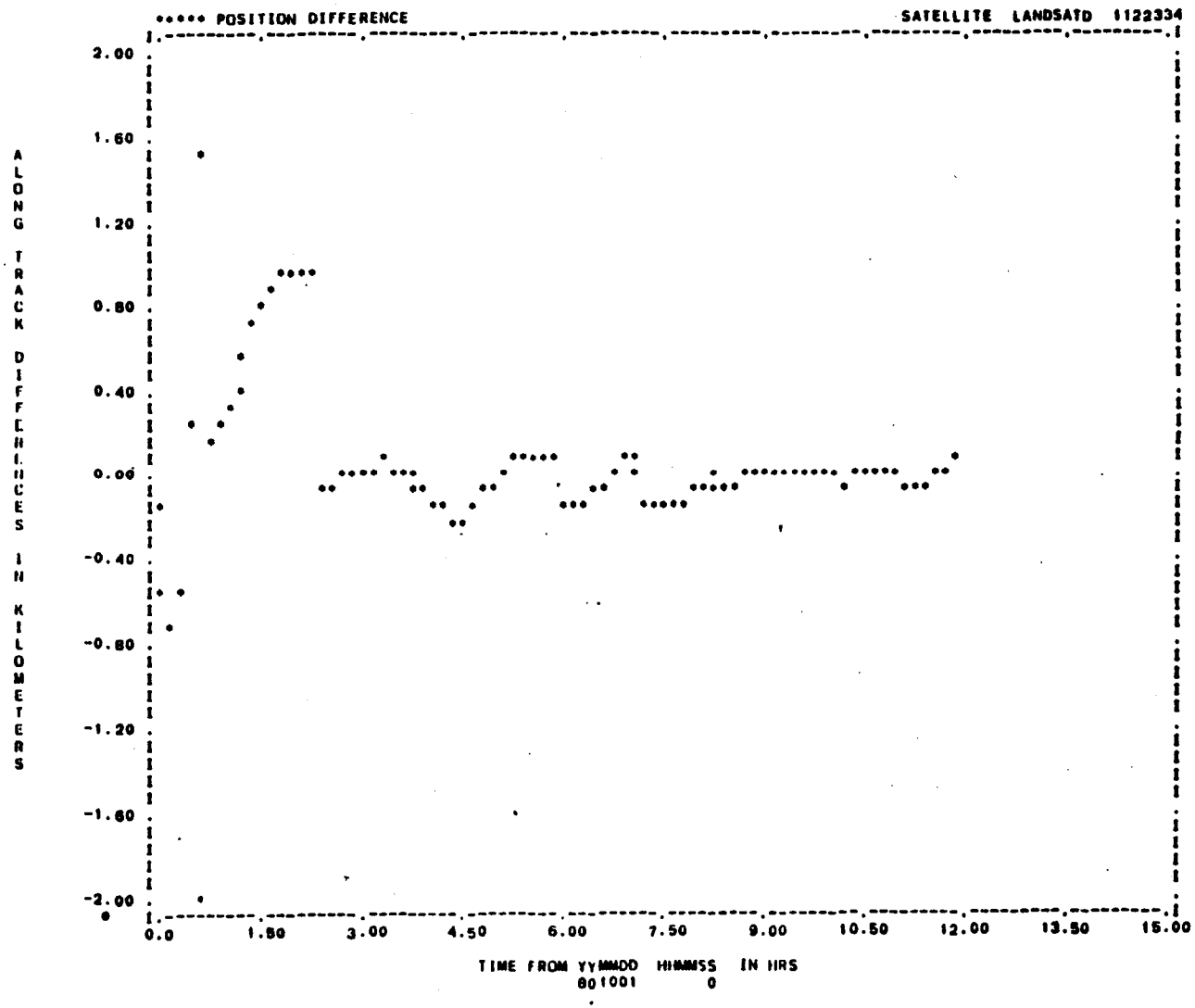

Figure A-18. Along-Track Differences for Run E4

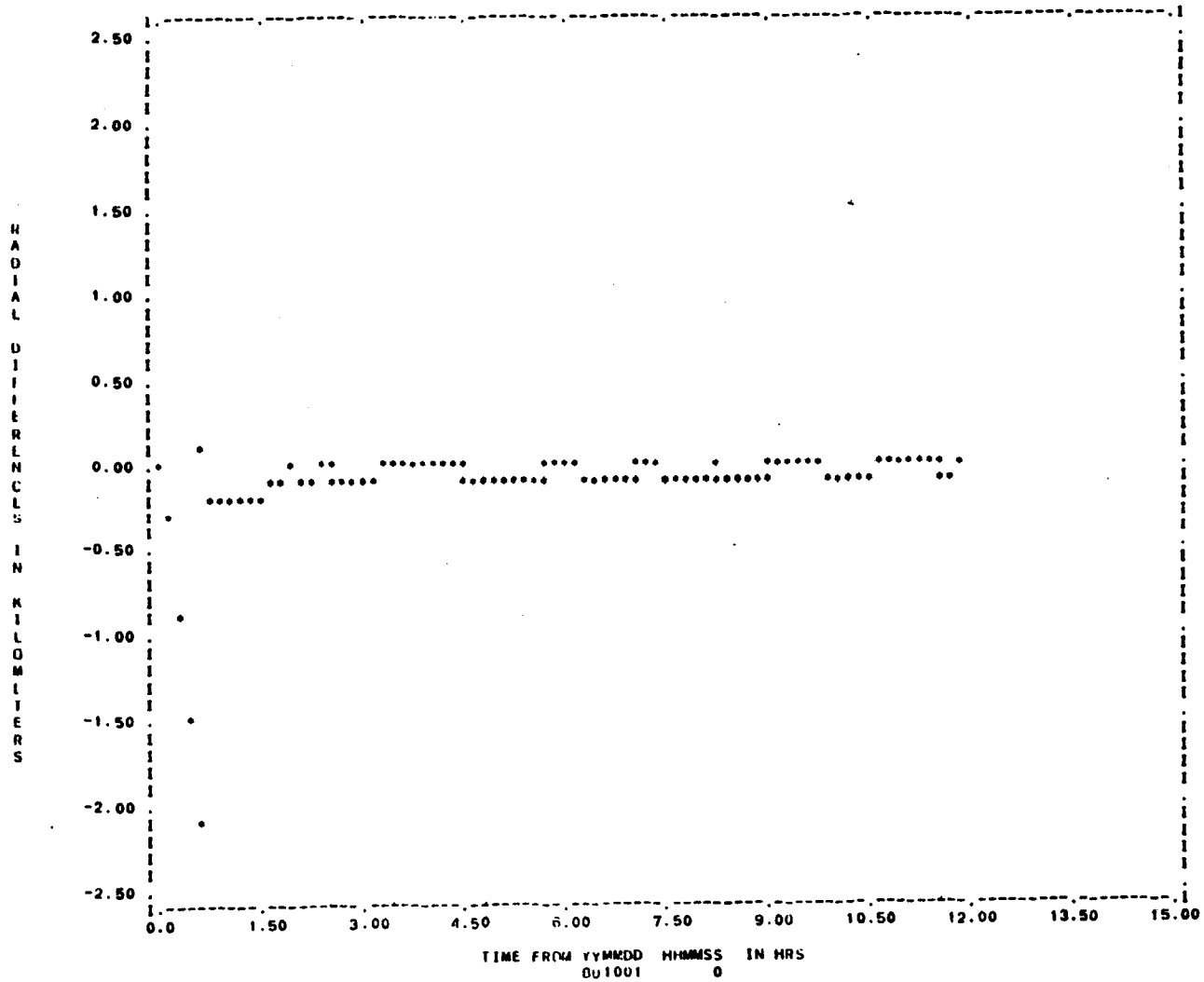

Figure A-19. Radial Differences for Run E5

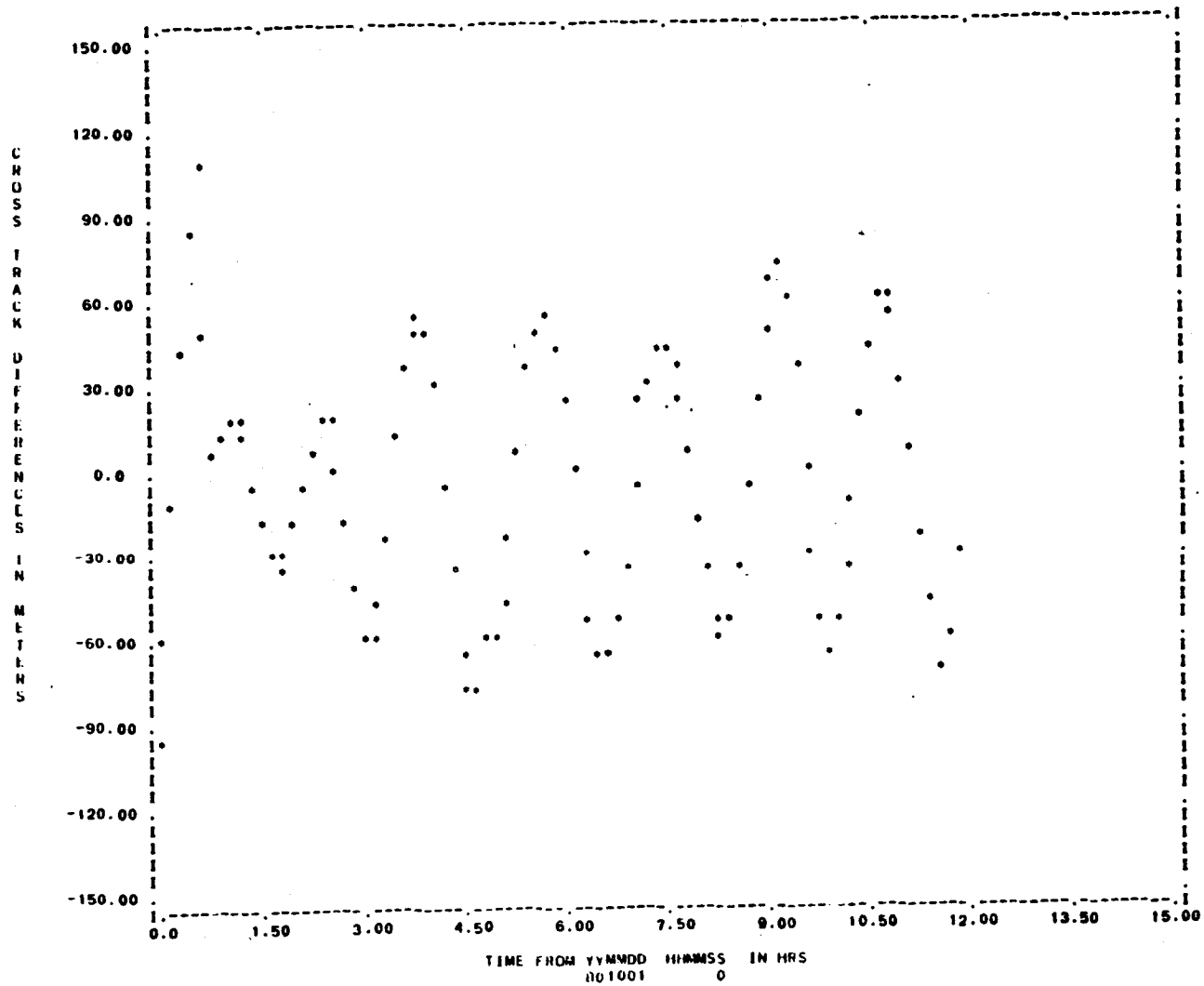

Figure A-20. Cross-Track Differences for Run E5

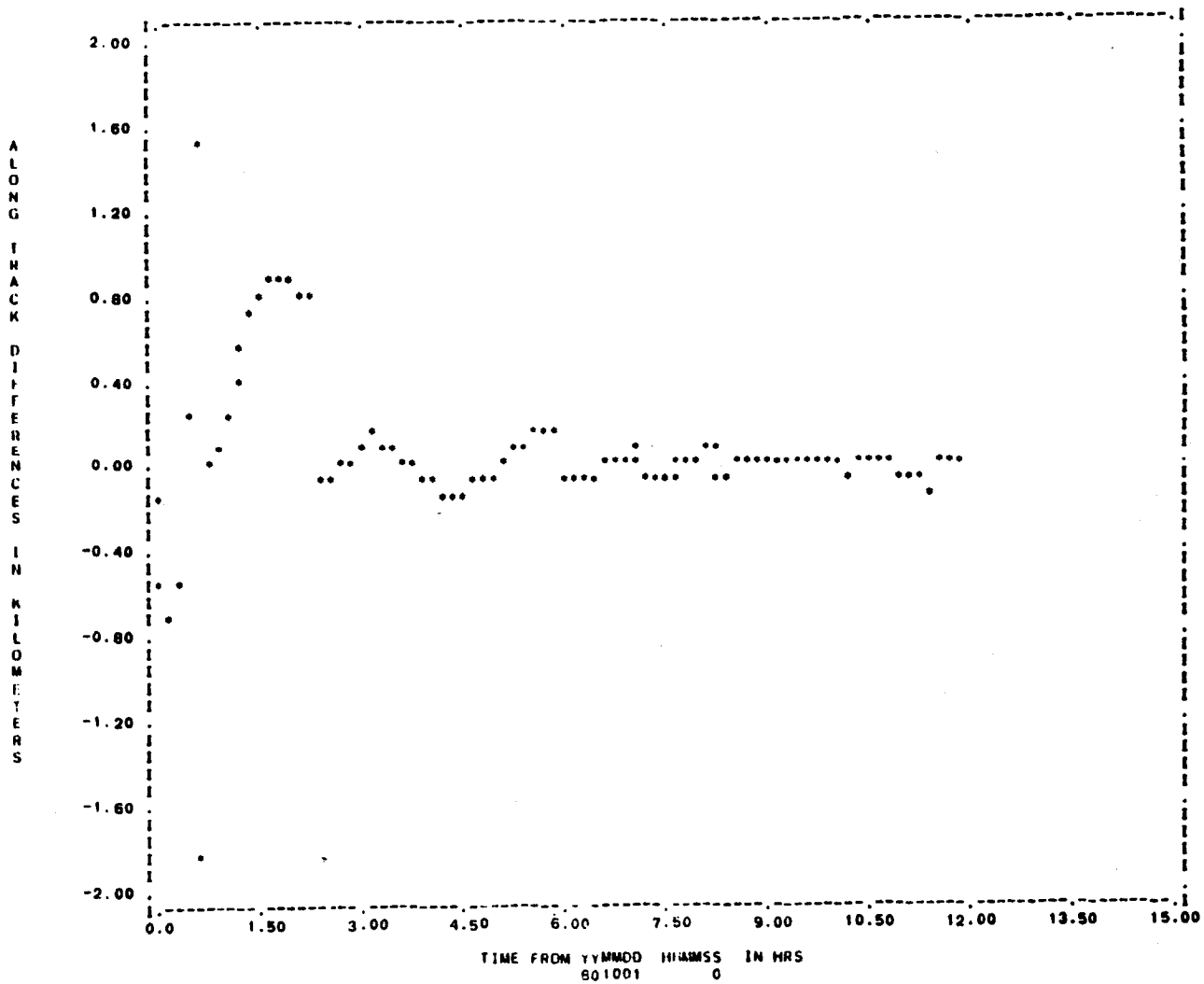

Figure A-21. Along-Track Differences for Run E5

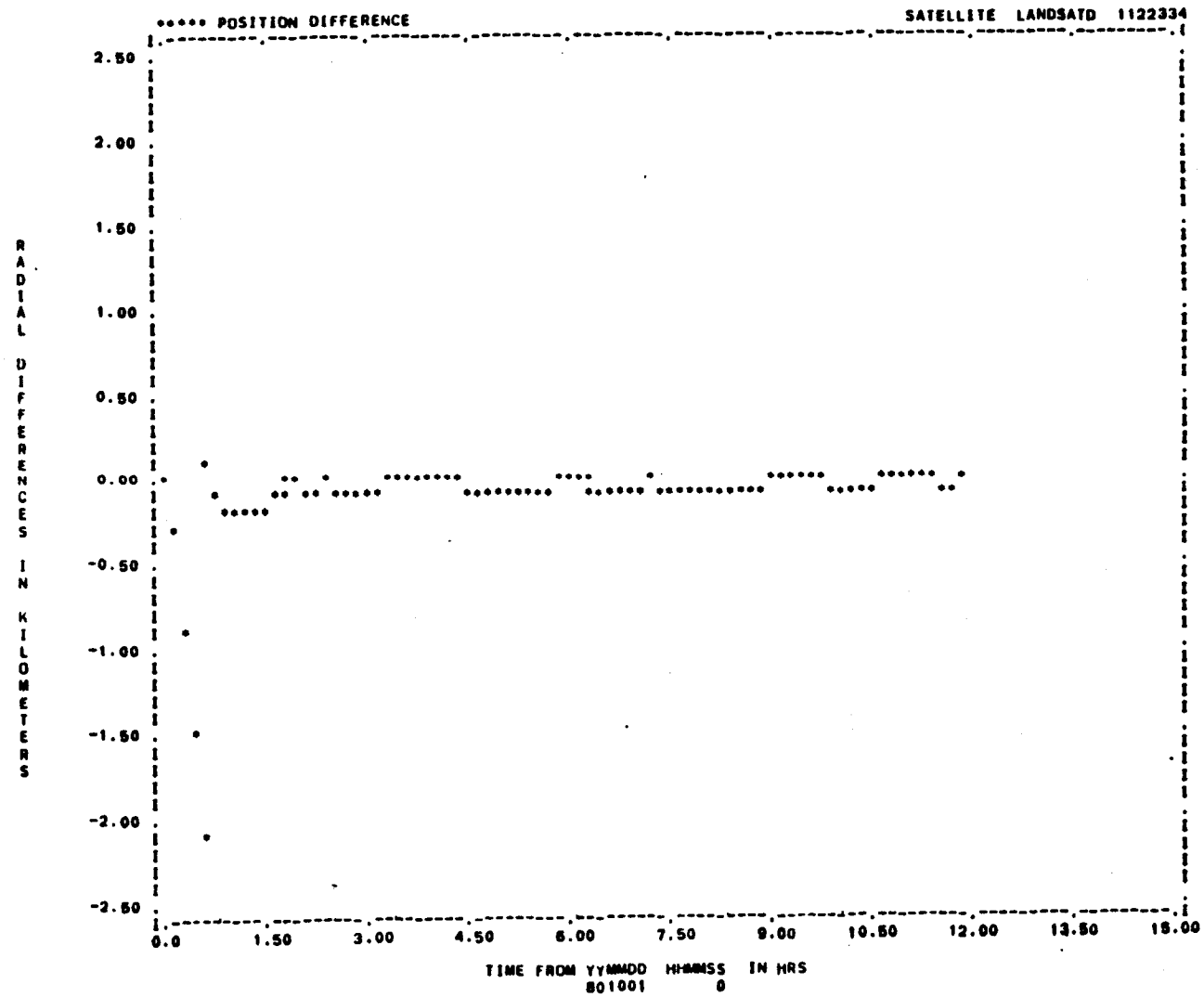

Figure A-22. Radial Differences for Run E7

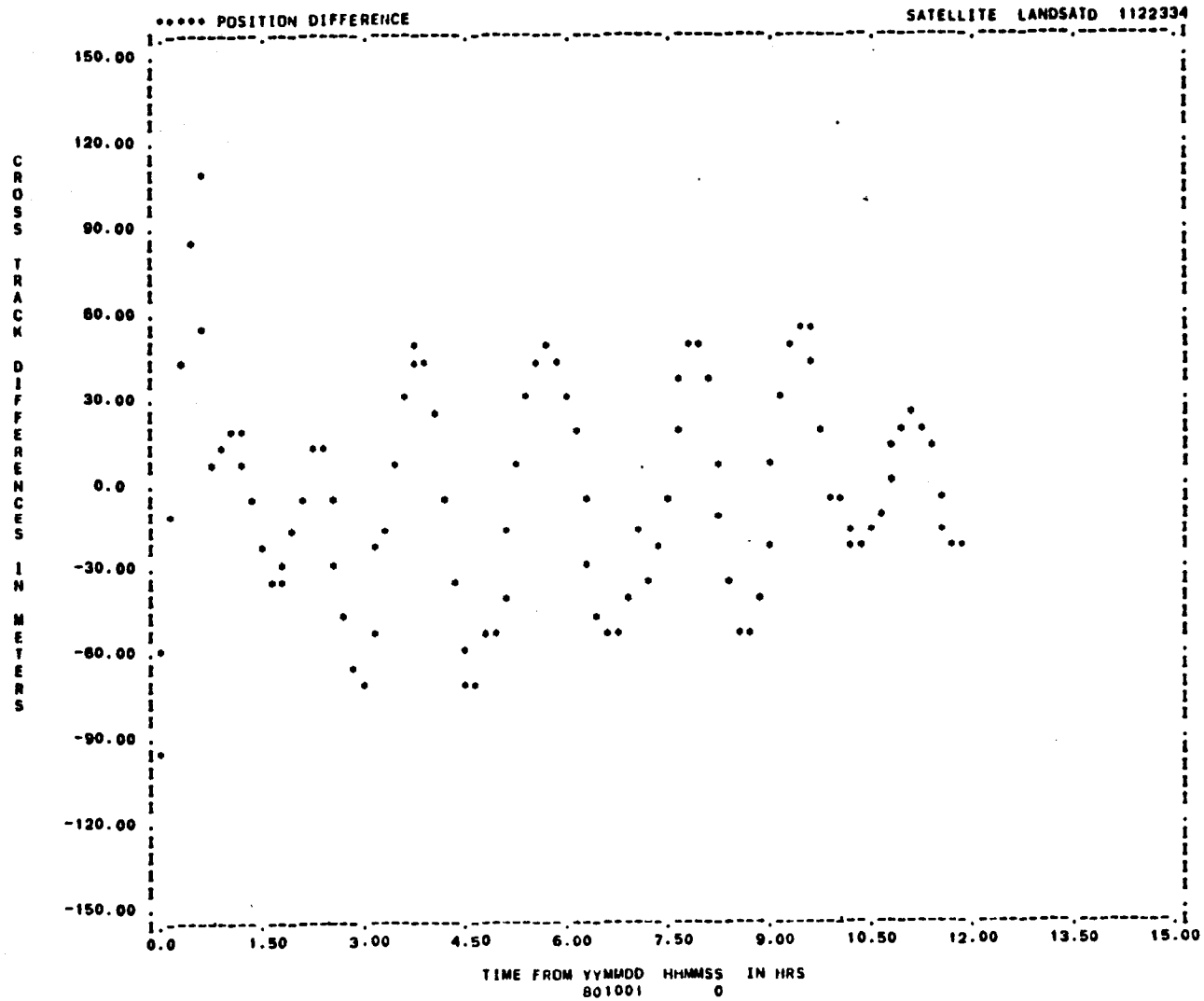

Figure A-23. Cross-Track Differences for Run E7

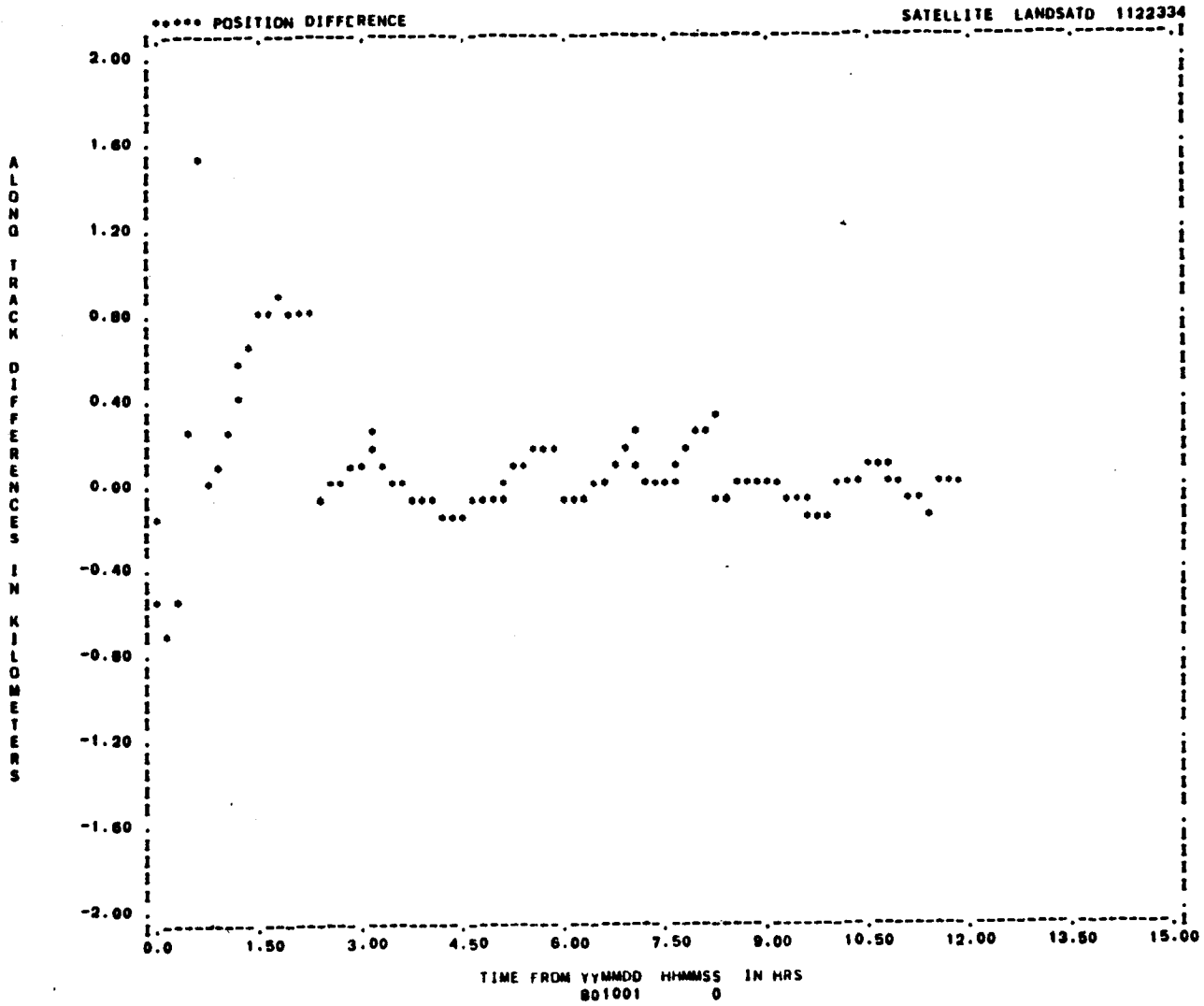

Figure A-24. Along-Track Differences for Run E7

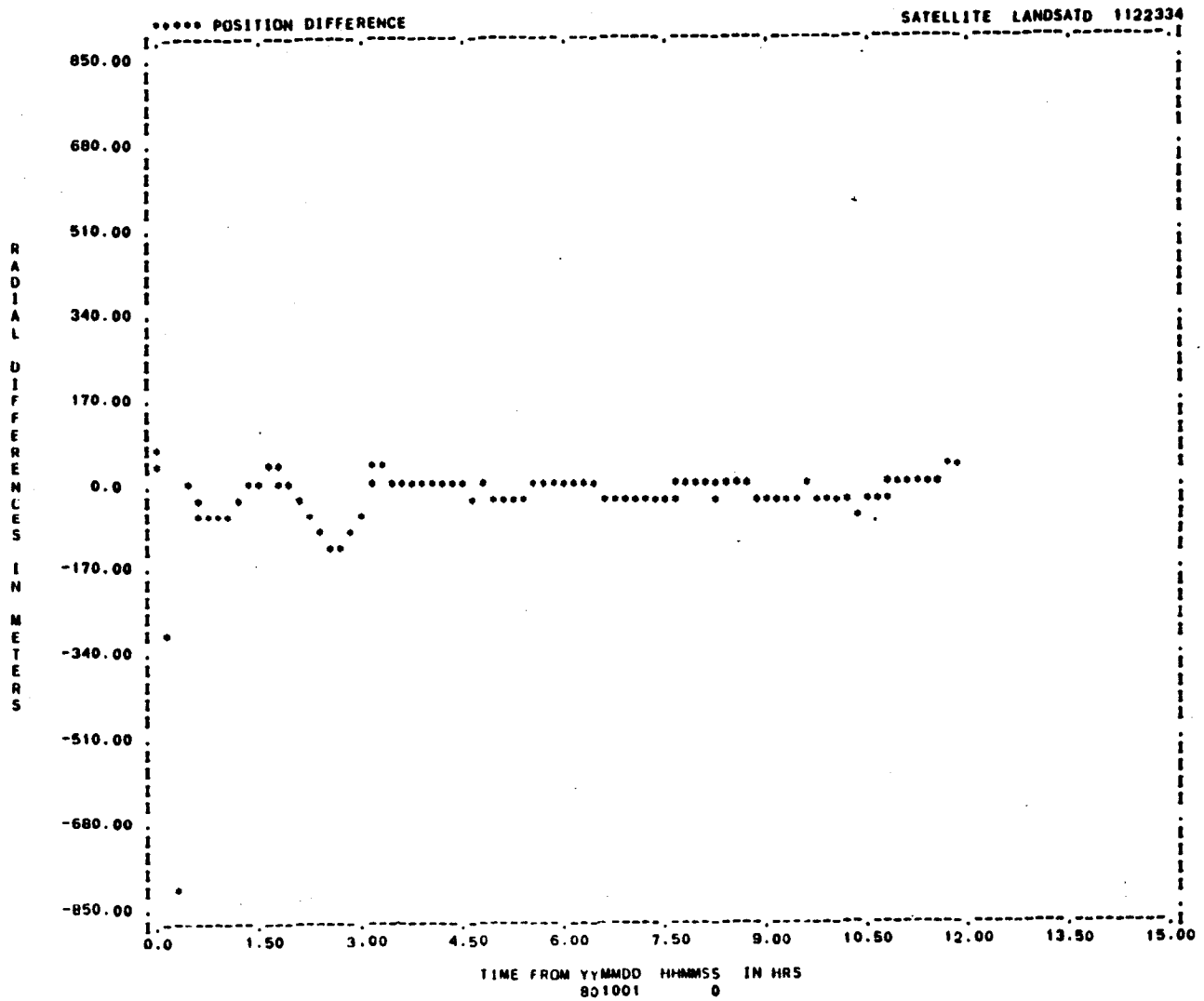

Figure A-25. Radial Differences for Run F1

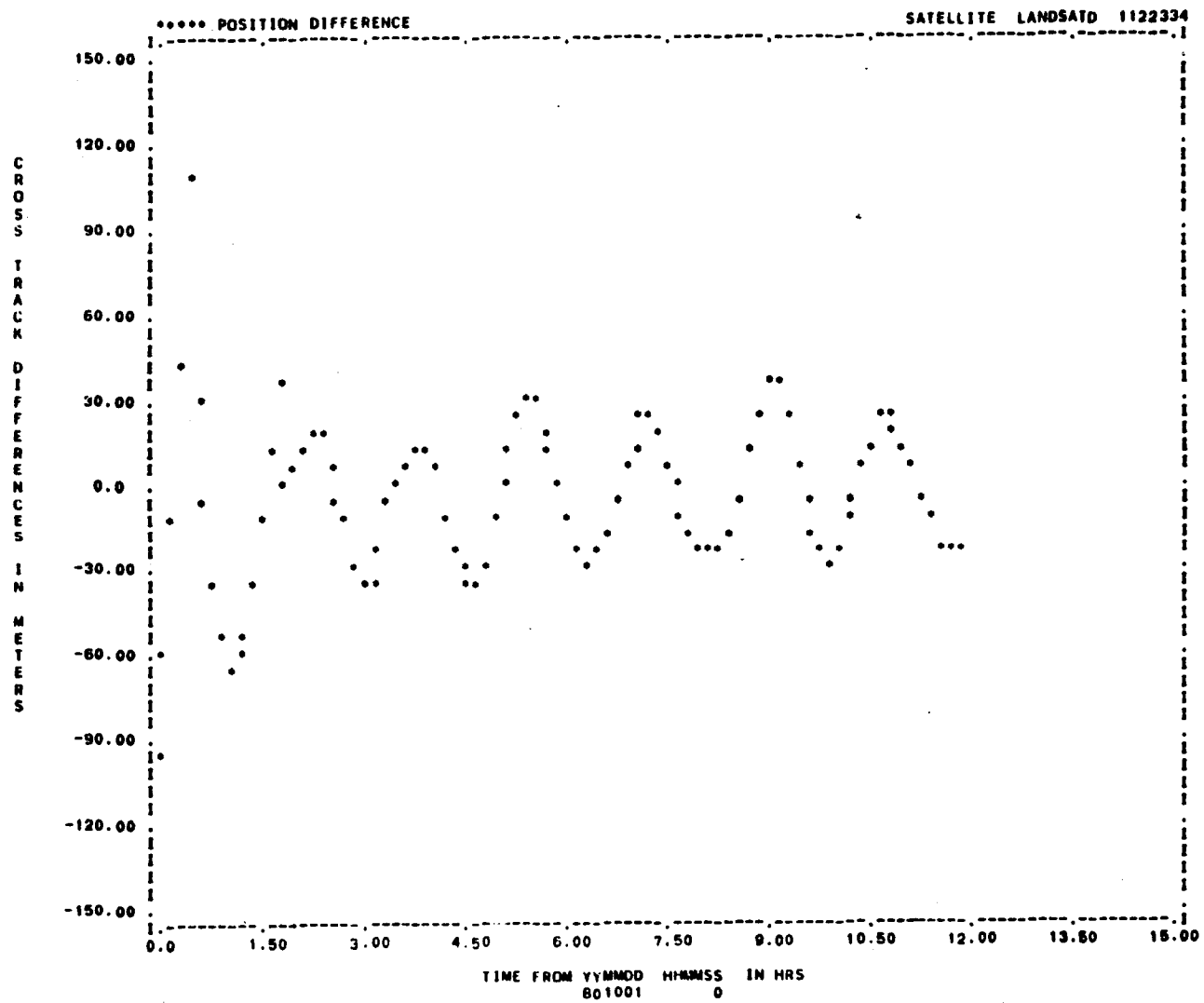

Figure A-26. Cross-Track Differences for Run F1

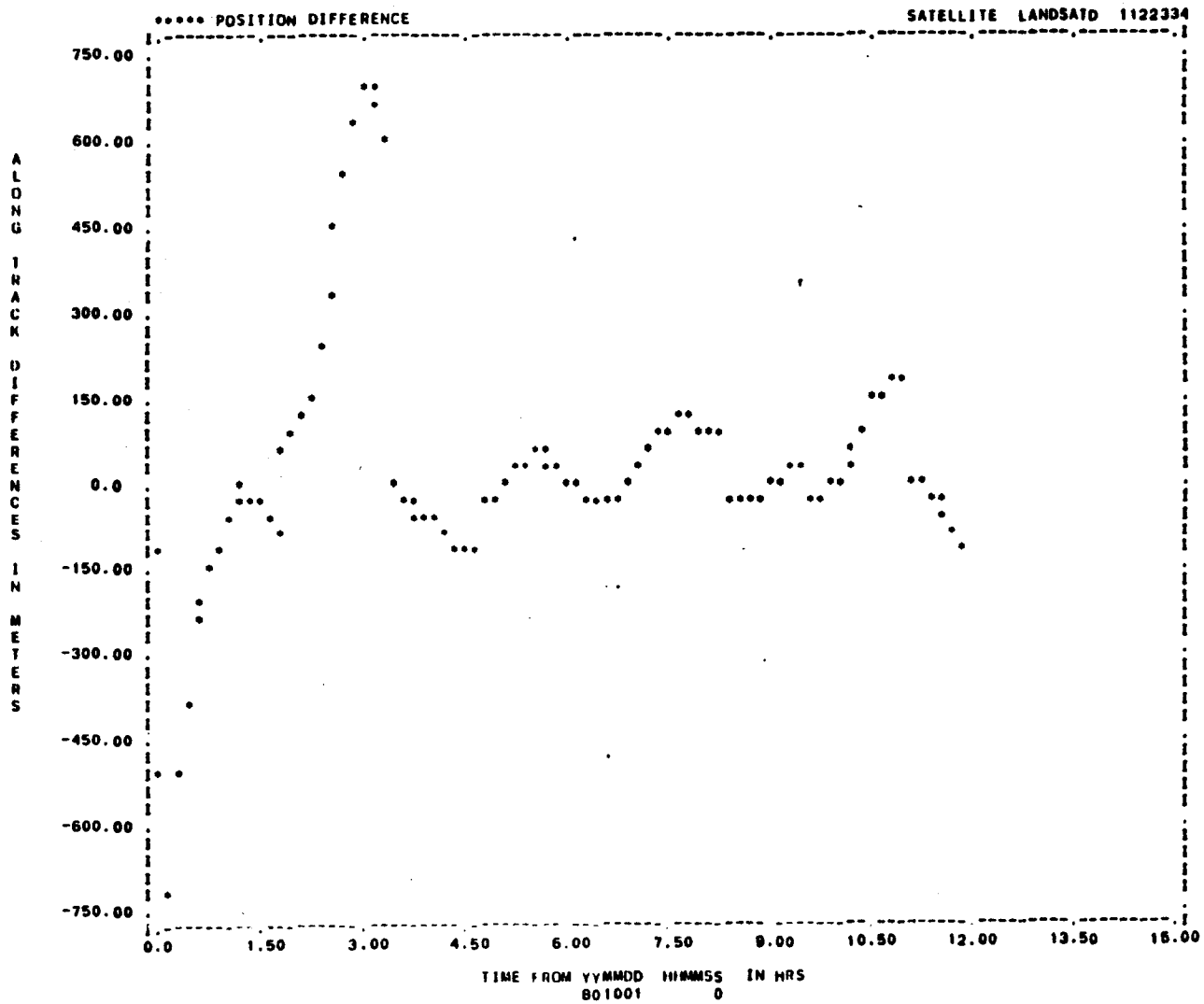

Figure A-27. Along-Track Differences for Run F1

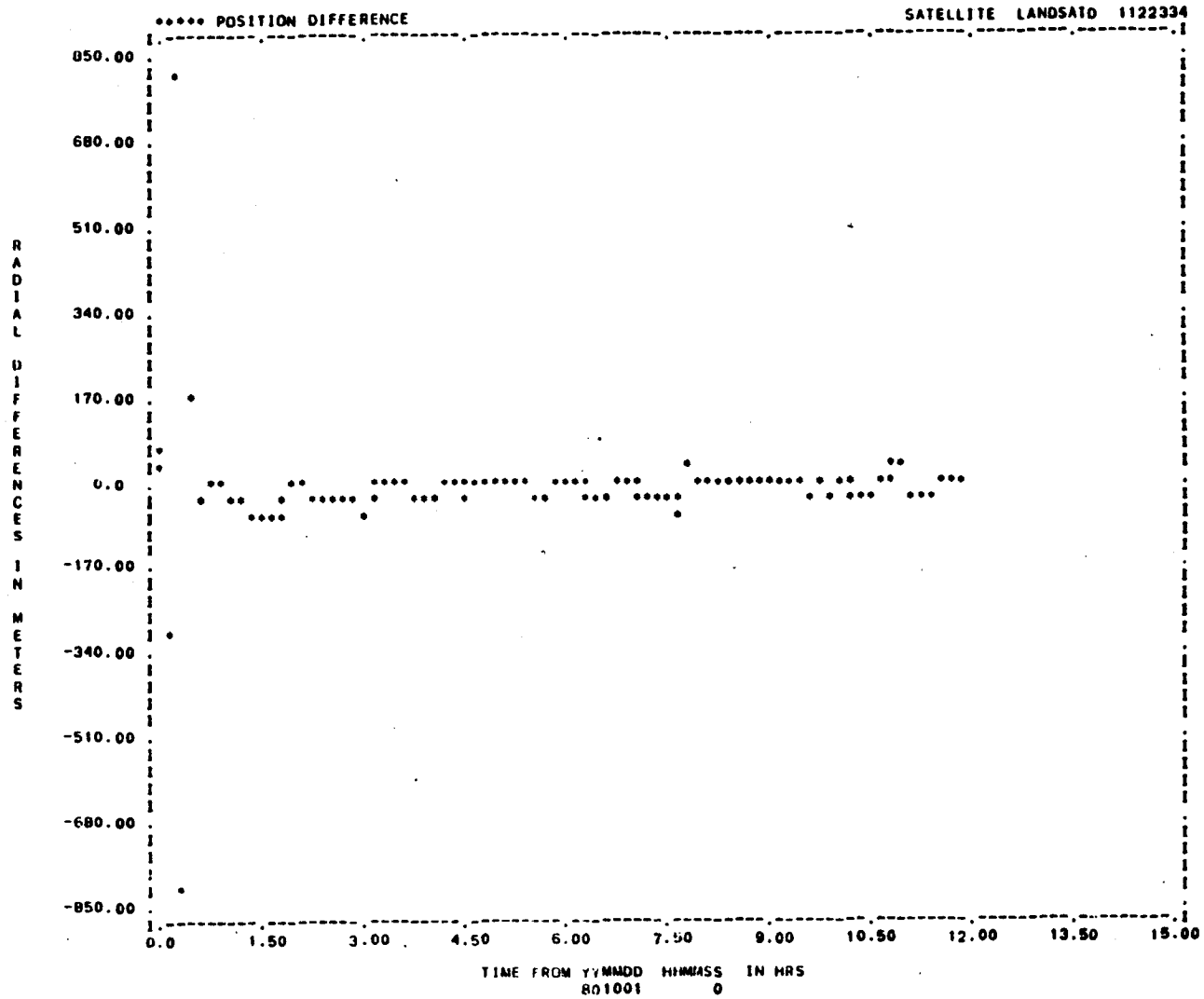

Figure A-28. Radial Differences for Run G1

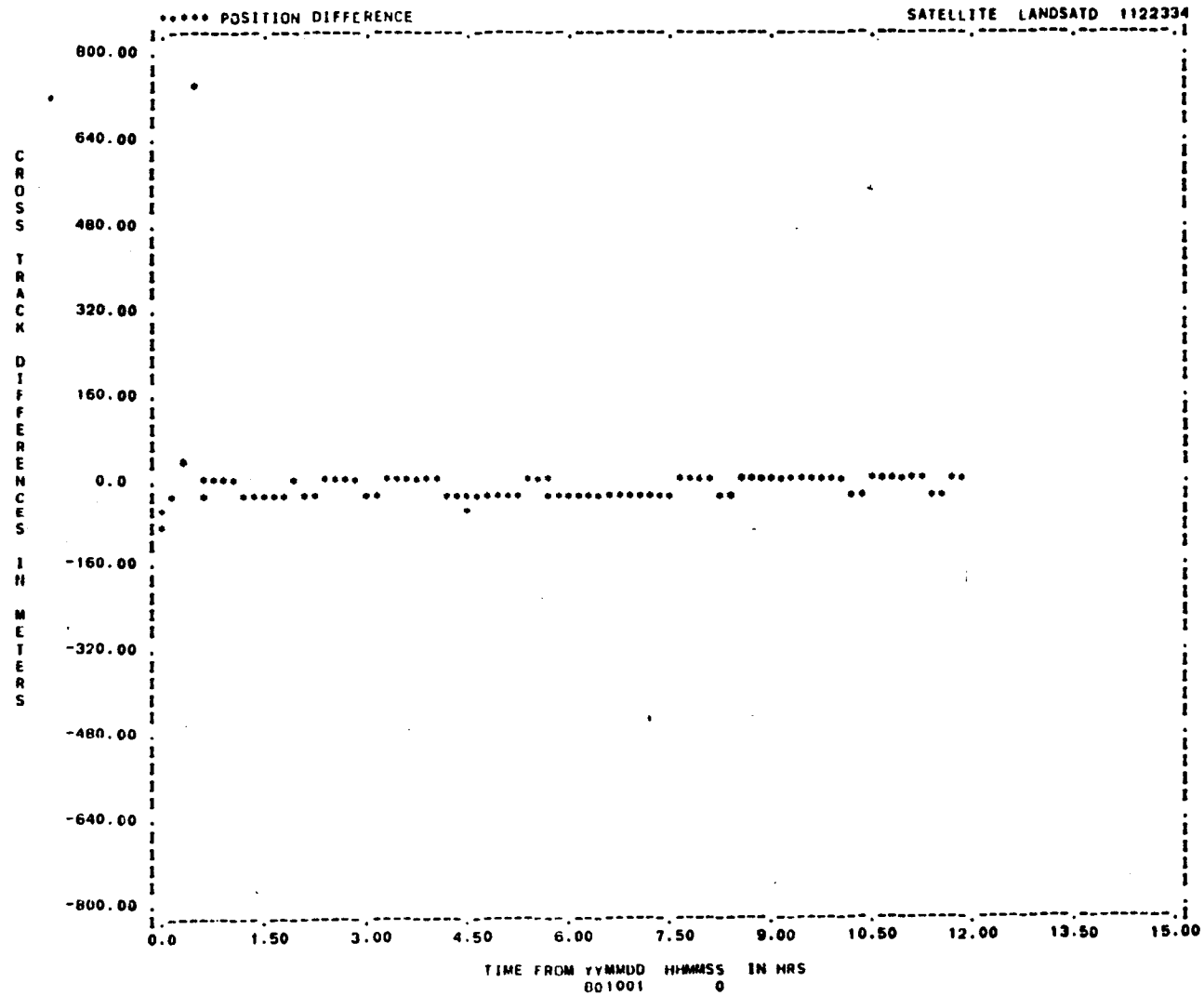

Figure A-29. Cross-Track Differences for Run G1

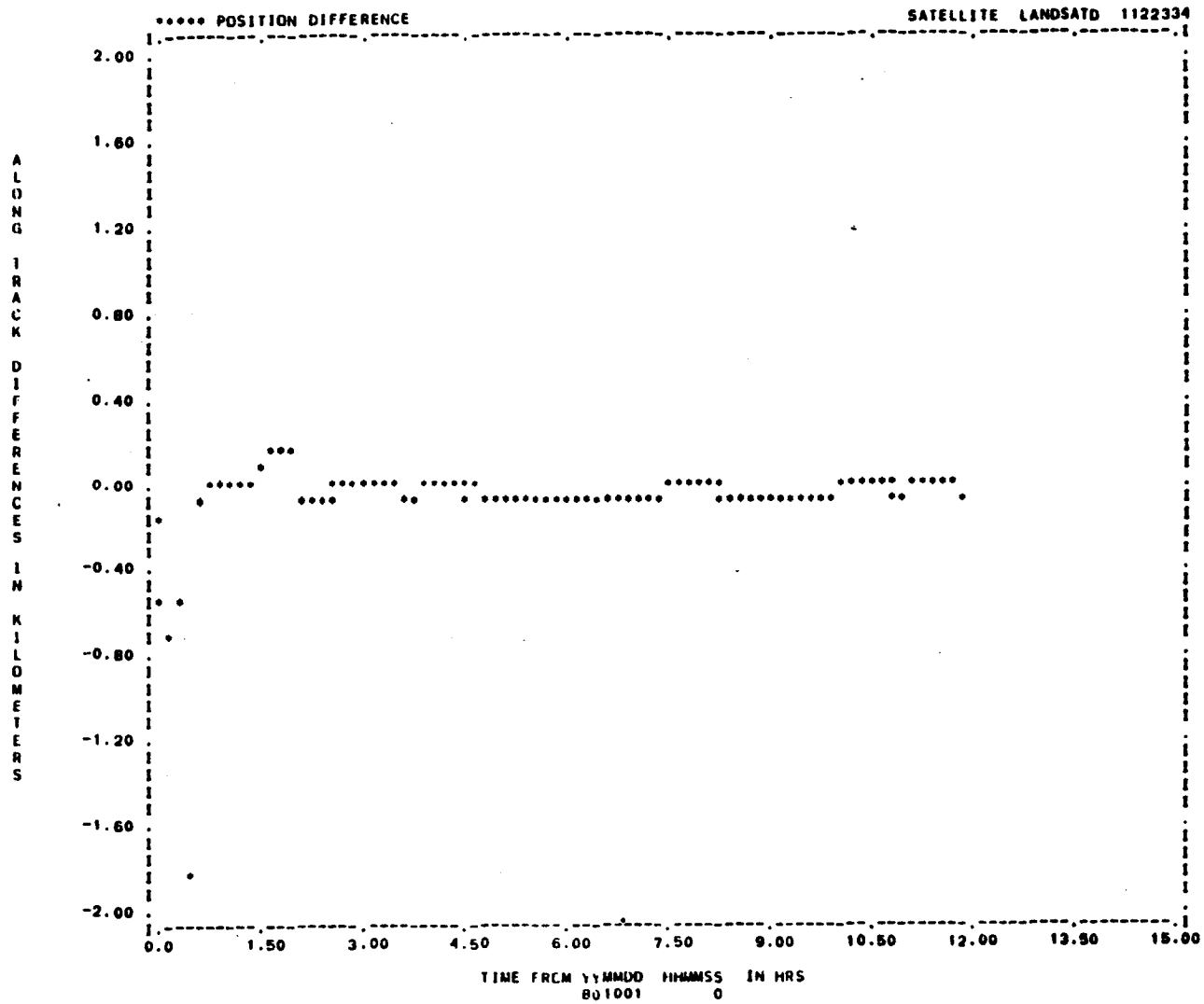

Figure A-30. Along-Track Differences for Run G1

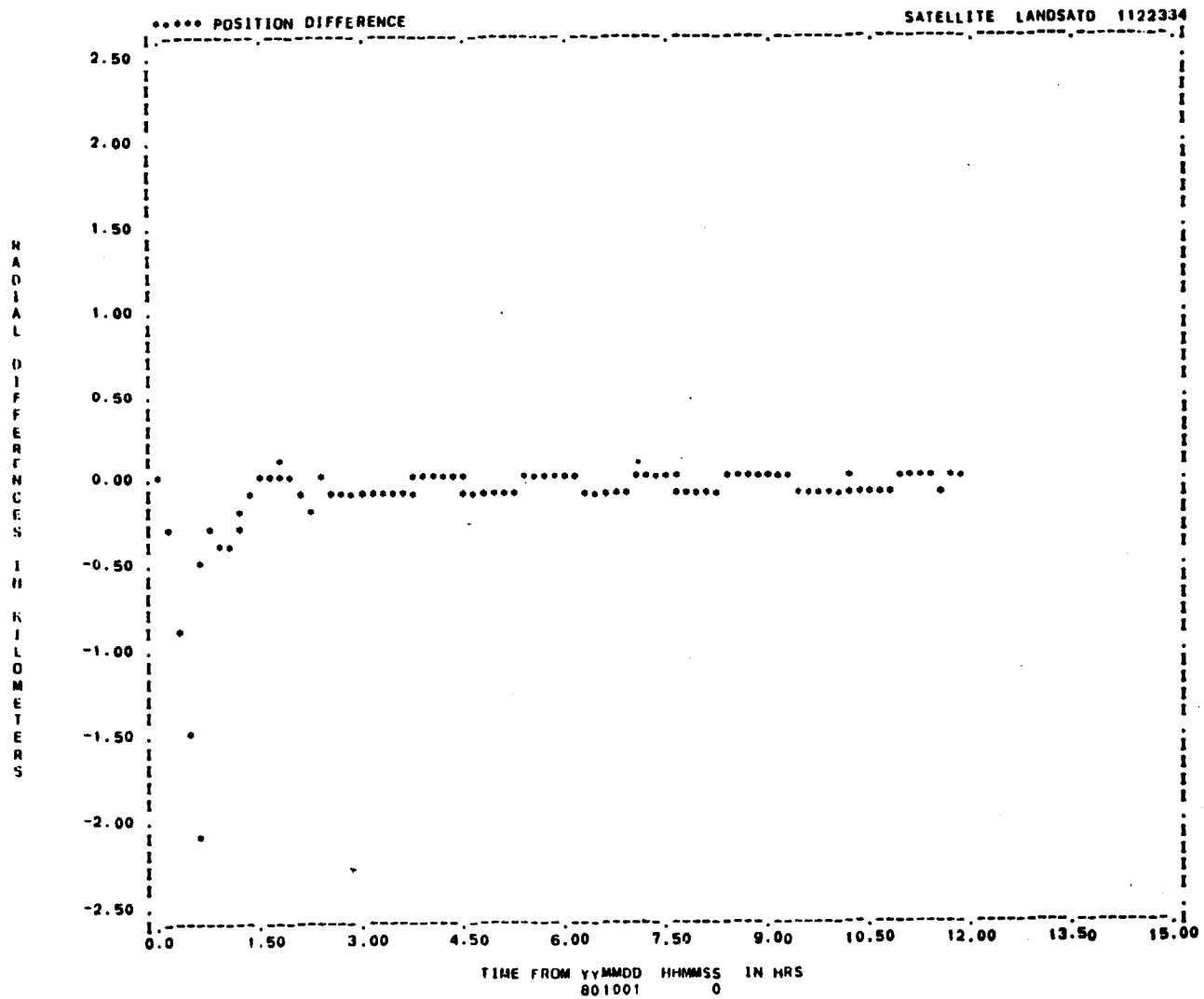

Figure A-31. Radial Differences for Run H3 (1 of 2)

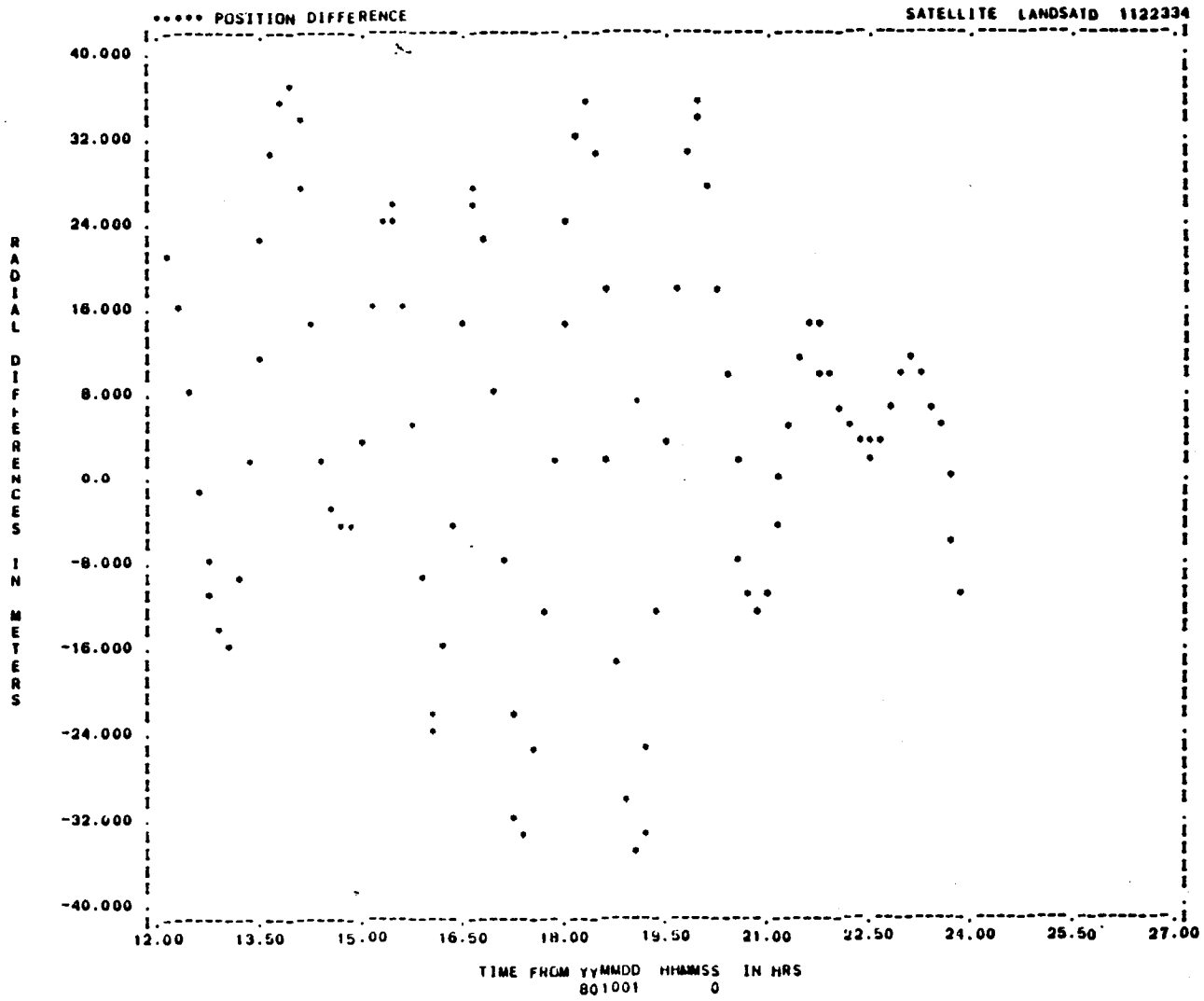

Figure A-31. Radial Differences for Run H3 (2 of 2)

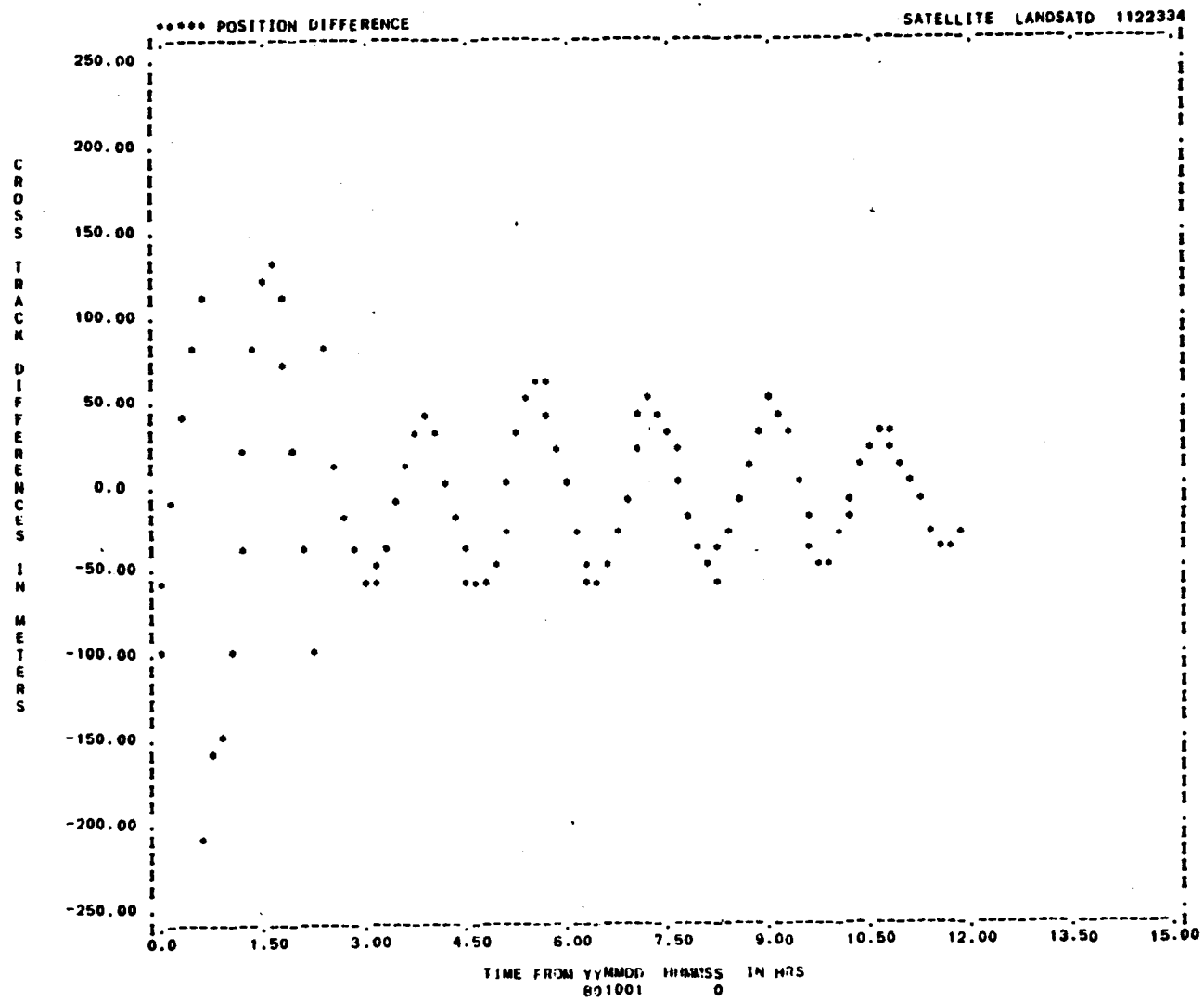

Figure A-32. Cross-Track Differences for Run H3 (1 of 2)

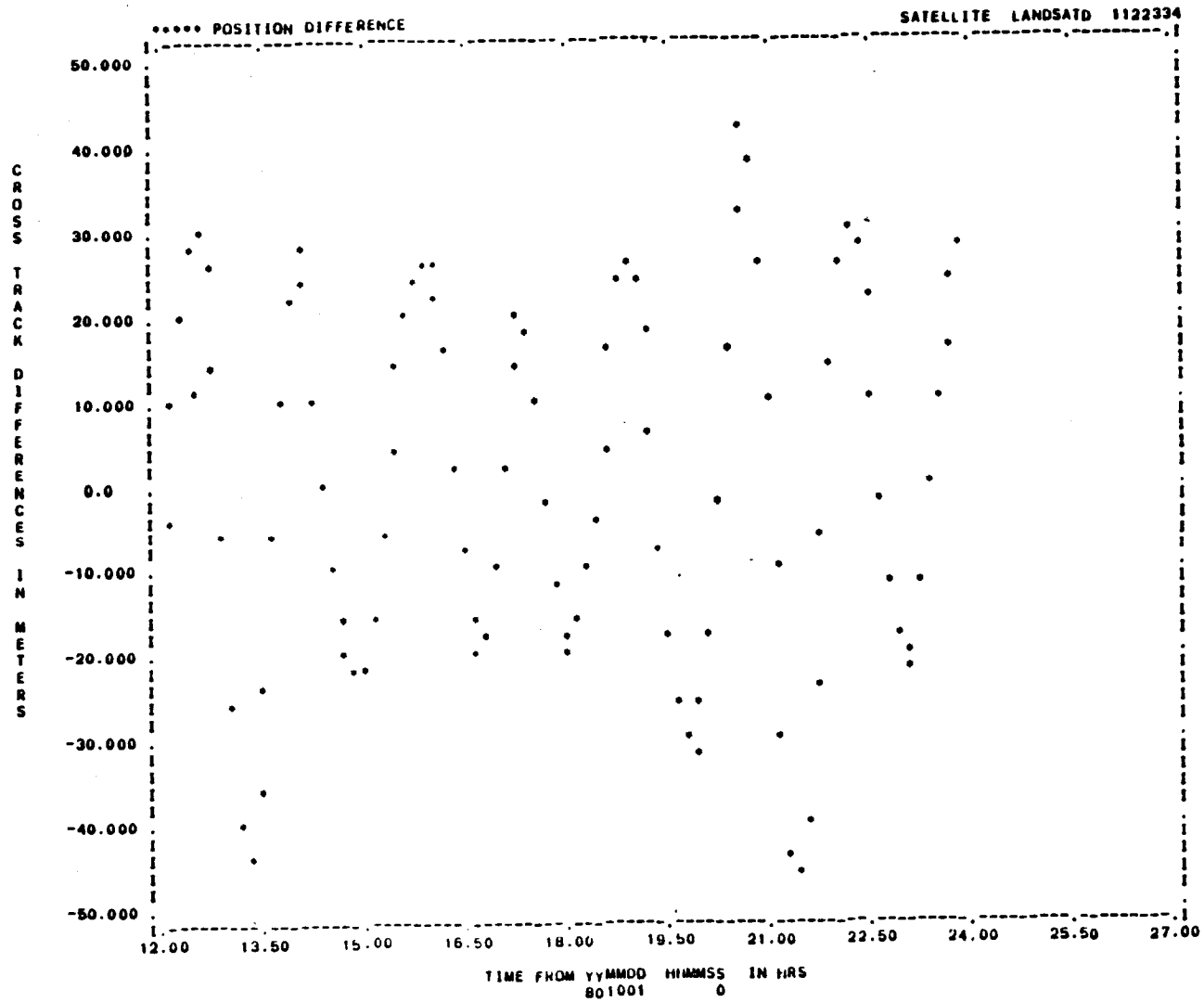

Figure A-32. Cross-Track Differences for Run H3 (2 of 2)

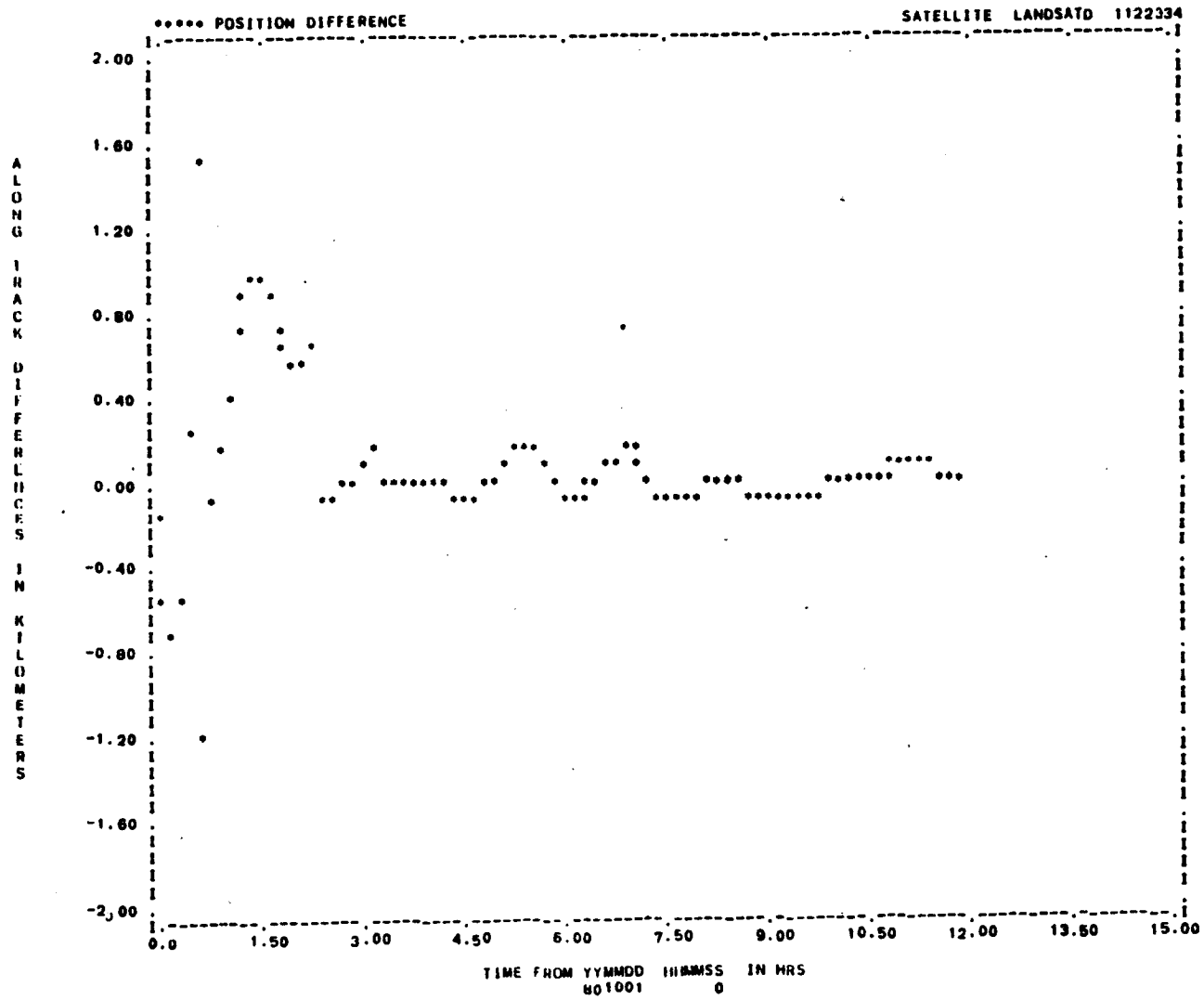

Figure A-33. Along-Track Differences for Run H3 (1 of 2)

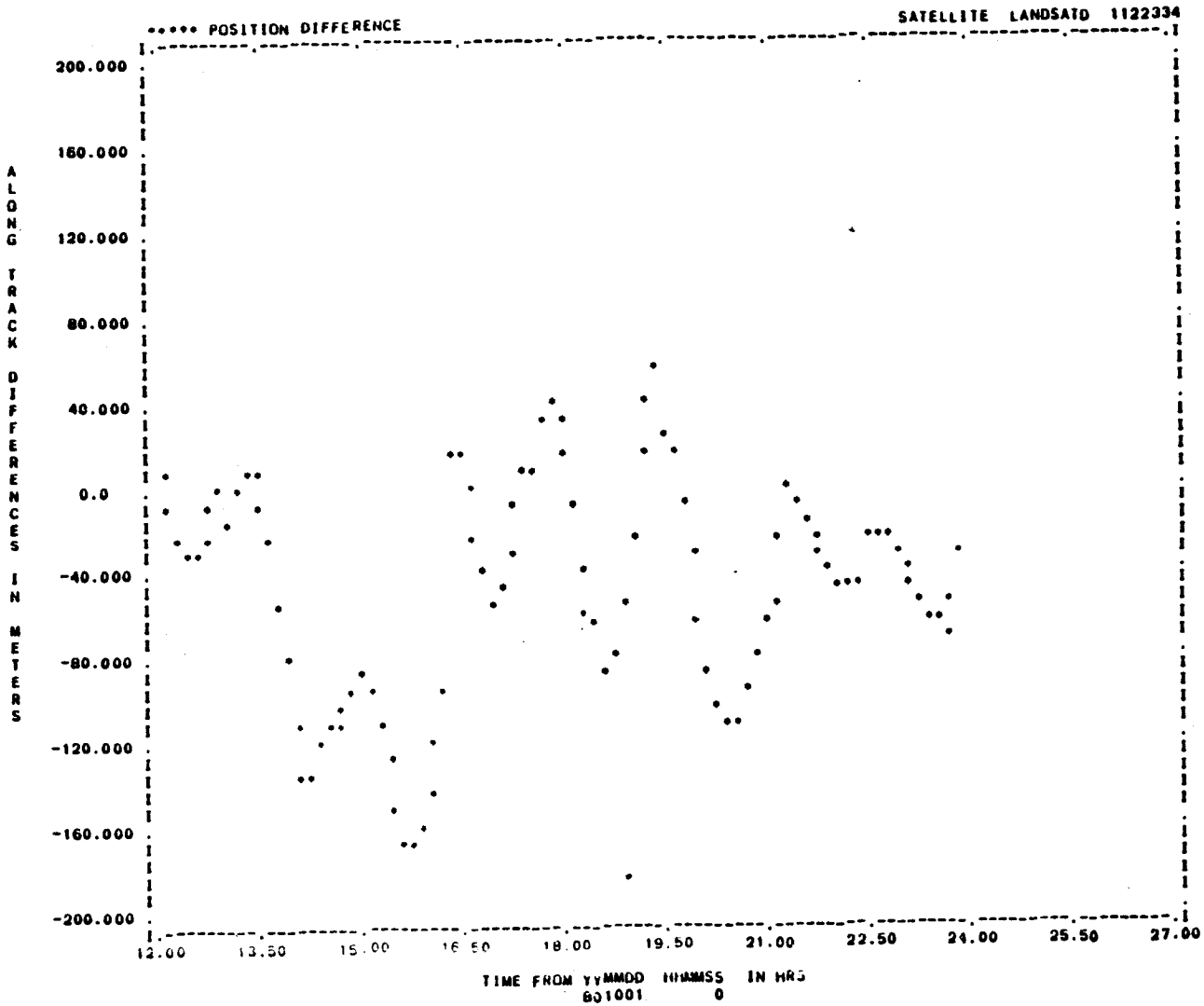

Figure A-33. Along-Track Differences for Run H3 (2 of 2)

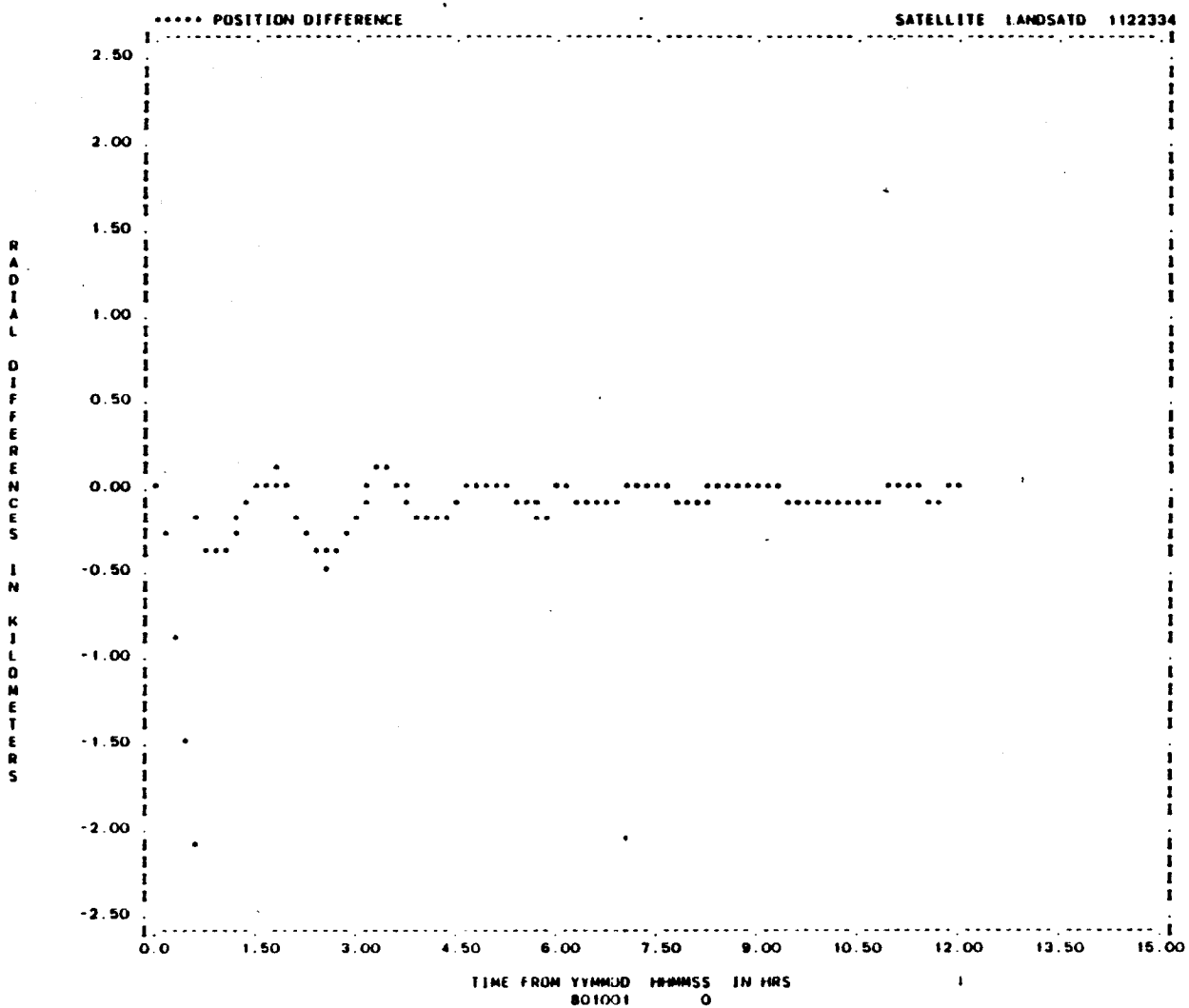

Figure A-34. Radial Differences for Run I6 (1 of 2)

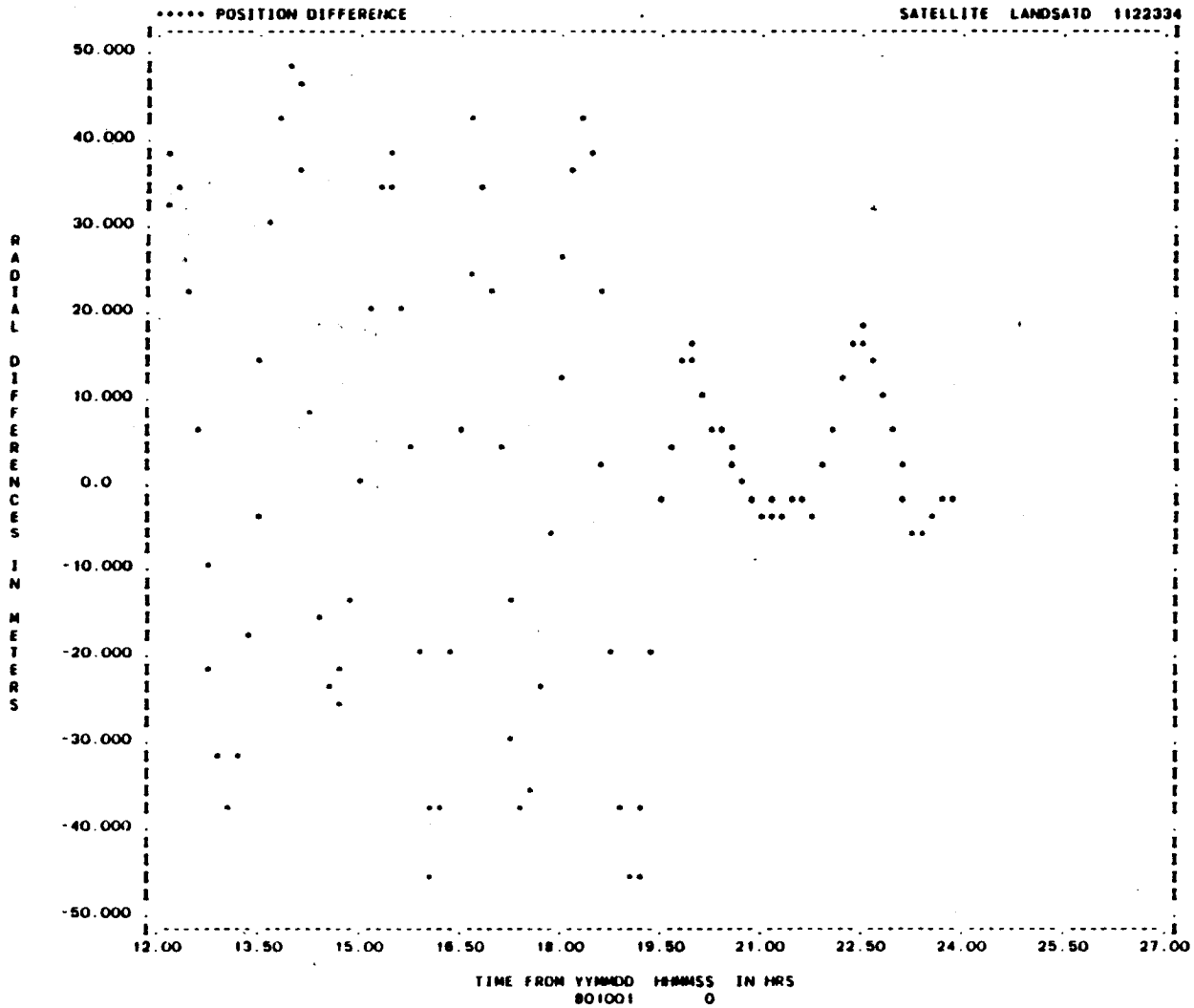

Figure A-34. Radial Differences for Run I6 (2 of 2)

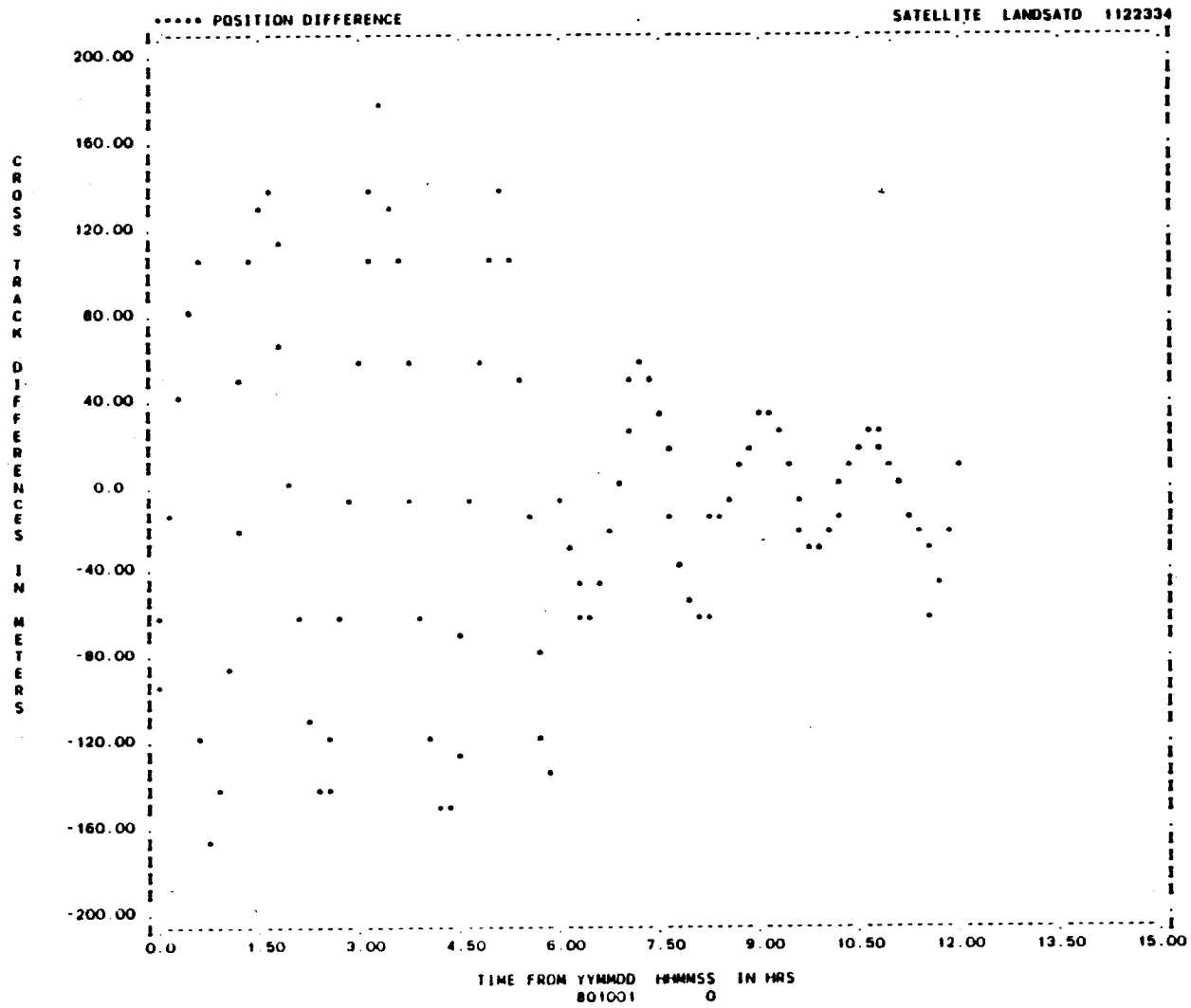

Figure A-35. Cross-Track Differences for Run I6 (1 of 2)

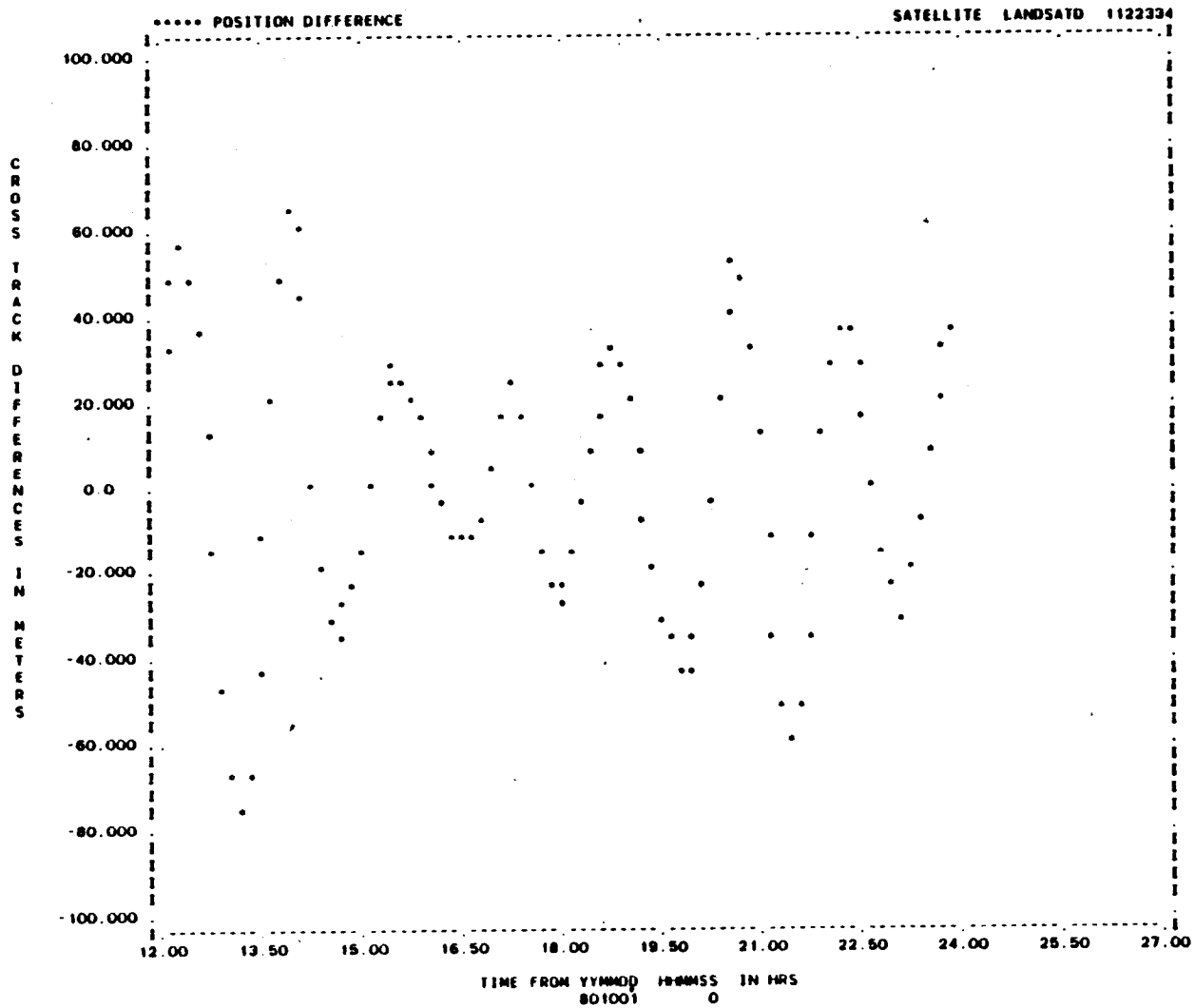

Figure A-35. Cross-Track Differences for Run I6 (2 of 2)

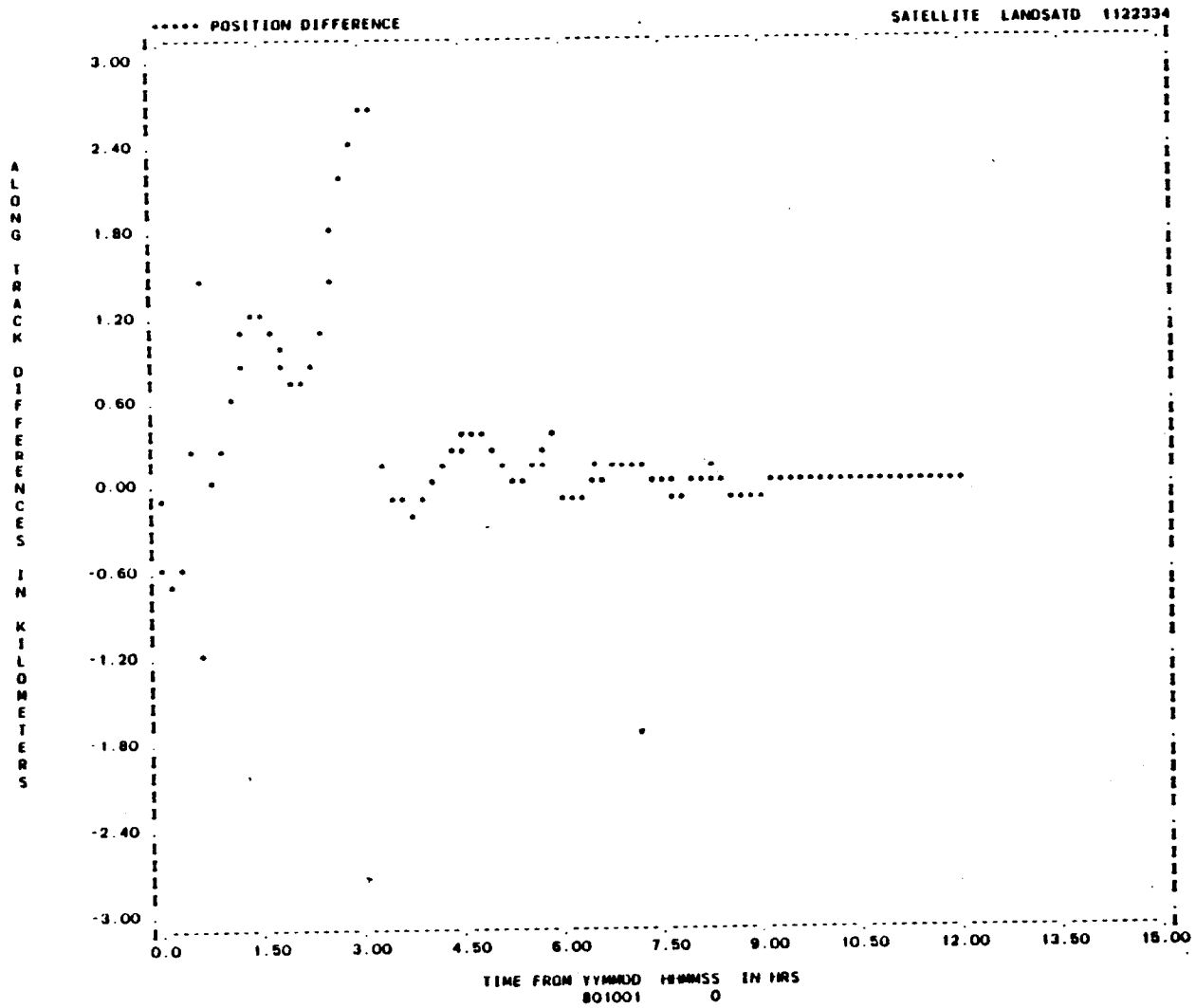

Figure A-36. Along-Track Differences for Run I6 (1 of 2)

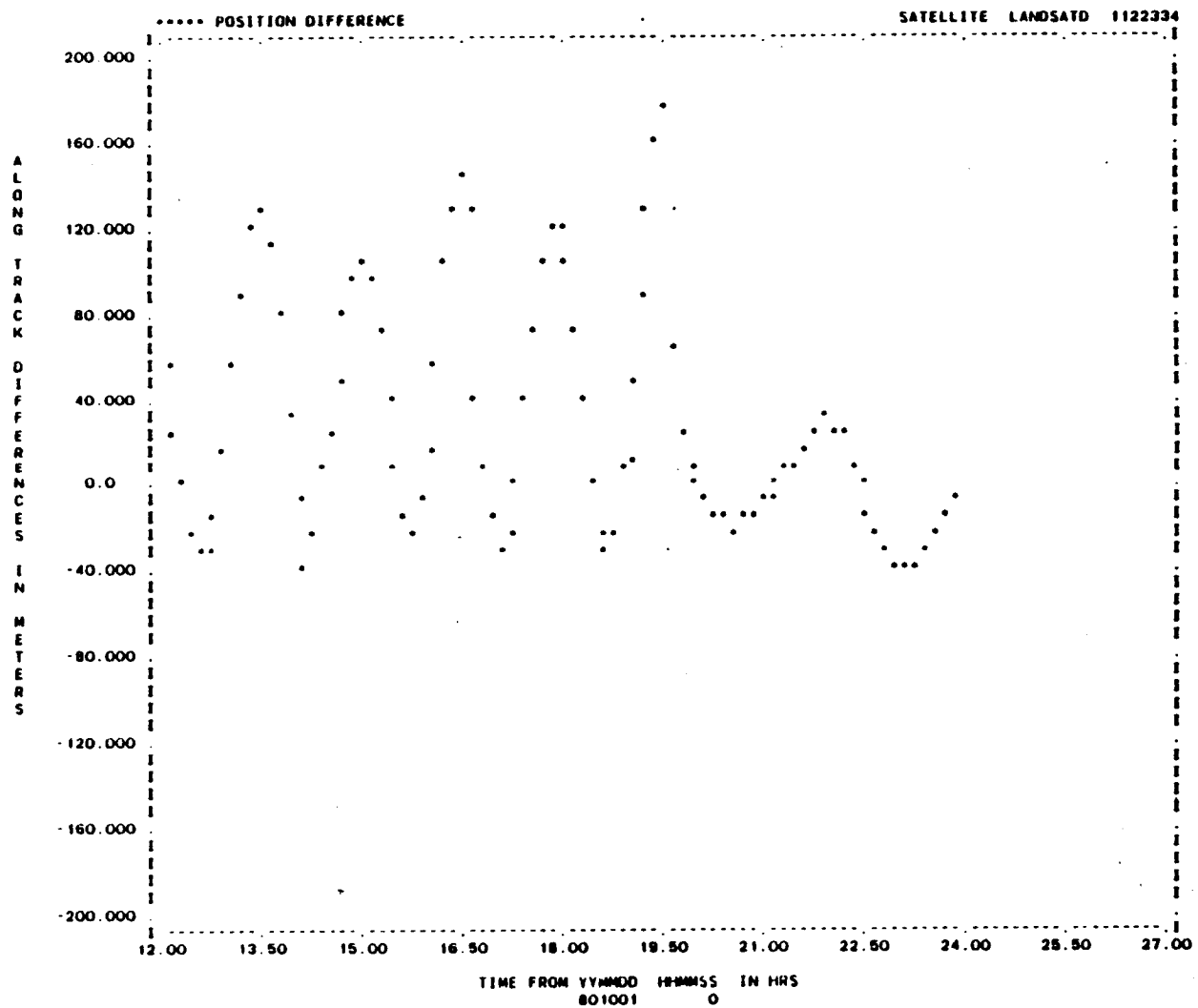

Figure A-36. Along-Track Differences for Run I6 (2 of 2)

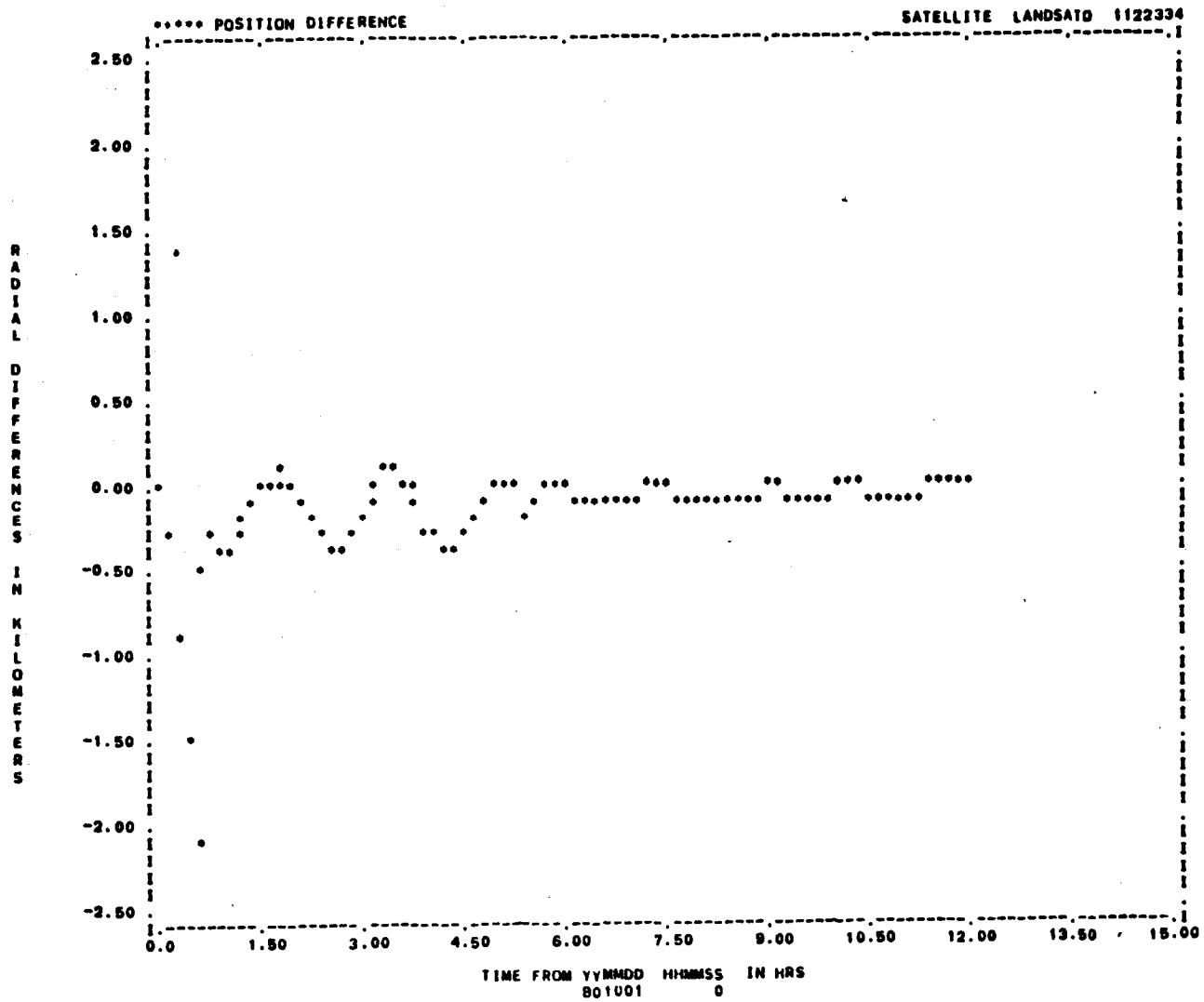

Figure A-37. Radial Differences for Run J3 (1 of 2)

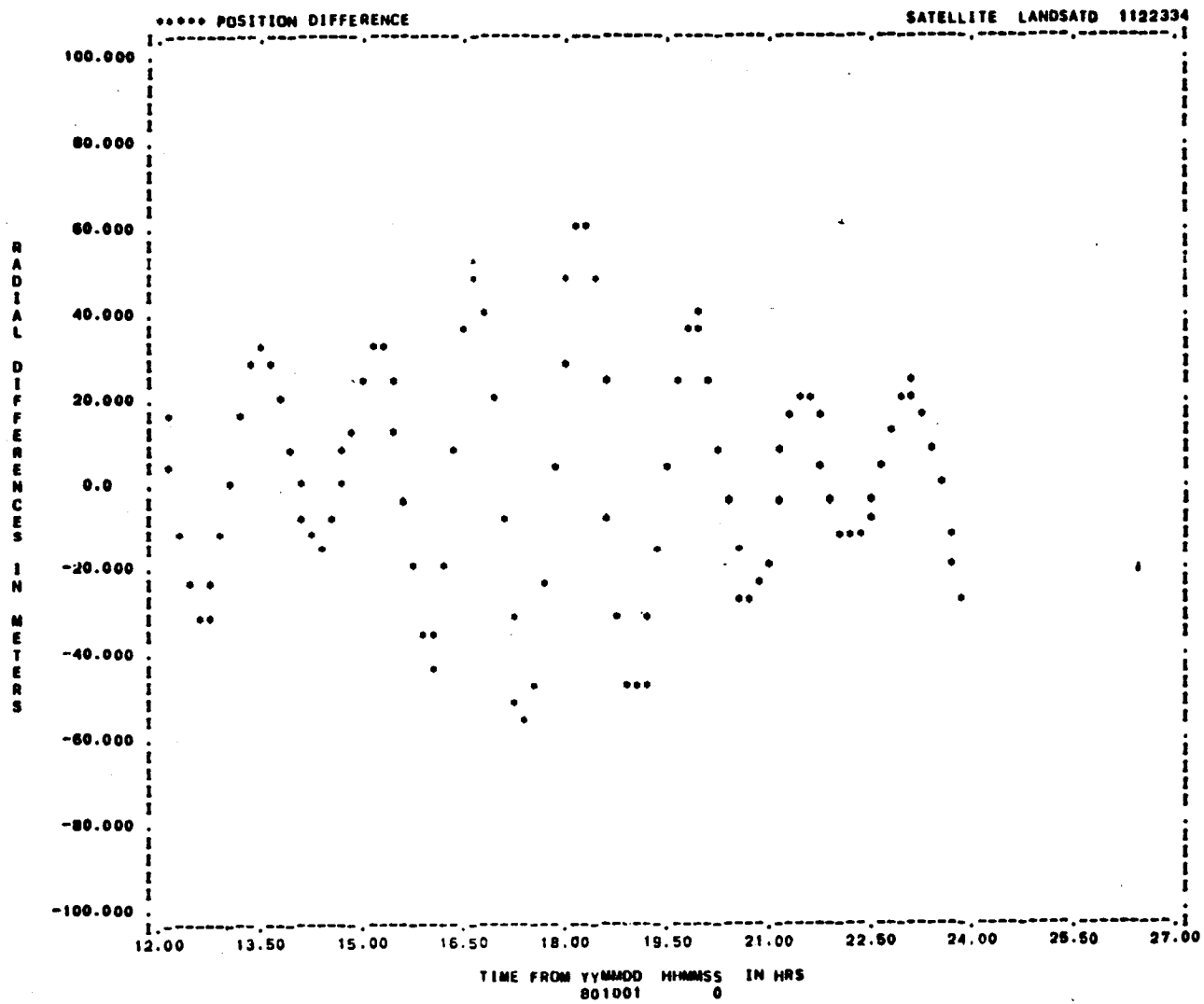

Figure A-37. Radial Differences for Run J3 (2 of 2)

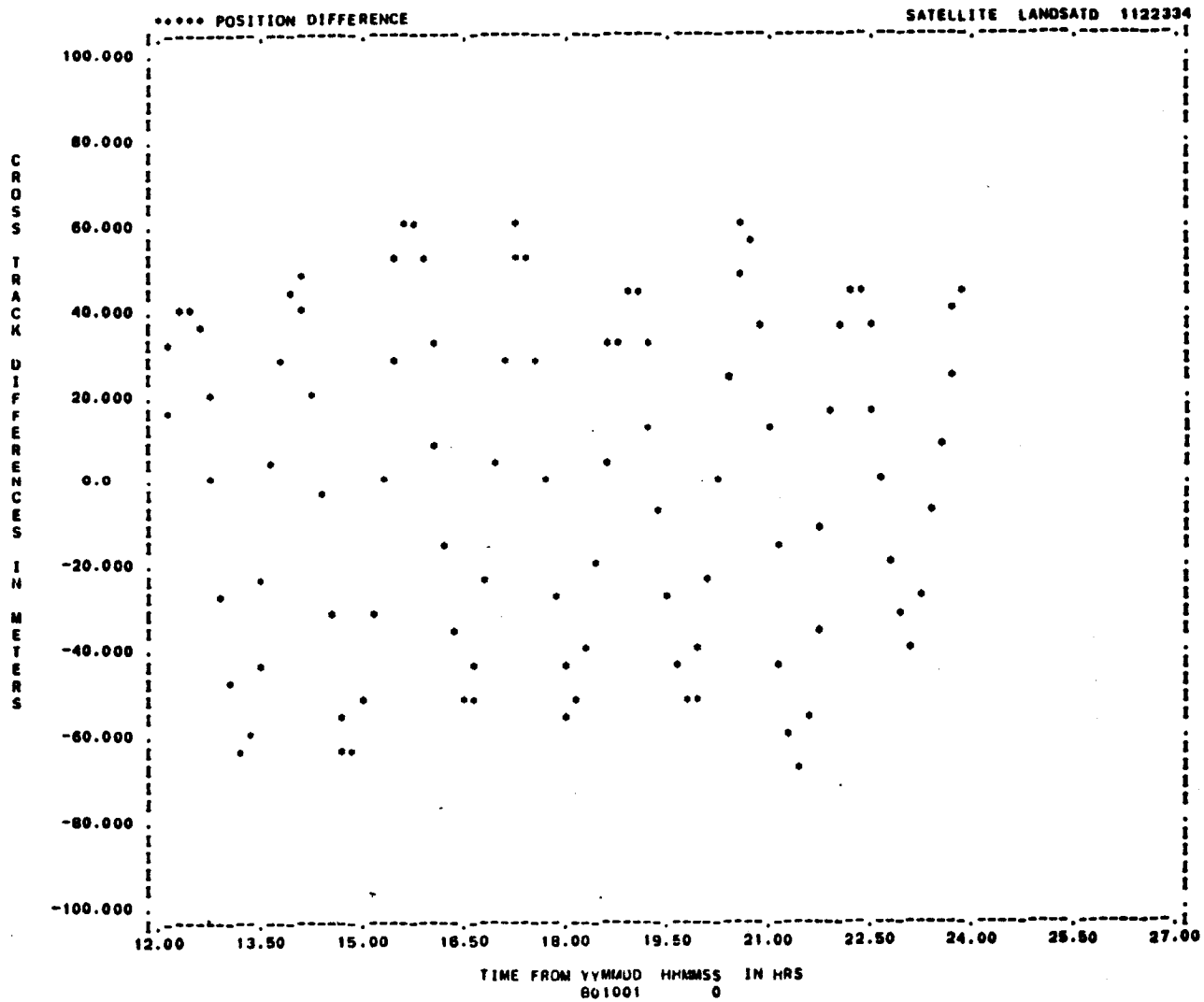

Figure A-38. Cross-Track Differences for Run J3 (2 of 2)

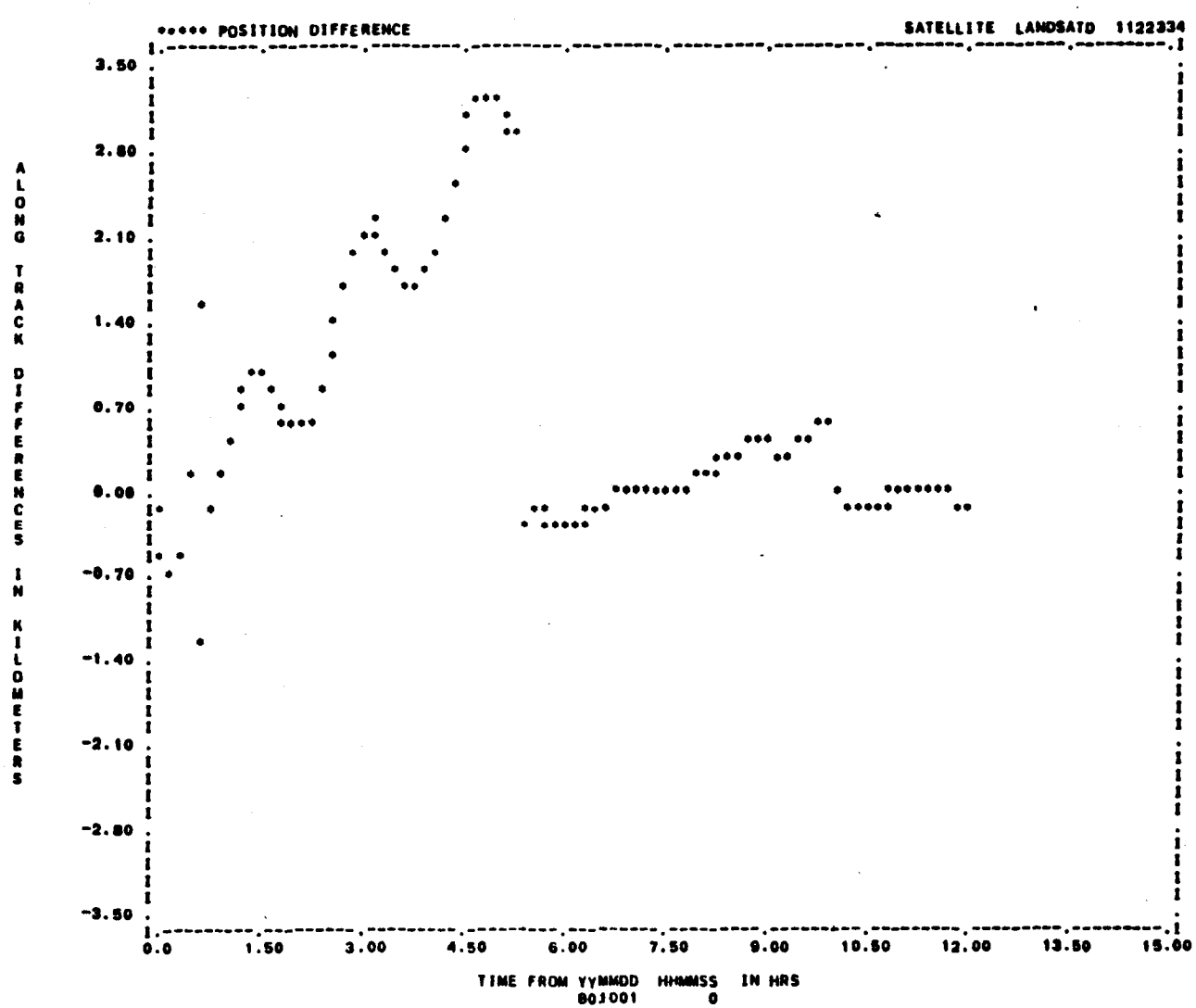

Figure A-39. Along-Track Differences for Run J3 (1 of 2)

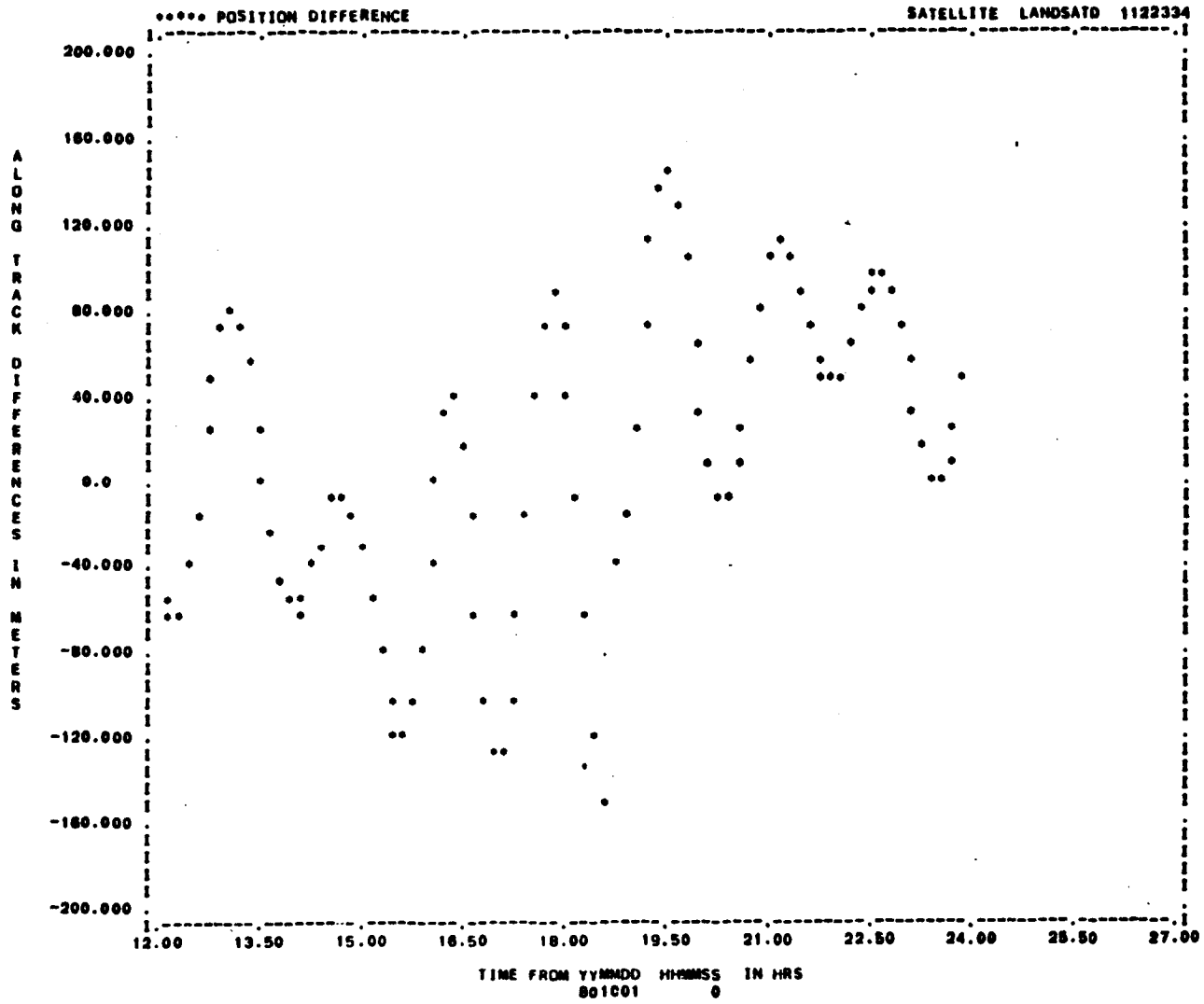

Figure A-39. Along-Track Differences for Run J3 (2 of 2)

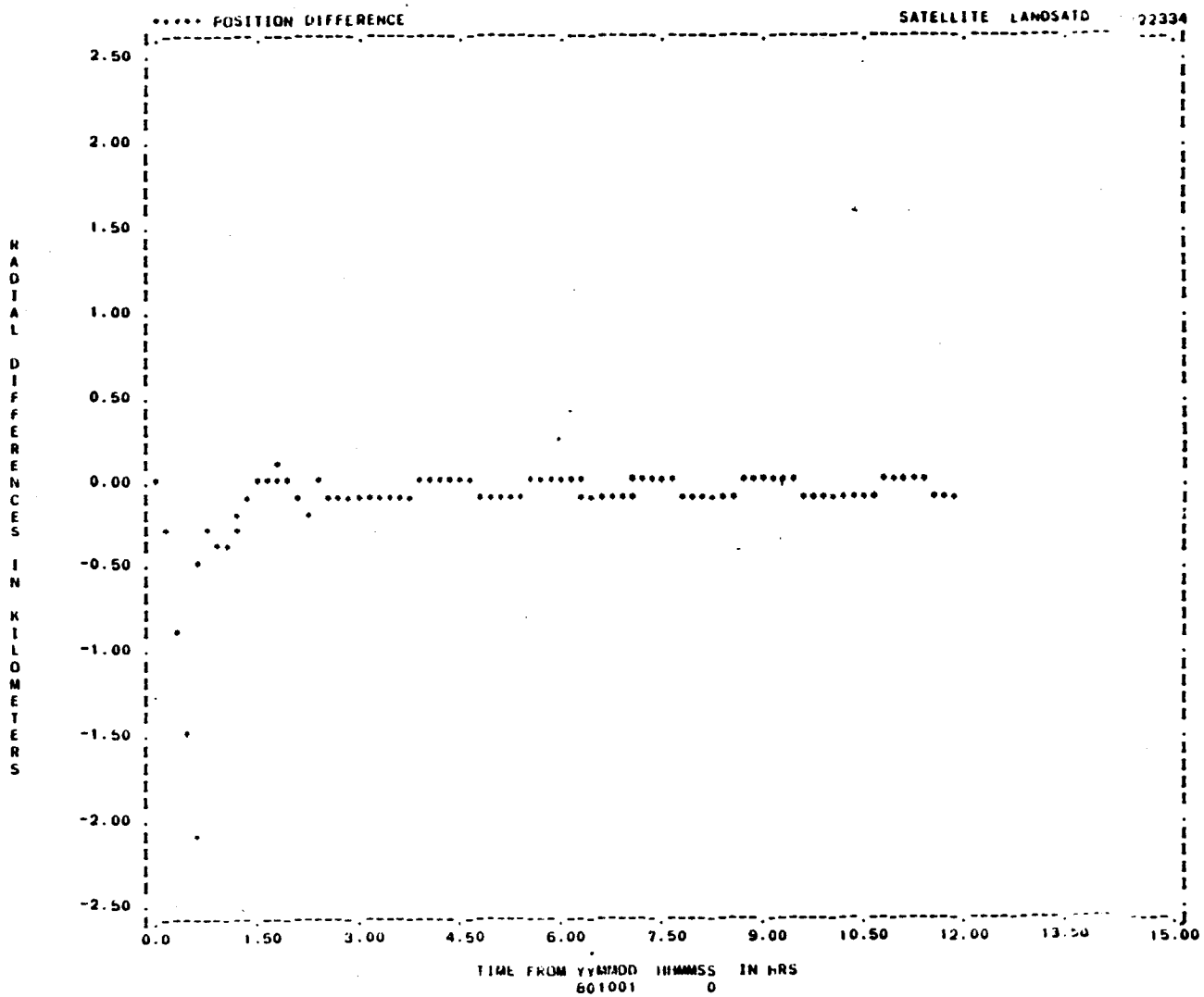

Figure A-40. Radial Differences for Run K2

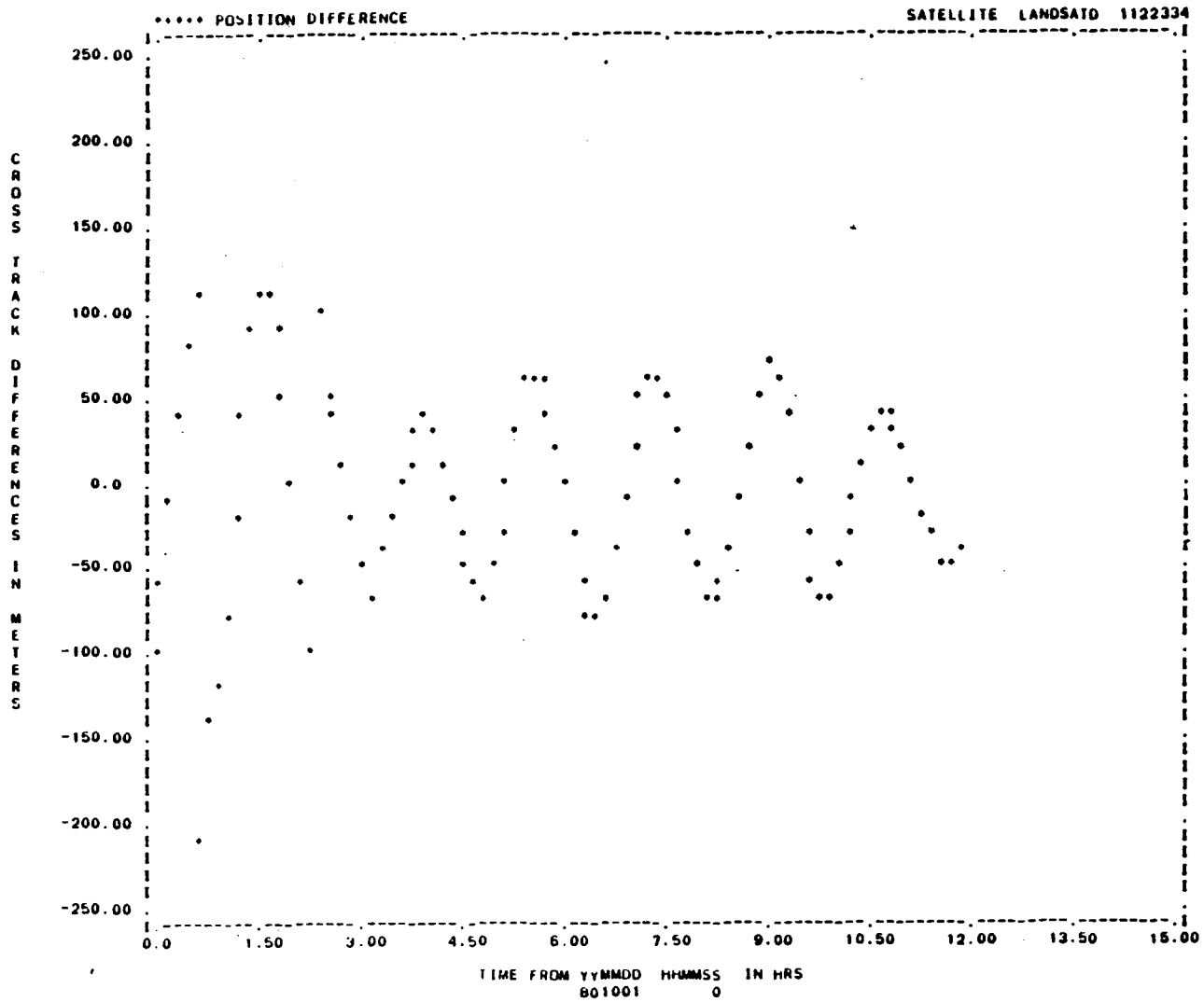

Figure A-41. Cross-Track Differences for Run K2

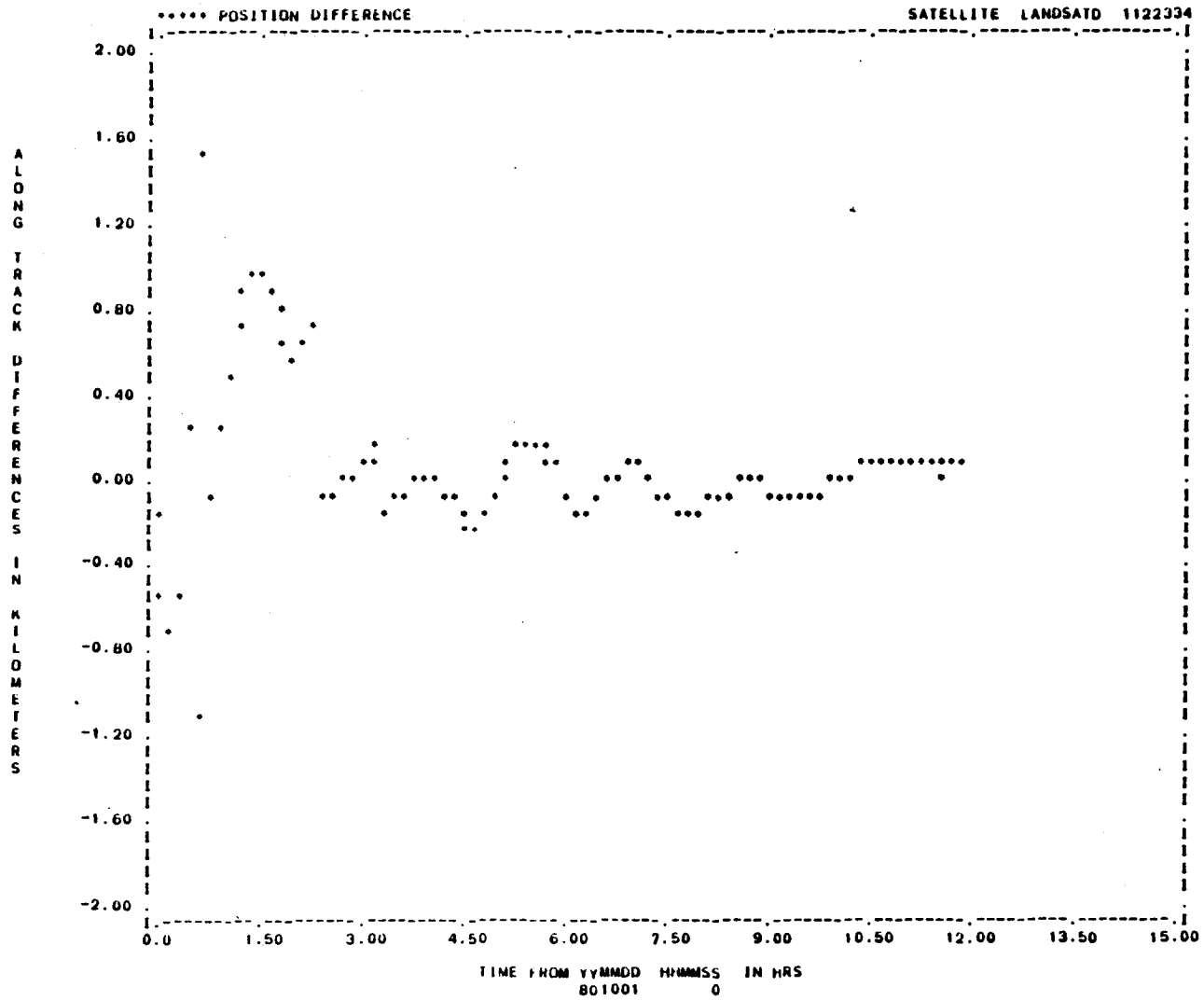

Figure A-42. Along-Track Differences for Run K2

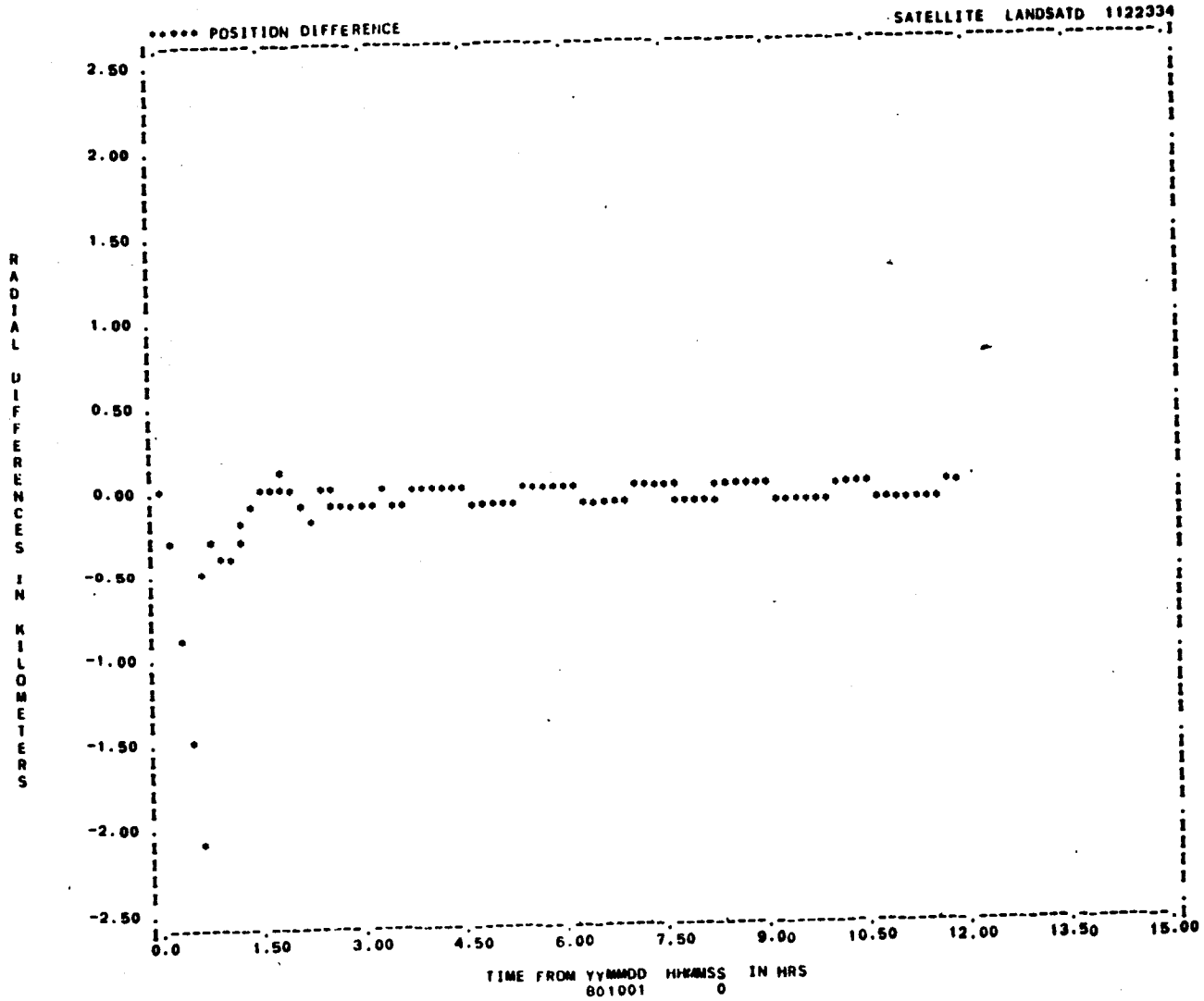

Figure A-43. Radial Differences for Run K3

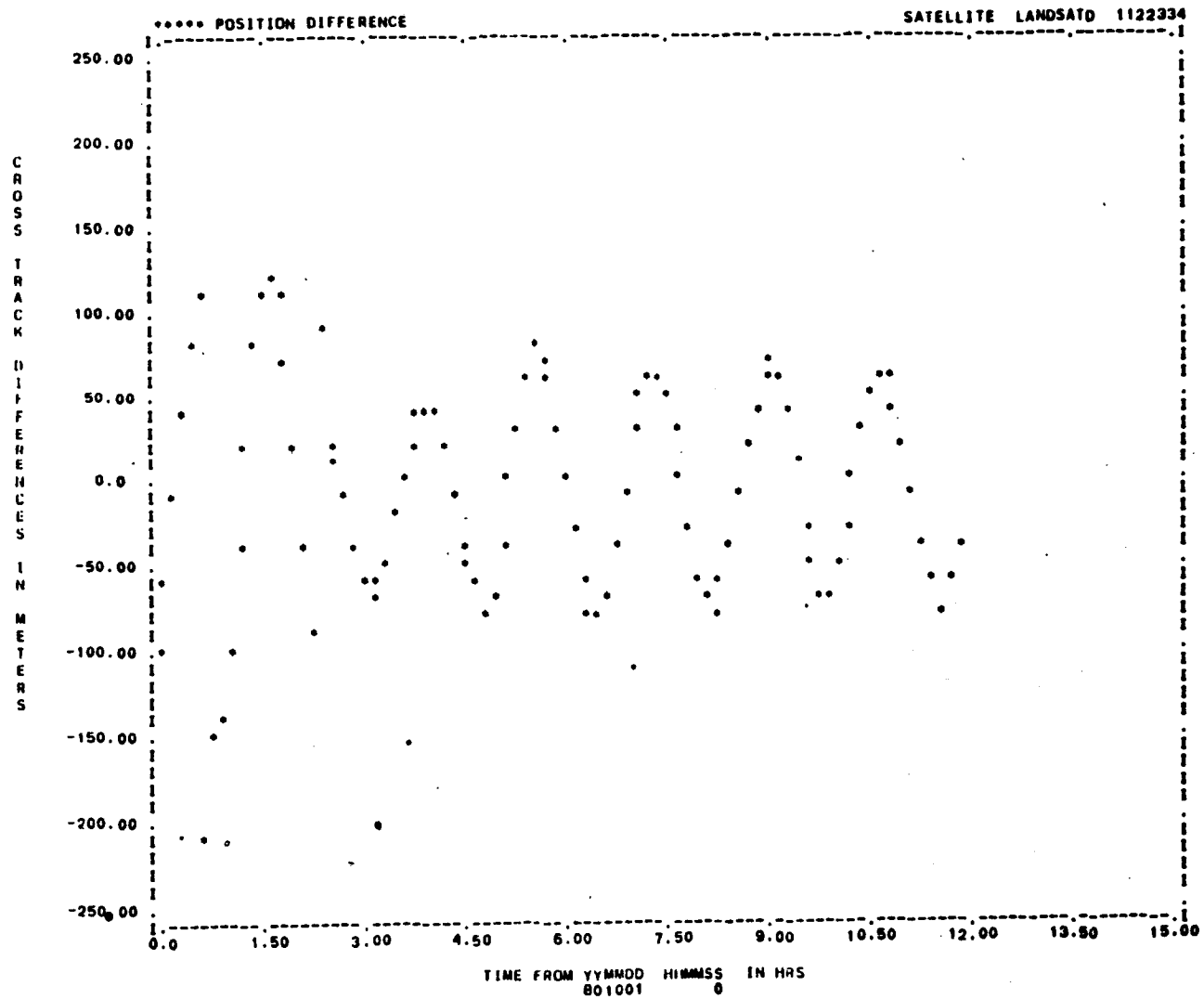

Figure A-44. Cross-Track Differences for Run K3

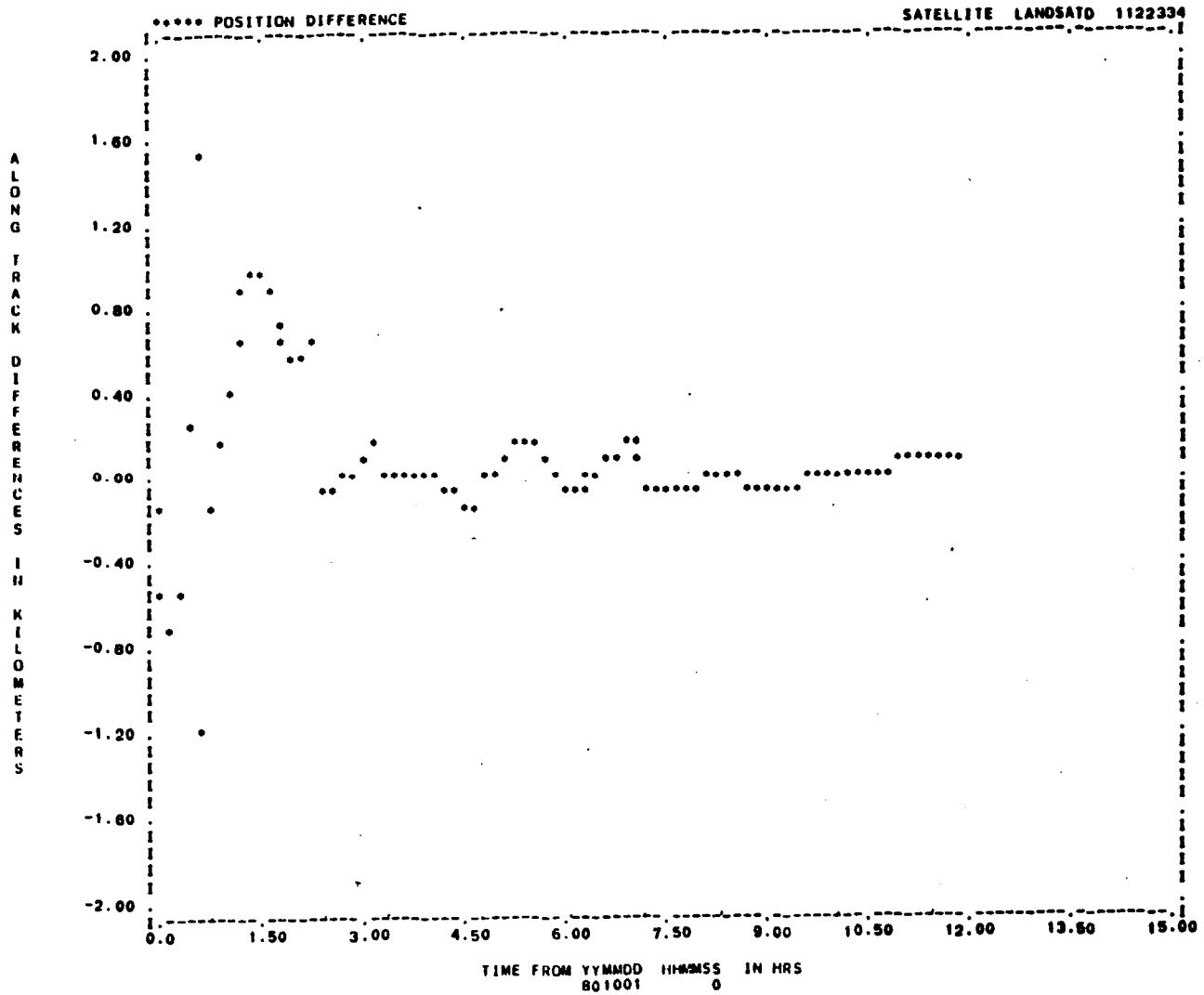

Figure A-45. Along-Track Differences for Run K3

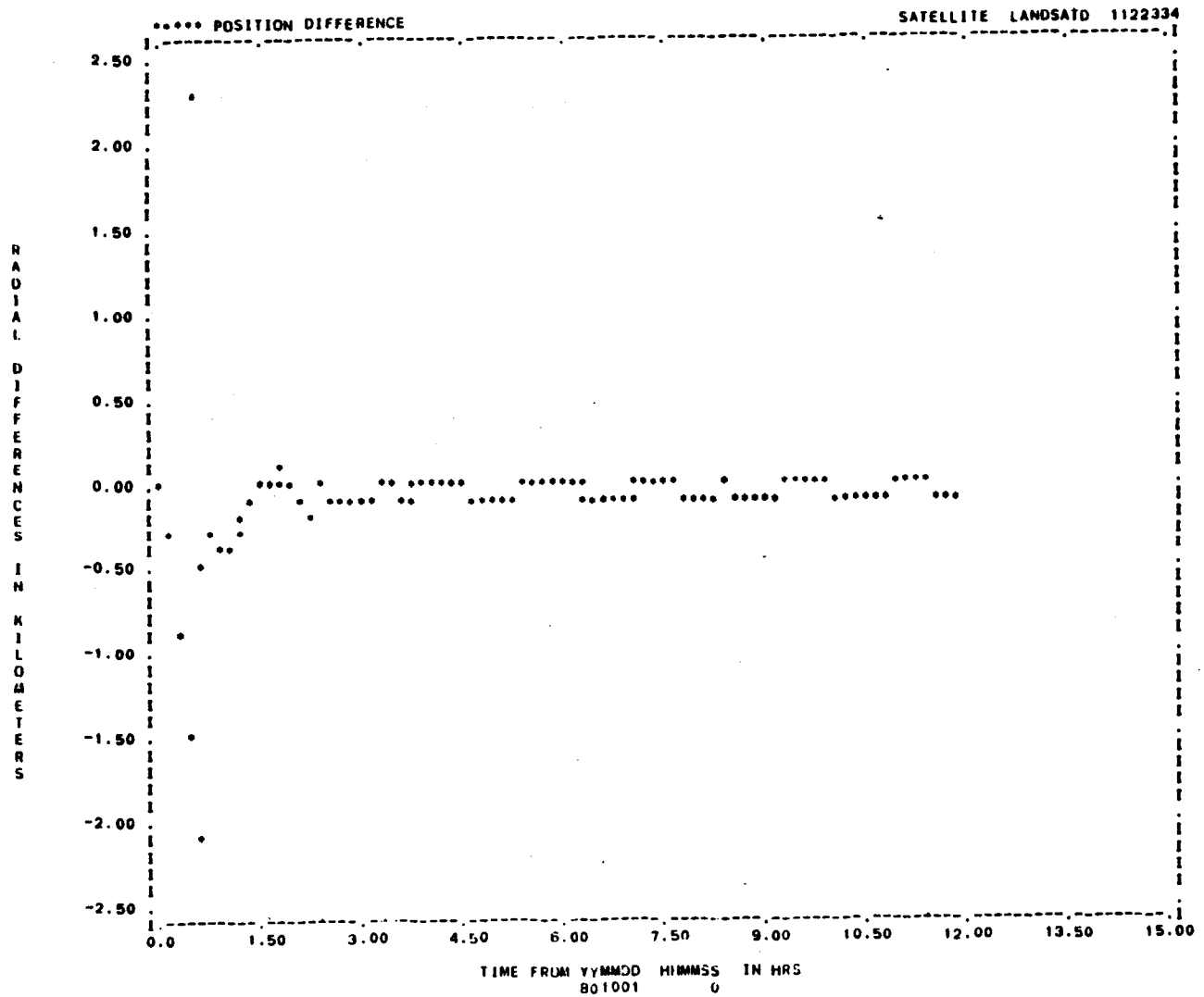

Figure A-46. Radial Differences for Run K6 (1 of 2)

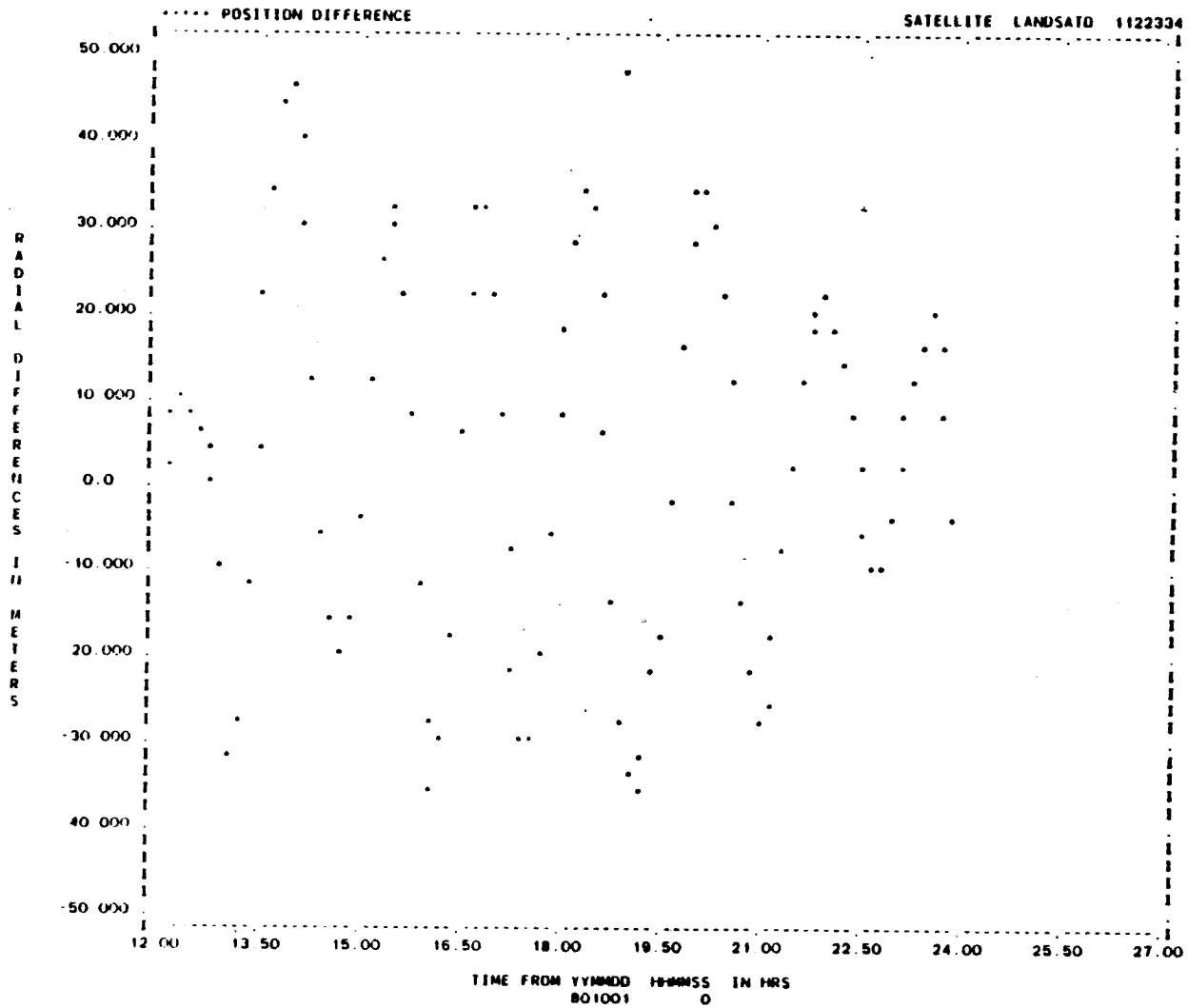

Figure A-46. Radial Differences for Run K6 (2 of 2)

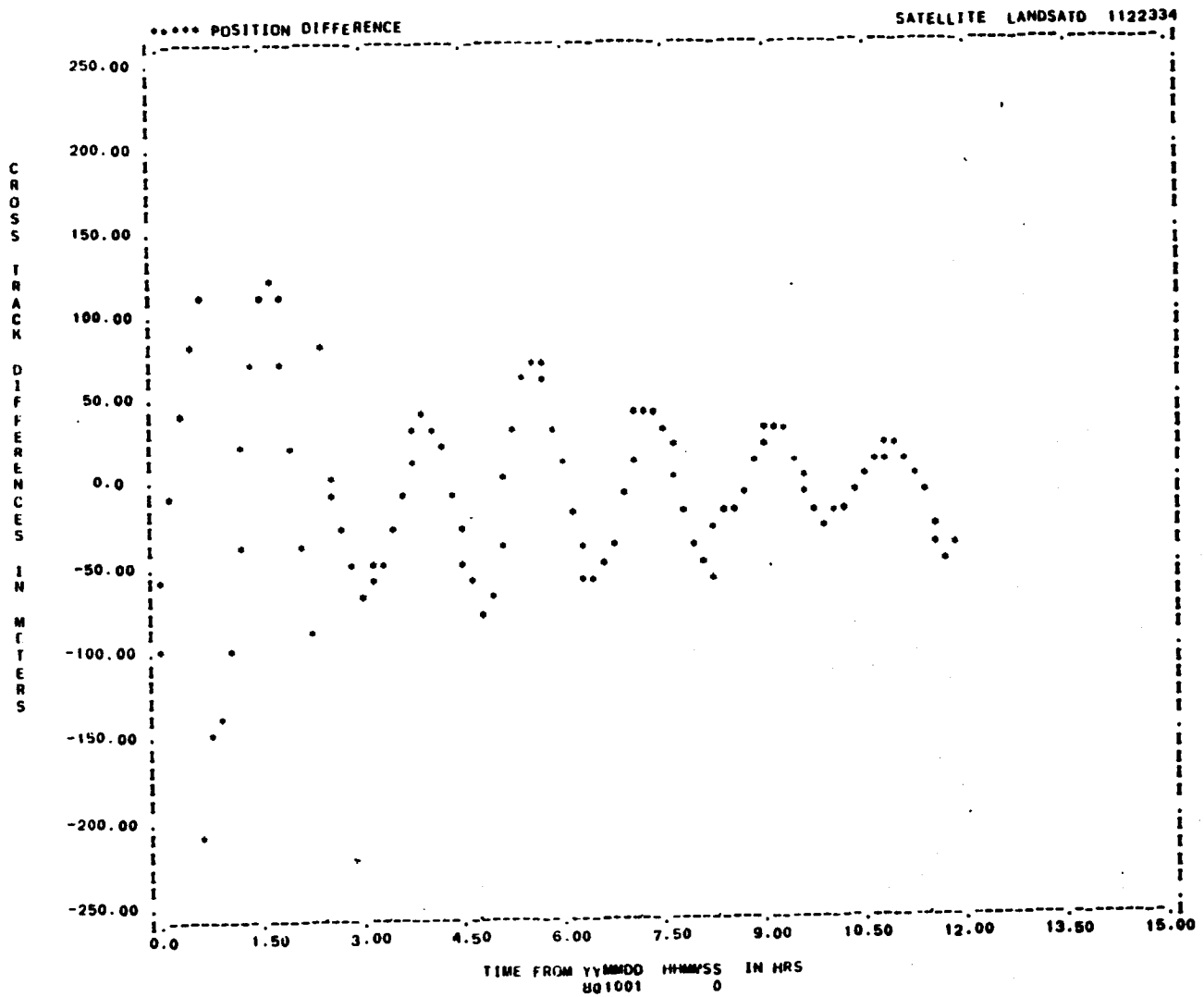

Figure A-47. Cross-Track Differences for Run K6 (1 of 2)

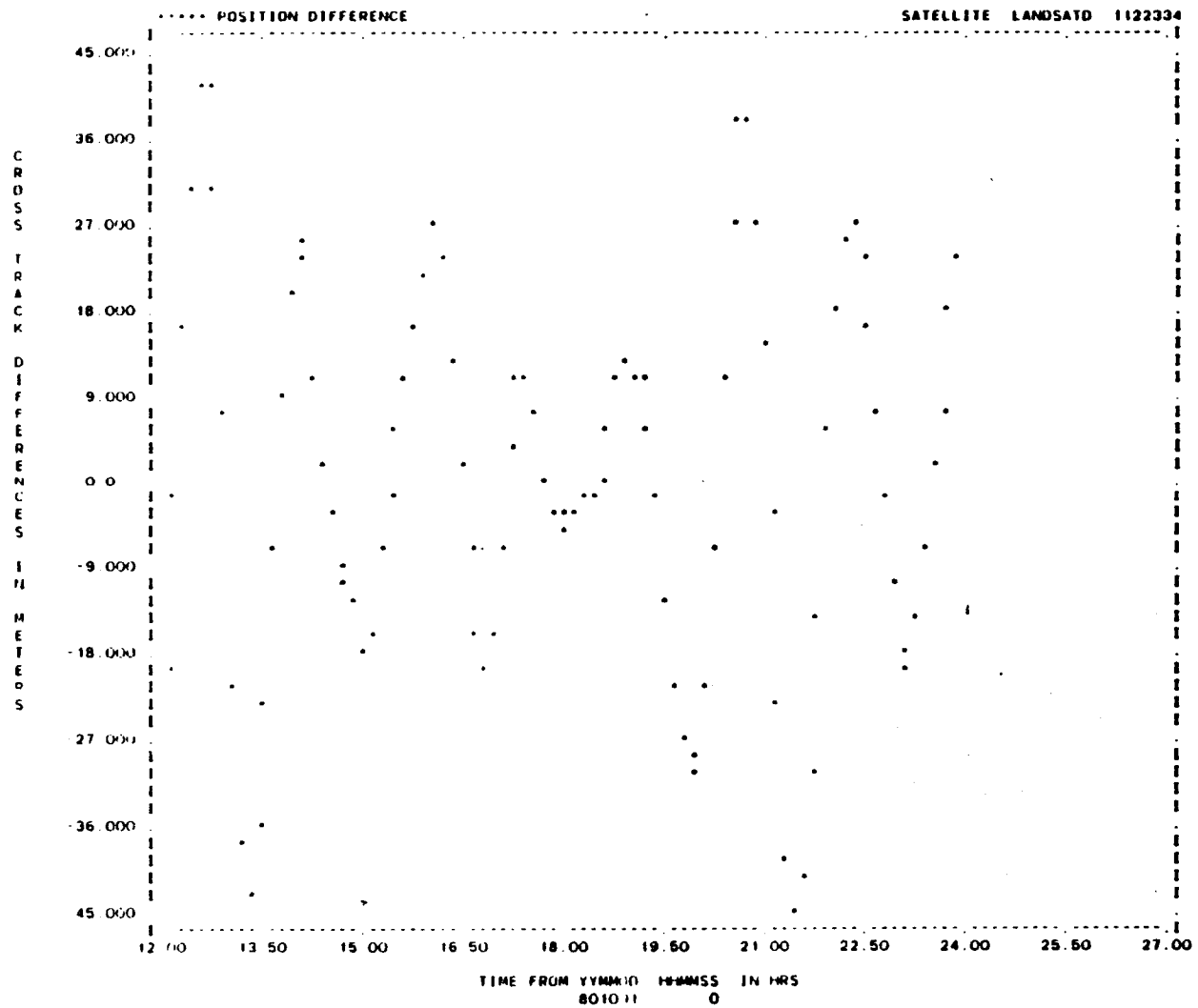

Figure A-47. Cross-Track Differences for Run K6 (2 of 2)

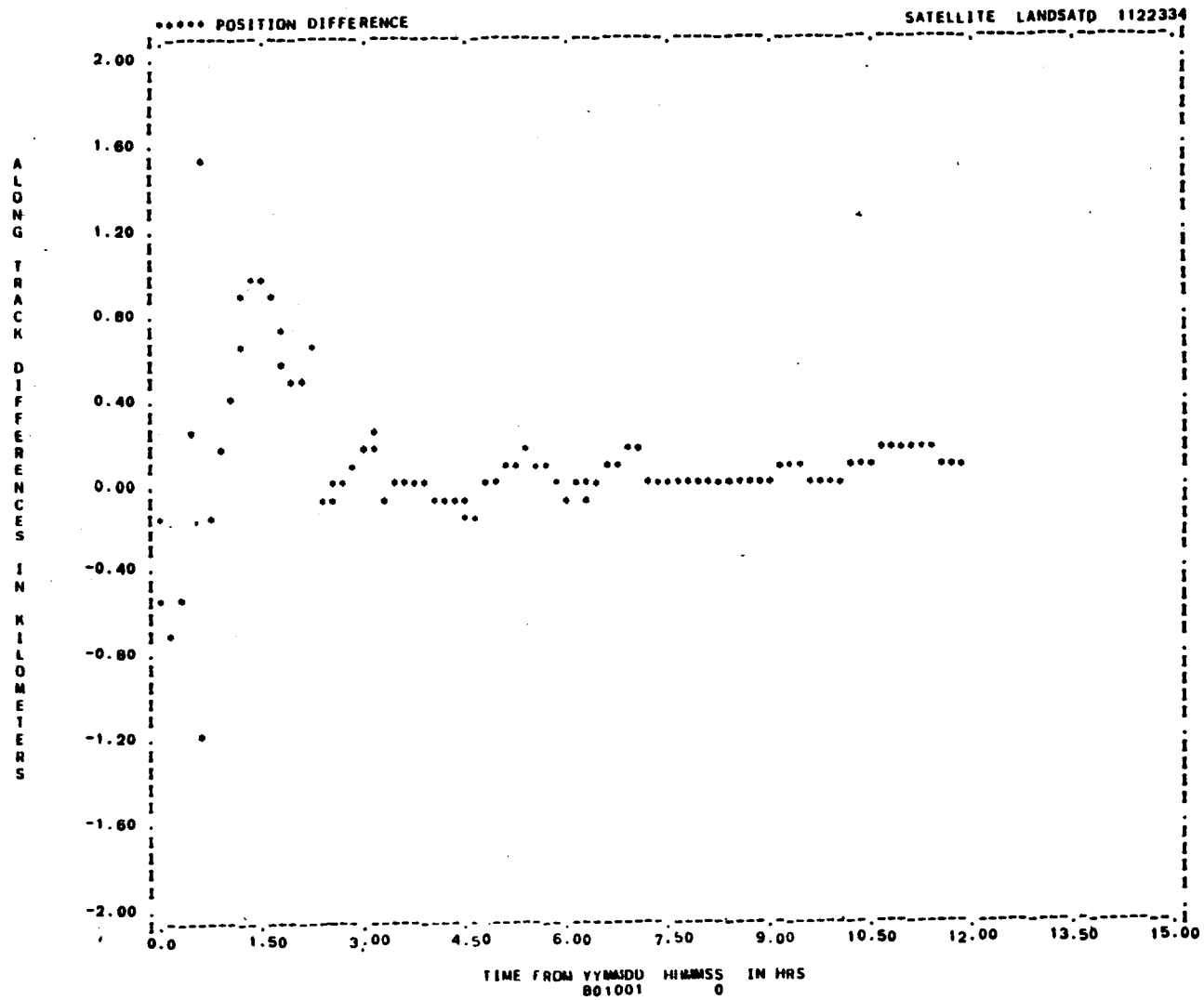

Figure A-48. Along-Track Differences for Run K6 (1 of 2)

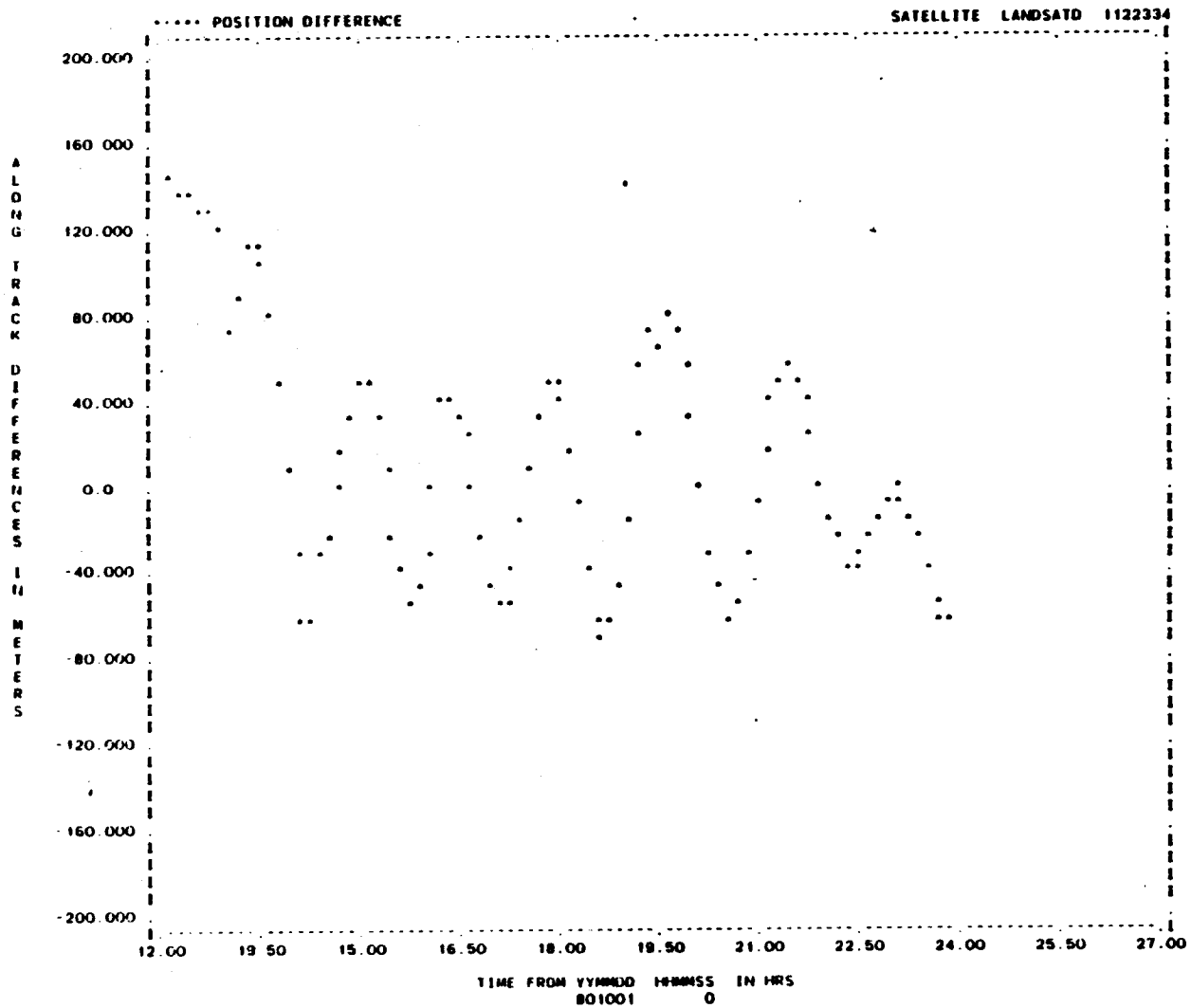

Figure A-48. Along-Track Differences for Run K6 (2 of 2)

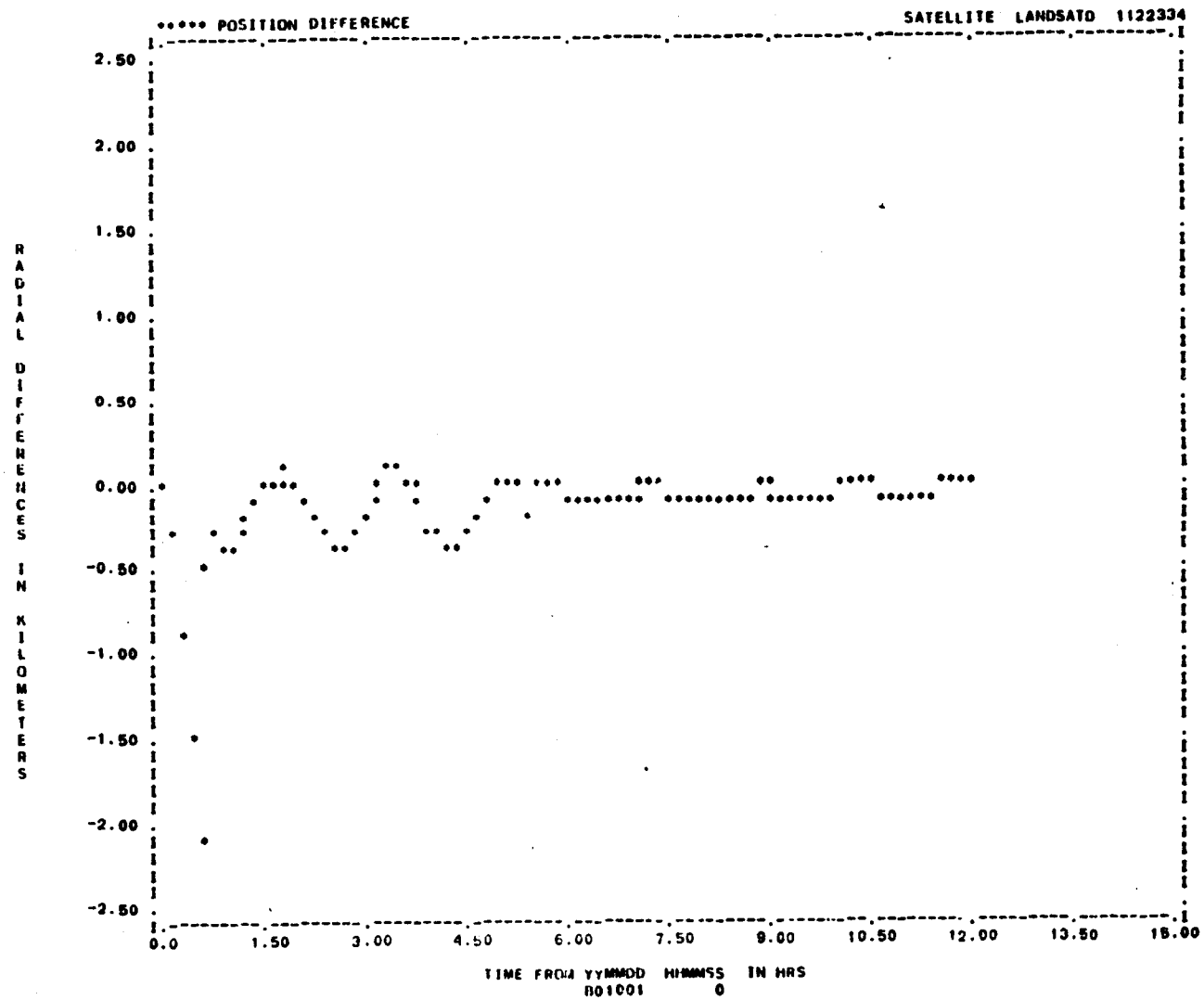

Figure A-49. Radial Differences for Run L4 (1 of 2)

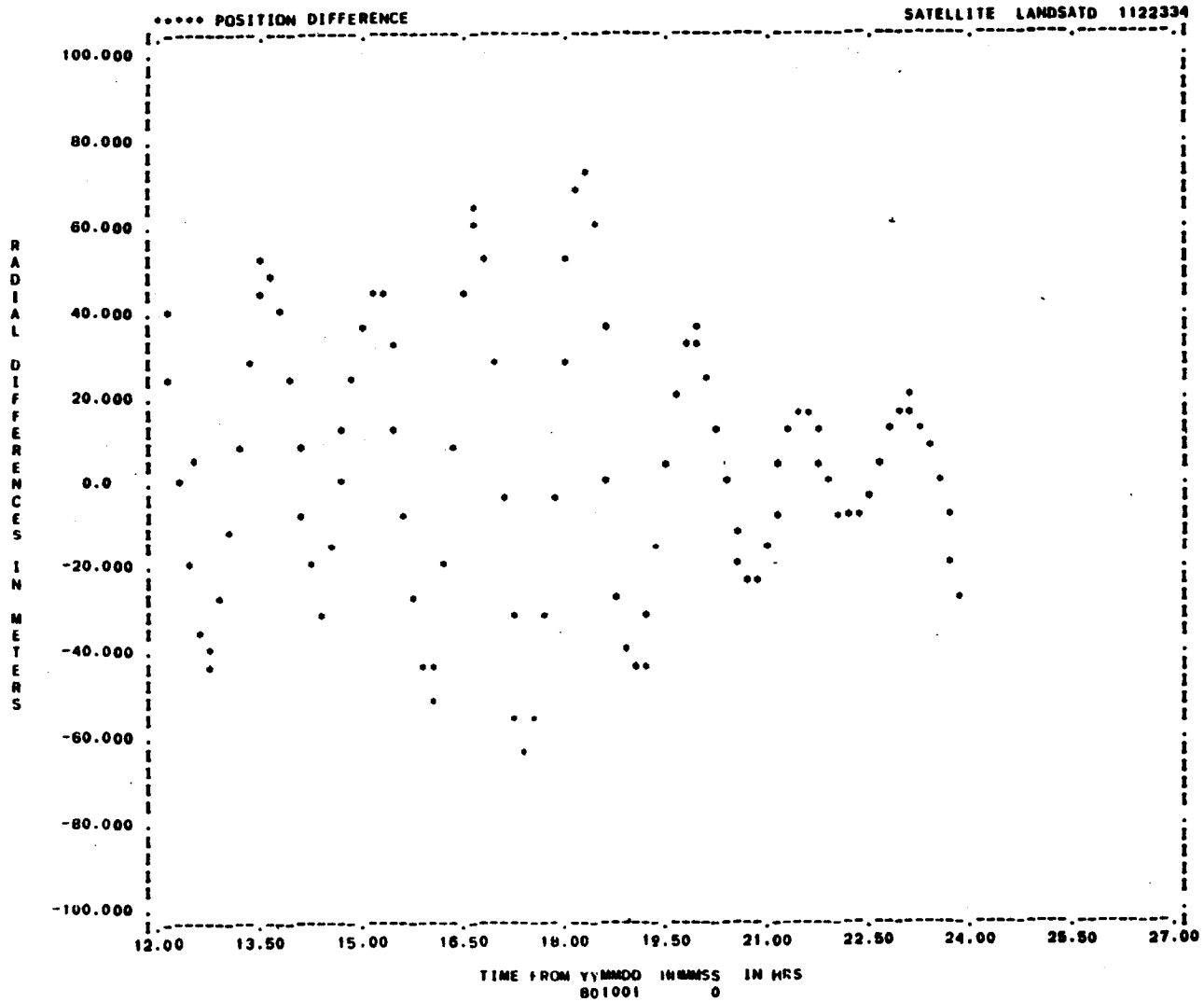

Figure A-49. Radial Differences for Run L4 (2 of 2)

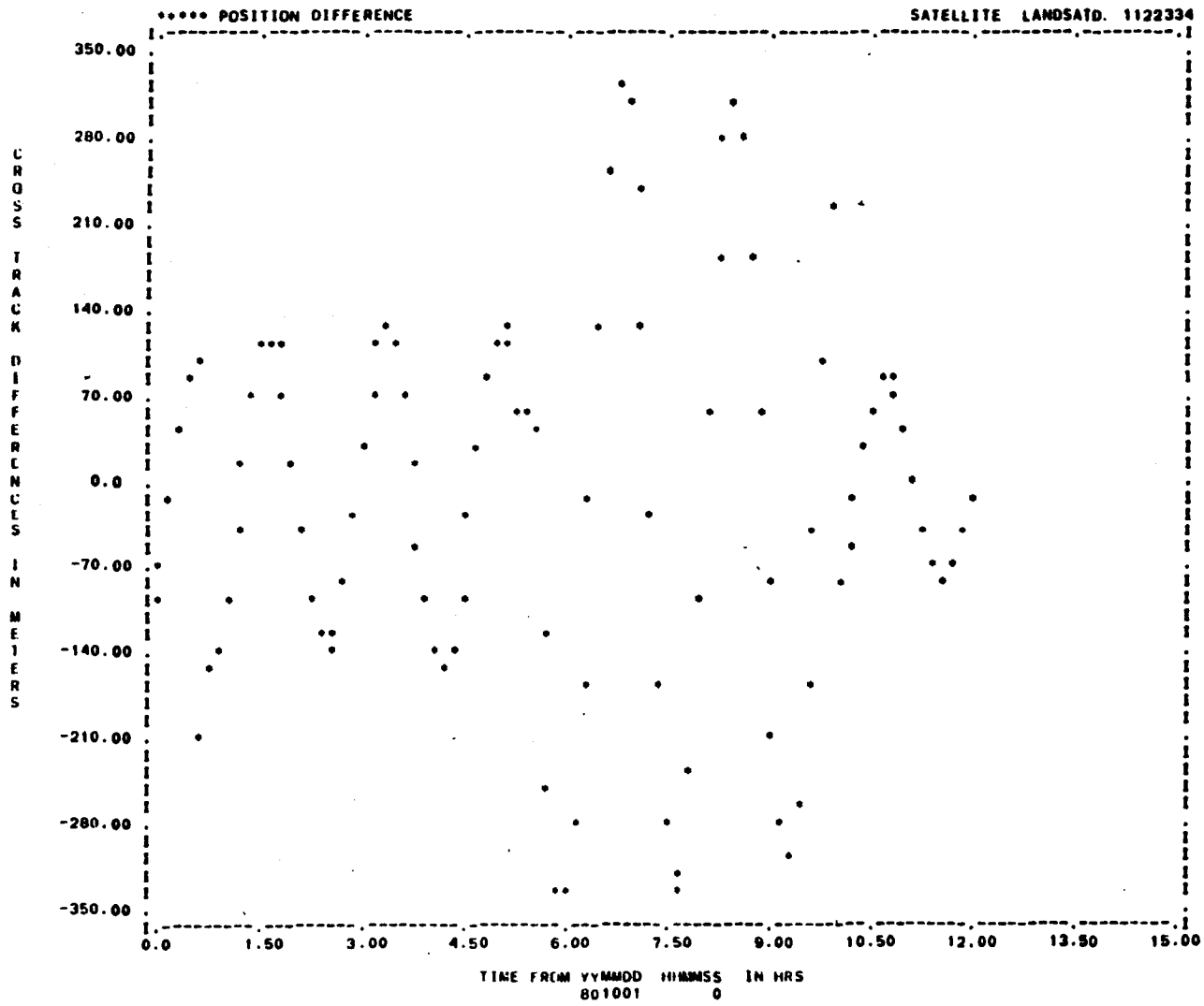

Figure A-50. Cross-Track Differences for Run L4 (1 of 2)

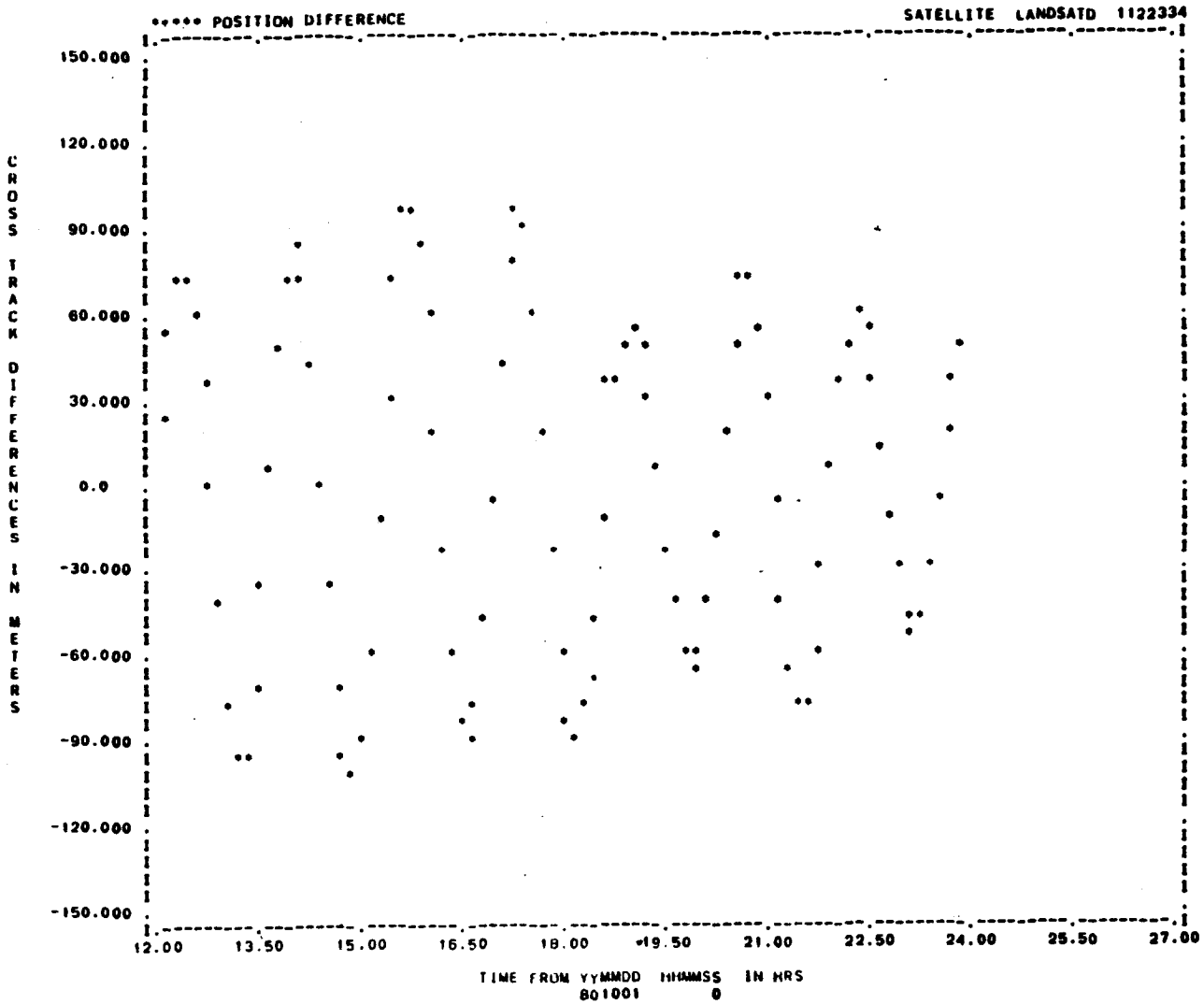

Figure A-50. Cross-Track Differences for Run L4 (2 of 2)

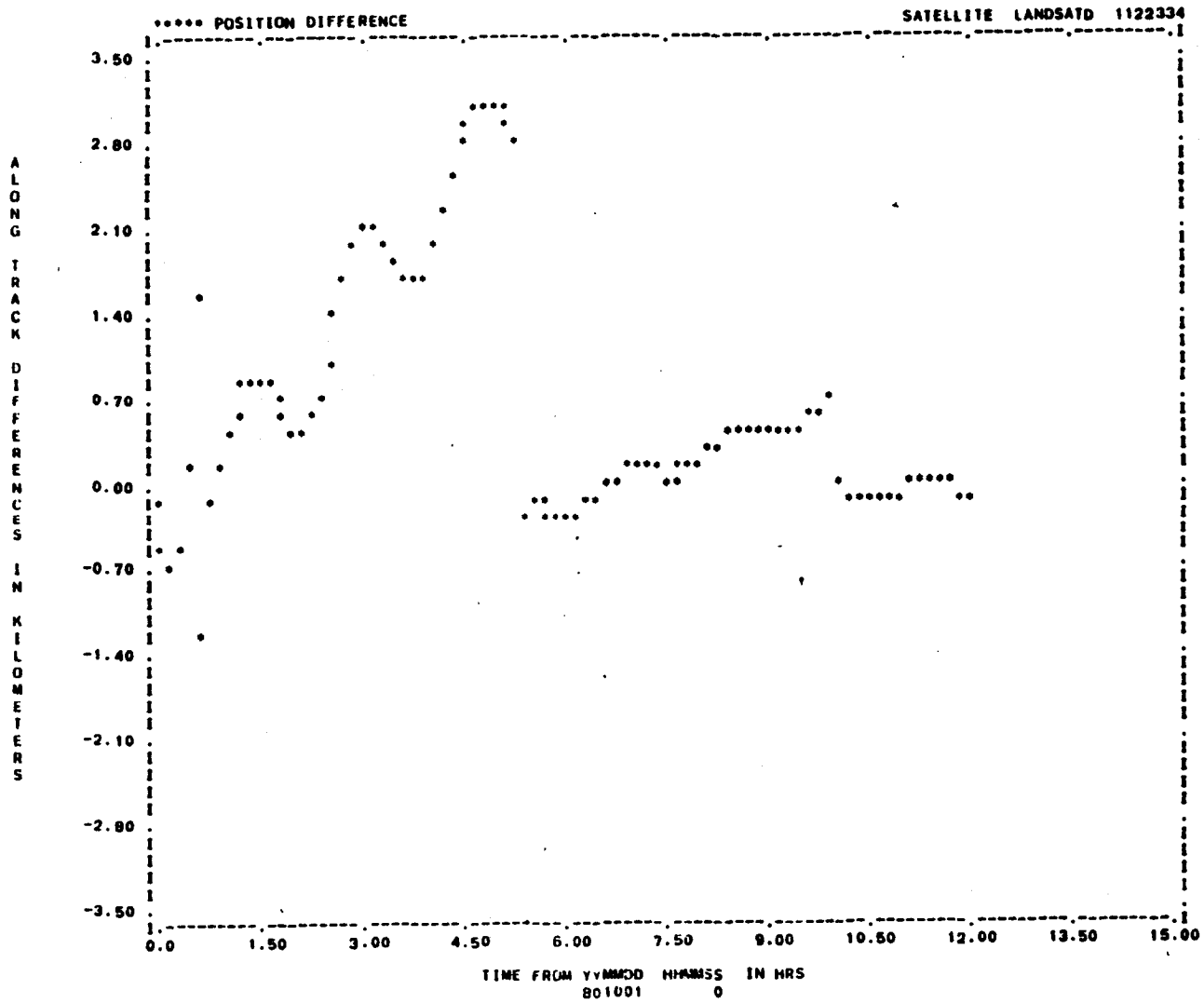

Figure A-51. Along-Track Differences for Run L4 (1 of 2)

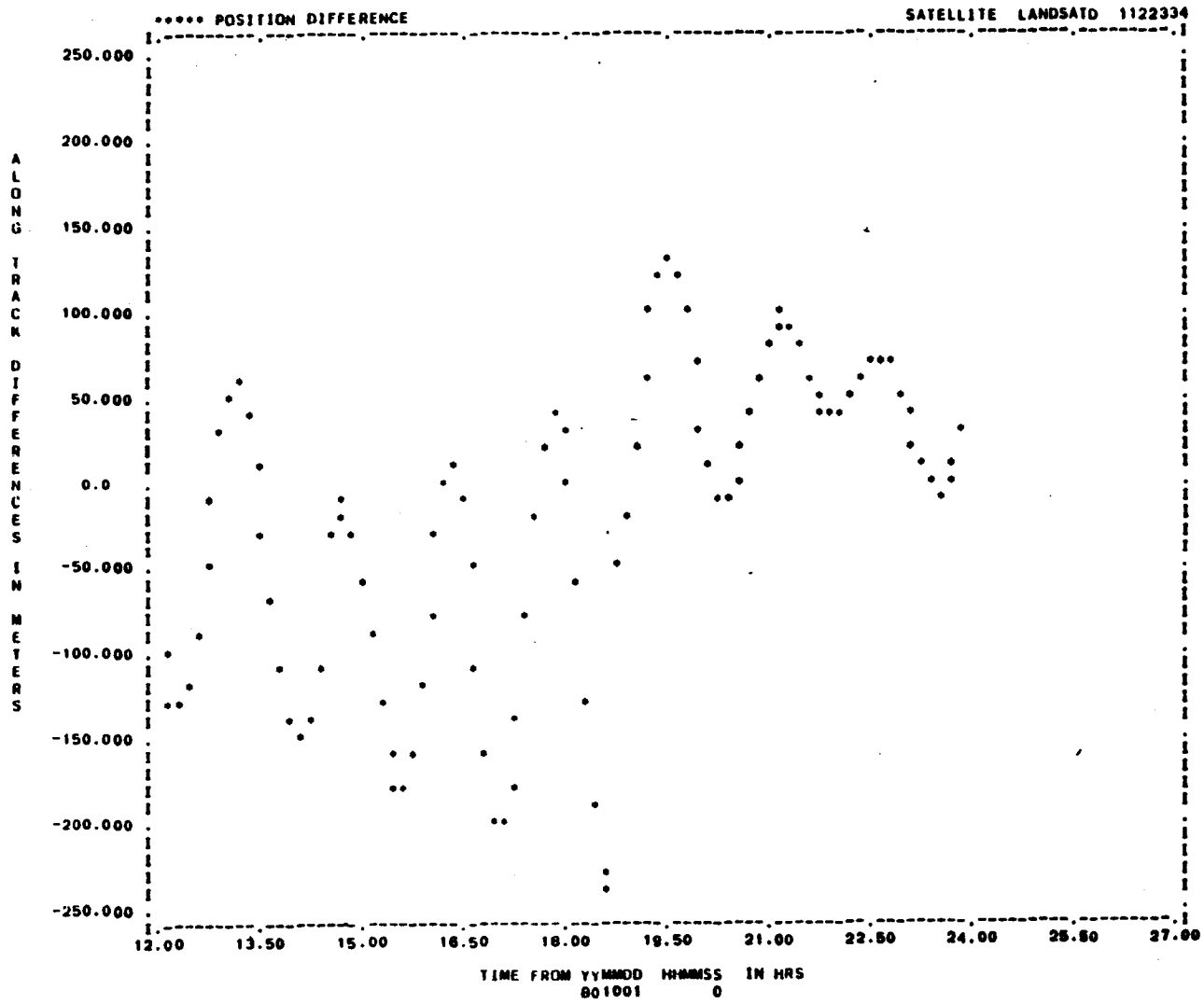

Figure A-51. Along-Track Differences for Run L4 (2 of 2)

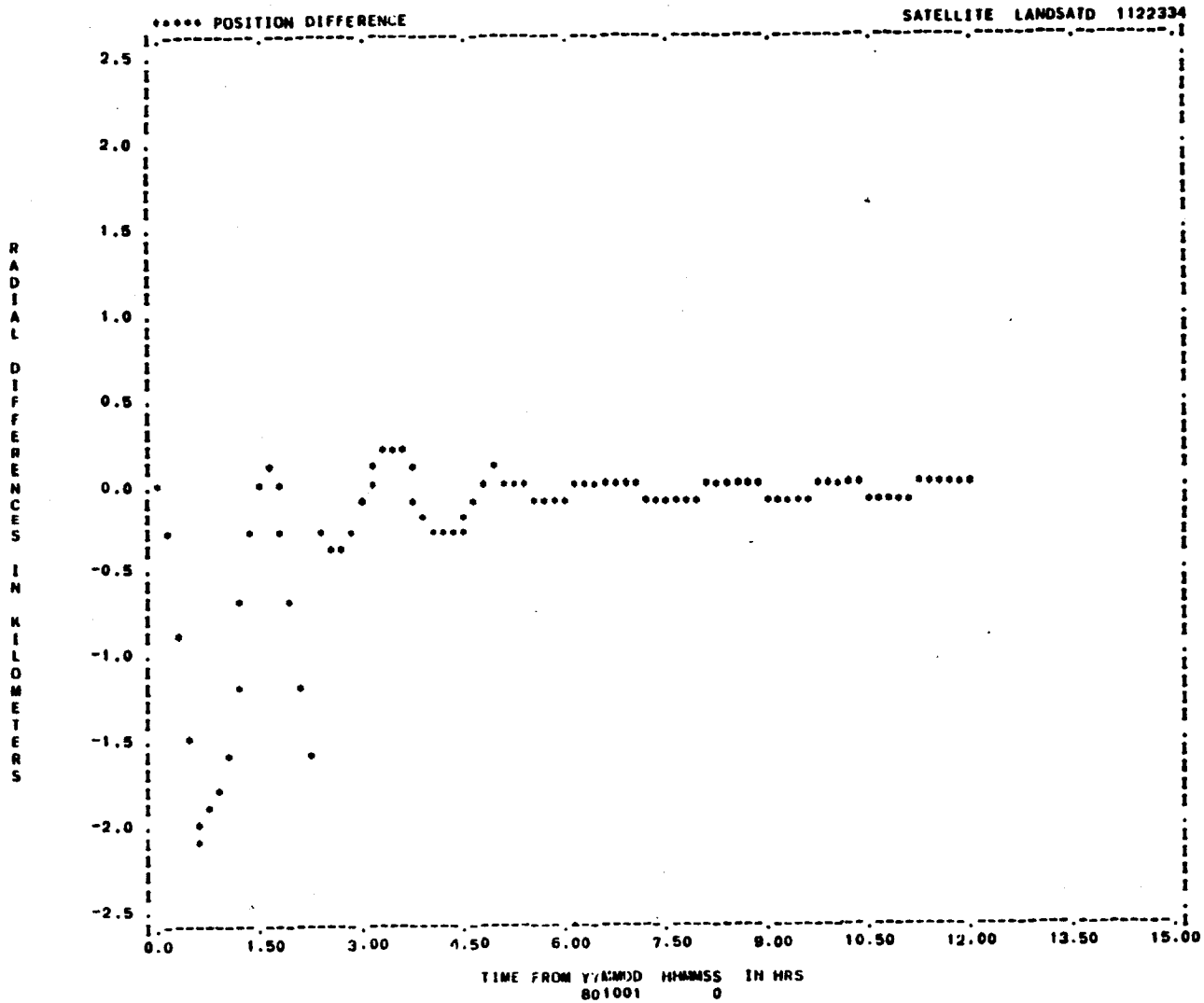

Figure A-52. Radial Differences for Run M3 (1 of 2)

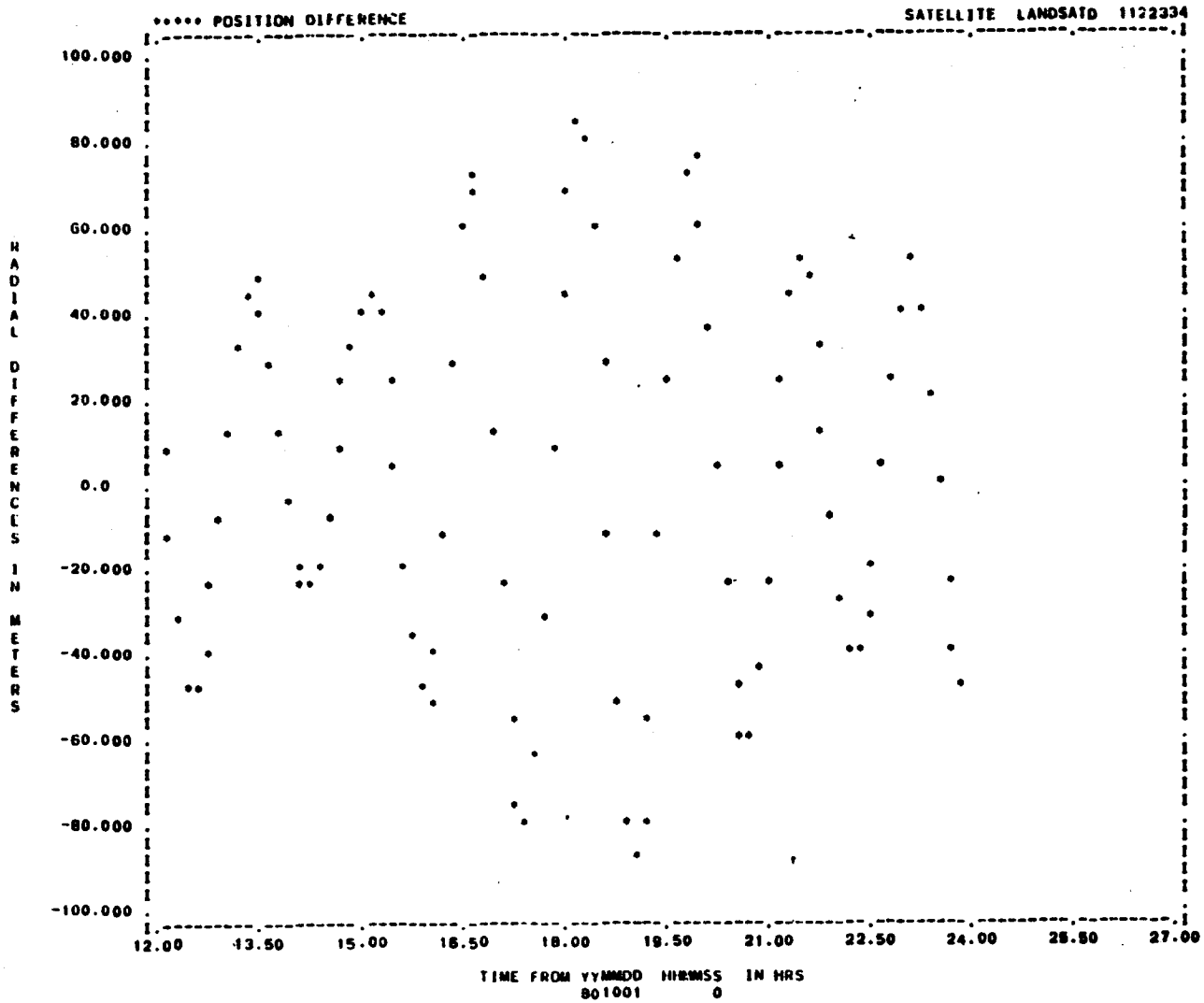

Figure A-52. Radial Differences for Run M3 (2 of 2)

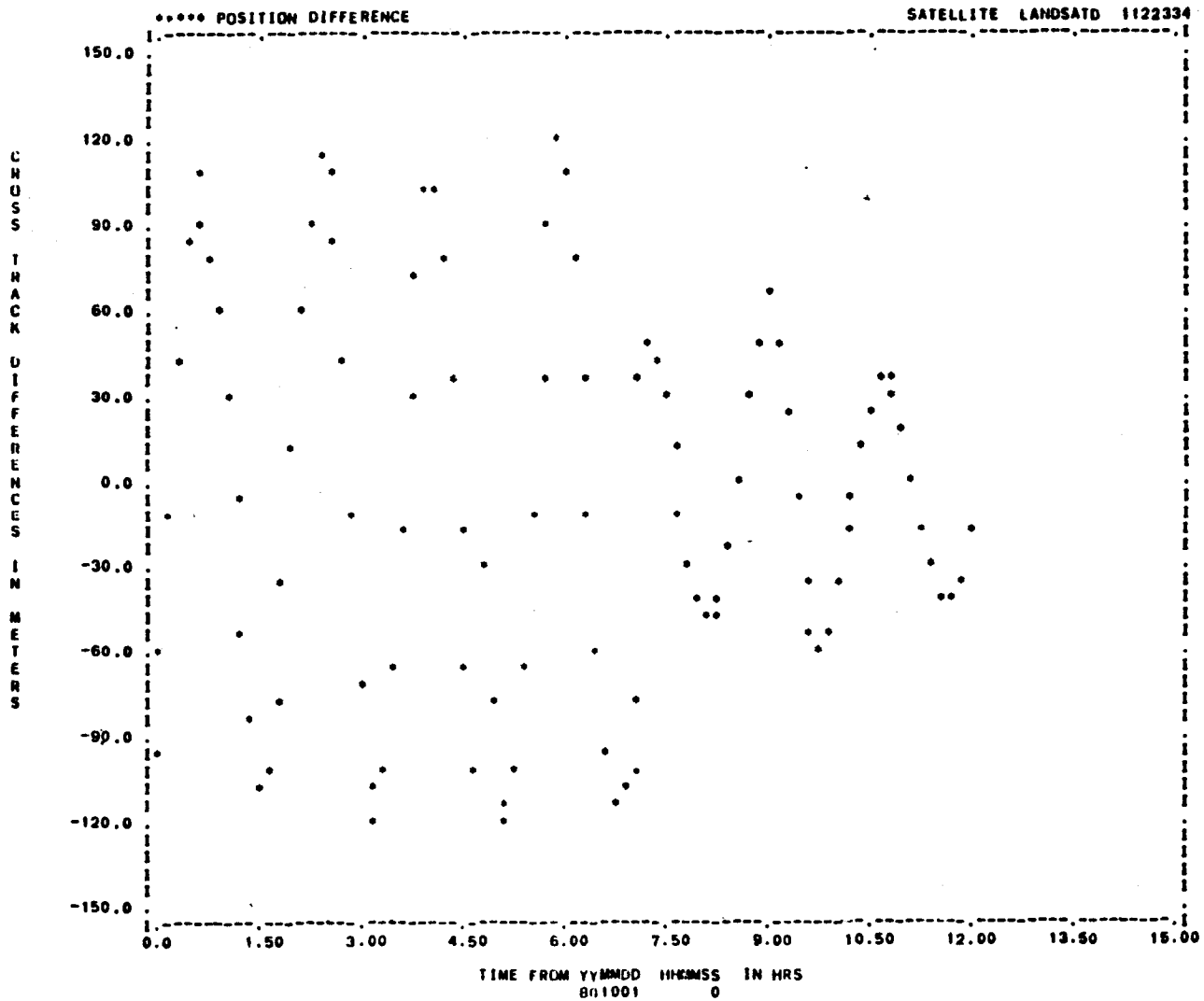

Figure A-53. Cross-Track Differences for Run M3 (1 of 2)

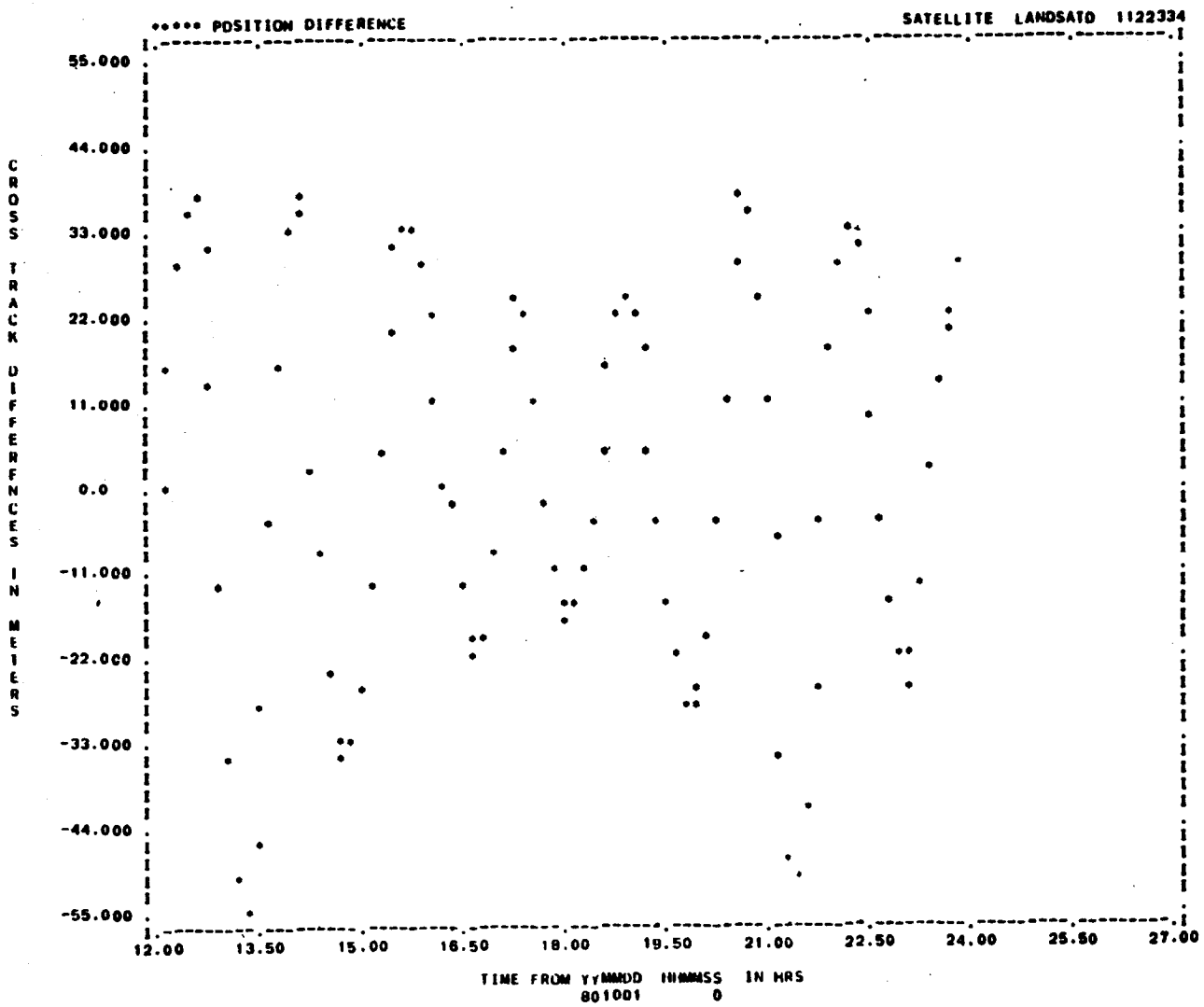

Figure A-53. Cross-Track Differences for Run M3 (2 of 2)

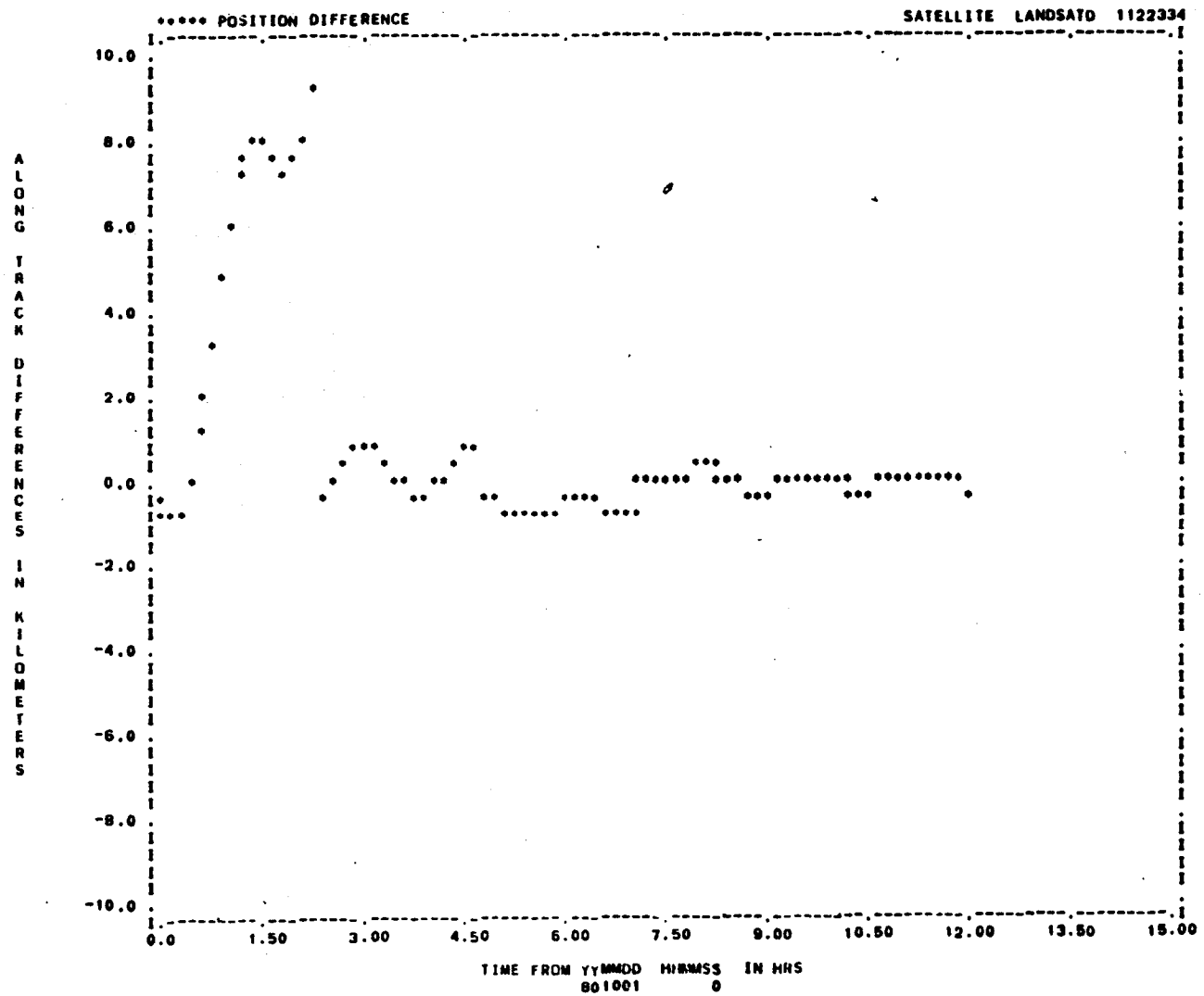

Figure A-54. Along-Track Differences for Run M3 (1 of 2)

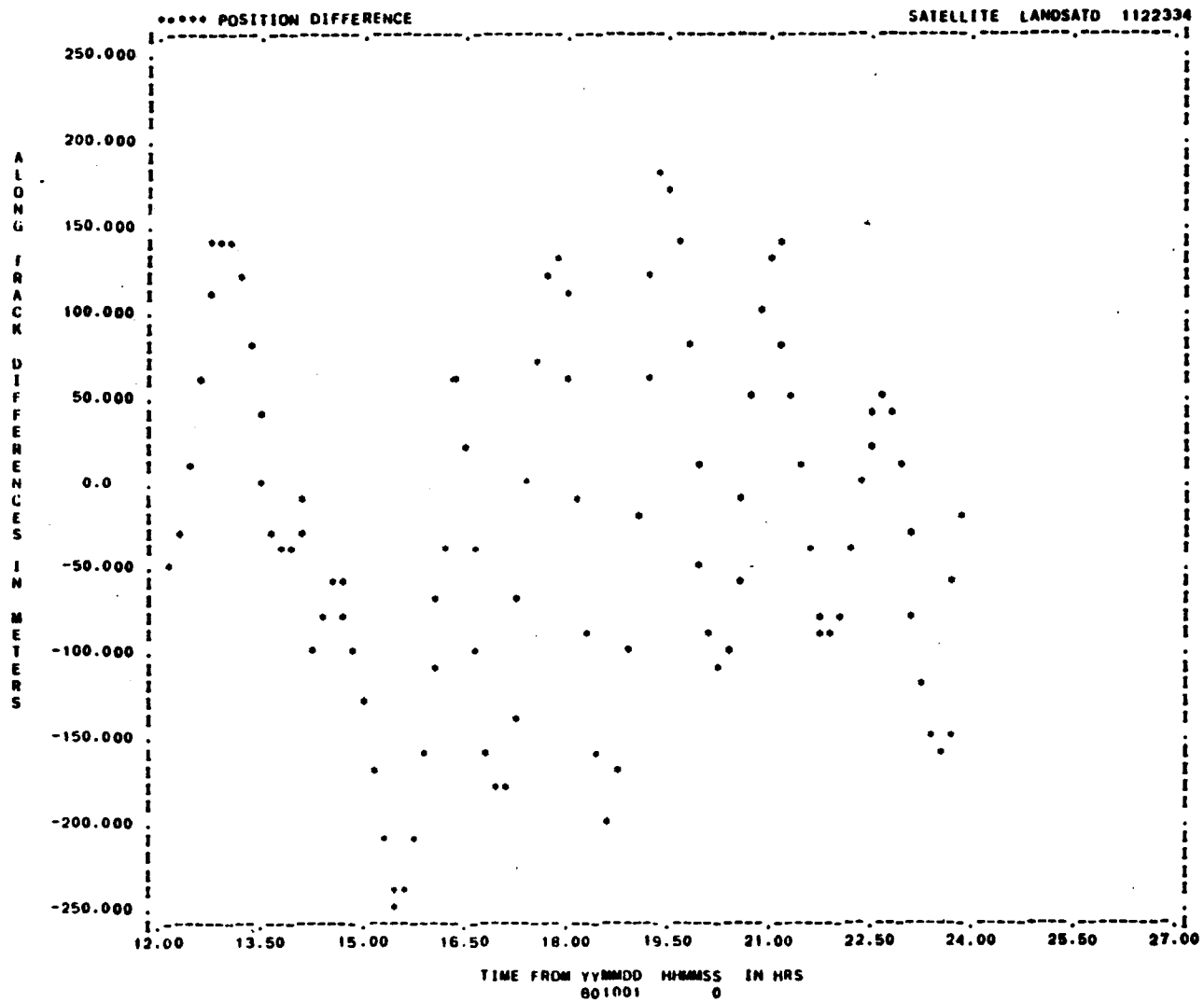

Figure A-54. Along-Track Differences for Run M3 (2 of 2)

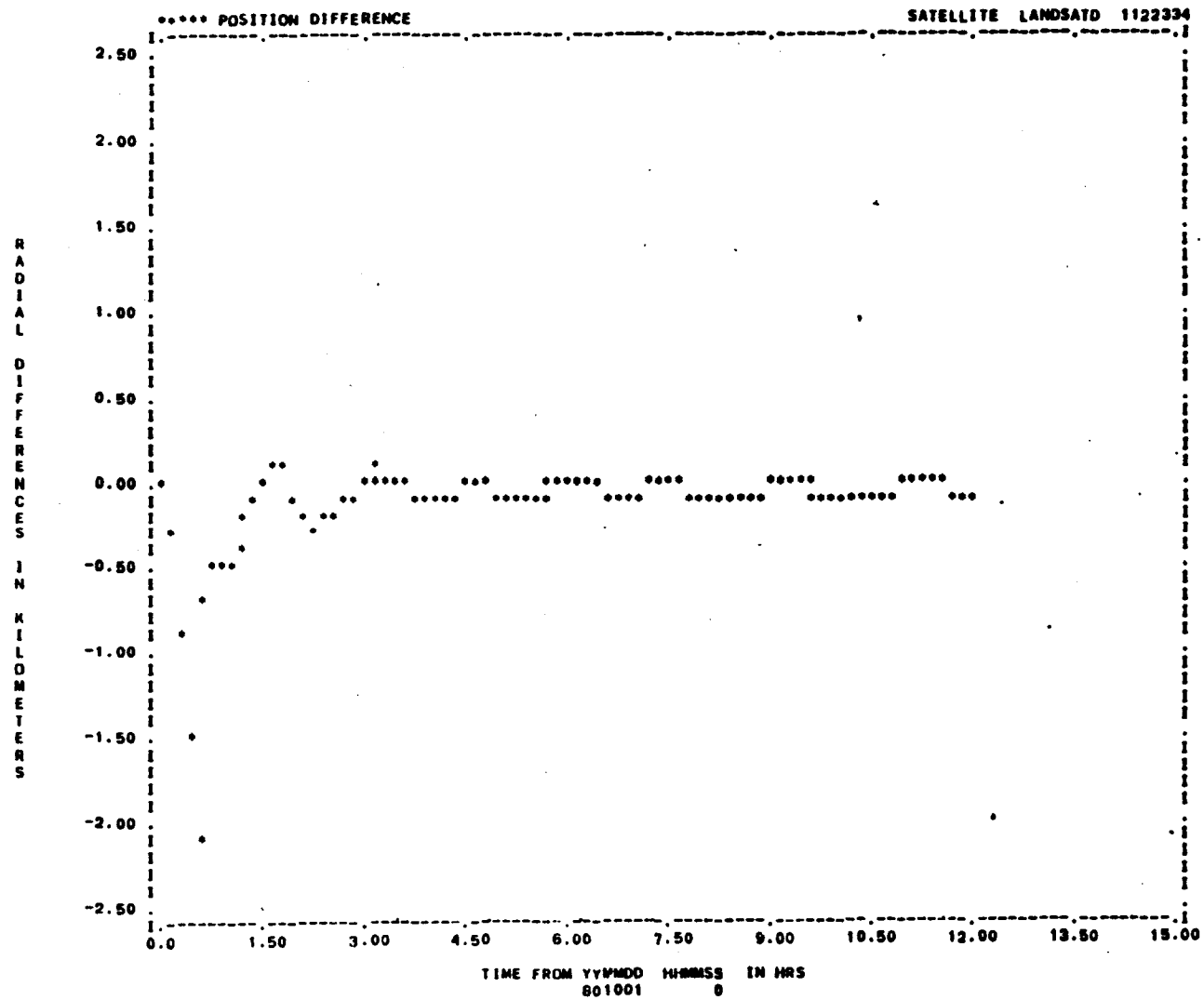

Figure A-55. Radial Differences for Run M4 (1 of 2)

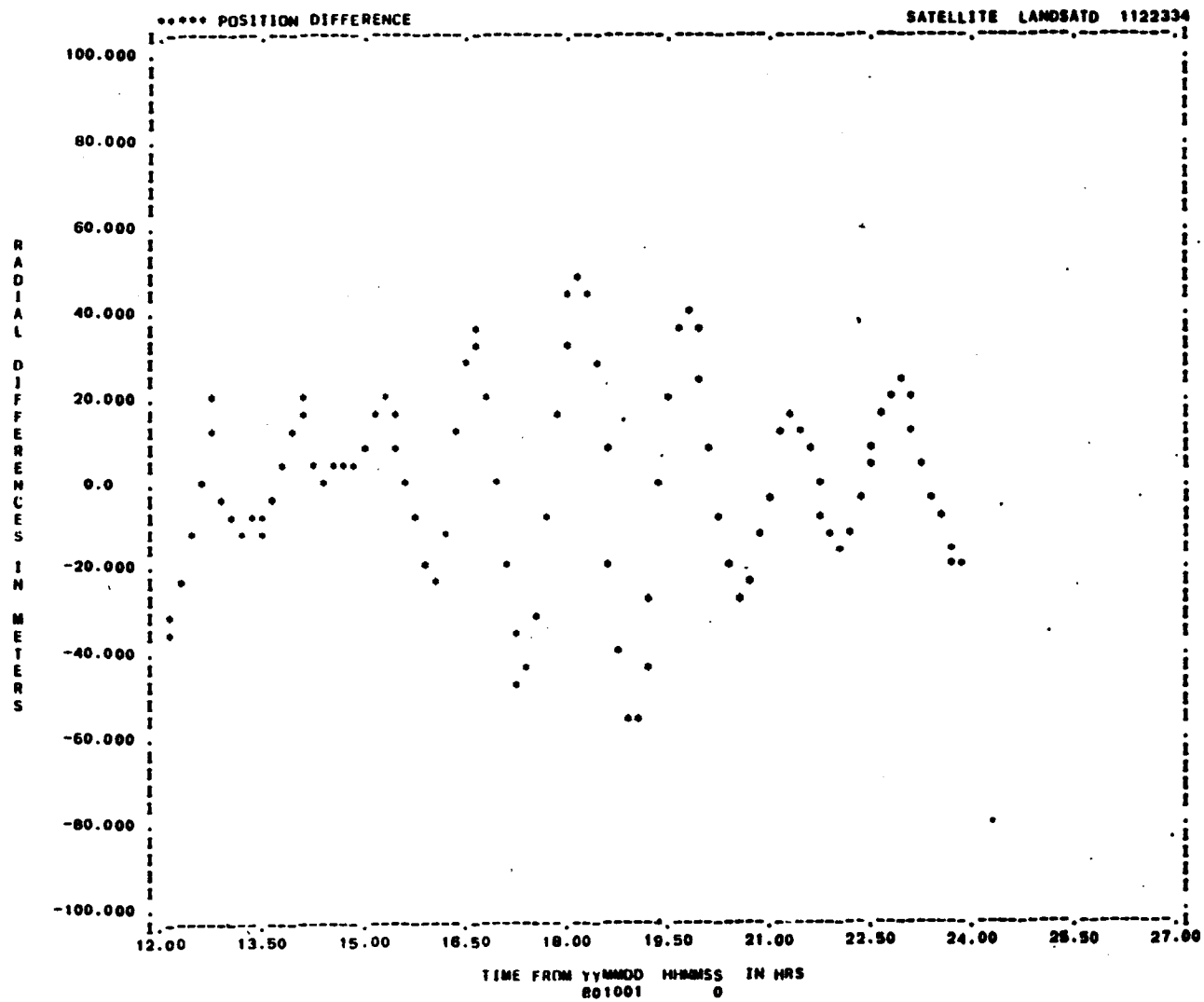

Figure A-55. Radial Differences for Run M4 (2 of 2)

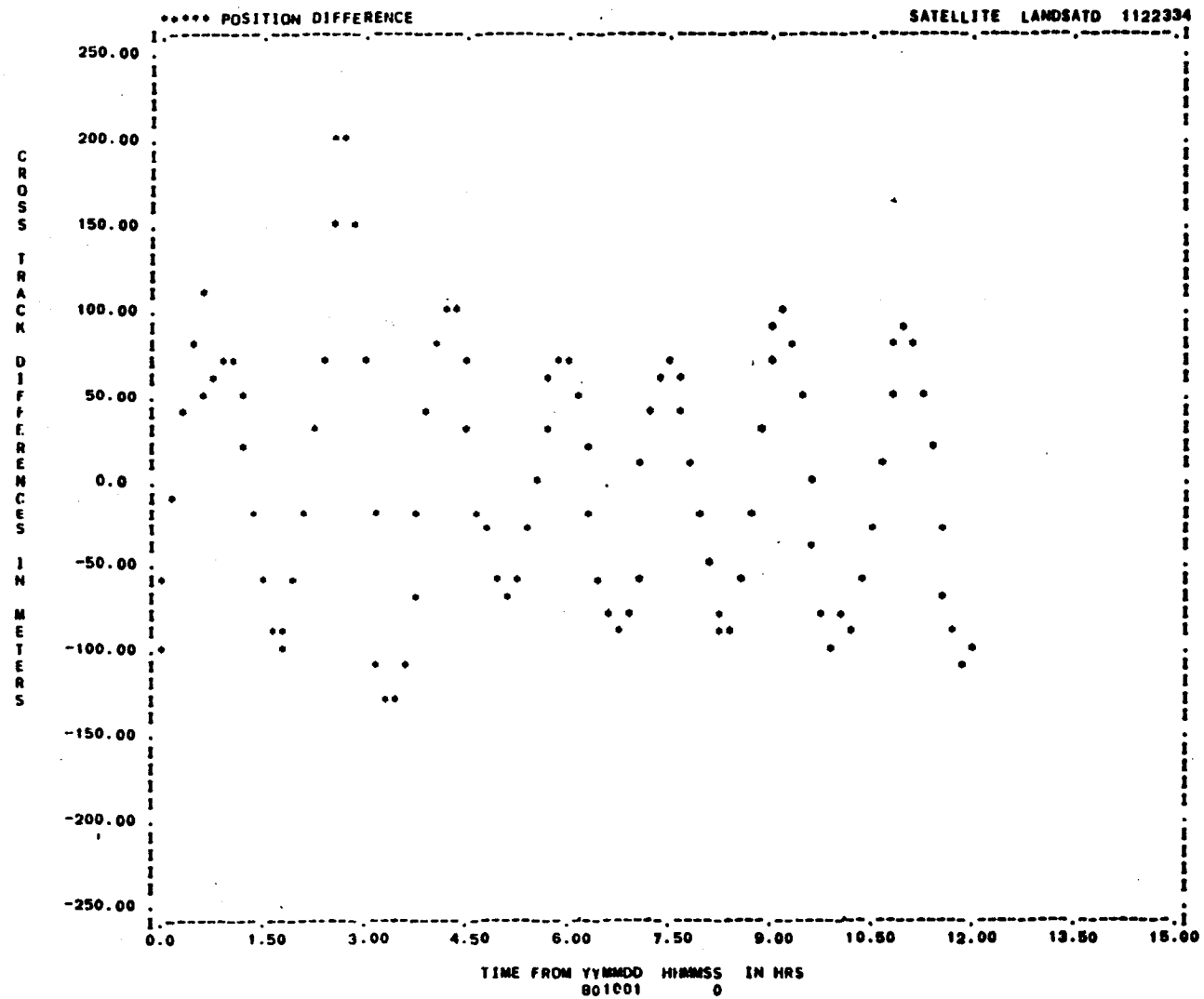

Figure A-56. Cross-Track Differences for Run M4 (1 of 2)

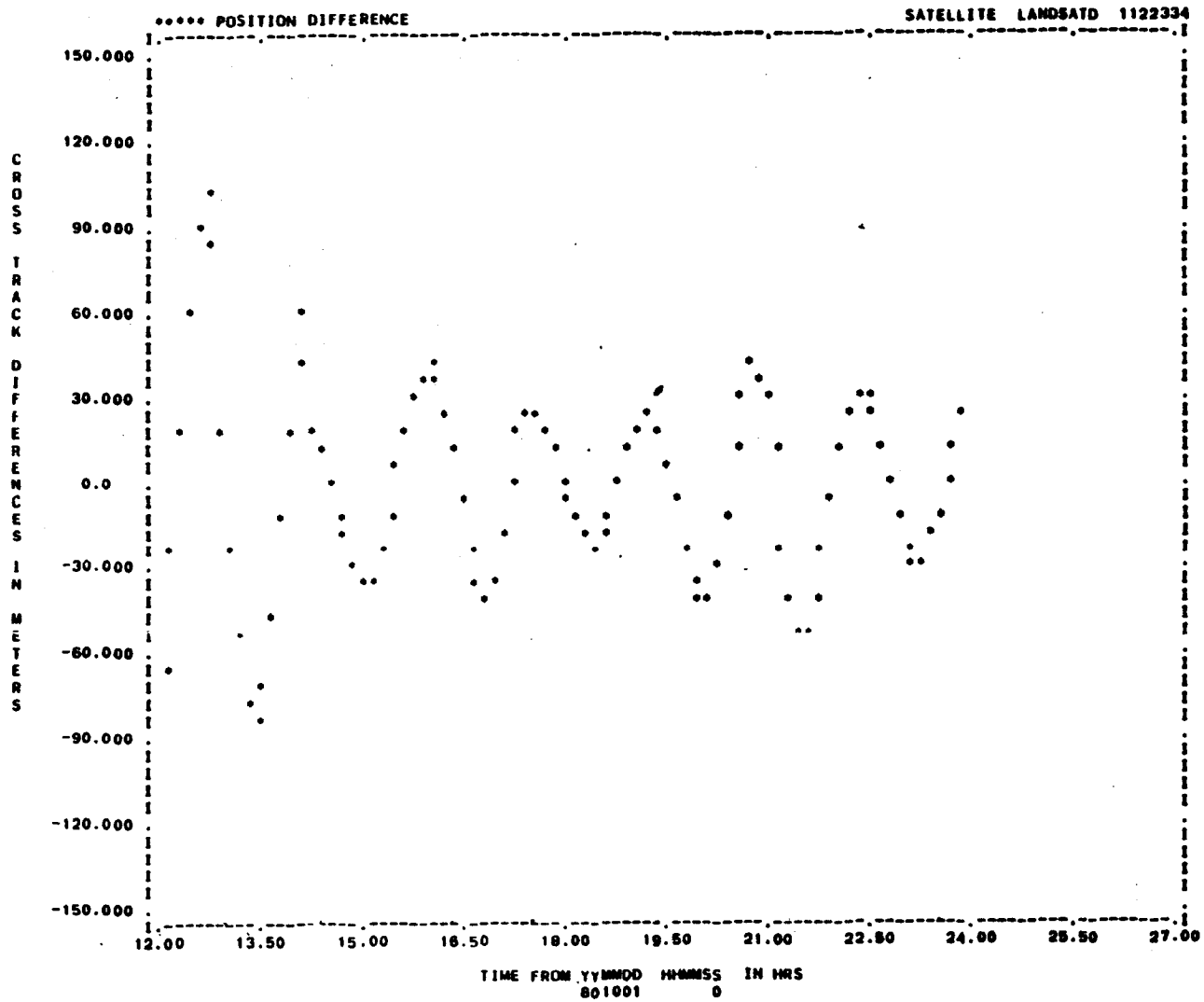

Figure A-56. Cross-Track Differences for Run M4 (2 of 2)

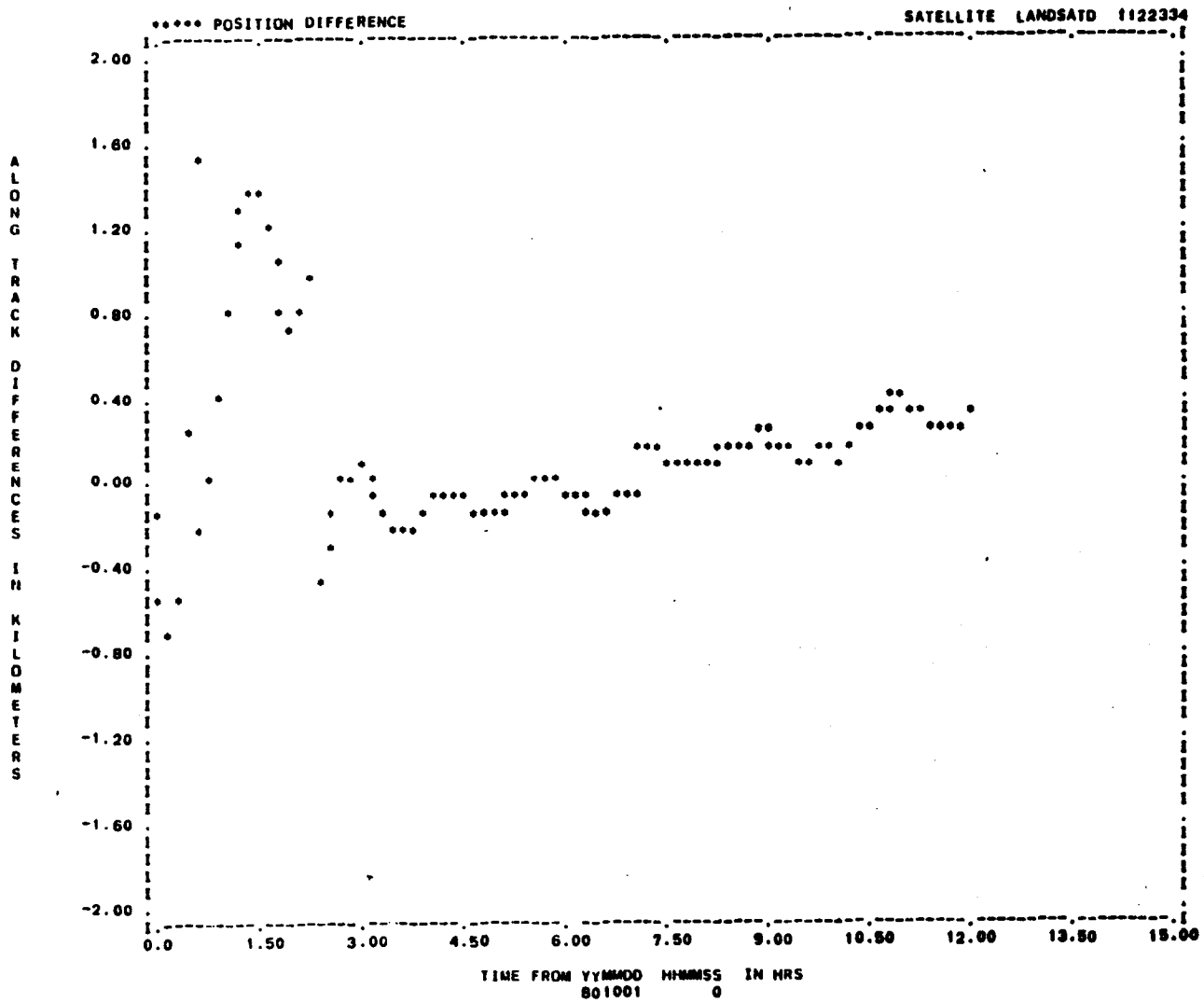

Figure A-57. Along-Track Differences for Run M4 (1 of 2)

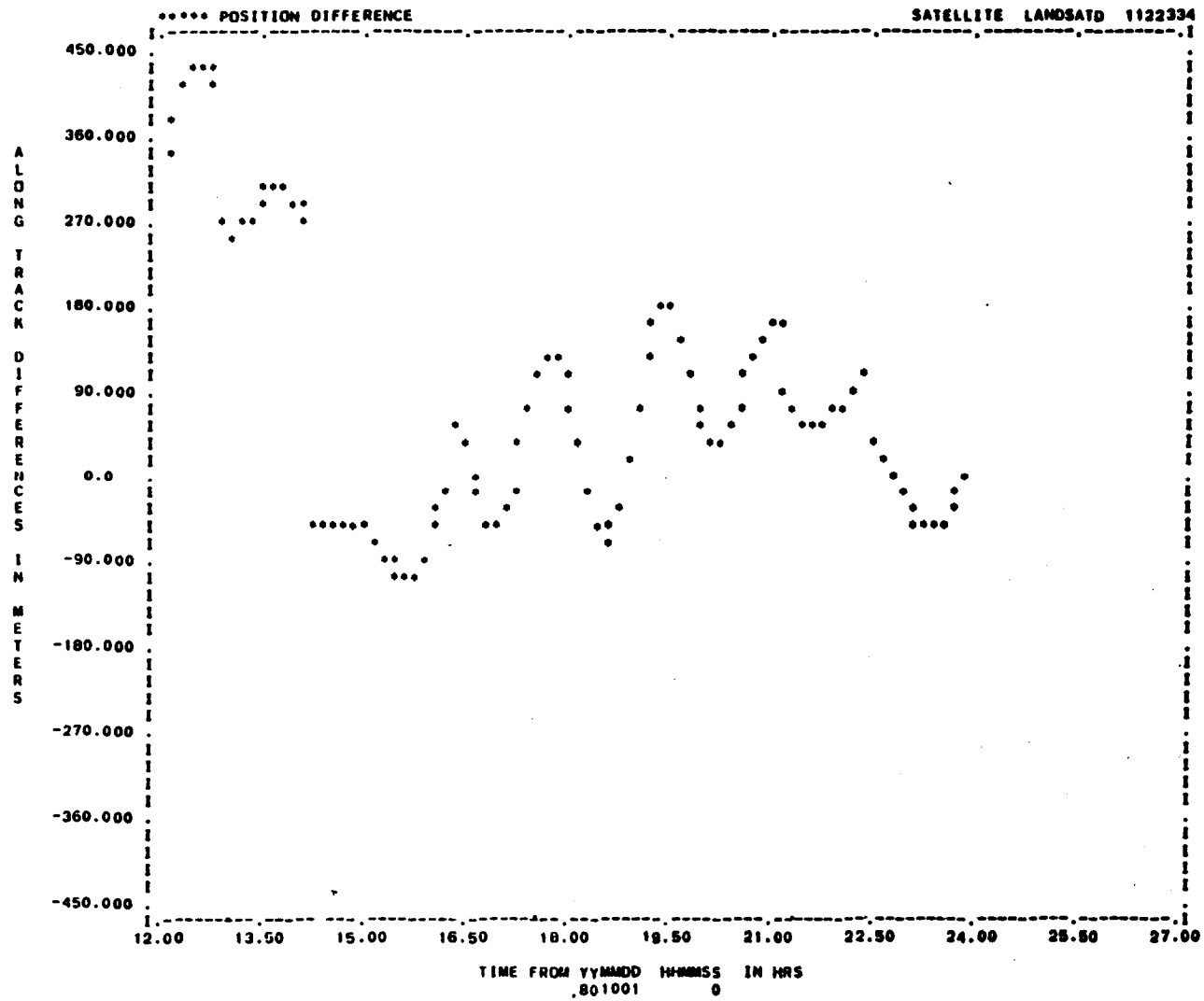

Figure A-57. Along-Track Differences for Run M4 (2 of 2)

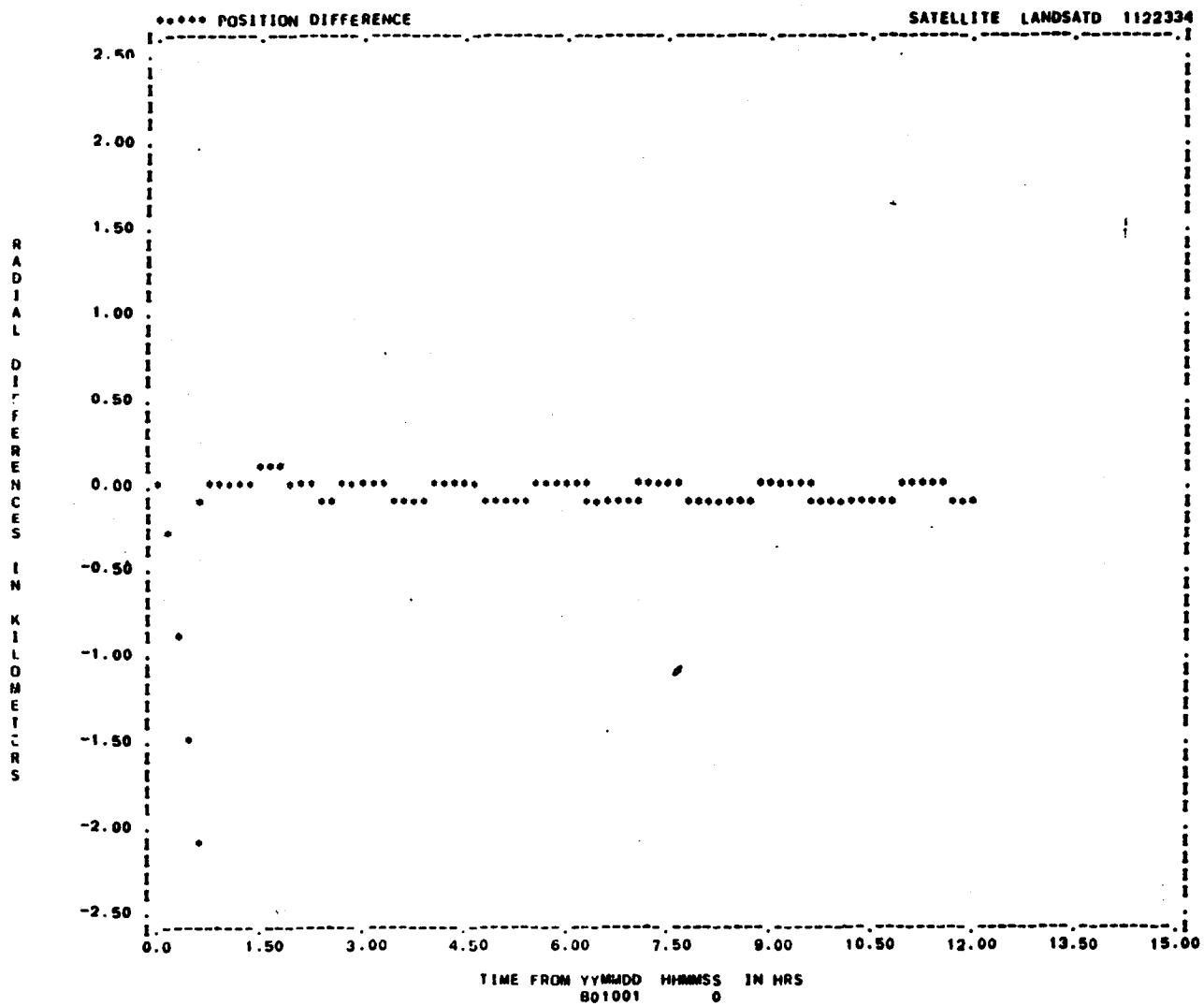

Figure A-58. Radial Differences for Run M5 (1 of 2)

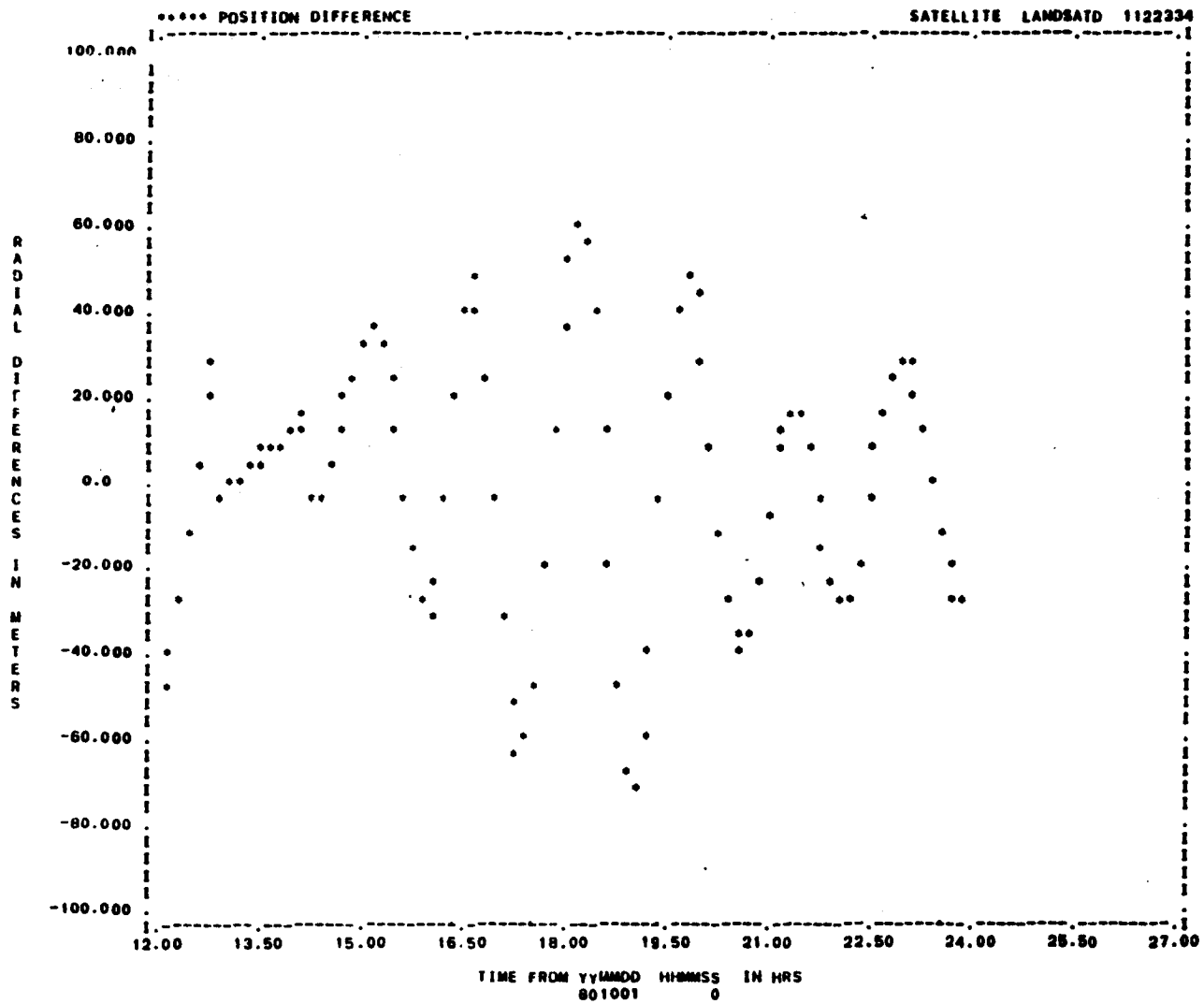

Figure A-58. Radial Differences for Run M5 (2 of 2)

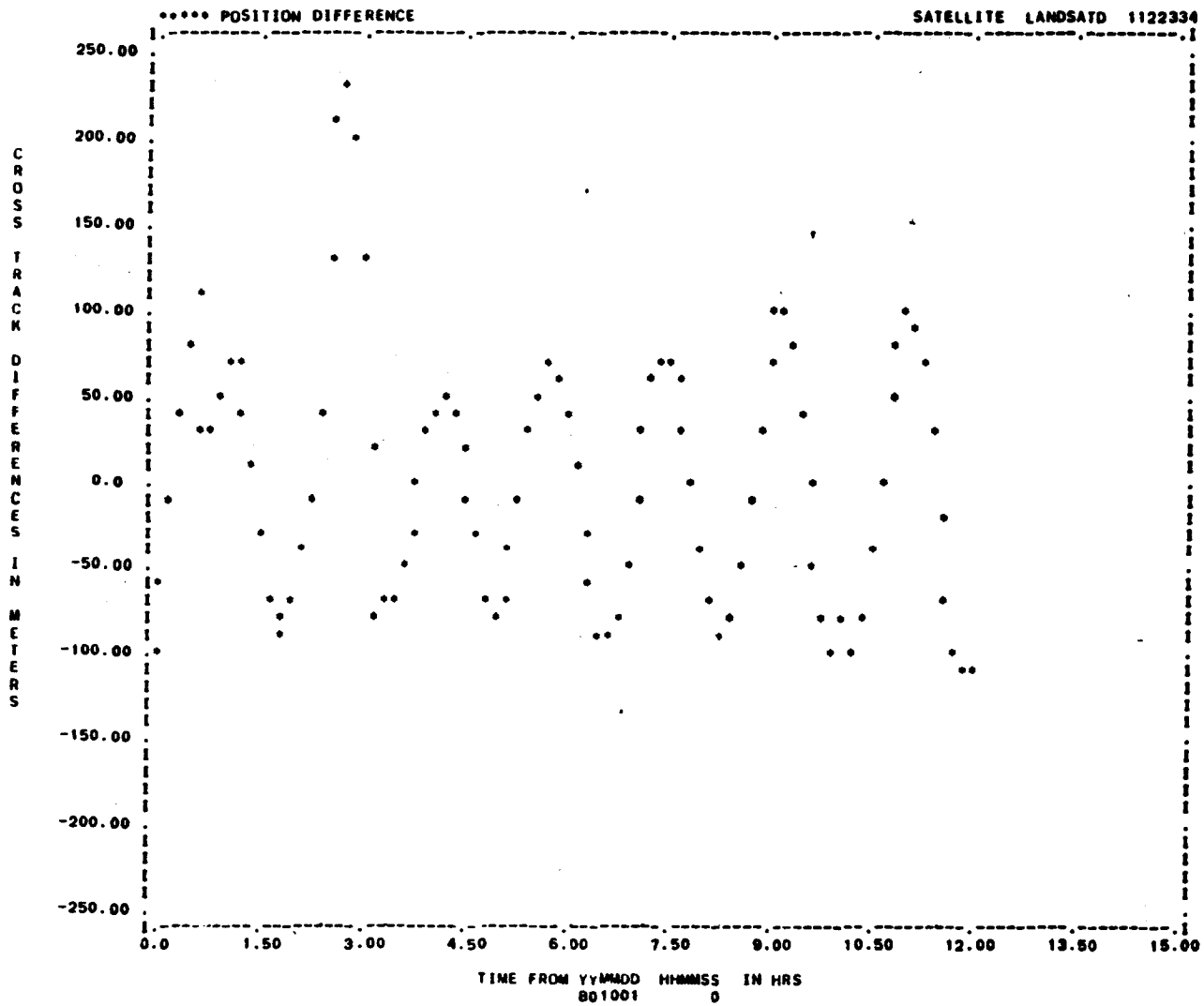

Figure A-59. Cross-Track Differences for Run M5 (1 of 2)

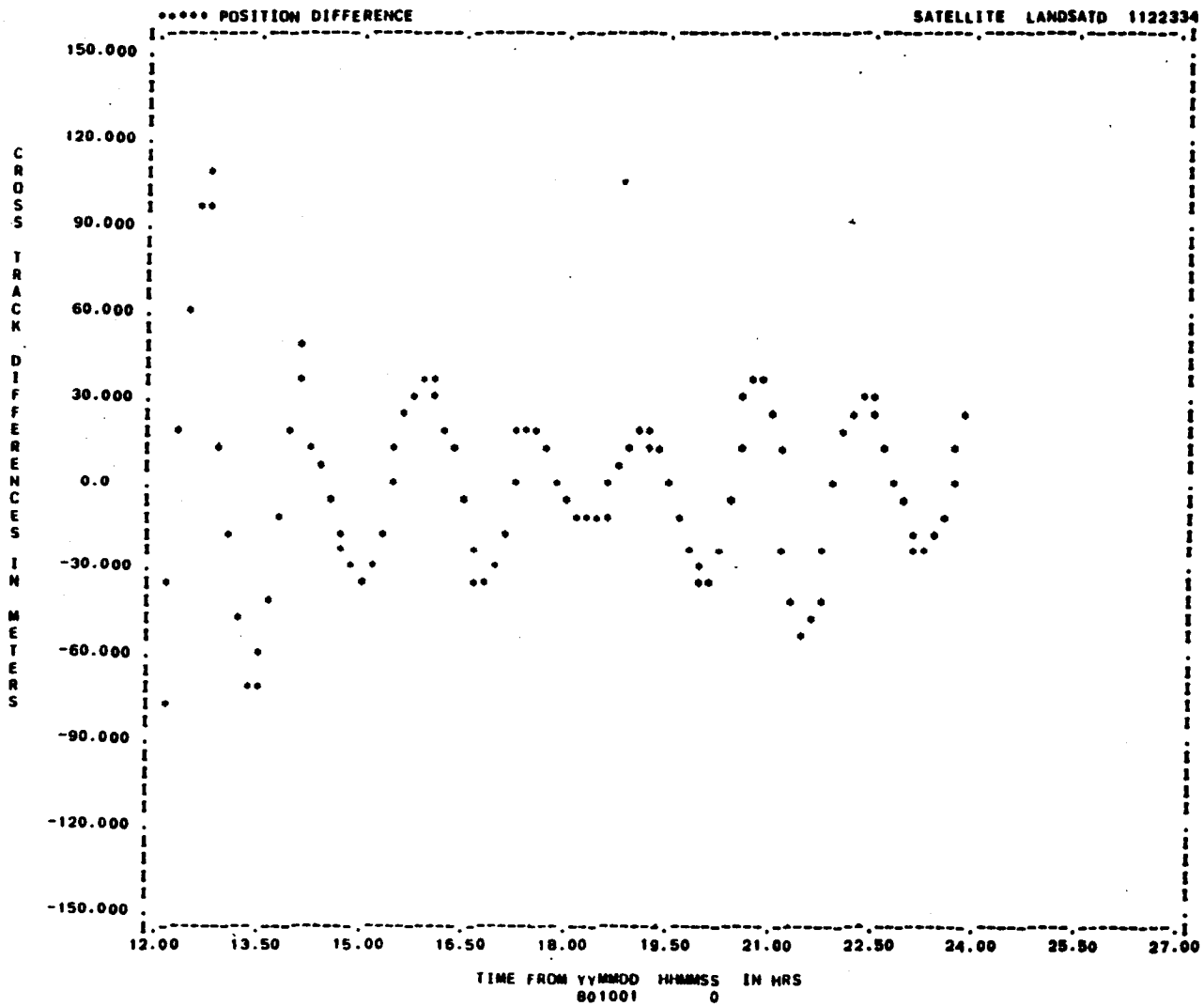

Figure A-59. Cross-Track Differences for Run M5 (2 of 2)

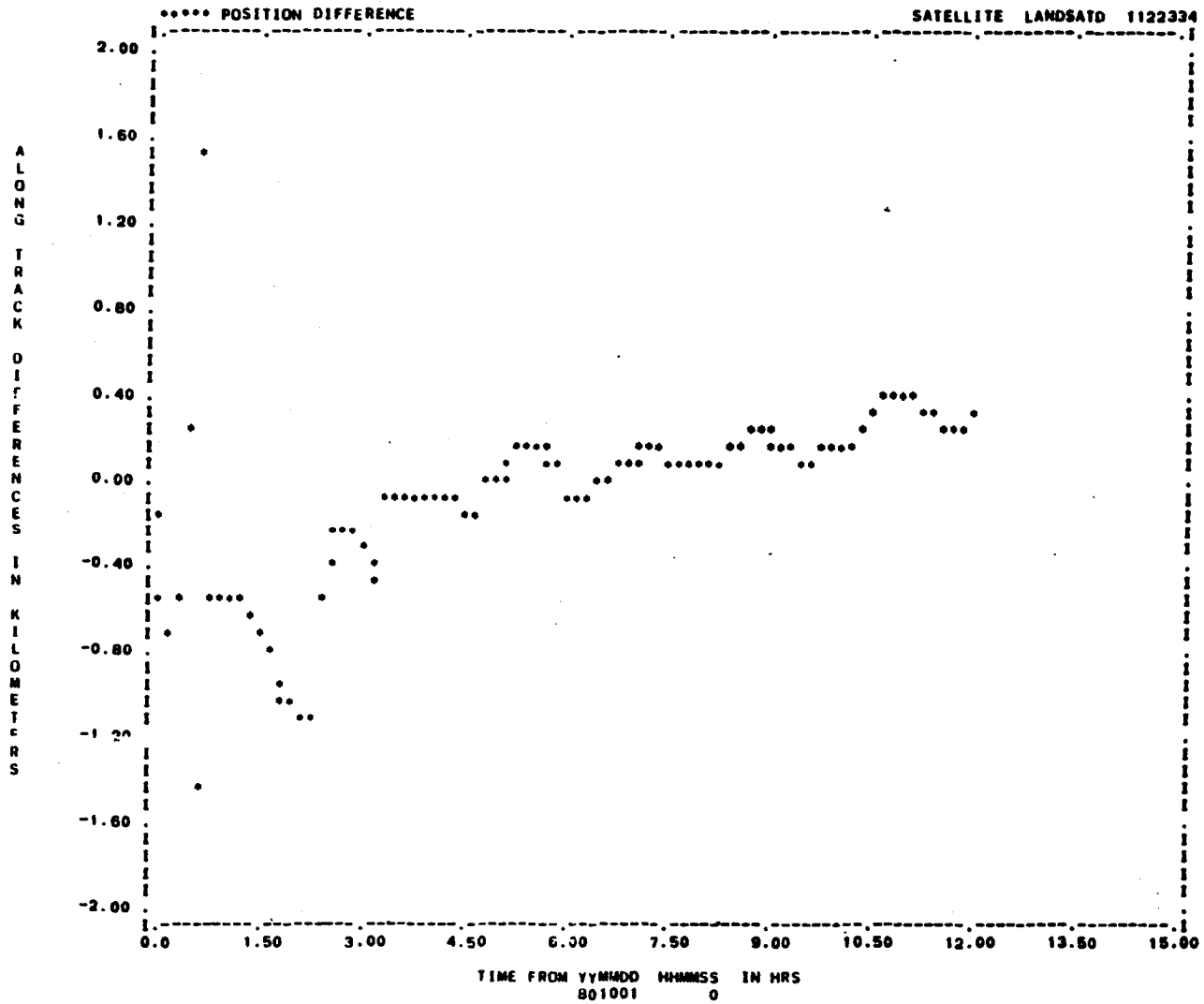

Figure A-60. Along-Track Differences for Run M5 (1 of 2)

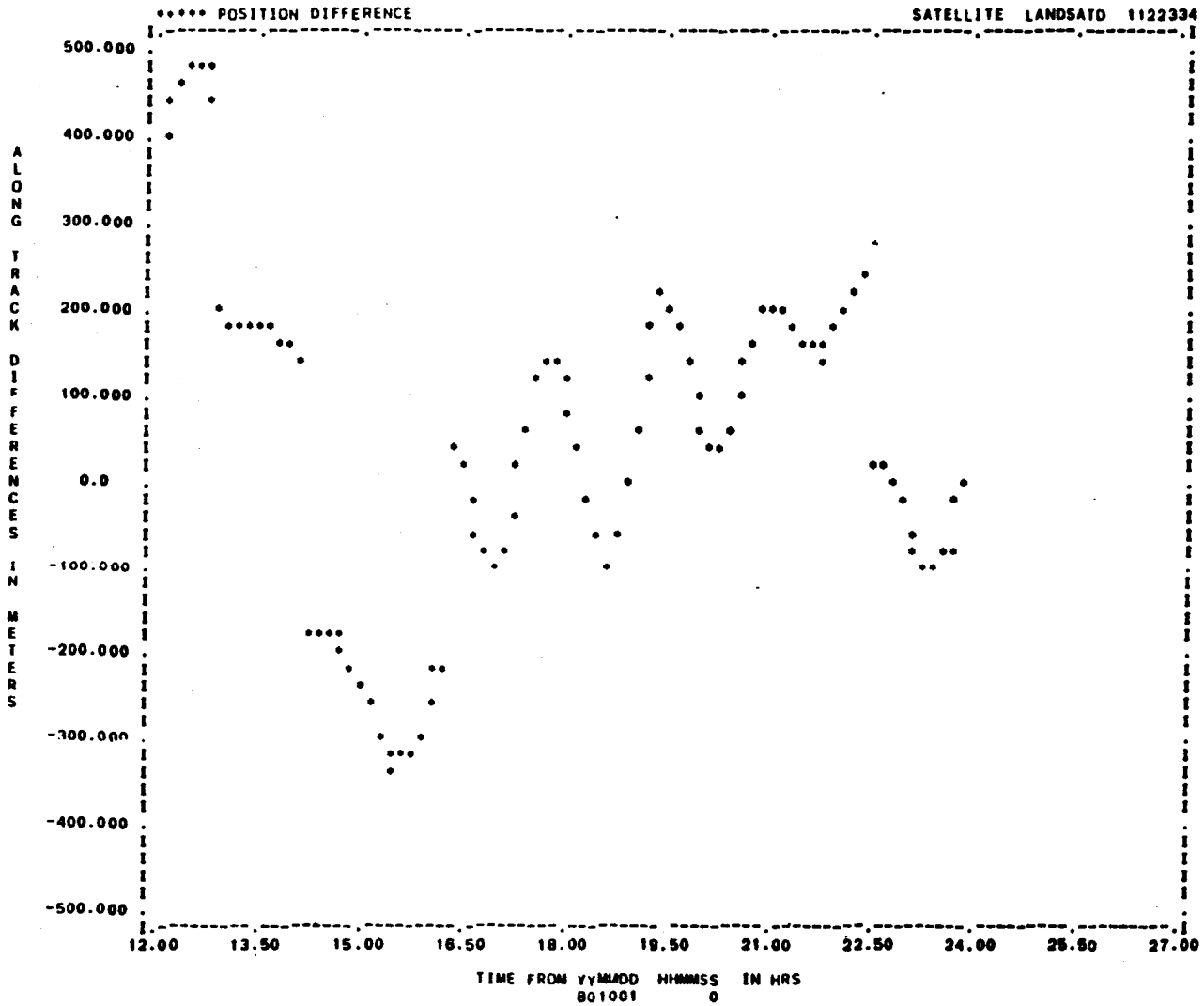

Figure A-60. Along-Track Differences for Run M5 (2 of 2)

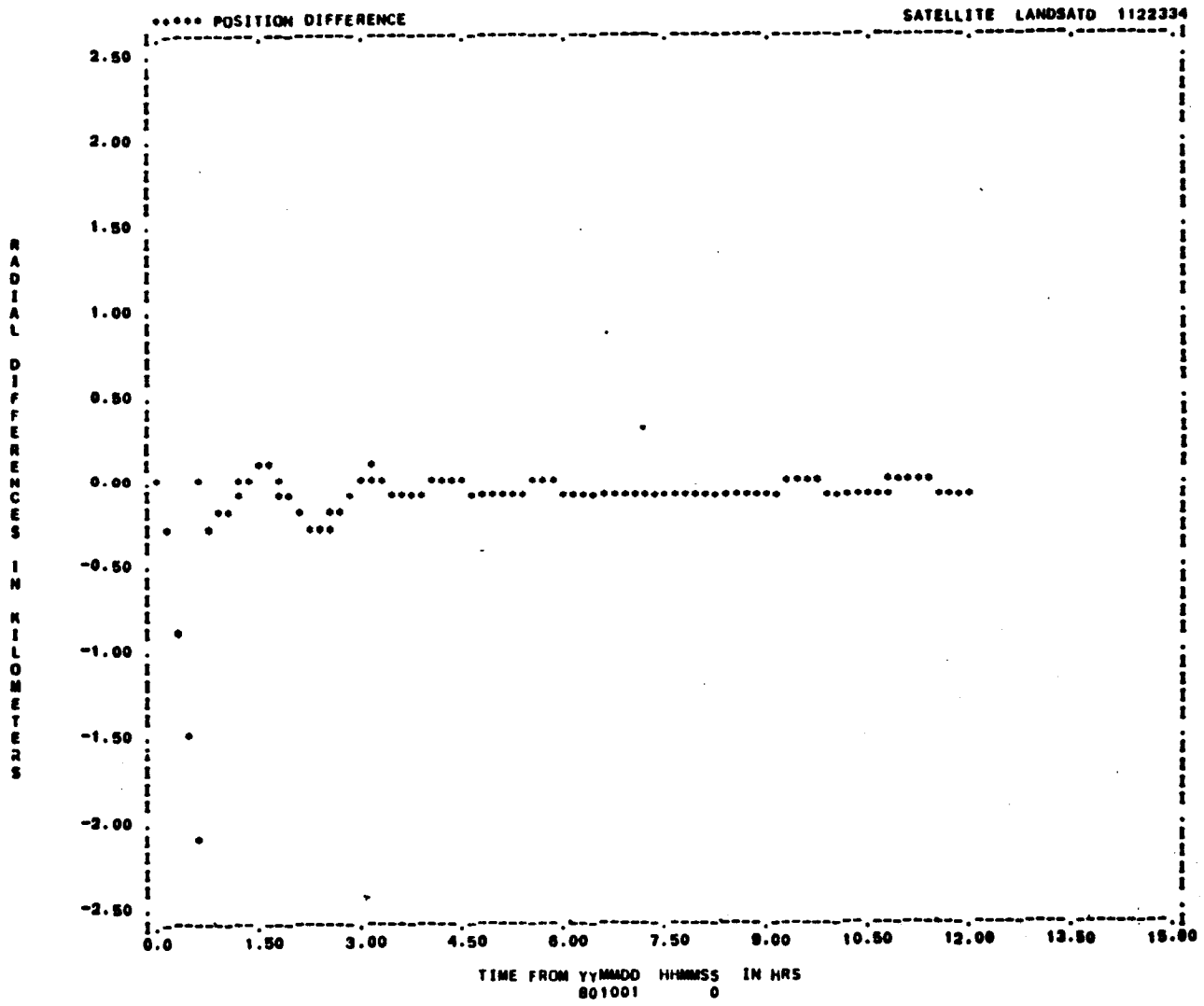

Figure A-61. Radial Differences for Run M14 (1 of 2)

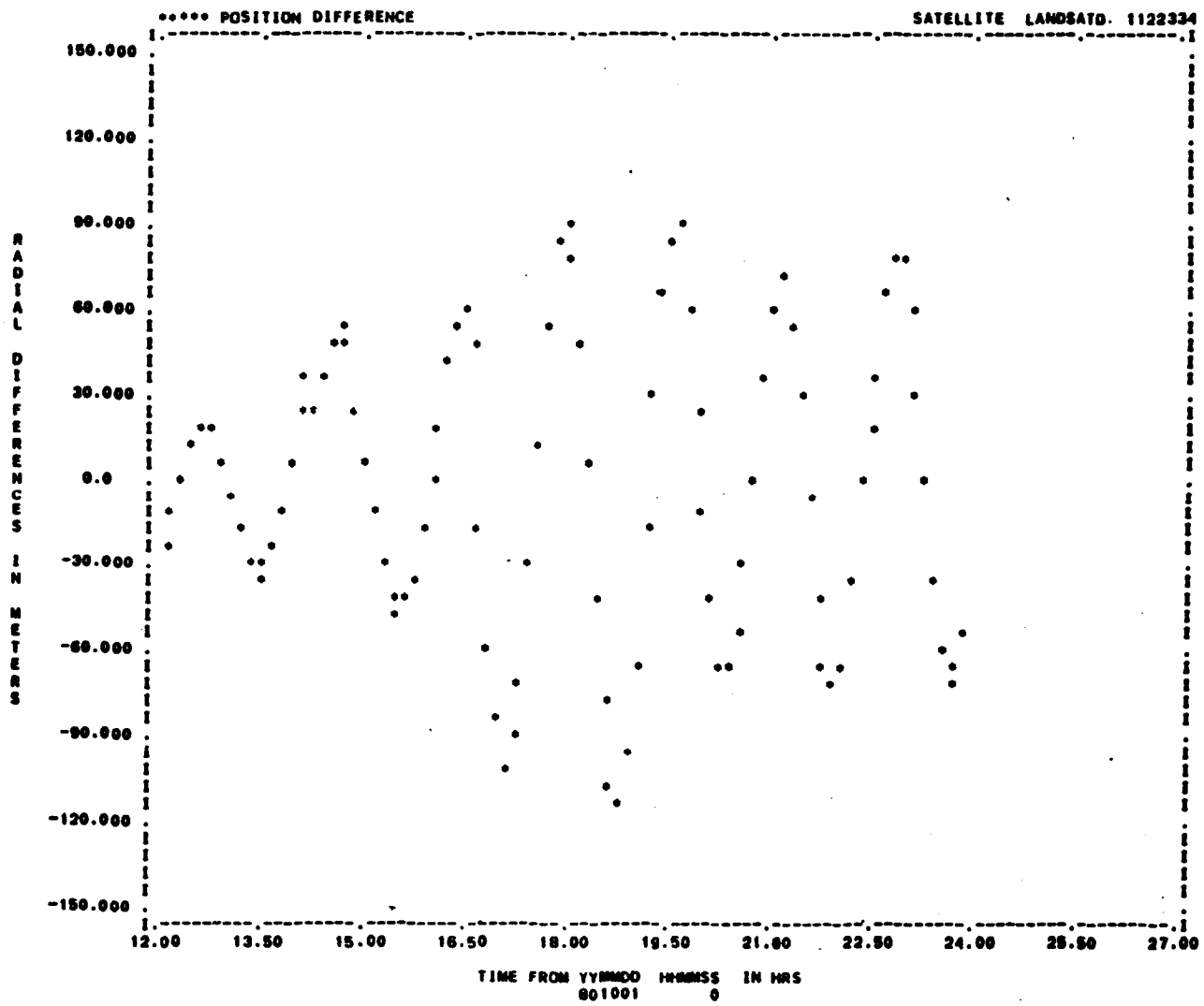

Figure A-61. Radial Differences for Run M14 (2 of 2)

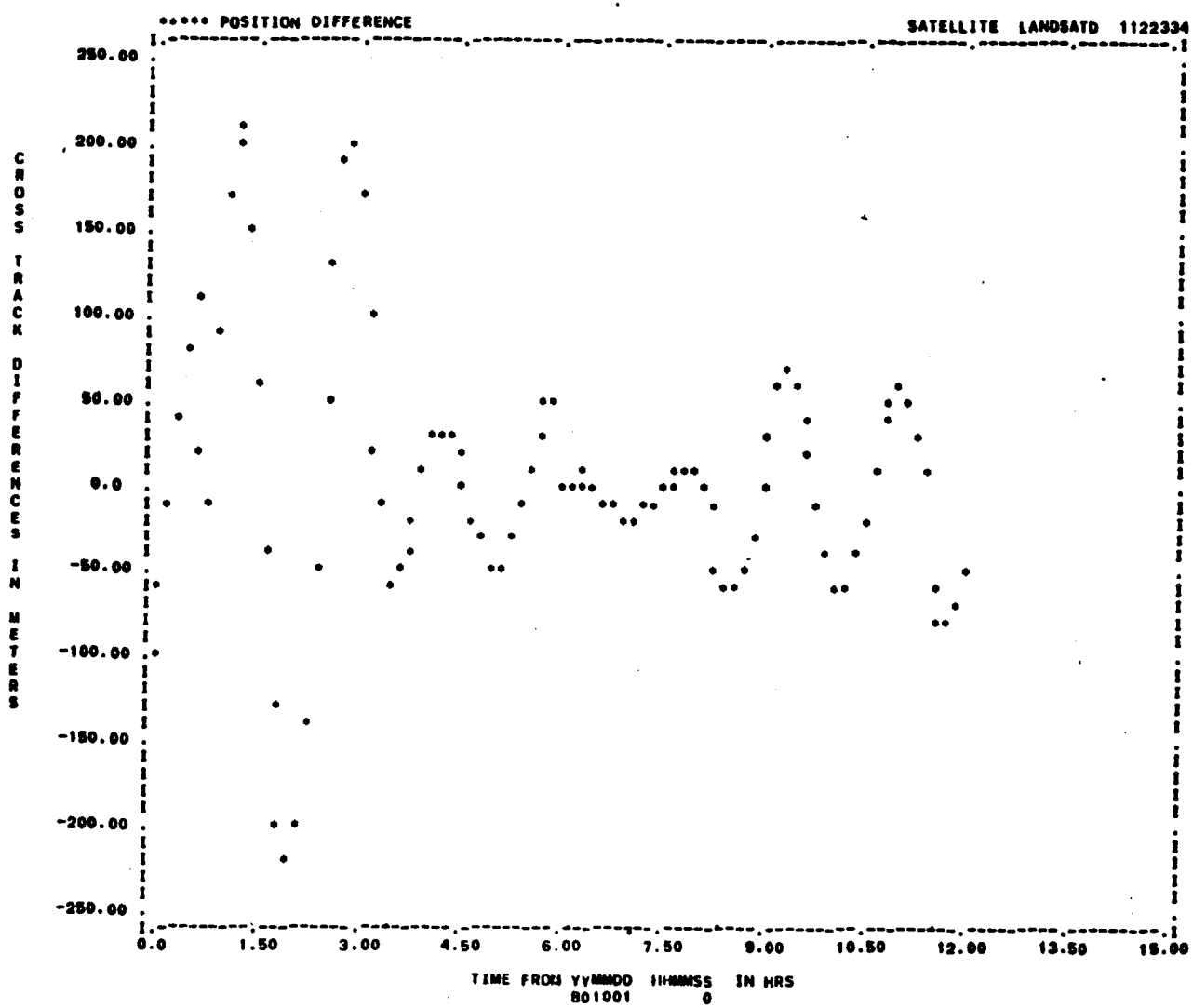

Figure A-62. Cross-Track Differences for Run M14 (1 of 2)

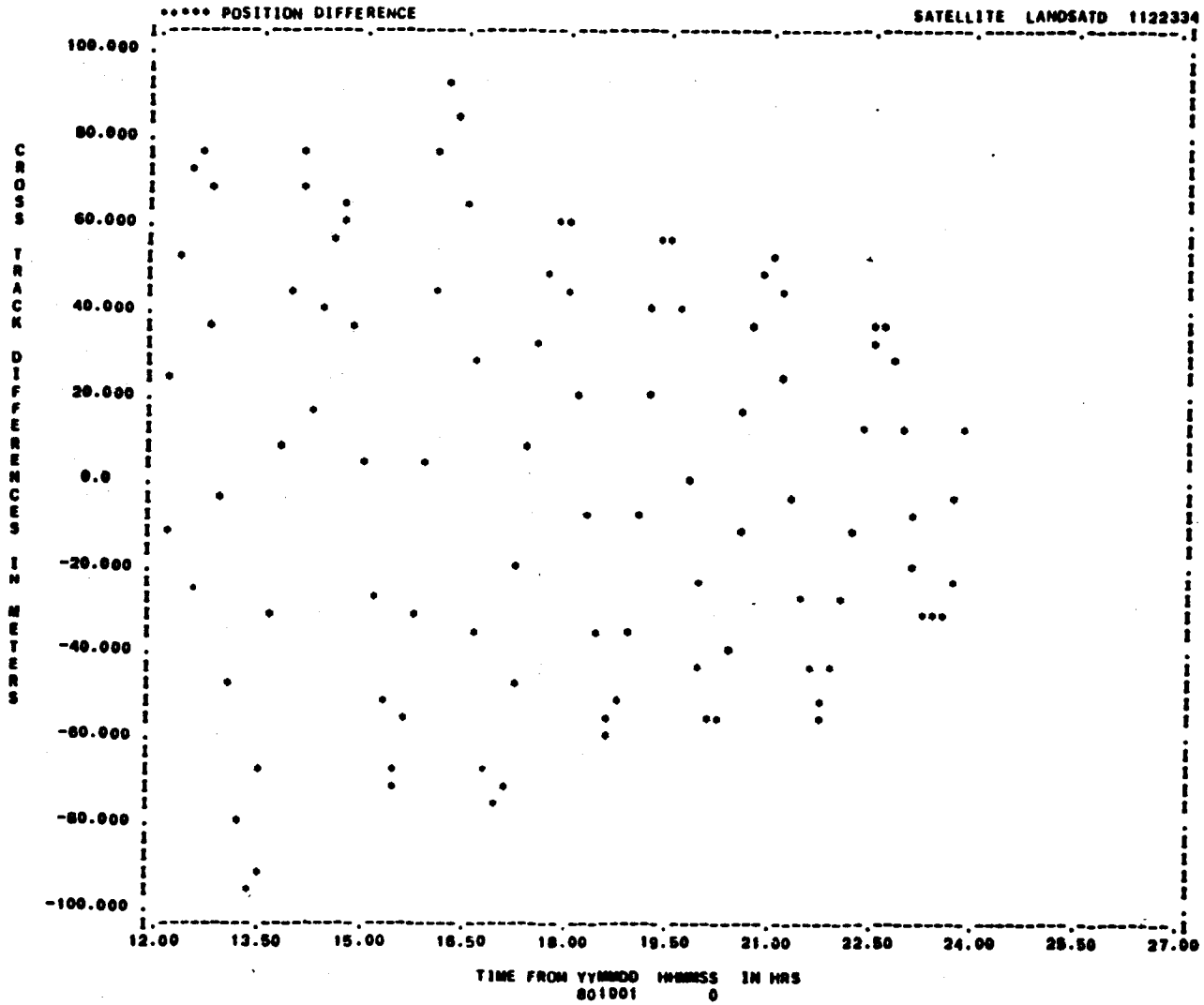

Figure A-62. Cross-Track Differences for Run M14 (2 of 2)

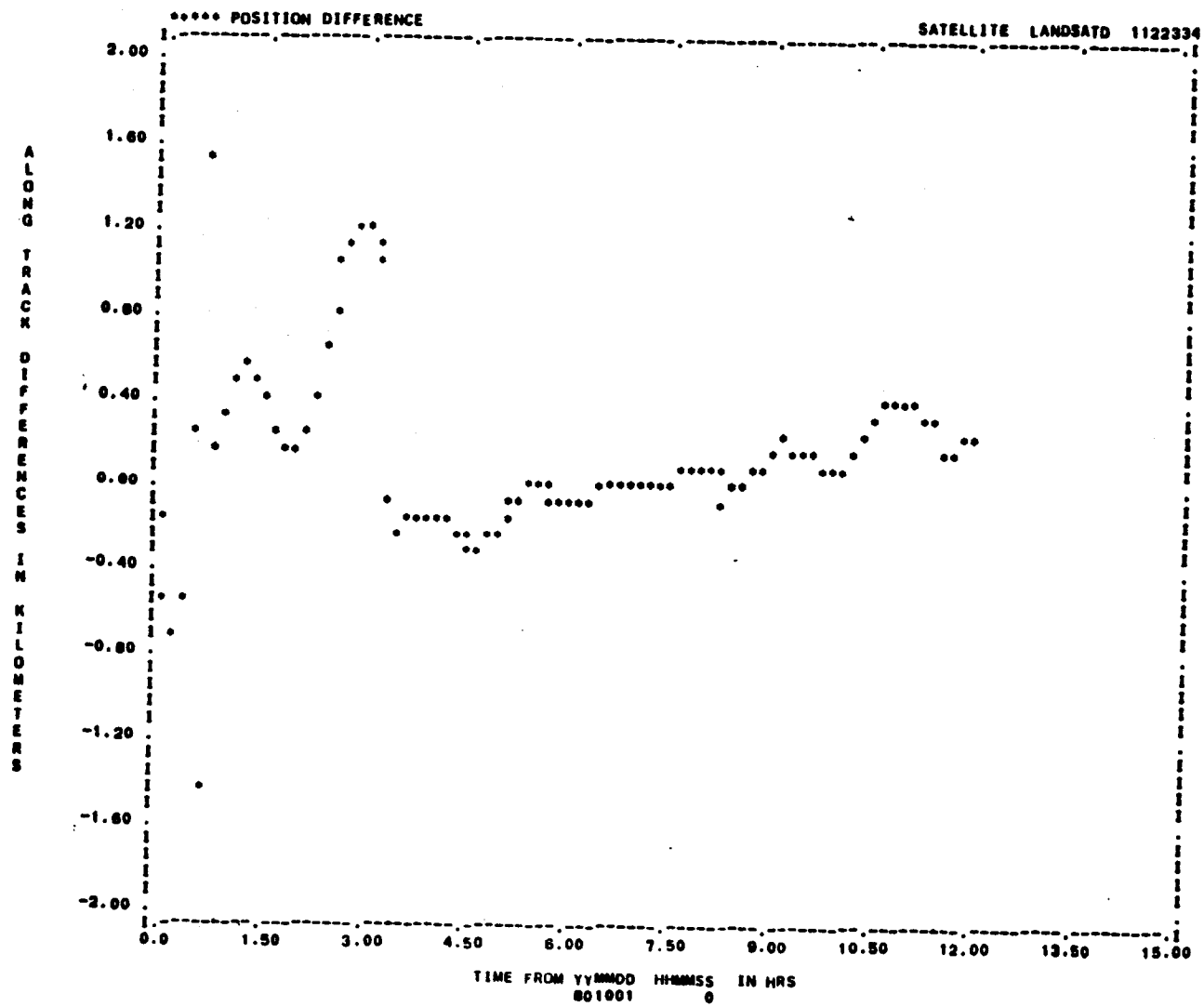

Figure A-63. Along-Track Differences for Run M14 (1 of 2)

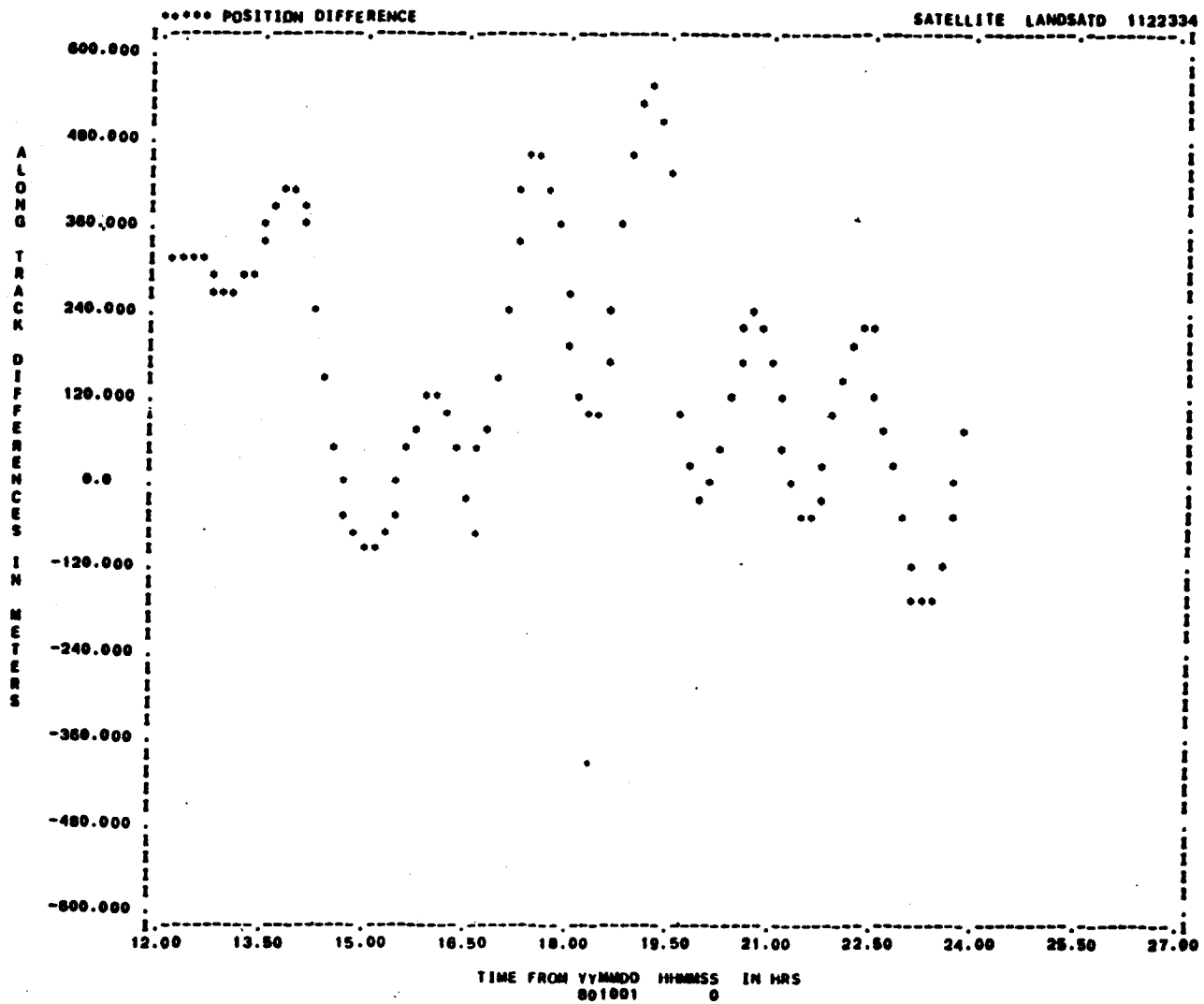

Figure A-63. Along-Track Differences for Run M14 (2 of 2)

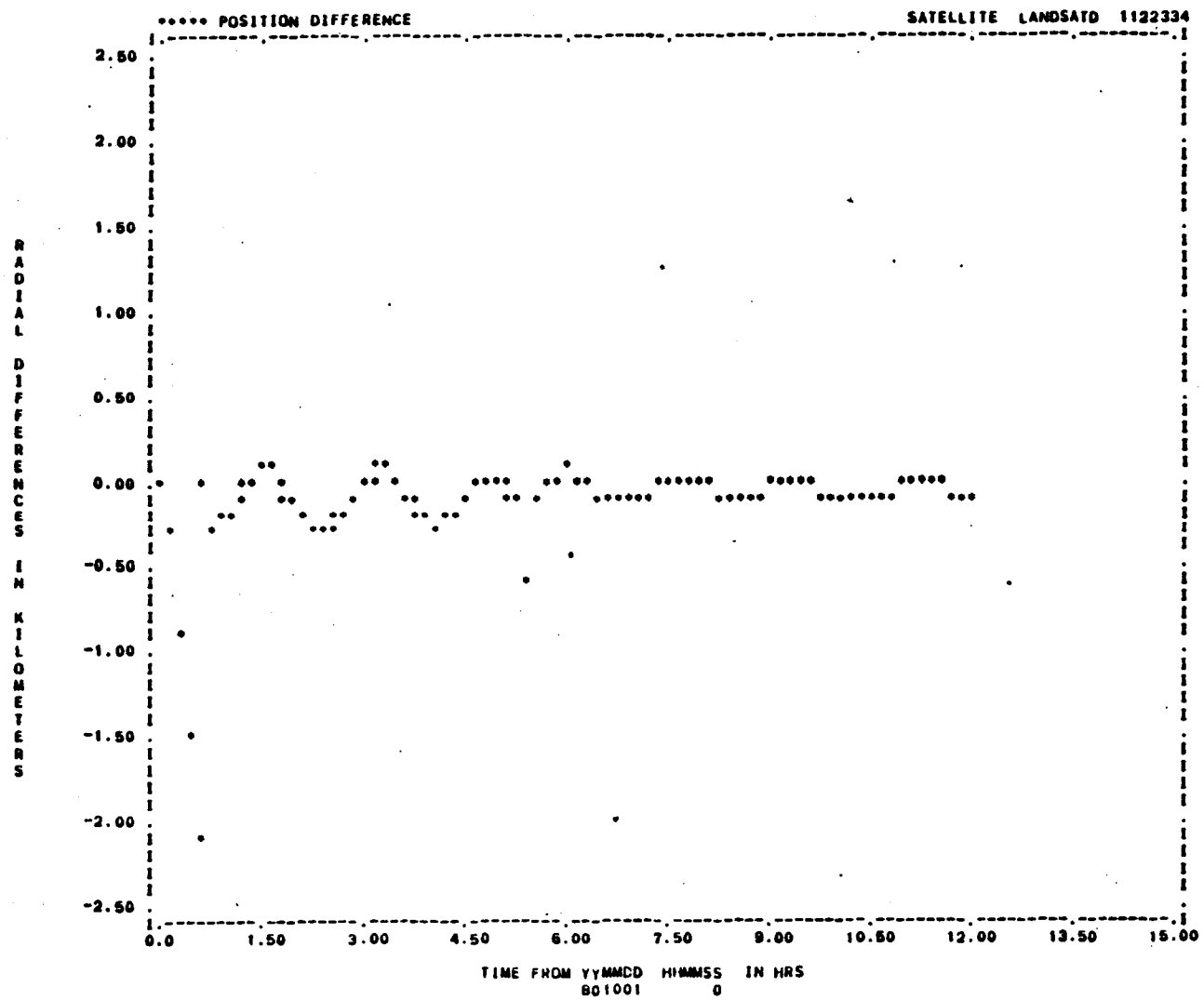

Figure A.64. Radial Differences for Run M26 (1 of 2)

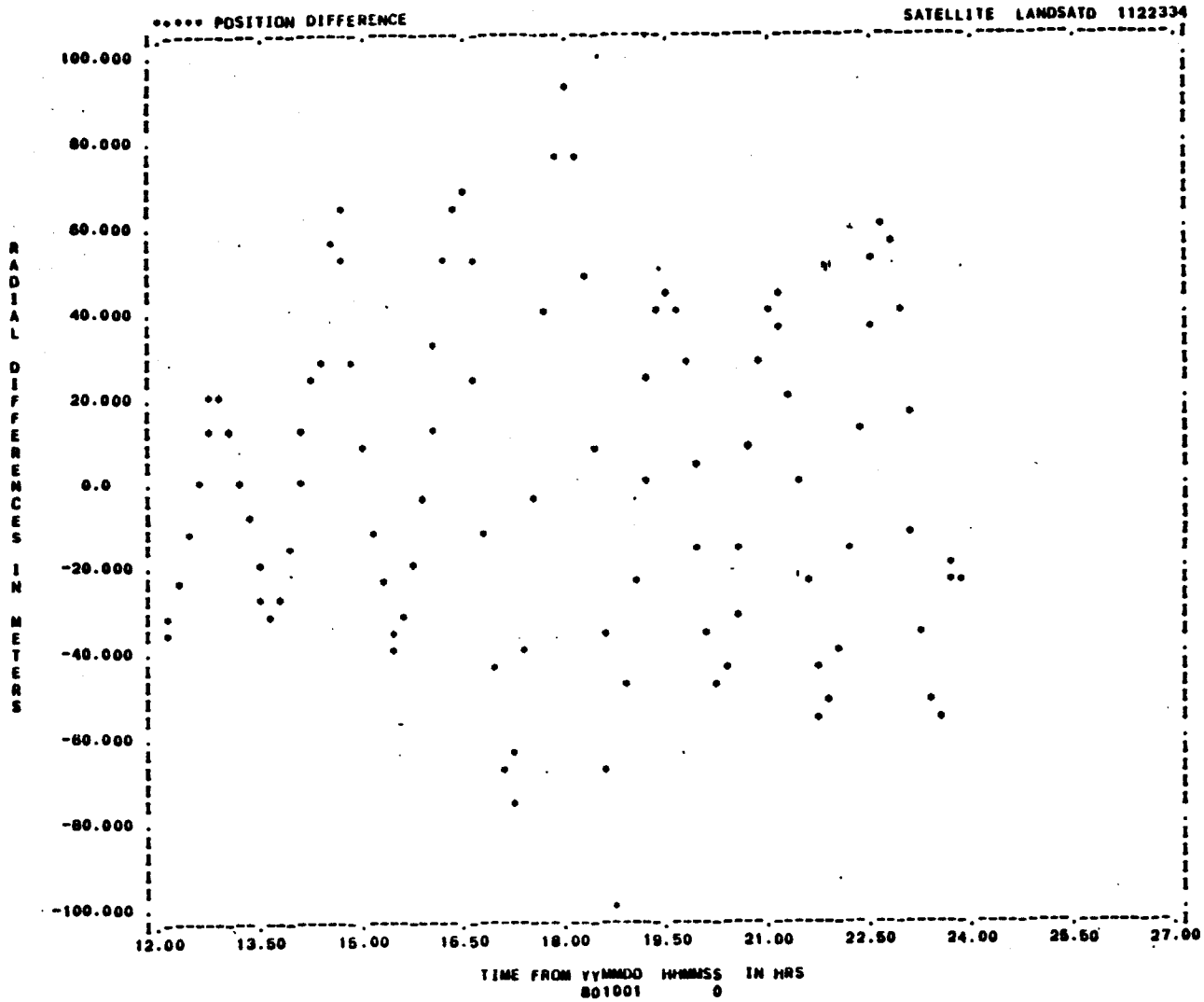

Figure A-64. Radial Differences for Run M26 (2 of 2)

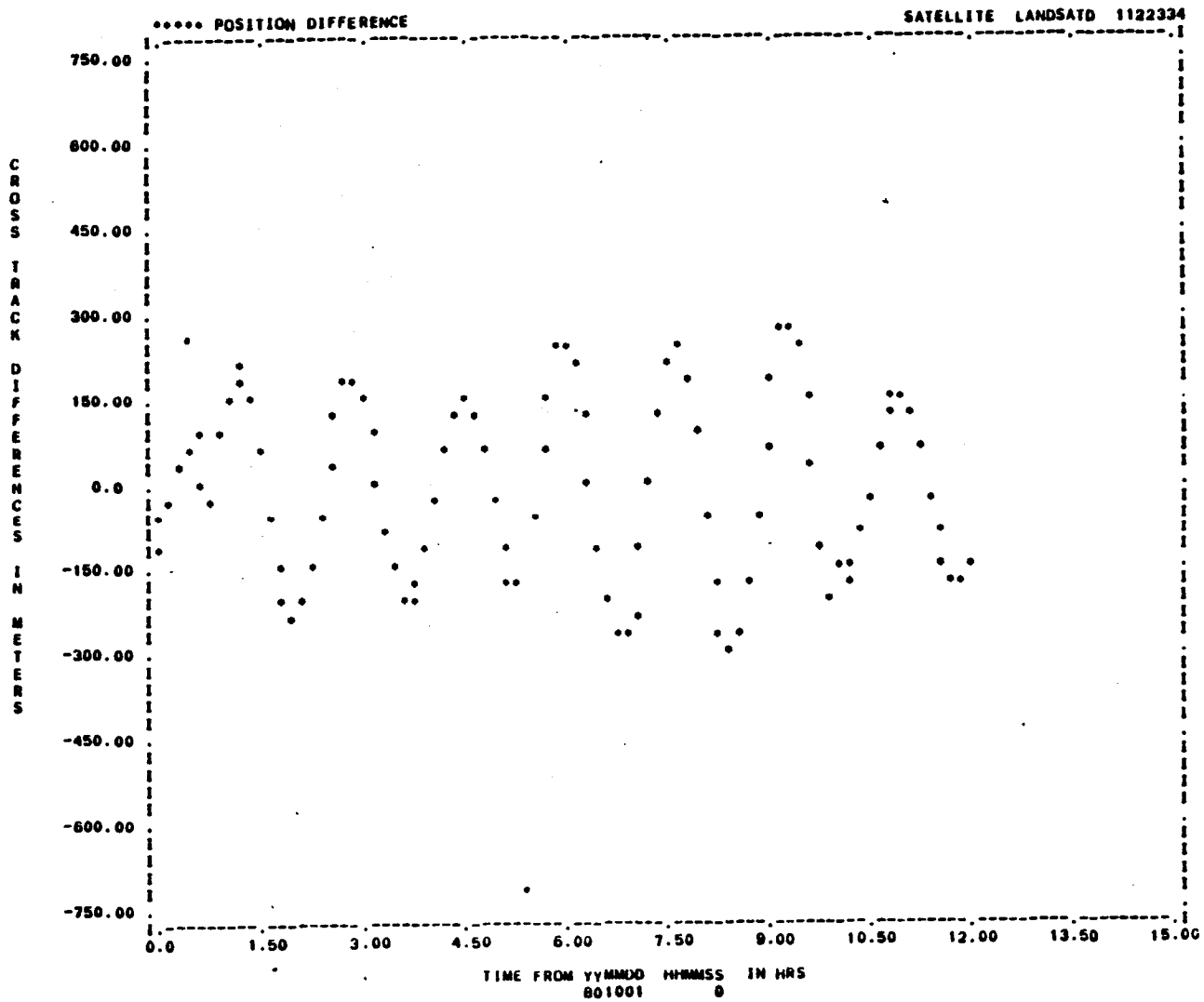

Figure A-65. Cross-Track Differences for Run M26 (1 of 2)

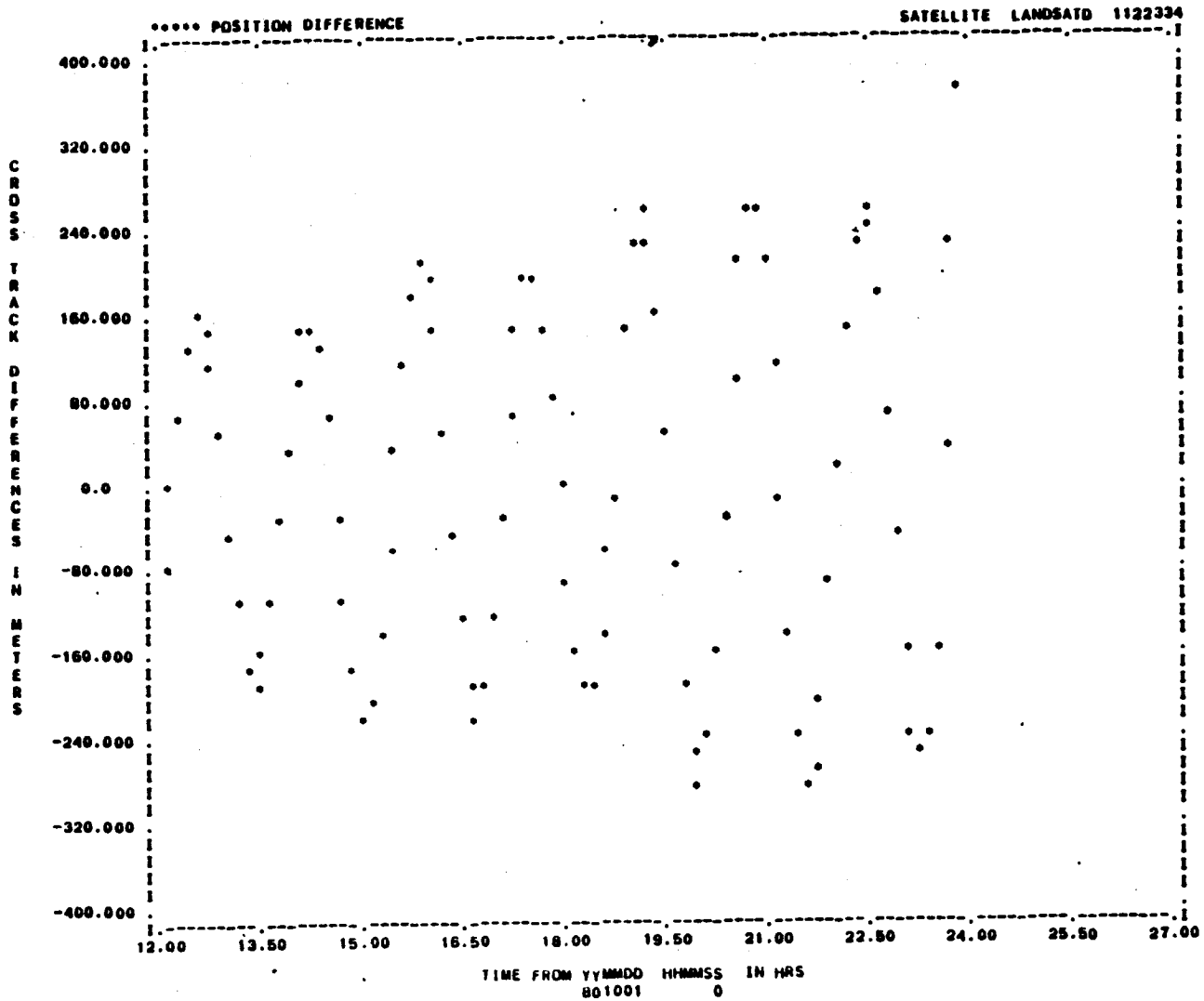

Figure A-65. Cross-Track Differences for Run M26 (2 of 2)

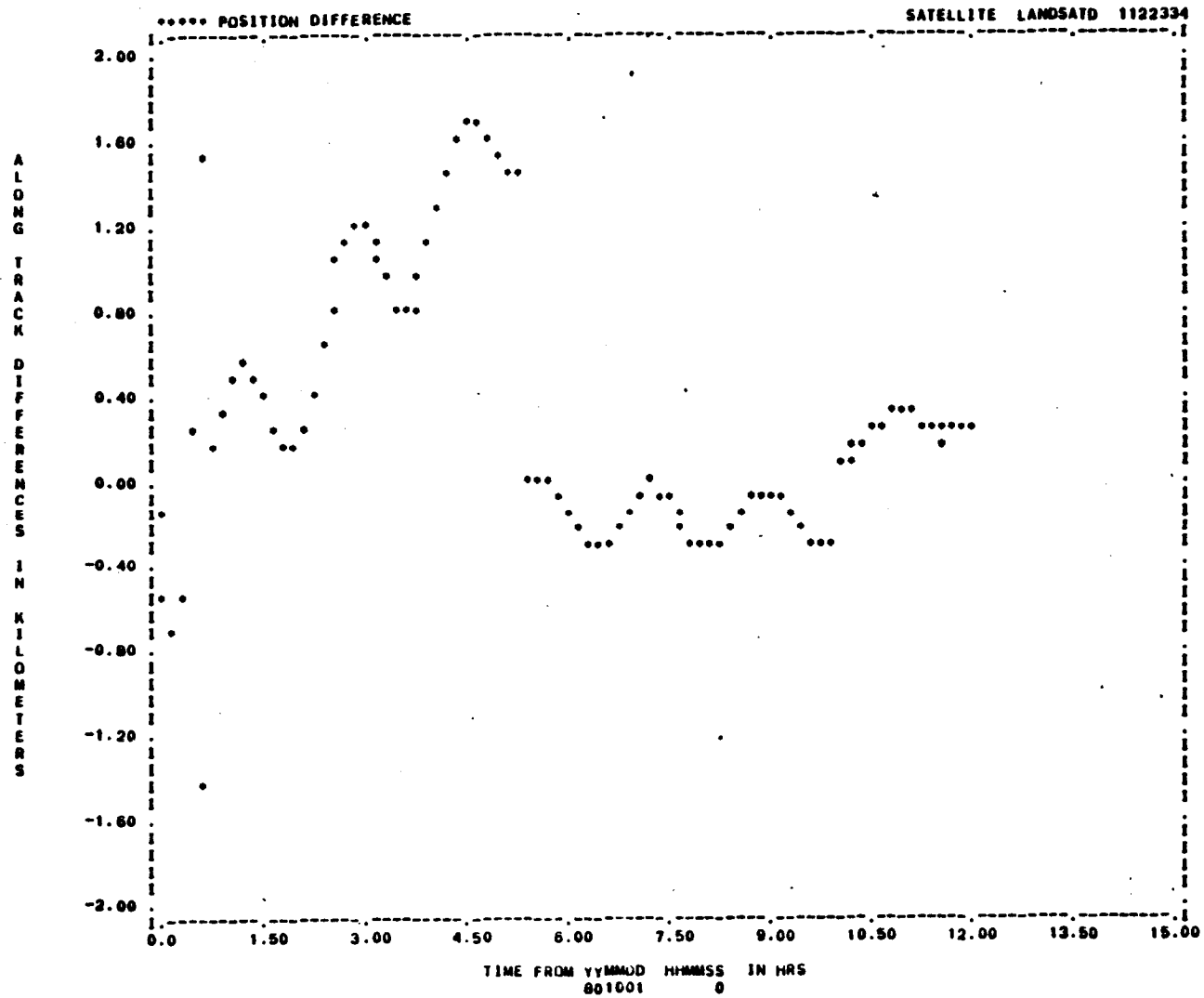

Figure A-66. Along-Track Differences for Run M26 (1 of 2

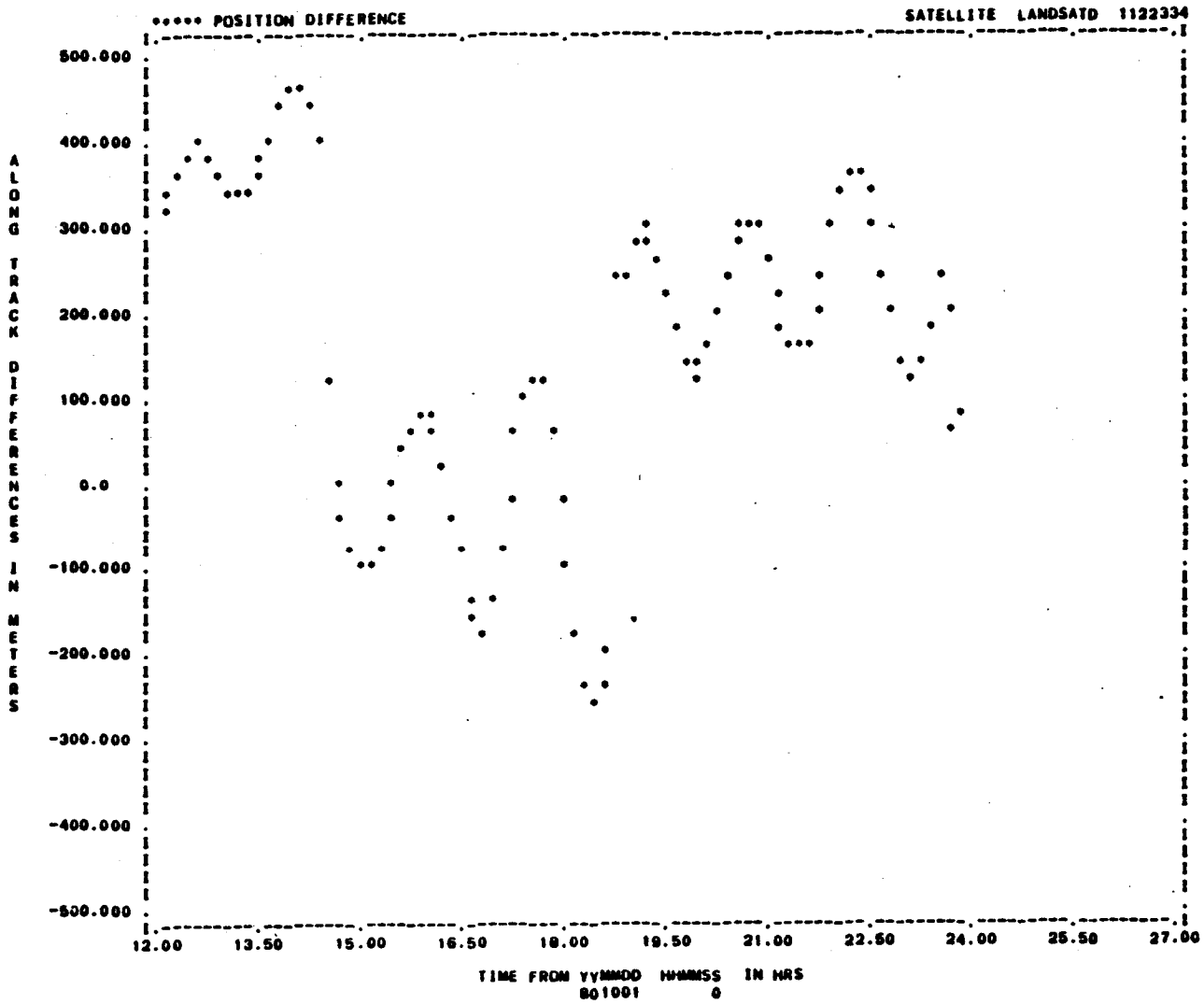

Figure A-66. Along-Track Differences for Run M26 (2 of 2)

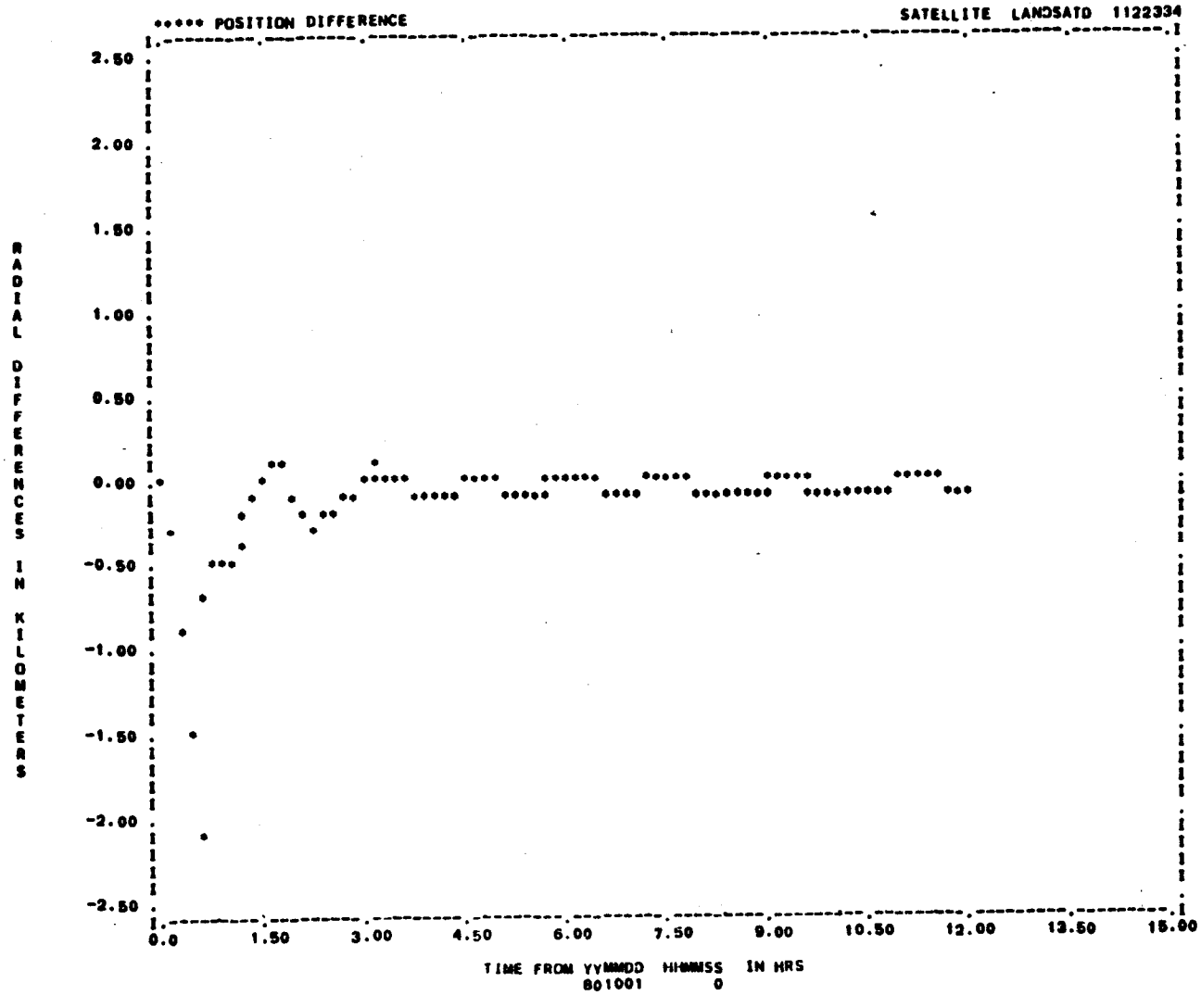

Figure A-67. Radial Differences for Run M33 (1 of 2)

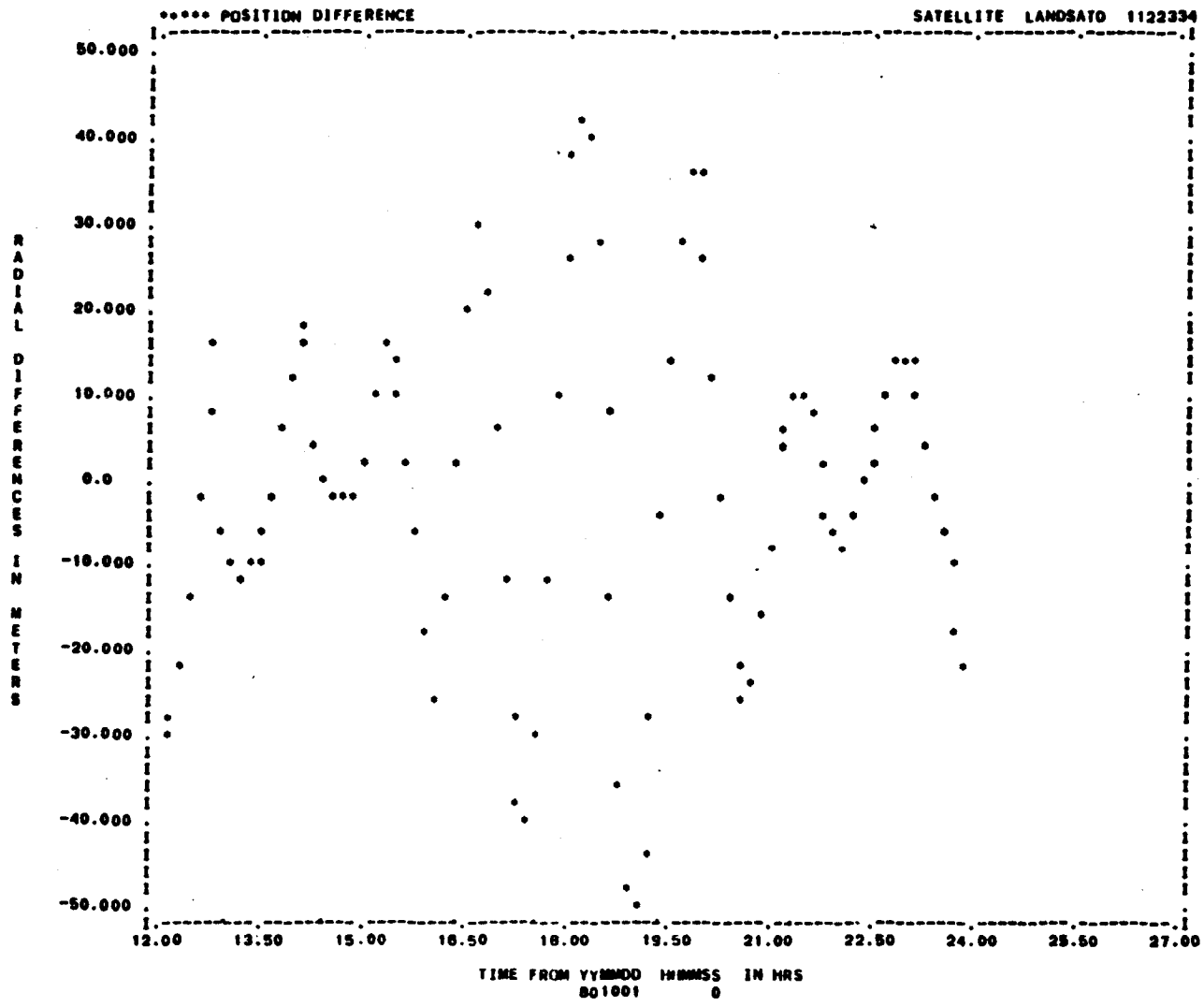

Figure A-67. Radial Differences for Run M33 (2 of 2)

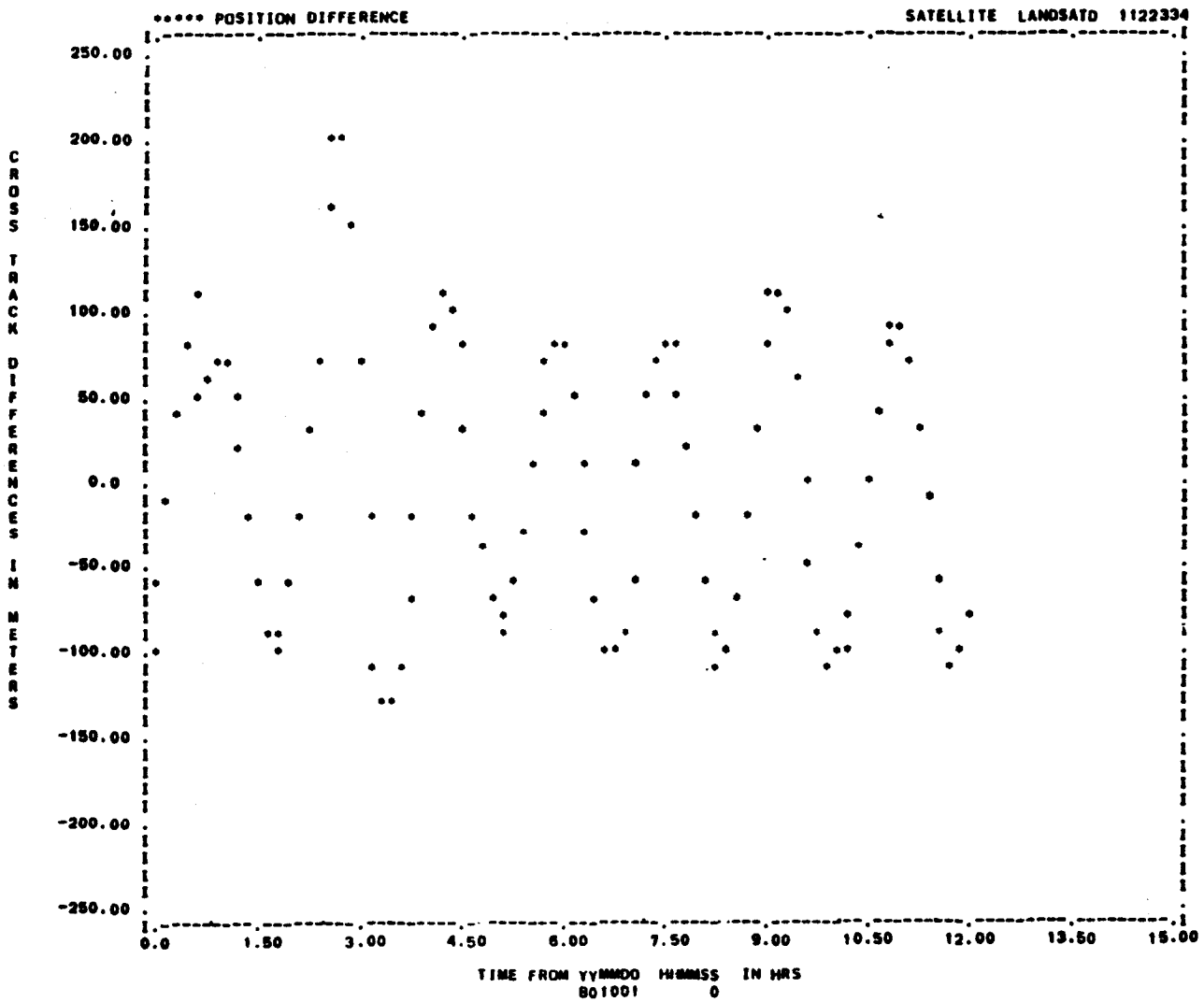

Figure A-68. Cross-Track Differences for Run M33 (1 of 2)

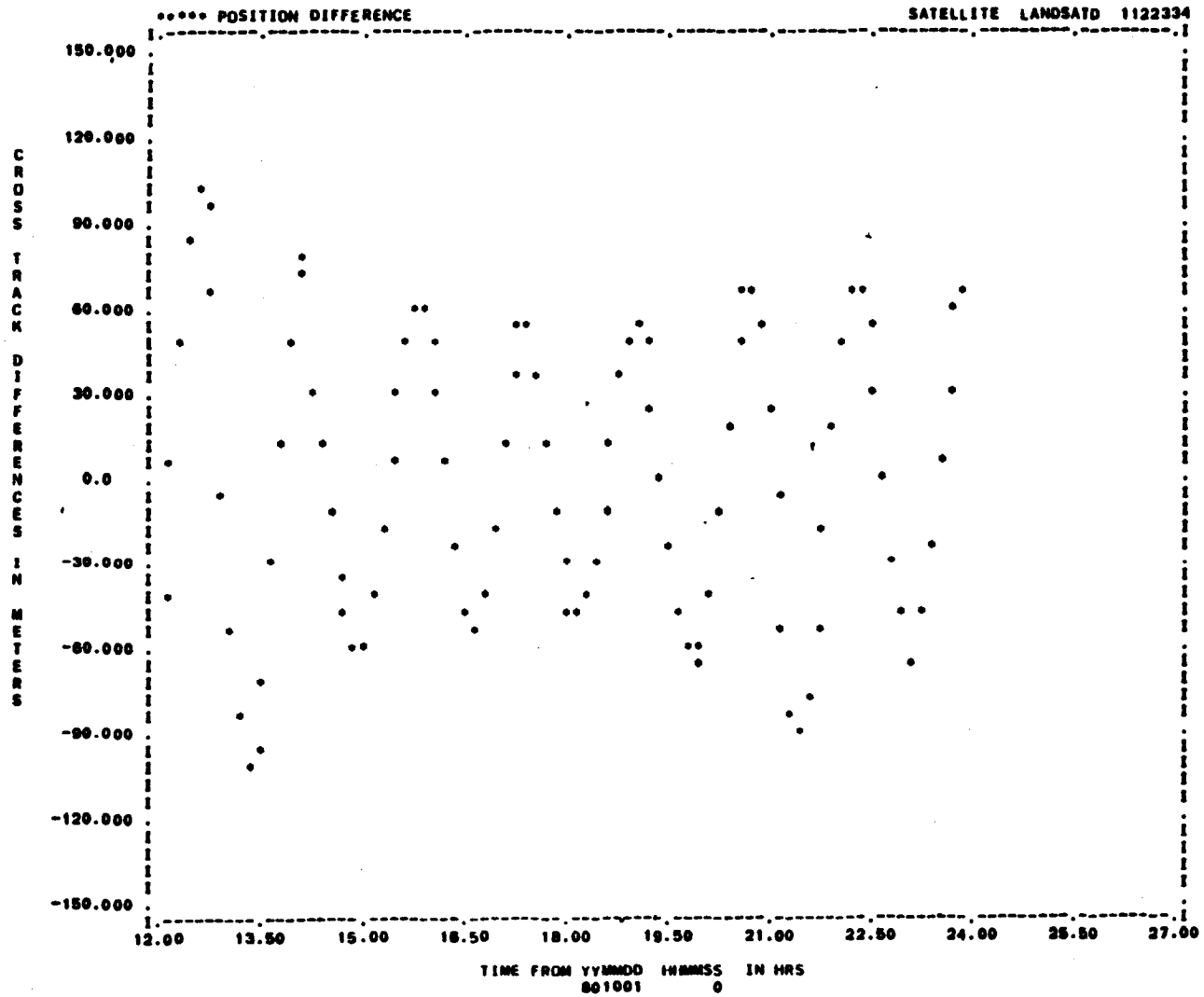

Figure A-68. Cross-Track Differences for Run M33 (2 of 2)

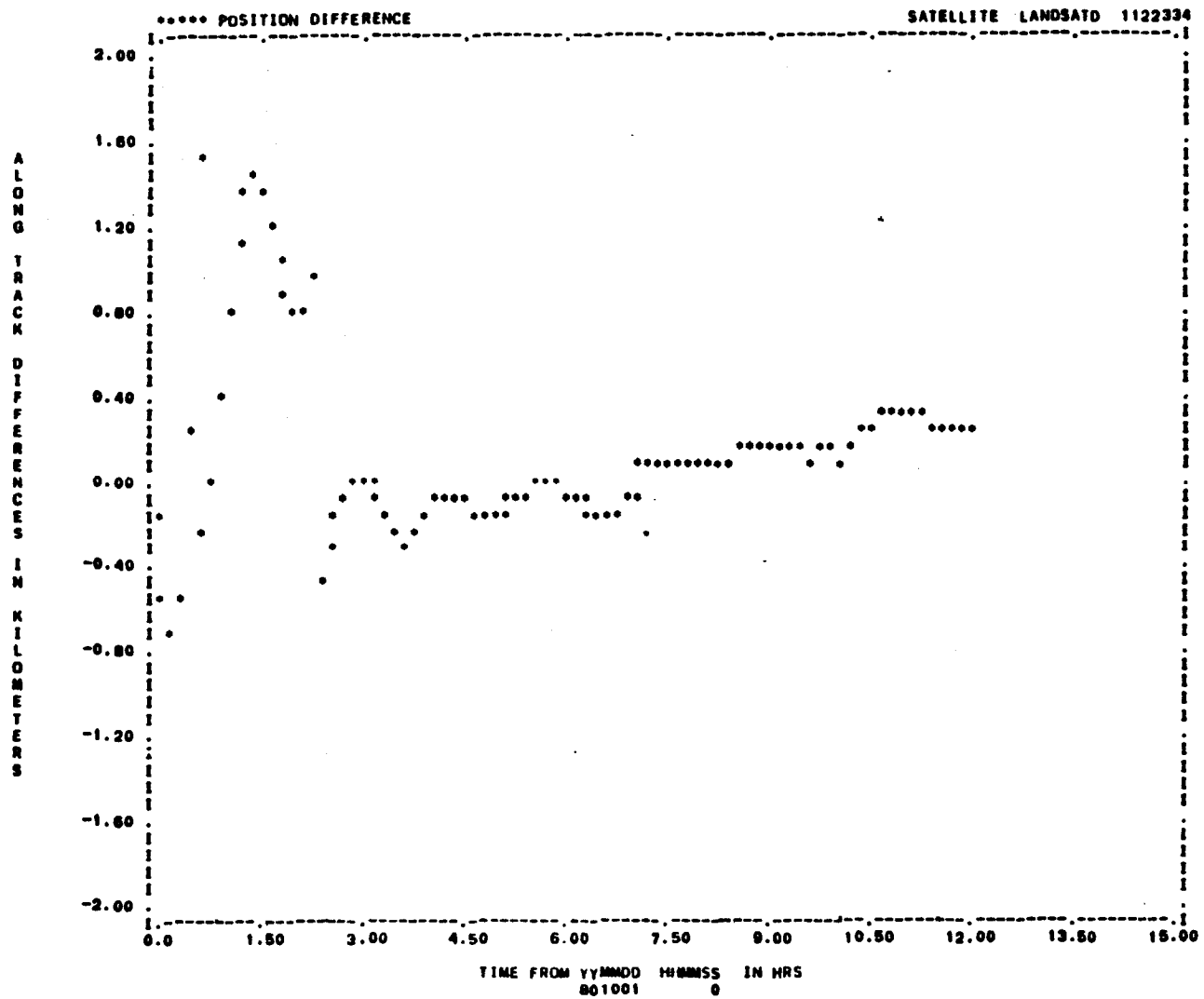

Figure A-69. Along-Track Differences for Run M33 (1 of 2)

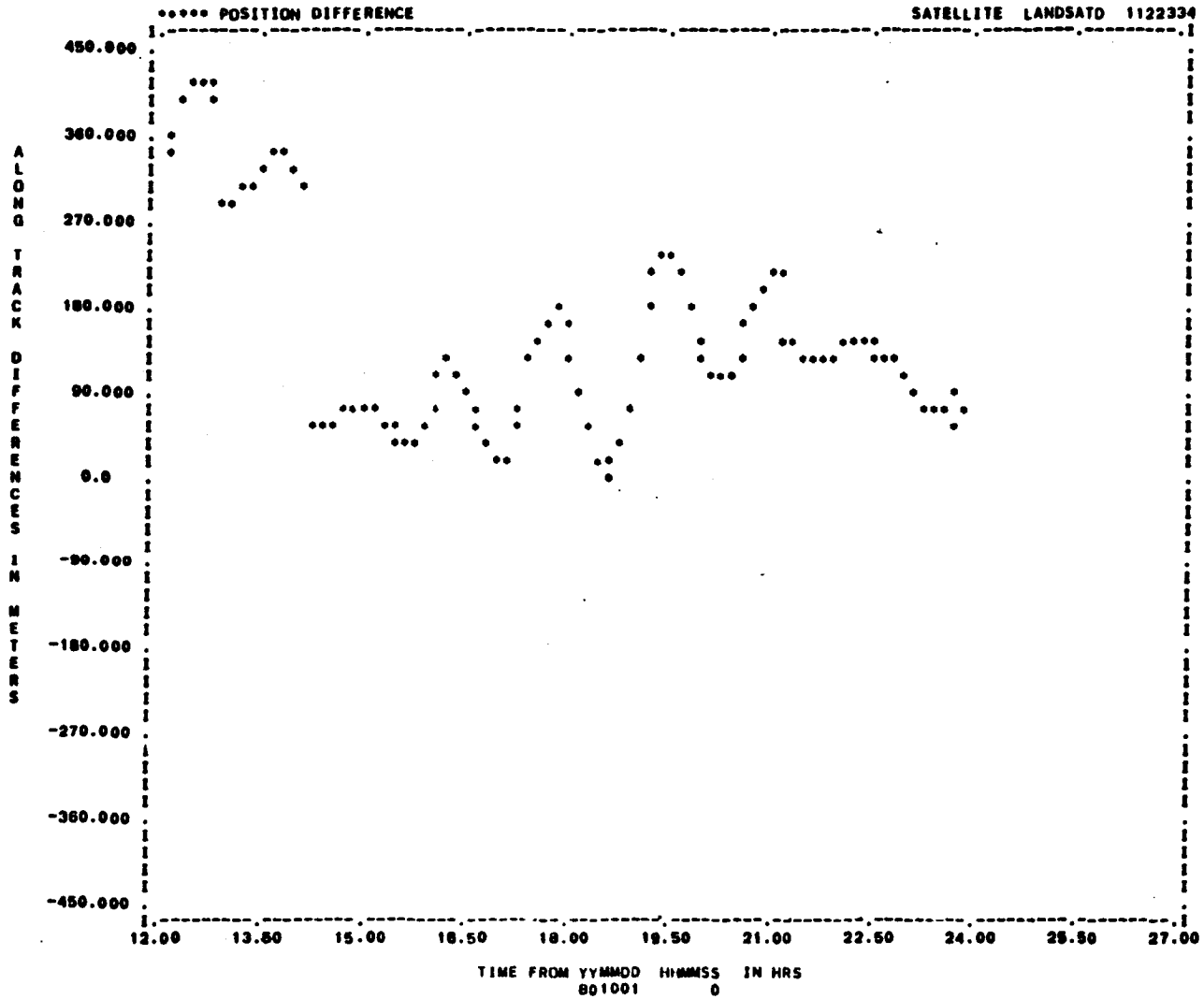

Figure A-69. Along-Track Differences for Run M33 (2 of 2)

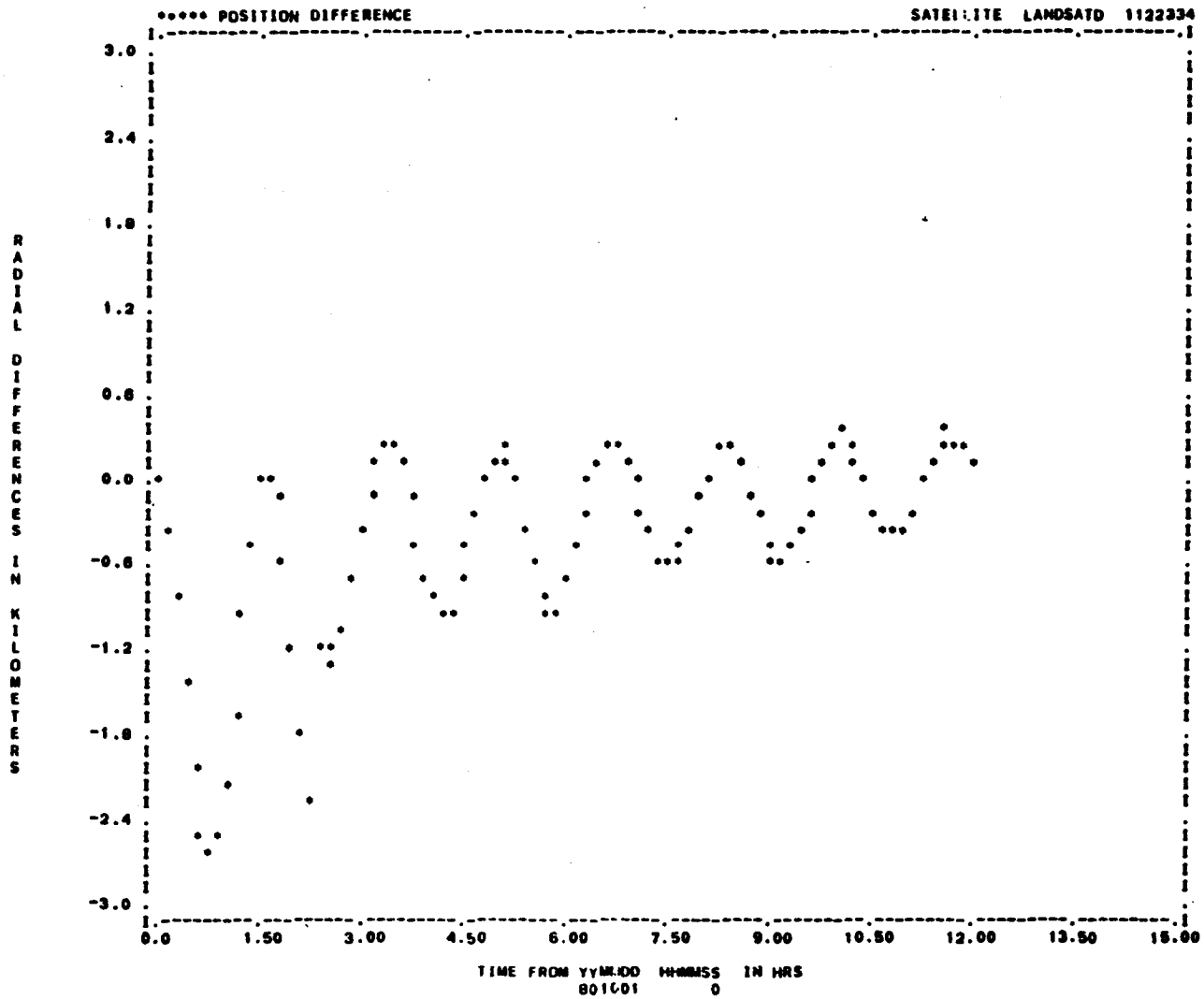

Figure A-70. Radial Differences for Run N6 (1 of 2)

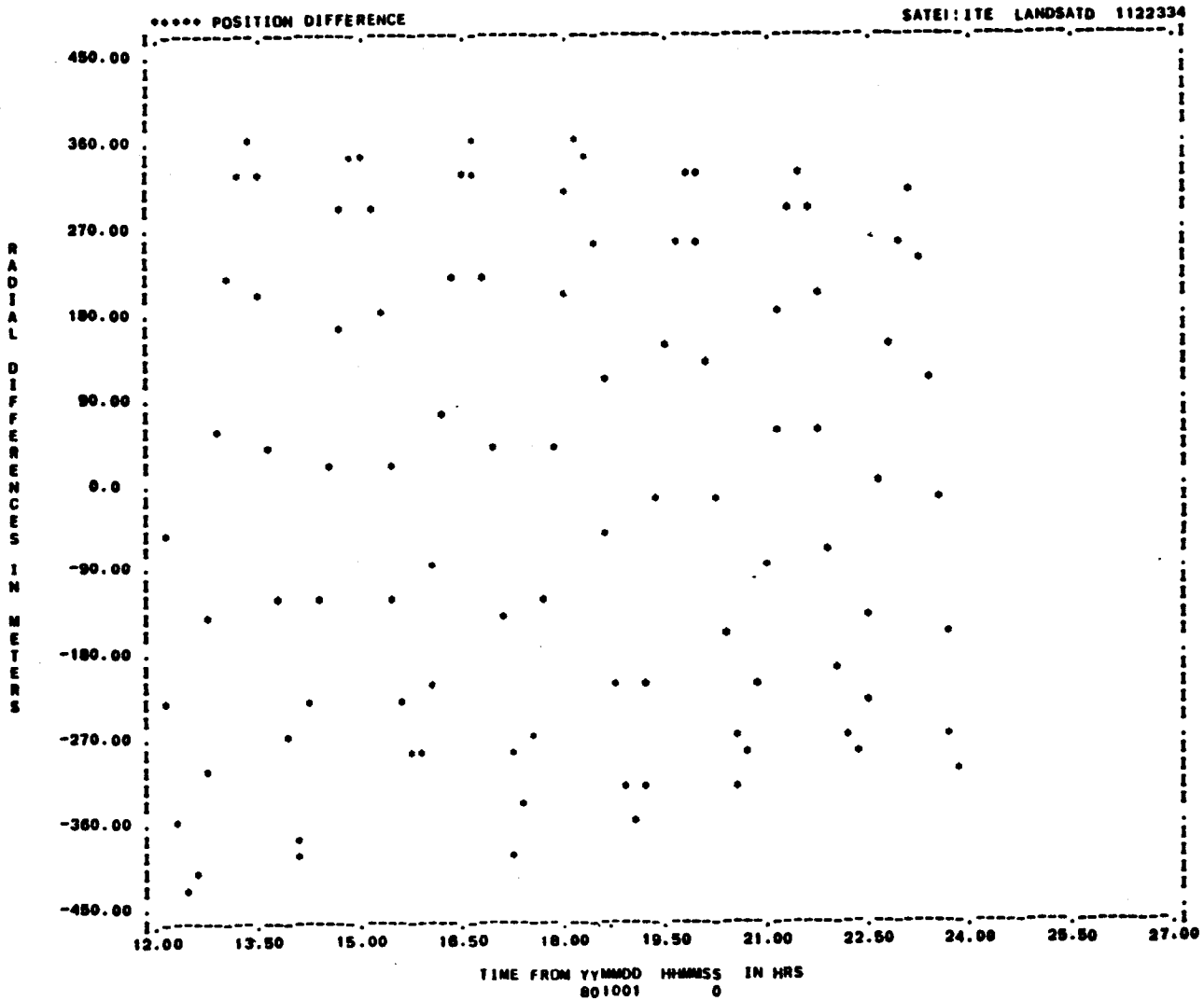

Figure A-70. Radial Differences for Run N6 (2 of 2)

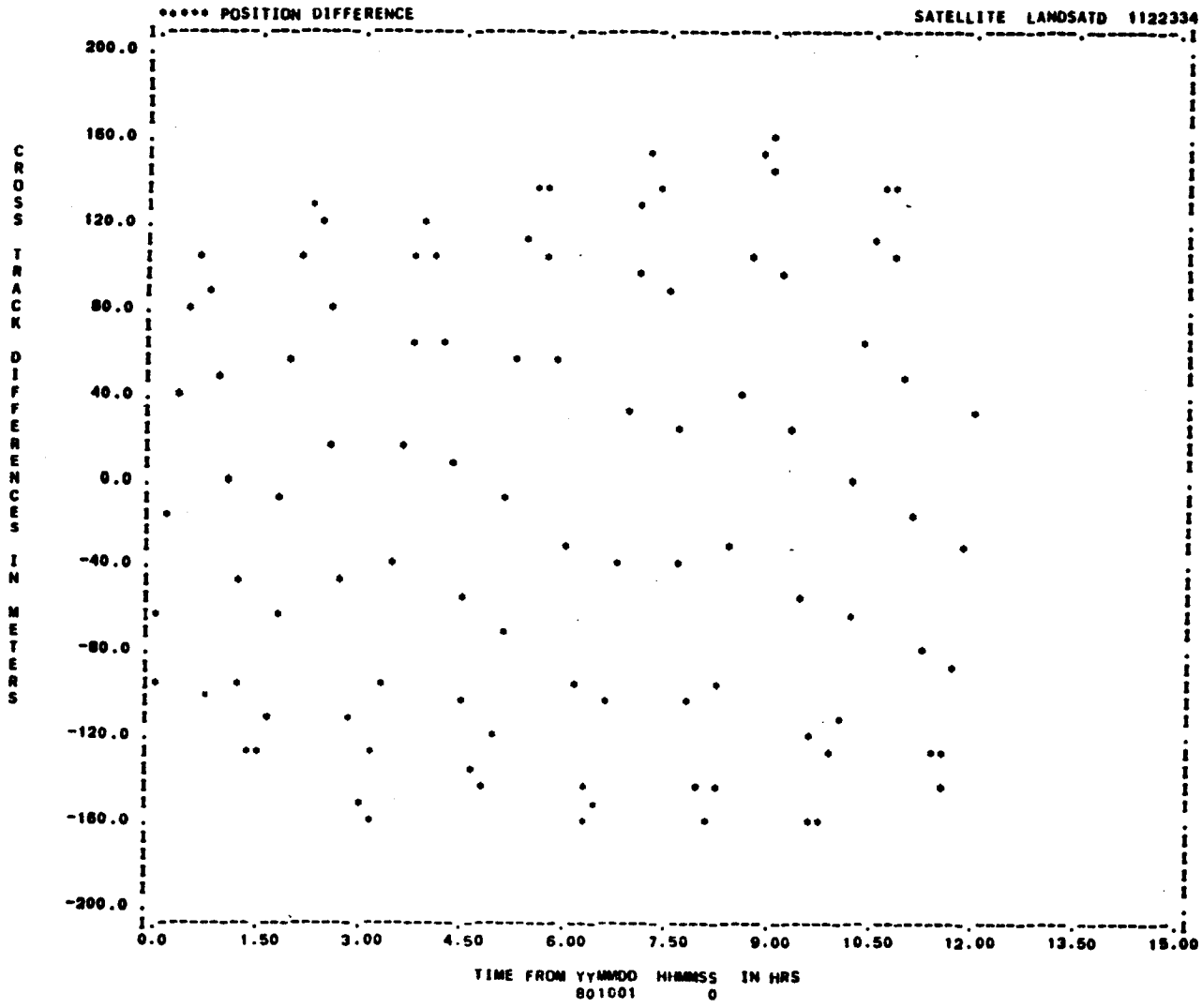

Figure A-71. Cross-Track Differences for Run N6 (1 of 2)

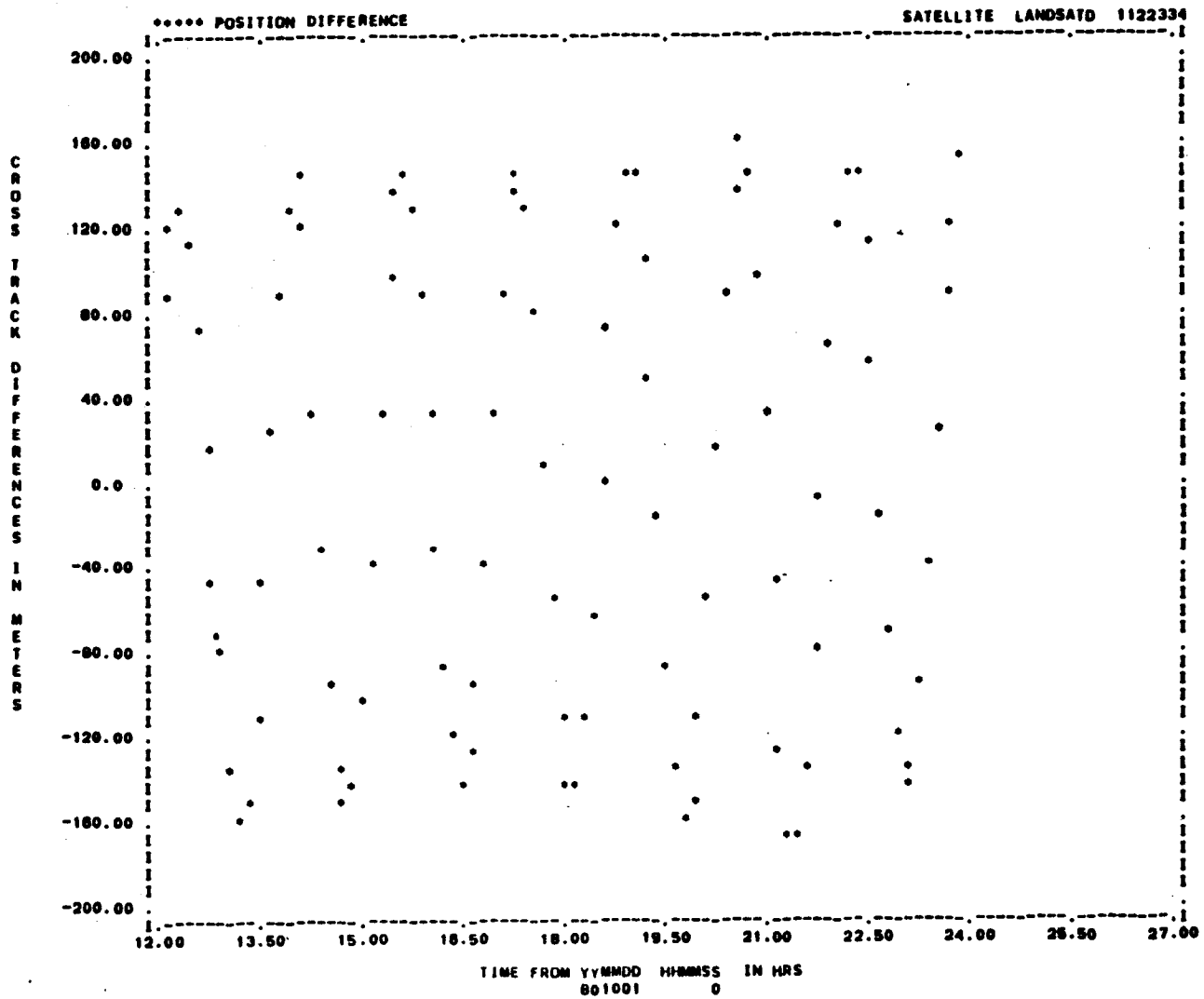

Figure A-71. Cross-Track Differences for Run N6 (2 of 2)

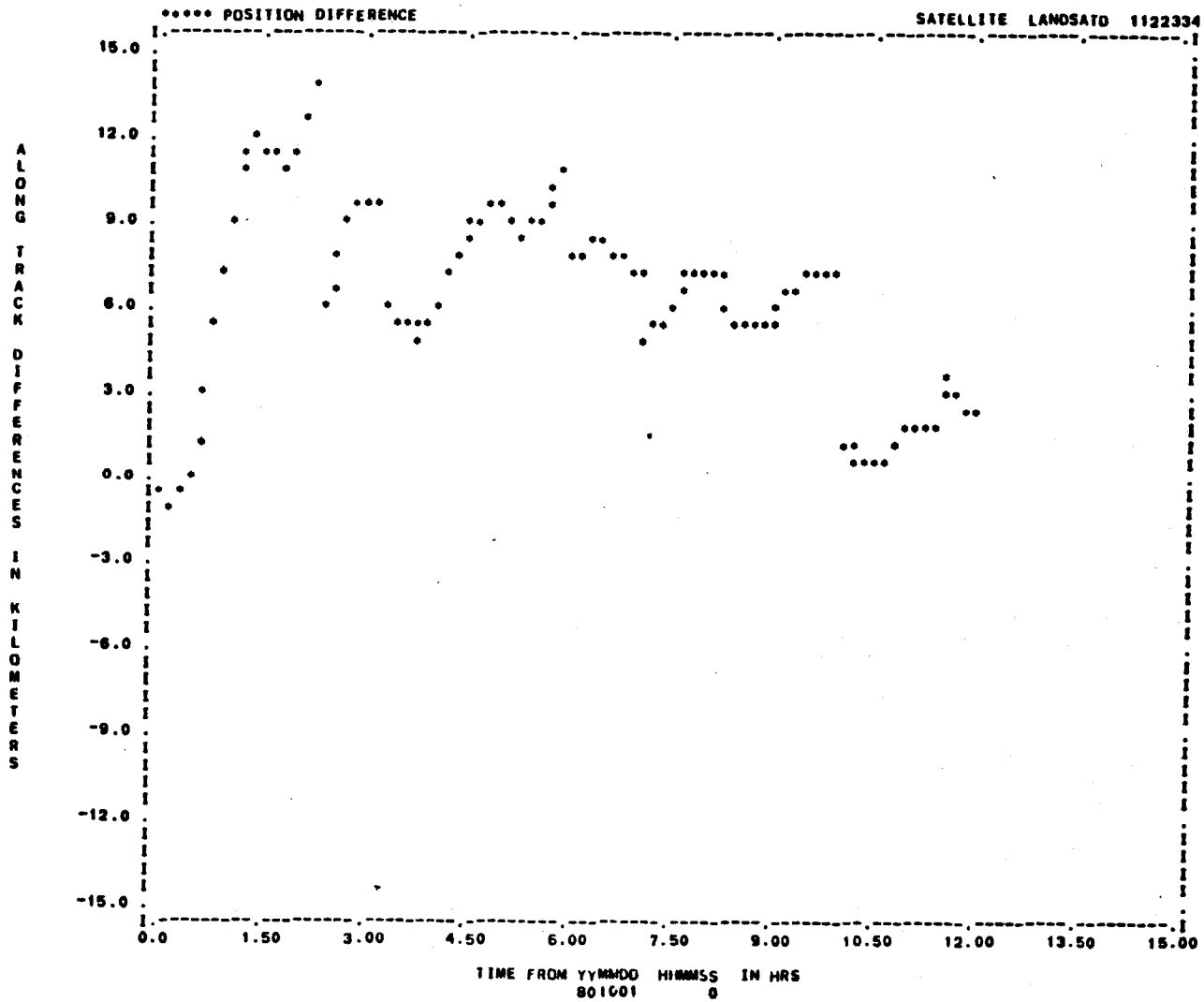

Figure A-72. Along-Track Differences for Run N6 (1 of 2)

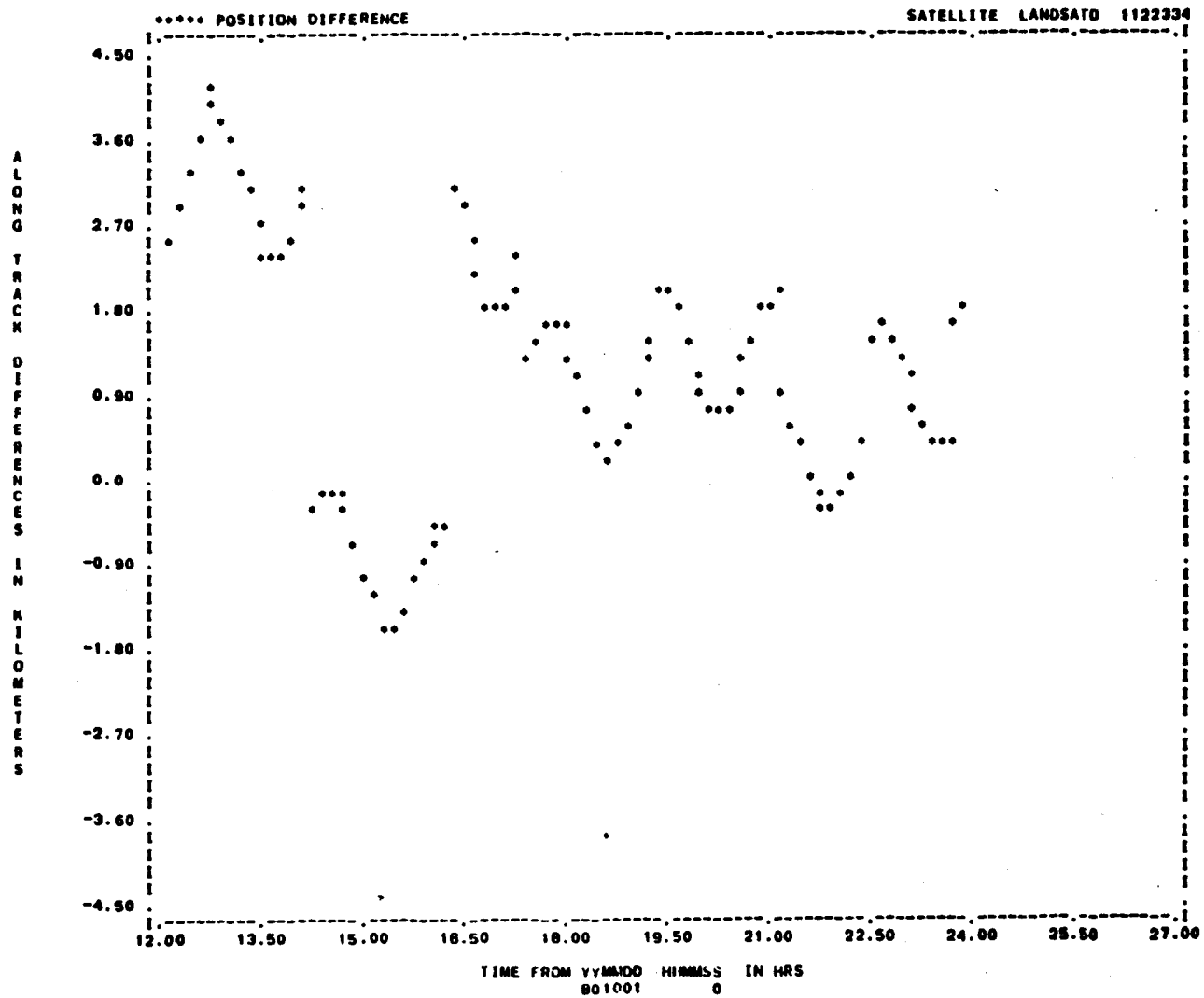

Figure A-72. Along-Track Differences for Run N6 (2 of 2)

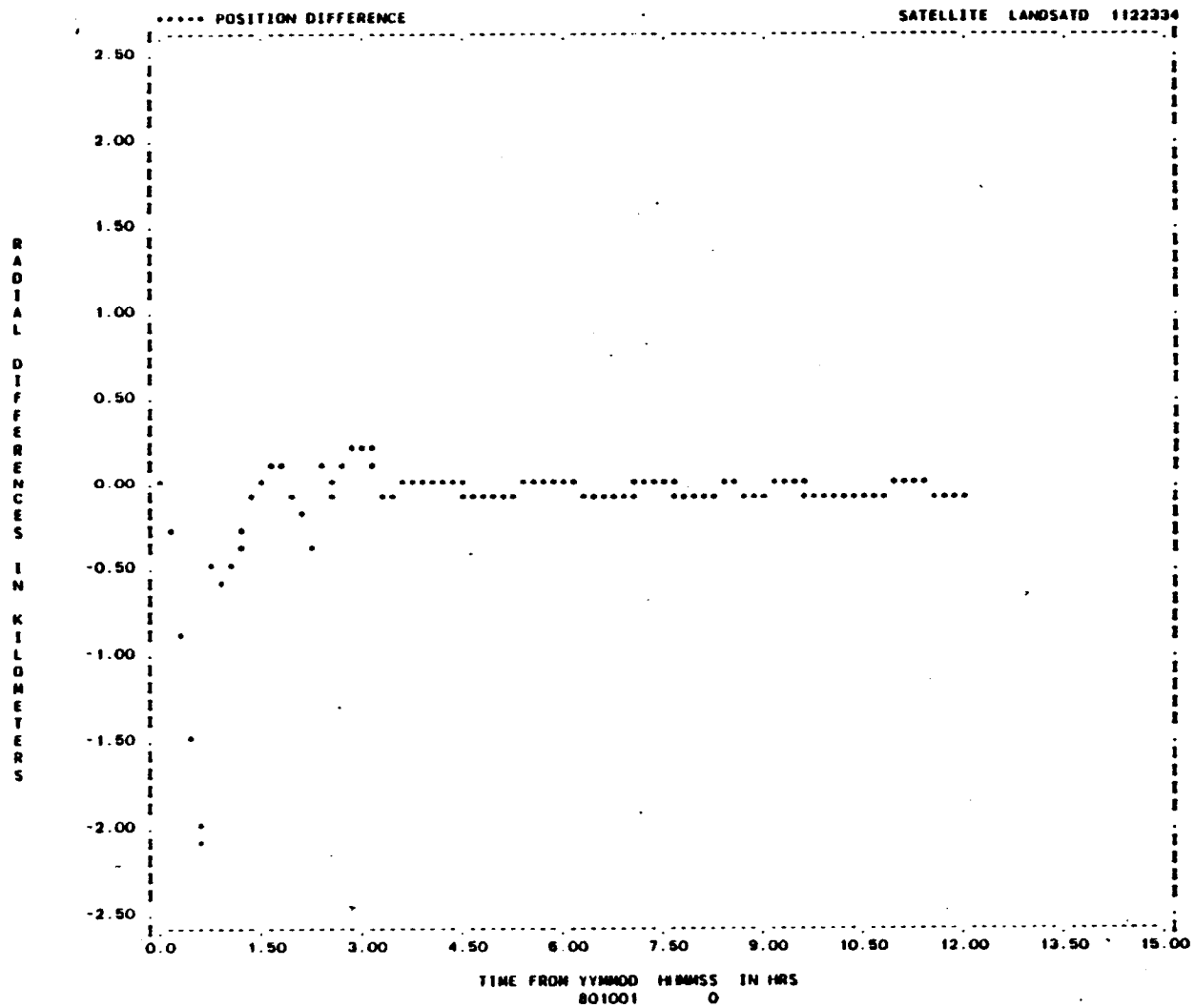

Figure A-73. Radial Differences for Run N14 (1 of 2)

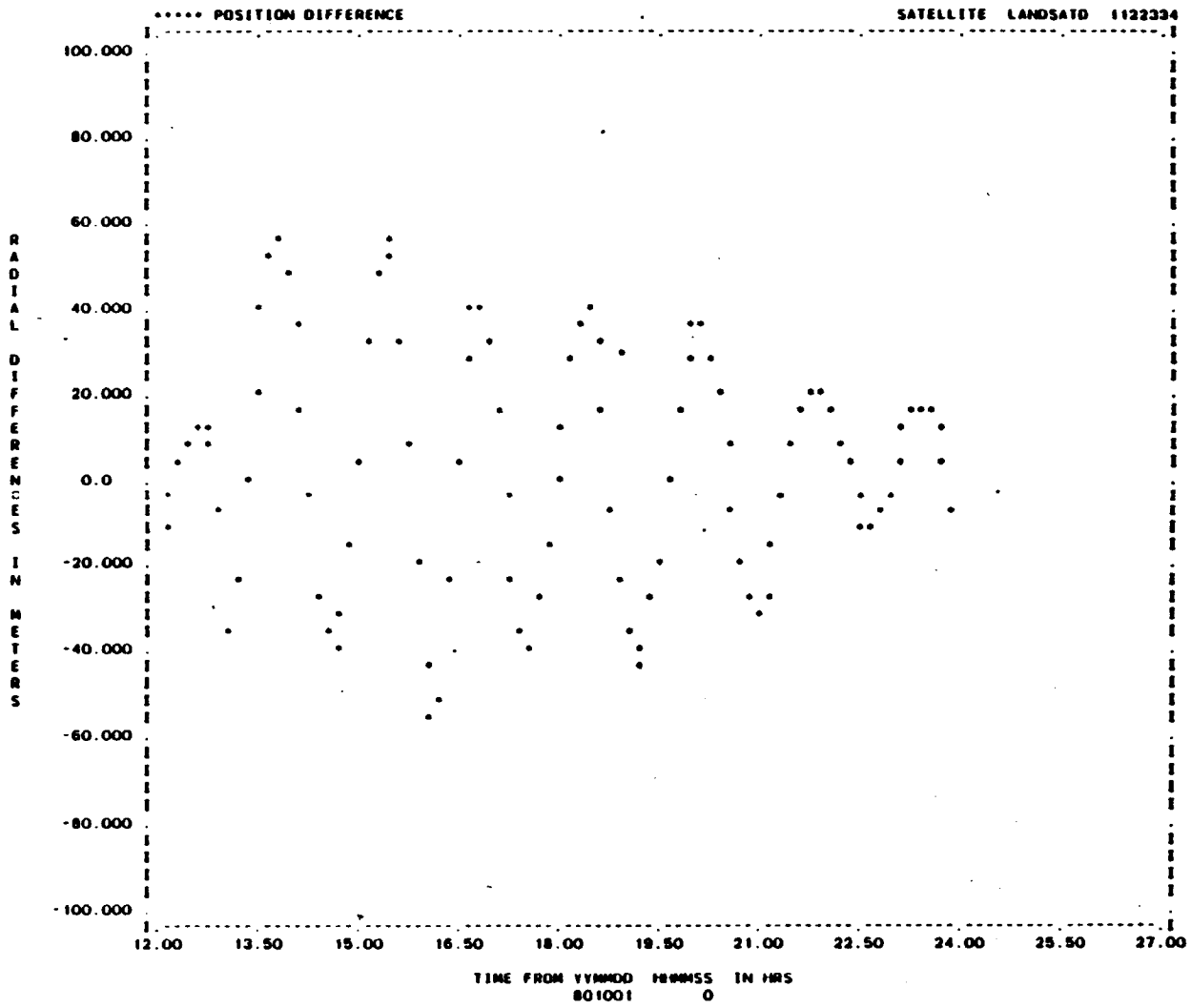

Figure A-73. Radial Differences for Run N14 (2 of 2)

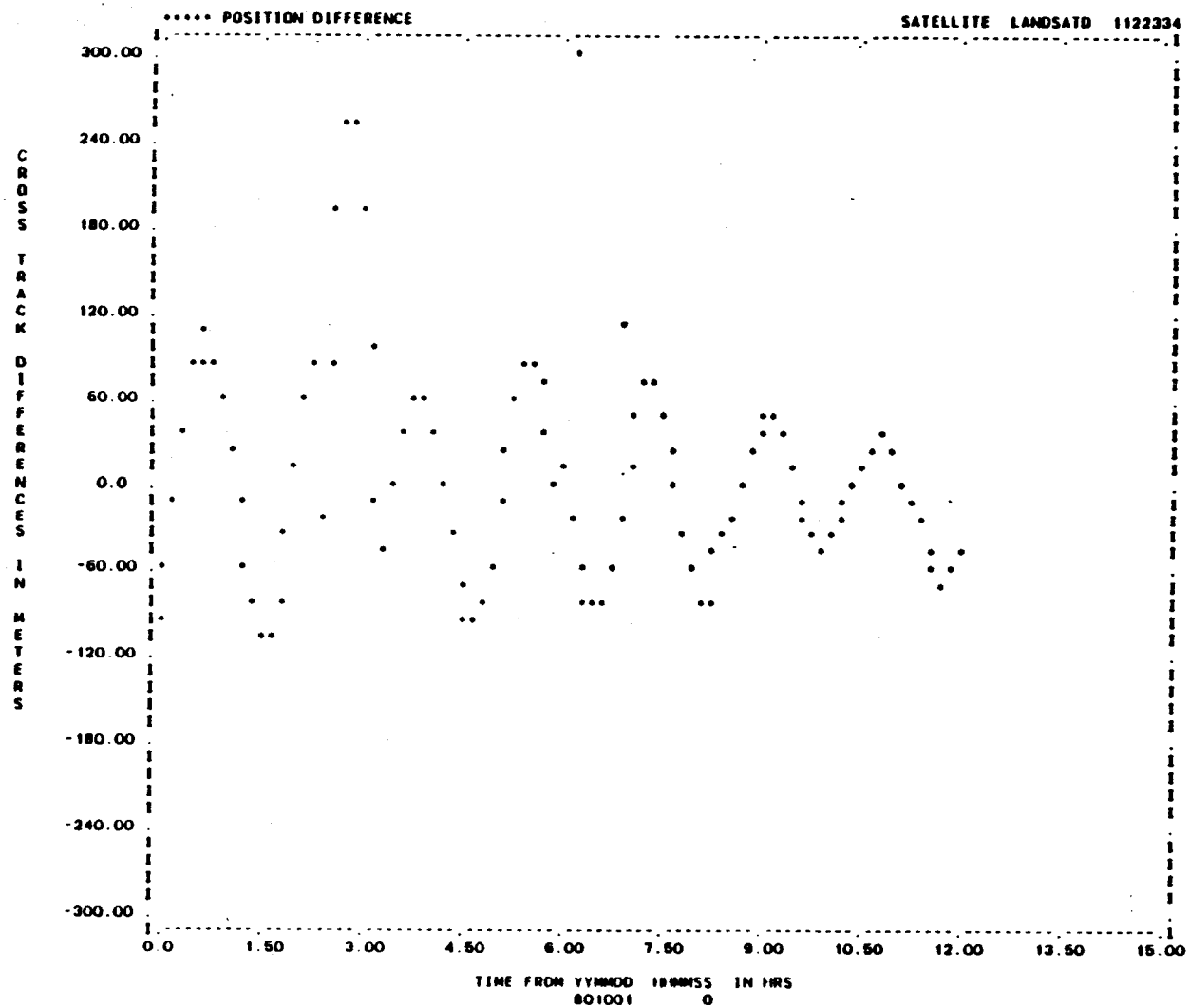

Figure A-74. Cross-Track Differences for Run N14 (1 of 2)

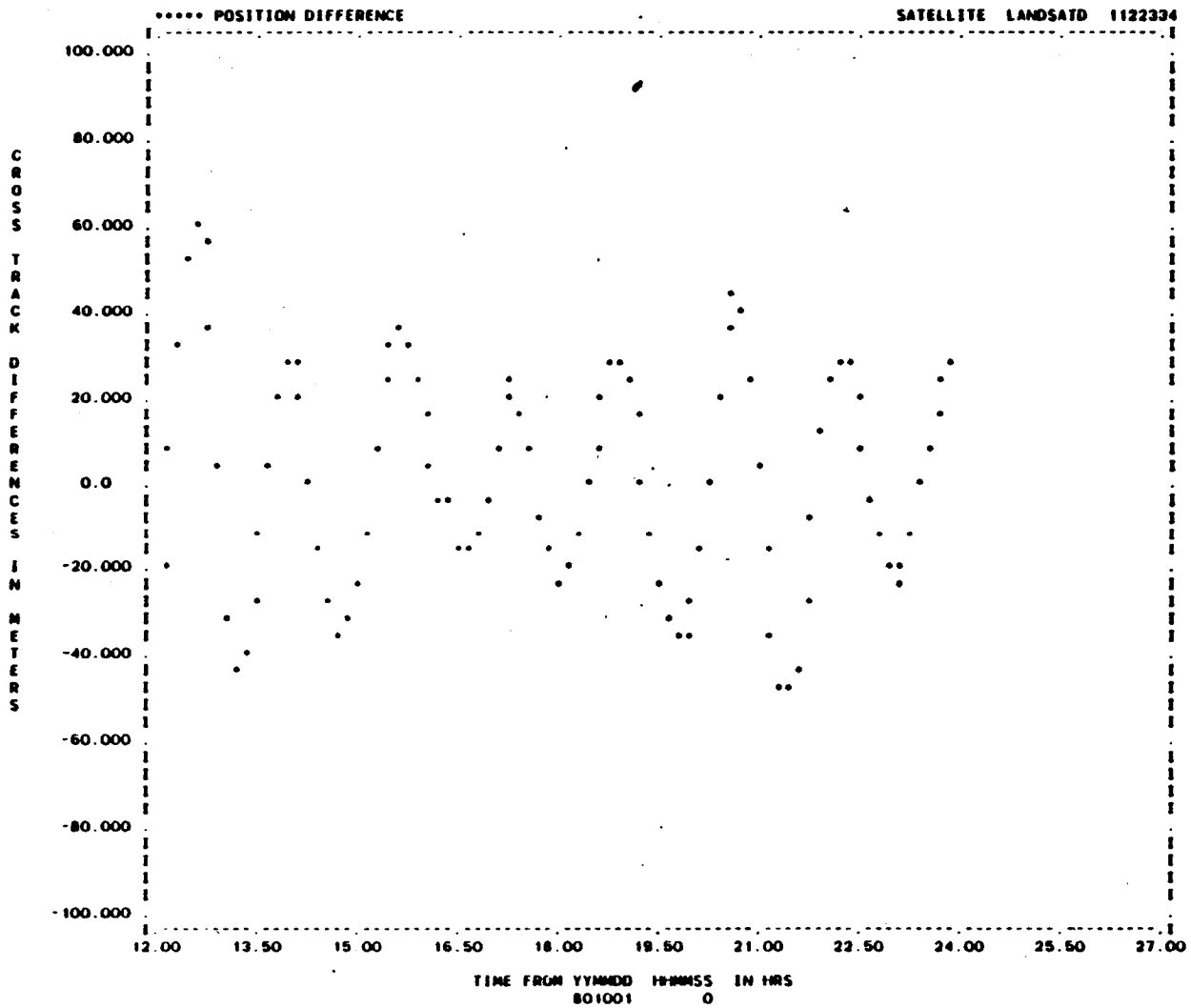

Figure A-74. Cross-Track Differences for Run N14 (2 of 2)

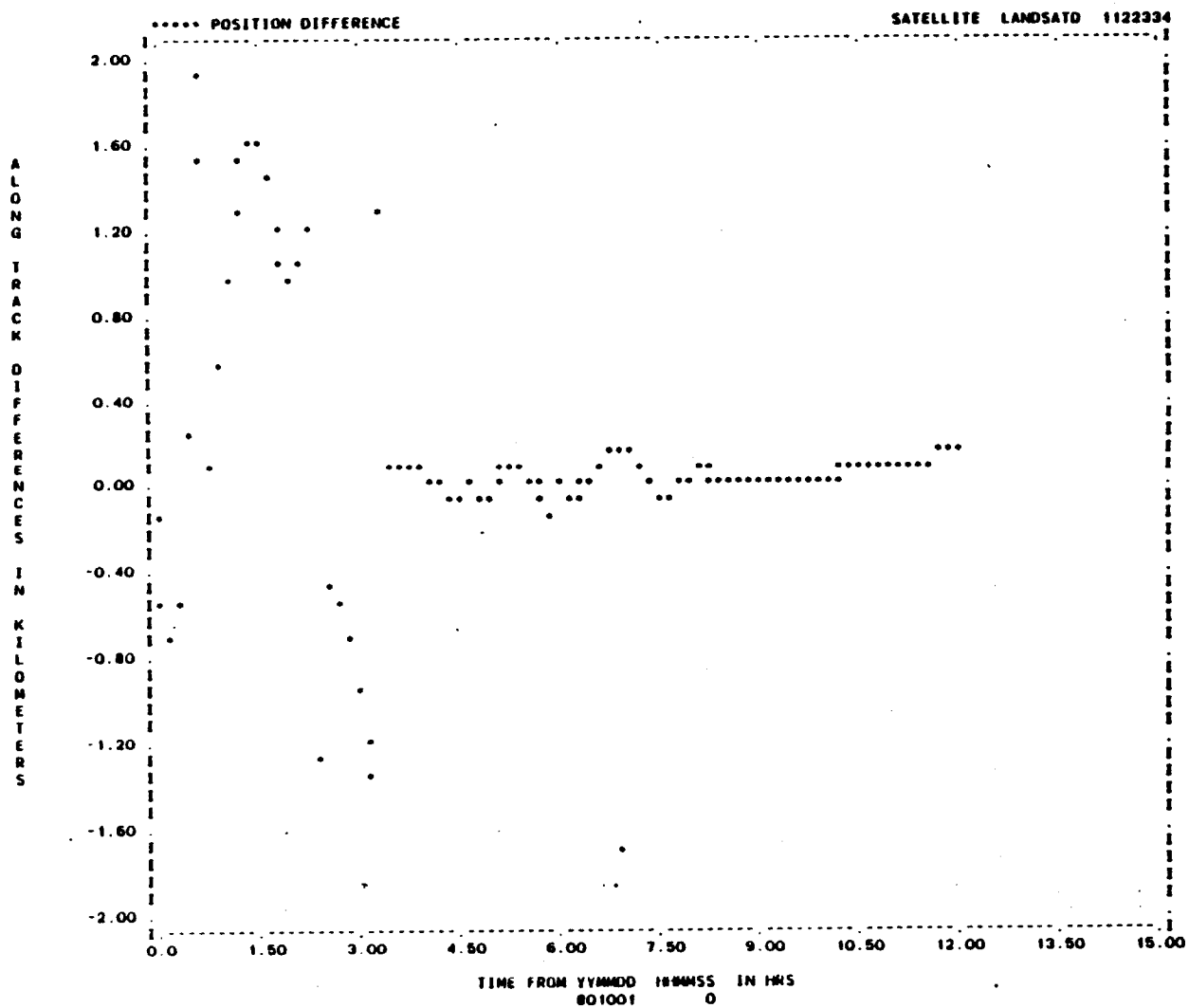

Figure A-75. Along-Track Differences for Run N14 (1 of 2)

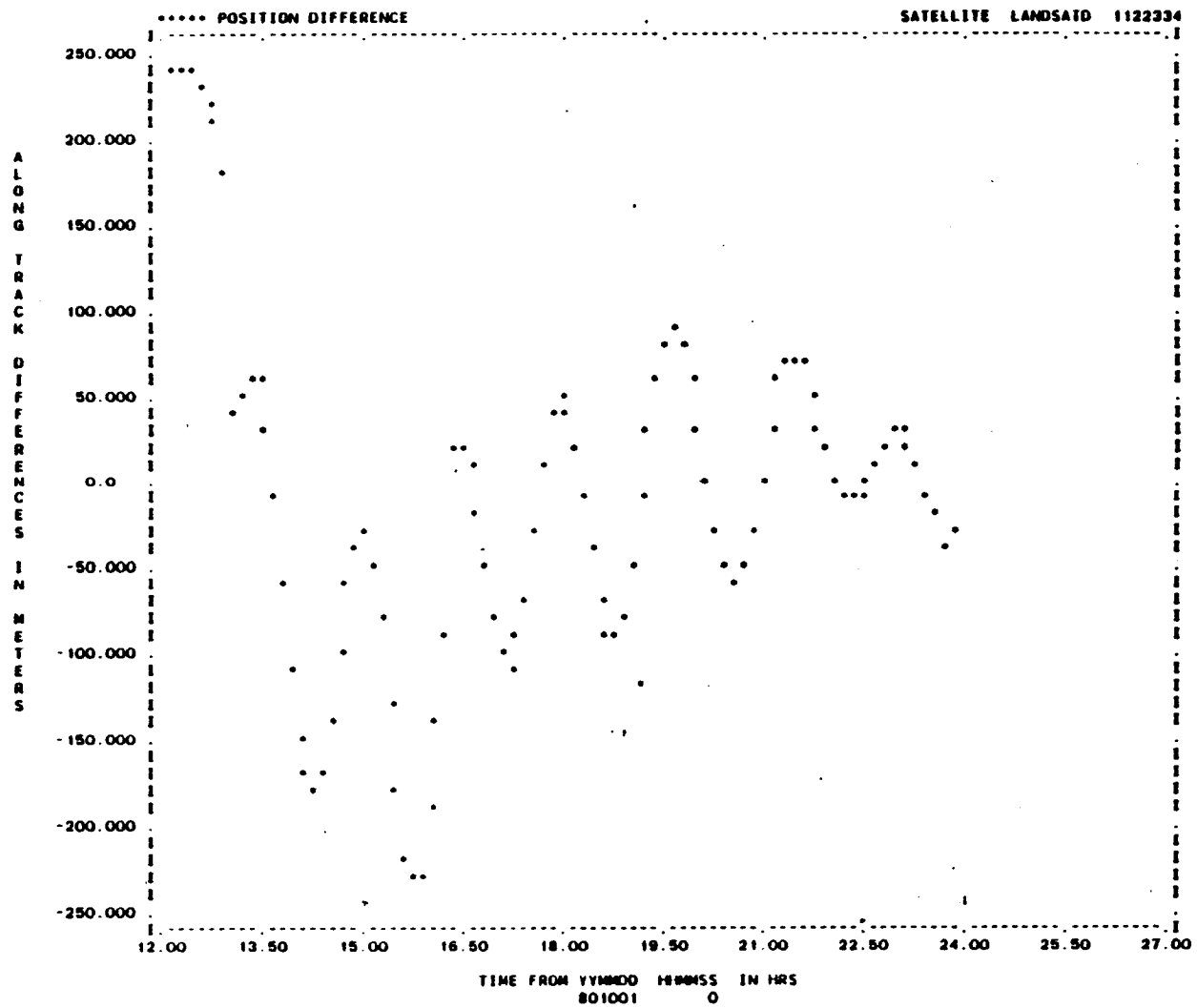

Figure A-75. Along-Track Differences for Run N14 (2 of 2)

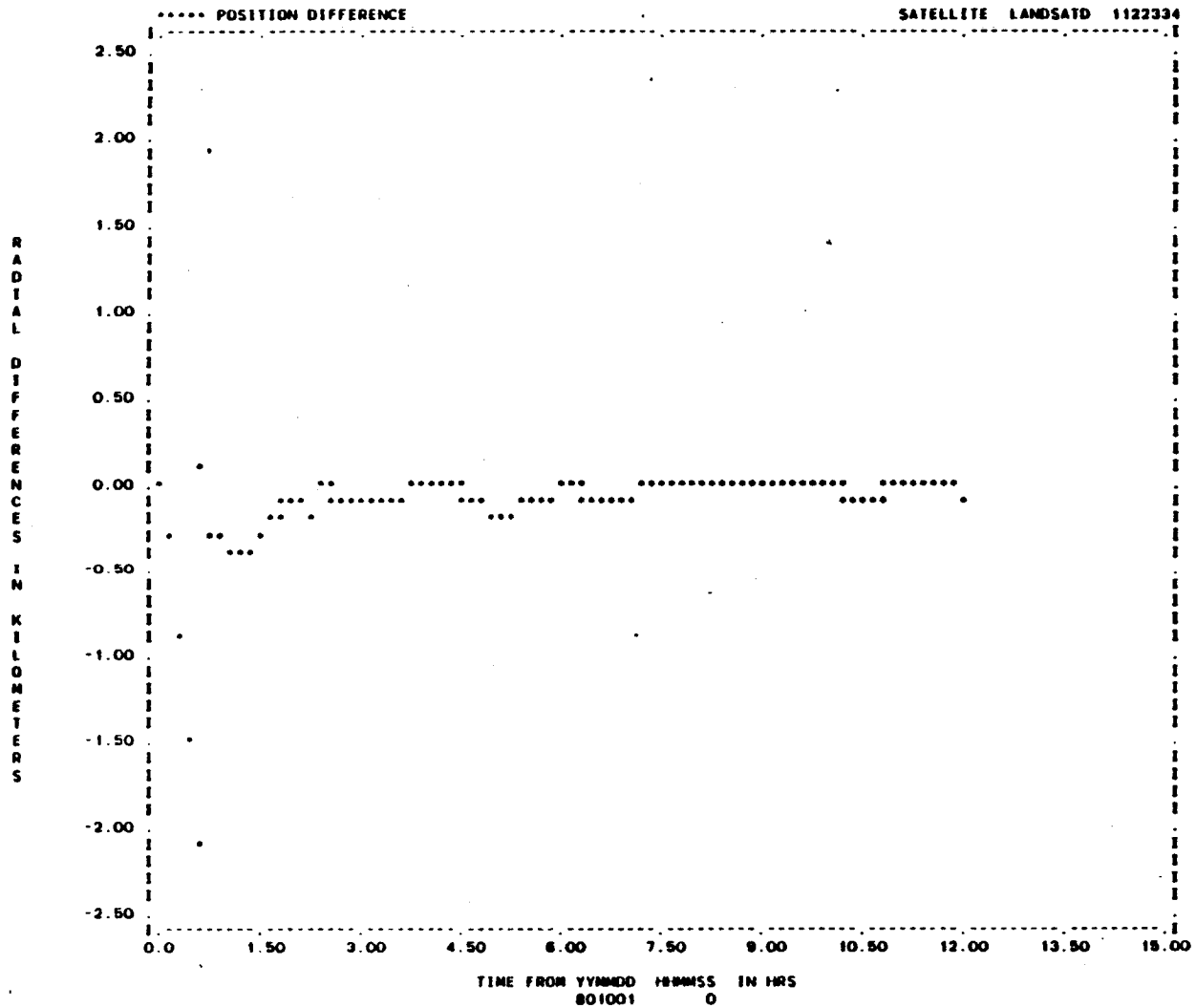

Figure A-76. Radial Differences for Run 01 (1 of 2)

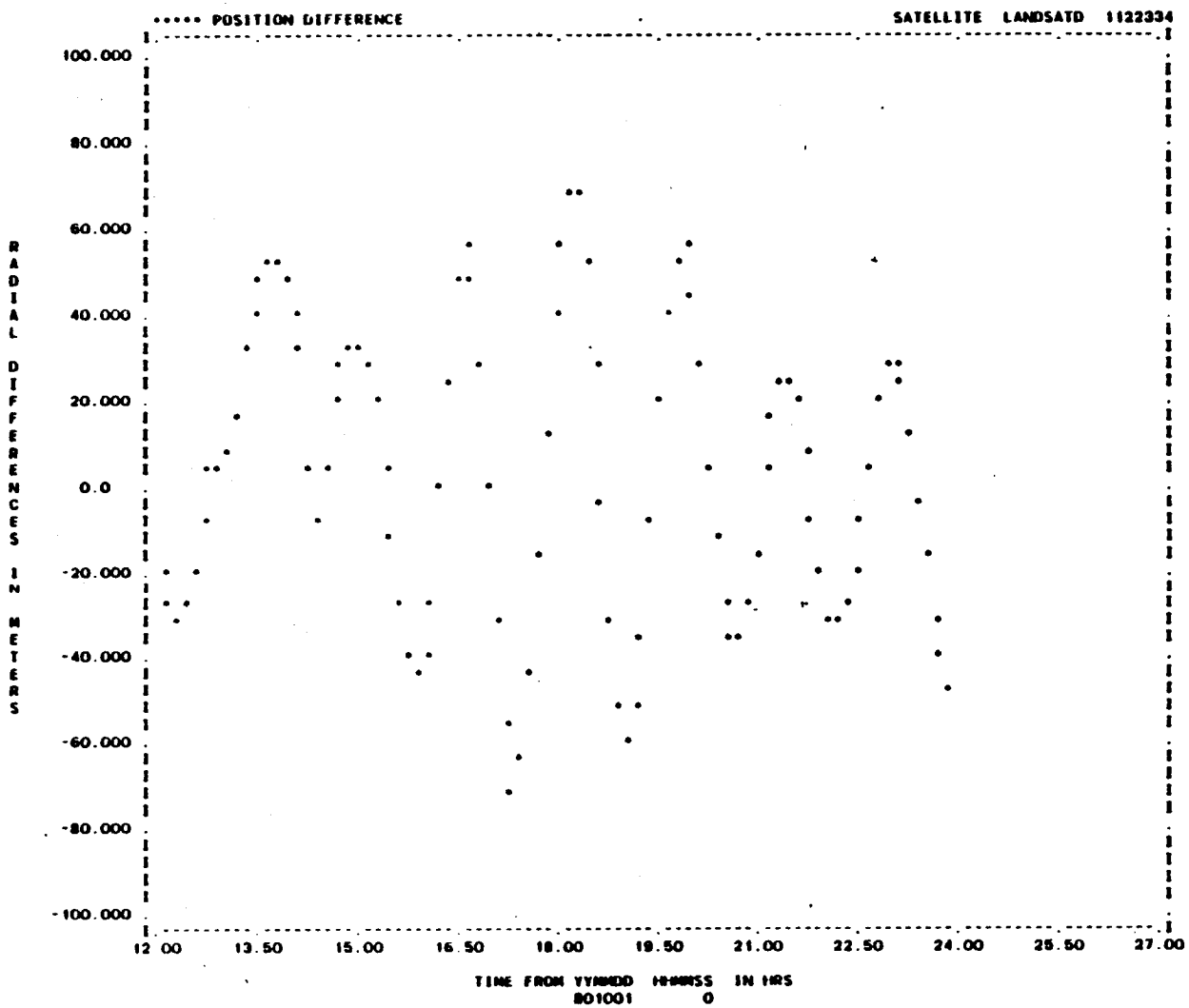

Figure A-76. Radial Differences for Run 01 (2 of 2)

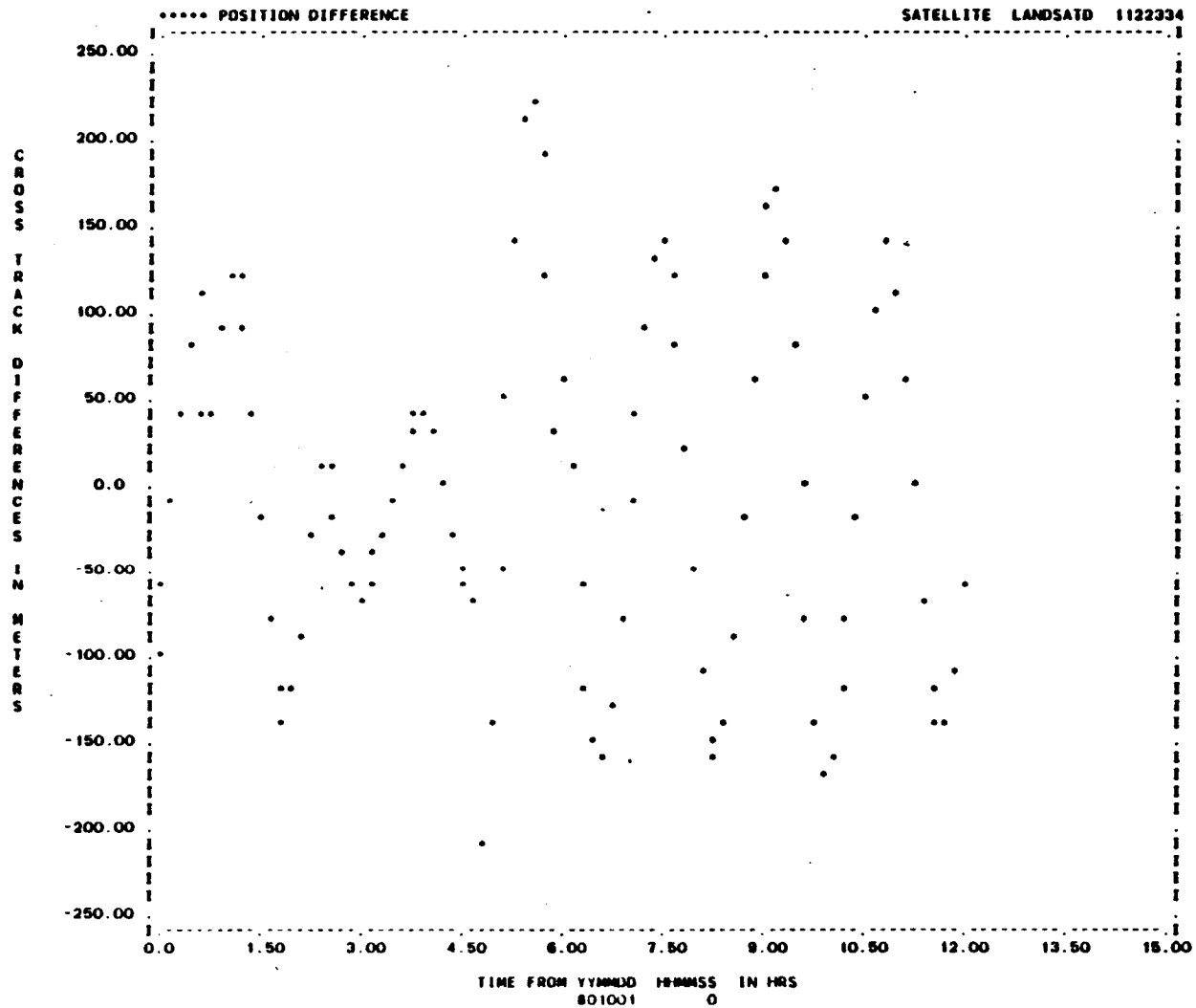

Figure A-77. Cross-Track Differences for Run 01 (1 of 2)

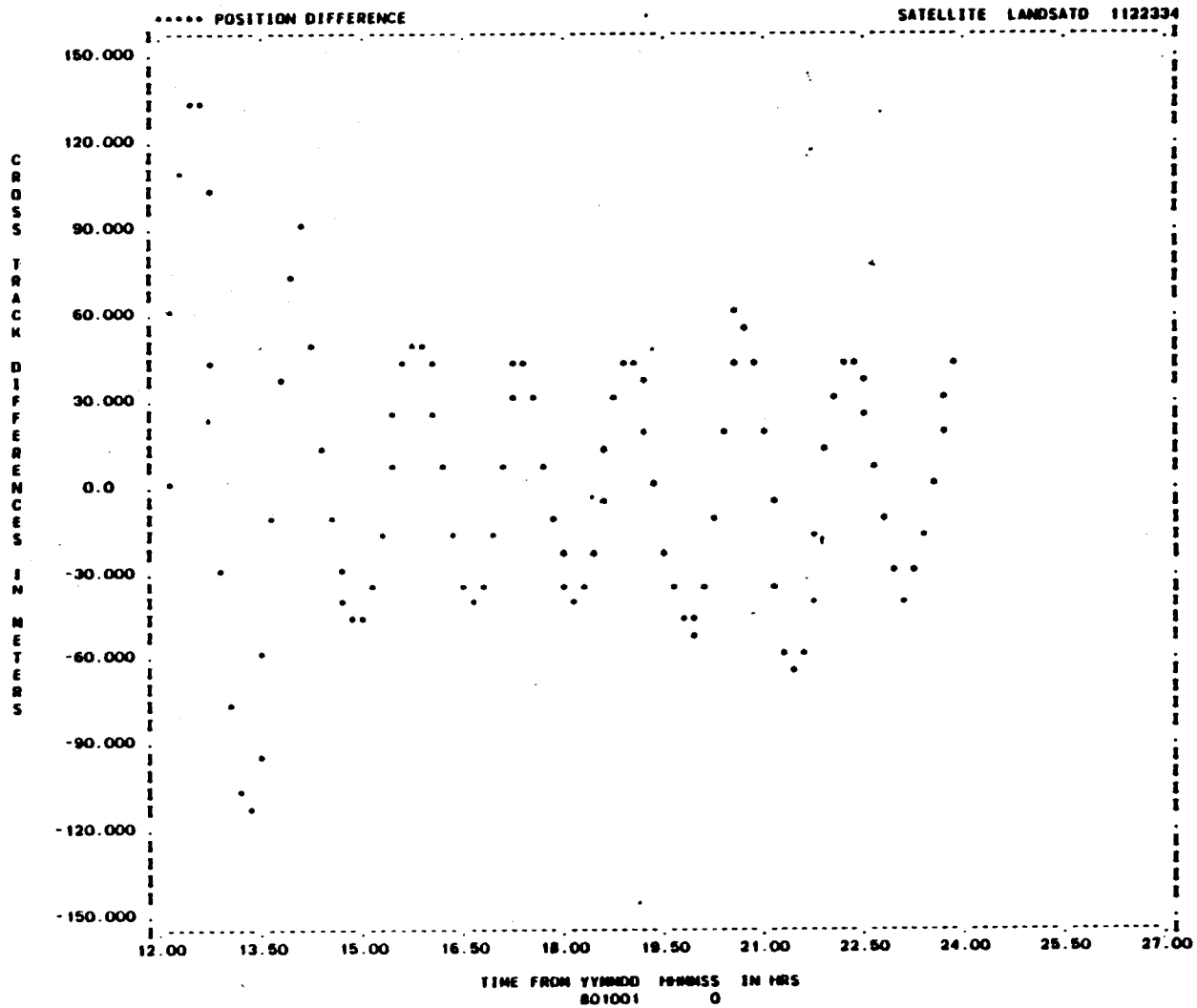

Figure A-77. Cross-Track Differences for Run 01 (2 of 2)

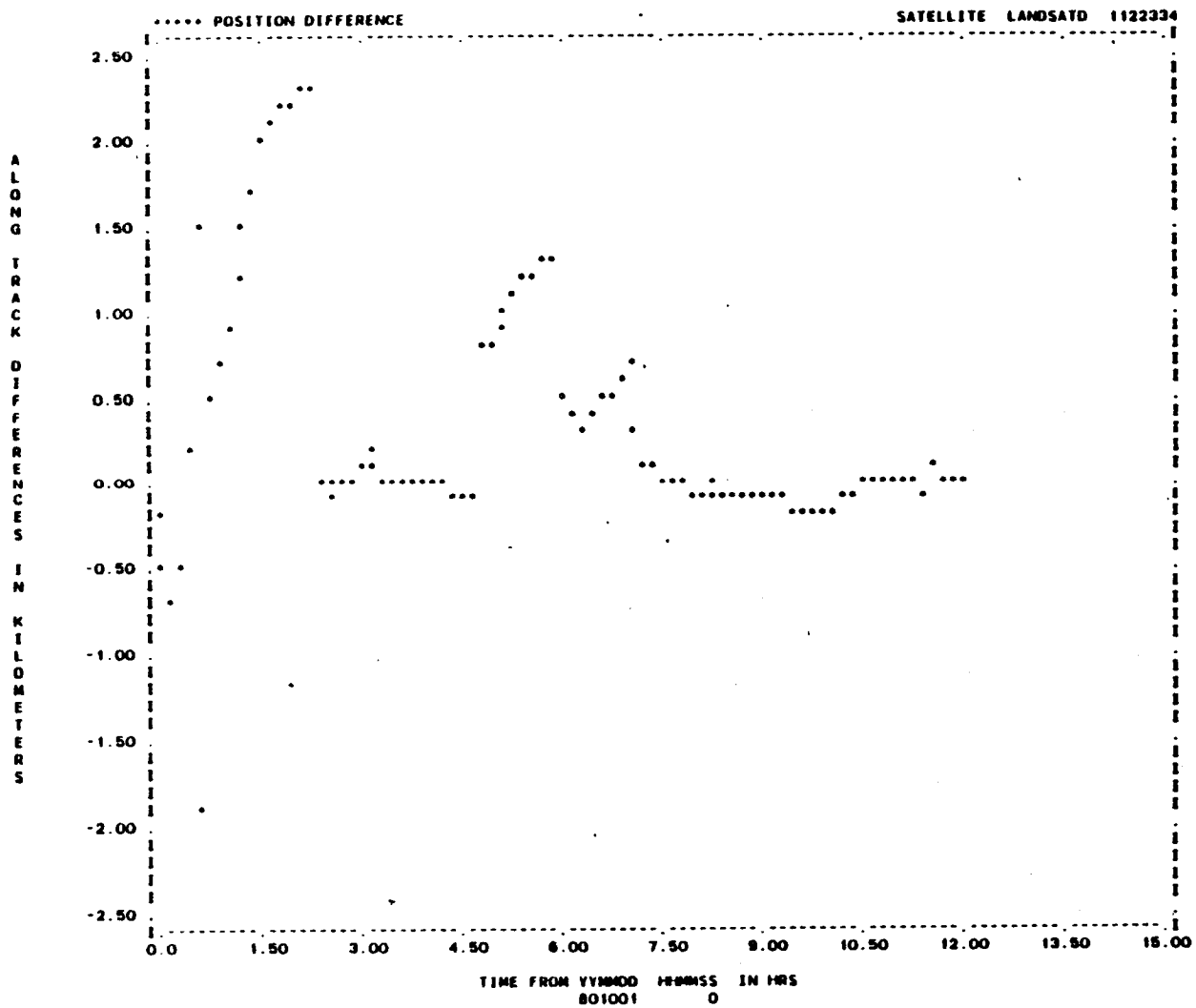

Figure A-78. Along-Track Differences for Run 01 (1 of 2)

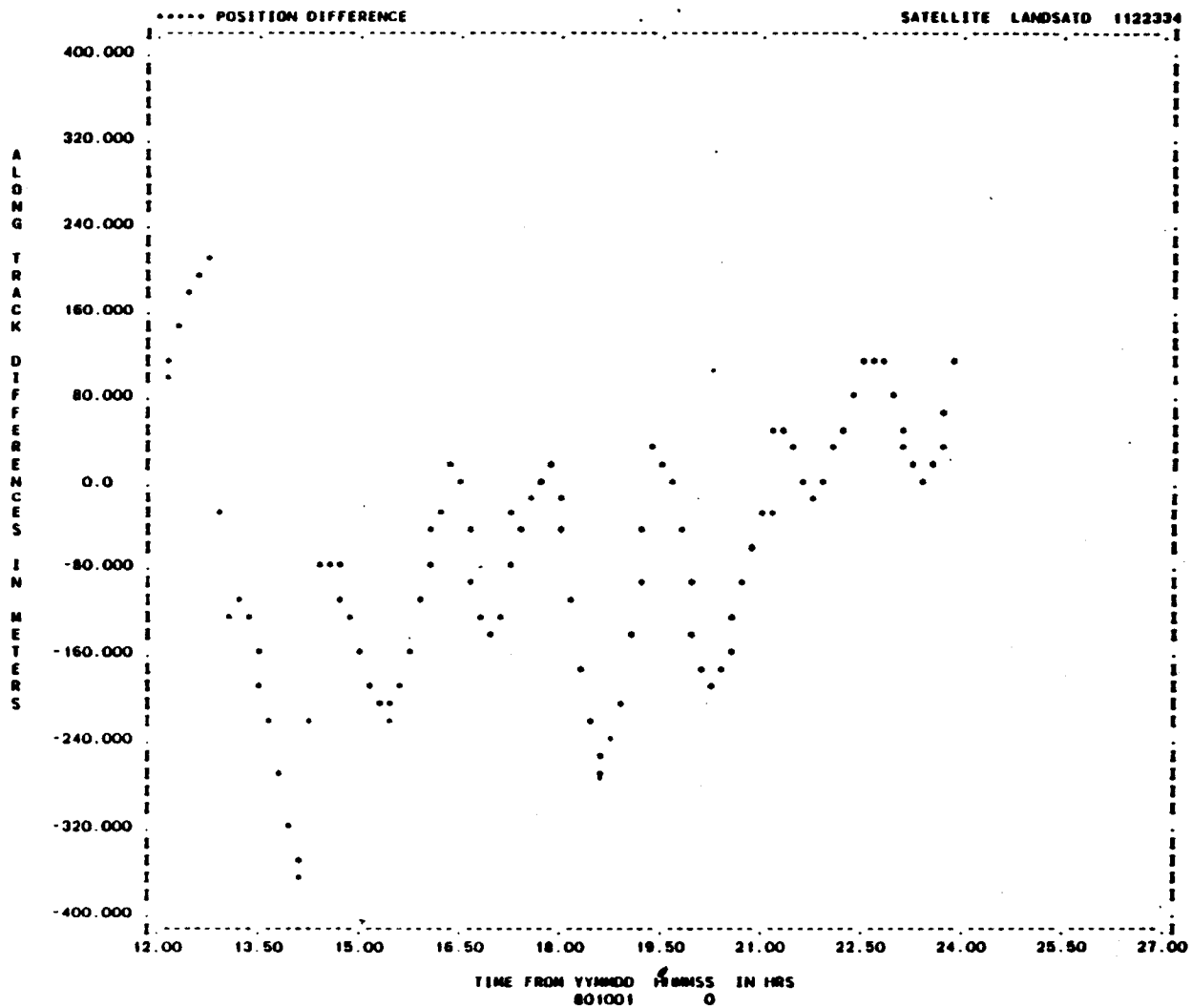

Figure A-78. Along-Track Differences for Run 01 (2 of 2)

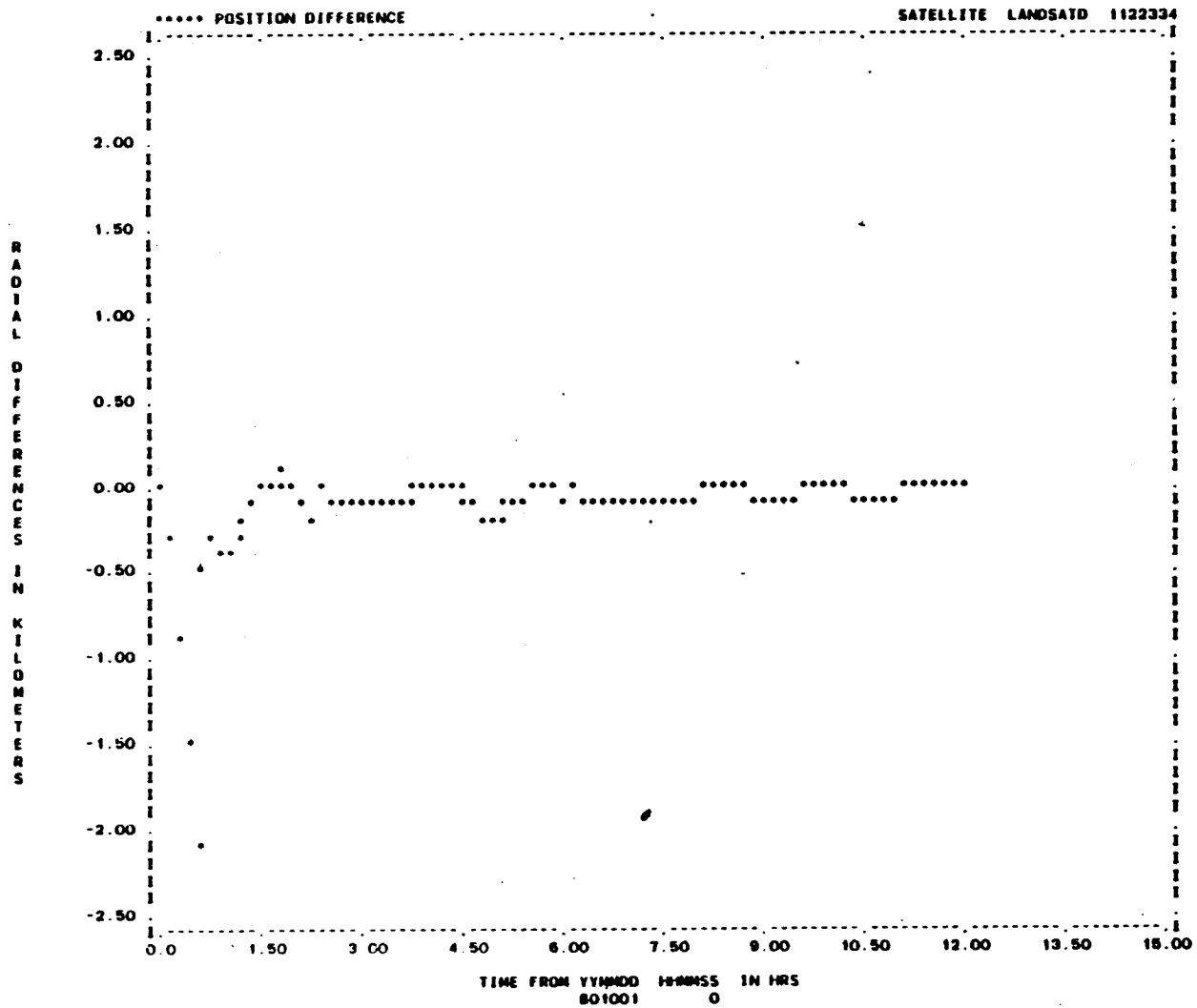

Figure A-79. Radial Differences for Run O2 (1 of 2)

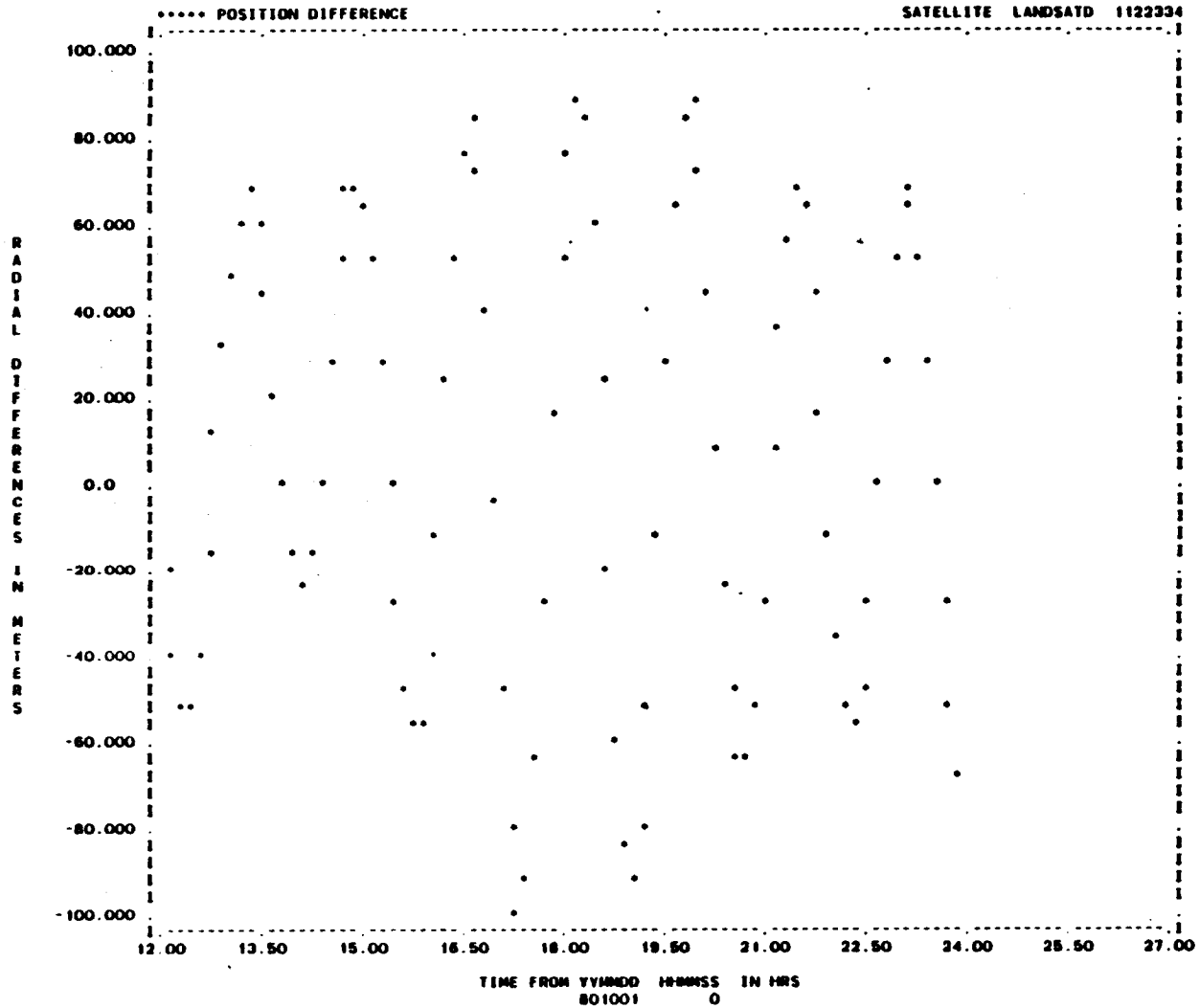

Figure A-79. Radial Differences for Run O2 (2 of 2)

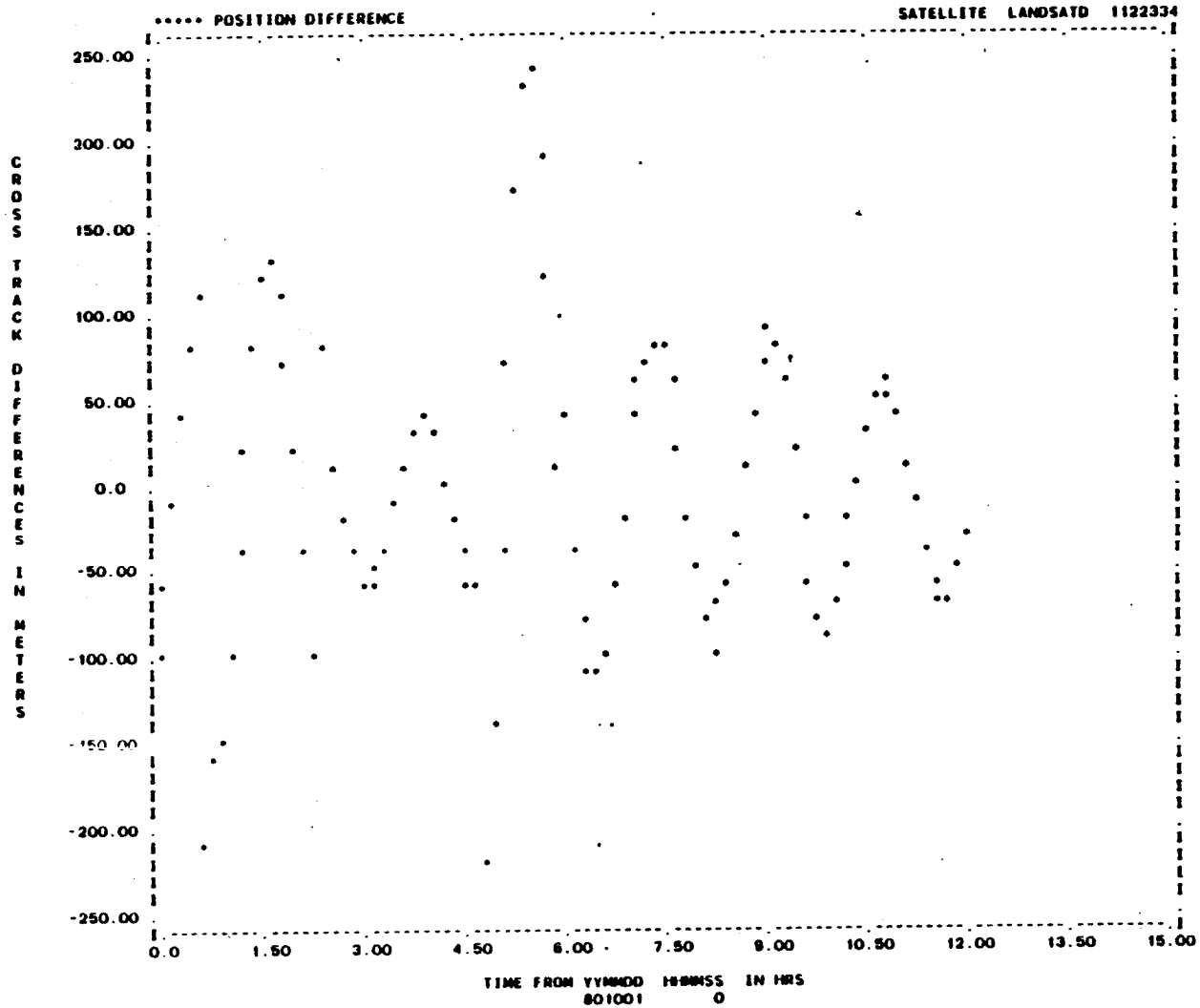

Figure A-80. Cross-Track Differences for Run 02 (1 of 2)

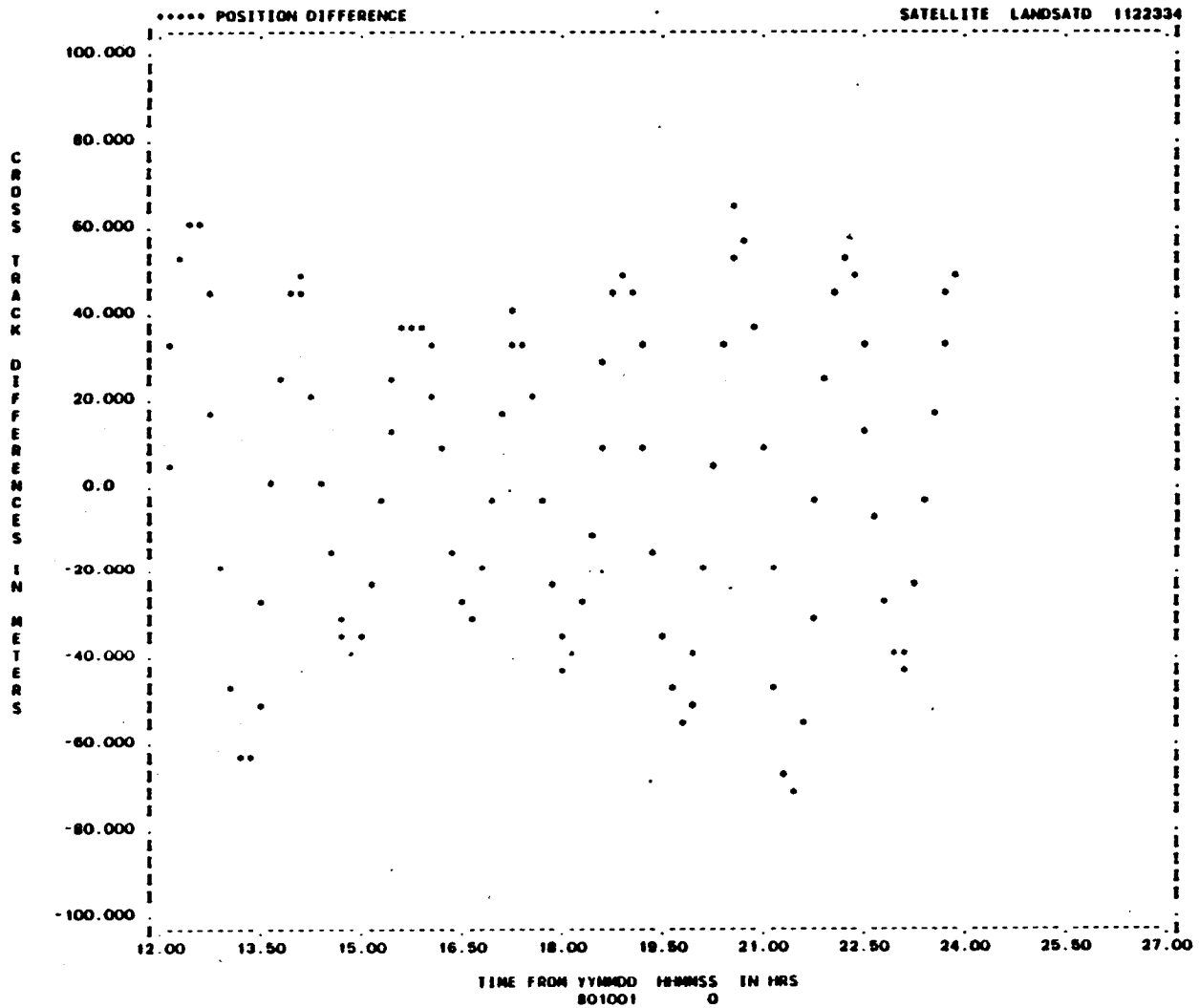

Figure A-80. Cross-Track Differences for Run O2 (2 of 2)

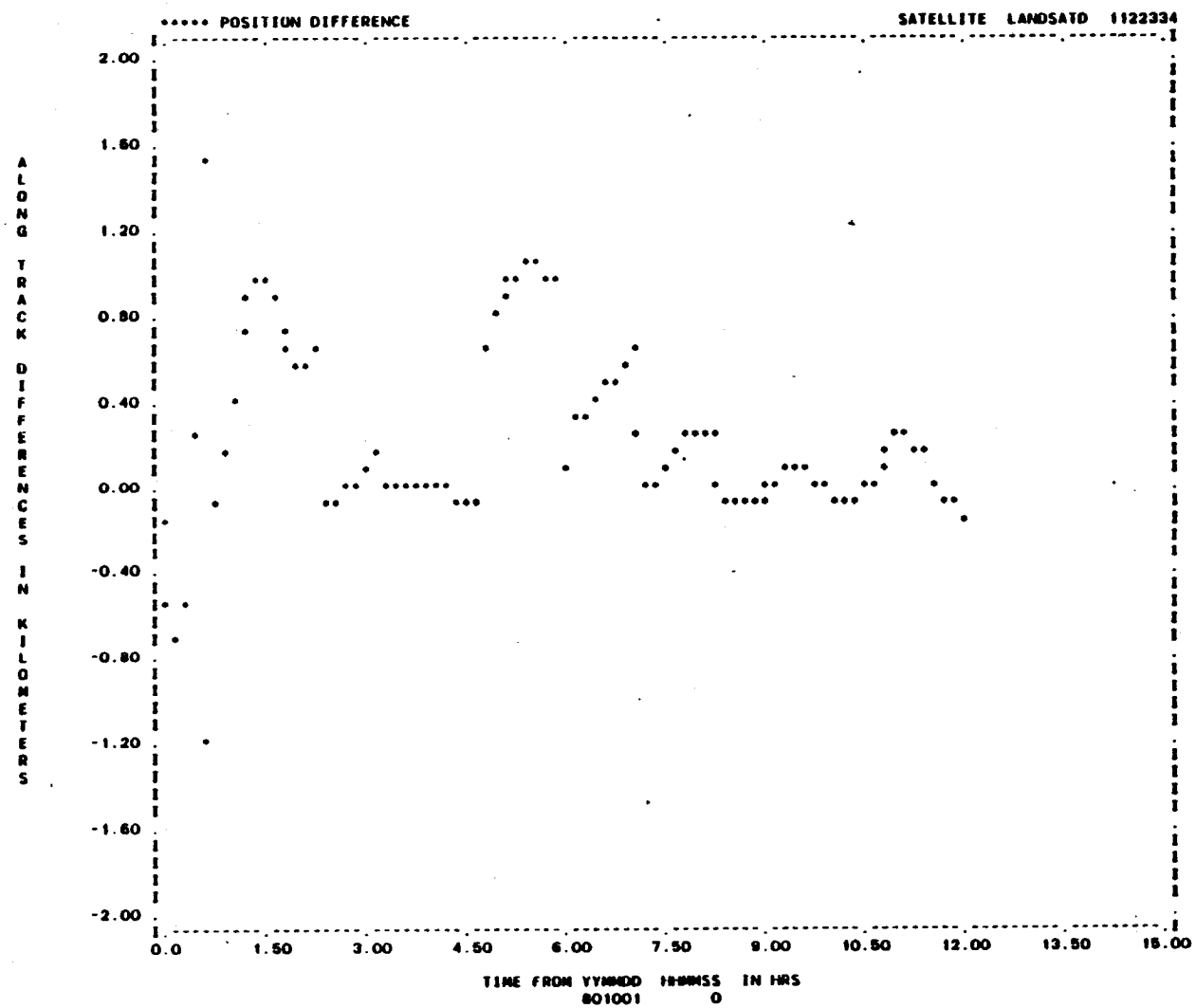

Figure A-81. Along-Track Differences for Run O2 (1 of 2)

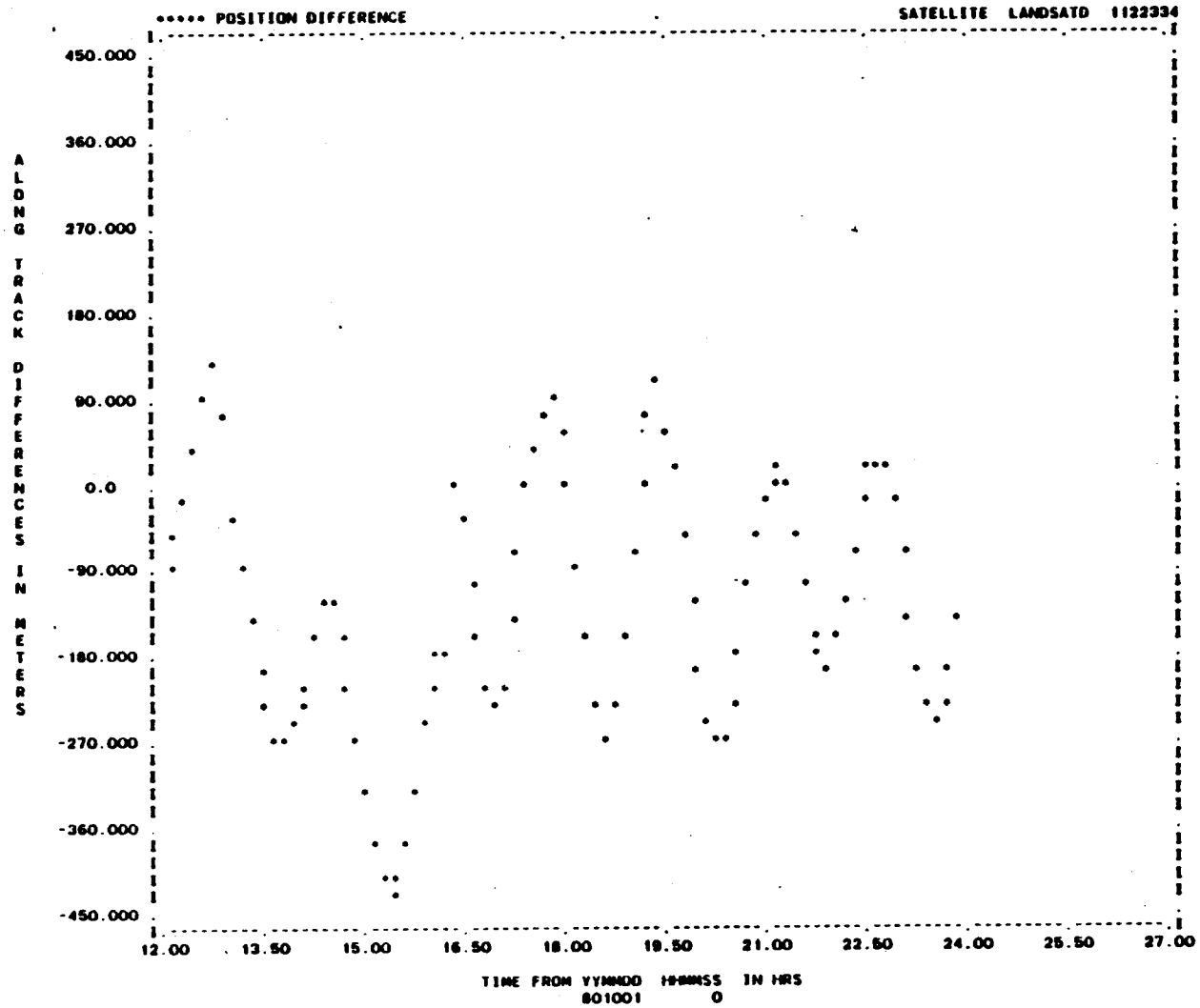

Figure A-81. Along-Track Differences for Run O2 (2 of 2)

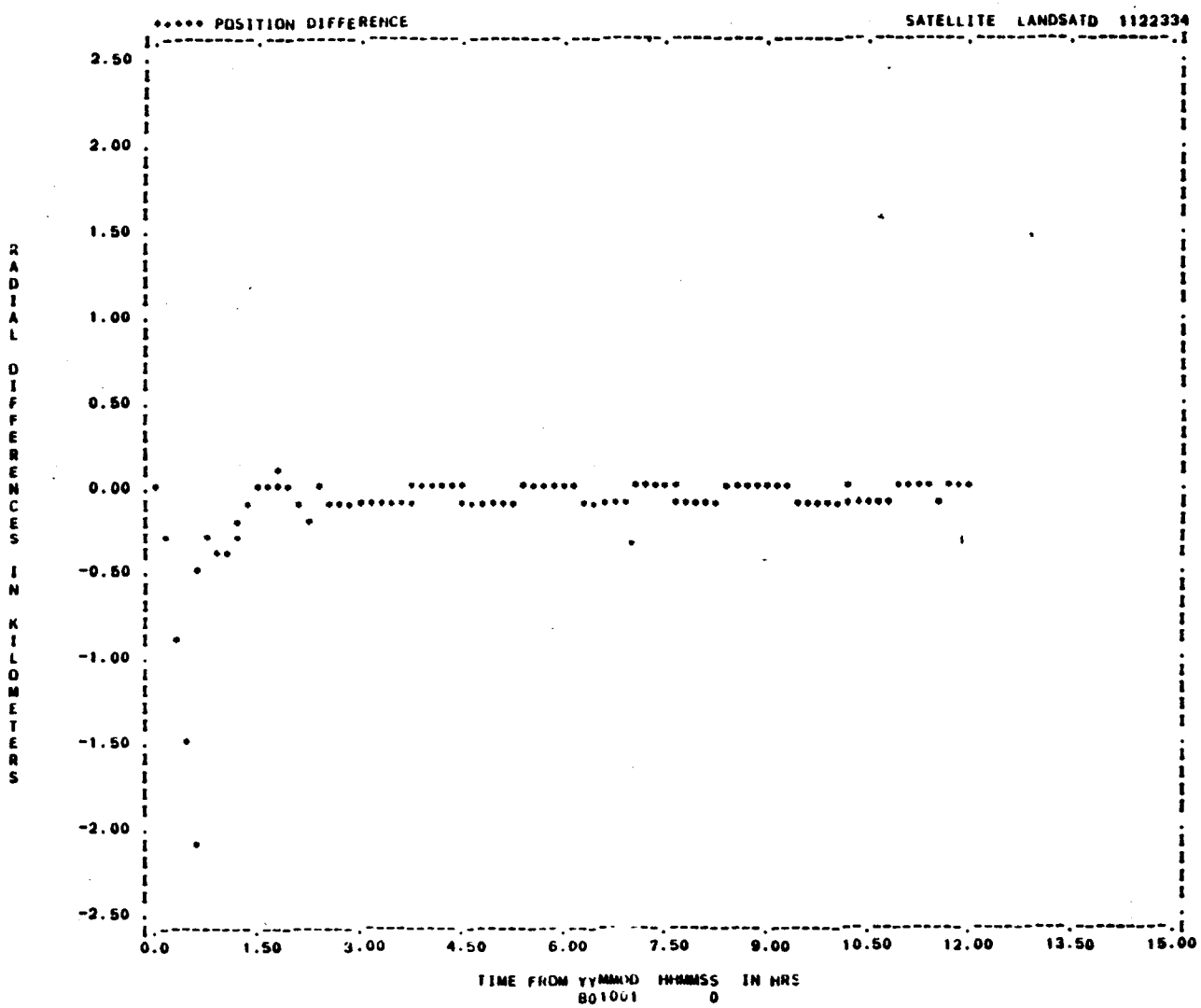

Figure A-82. Radial Differences for Run 03 (1 of 2)

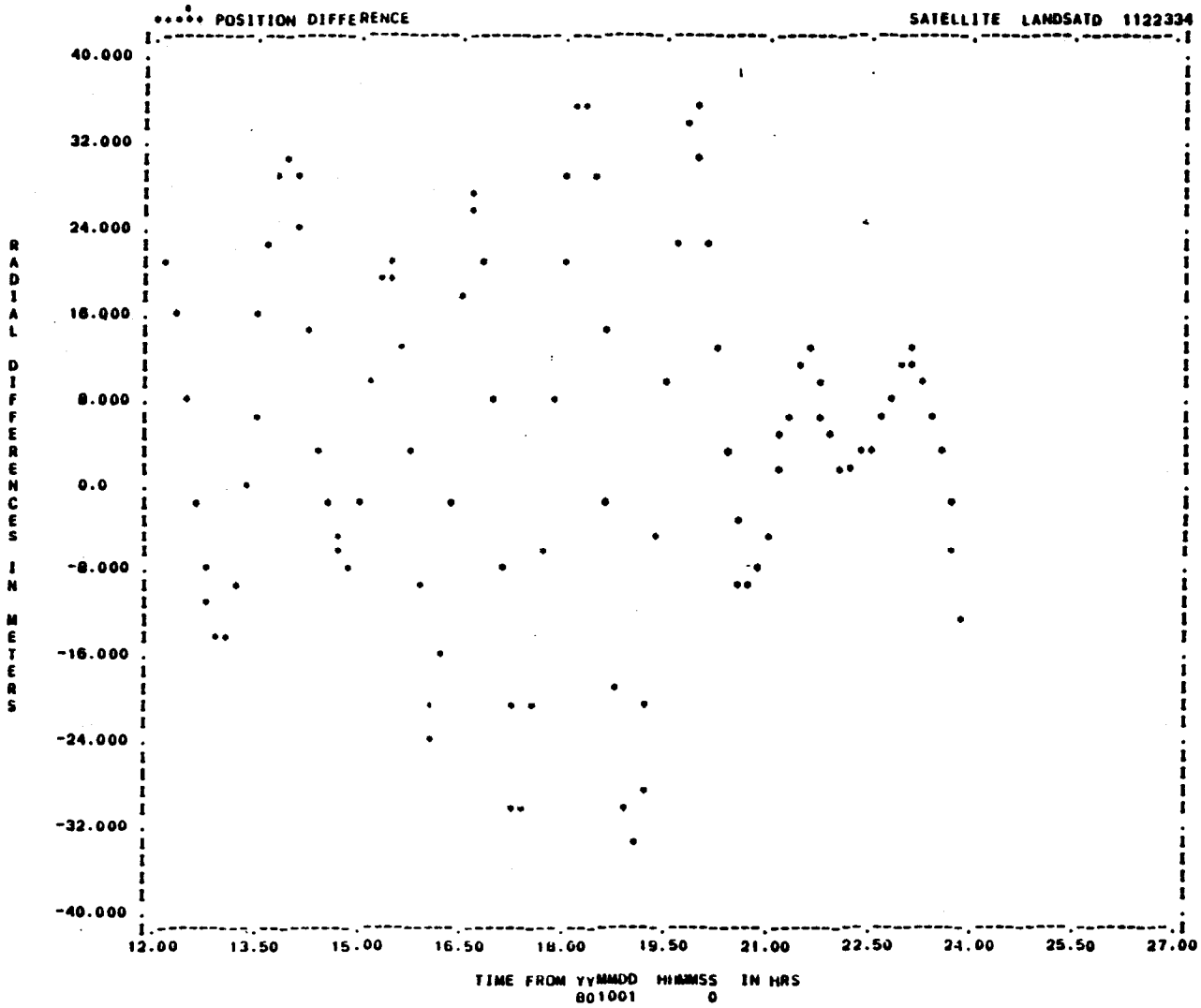

Figure A-82. Radial Differences for Run O3 (2 of 2)

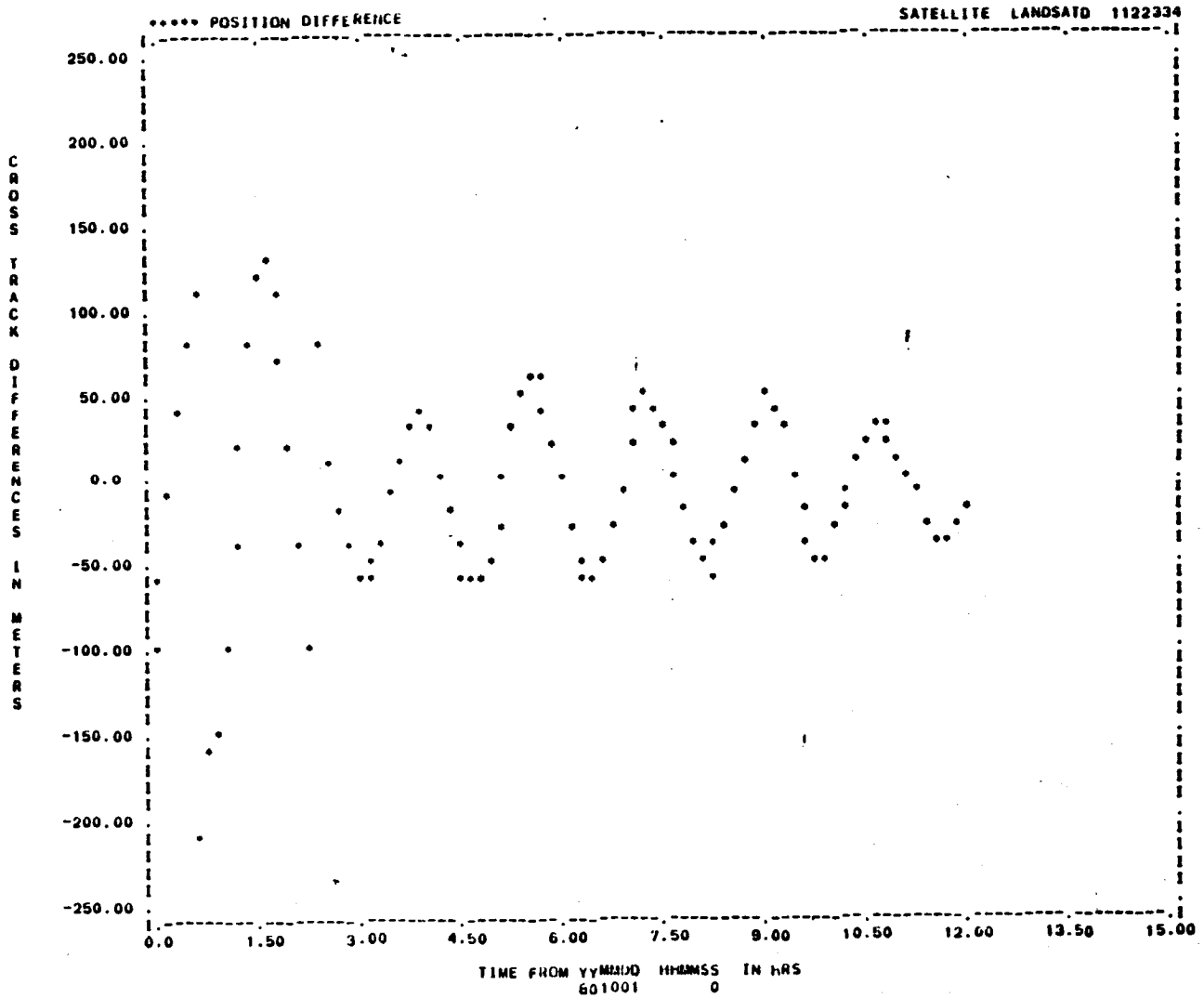

Figure A-83. Cross-Track Differences for Run 03 (1 of 2)

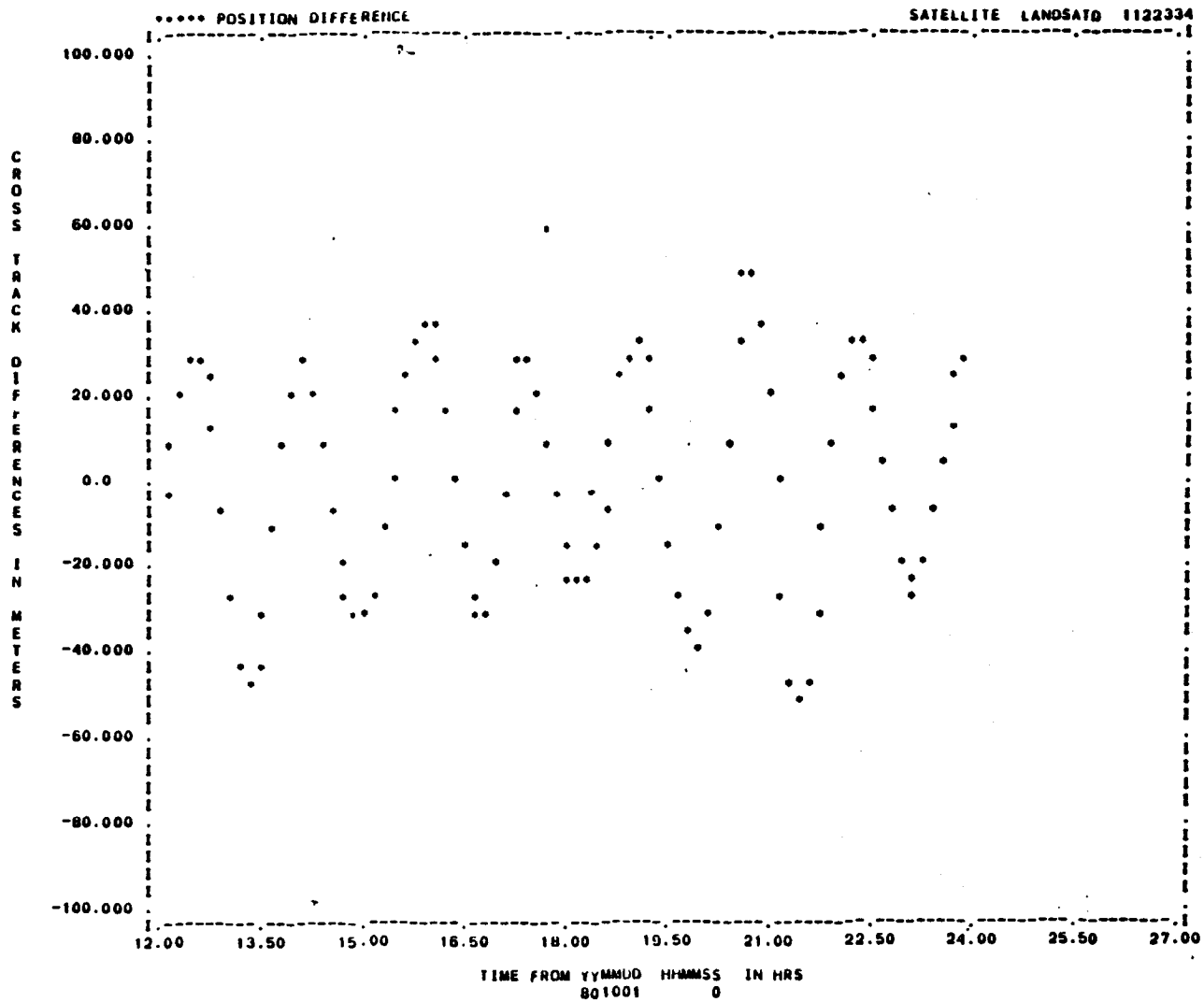

Figure A-83. Cross-Track Differences for Run 03 (2 of 2)

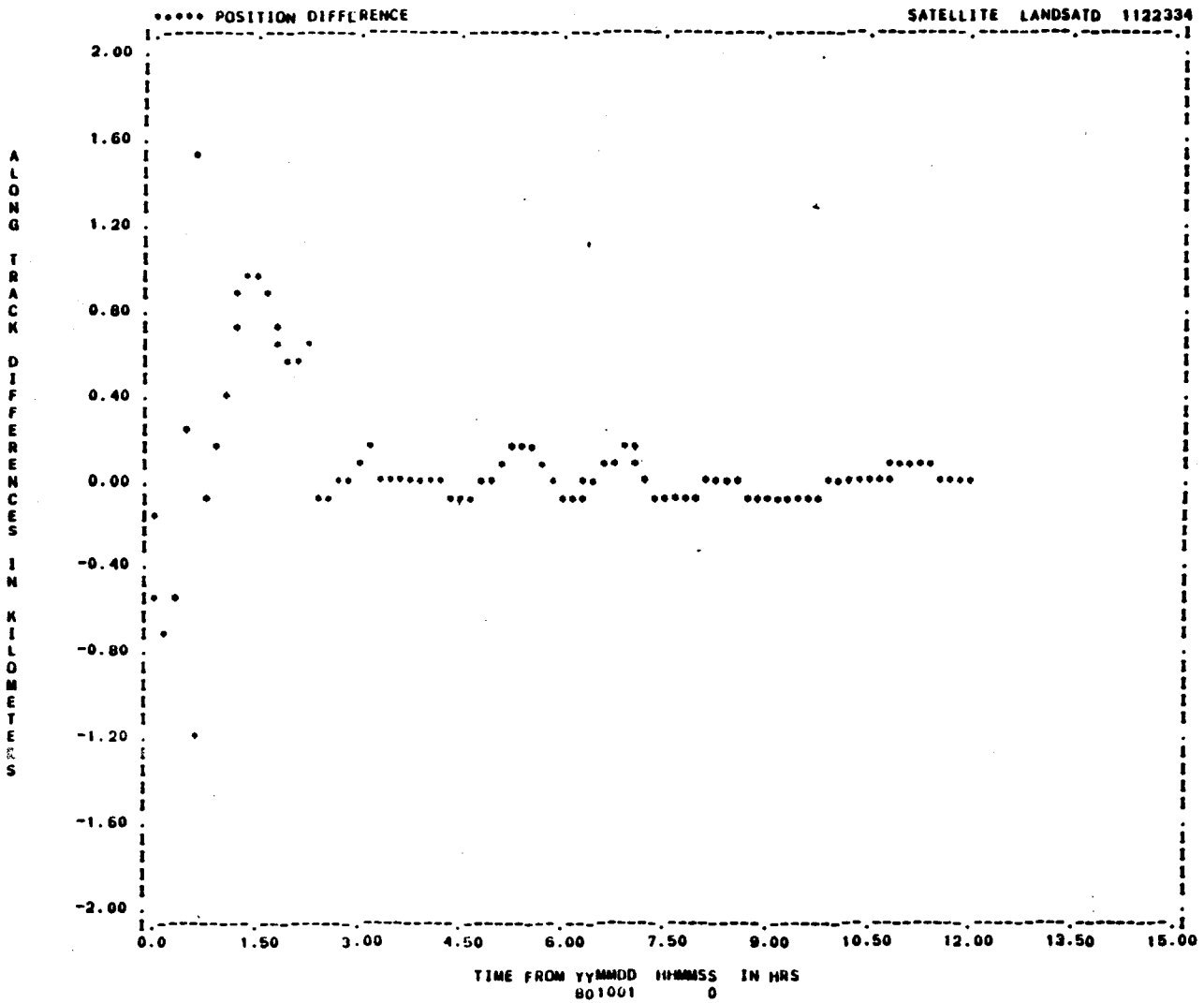

Figure A-84. Along-Track Differences for Run 03 (1 of 2)

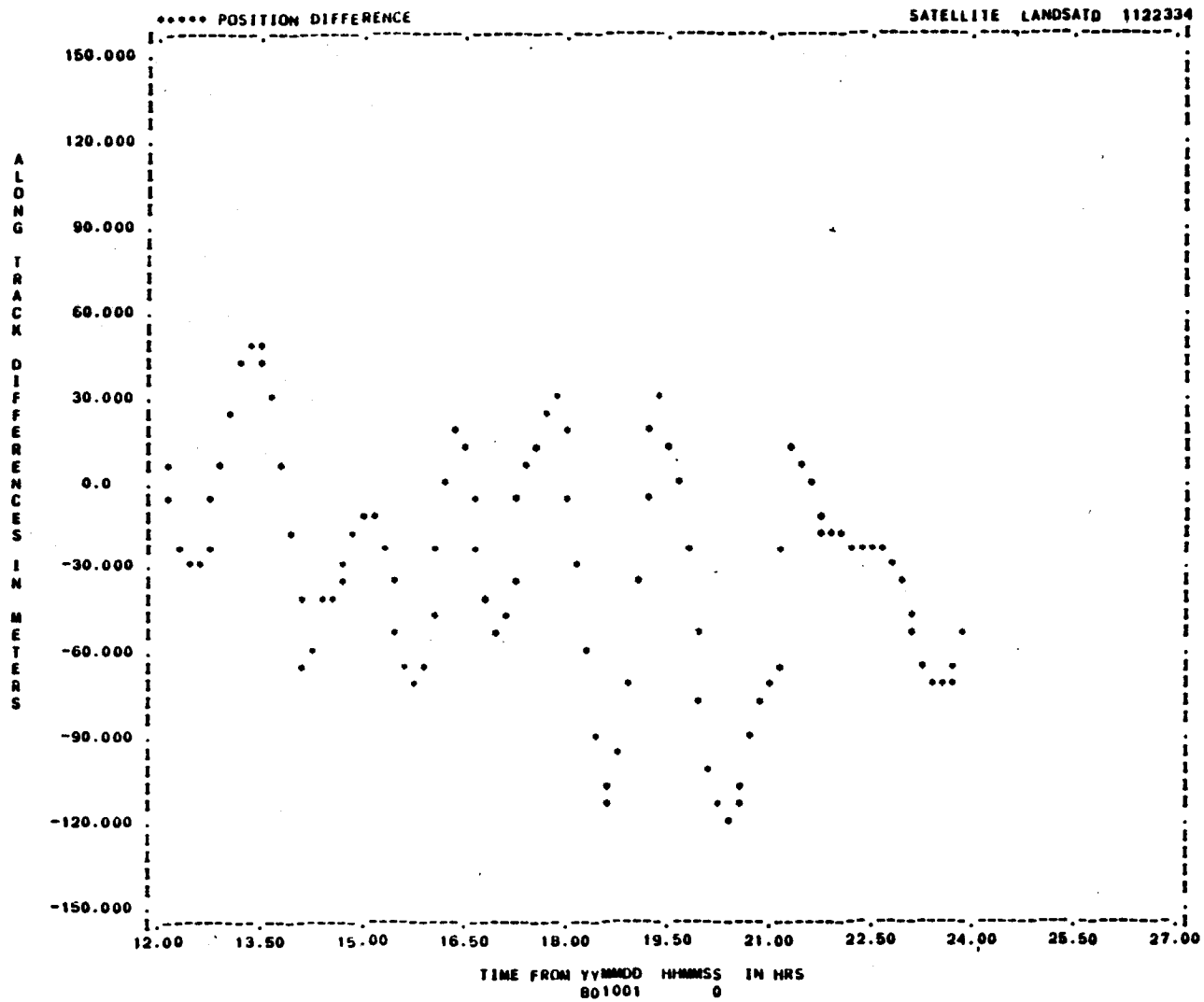

Figure A-84. Along-Track Differences for Run 03 (2 of 2)

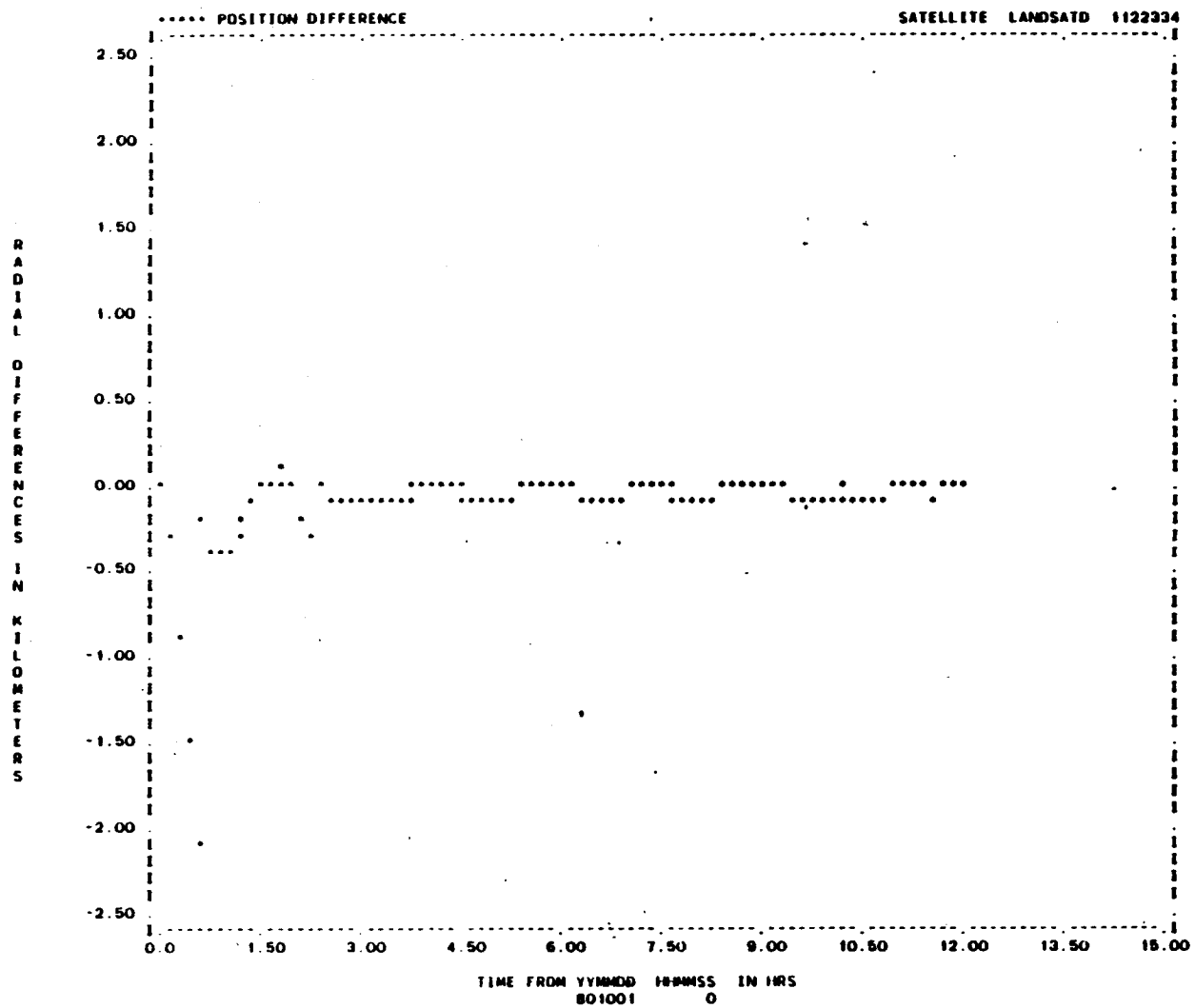

Figure A-85. Radial Differences for Run O4 (1 of 2)

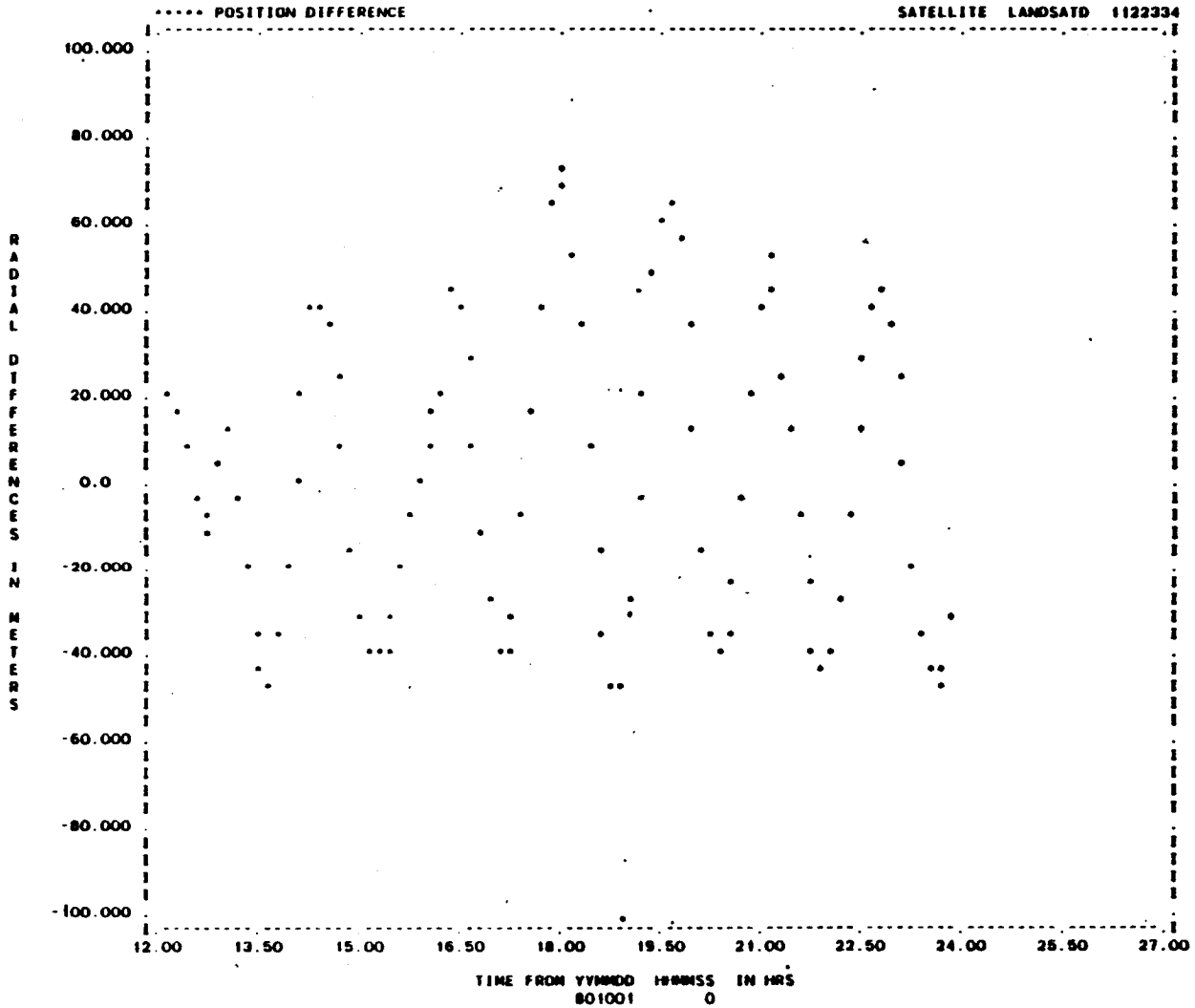

Figure A-85. Radial Differences for Run O4 (2 of 2)

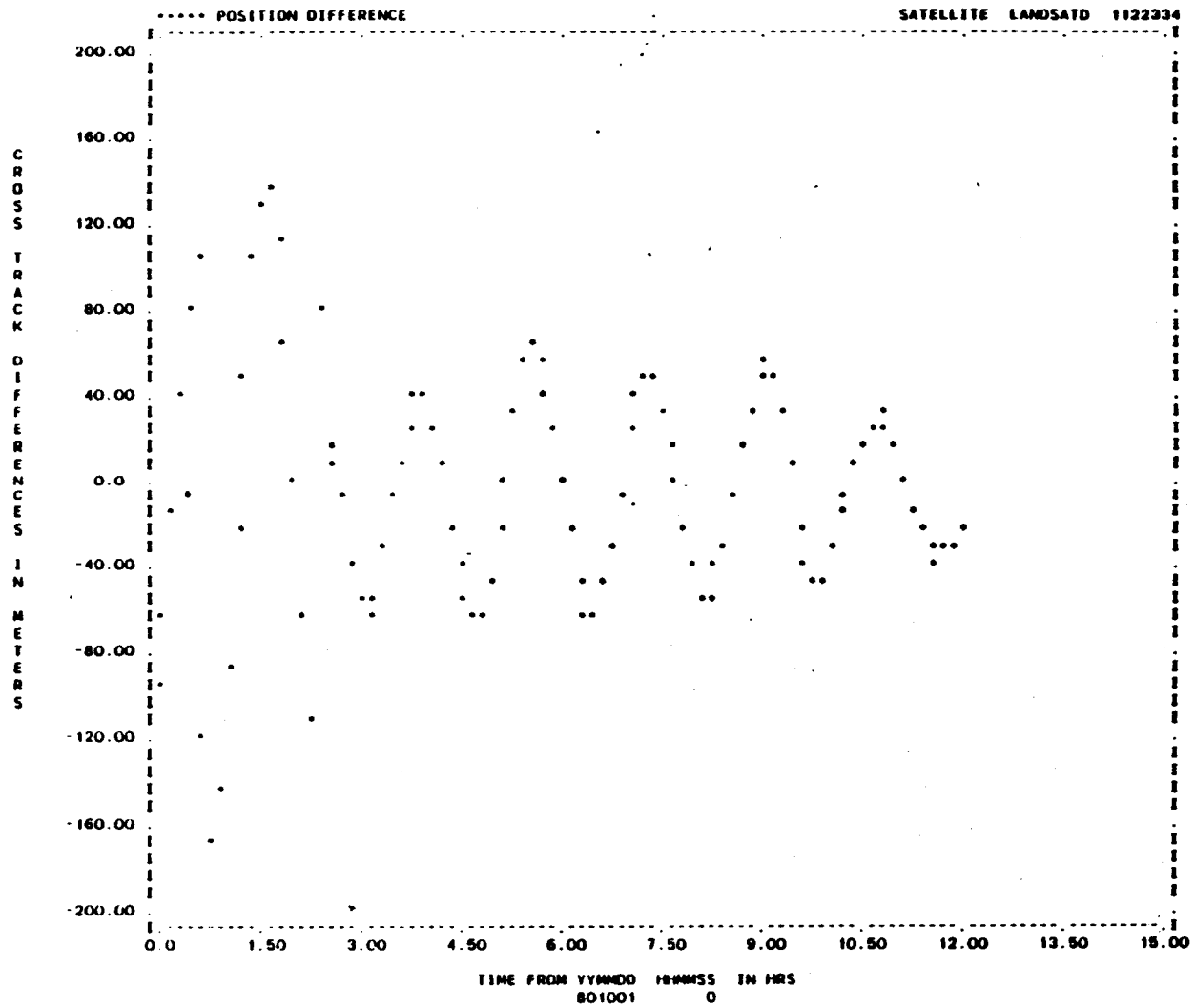

Figure A-86. Cross-Track Differences for Run 04 (1 of 2)

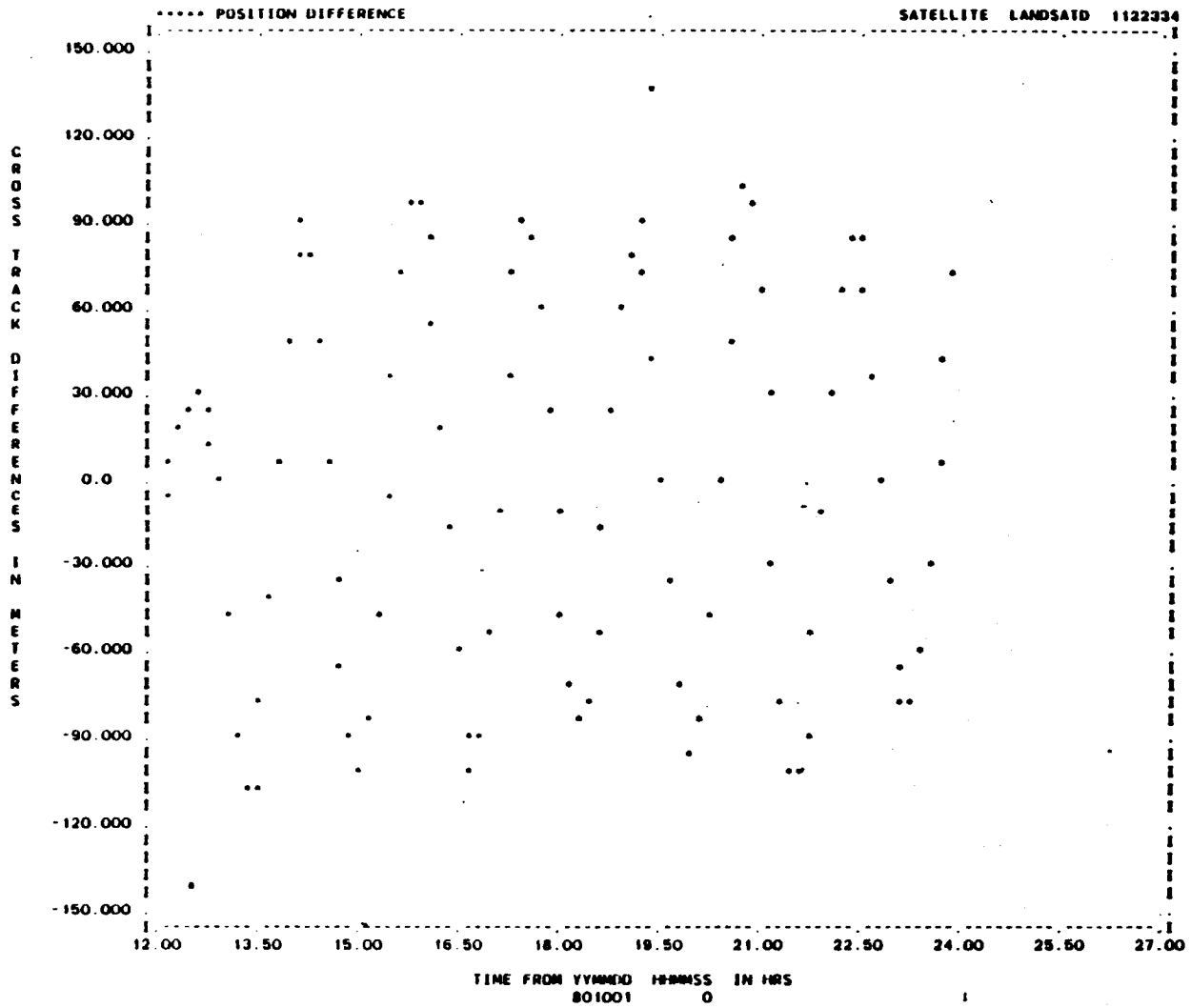

Figure A-86. Cross-Track Differences for Run O4 (2 of 2)

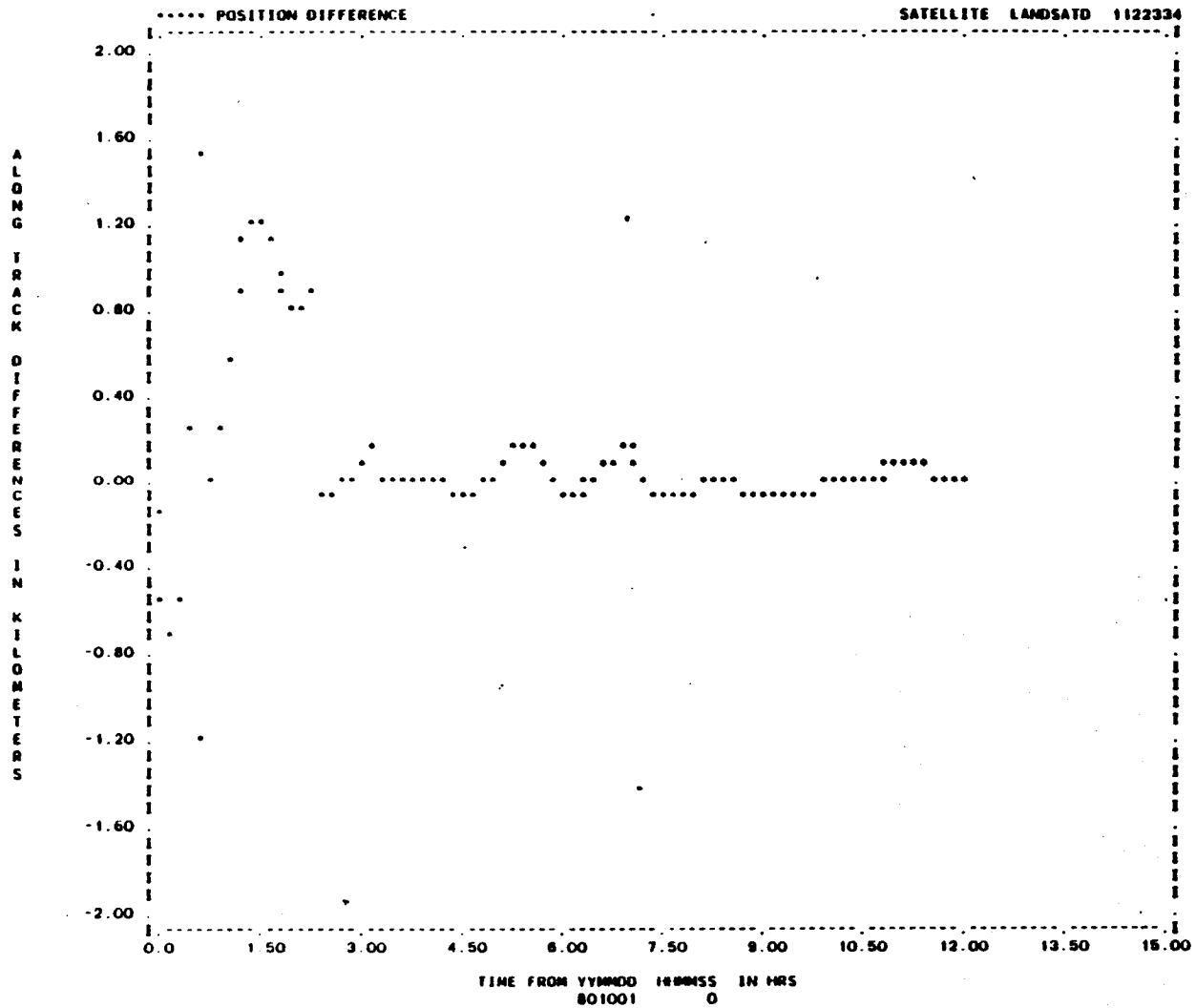

Figure A-87. Along-Track Differences for Run 04 (1 of 2)

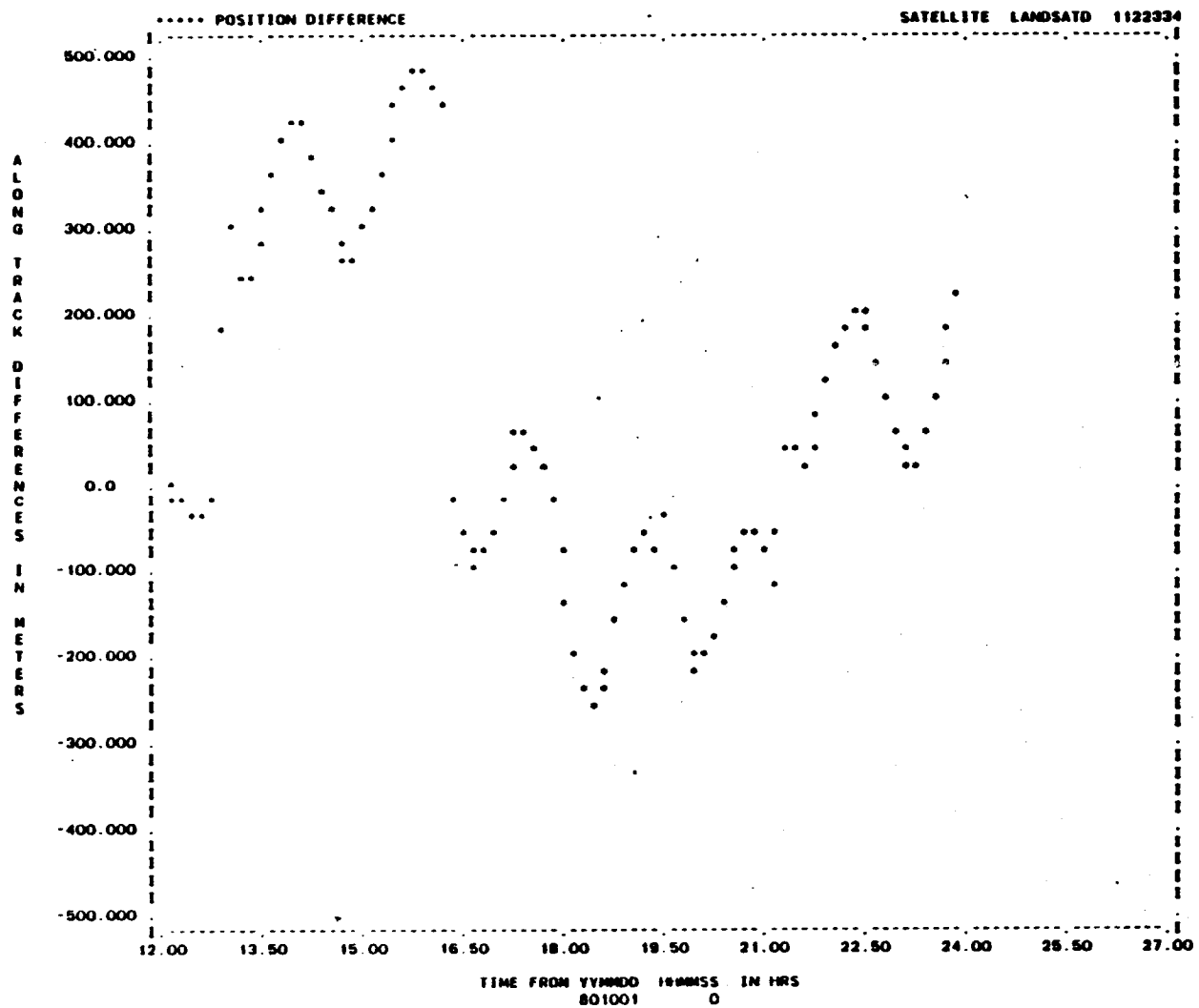

Figure A-87. Along-Track Differences for Run 04 (2 of 2)

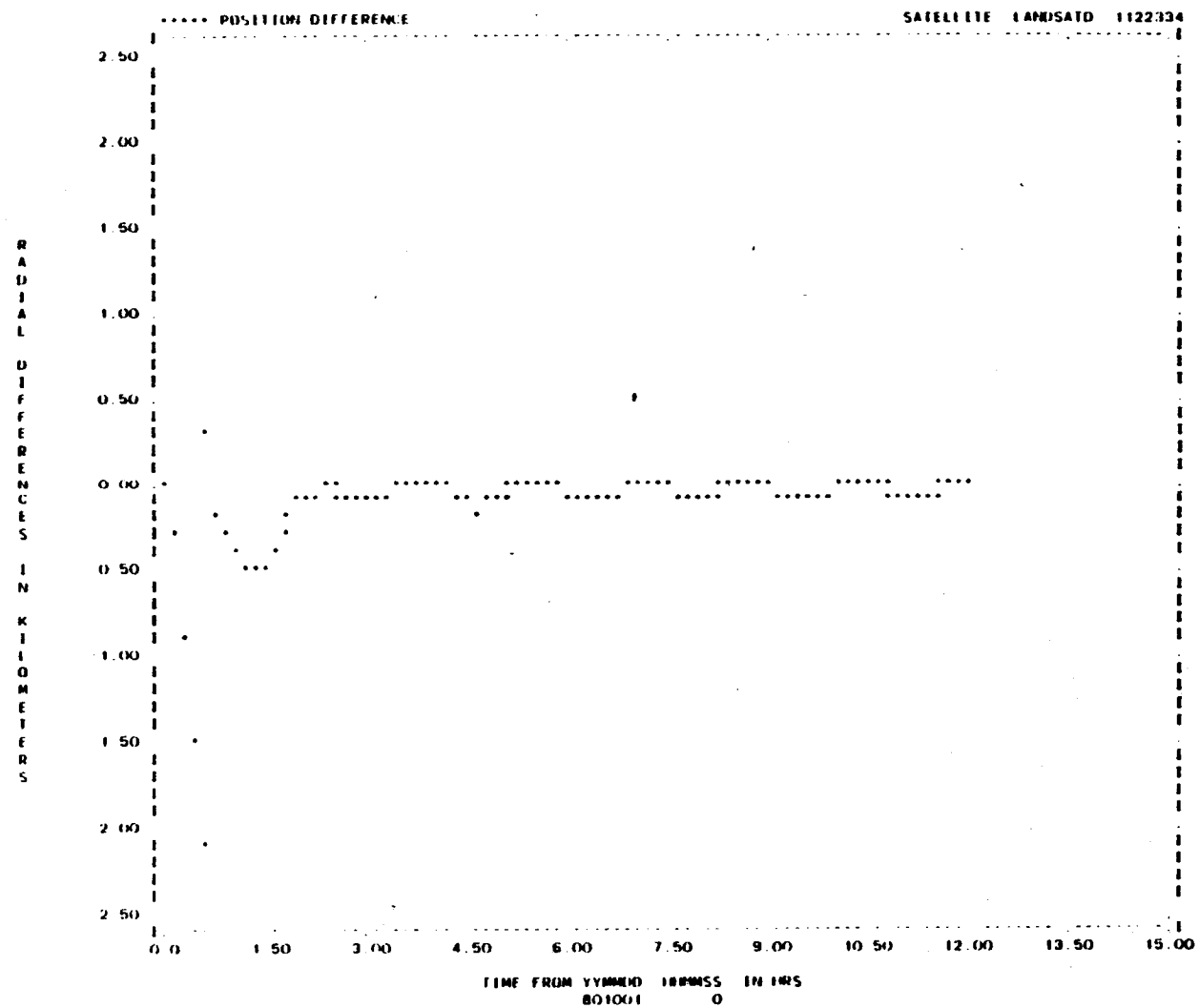

Figure A-88. Radial Differences for Run 05 (1 of 2)

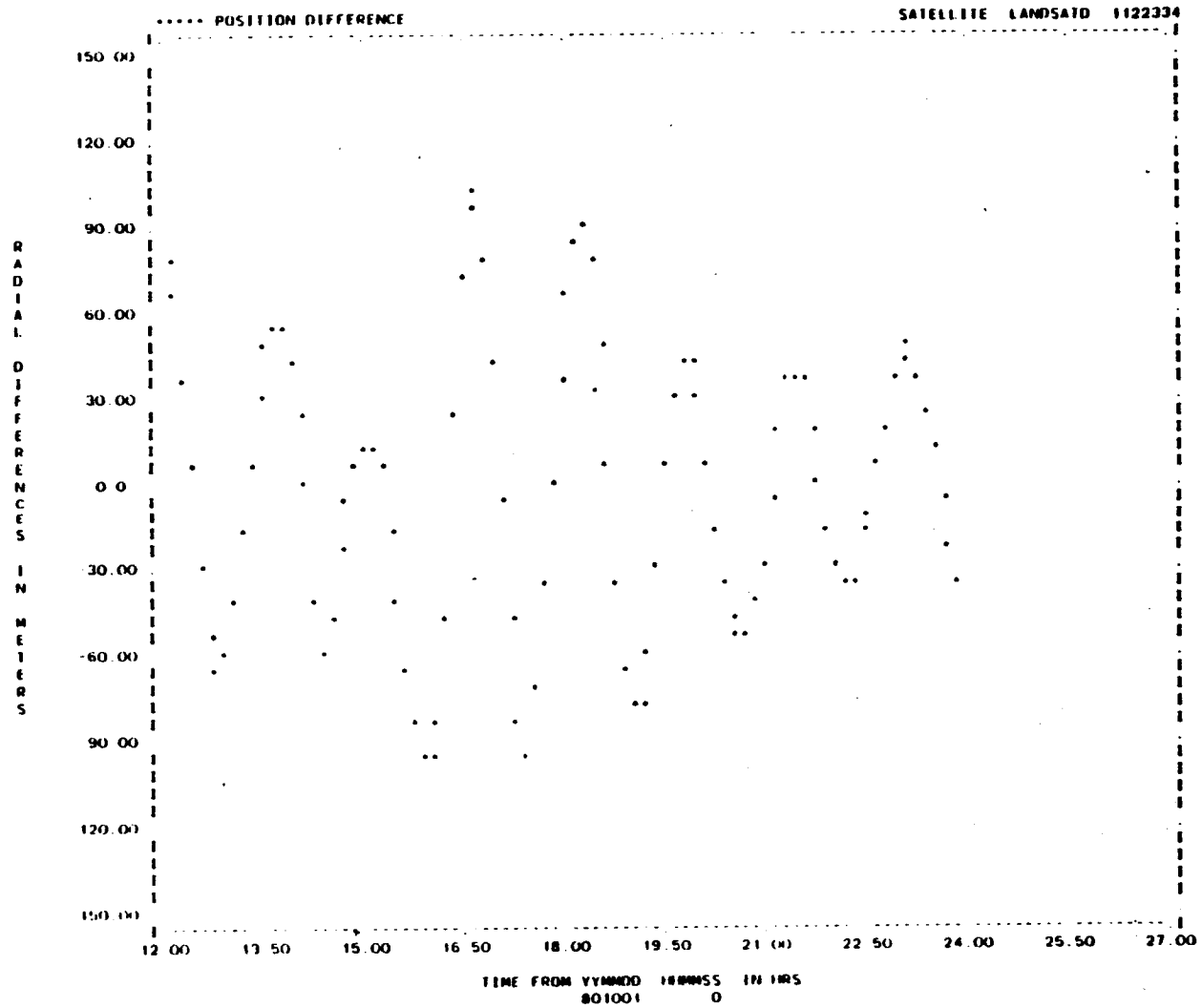

Figure A-88. Radial Differences for Run 05 (1 of 2)

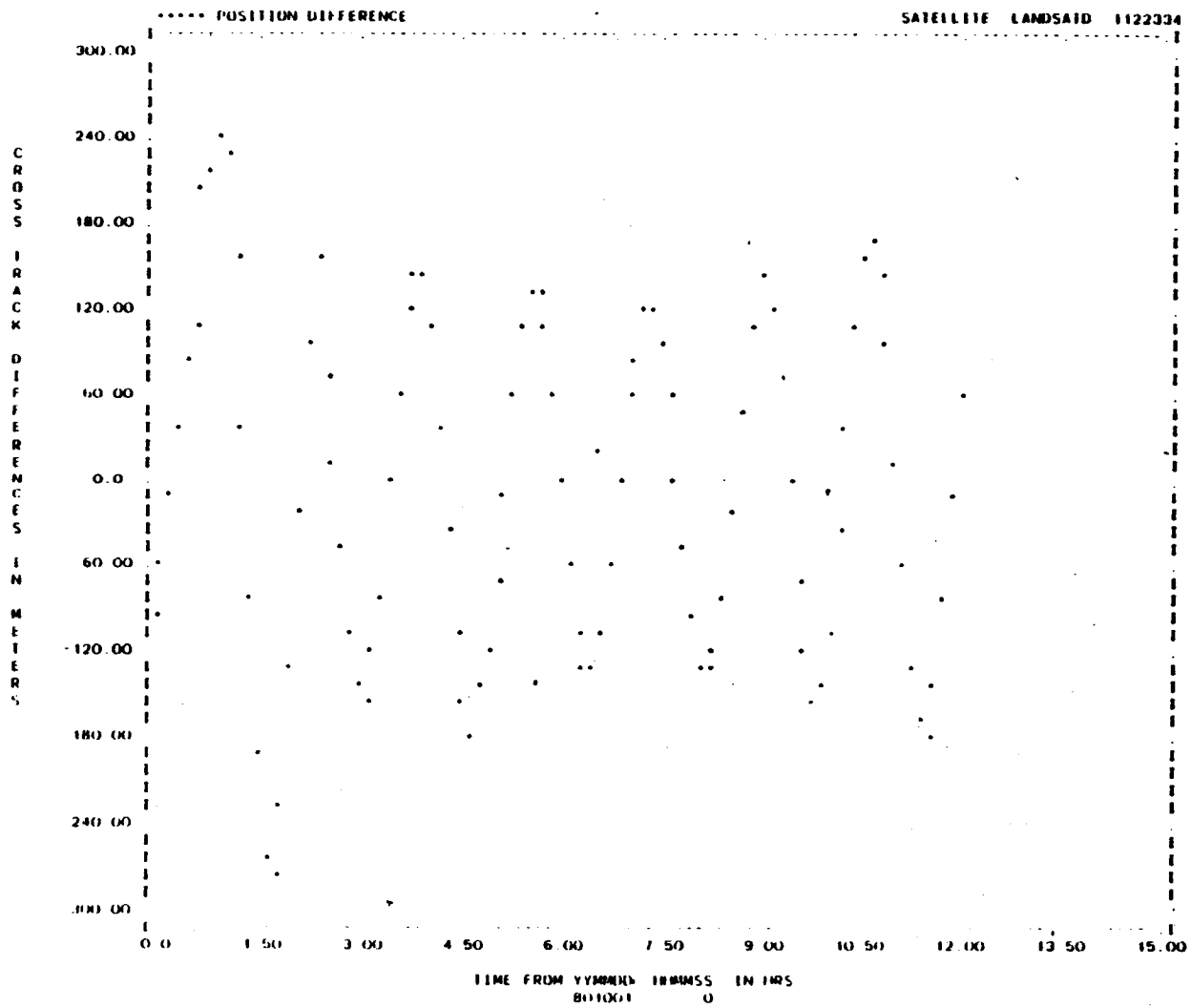

Figure A-89. Cross-Track Differences for Run 05 (1 of 2)

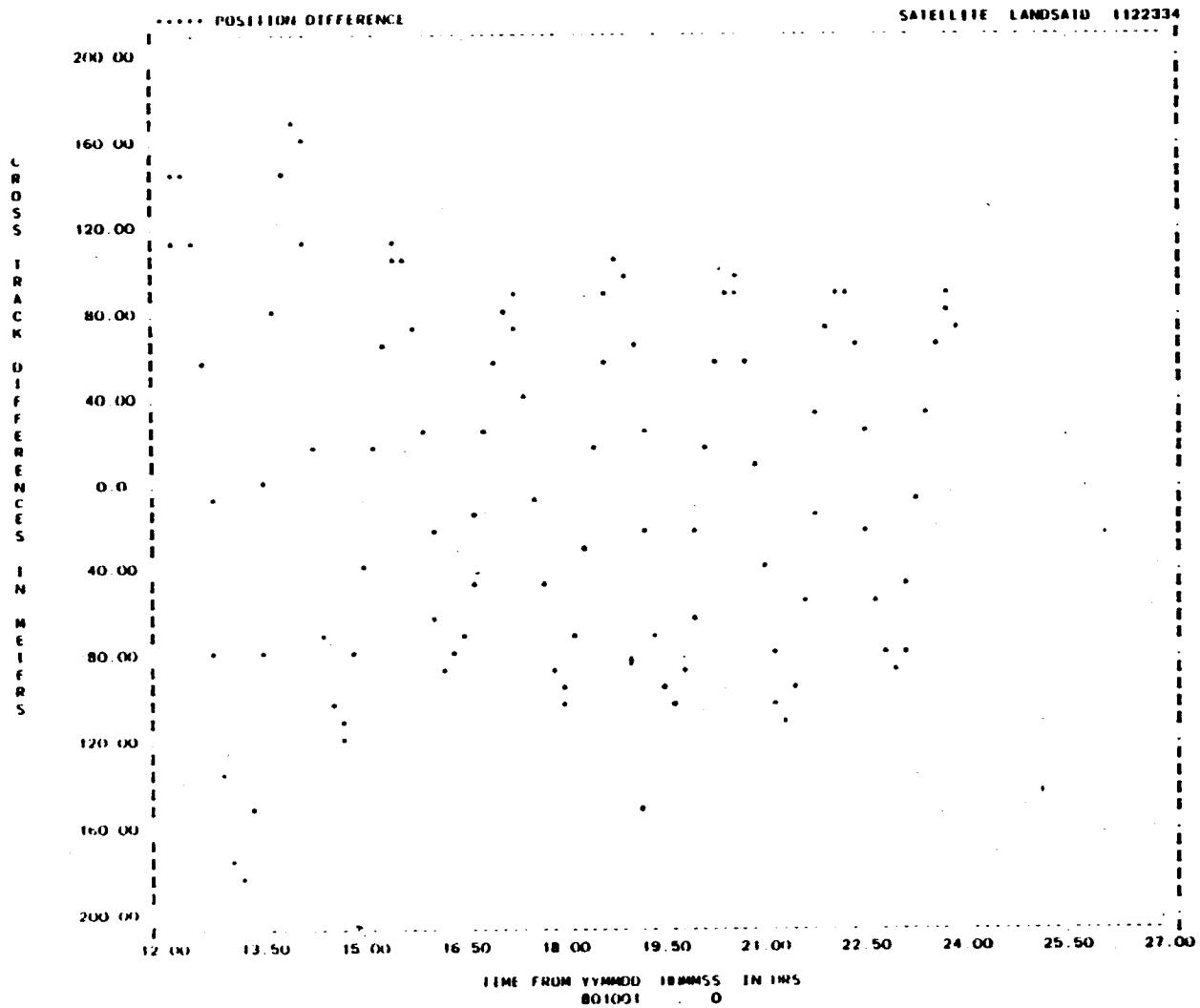

Figure A-89. Cross-Track Differences for Run 05 (2 of 2)

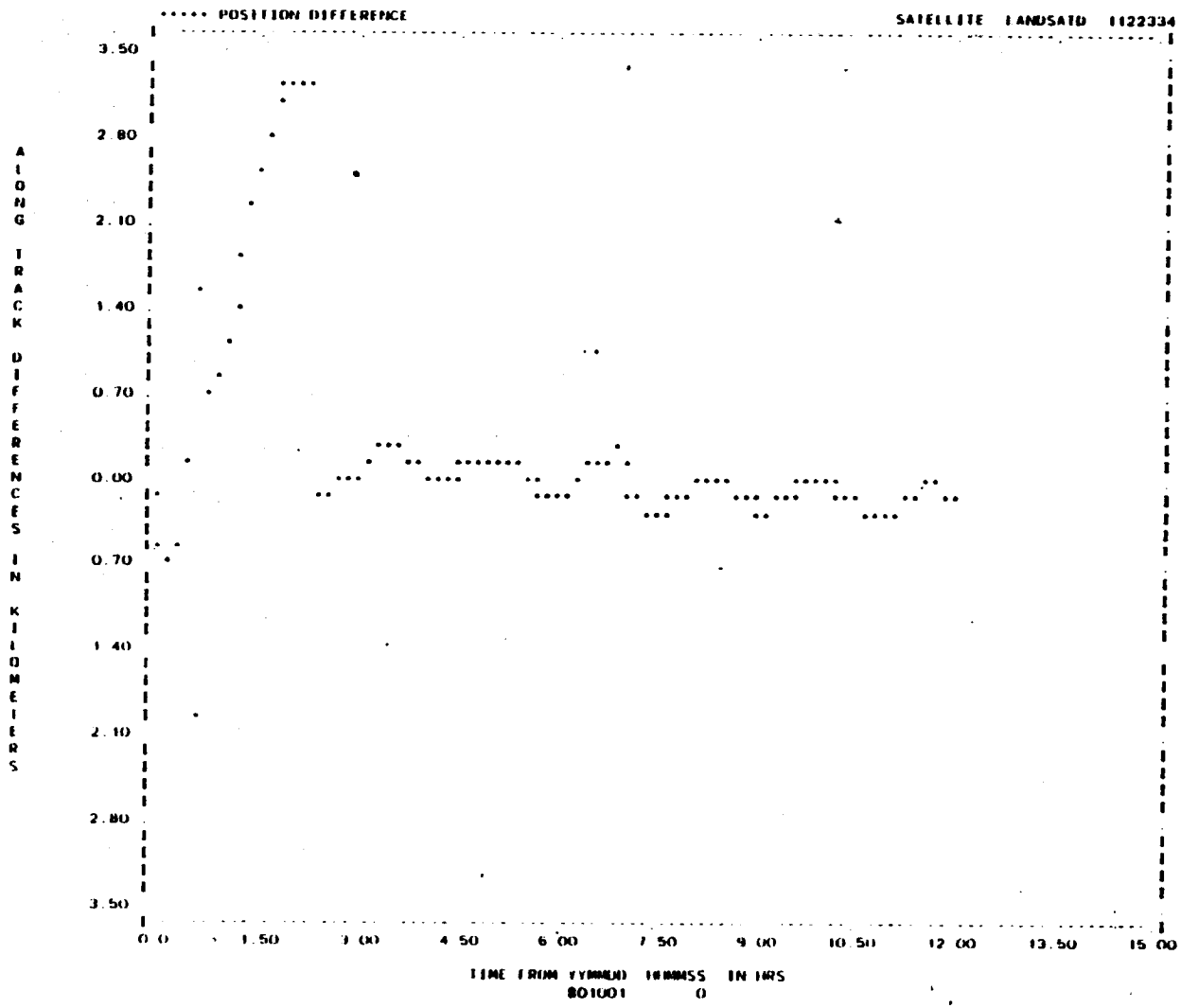

Figure A-90. Along-Track Differences for Run 05 (1 of 2)

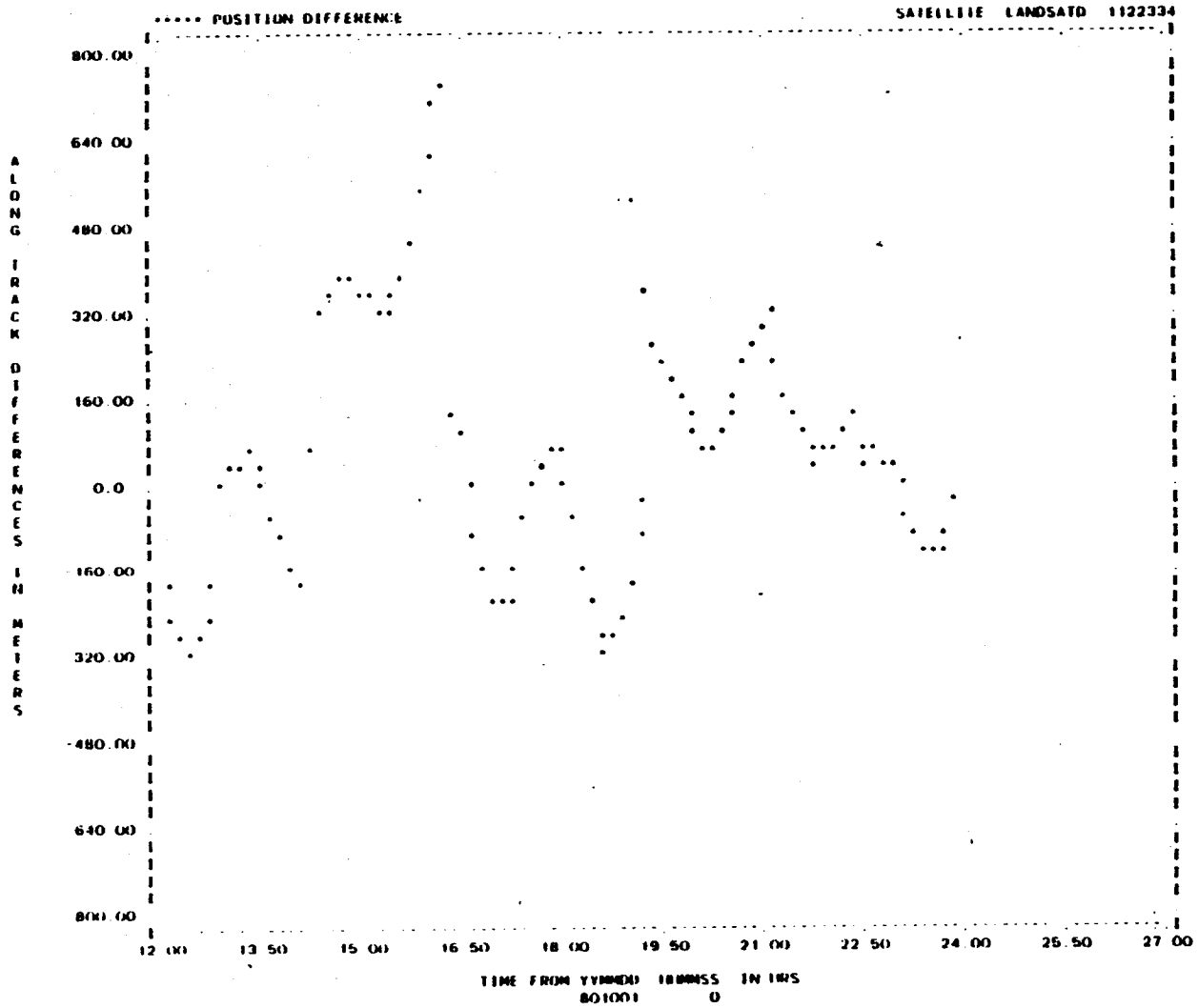

Figure A-90. Along-Track Differences for Run 05 (2 of 2)

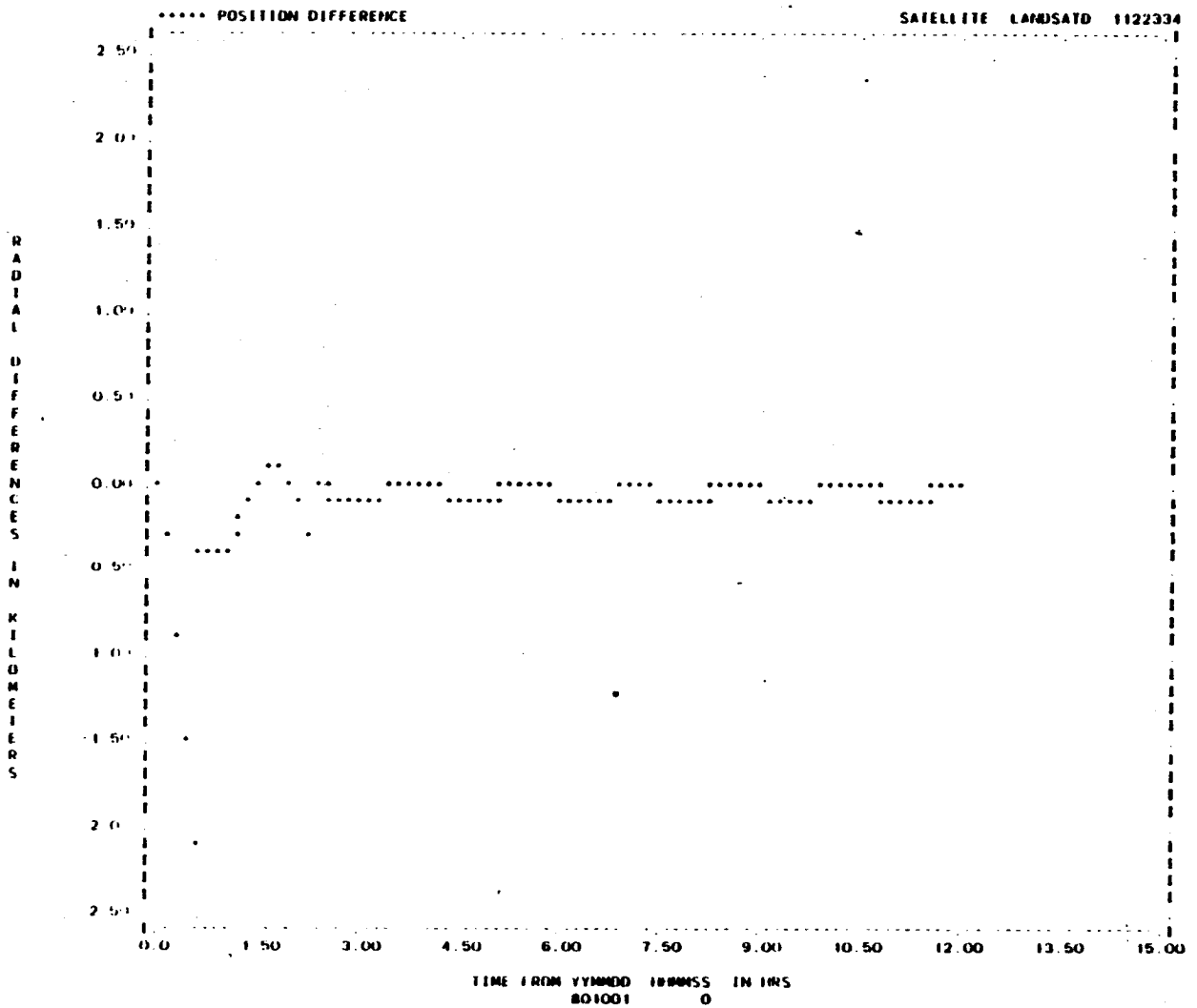

Figure A-91. Raidal Differences for Run 06 (1 of 2)

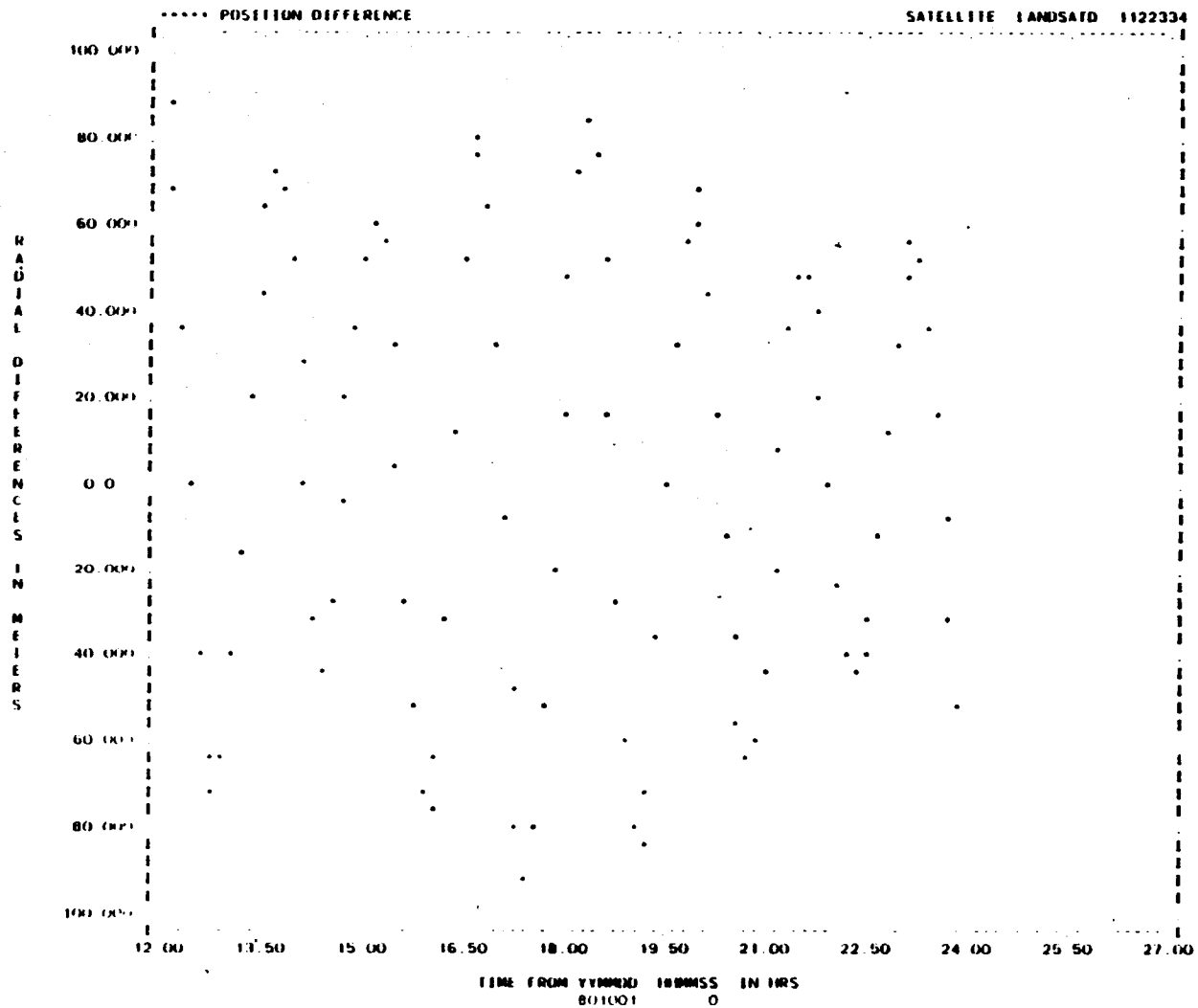

Figure A-91. Radial Differences for Run 06 (2 of 2)

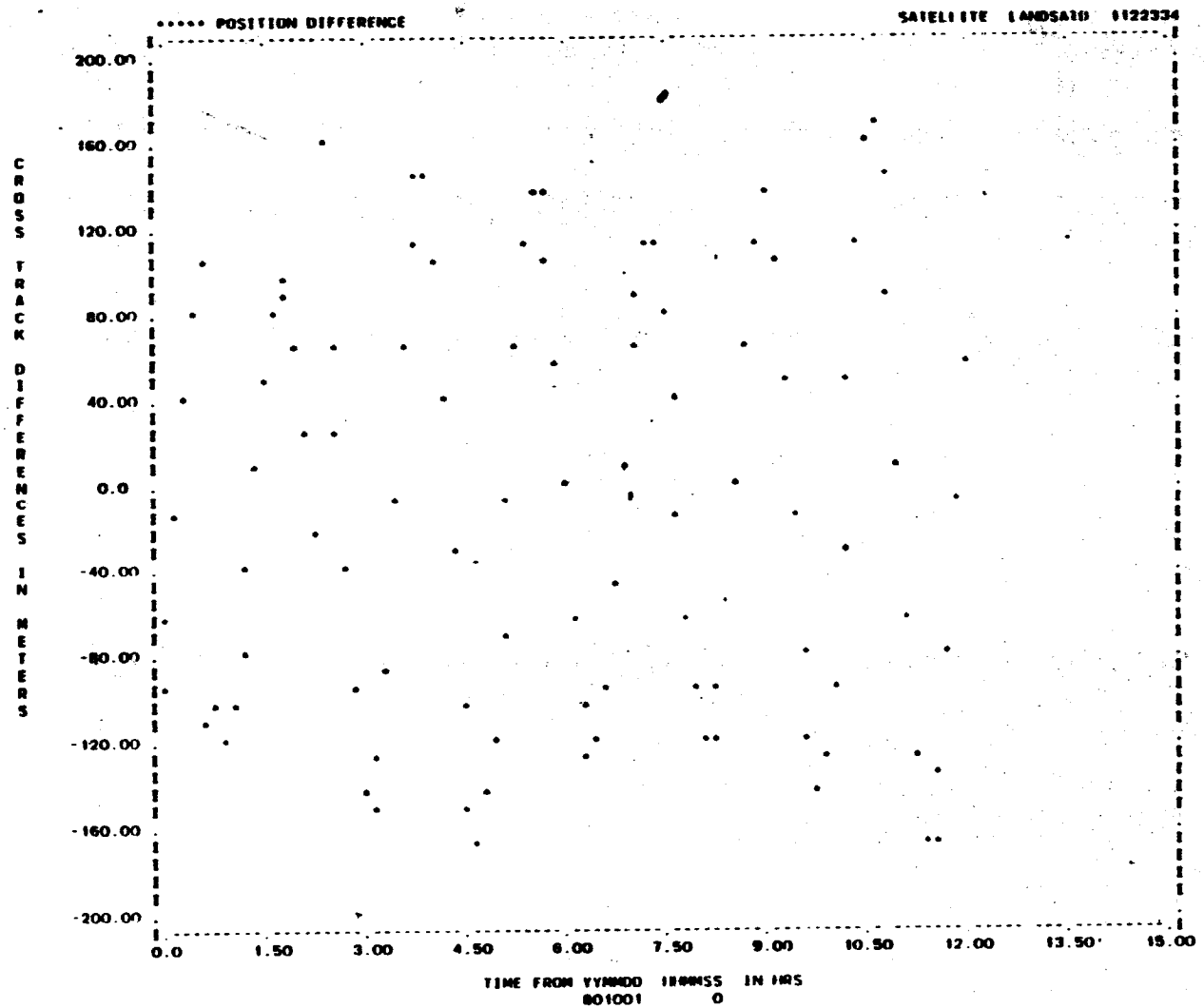

Figure A-92. Cross-Track Differences for Run 06 (1 of 2)

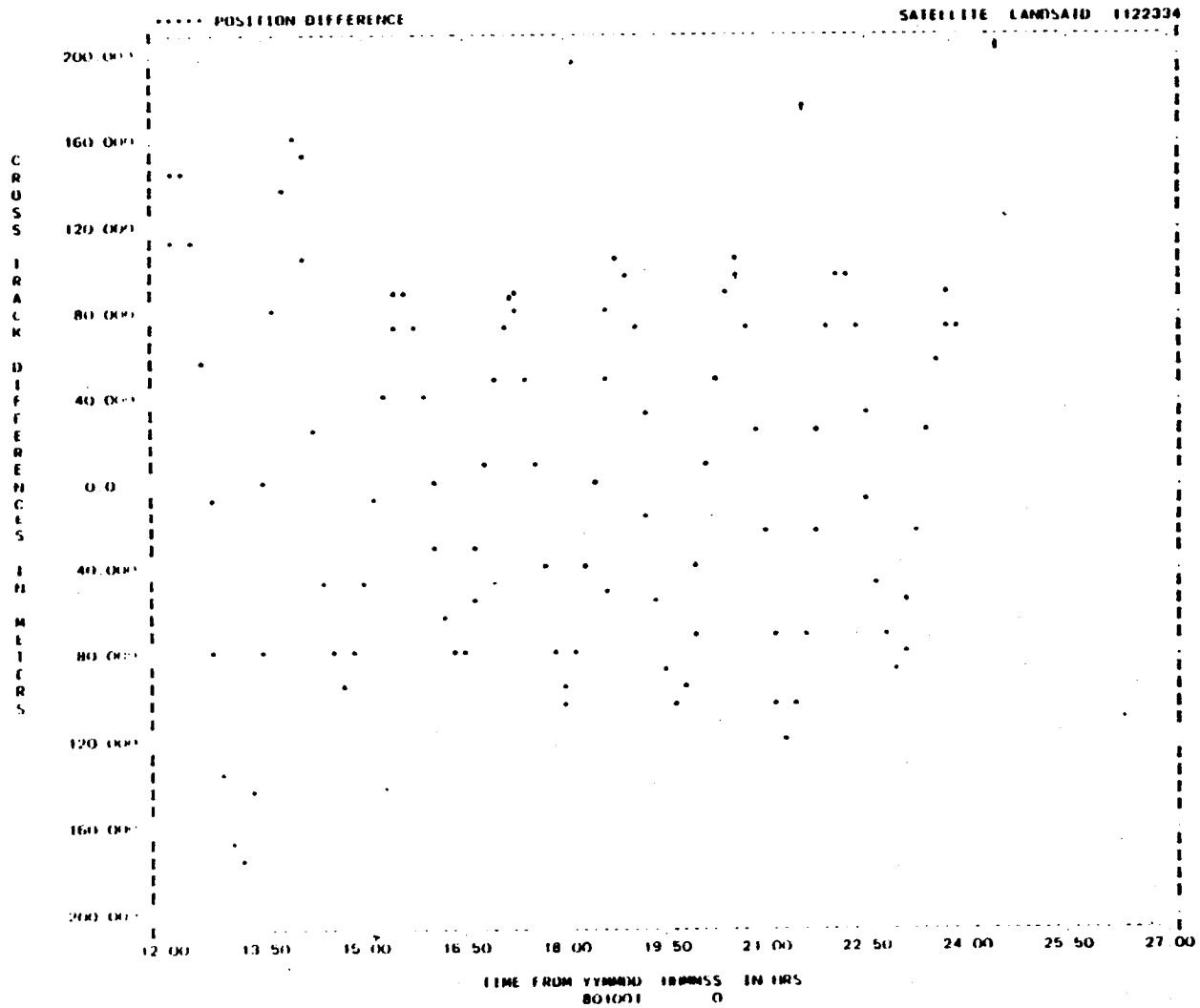

Figure A-92. Cross-Track Differences for Run 06 (2 of 2)

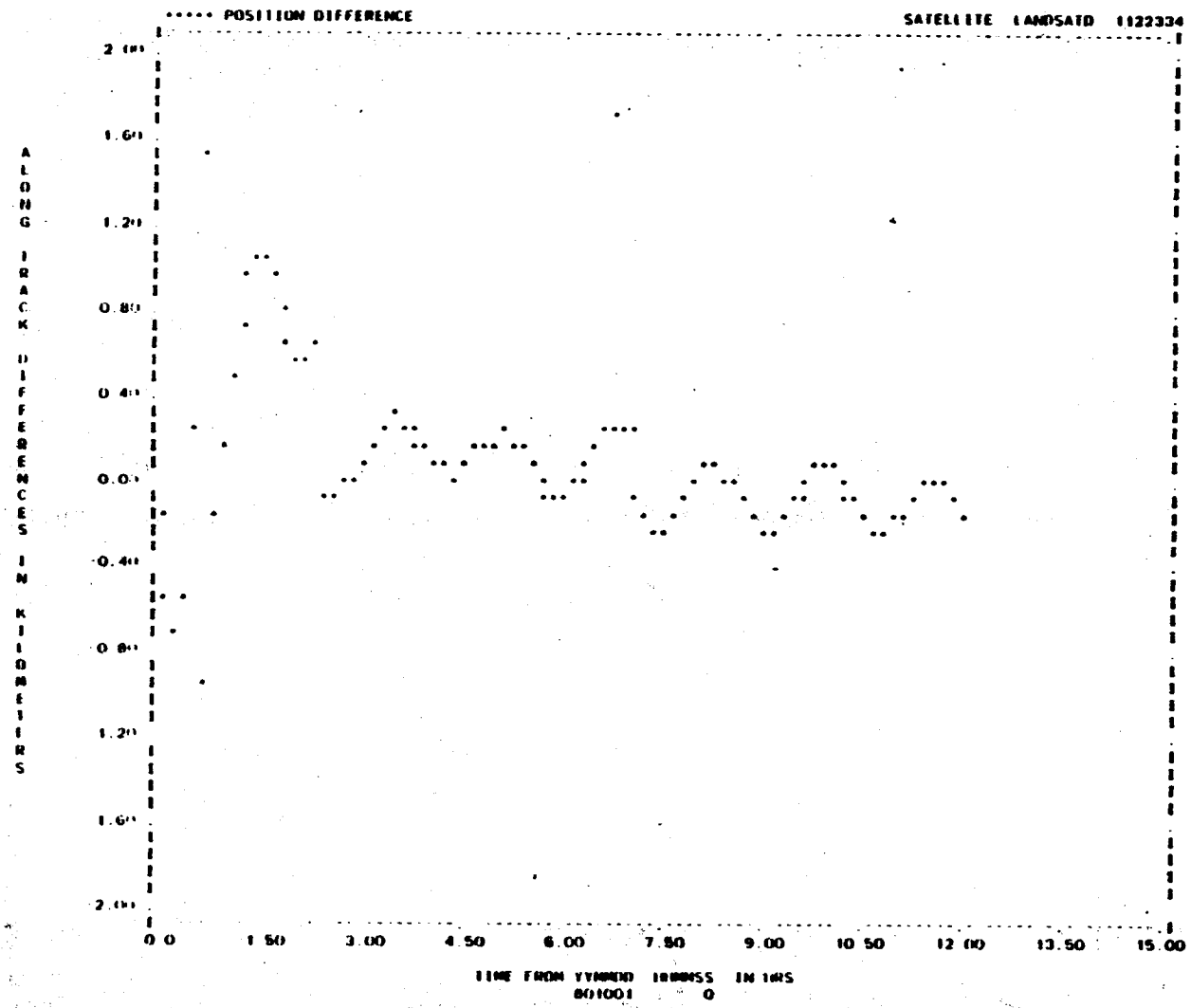

Figure A-93. Along-Track Differences for Run 06 (1 of 2)

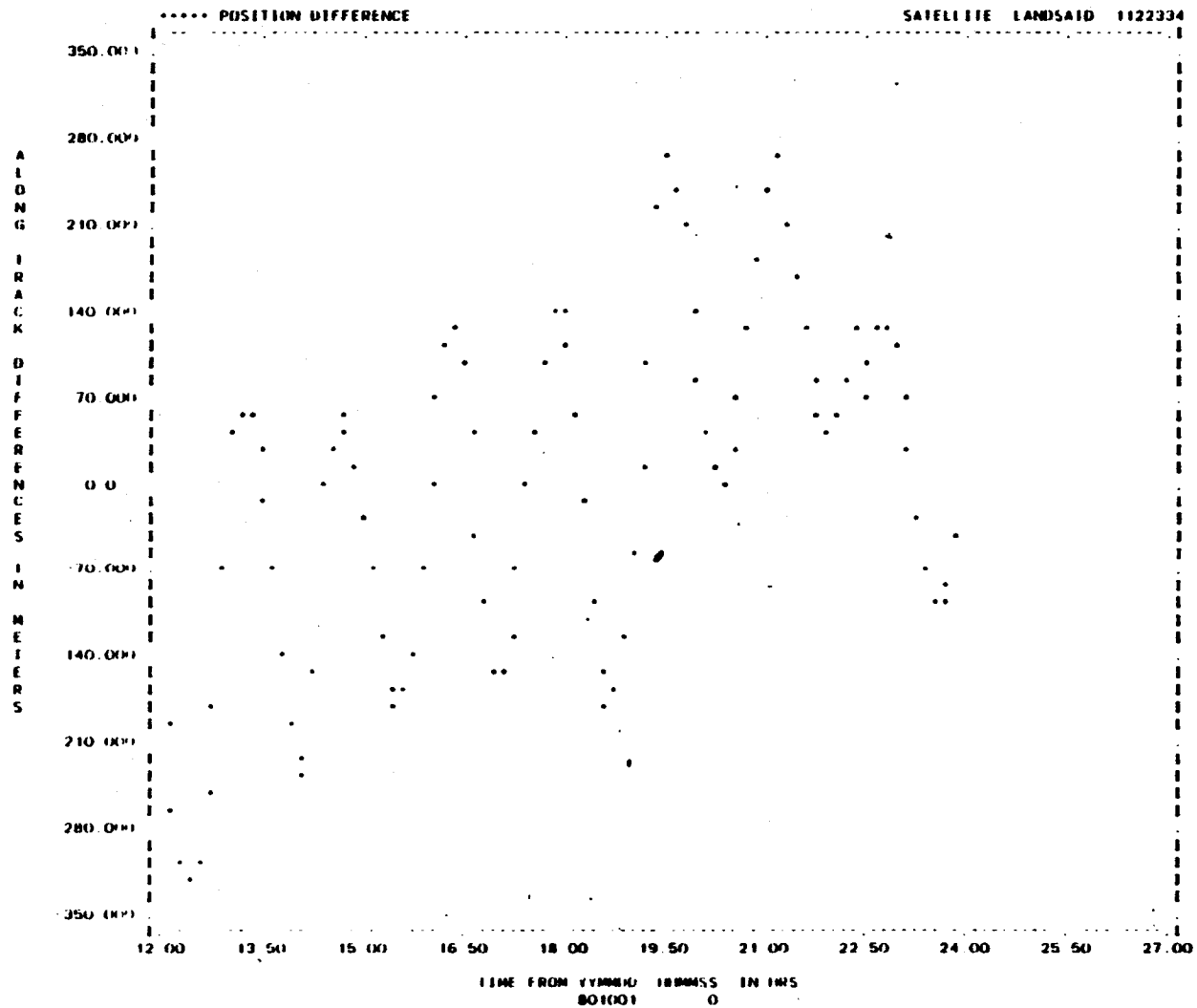

Figure A-93. Along-Track Differences for Run 06 (2 of 2)

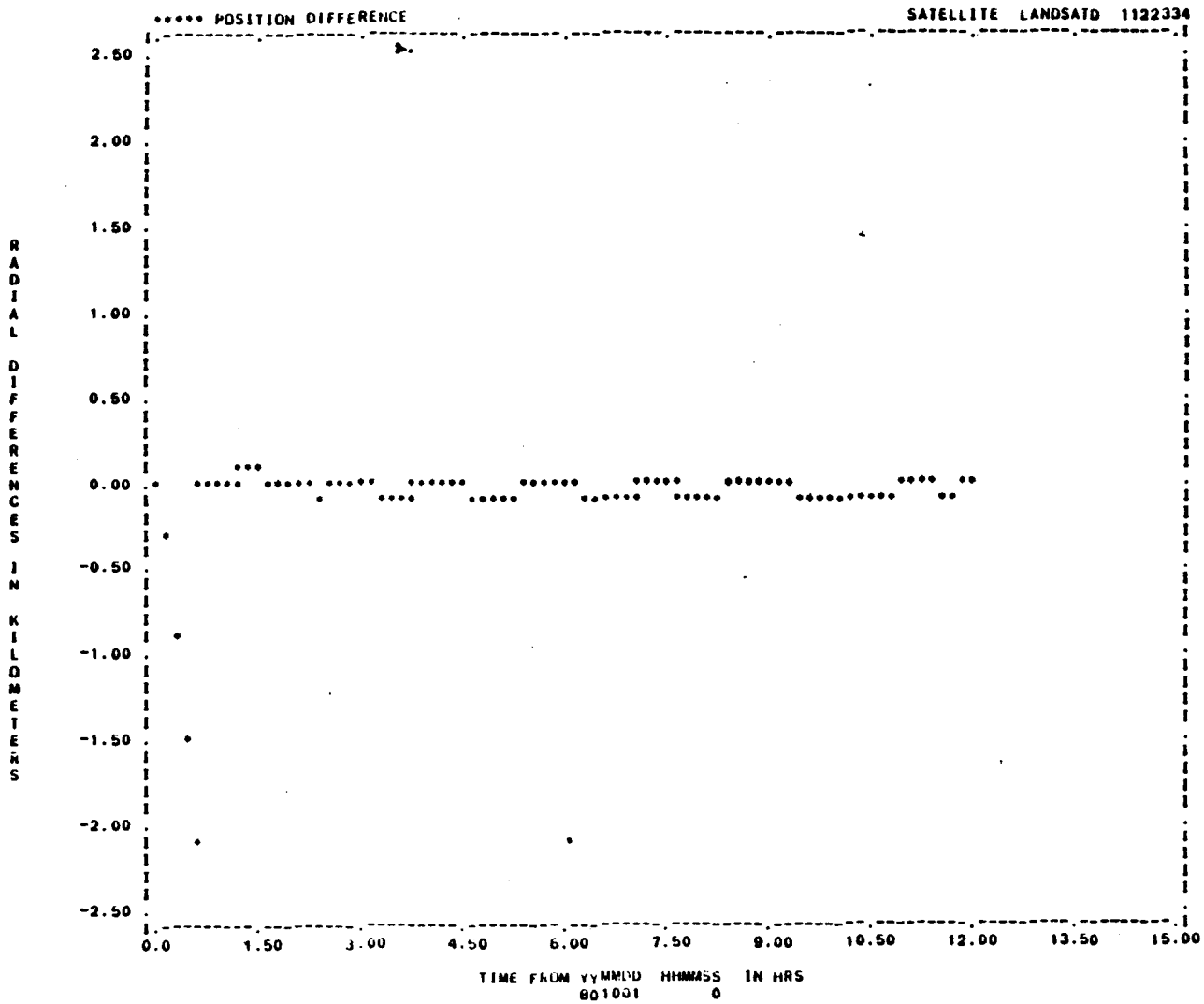

Figure A-94. Radial Differences for Run 07 (1 of 2)

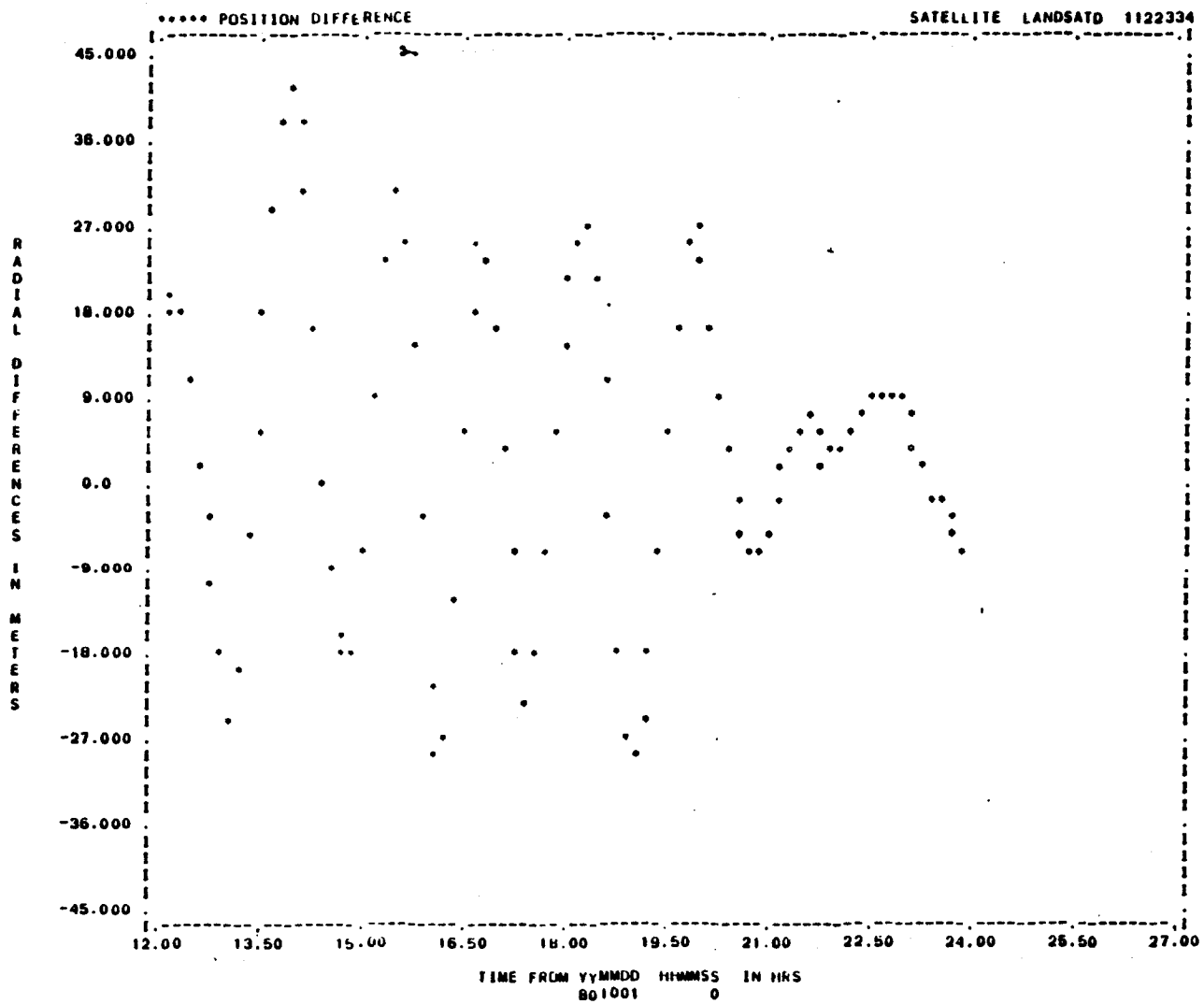

Figure A-94. Radial Differences for Run 07 (2 of 2)

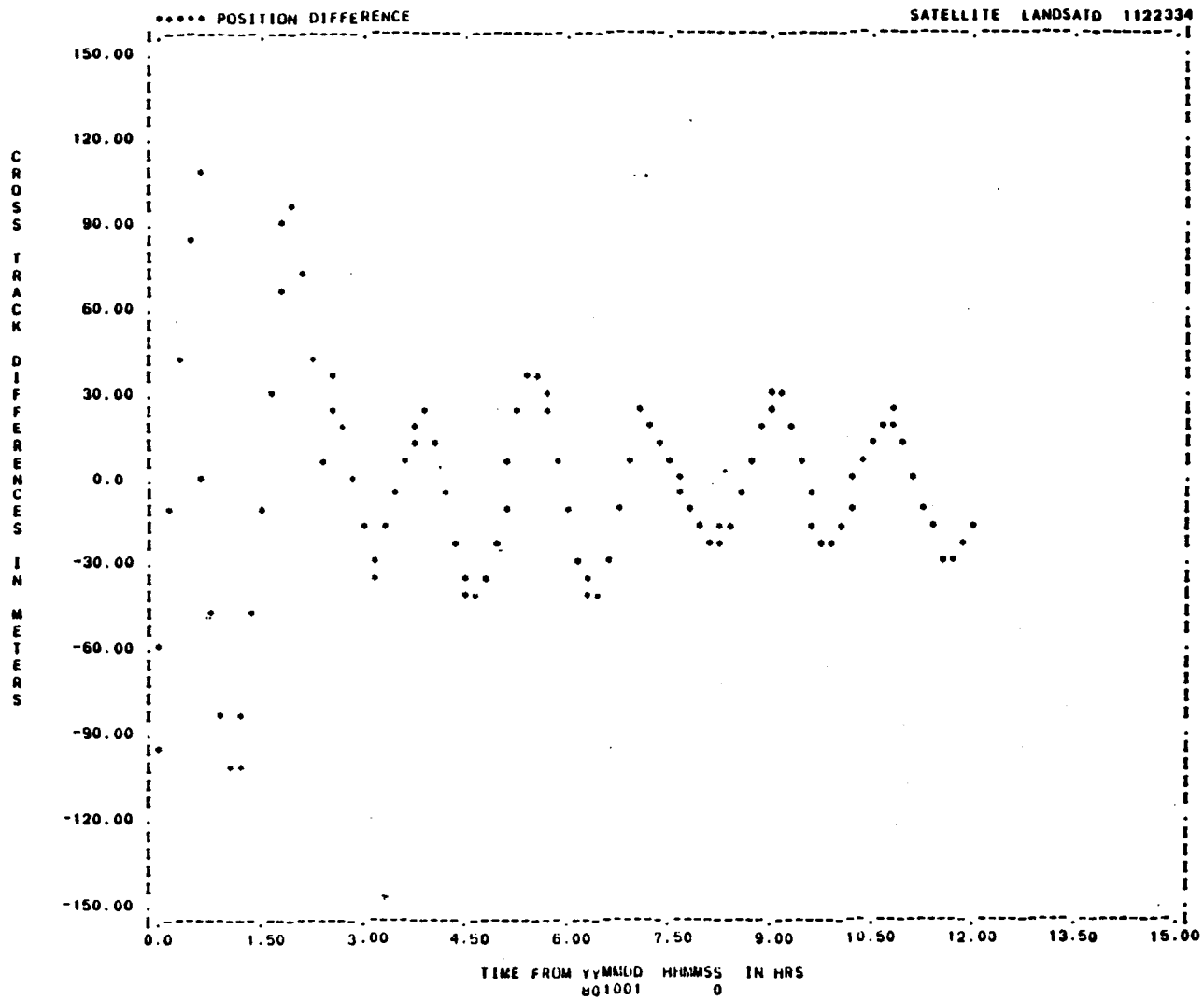

Figure A-95. Cross-Track Differences for Run 07 (1 of 2)

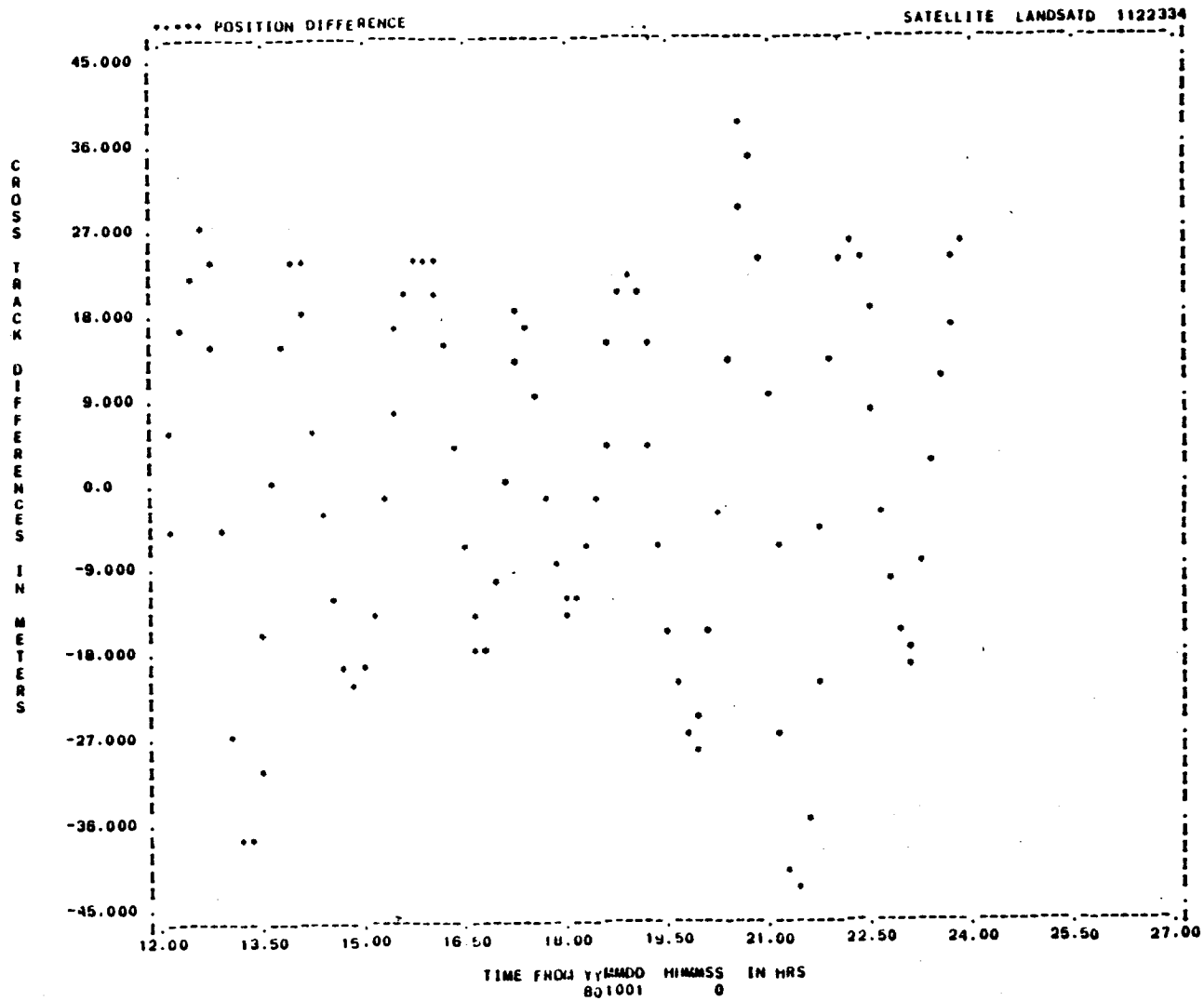

Figure A-95. Cross-Track Differences for Run O7 (2 of 2)

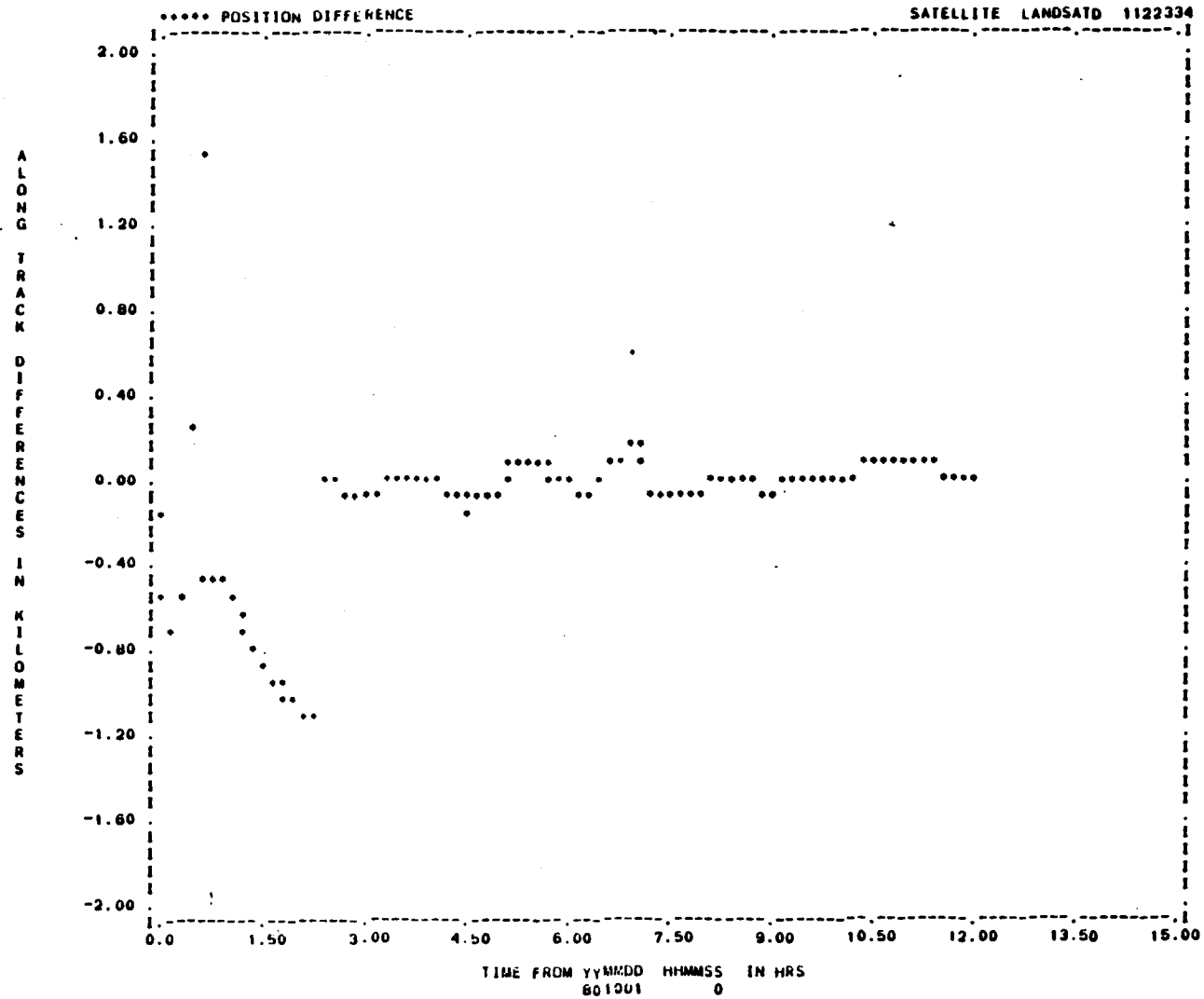

Figure A-96. Along-Track Differences for Run 07 (1 of 2)

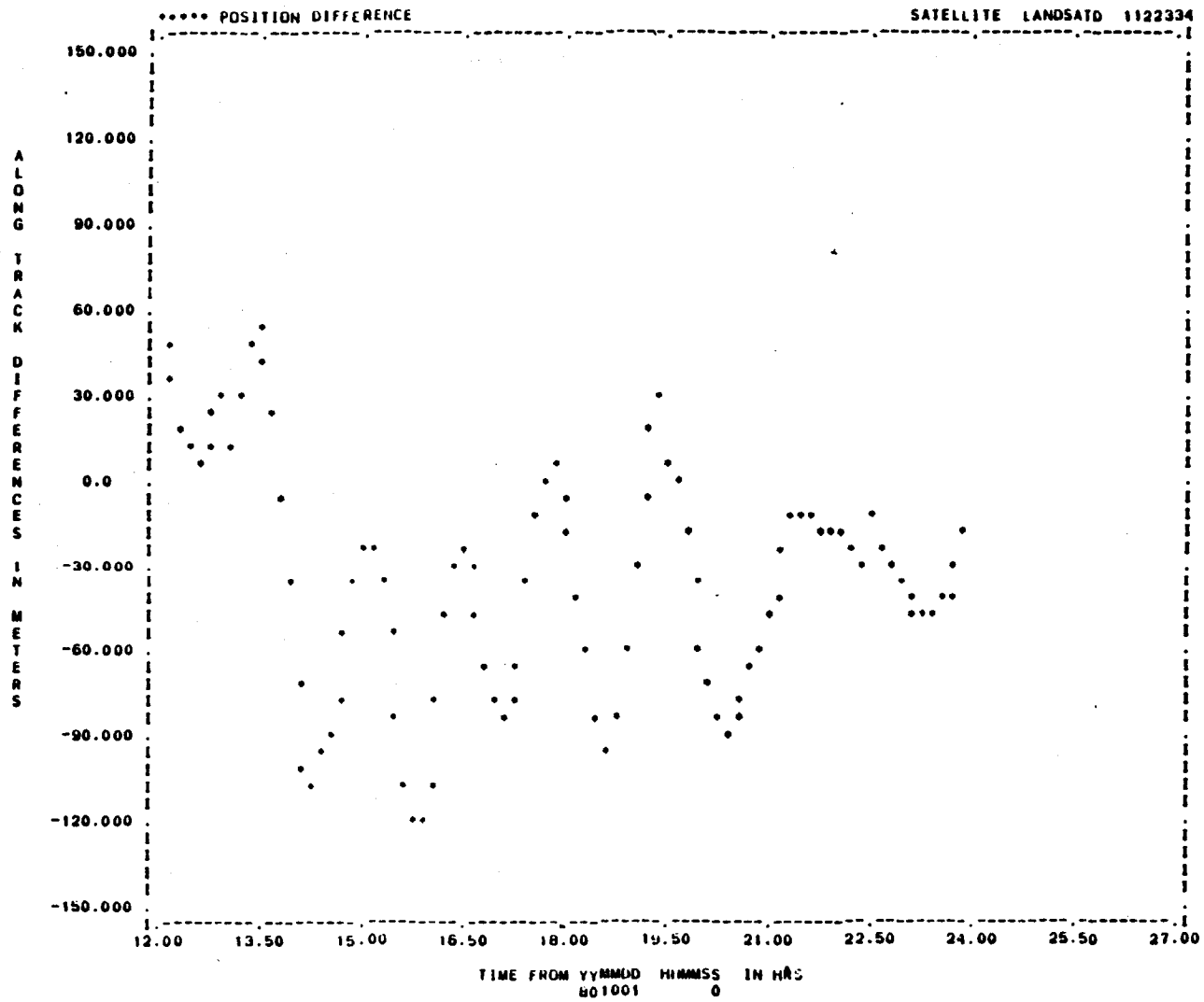

Figure A-96. Along-Track Differences for Run 07 (2 of 2)

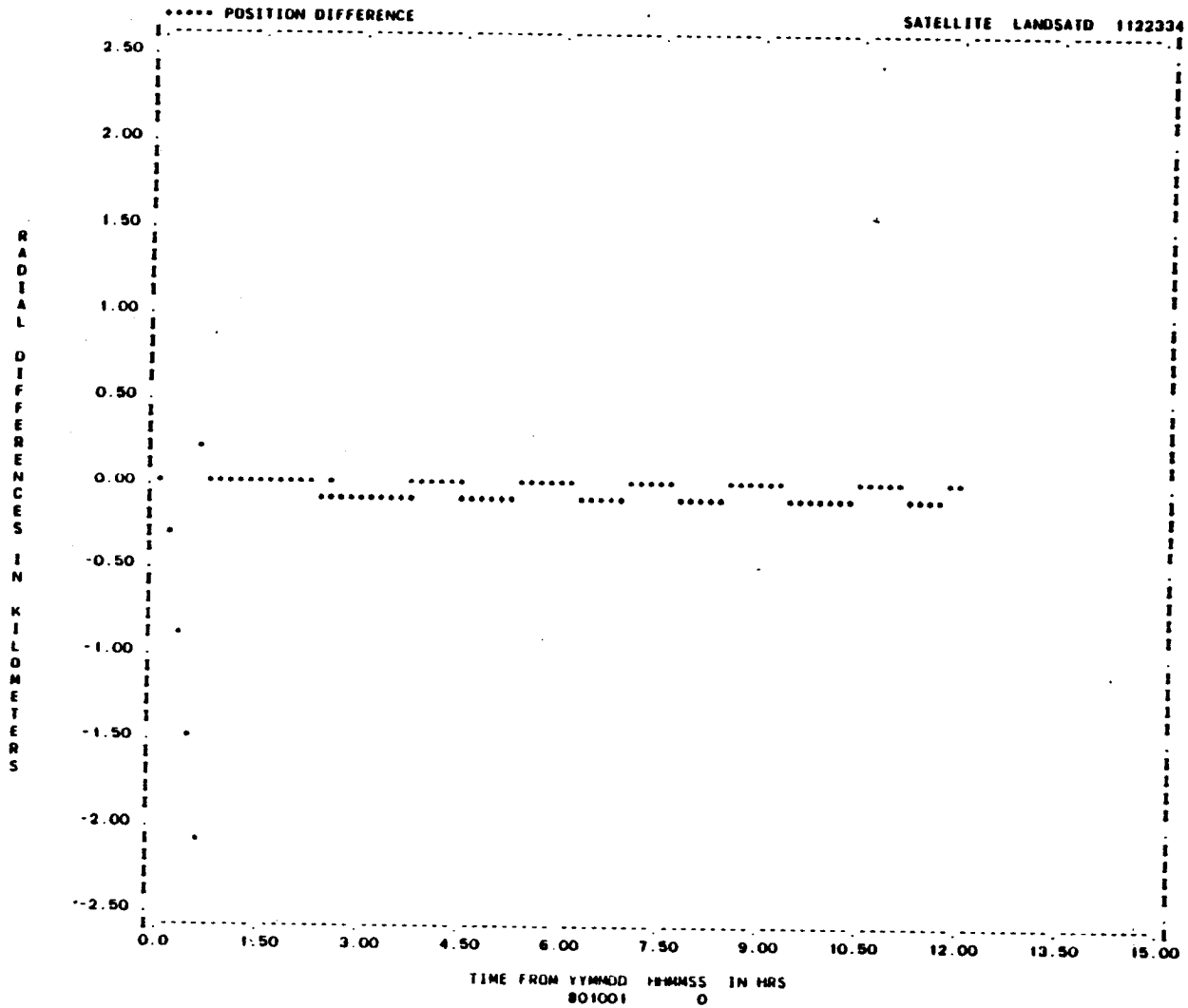

Figure A-97. Radial Differences for Run 08 (1 of 2)

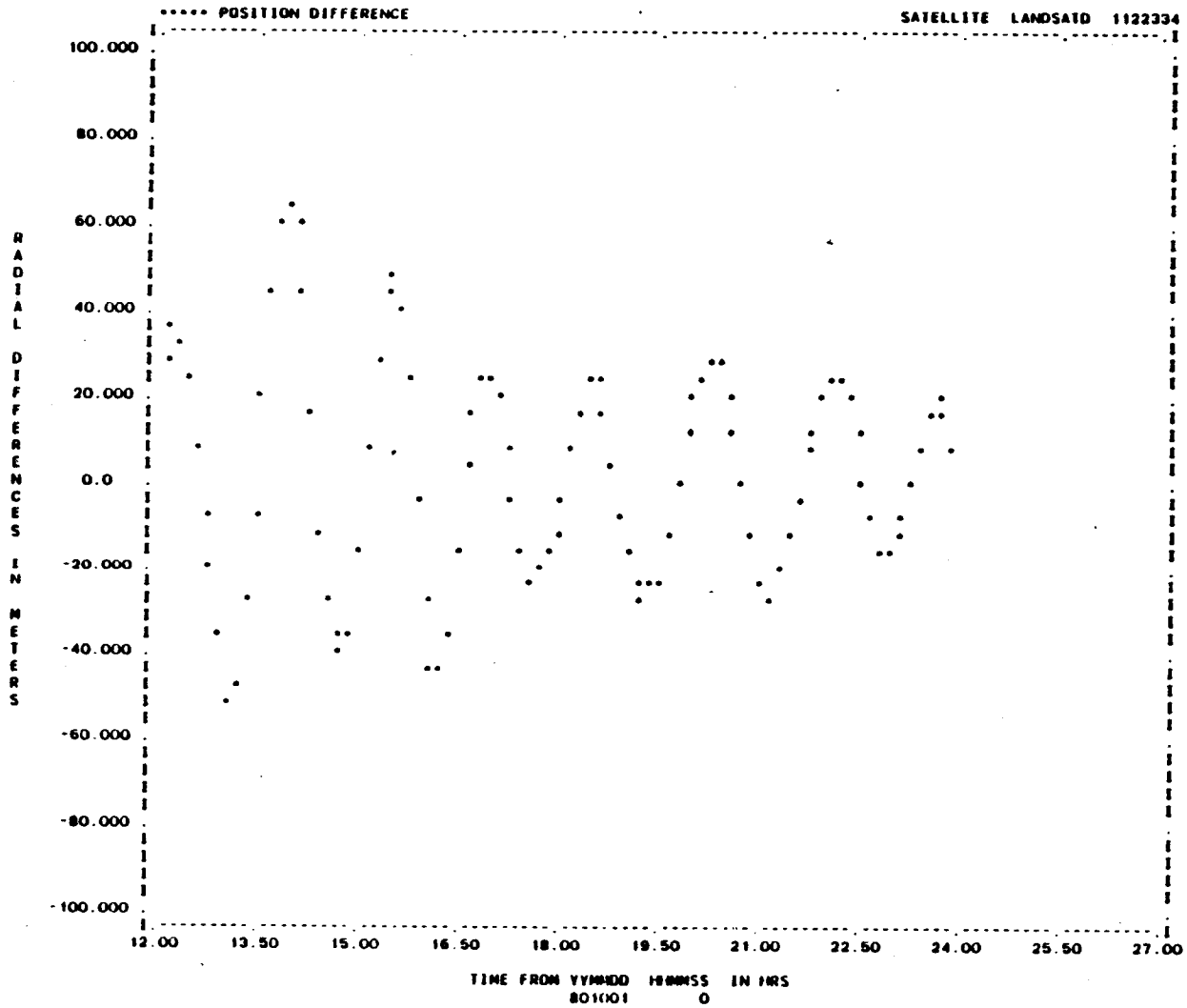

Figure A-97. Radial Differences for Run 08 (2 of 2)

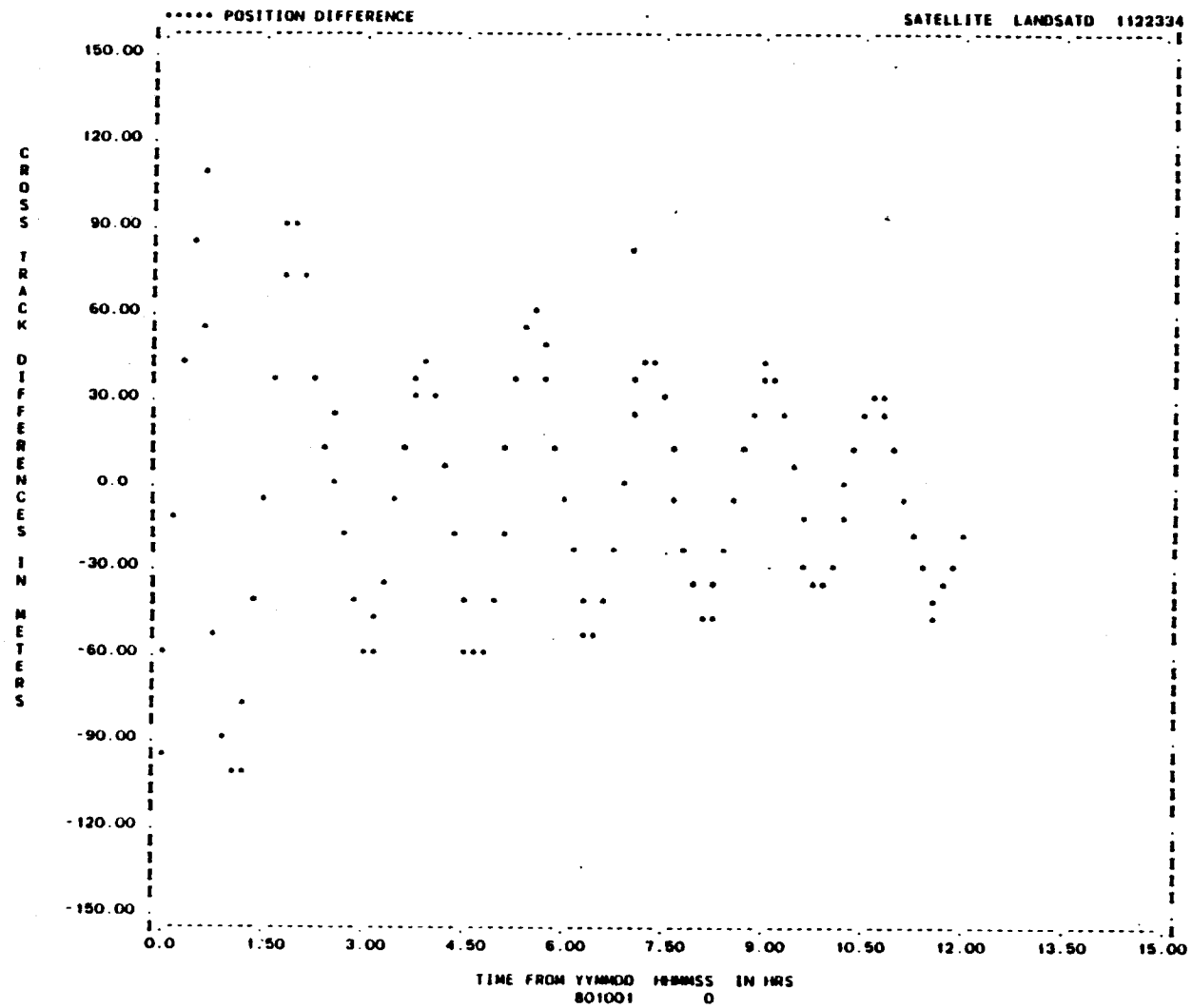

Figure A-98. Cross-Track Differences for Run 08 (1 of 2)

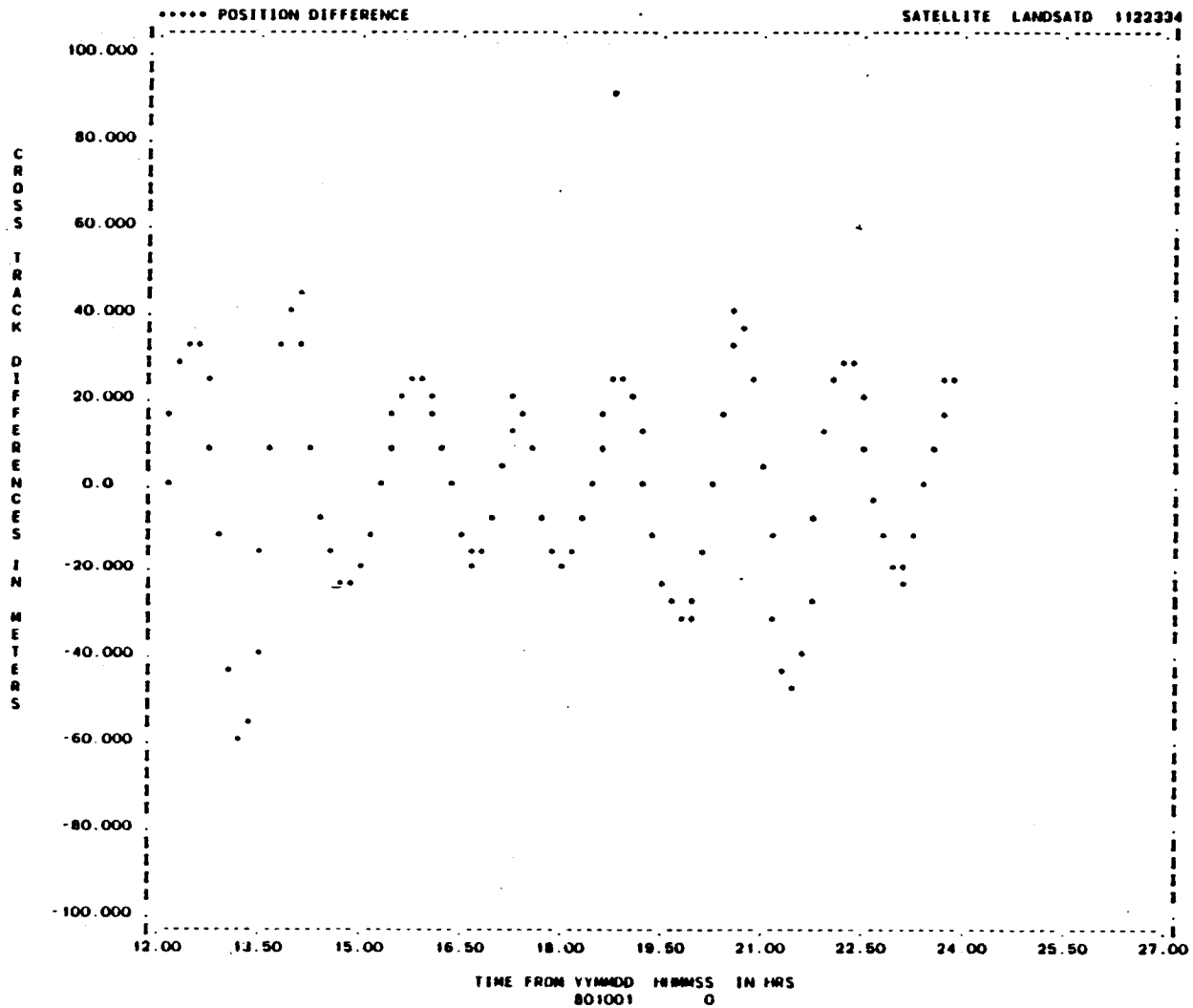

Figure A-98. Cross-Track Differences for Run 08 (2 of 2)

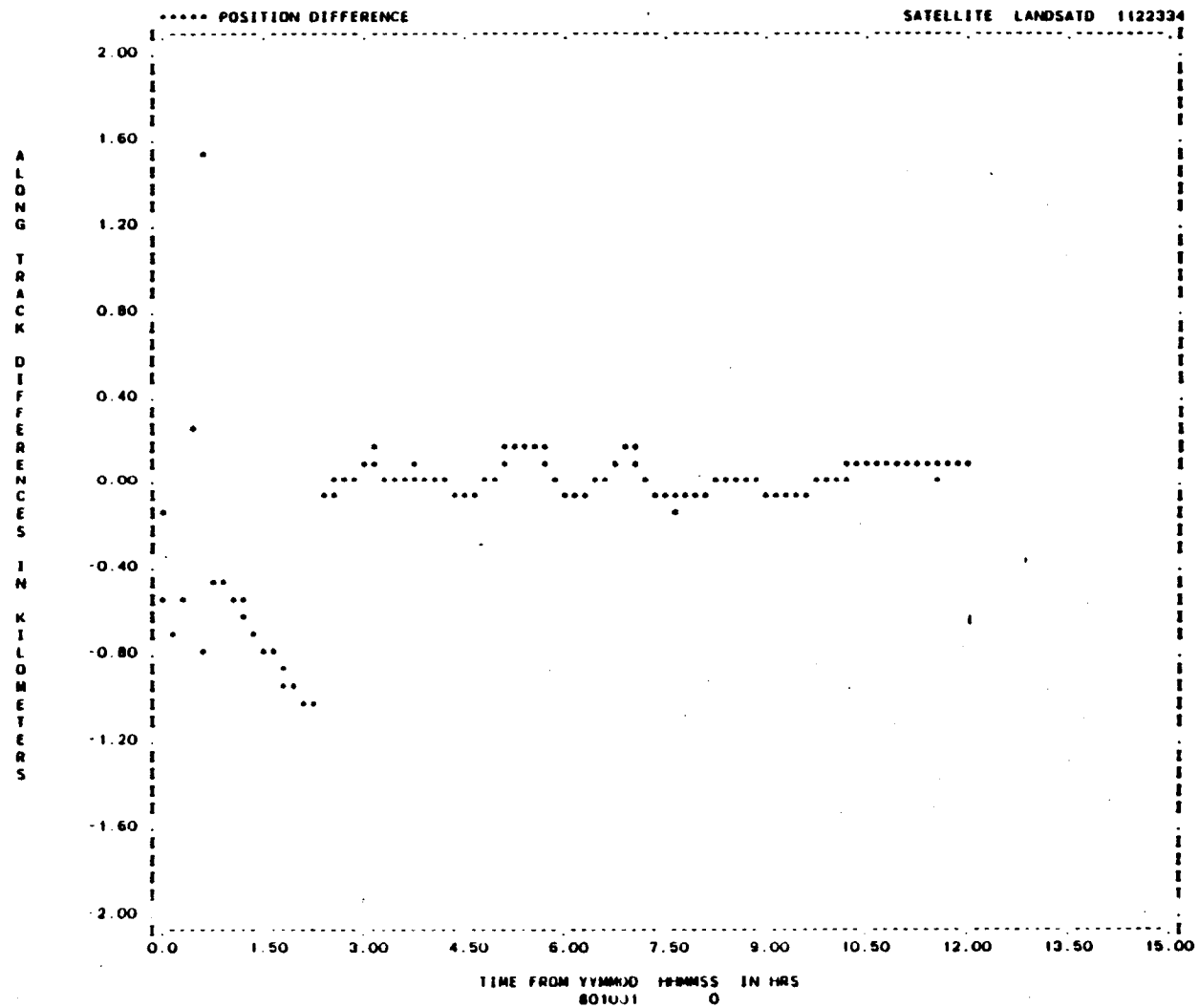

Figure A-99. Along-Track Differences for Run 08 (1 of 2)

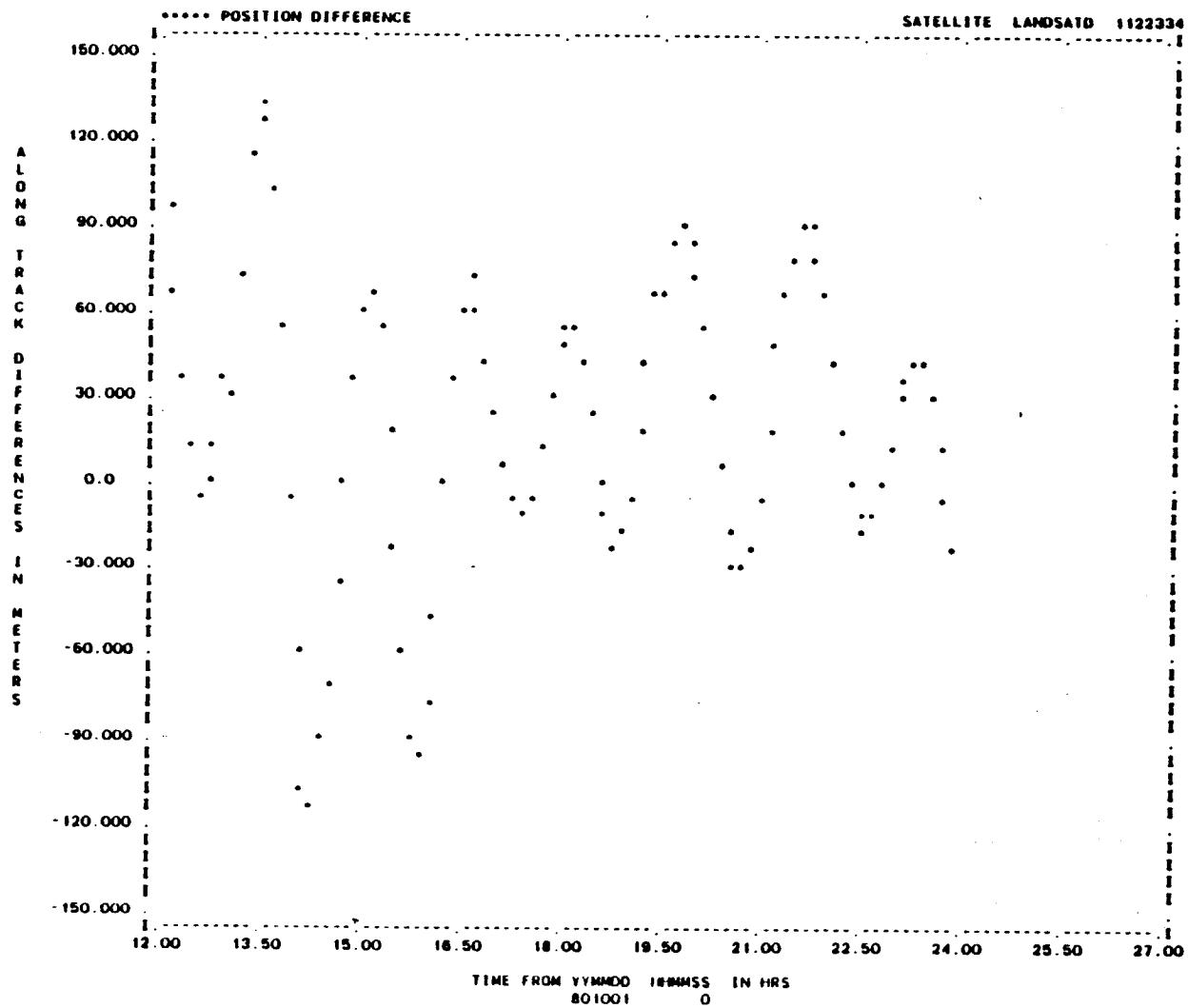

Figure A-99. Along-Track Differences for Run 08 (2 of 2)

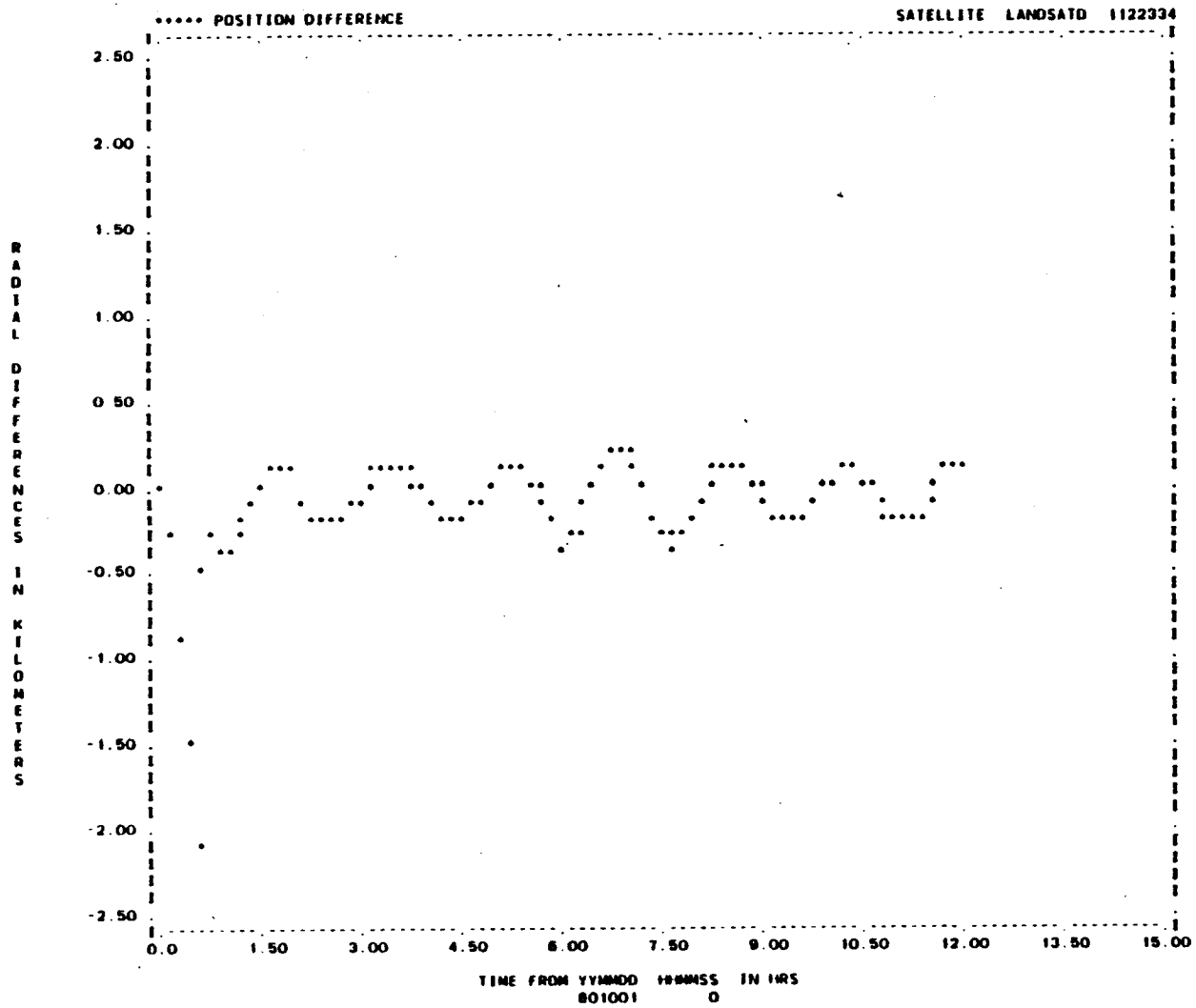

Figure A-100. Radial Differences for Run 010 (1 of 2)

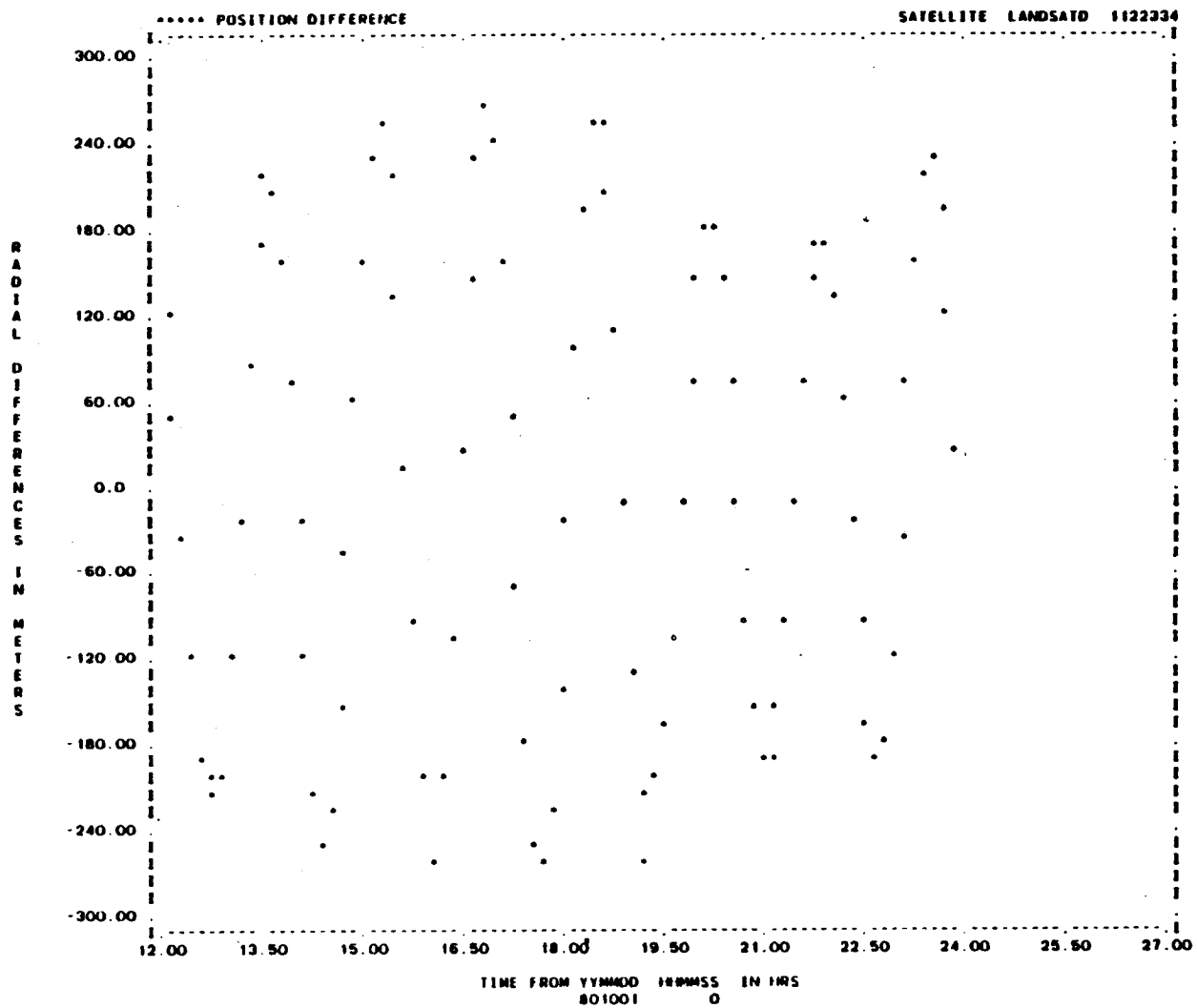

Figure A-100. Radial Differences for Run 010 (2 of 2)

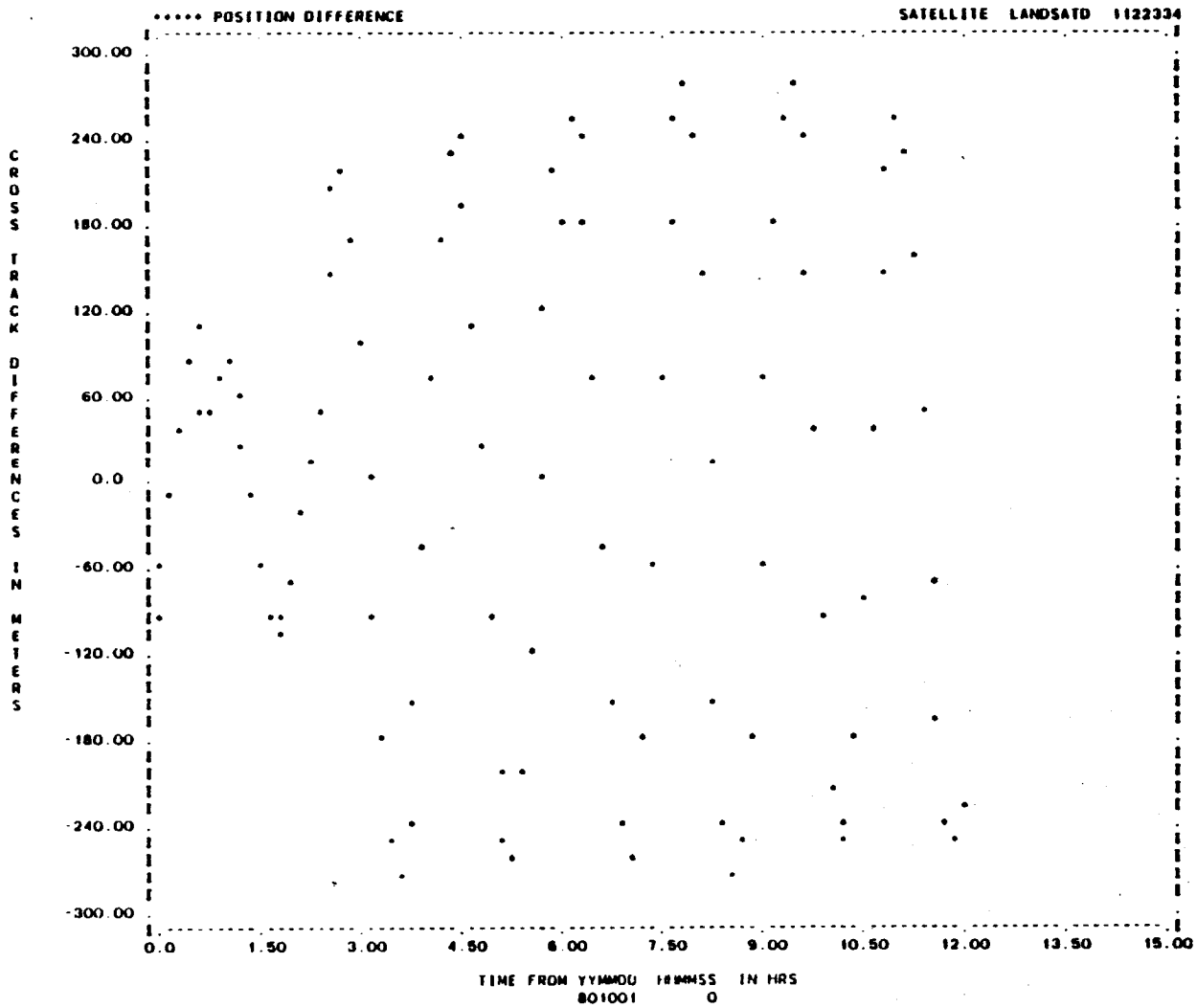

Figure A-101. Cross-Track Differences for Run 010 (1 of 2)

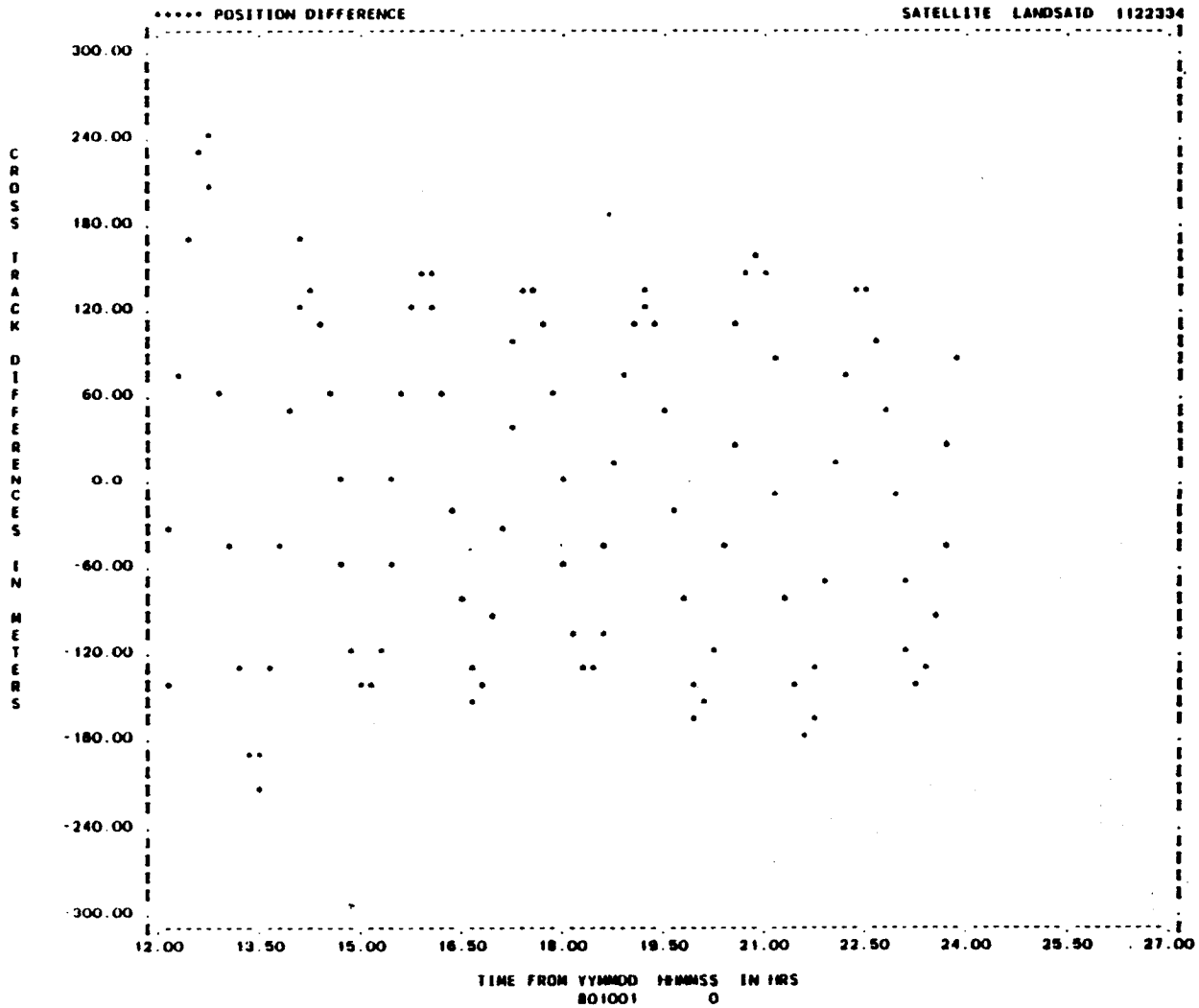

Figure A-101. Cross-Track Differences for Run 010 (2 of 2)

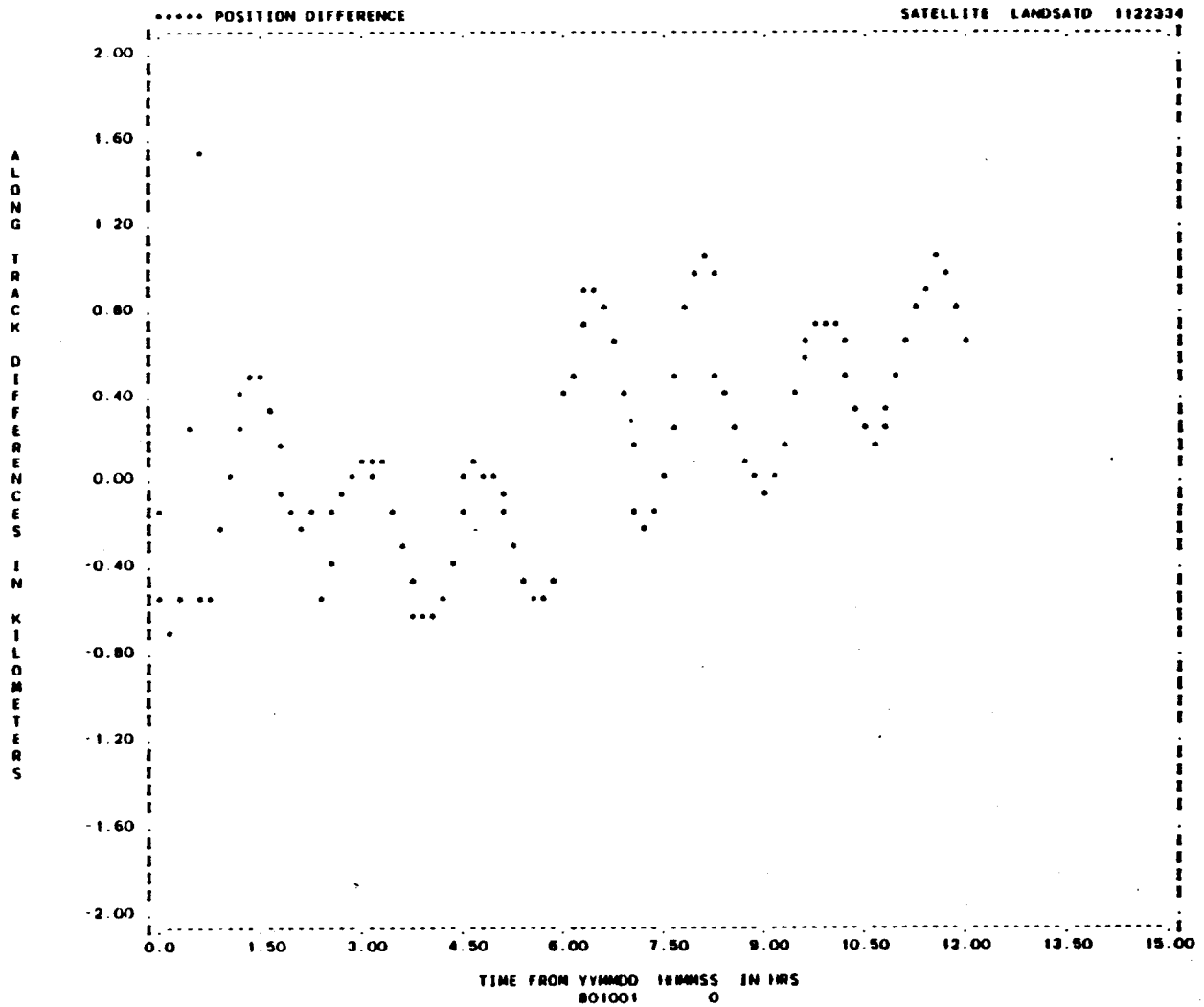

Figure A-102. Along-Track Differences for Run 010 (1 of 2)

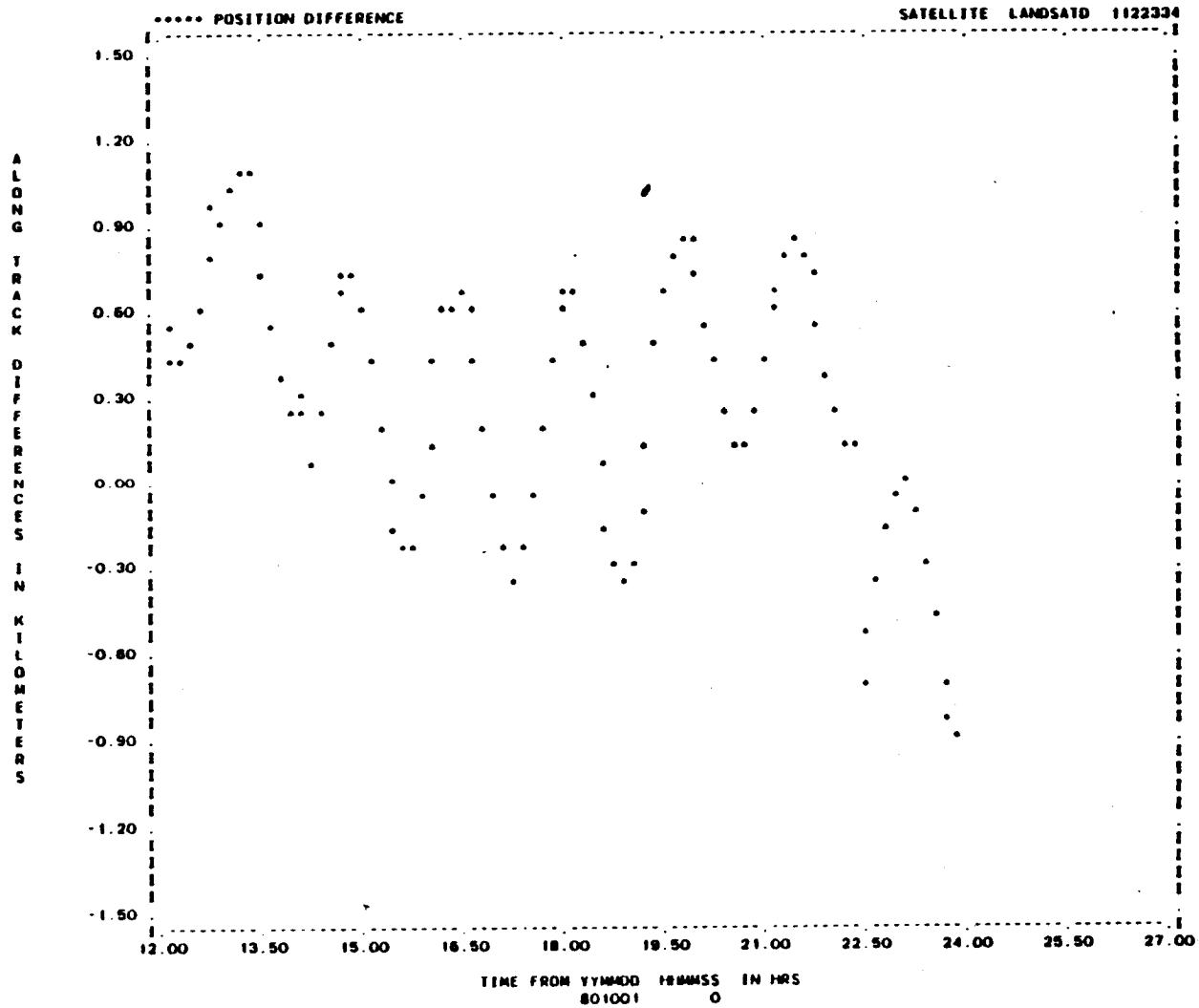

Figure A-102. Along-Track Differences for Run 010 (2 of 2)

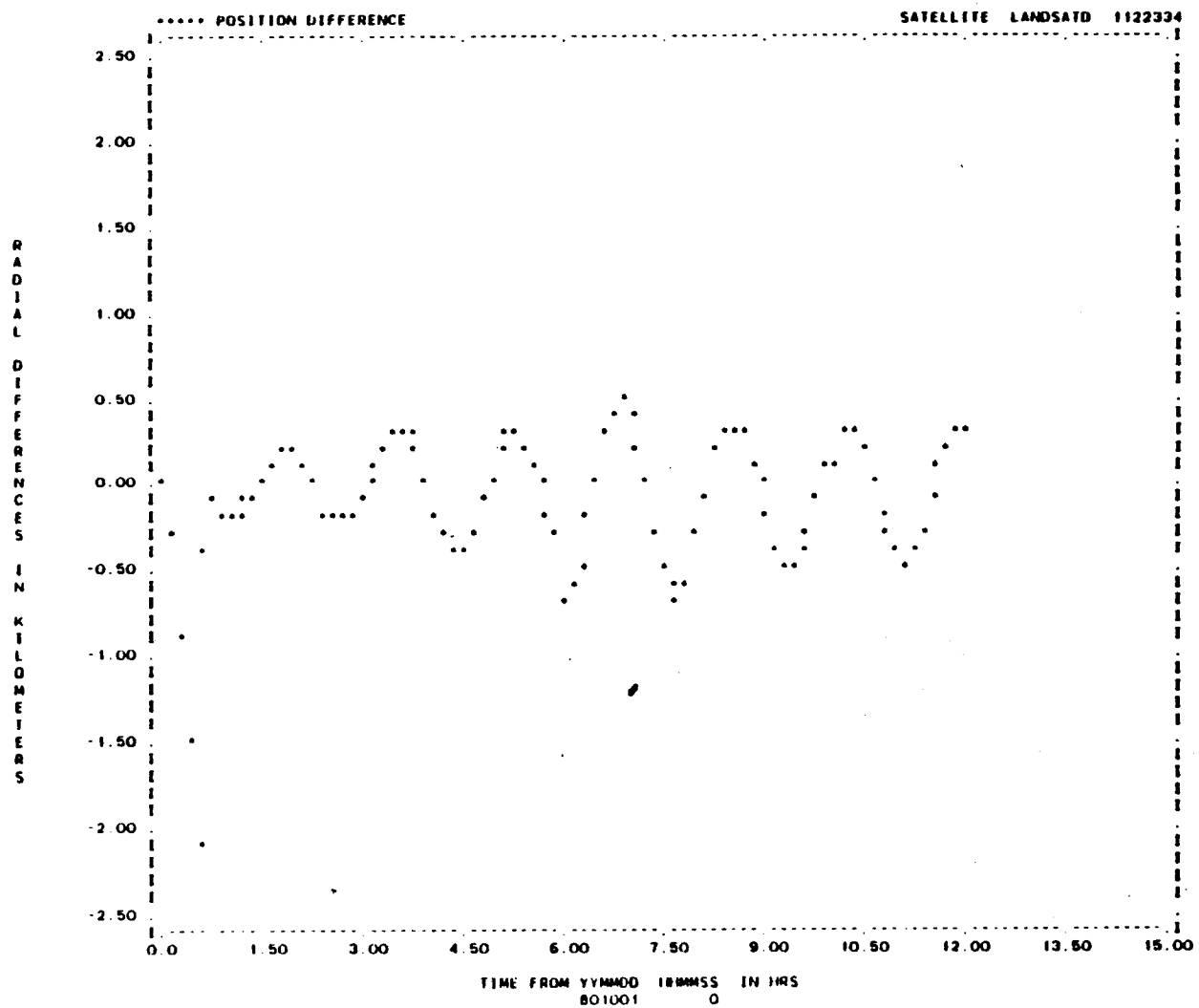

Figure A-103. Radial Differences for Run O11 (1 of 2)

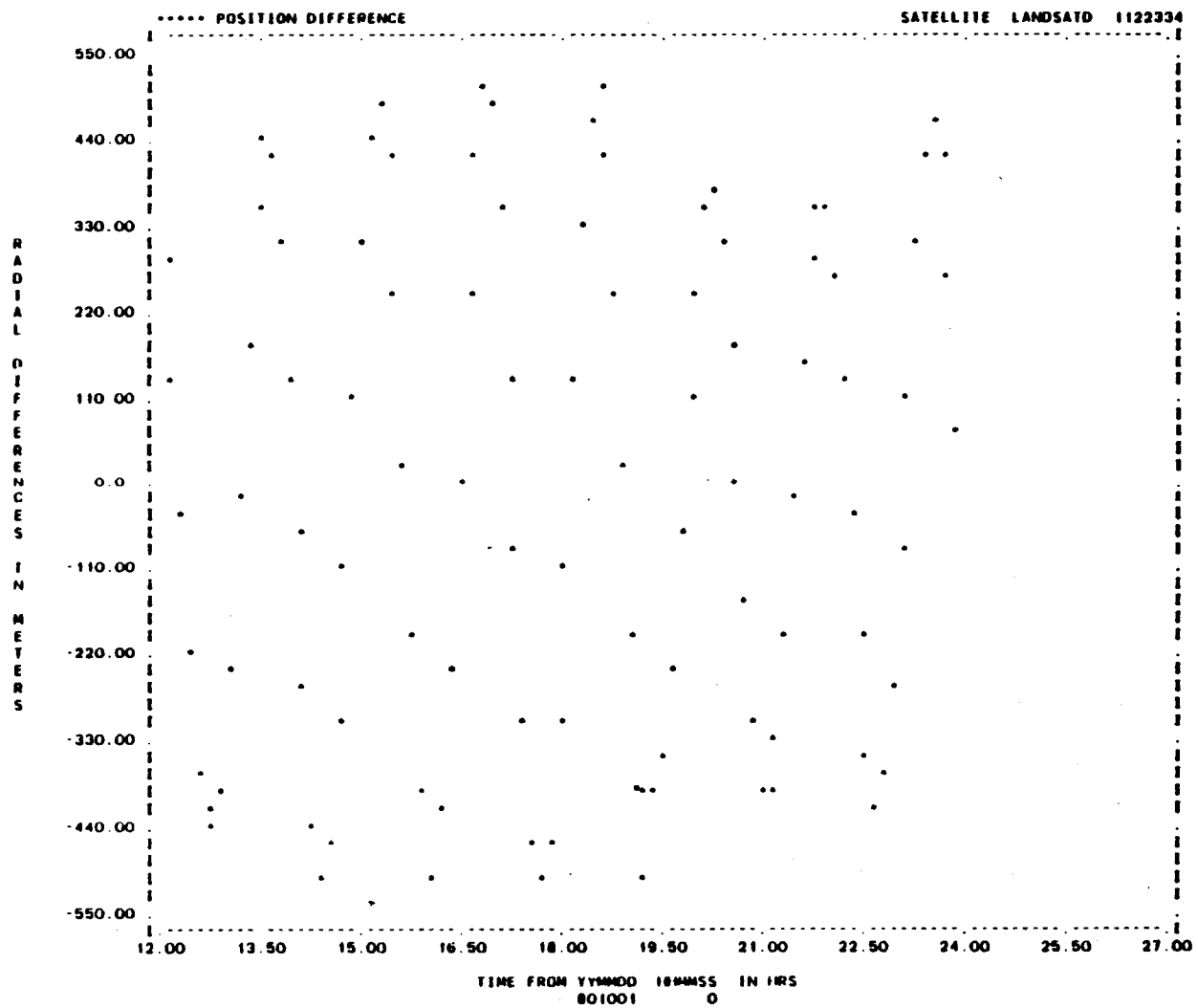

Figure A-103. Radial Differences for Run 011 (2 of 2)

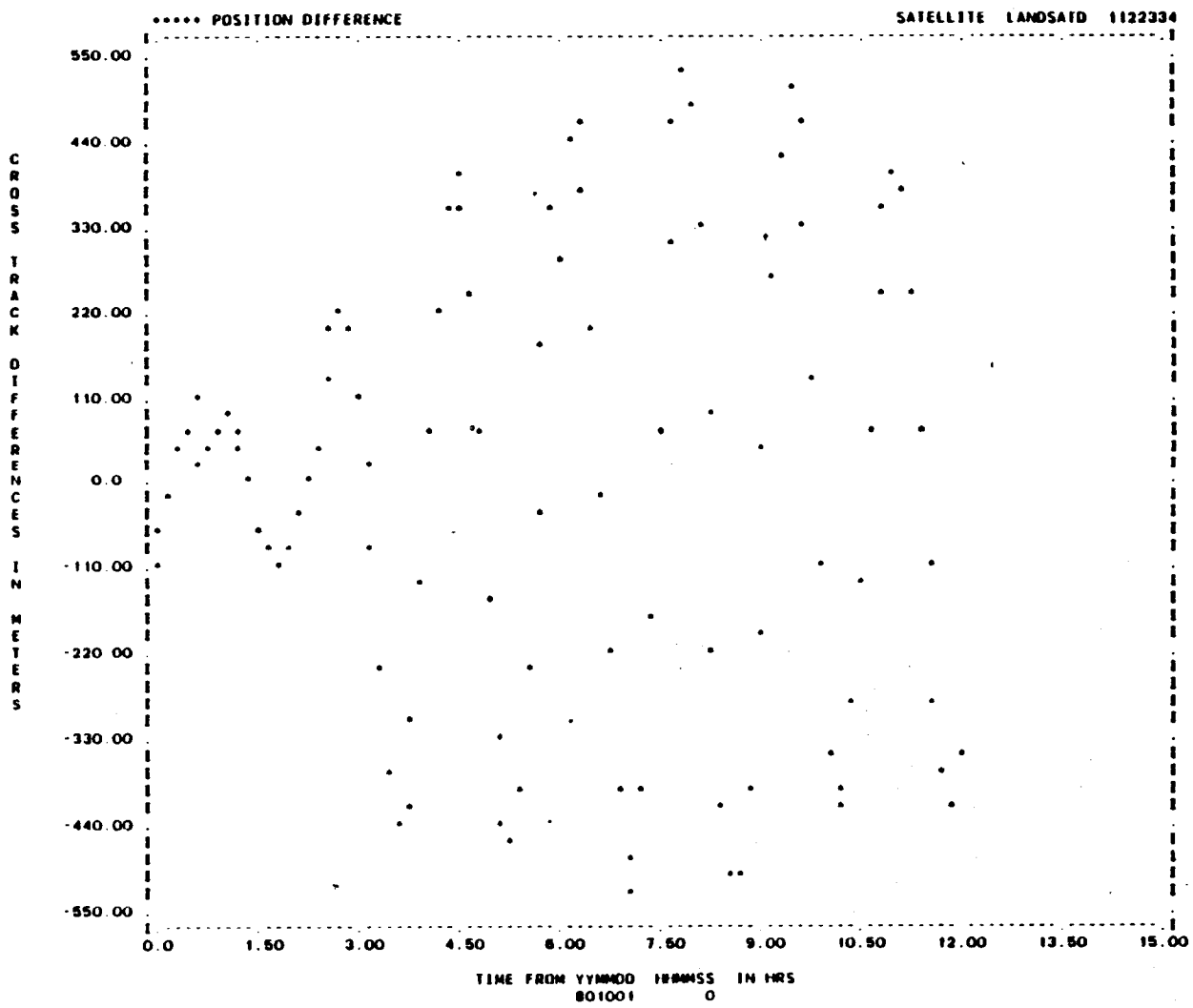

Figure A-104. Cross-Track Differences for Run O11 (1 of 2)

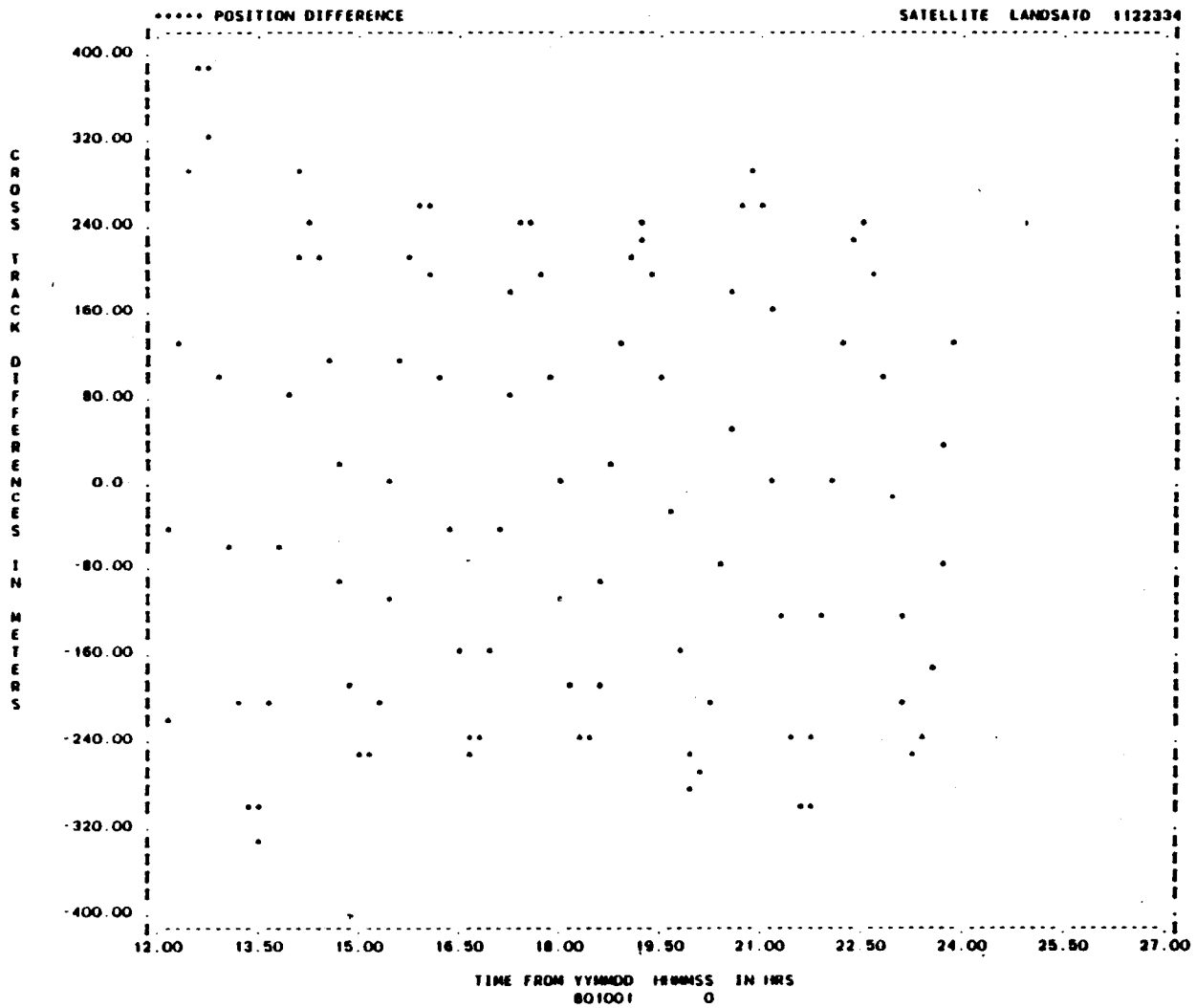

Figure A-104. Cross-Track Differences for Run O11 (2 of 2)

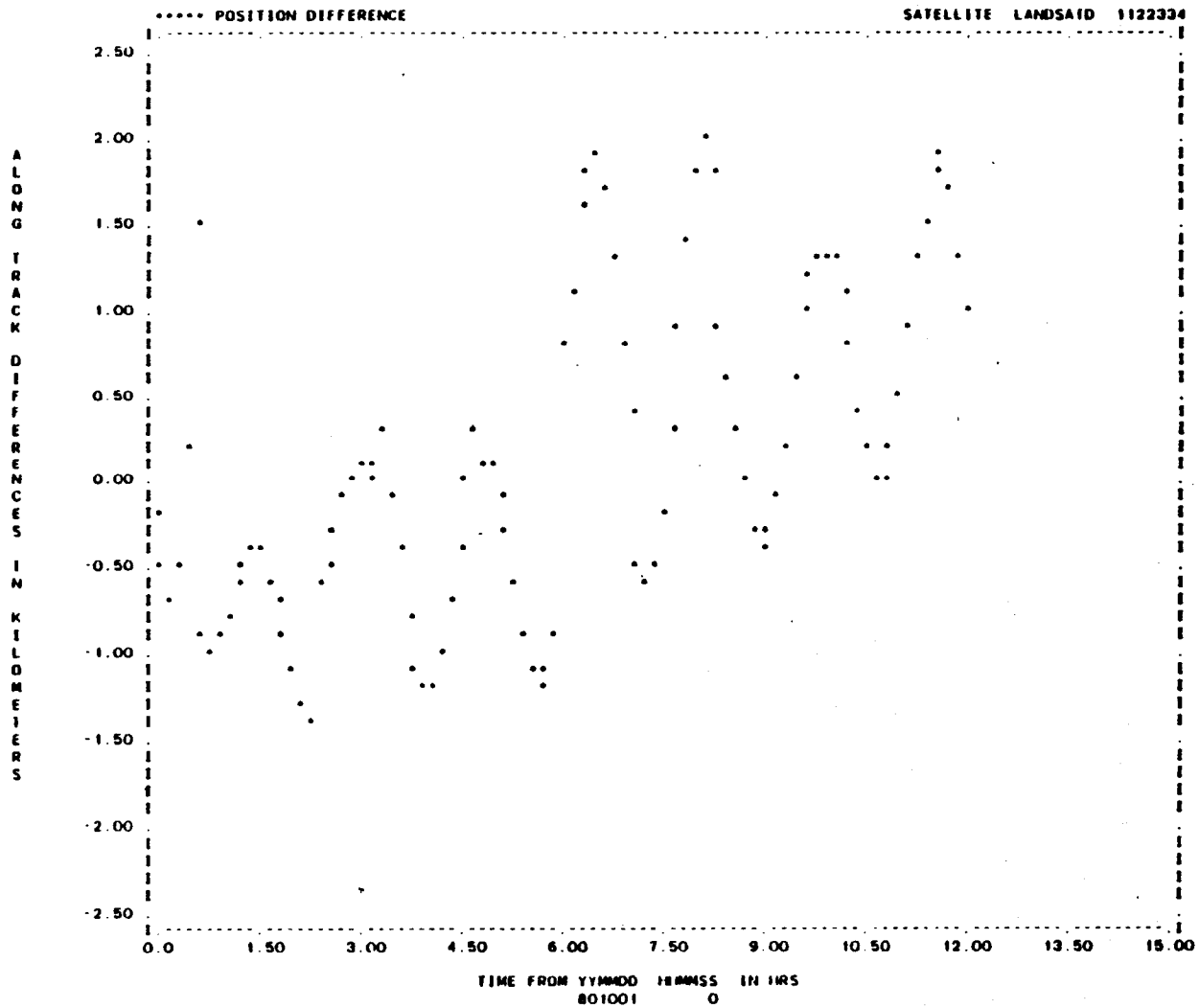

Figure A-105. Along-Track Differences for Run 011 (1 of 2)

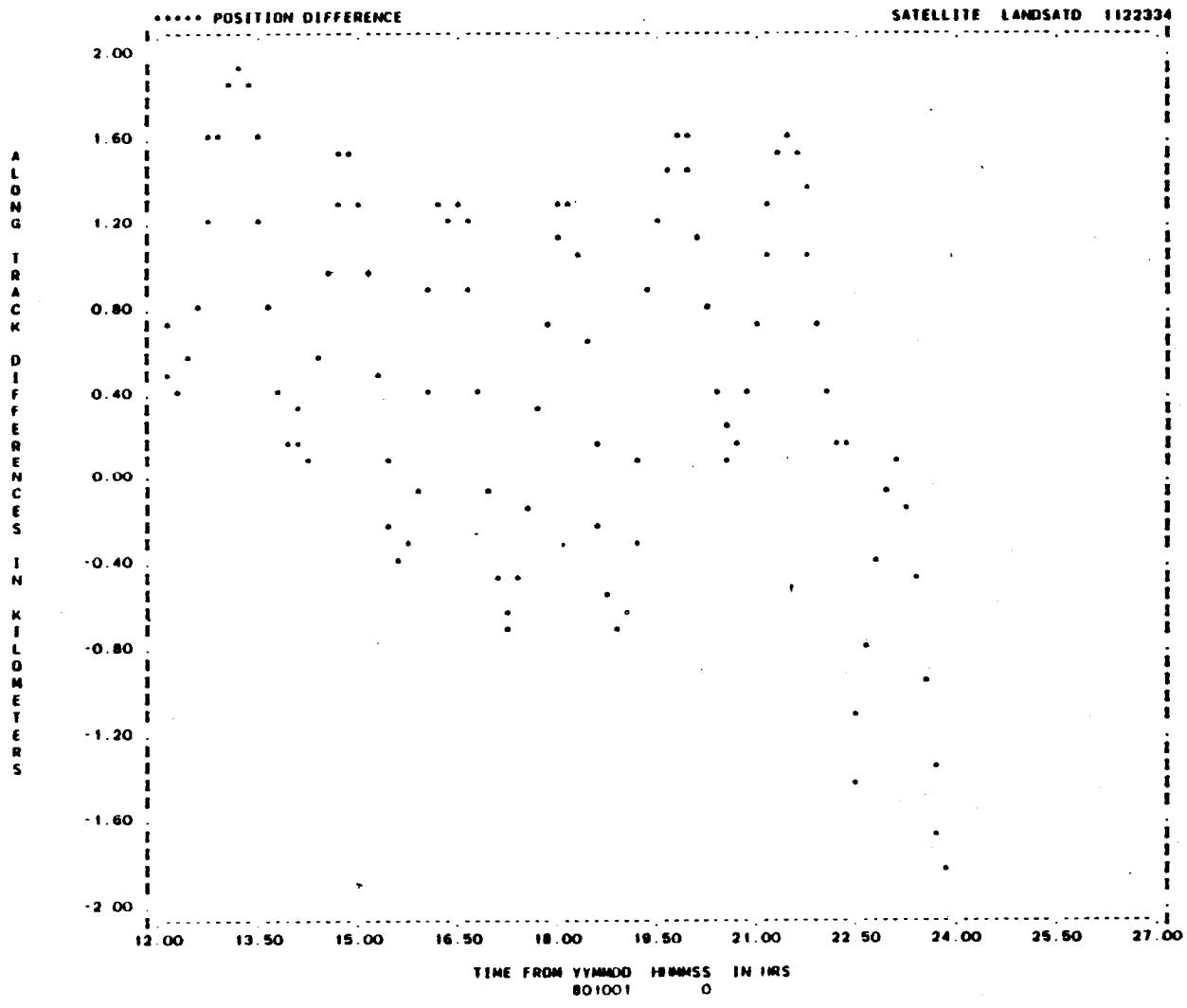

Figure A-105. Along-Track Differences for Run O11 (2 of 2)

APPENDIX B - GRO ERROR PLOTS

This appendix contains plots of the radial, cross-track, and along-track position differences that were obtained by differencing the "truth" and EKF estimated ephemerides for GRO. Table B-1 is an index to this appendix.

Table B-1. Appendix B Index

RUN NUMBER	TABLE REFERENCE	DATA PLOTTED[1]	TIME SPAN	FIGURE NUMBERS (B–)
P3	5–1	ΔR, ΔC, ΔL	0^h–24^h	1, 2, 3
P12	5–1	ΔR, ΔC, ΔL	0^h–24^h	4, 5, 6
P21	5–1	ΔR, ΔC, ΔL	0^h–24^h	7, 8, 9
P24	5–1	ΔR, ΔC, ΔL	0^h–24^h	10, 11, 12
P32	5–1	ΔR, ΔC, ΔL	0^h–24^h	13, 14, 15
P34	5–1	ΔR, ΔC, ΔL	0^h–24^h	16, 17, 18
P37	5–1	ΔR, ΔC, ΔL	0^h–24^h	19, 20, 21
Q3	5–2	ΔR, ΔC, ΔL	0^h–24^h	22, 23, 24
Q5	5–2	ΔR, ΔC, ΔL	0^h–24^h	25, 26, 27
Q9	5–2	ΔR, ΔC, ΔL	0^h–24^h	28, 29, 30
Q13	5–2	ΔR, ΔC, ΔL	0^h–24^h	31, 32, 33
Q17	5–2	ΔR, ΔC, ΔL	0^h–24^h	34, 35, 36
Q20	5–2	ΔR, ΔC, ΔL	0^h–24^h	37, 38, 39
R8	5–3	ΔR, ΔC, ΔL	0^h–24^h	40, 41, 42
R11	5–3	ΔR, ΔC, ΔL	0^h–24^h	43, 44, 45
R15	5–3	ΔR, ΔC, ΔL	0^h–24^h	46, 47, 48
S3	5–4	ΔR, ΔC, ΔL	0^h–24^h	49, 50, 51
T1	5–6	ΔR, ΔC, ΔL	0^h–24^h	52, 53, 54
T2	5–6	ΔR, ΔC, ΔL	0^h–24^h	55, 56, 57
T3	5–6	ΔR, ΔC, ΔL	0^h–24^h	58, 59, 60
T4	5–6	ΔR, ΔC, ΔL	0^h–24^h	61, 62, 63
T5	5–6	ΔR, ΔC, ΔL	0^h–24^h	64, 65, 66
T7	5–7	ΔR, ΔC, ΔL	0^h–24^h	67, 68, 69
T10	5–7	ΔR, ΔC, ΔL	0^h–24^h	70, 71, 72
T11	5–7	ΔR, ΔC, ΔL	0^h–24^h	73, 74, 75

7526/80

[1] ΔR = RADIAL POSITION DIFFERENCE; ΔC = CROSS-TRACK POSITION DIFFERENCE; ΔL = ALONG-TRACK POSITION DIFFERENCE.

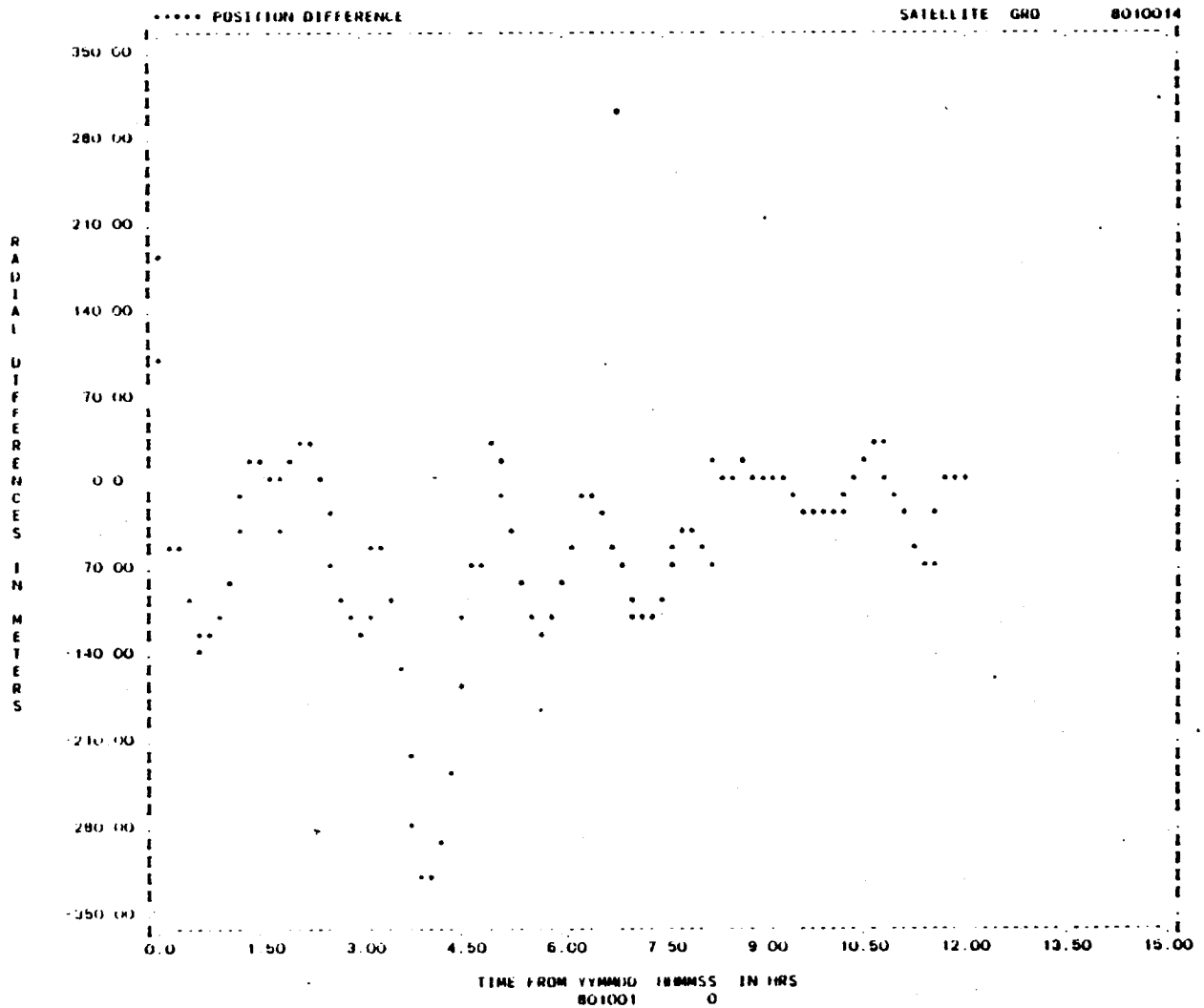

Figure B-1. Radial Differences for Run P3 (1 of 2)

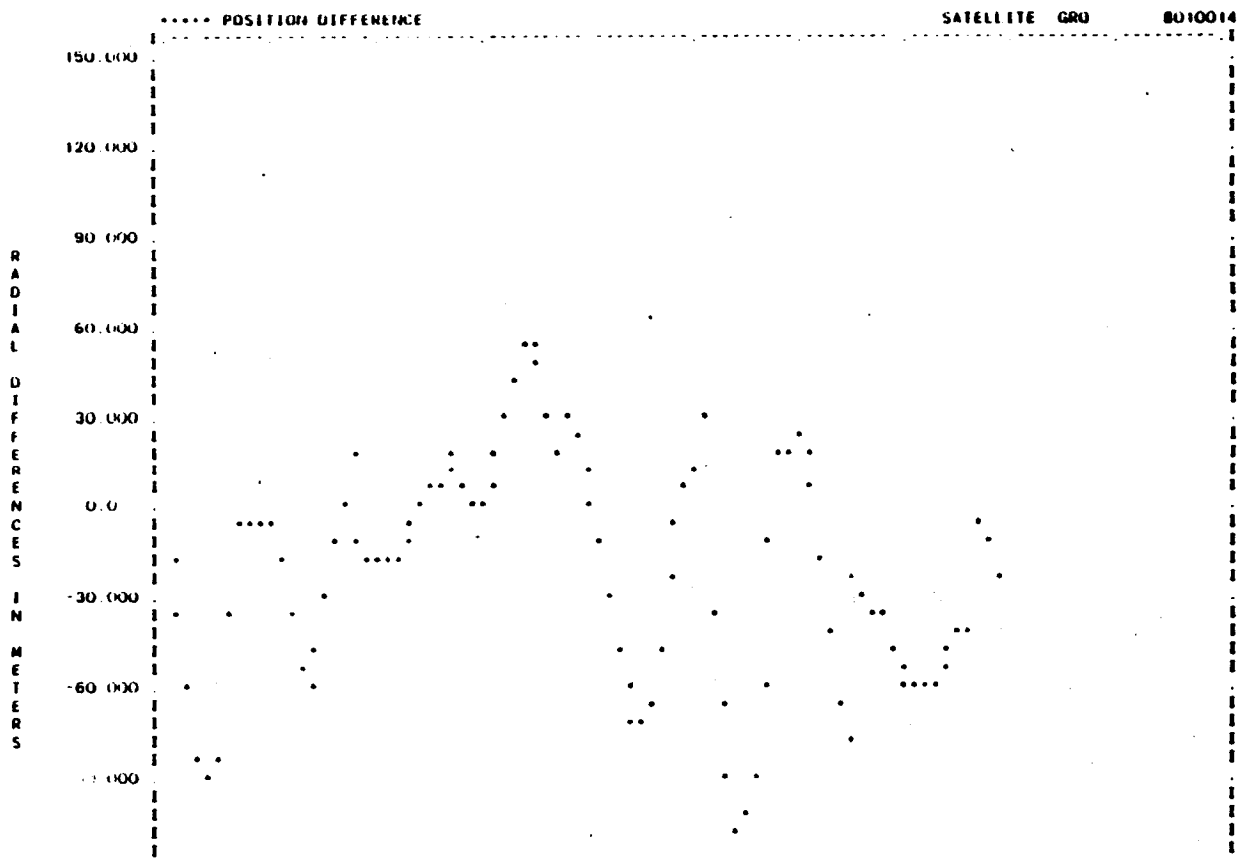

Figure B-1. Radial Differences for Run P3 (2 of 2)

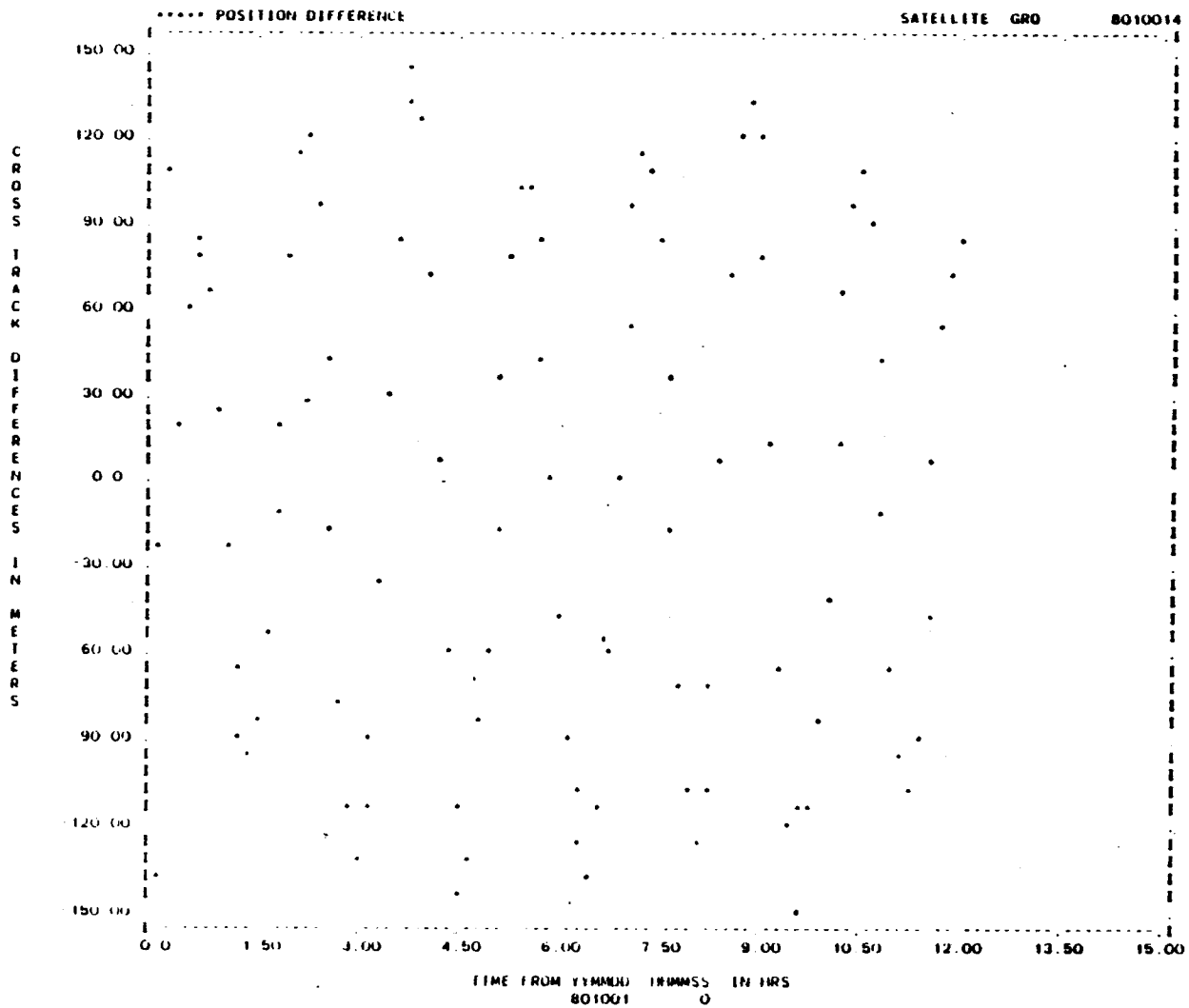

Figure B-2. Cross-Track Differences for Run P3 (1 of 2)

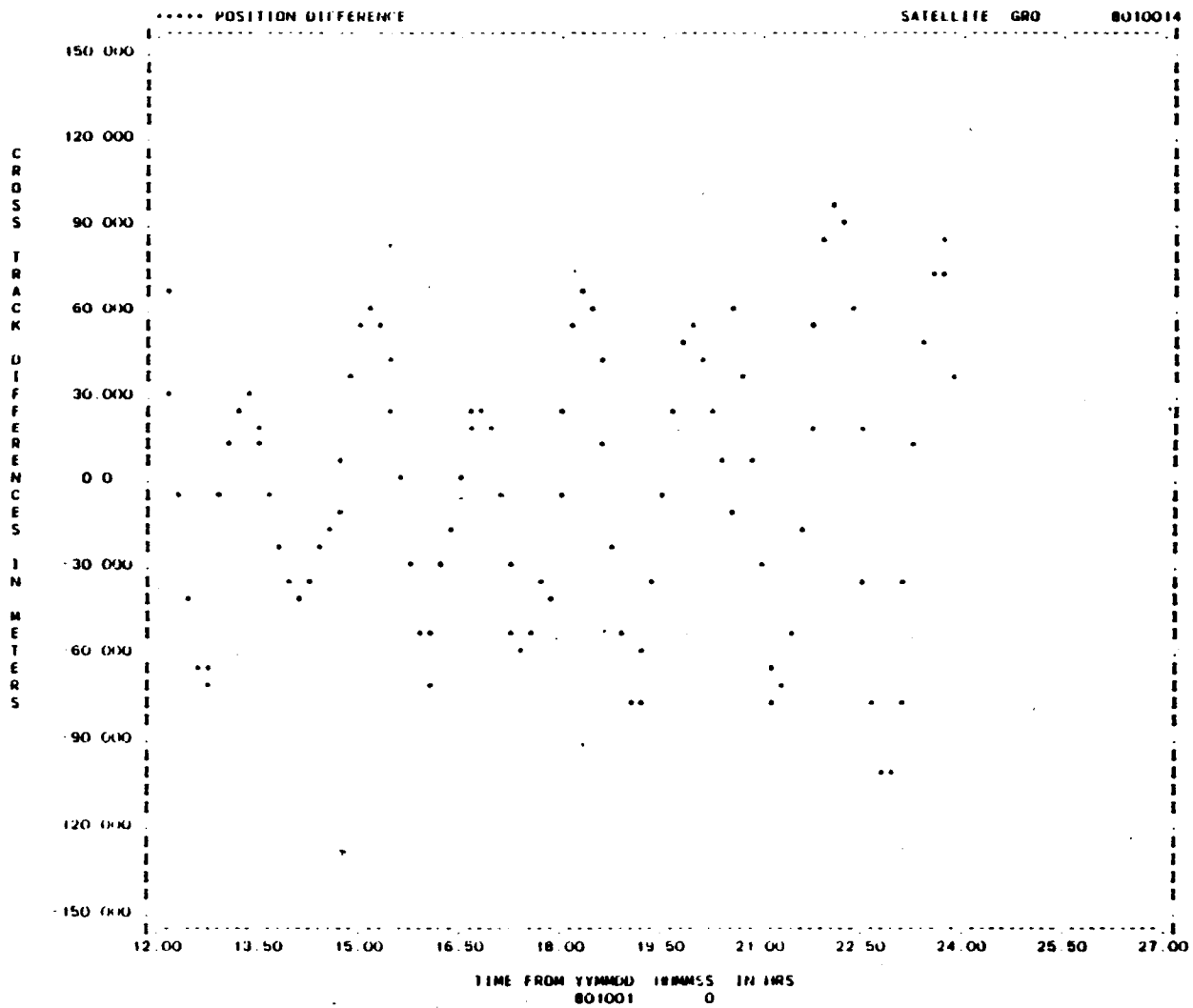

Figure B-2. Cross-Track Differences for Run P3 (2 of 2)

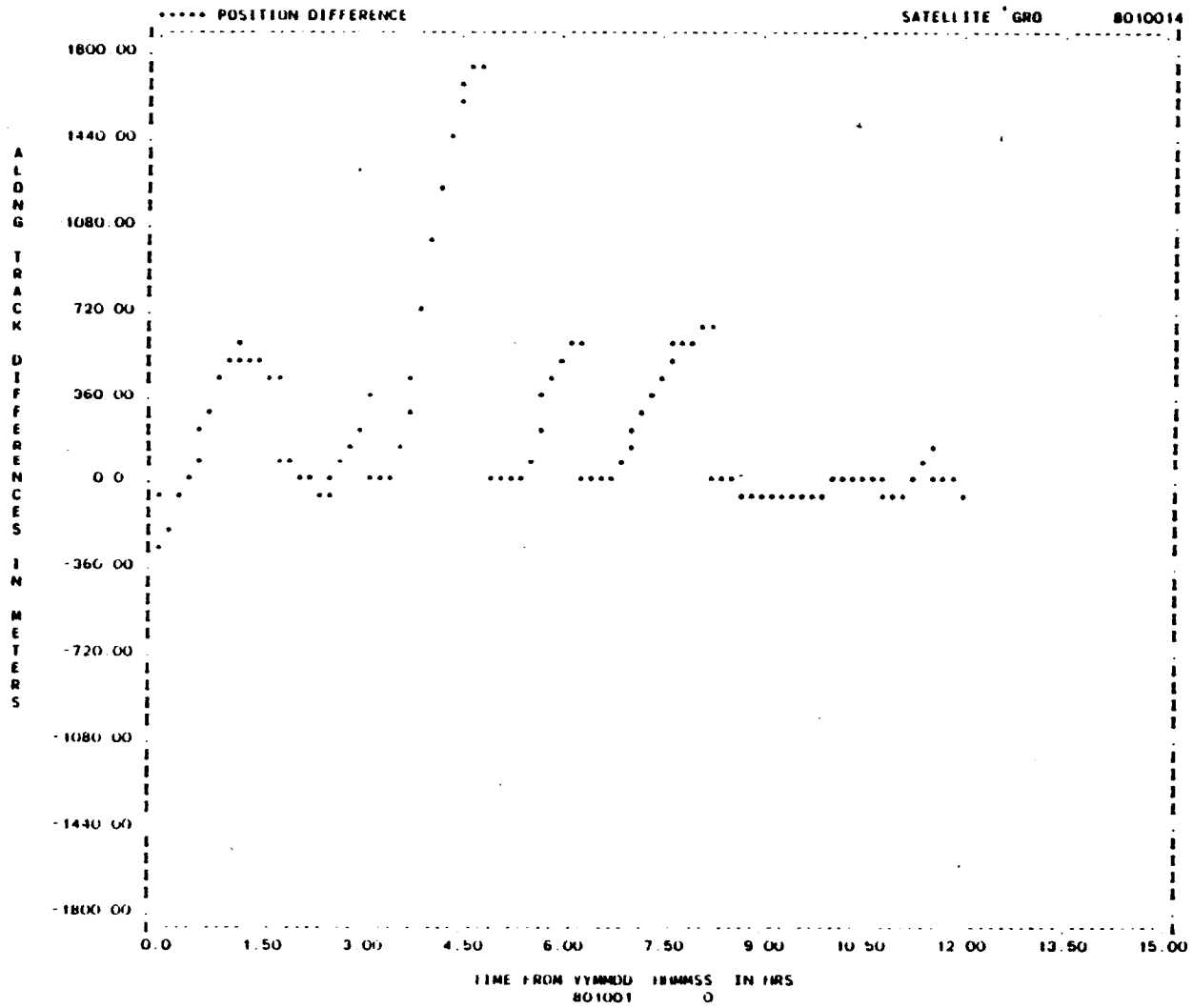

Figure B-3. Along-Track Differences for Run P3 (1 of 2)

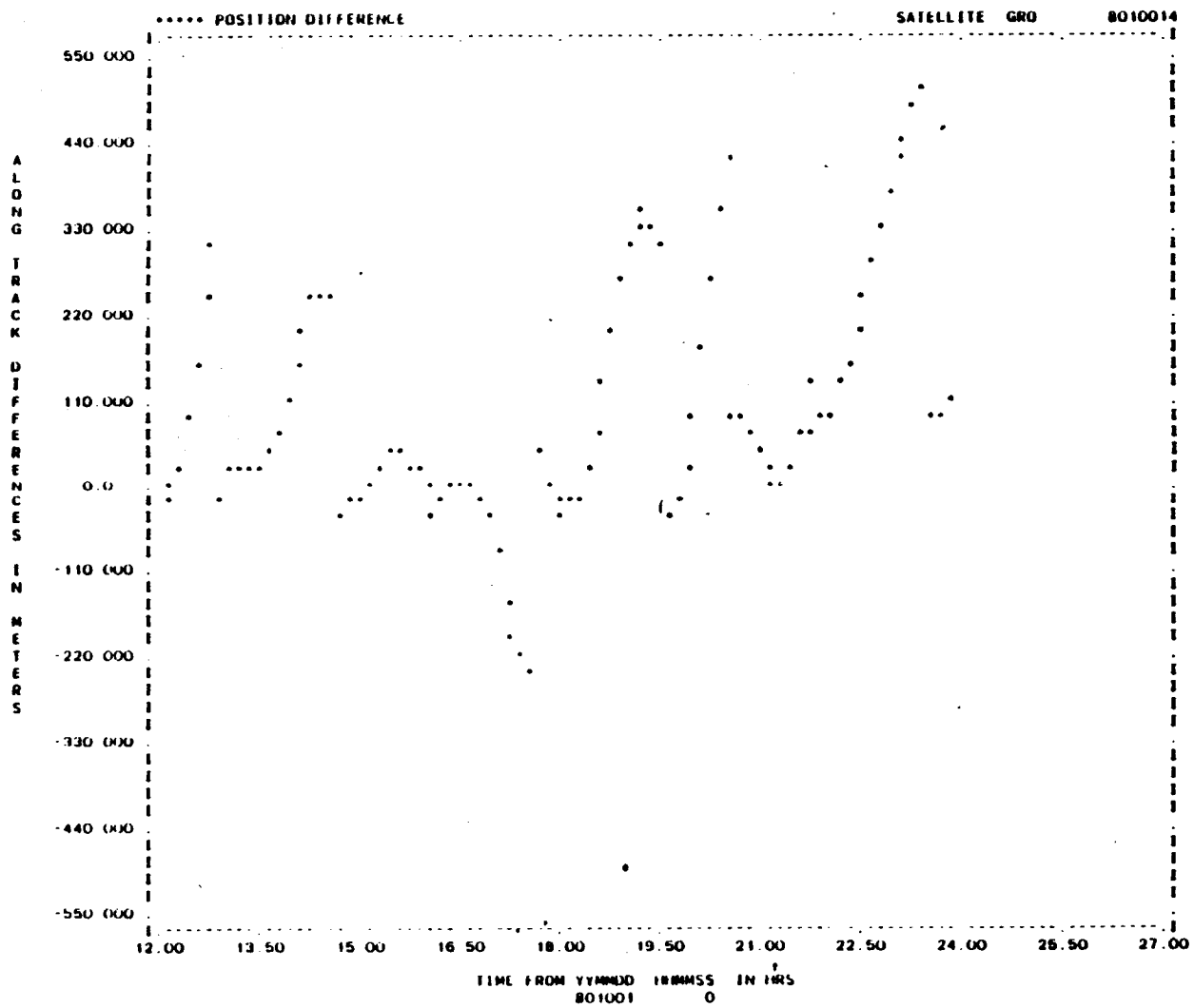

Figure B-3. Along-Track Differences for Run P3 (2 of 2)

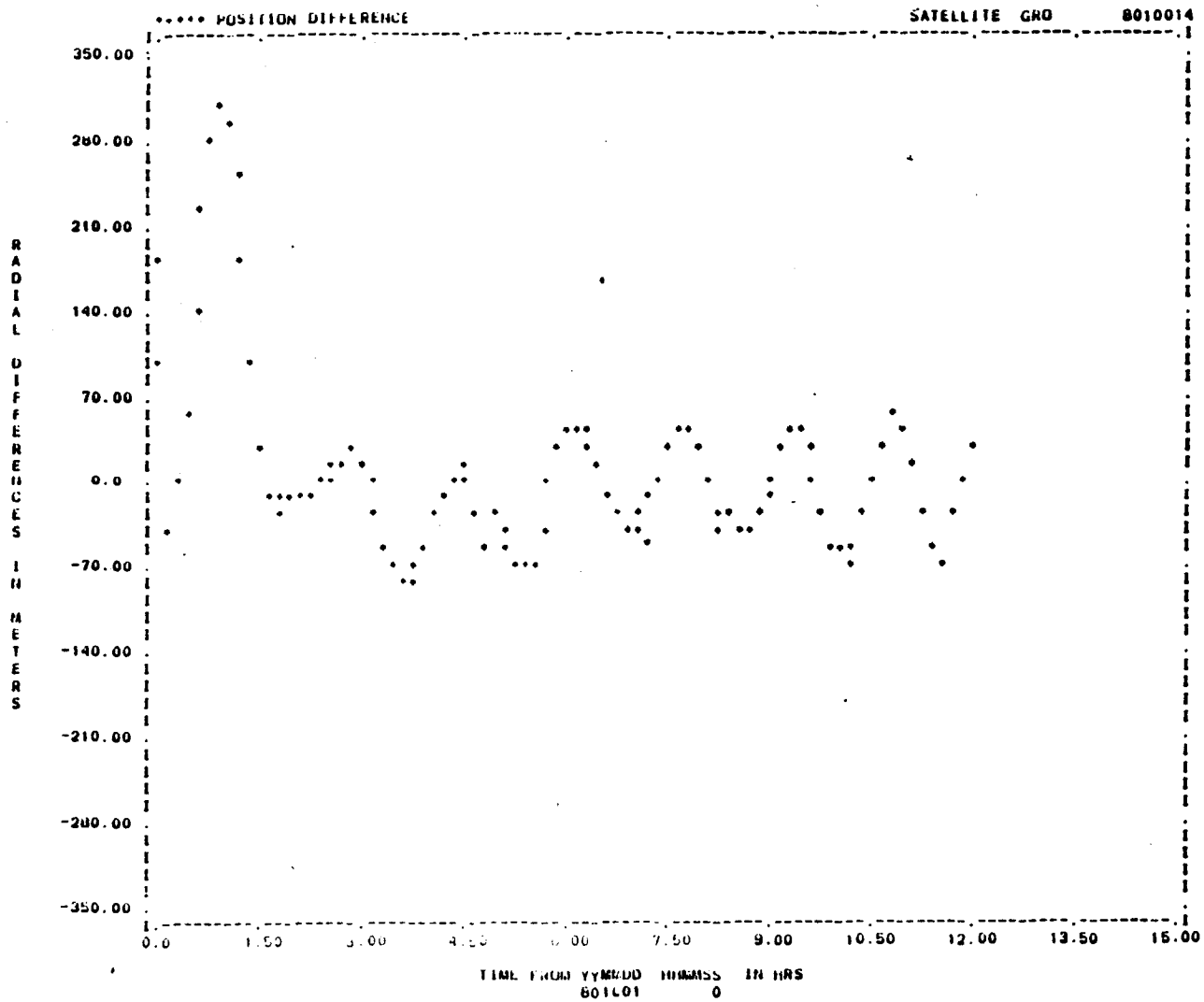

Figure B-4. Radial Differences for Run P12 (1 of 2)

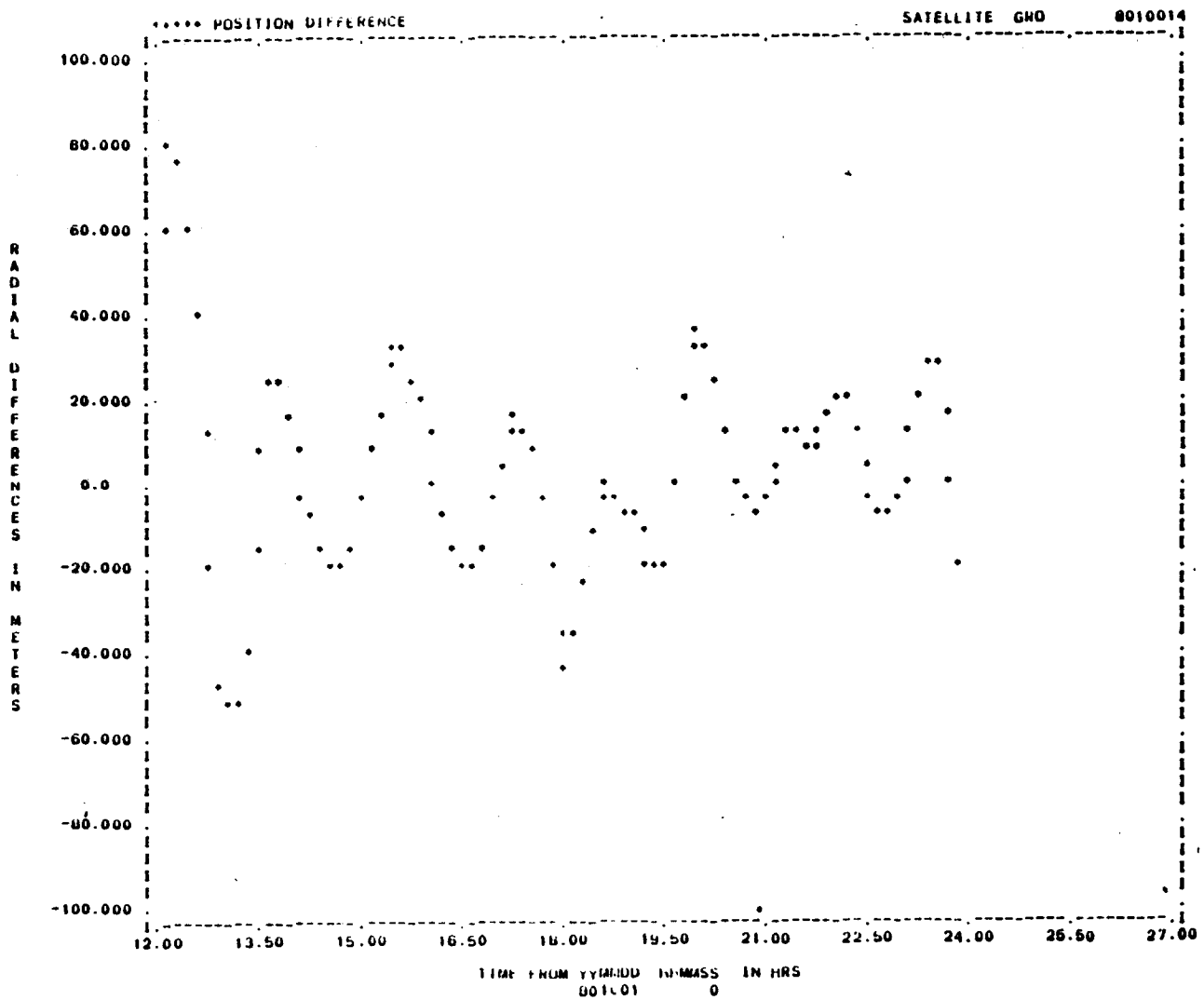

Figure B-4. Radial Differences for Run P12 (2 of 2)

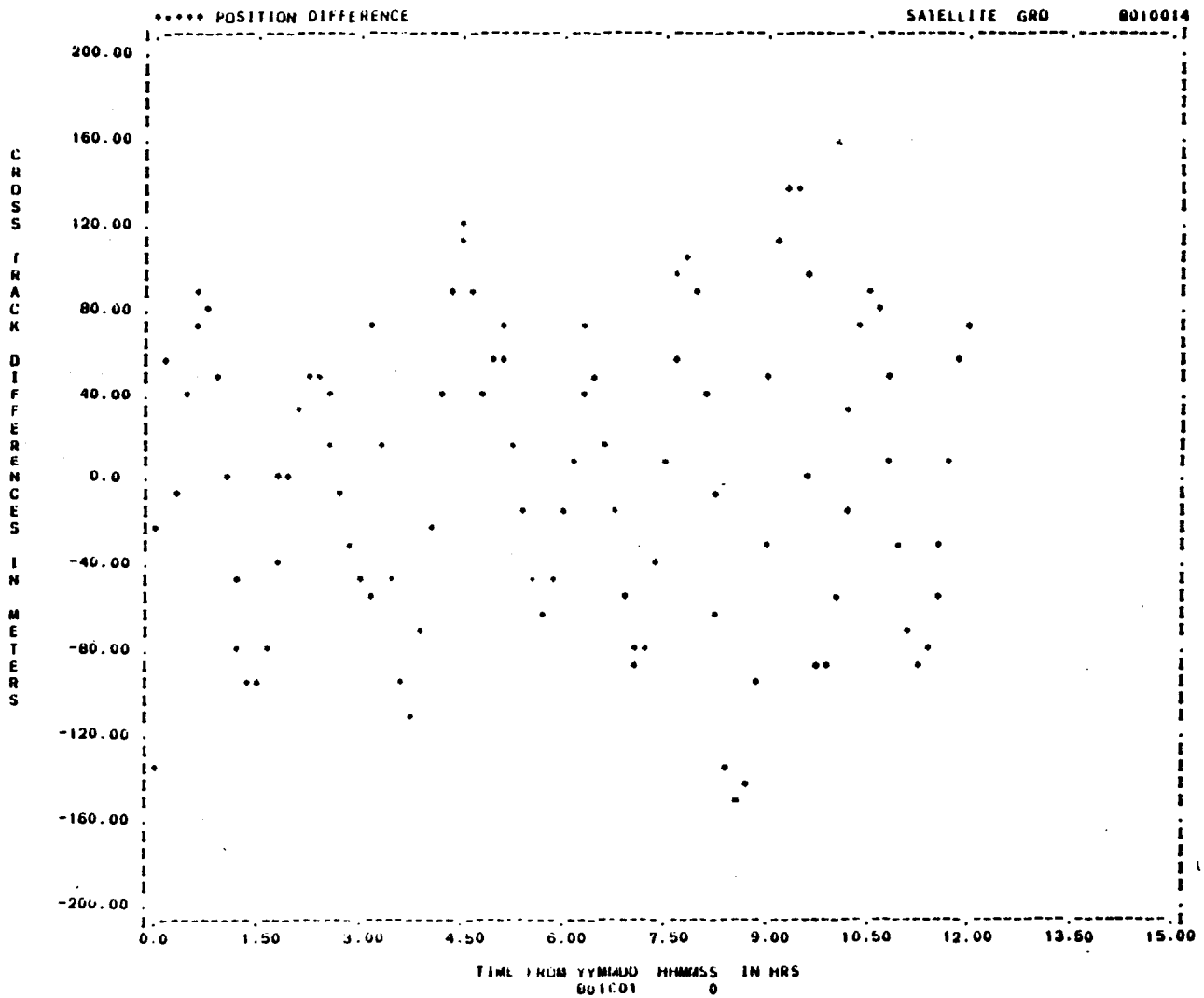

Figure B-5. Cross-Track Differences for Run P12 (1 of 2)

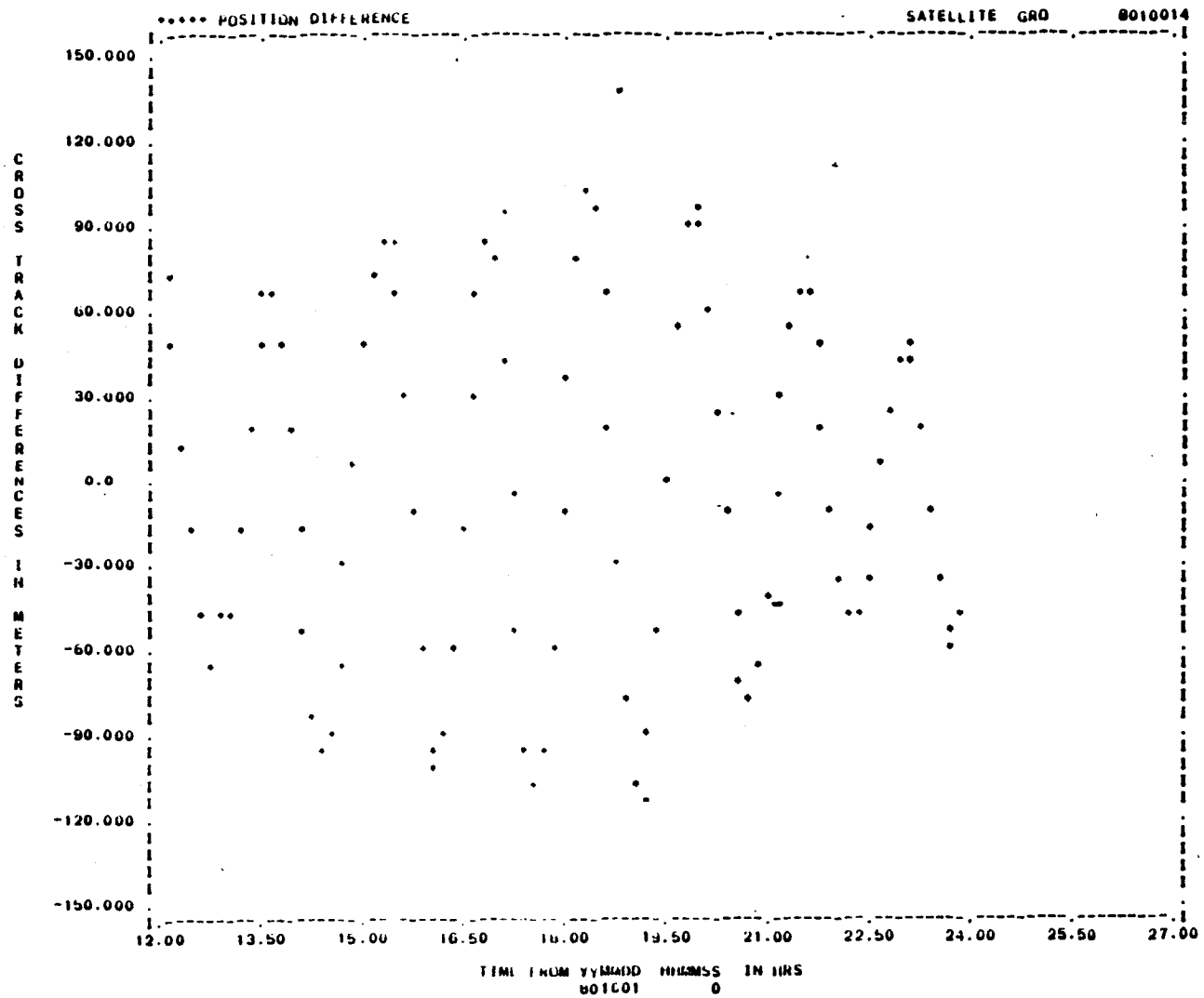

Figure B-5. Cross-Track Differences for Run P12 (2 of 2)

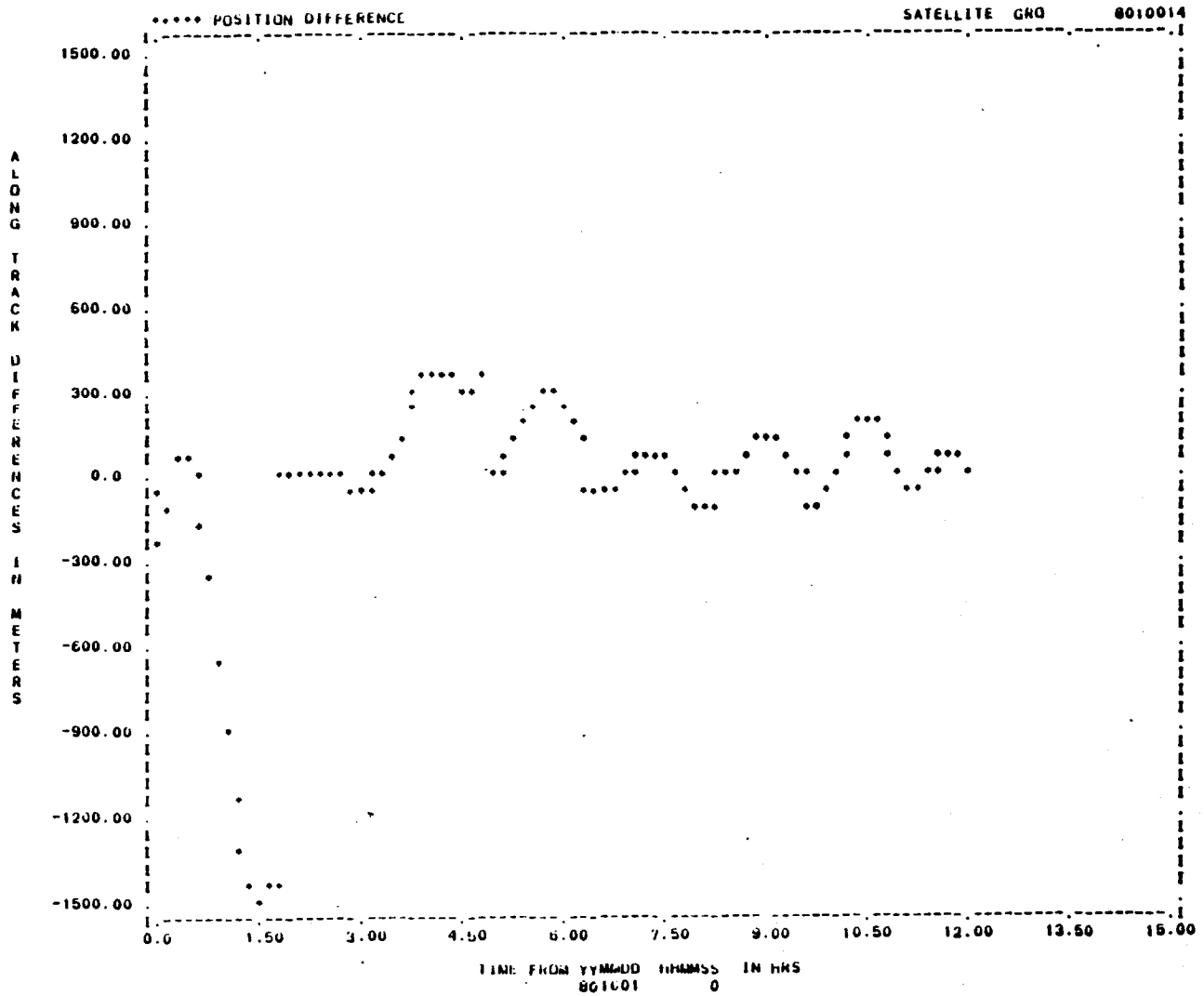

Figure B-6. Along-Track Differences for Run P12 (1 of 2)

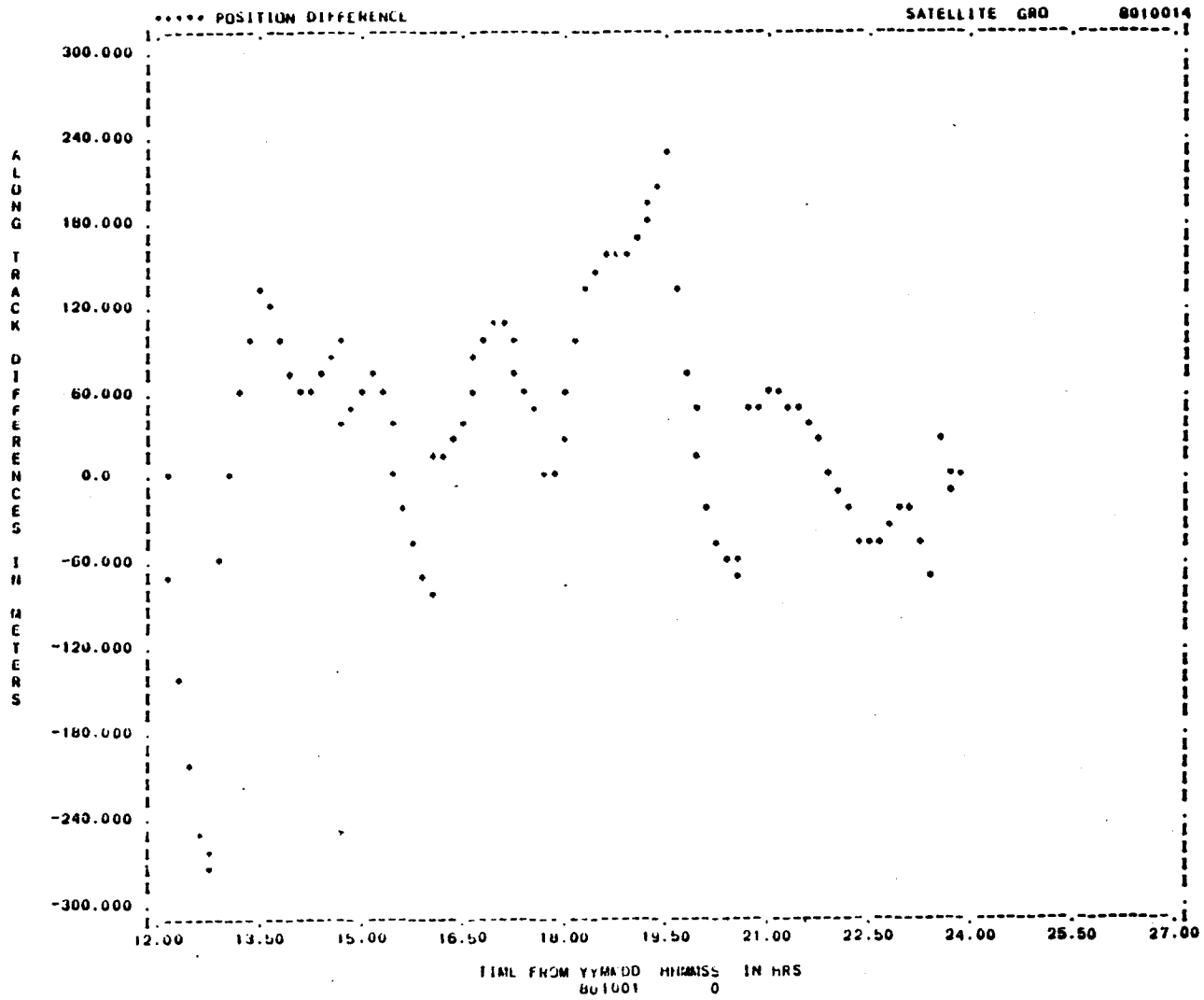

Figure B-6. Along-Track Differences for Run P12 (2 of 2)

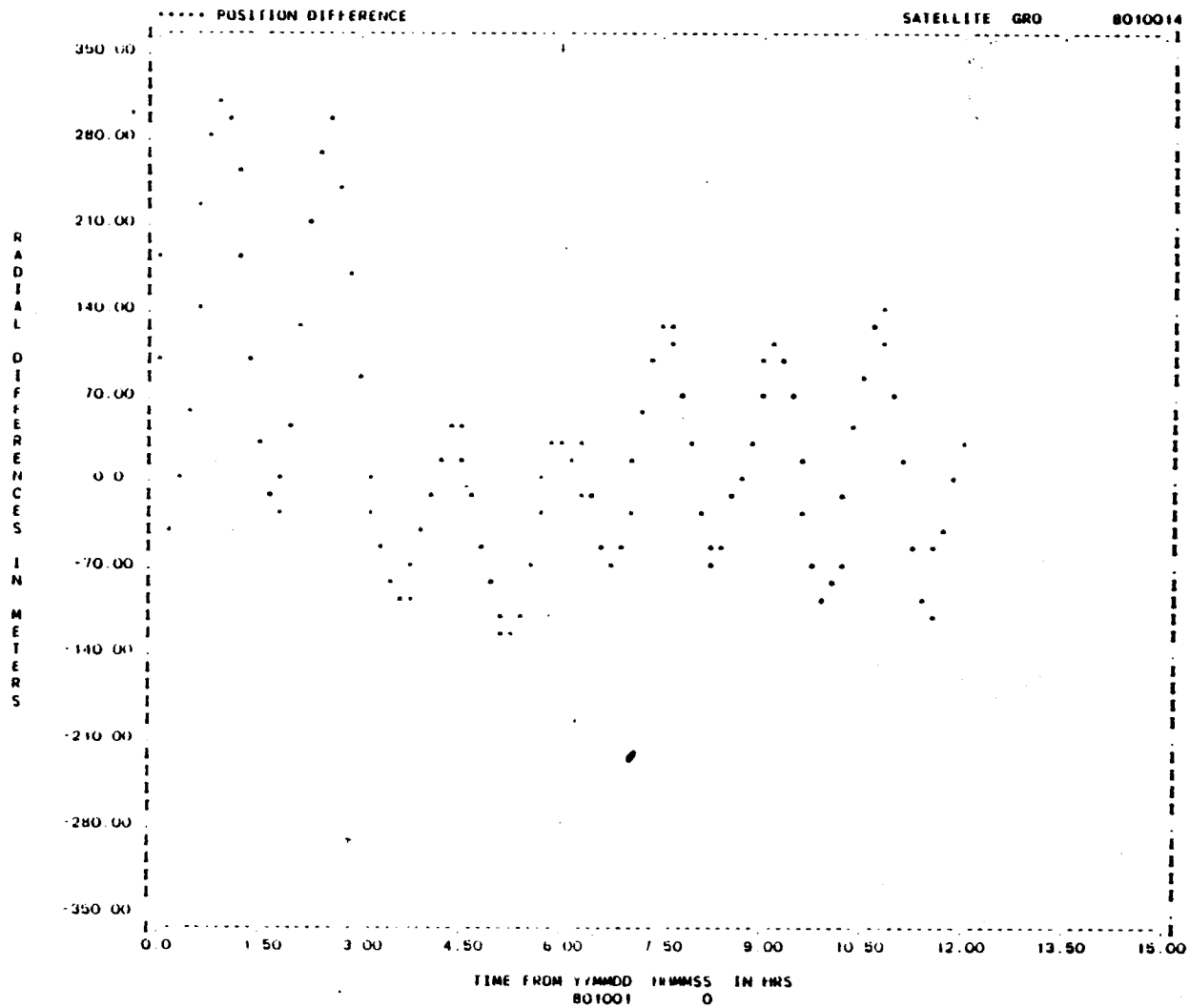

Figure B-7. Radial Differences for Run P21 (1 of 2)

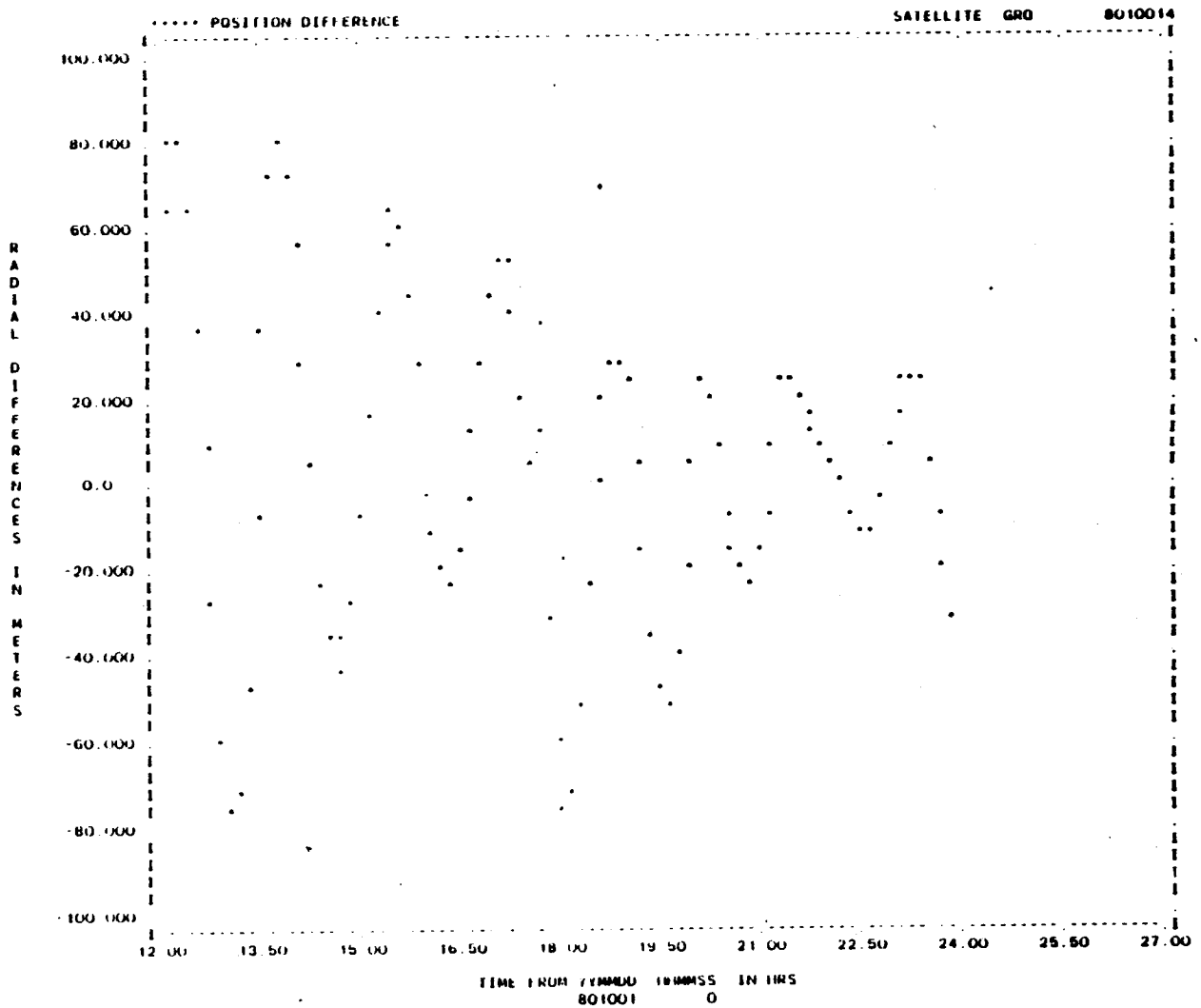

Figure B-7. Radial Differences for Run P21 (2 of 2)

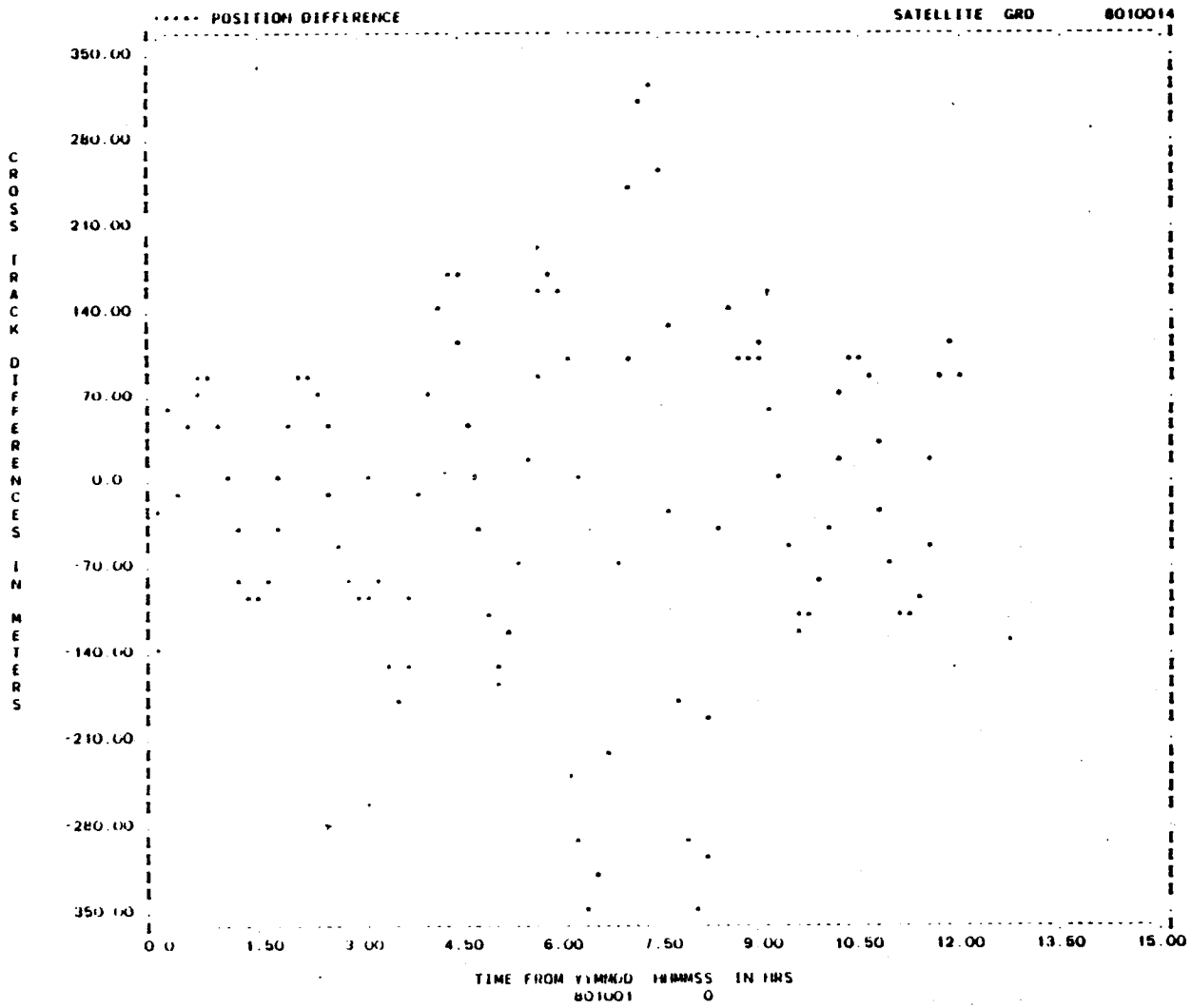

Figure B-8. Cross-Track Differences for Run P21 (1 of 2)

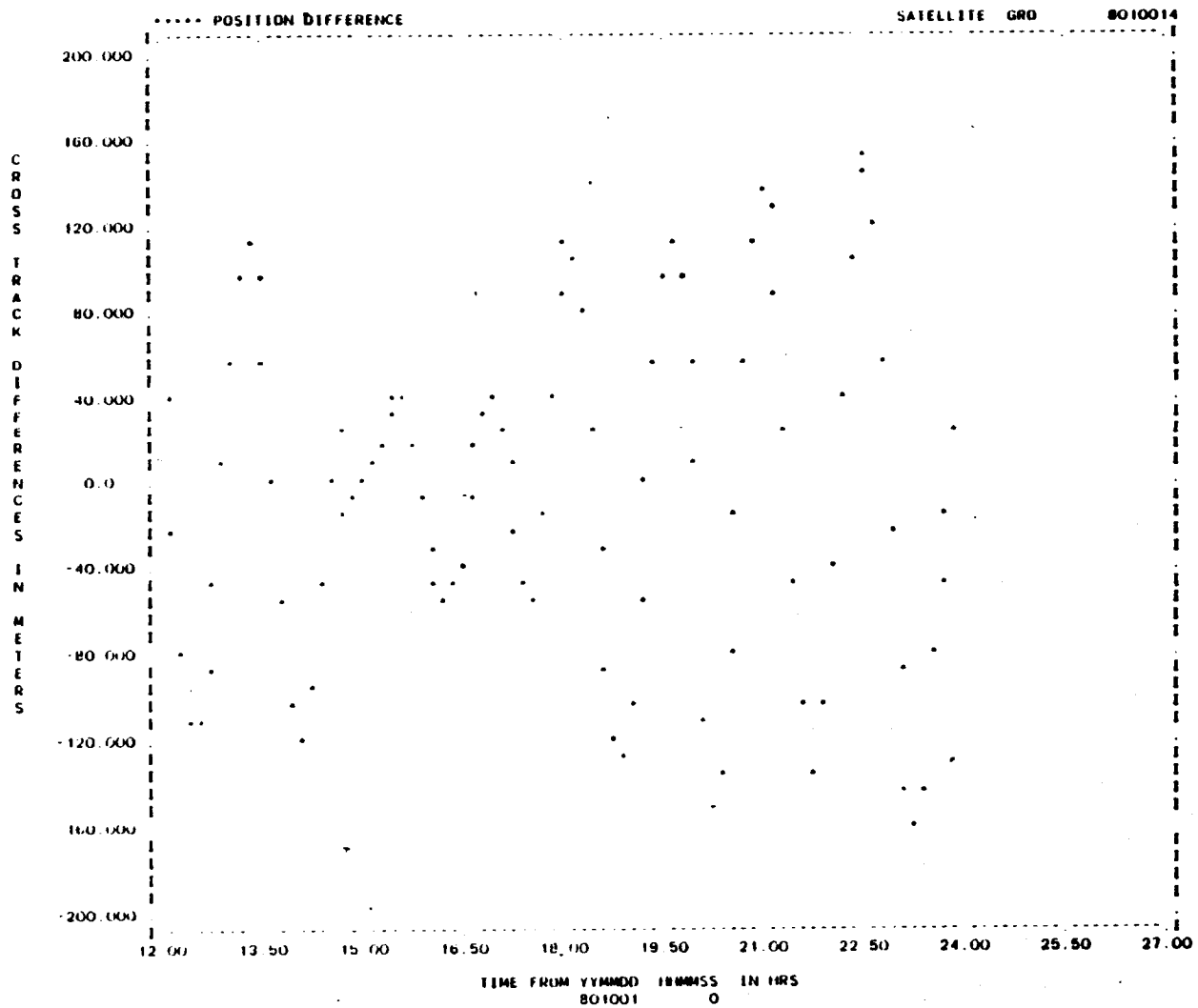

Figure B-8. Cross-Track Differences for Run P21 (2 of 2)

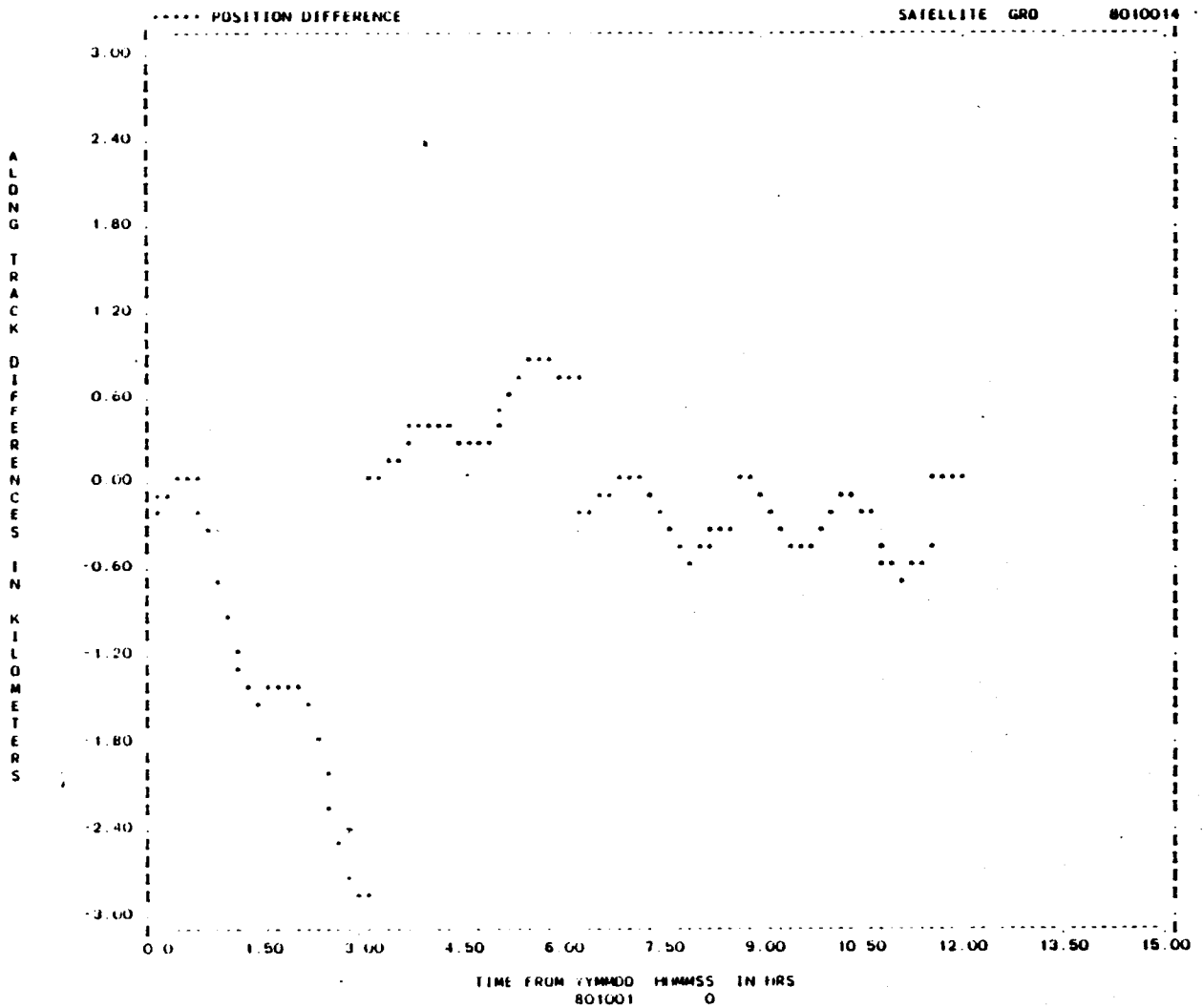

Figure B-9. Along-Track Differences for Run P21 (1 of 2)

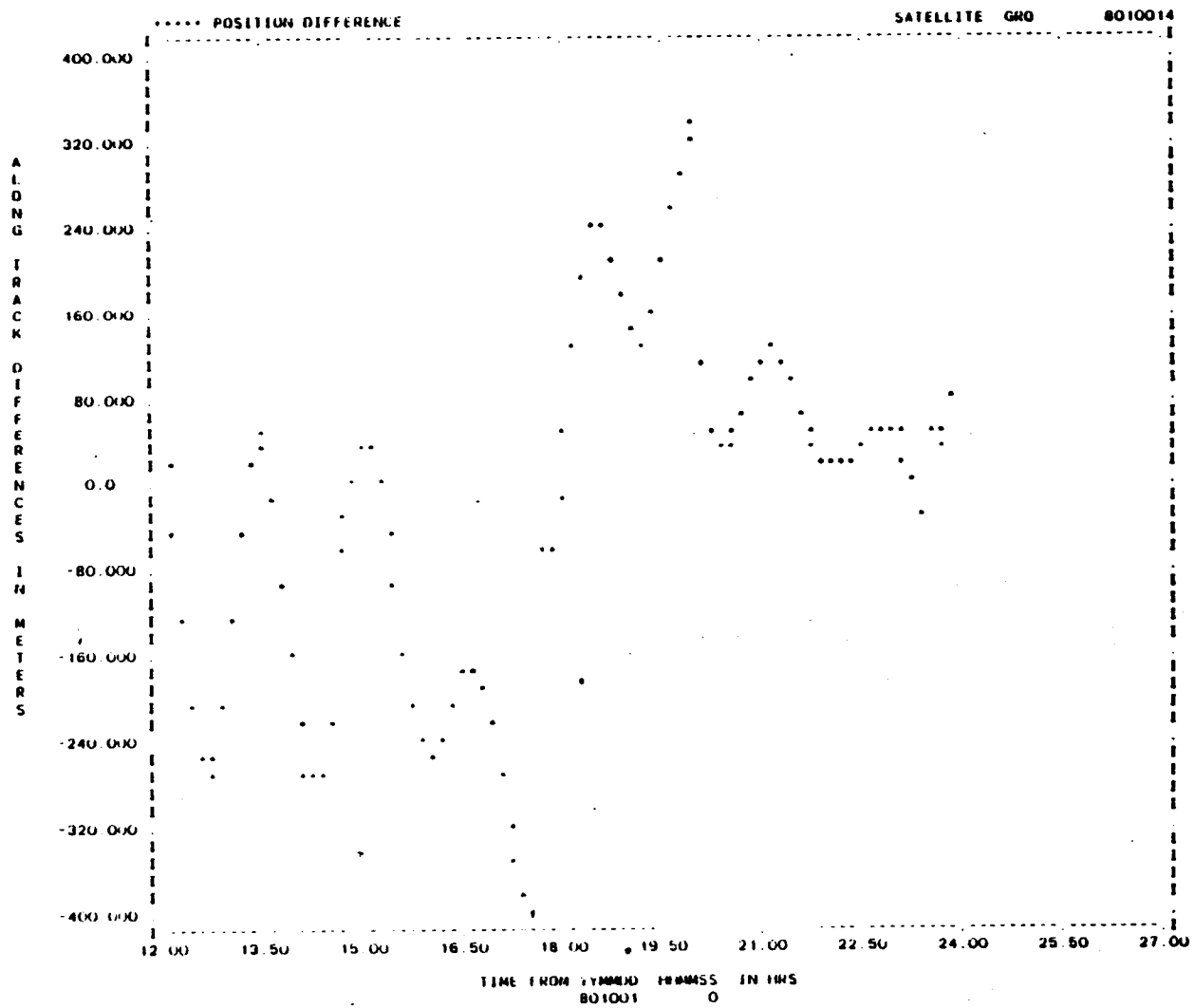

Figure B-9. Along-Track Differences for Run P21 (1 of 2)

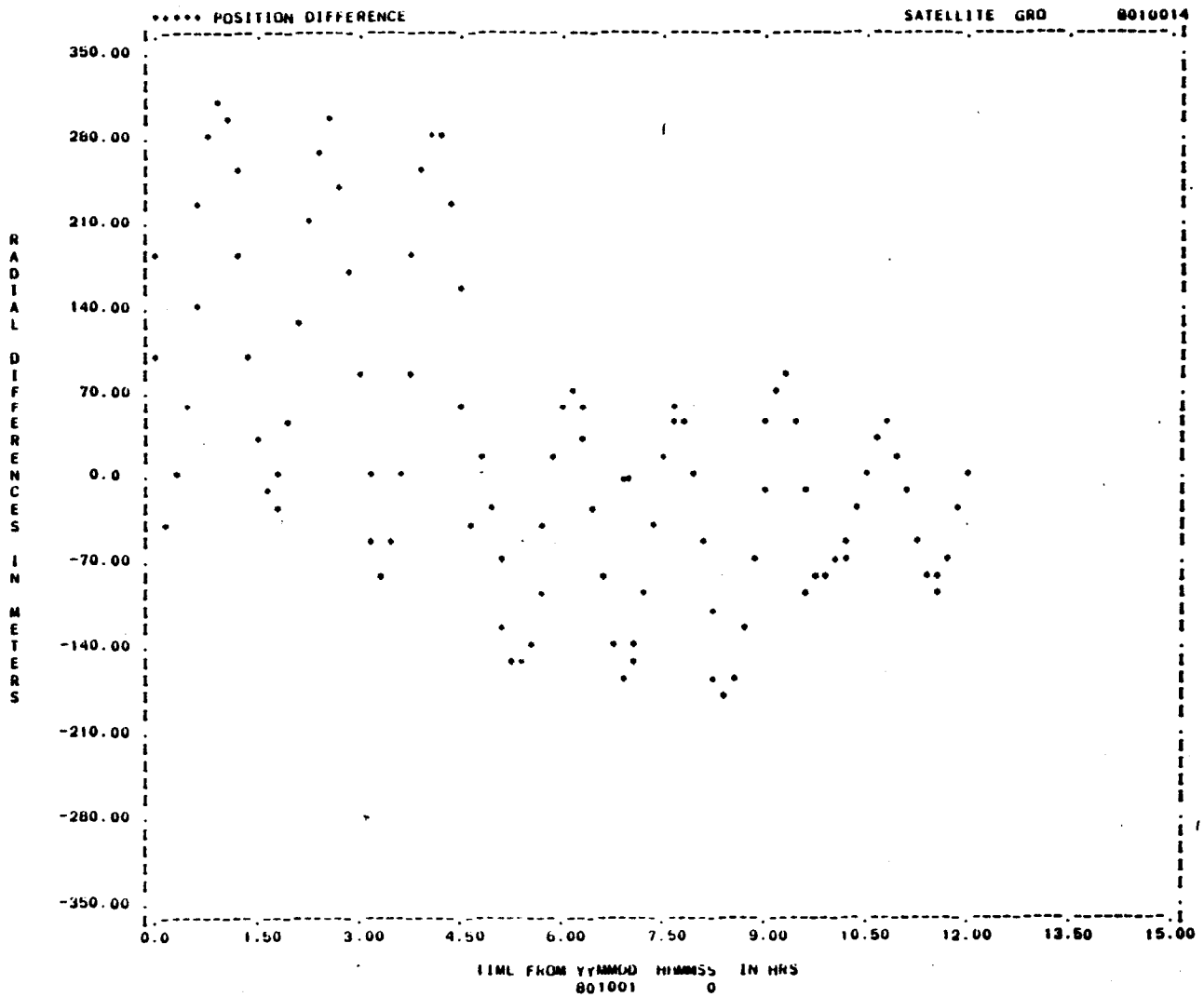

Figure B-10. Radial Differences for Run P24 (1 of 2)

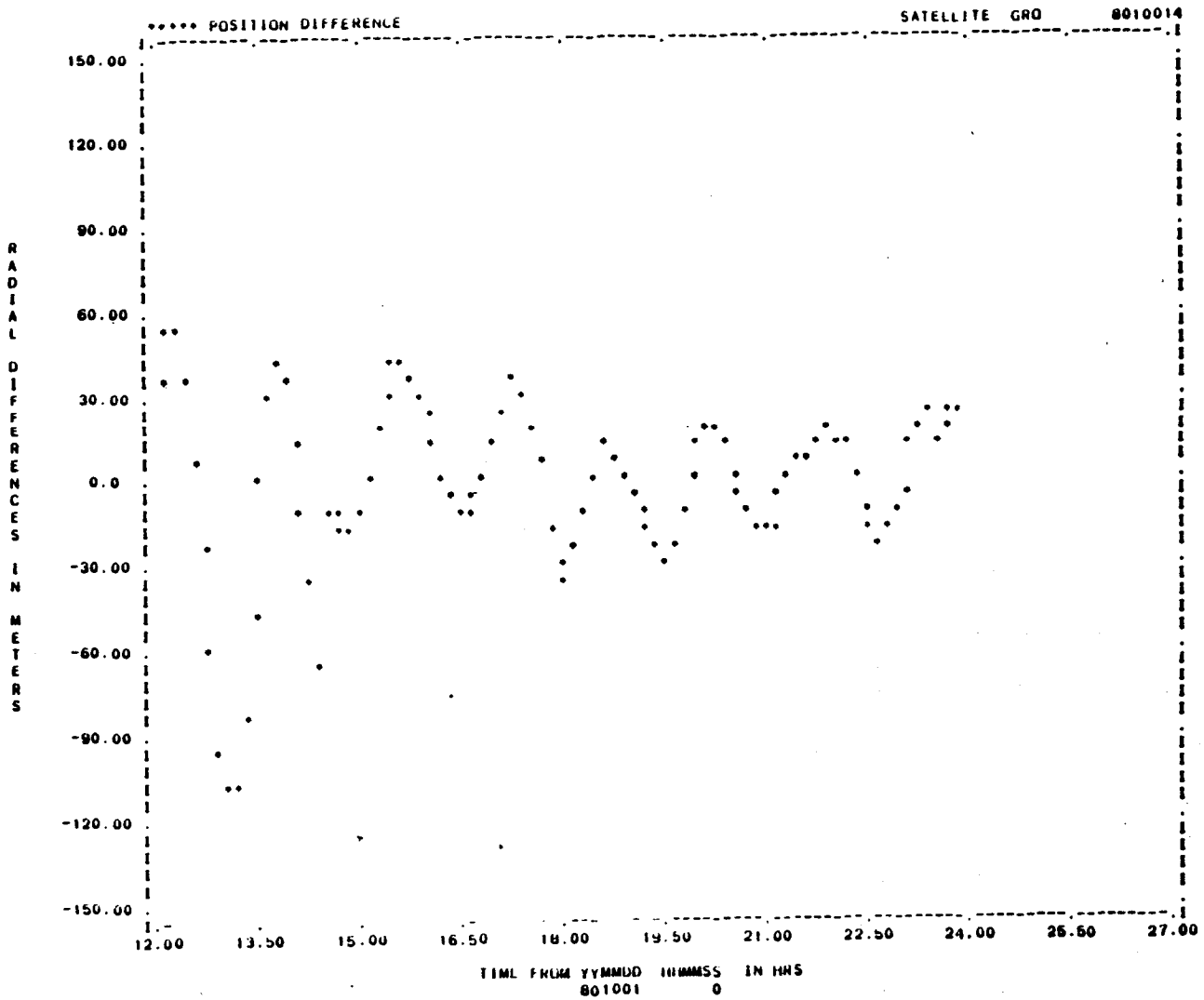

Figure B-10. Radial Differences for Run P24 (2 of 2)

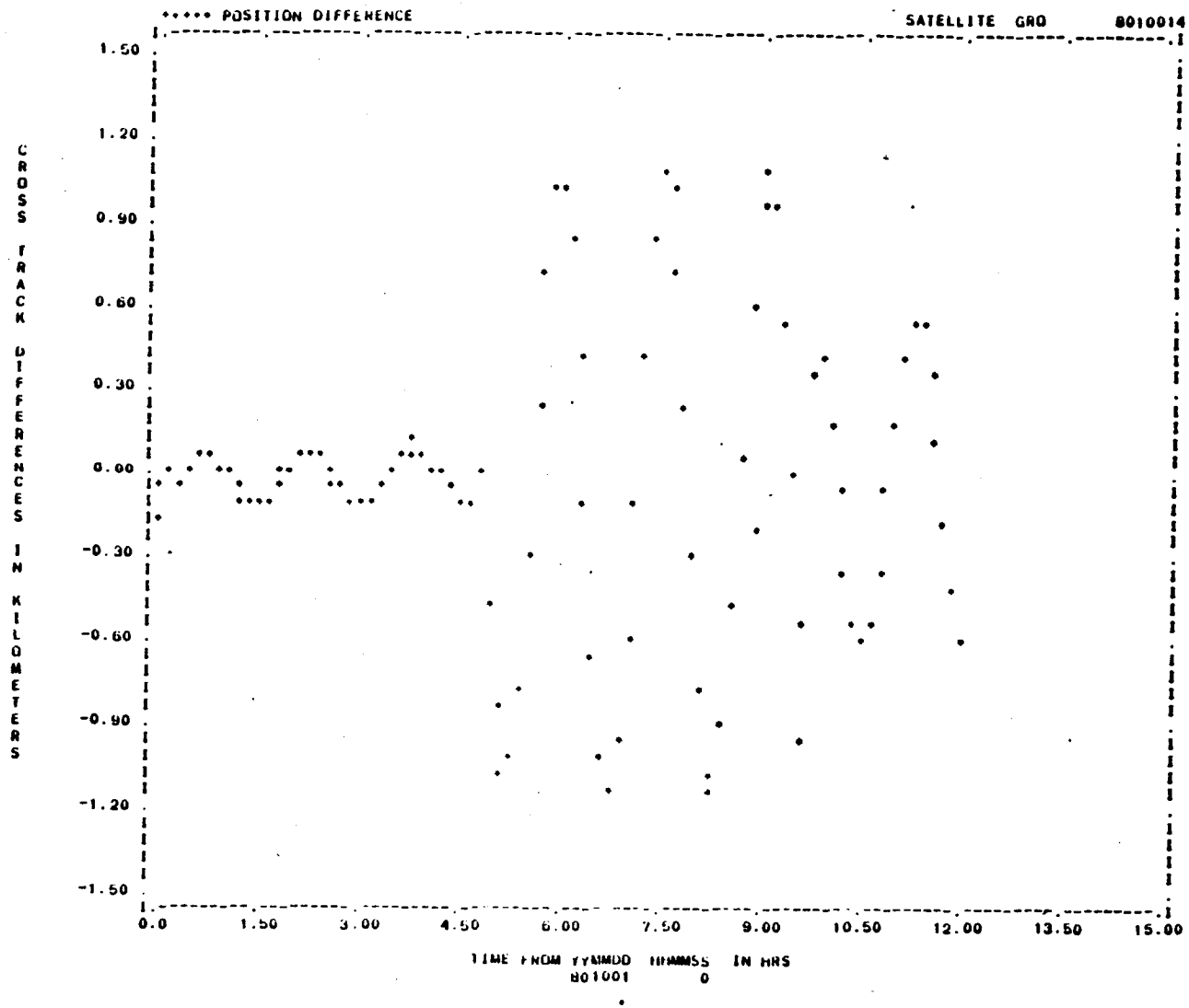

Figure B-11. Cross-Track Differences for Run P24 (1 of 2)

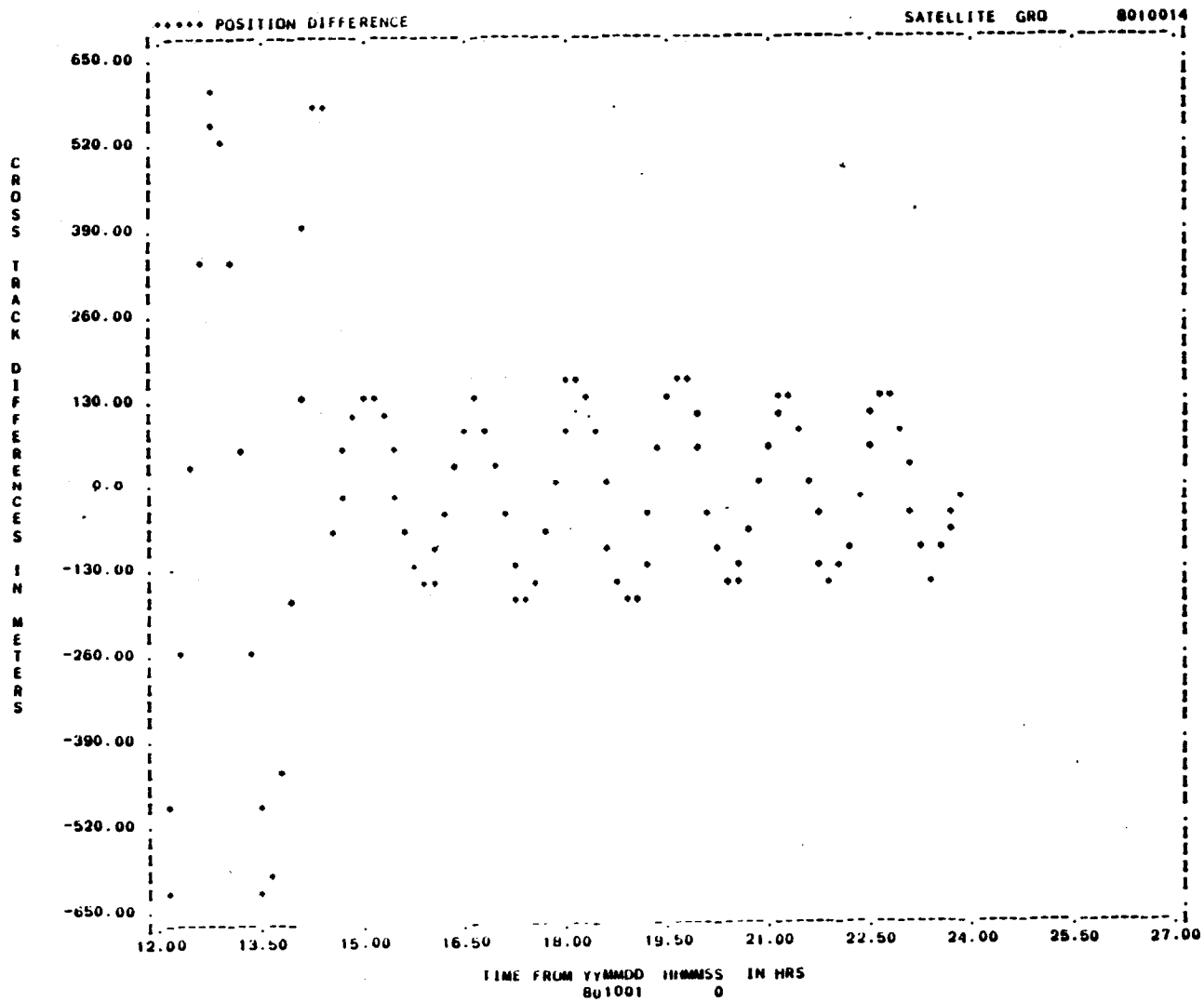

Figure B-11. Cross-Track Differences for Run P24 (2 of 2)

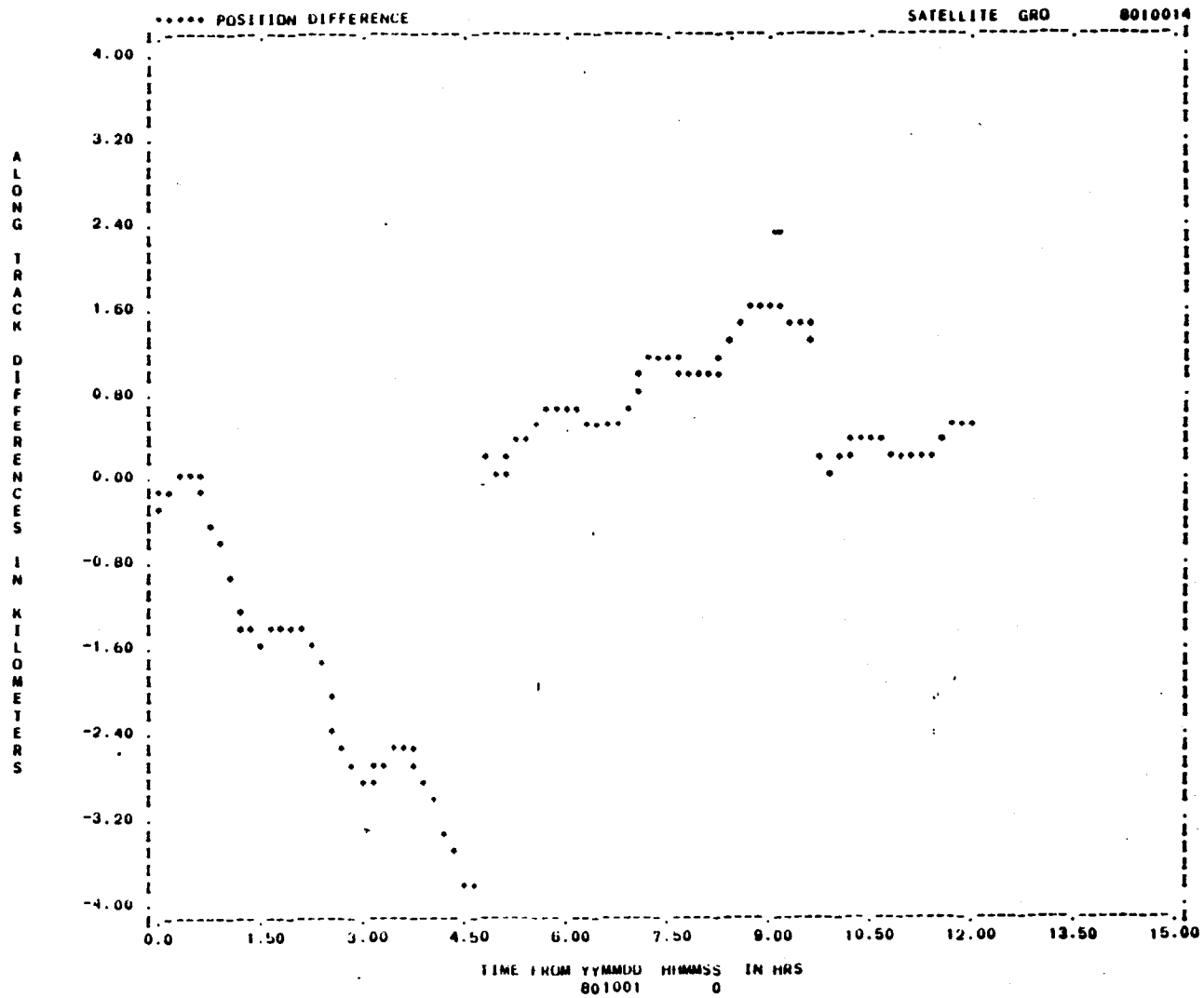

Figure B-12. Along-Track Differences for Run P24 (1 of 2)

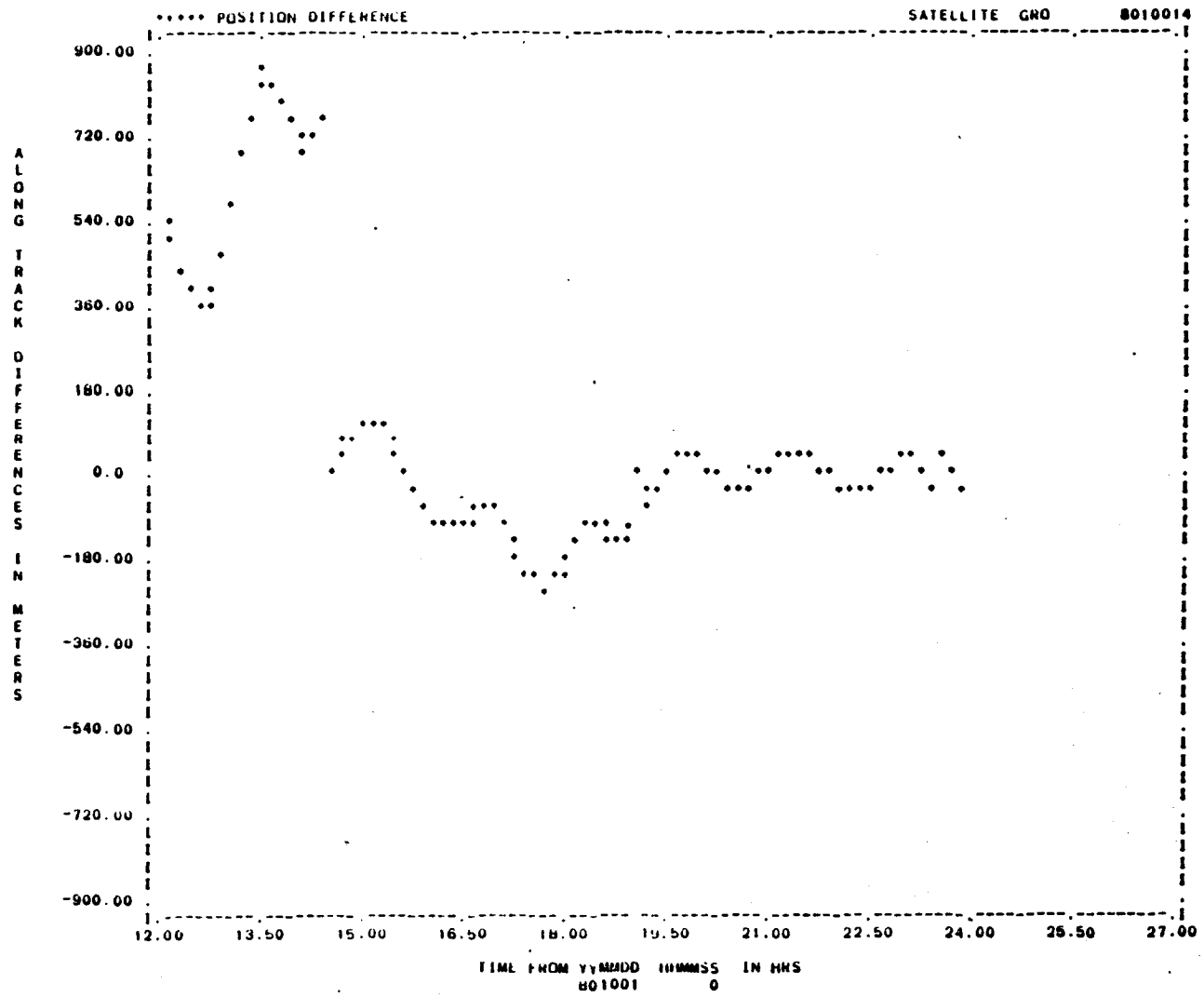

Figure B-12. Along-Track Differences for Run P24 (2 of 2)

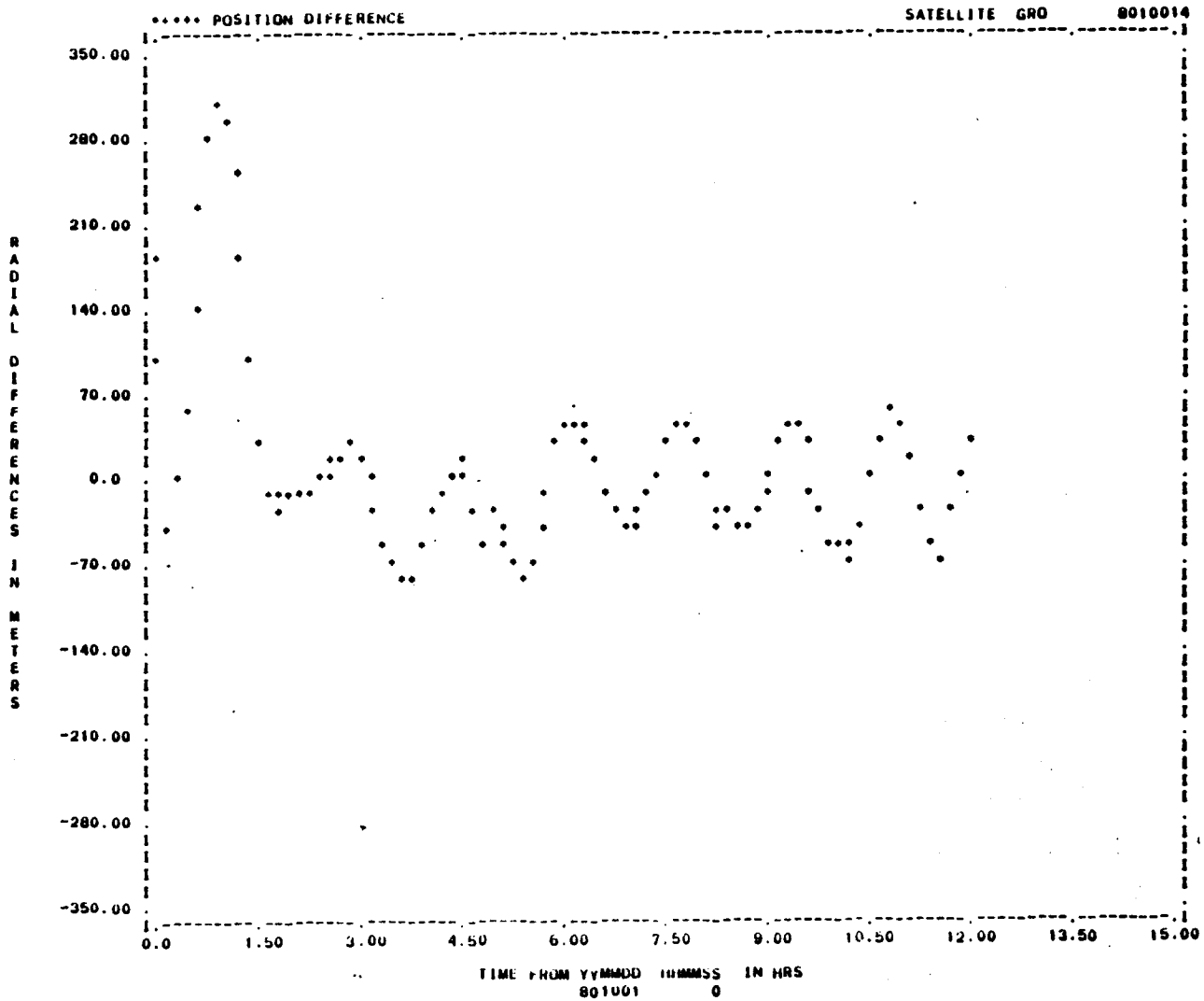

Figure B-13. Radial Differences for Run P32 (1 of 2)

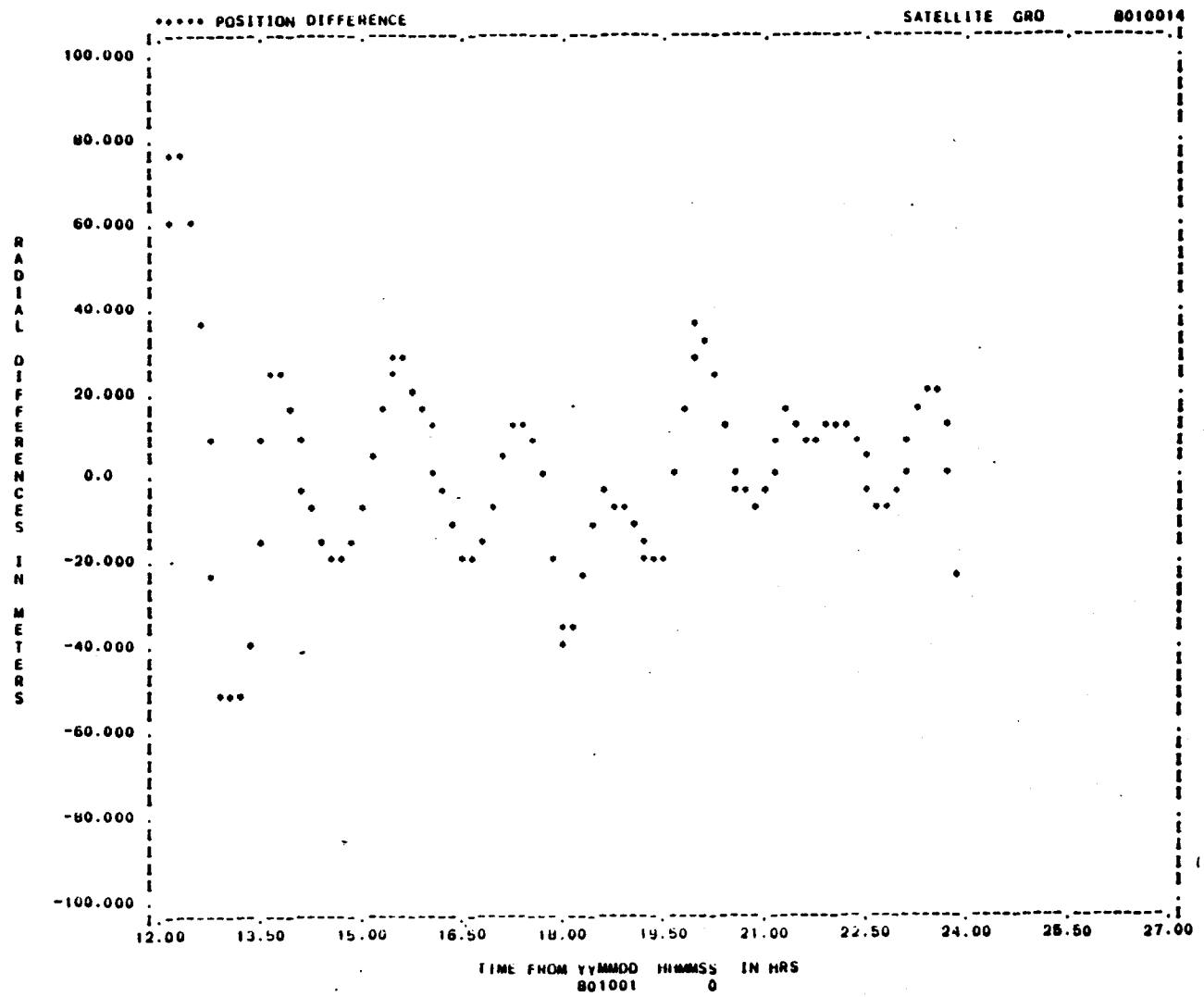

Figure B-13. Radial Differences for Run P32 (2 of 2)

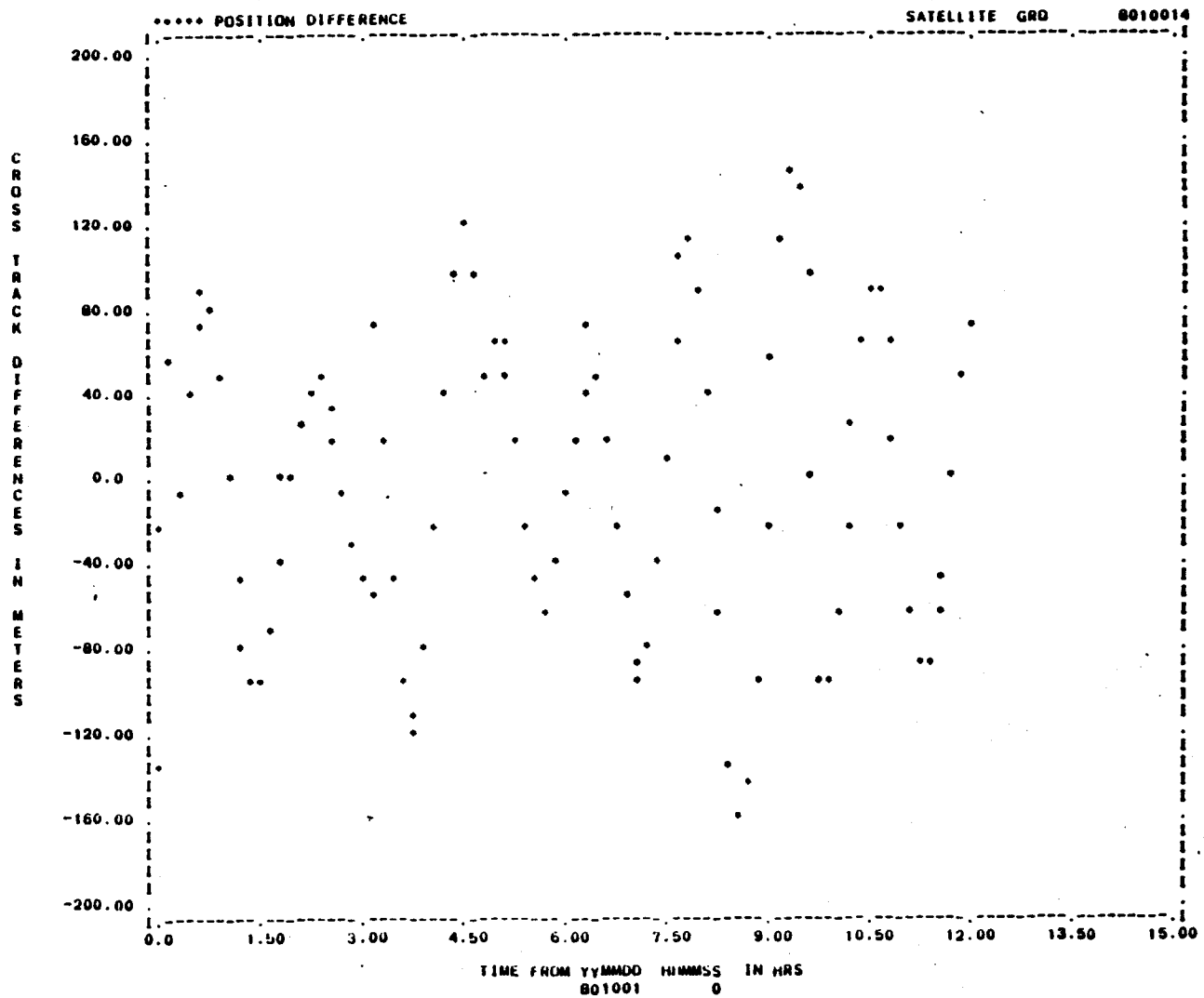

Figure B-14. Cross-Track Differences for Run P32 (1 of 2)

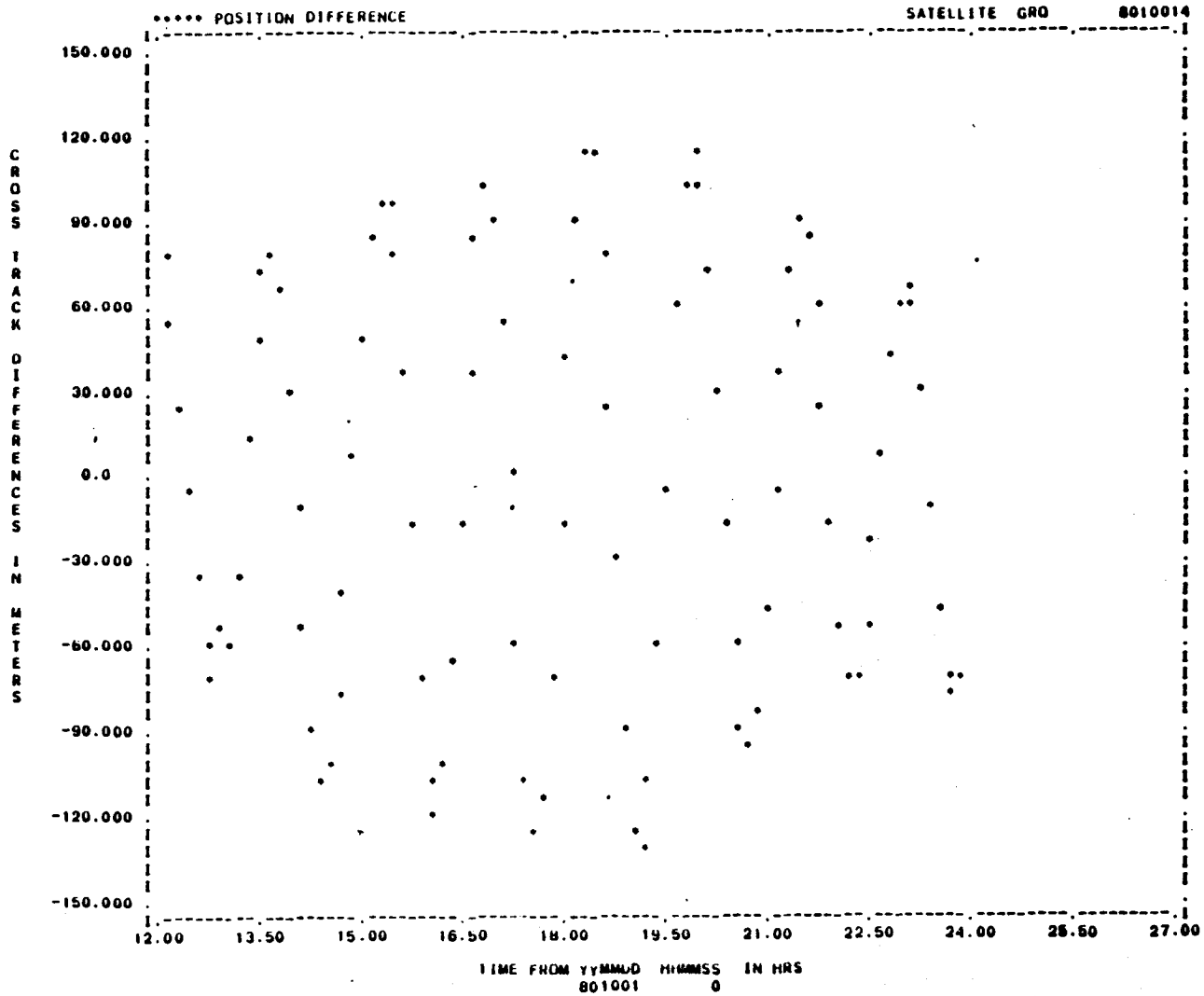

Figure B-14. Cross-Track Differences for Run P32 (2 of 2)

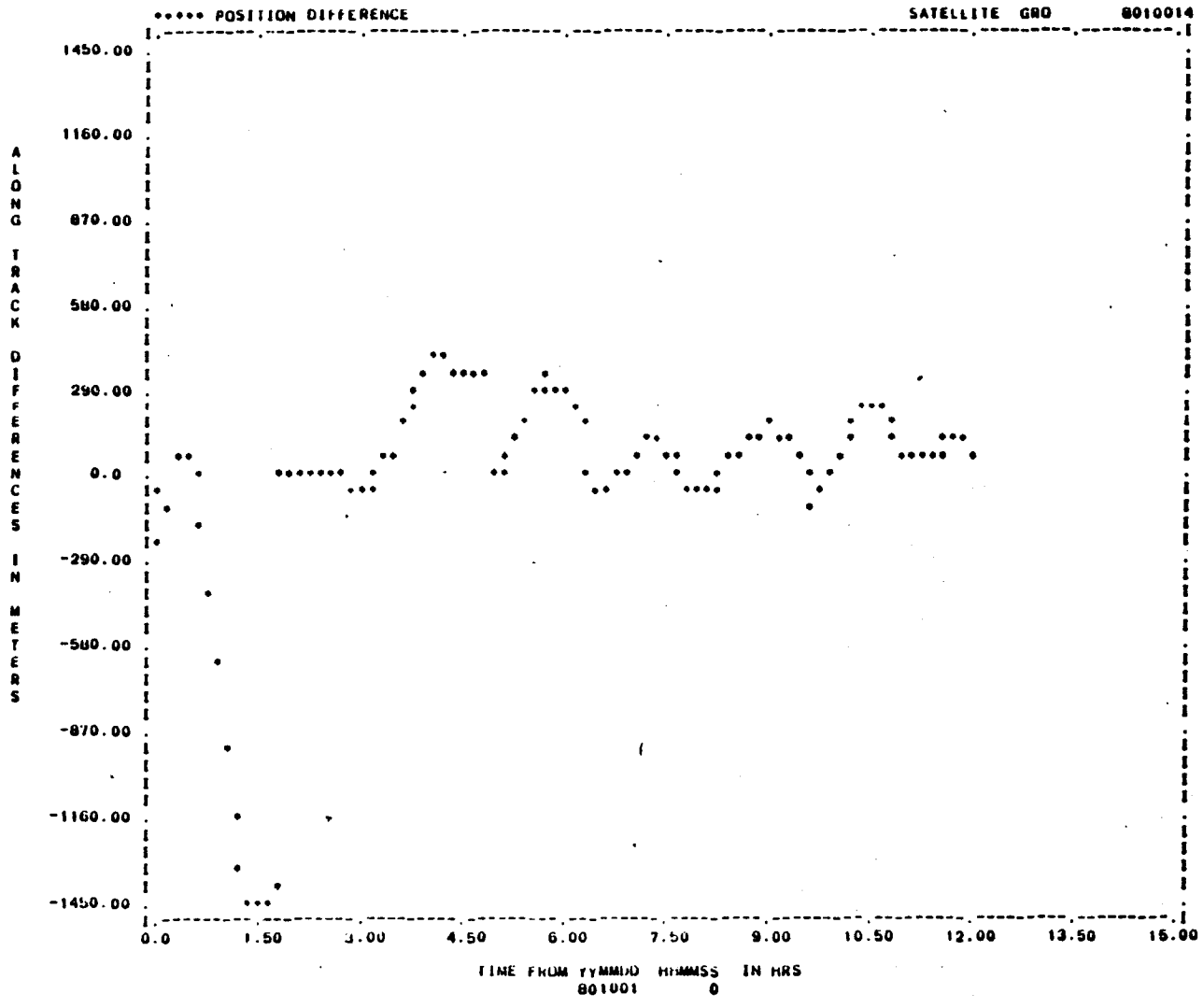

Figure B-15. Along-Track Differences for Run P32 (1 of 2)

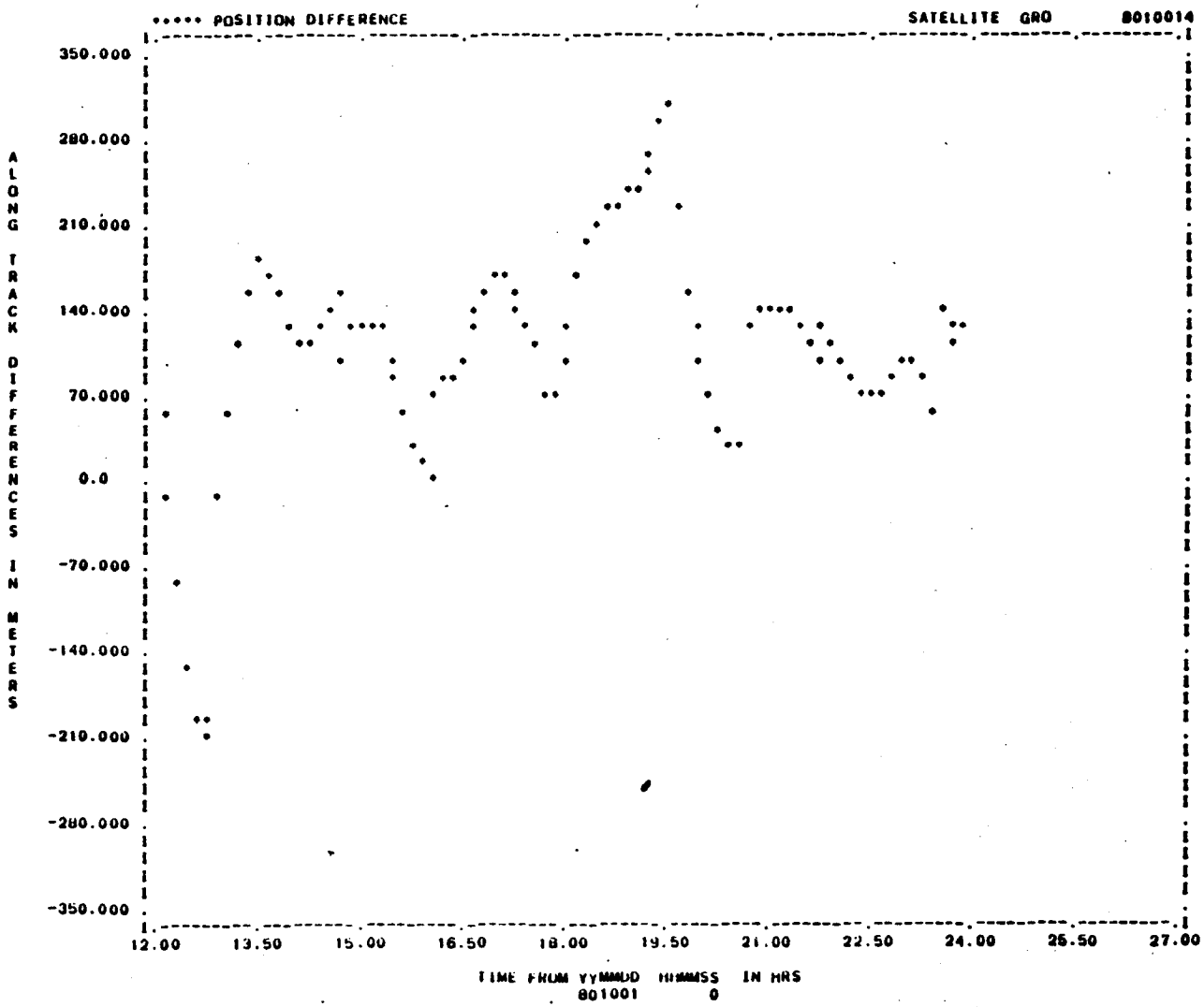

Figure B-15. Along-track Differences for Run P32 (2 of 2)

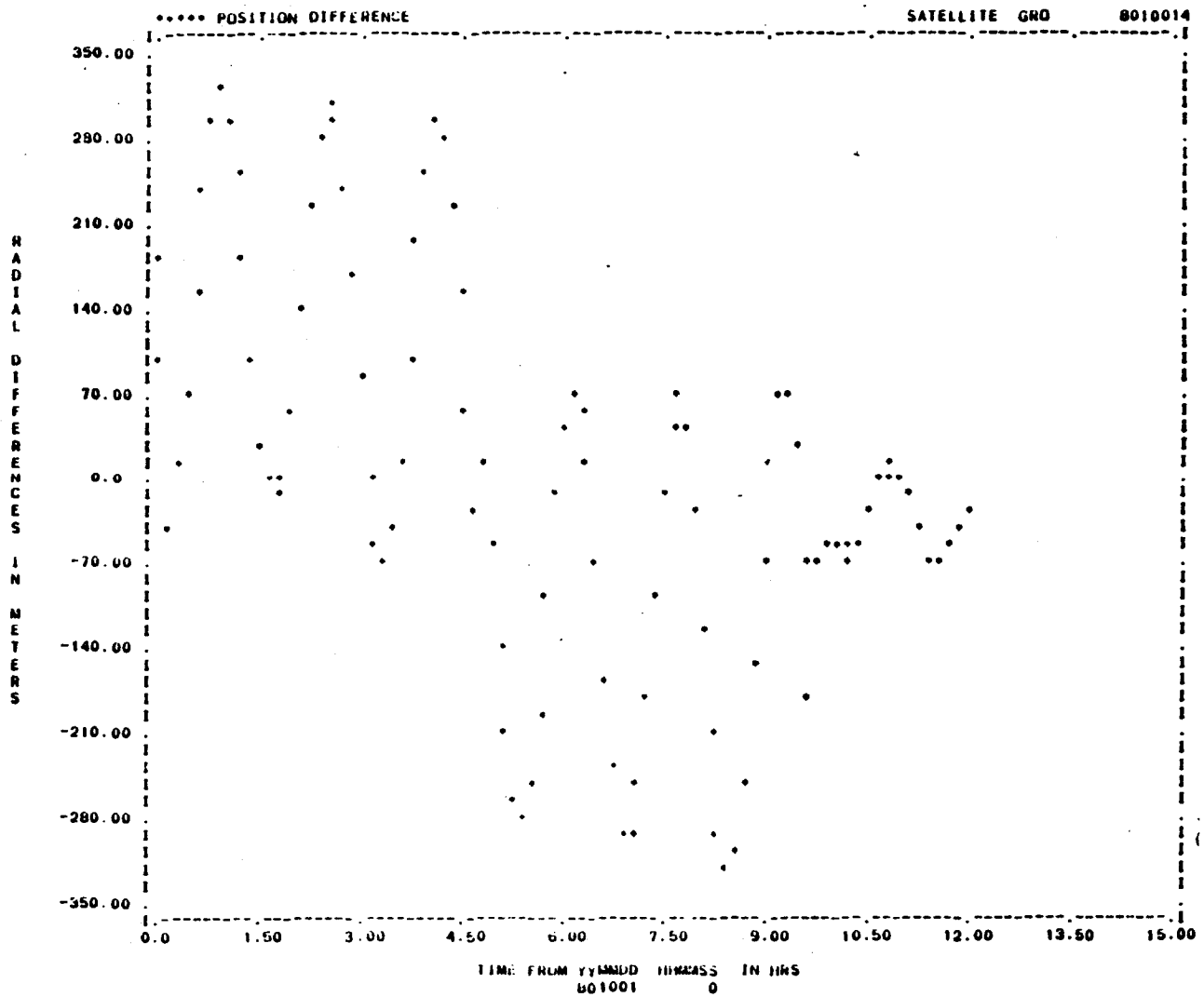

Figure B-16. Radial Differences for Run P34 (1 of 2)

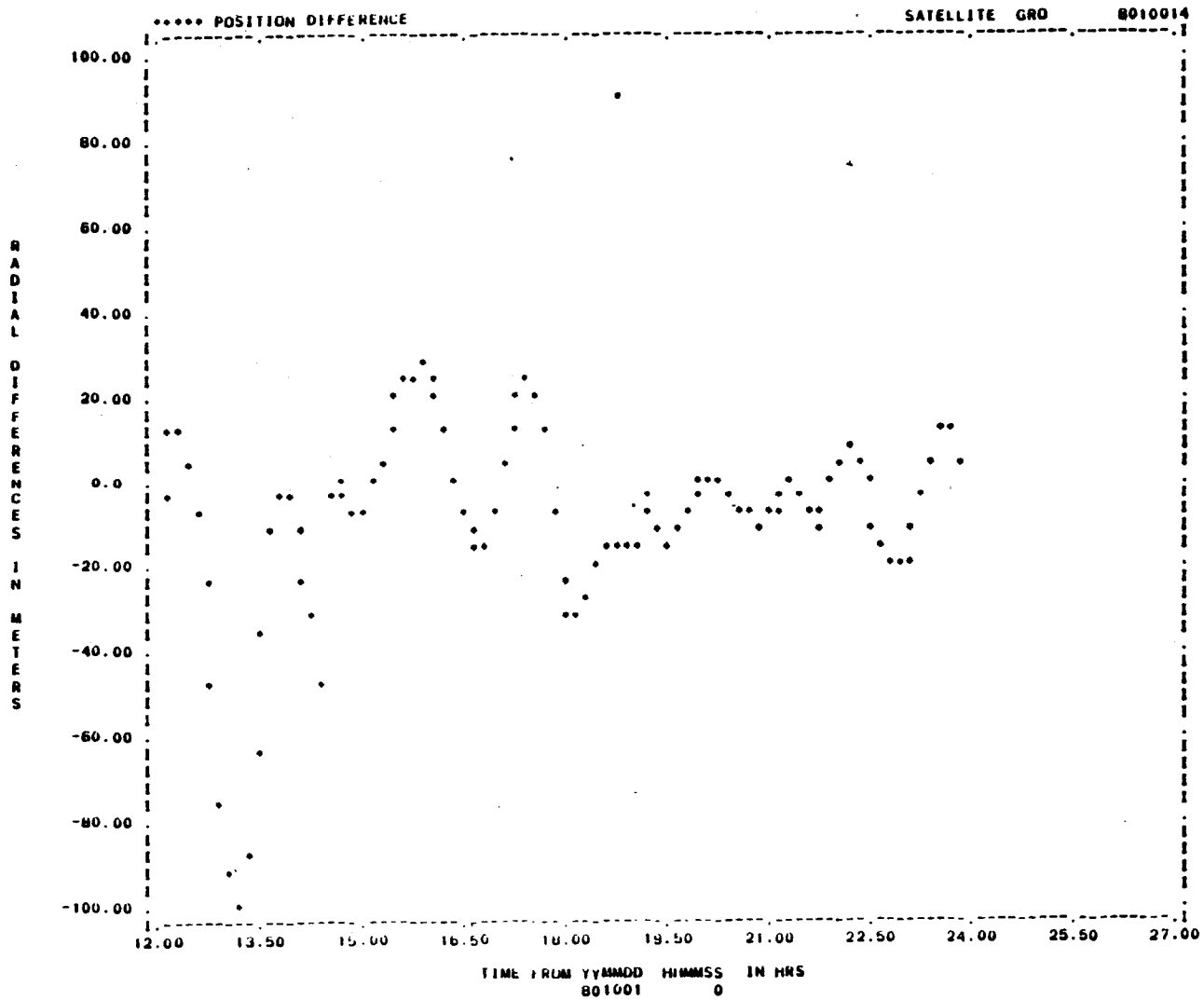

Figure B-16. Radial Differences for Run P34 (2 of 2)

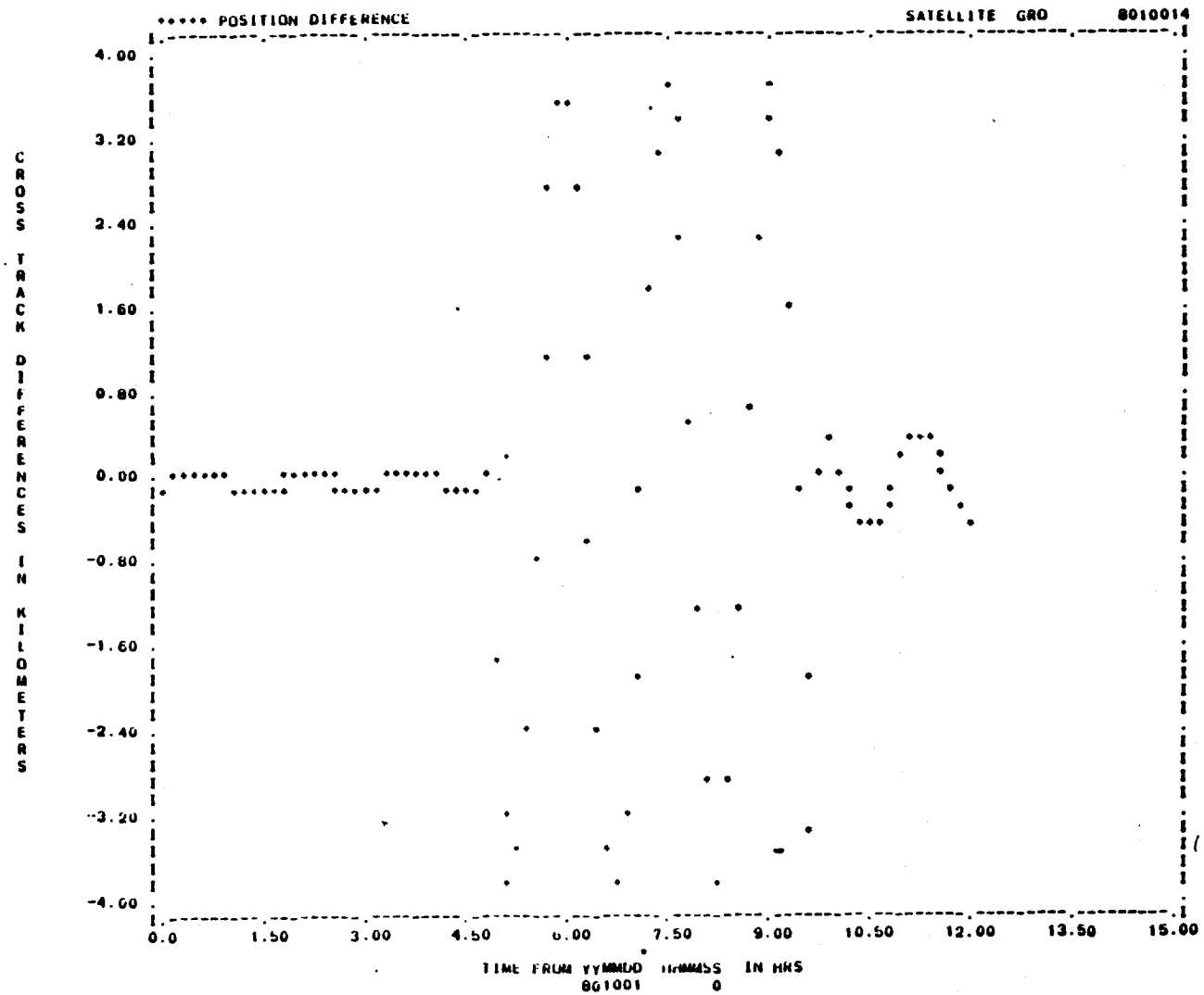

Figure B-17. Cross-Track Differences for Run P34 (1 of 2)

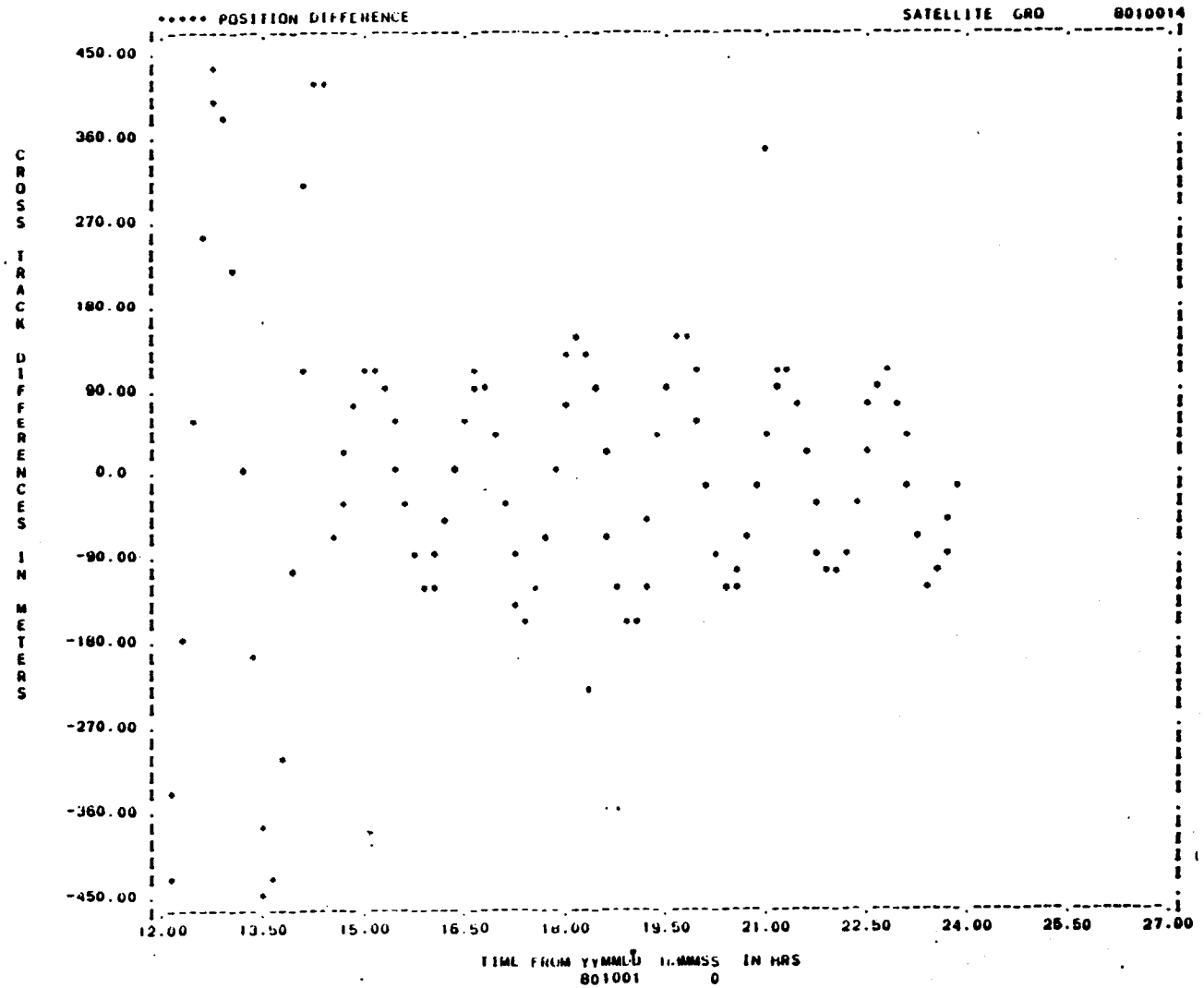

Figure B-17. Cross-Track Differences for Run P34 (2 of 2)

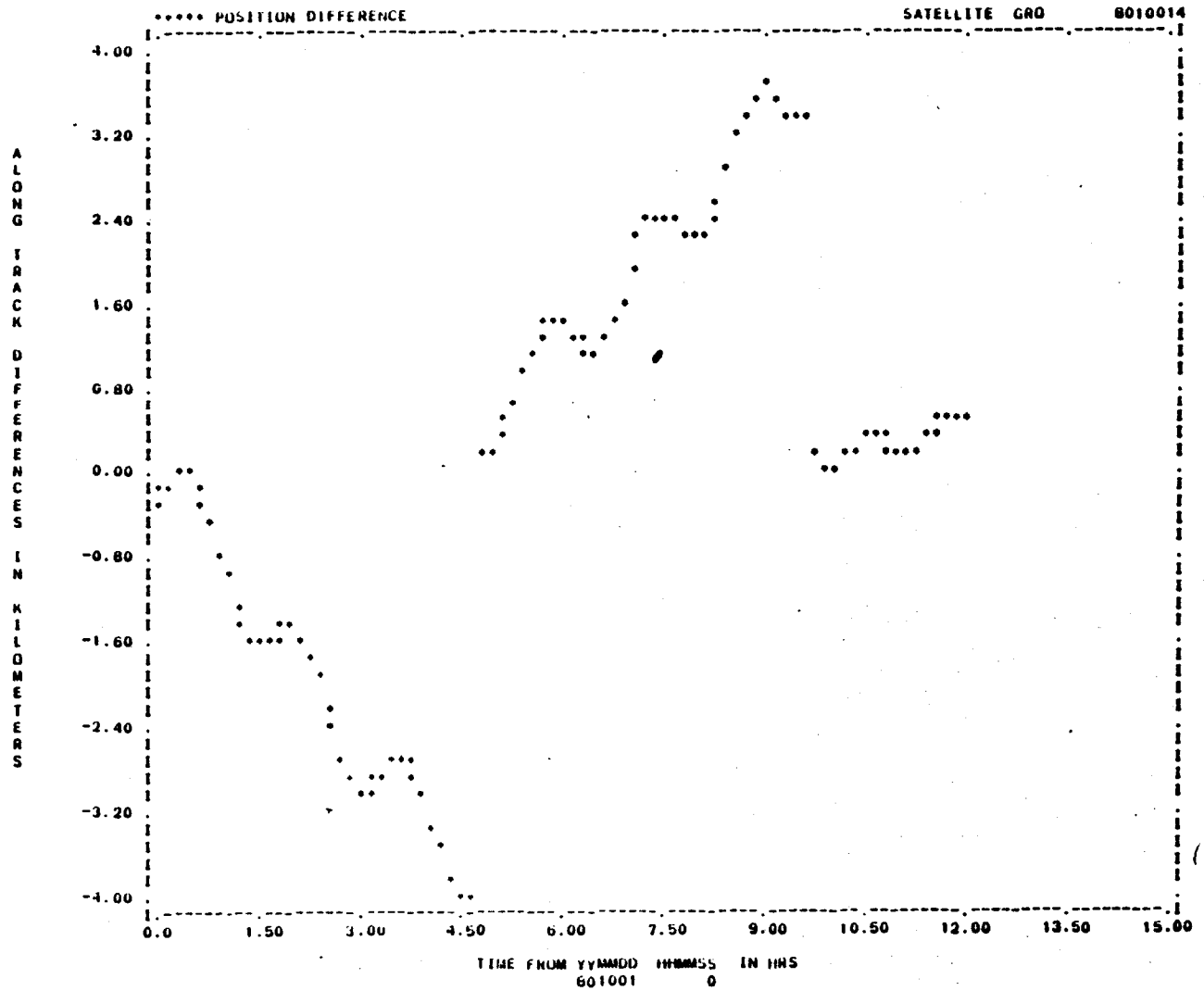

Figure B-18. Along-Track Differences for Run P34 (1 of 2)

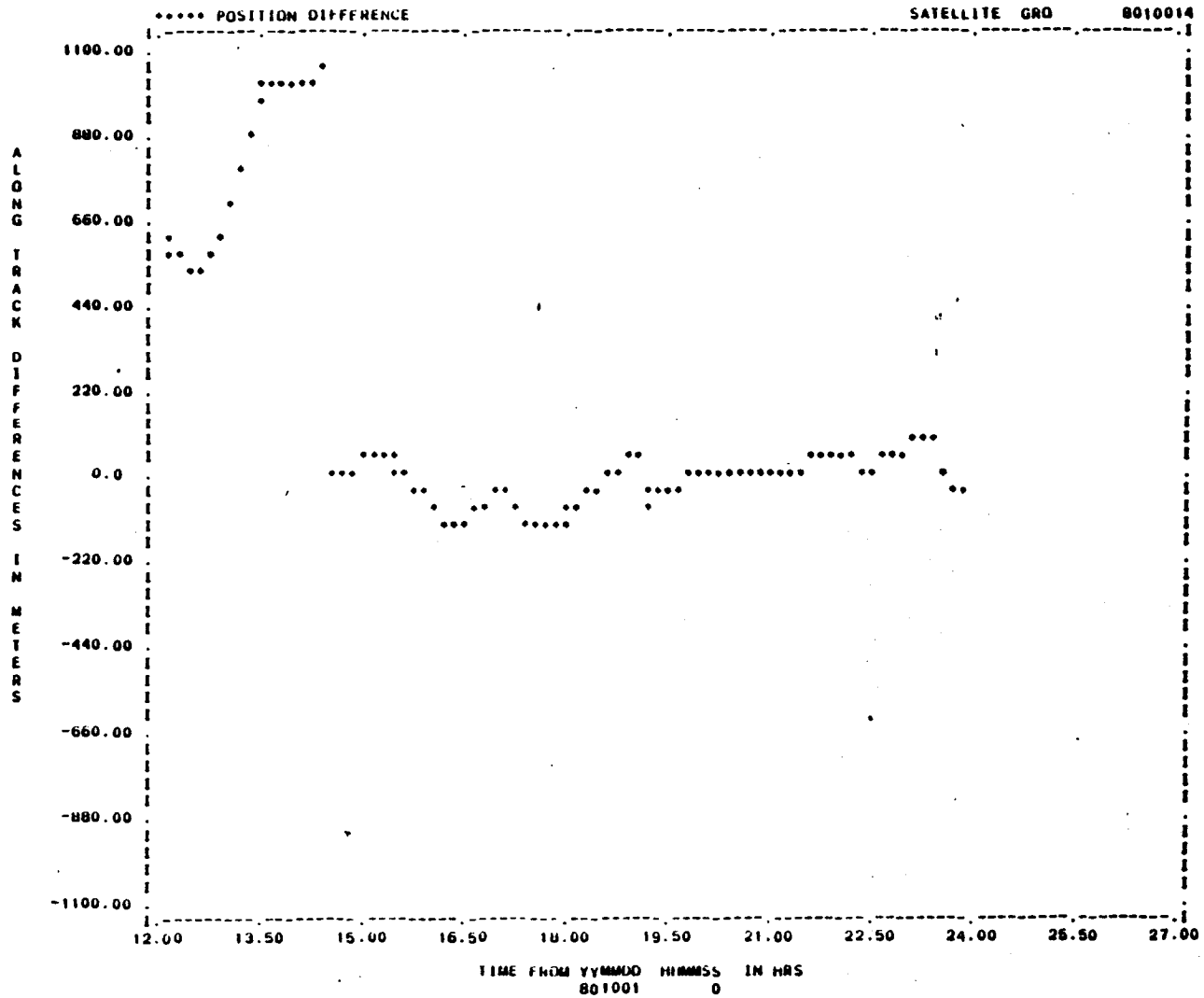

Figure B-18. Along-Track Differences for Run P34 (2 of 2)

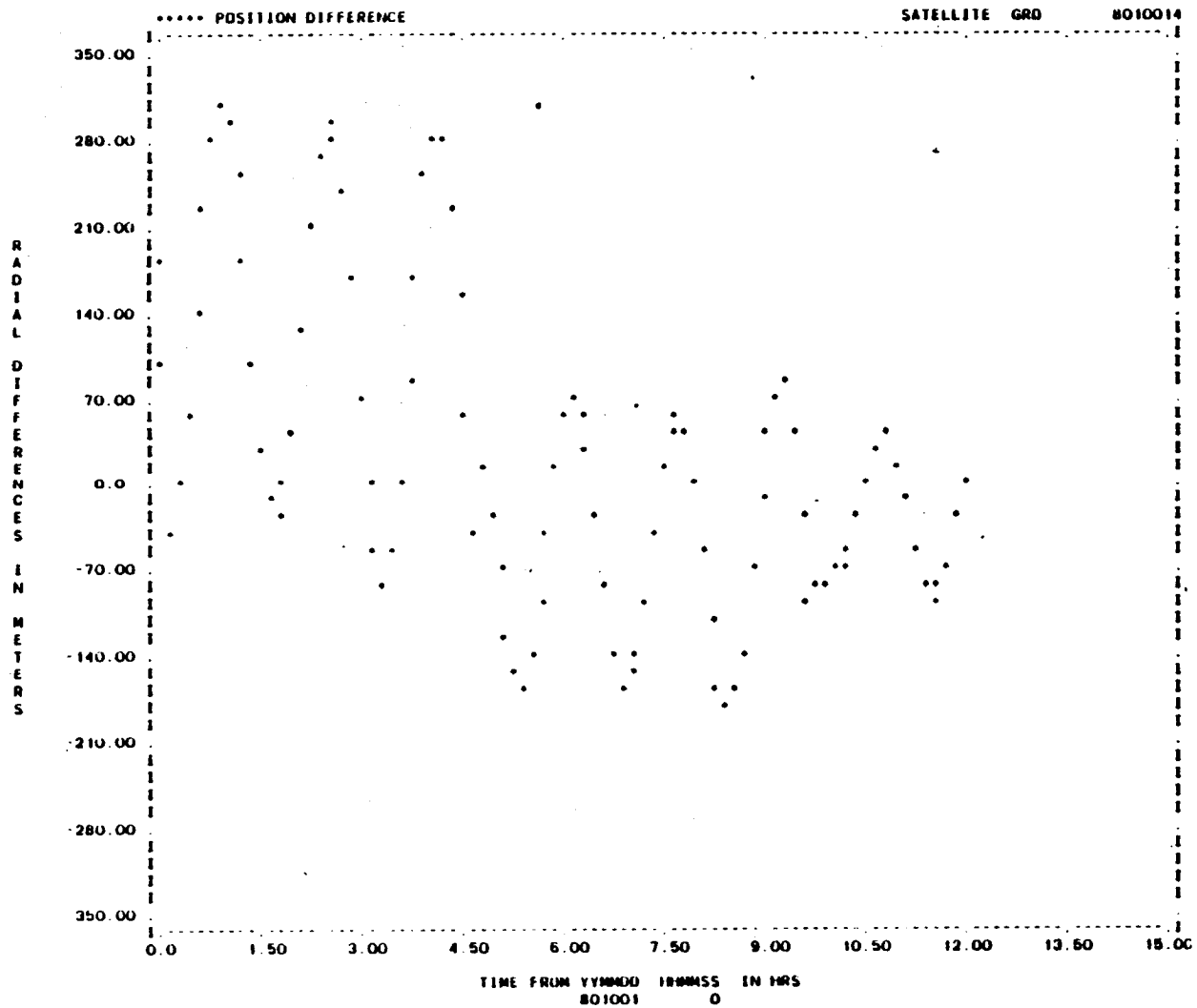

Figure B-19. Radial Differences for Run P37 (1 of 2)

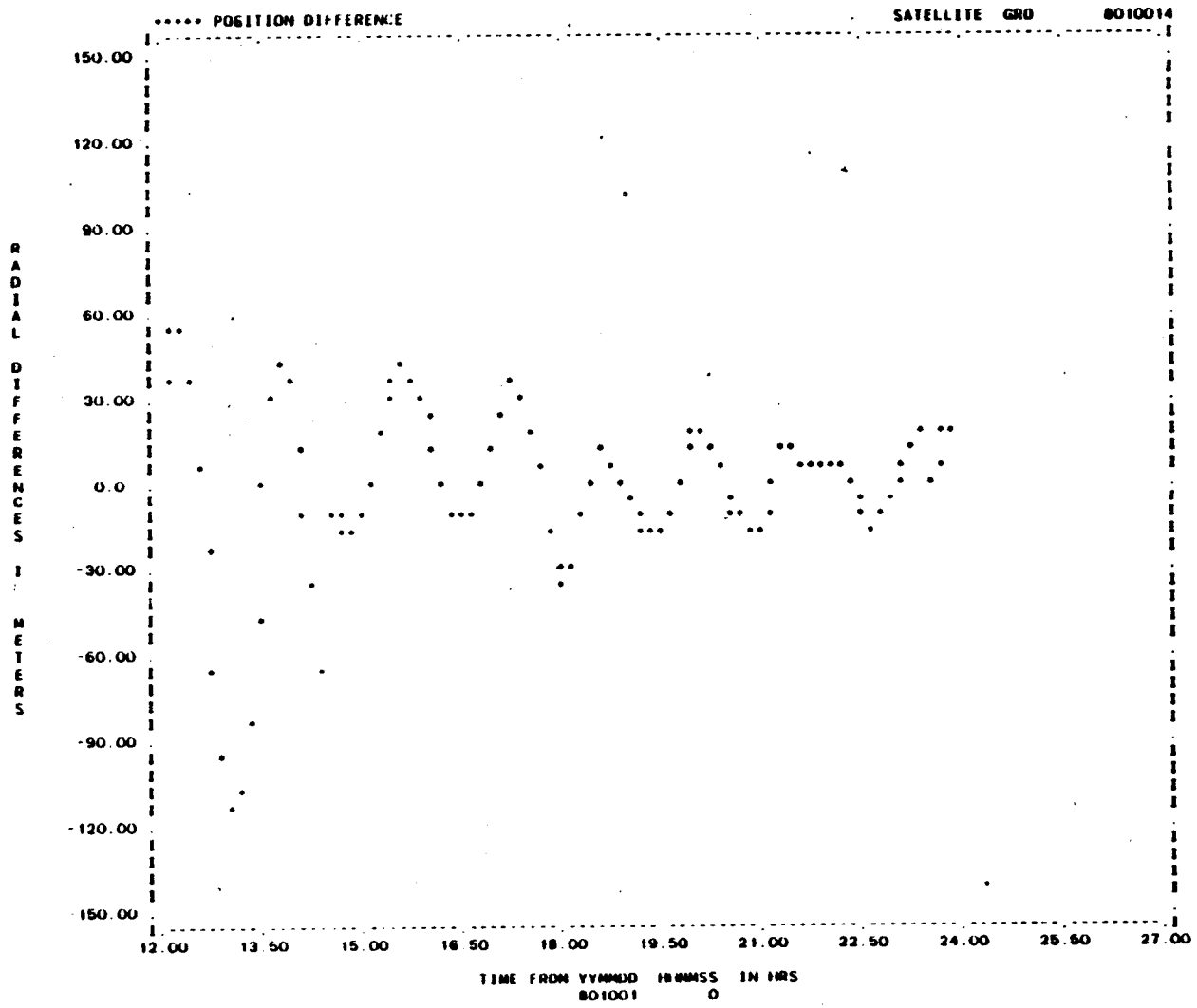

Figure B-19. Radial Differences for Run P37 (2 of 2)

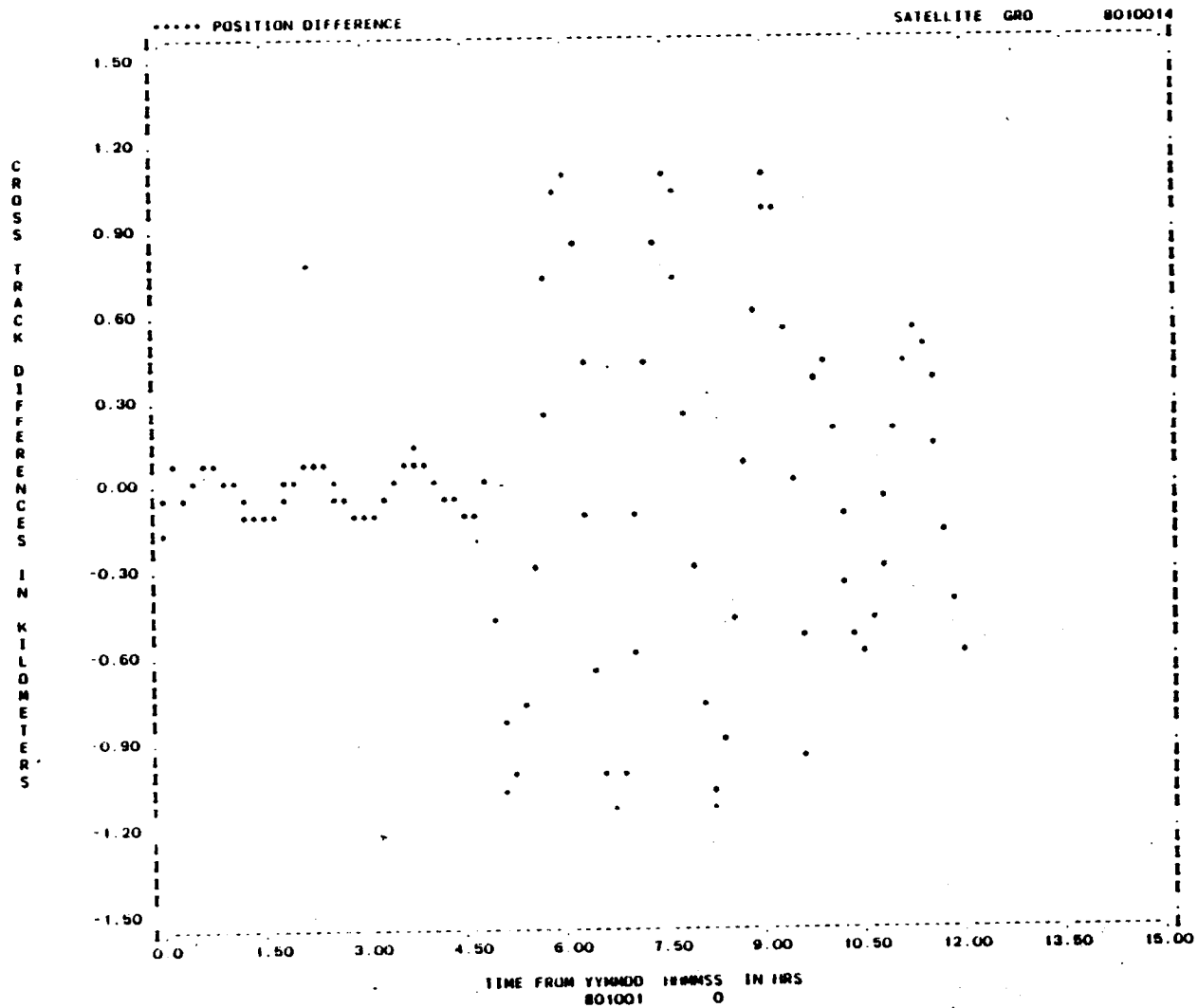

Figure B-20. Cross-Track Differences for Run P37 (1 of 2)

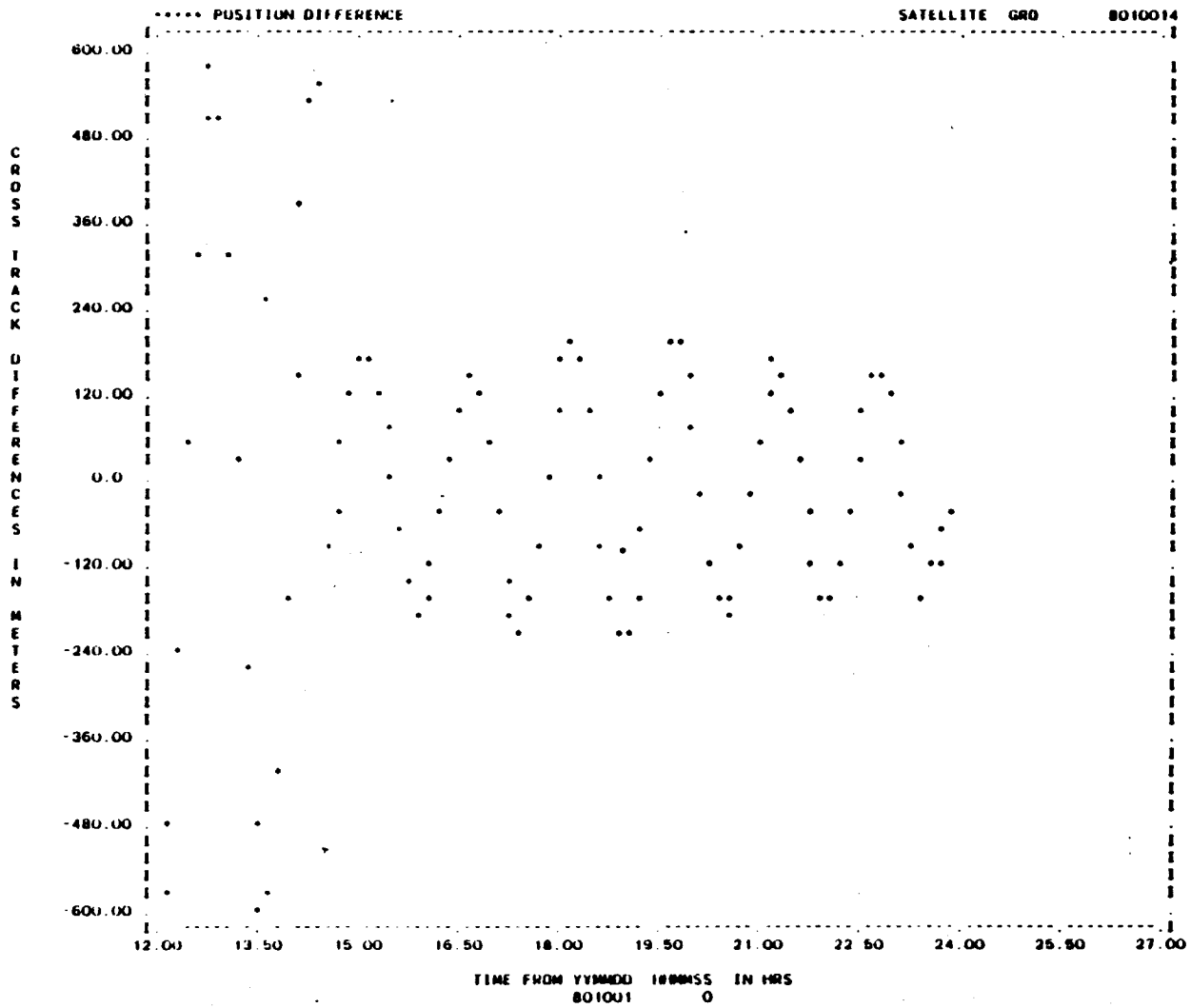

Figure B-20. Cross-Track Differences for Run P37 (2 of 2)

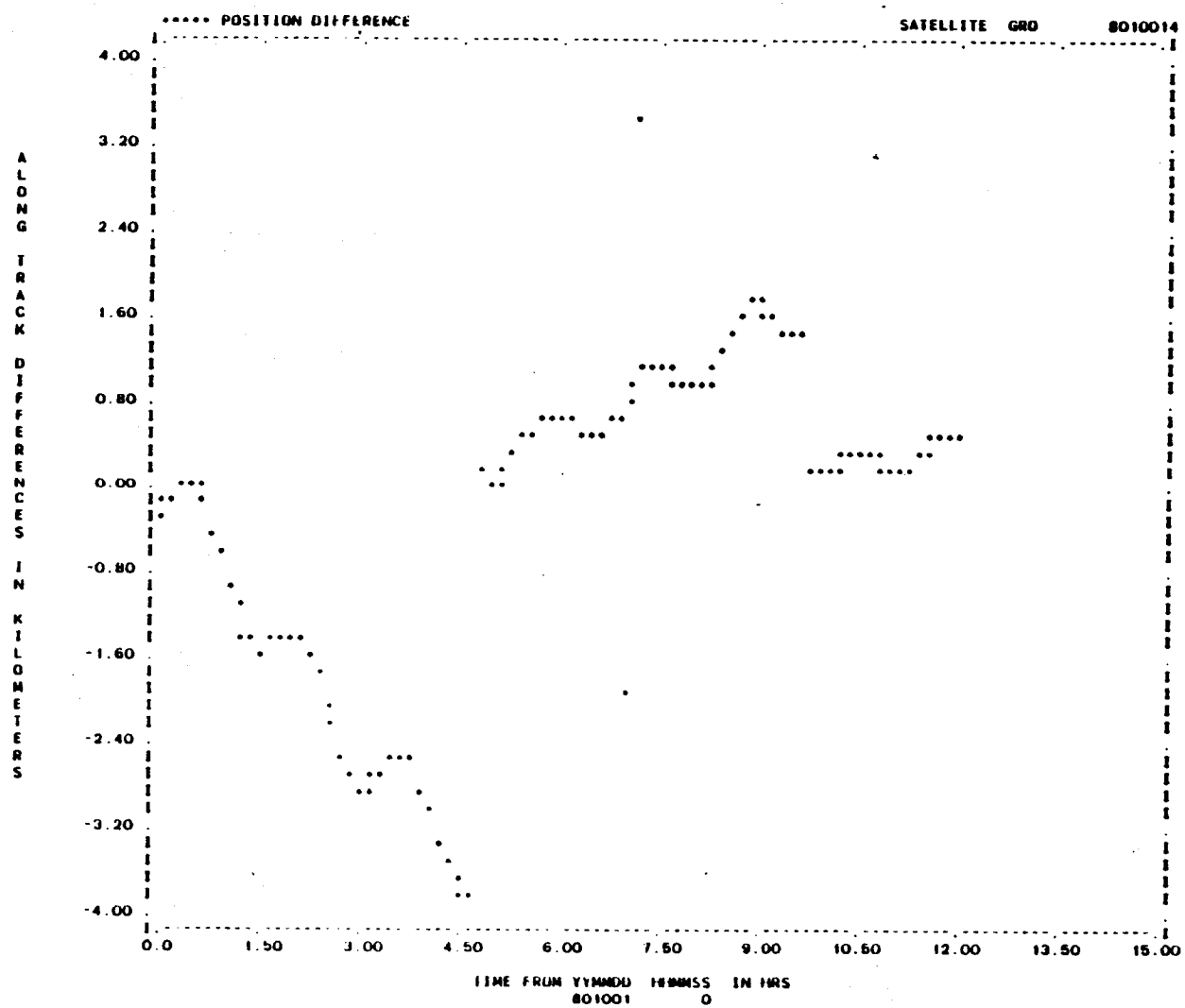

Figure B-21. Along-Track Differences for Run P37 (1 of 2)

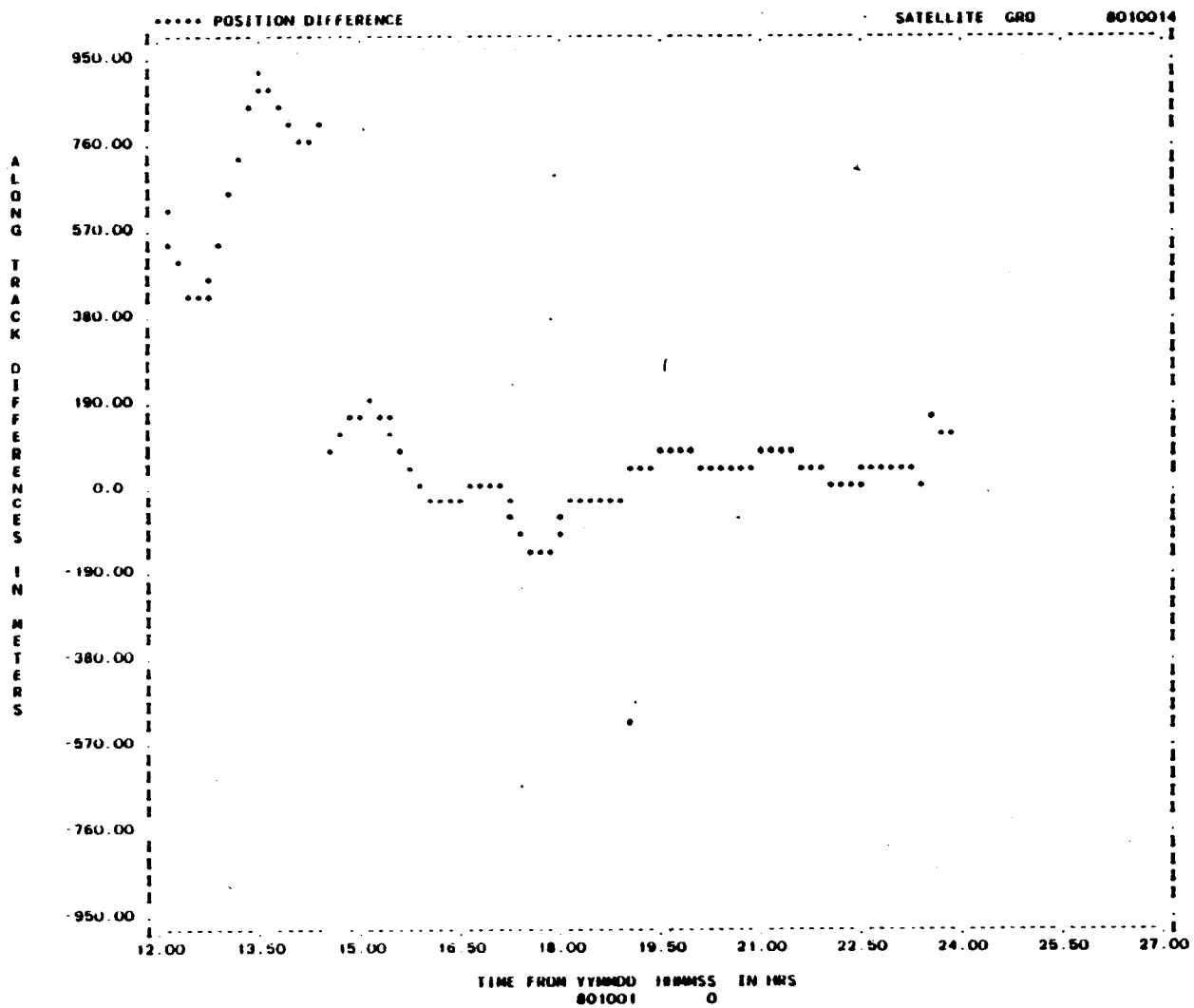

Figure B-21. Along-Track Differences for Run P37 (2 of 2)

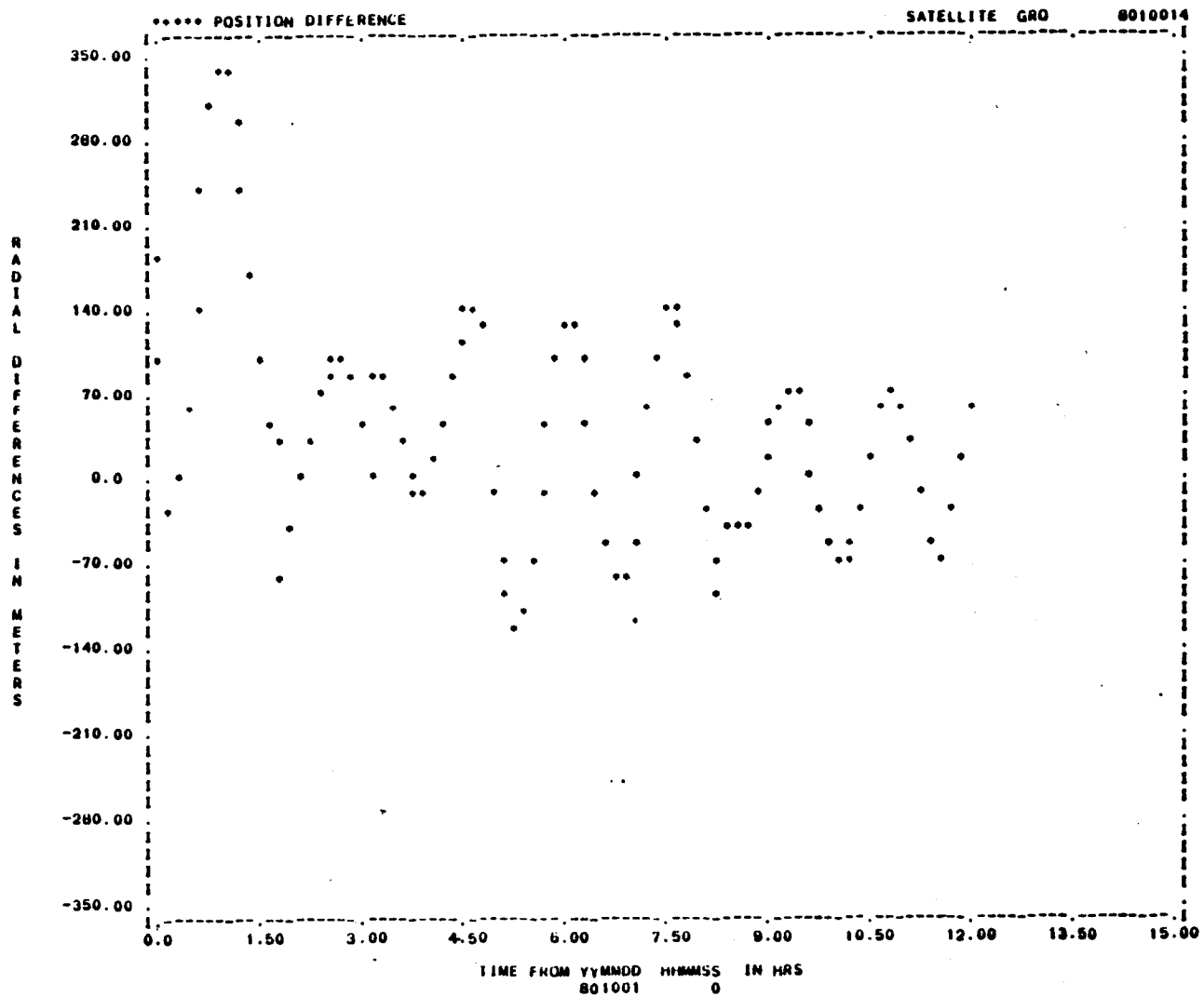

Figure B-22. Radial Differences for Run Q3 (1 of 2)

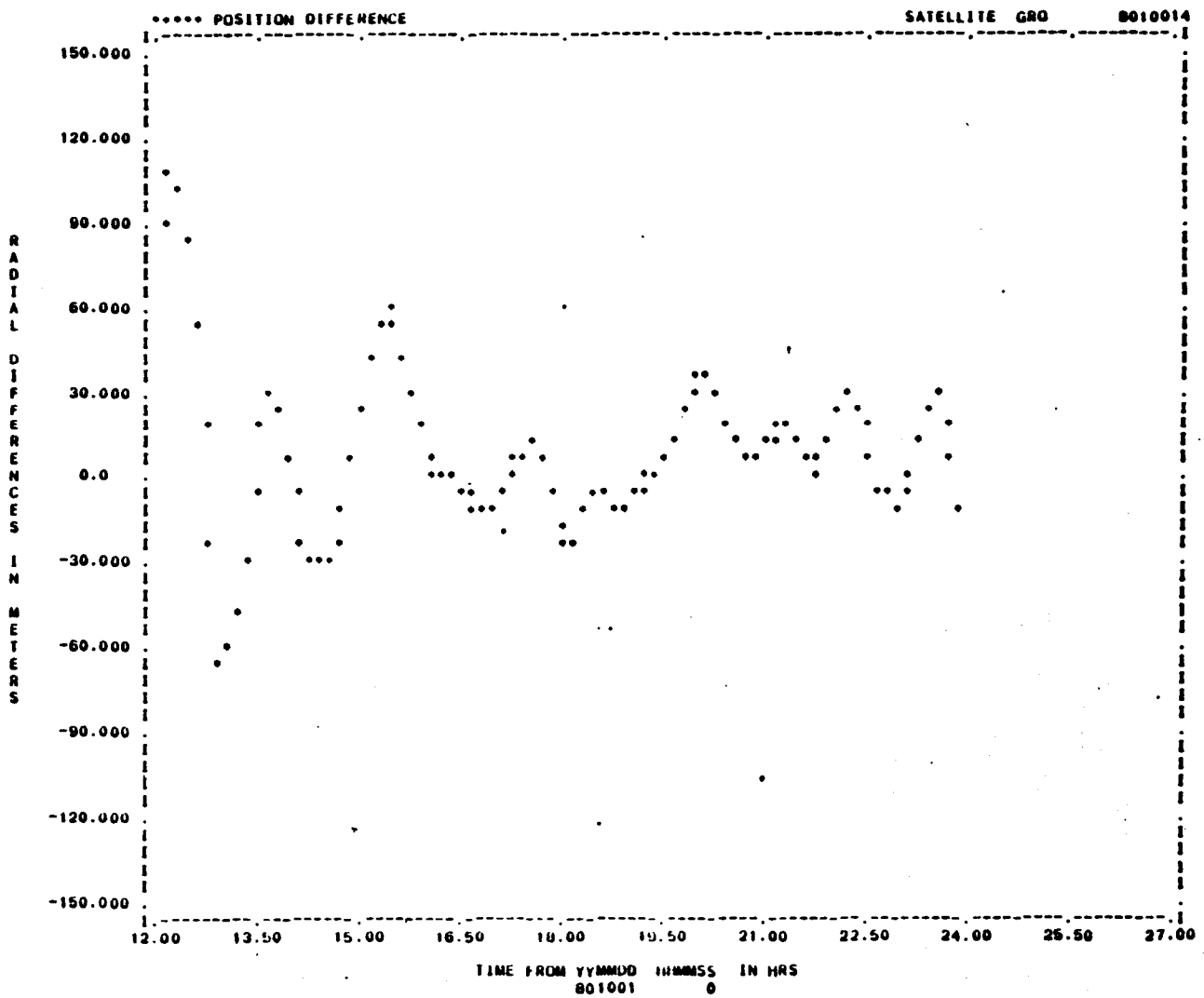

Figure B-22. Radial Differences for Run Q3 (2 of 2)

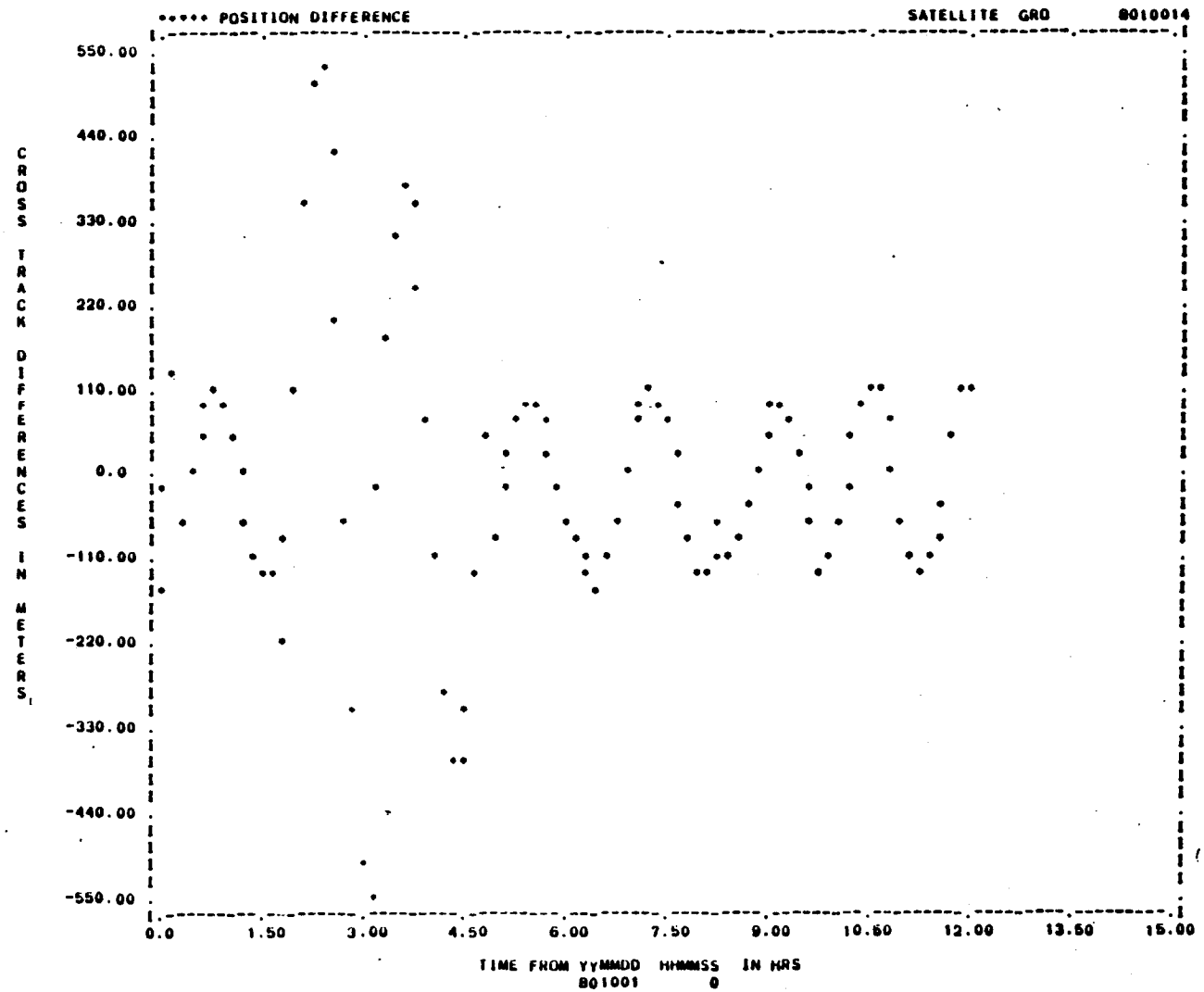

Figure B-23. Cross-Track Differences for Run Q3 (1 of 2)

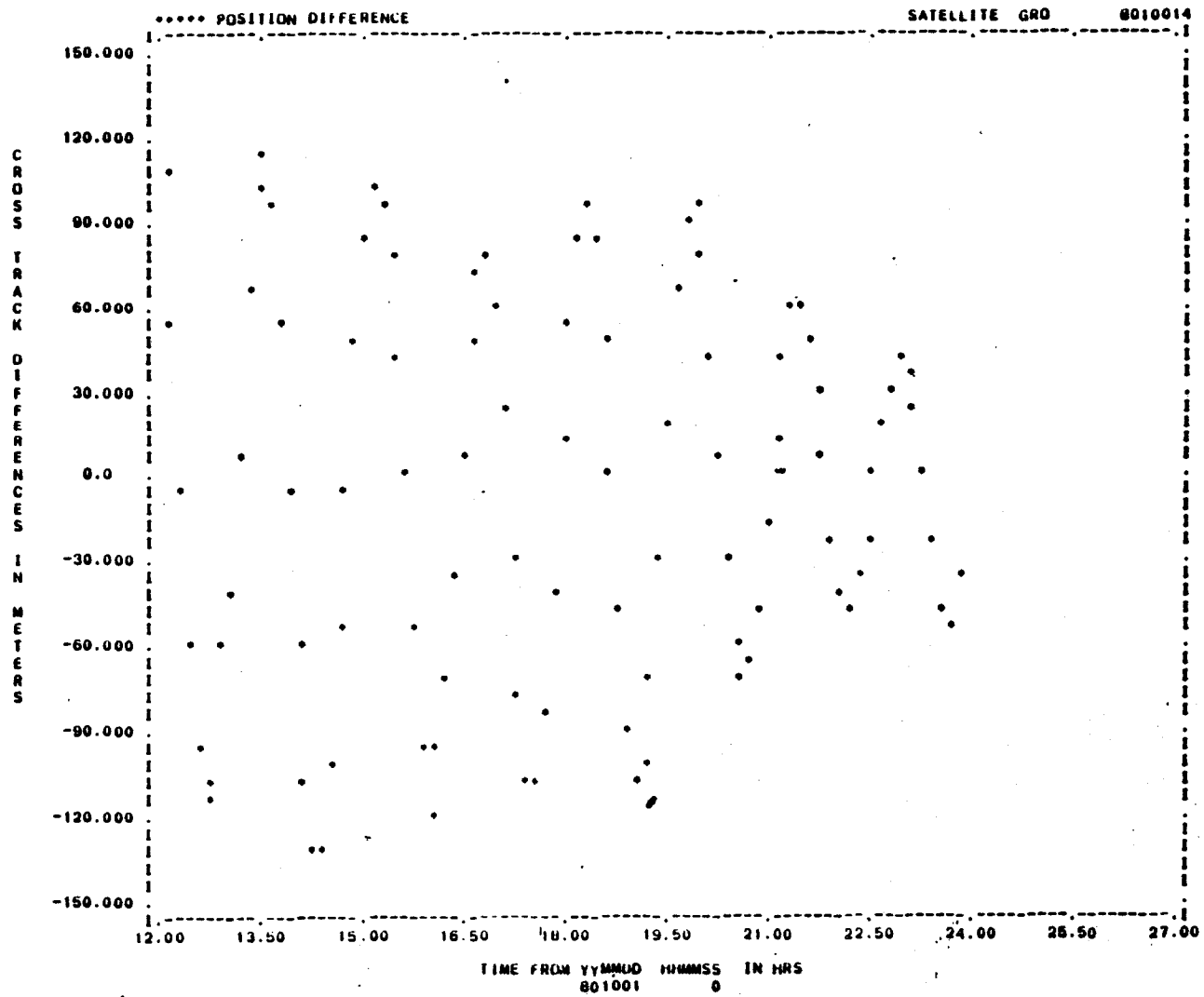

Figure B-23. Cross-Track Differences for Run Q3 (2 of 2)

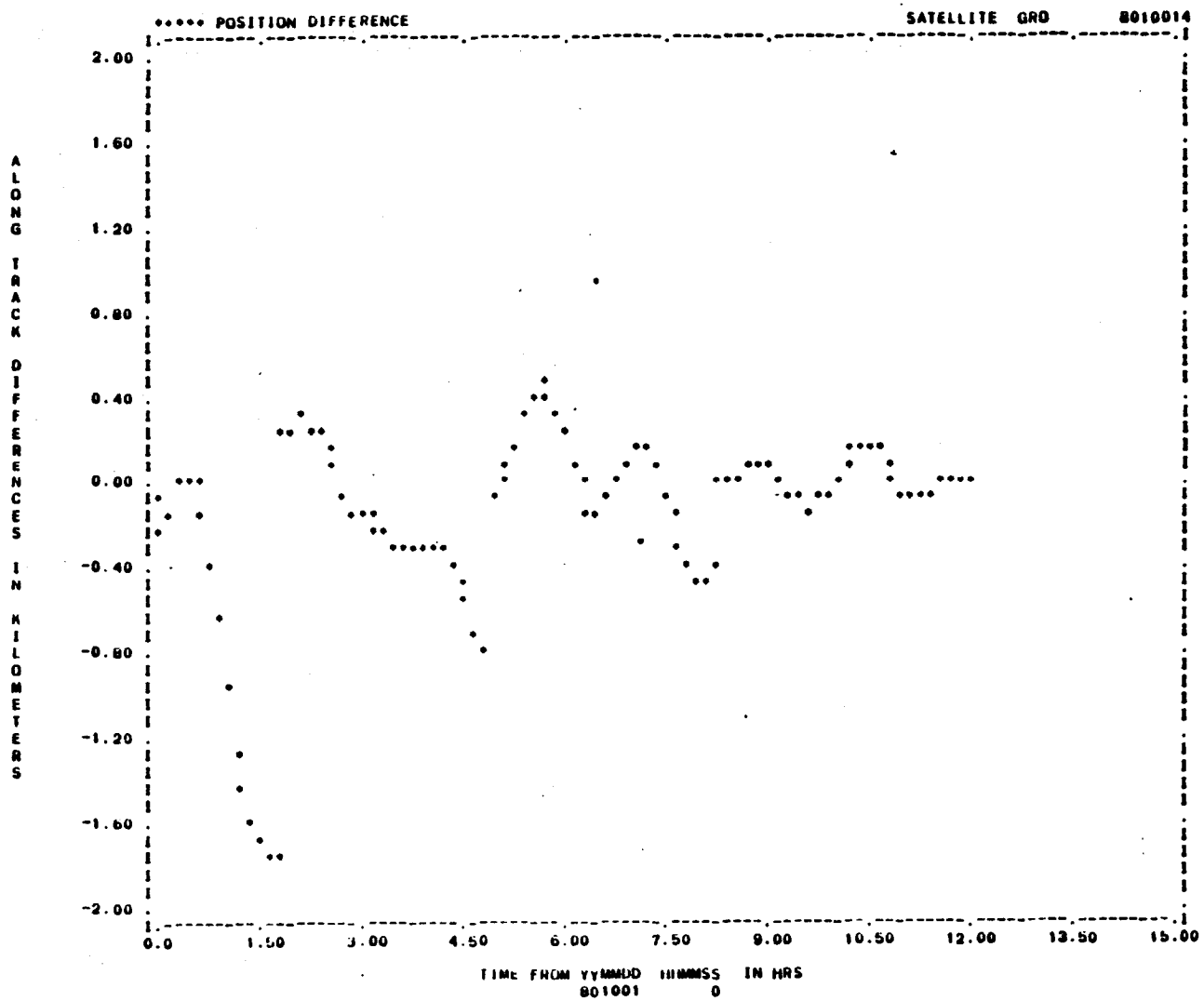

Figure B-24. Along-Track Differences for Run Q3 (1 of 2)

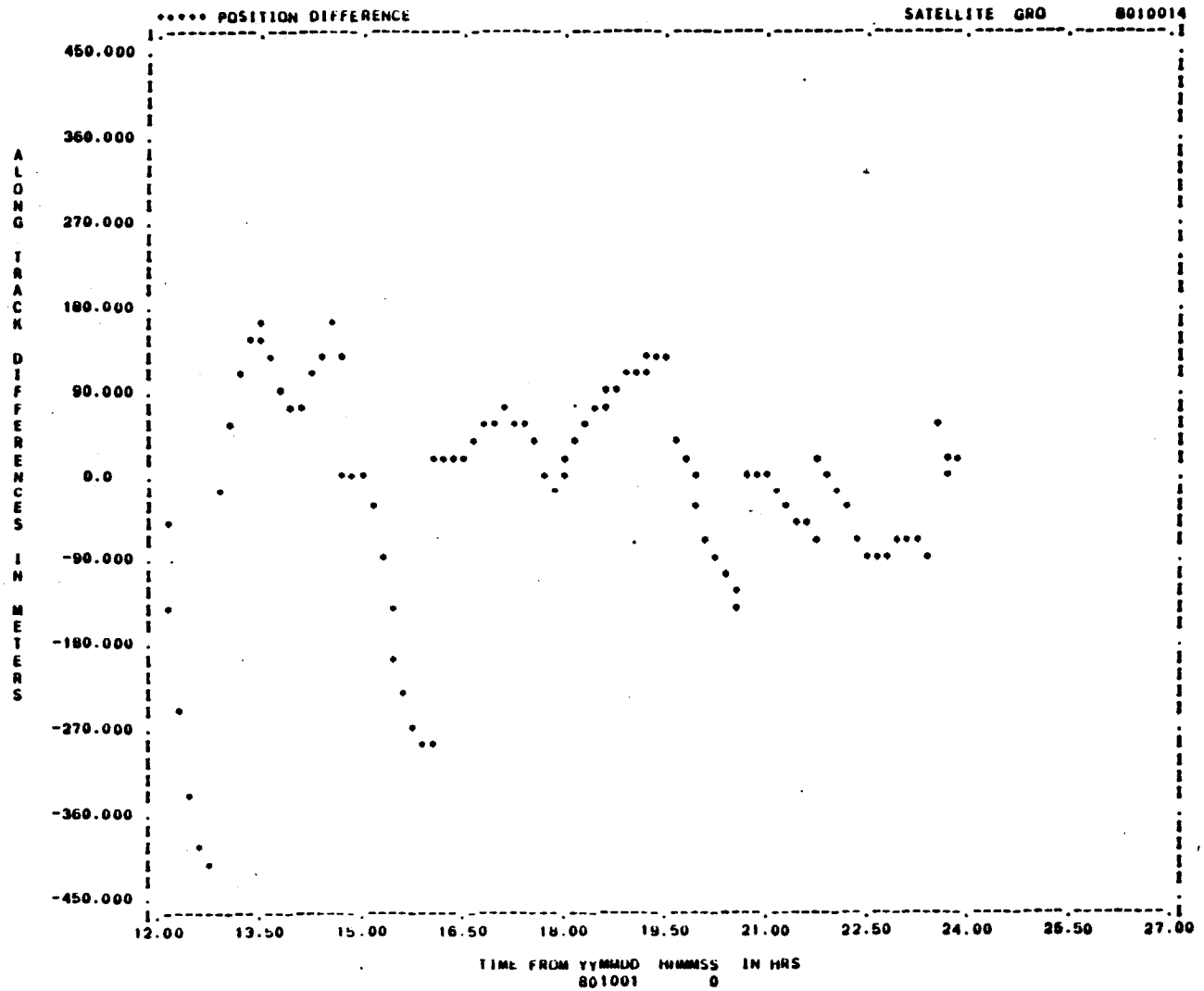

Figure B-24. Along-Track Differences for Run Q3 (2 of 2)

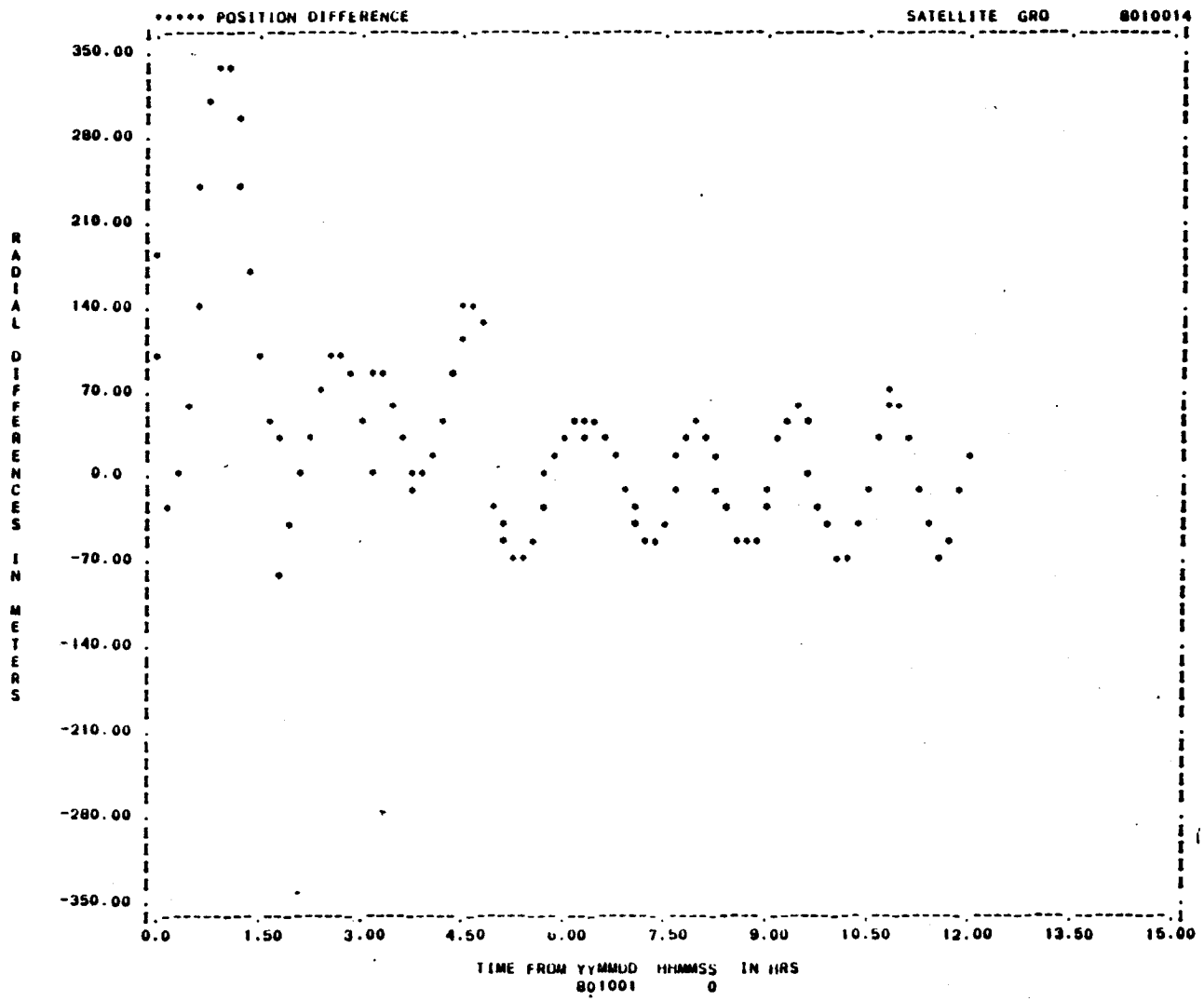

Figure B-25. Radial Differences for Run Q5 (1 of 2)

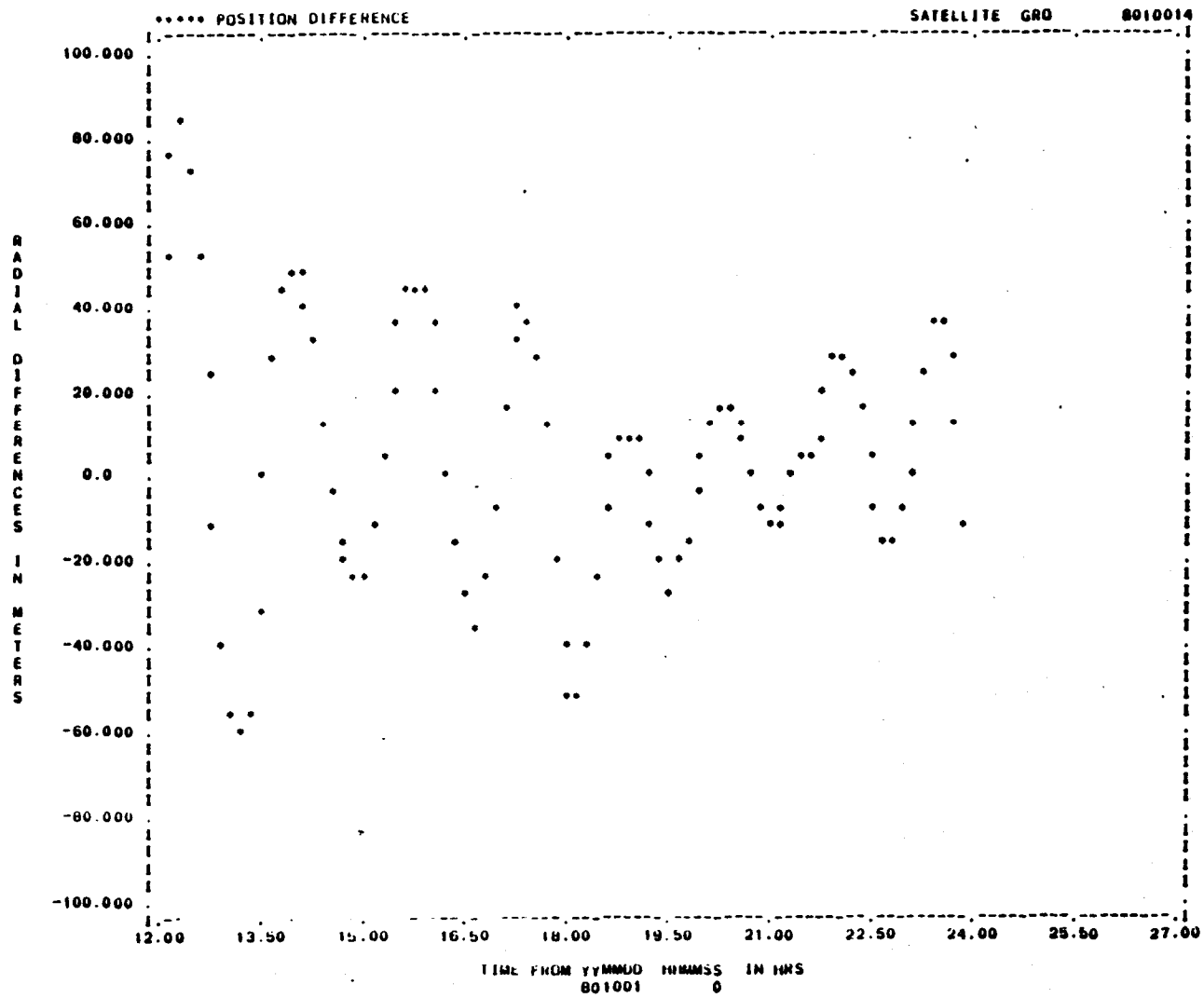

Figure B-25. Radial Differences for Run Q5 (2 of 2)

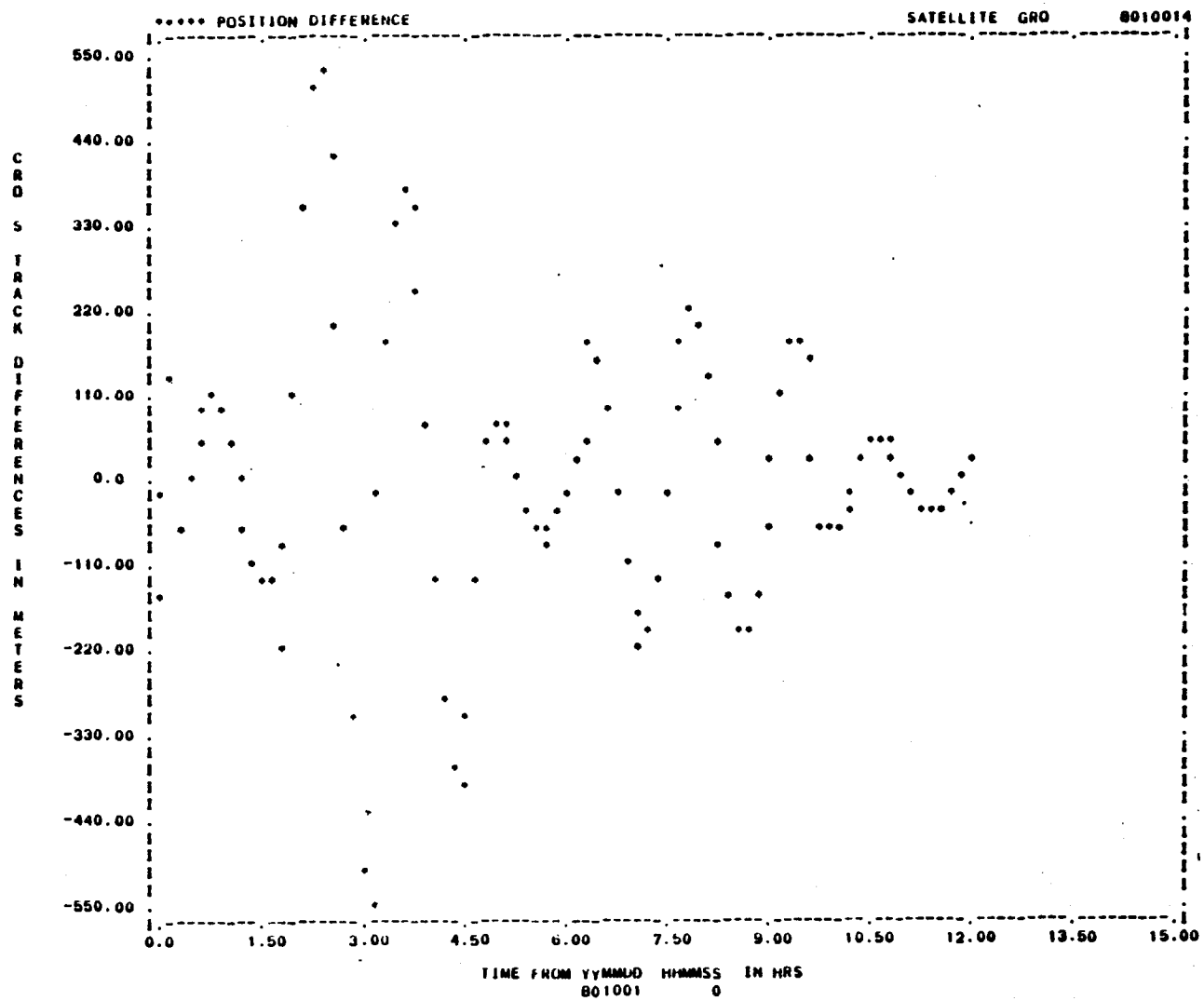

Figure B-26. Cross-Track Differences for Run Q5 (1 of 2)

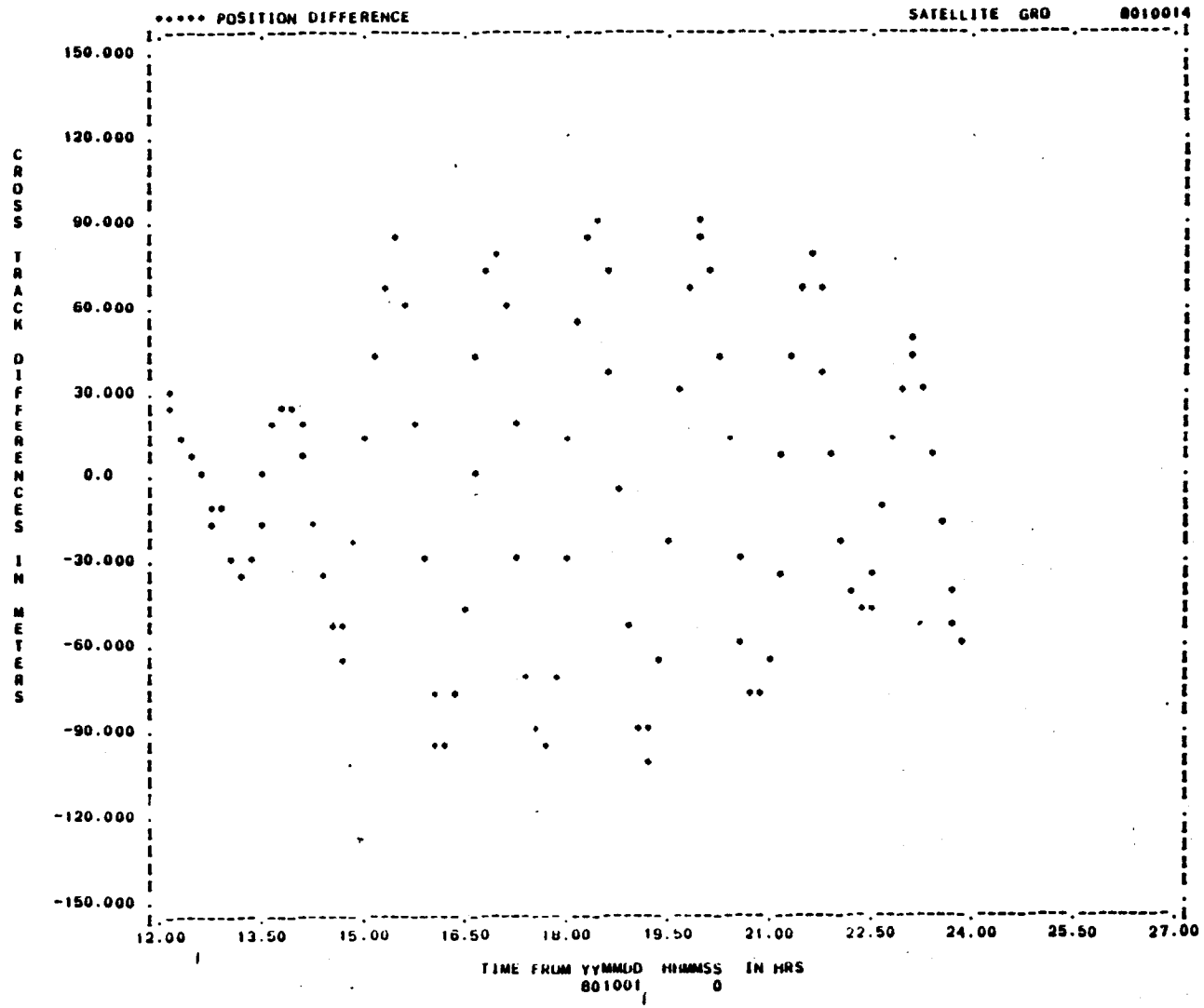

Figure B-26. Cross-Track Differences for Run Q5 (2 of 2)

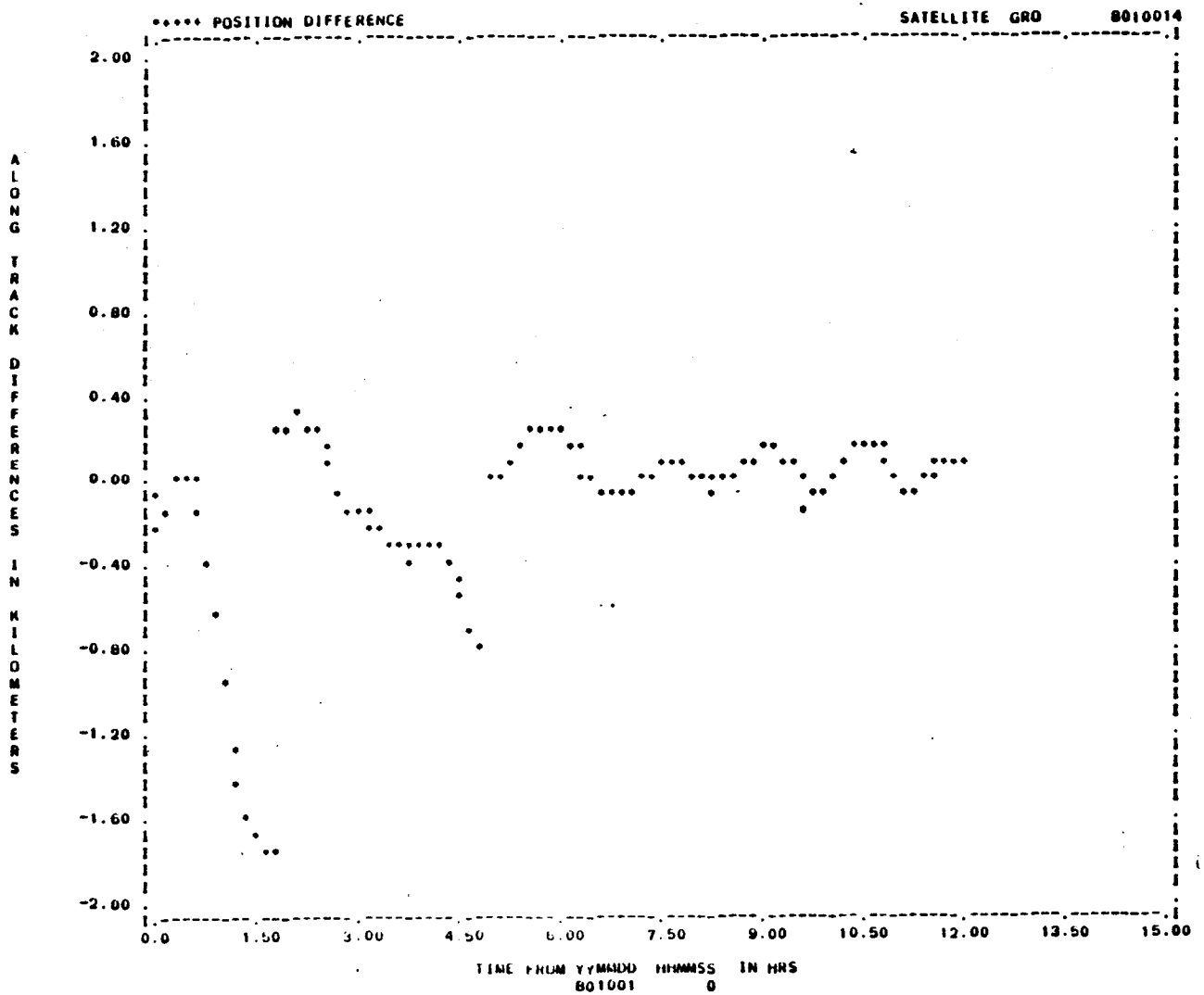

Figure B-27. Along-Track Differences for Run Q5 (1 of 2)

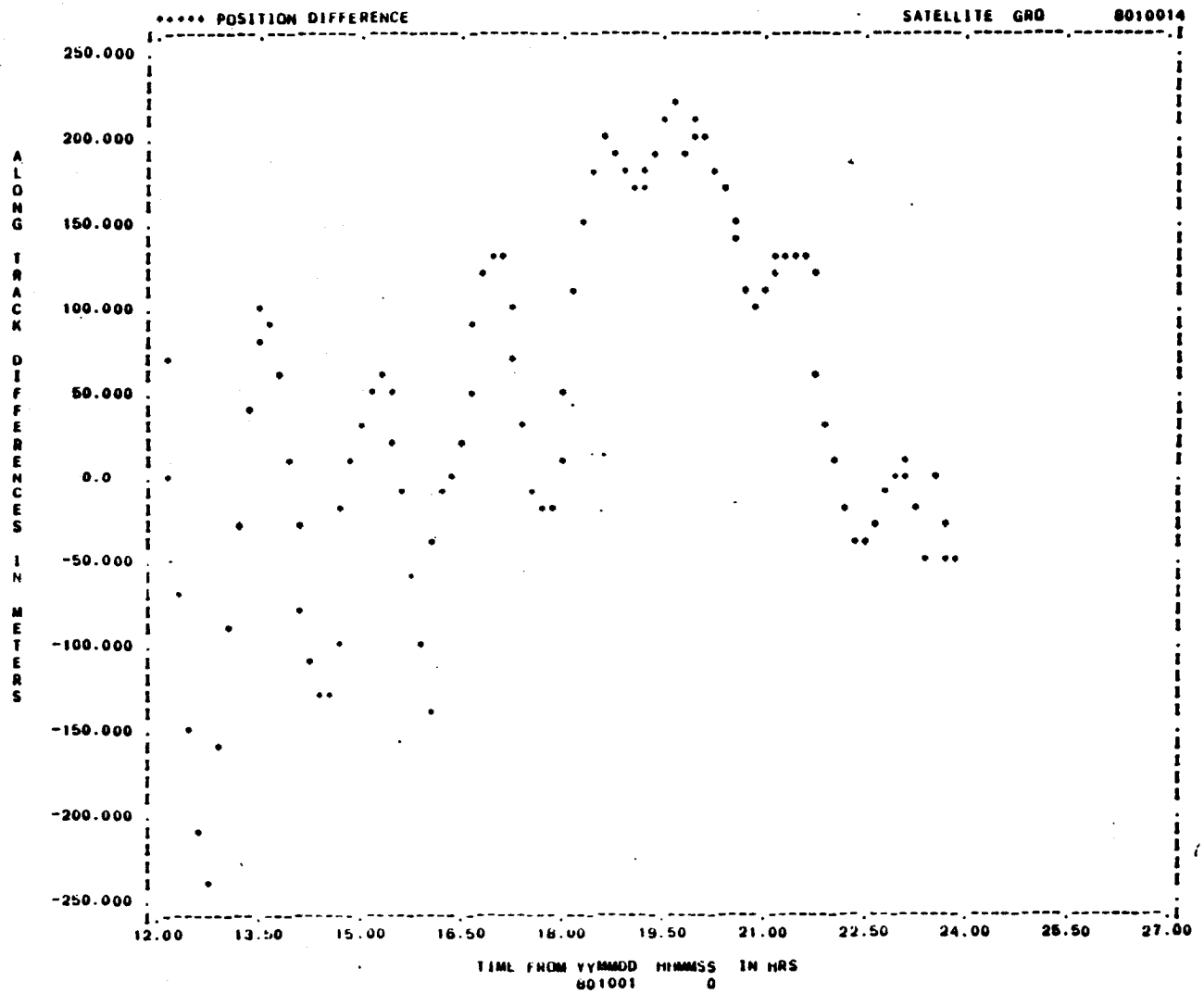

Figure B-27. Along-Track Differences for Run Q5 (2 of 2)

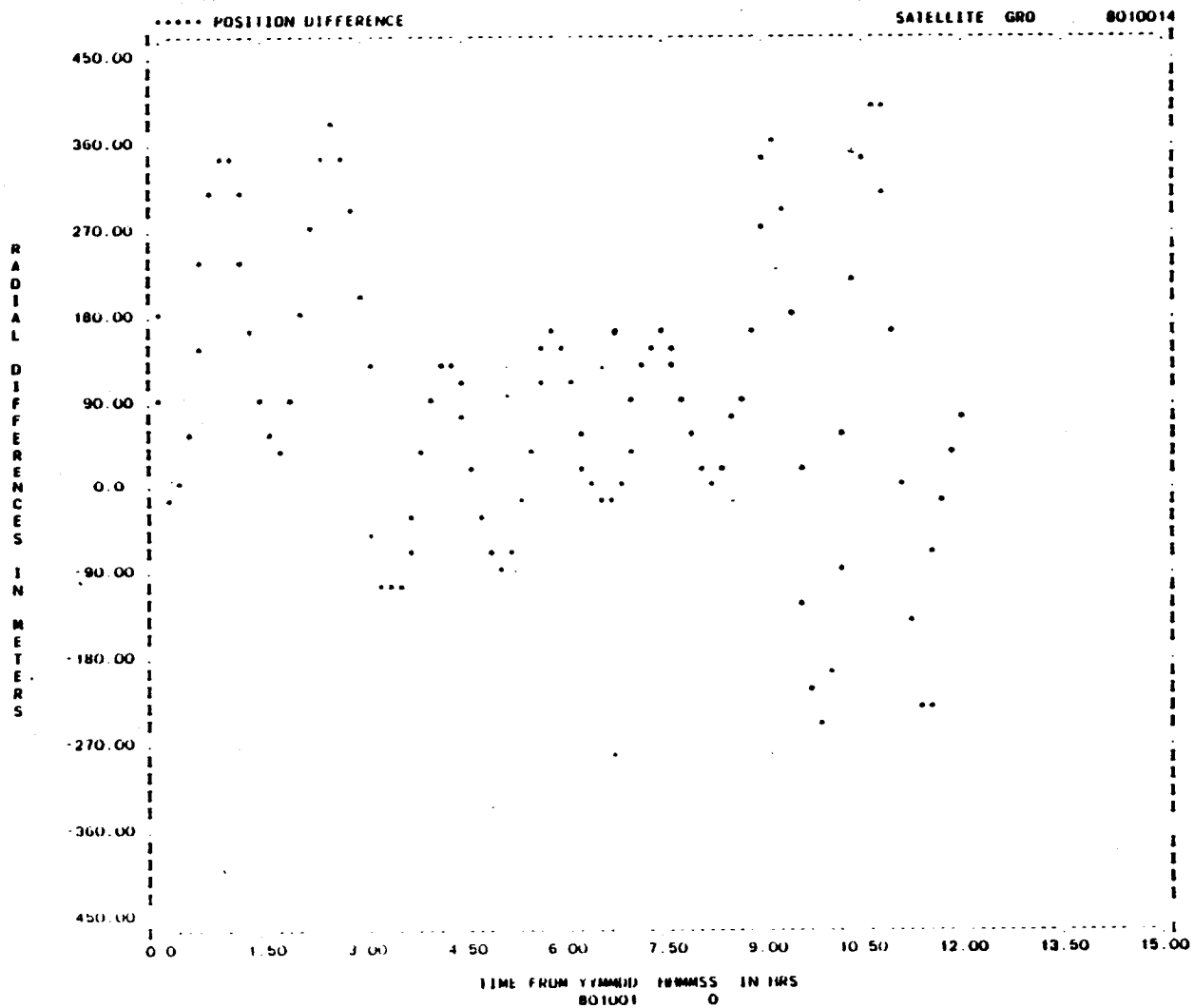

Figure B-28. Radial Differences for Run Q9 (1 of 2)

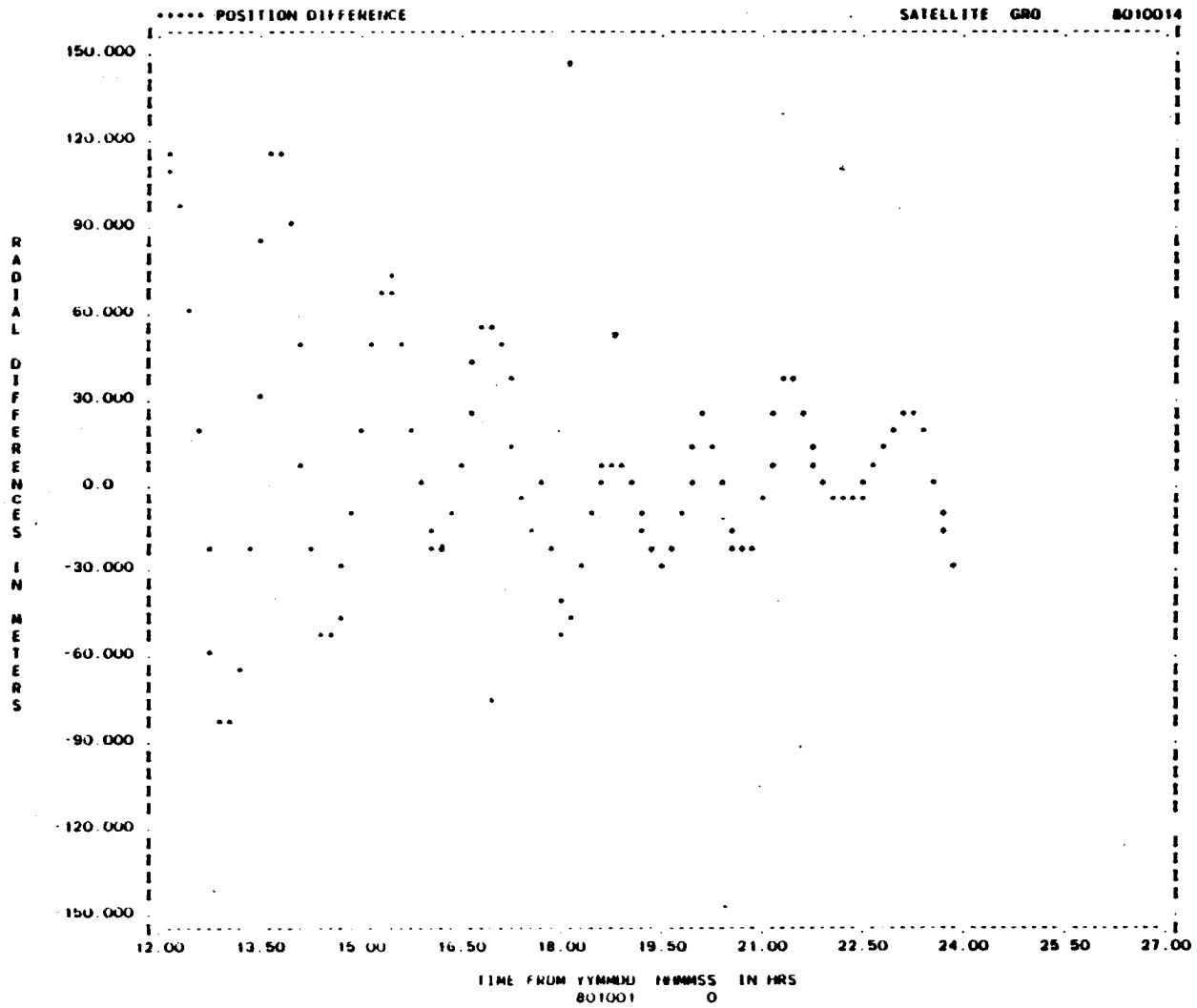

Figure B-28. Radial Differences for Run Q9 (2 of 2)

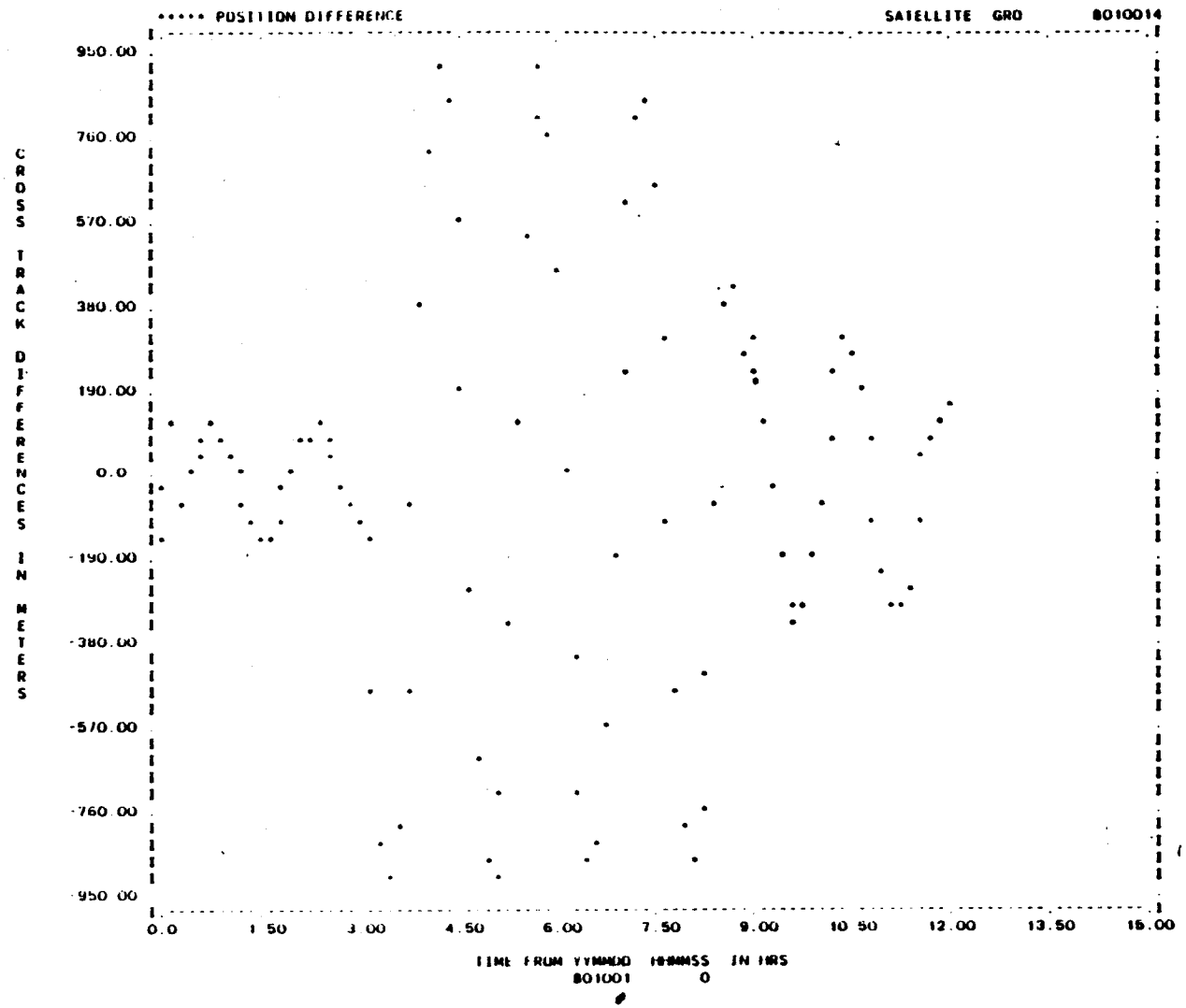

Figure B-29. Cross-Track Differences for Run Q9 (1 of 2)

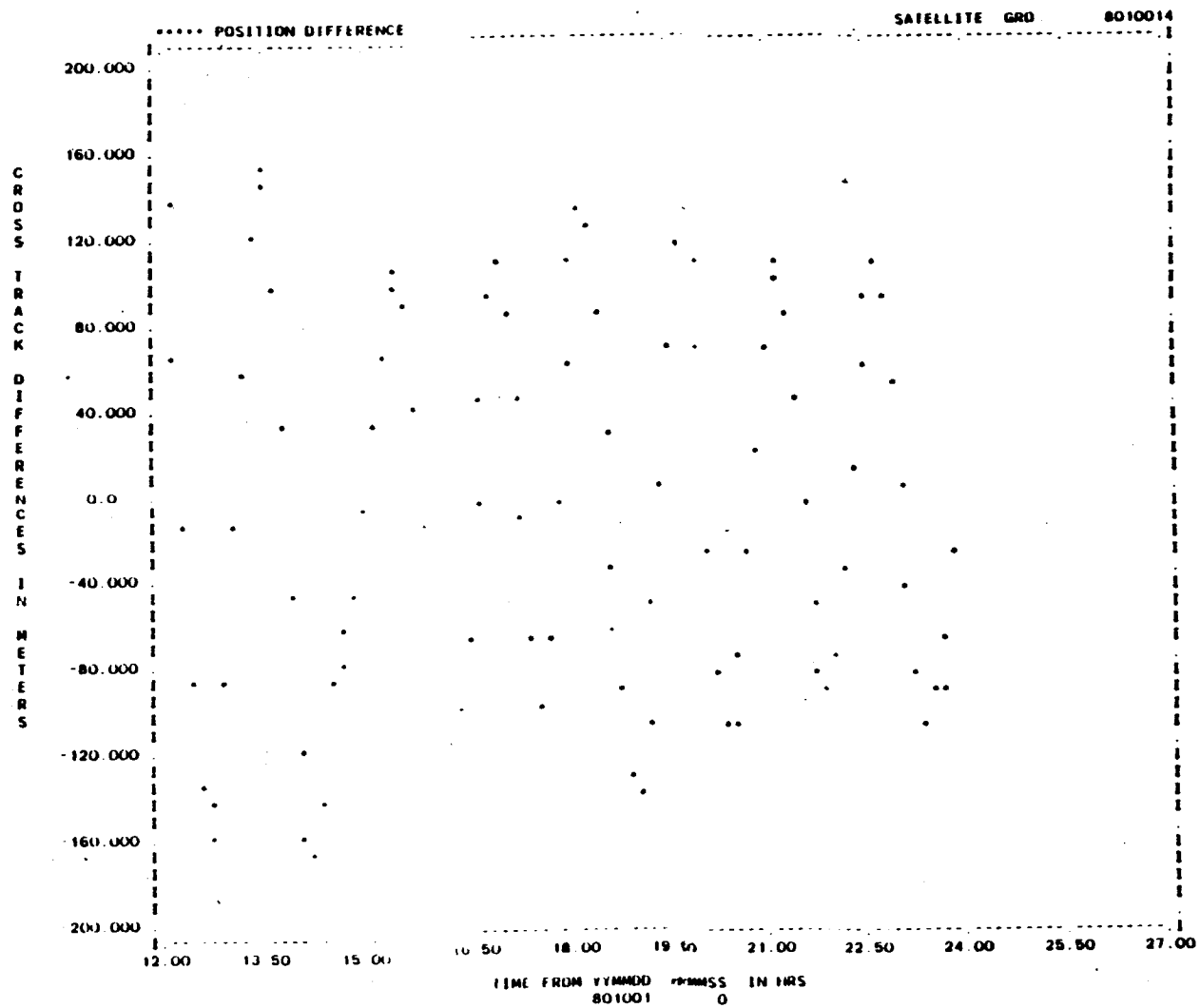

Figure B-29. Cross-Track Differences for Run Q9 (2 of 2)

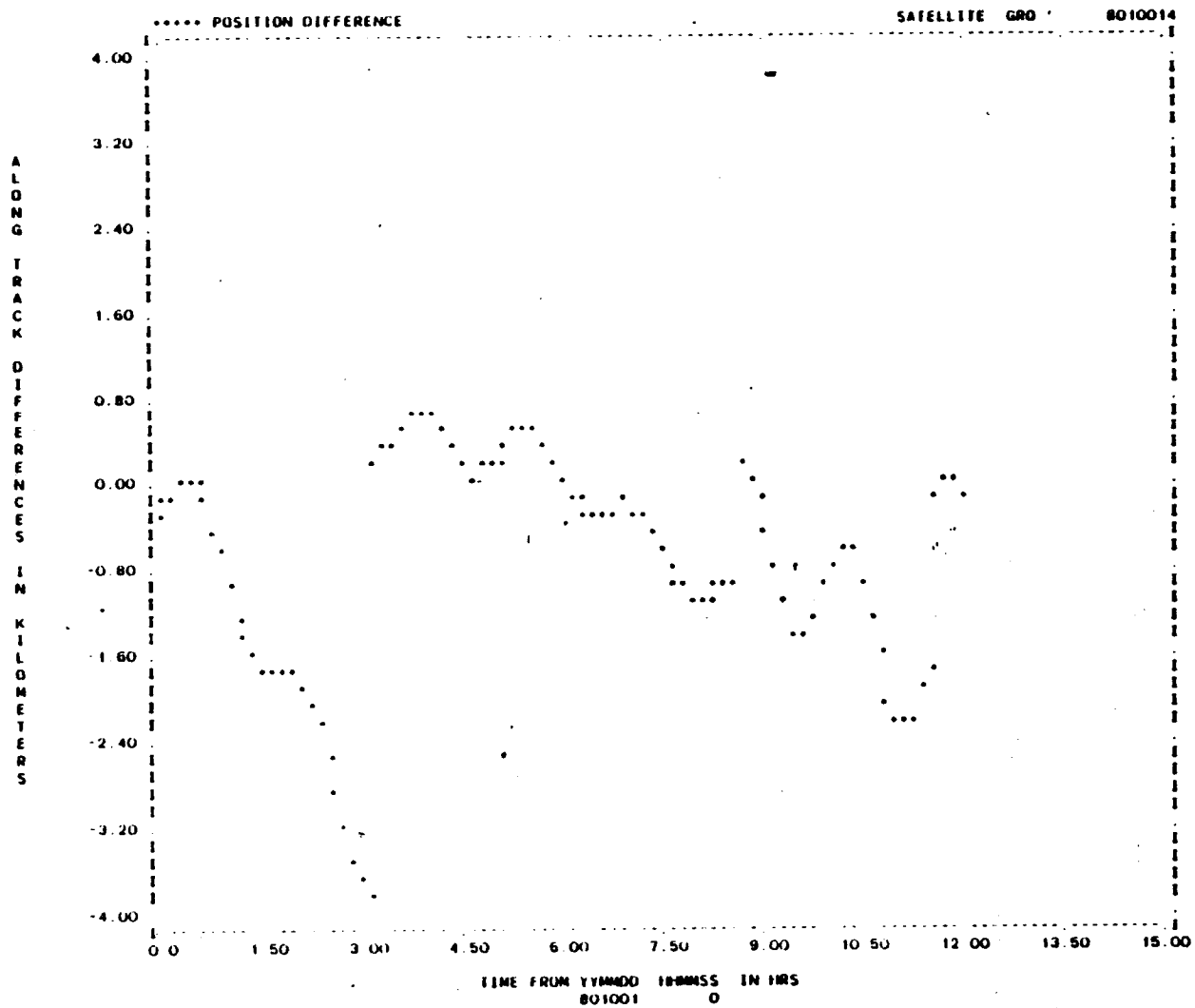

Figure B-30. Along-Track Differences for Run Q9 (1 of 2)

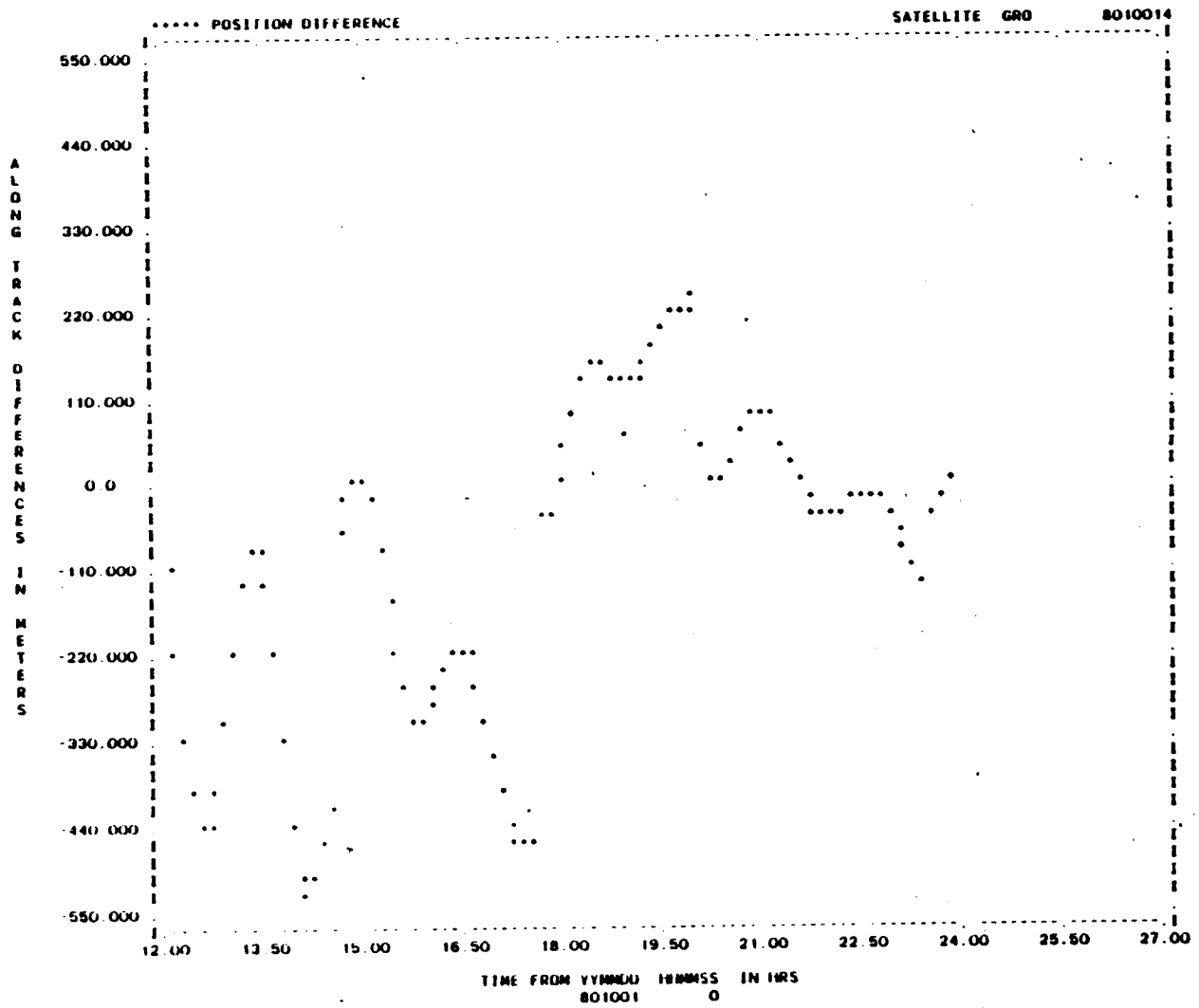

Figure B-30. Along-Track Differences for Run Q9 (2 of 2)

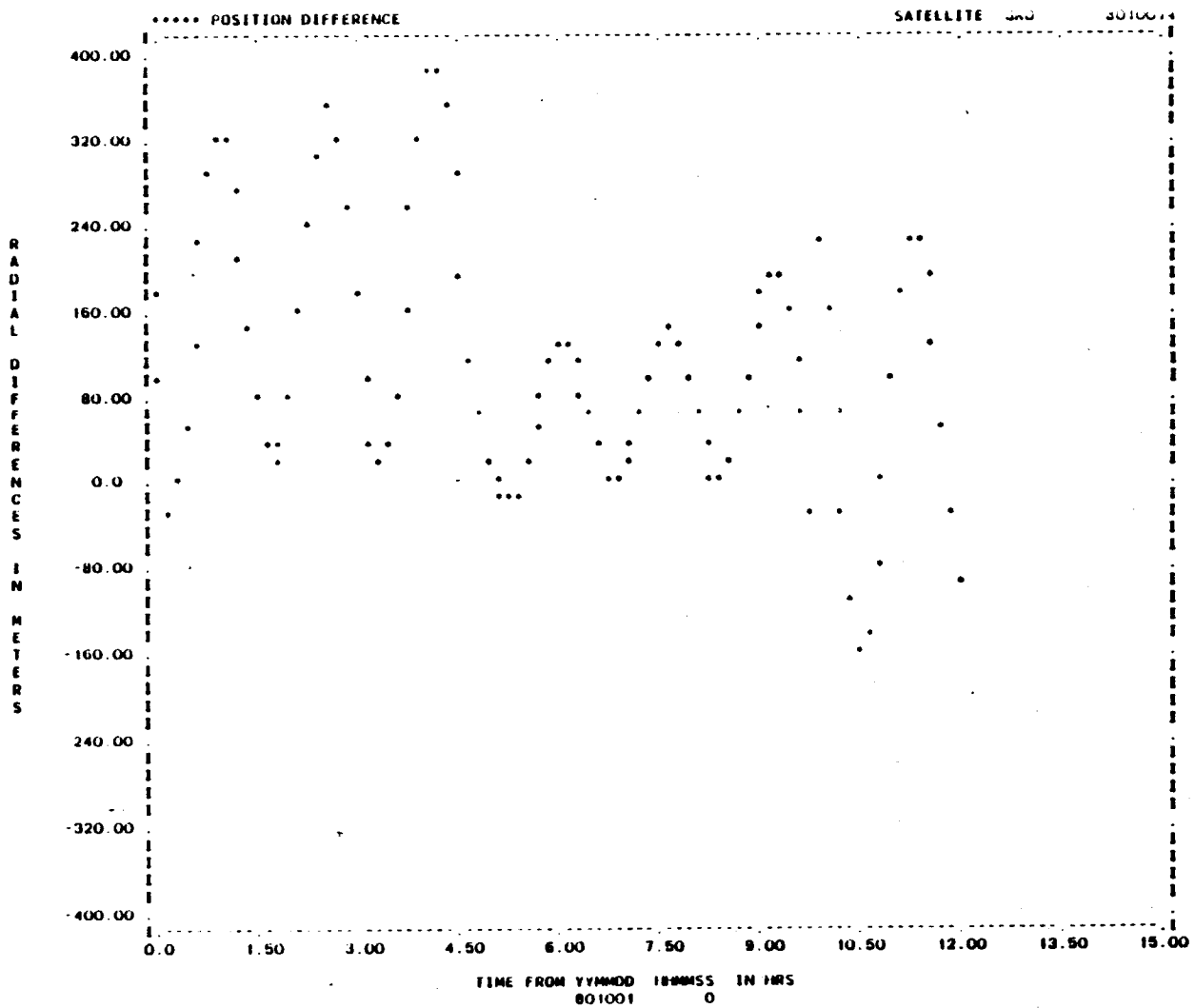

Figure B-31. Radial Differences for Run Q13 (1 of 2)

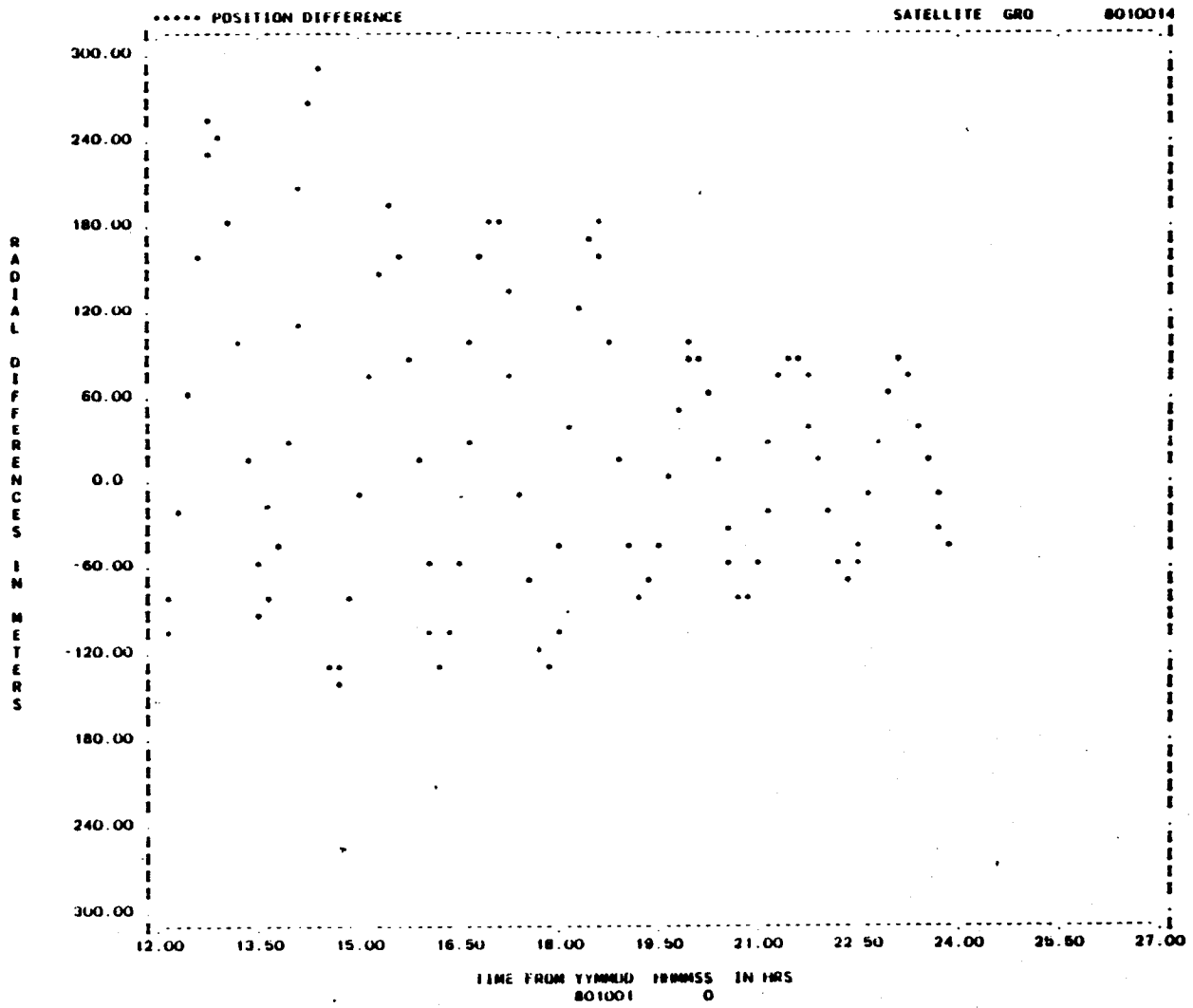

Figure B-31. Radial Differences for Run Q13 (2 of 2)

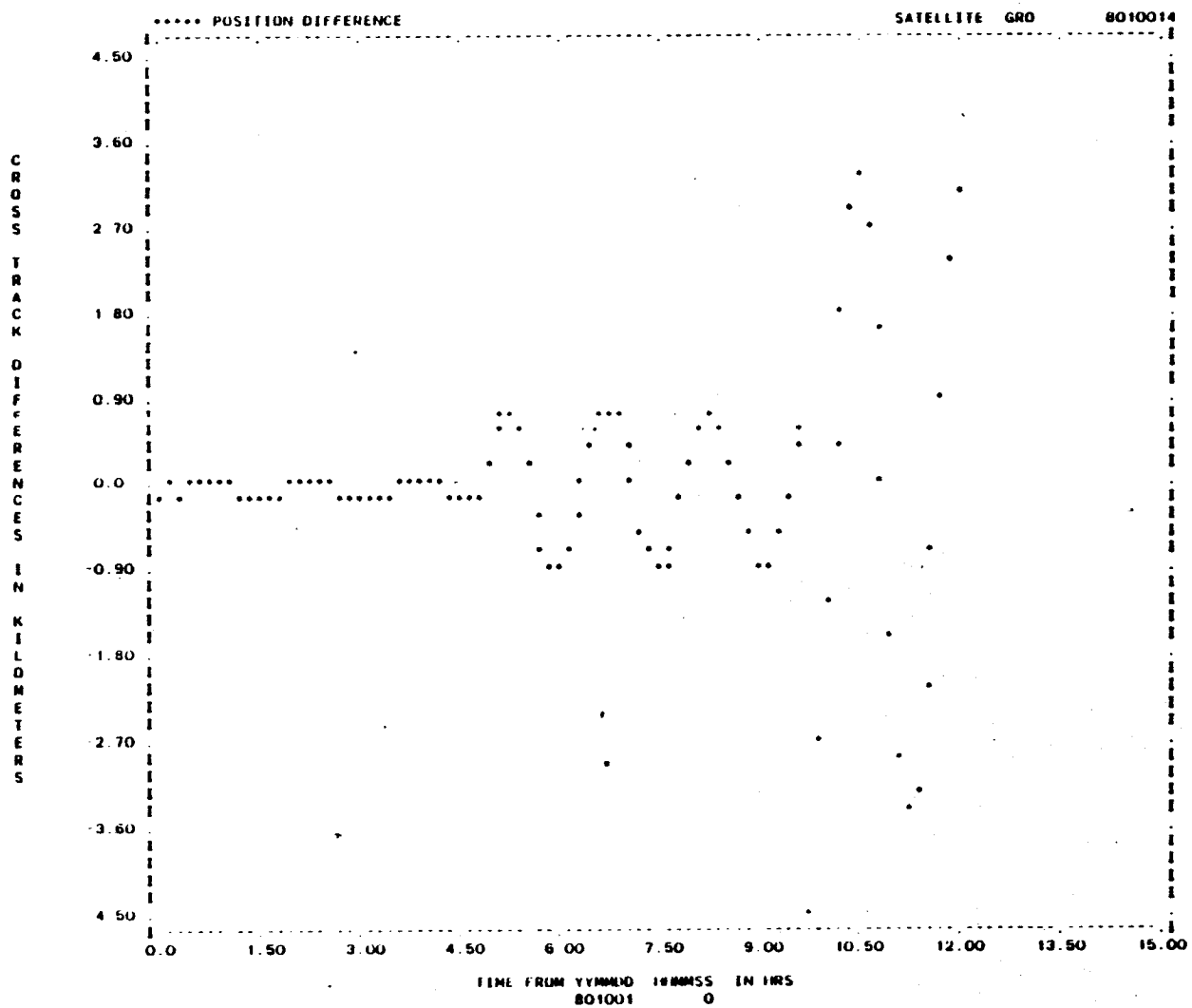

Figure B-32. Cross-Track Differences for Run Q13 (1 of 2)

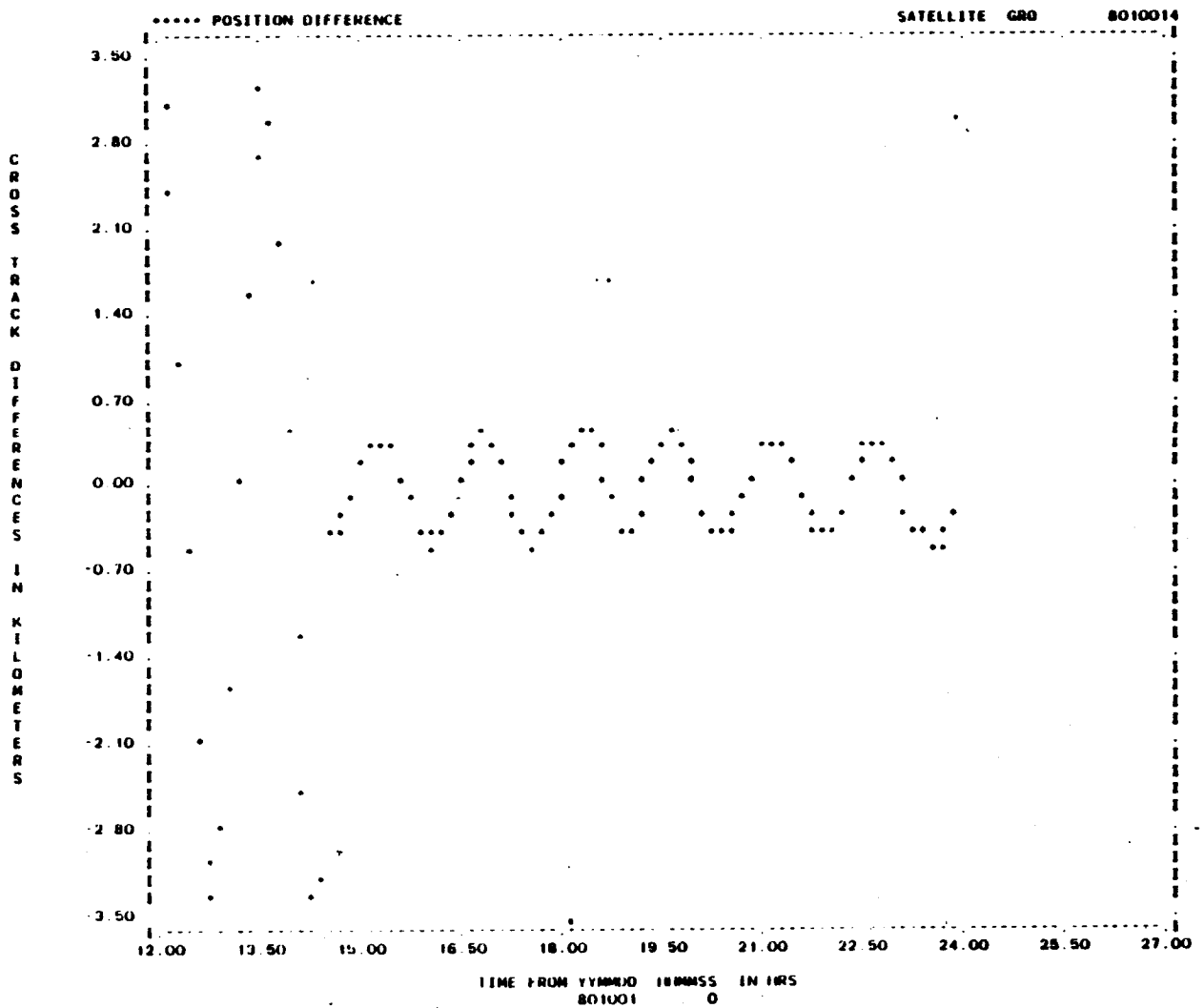

Figure B-32. Cross-Track Differences for Run Q13 (2 of 2)

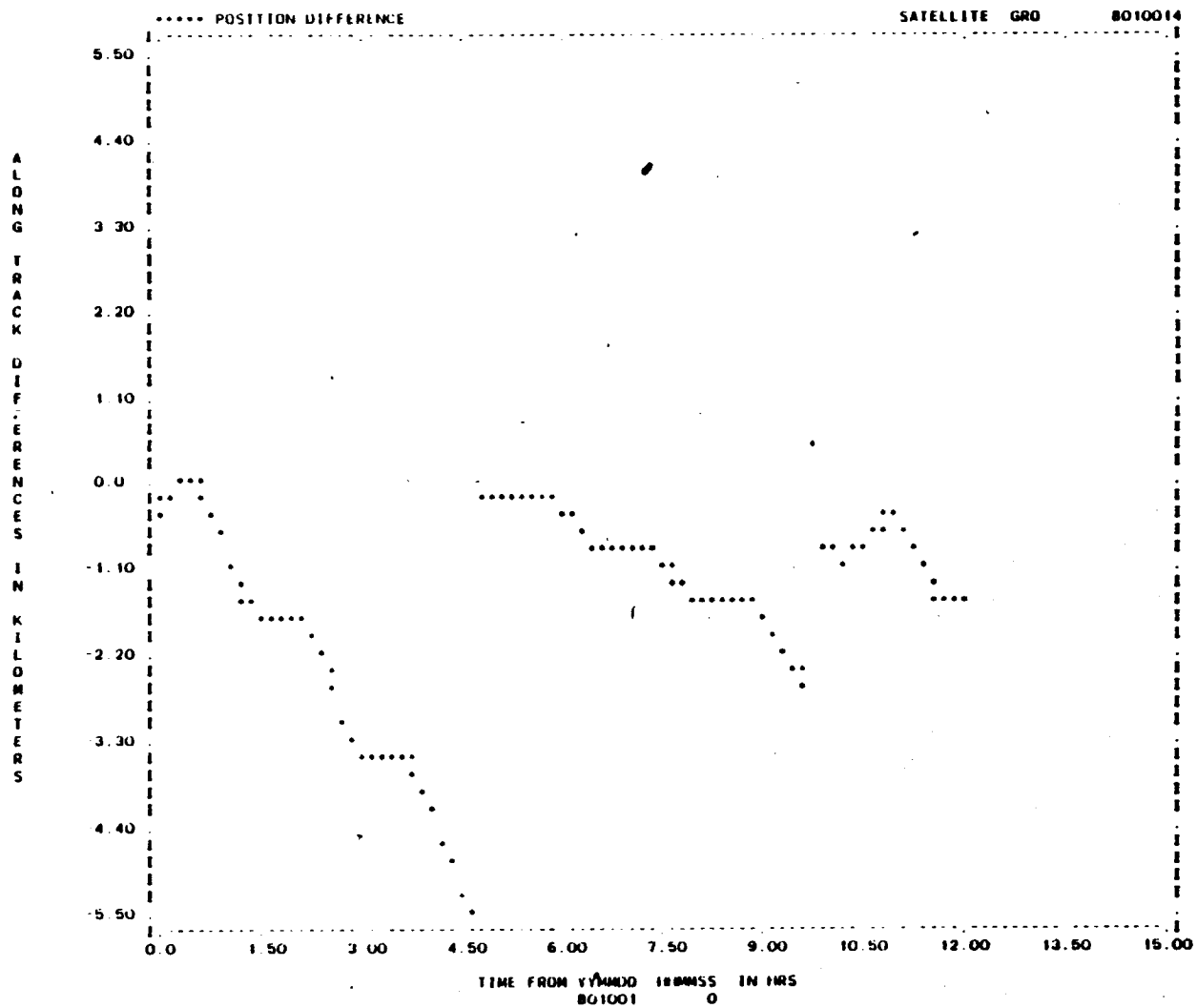

Figure B-33. Along-Track Differences for Run Q13 (1 of 2)

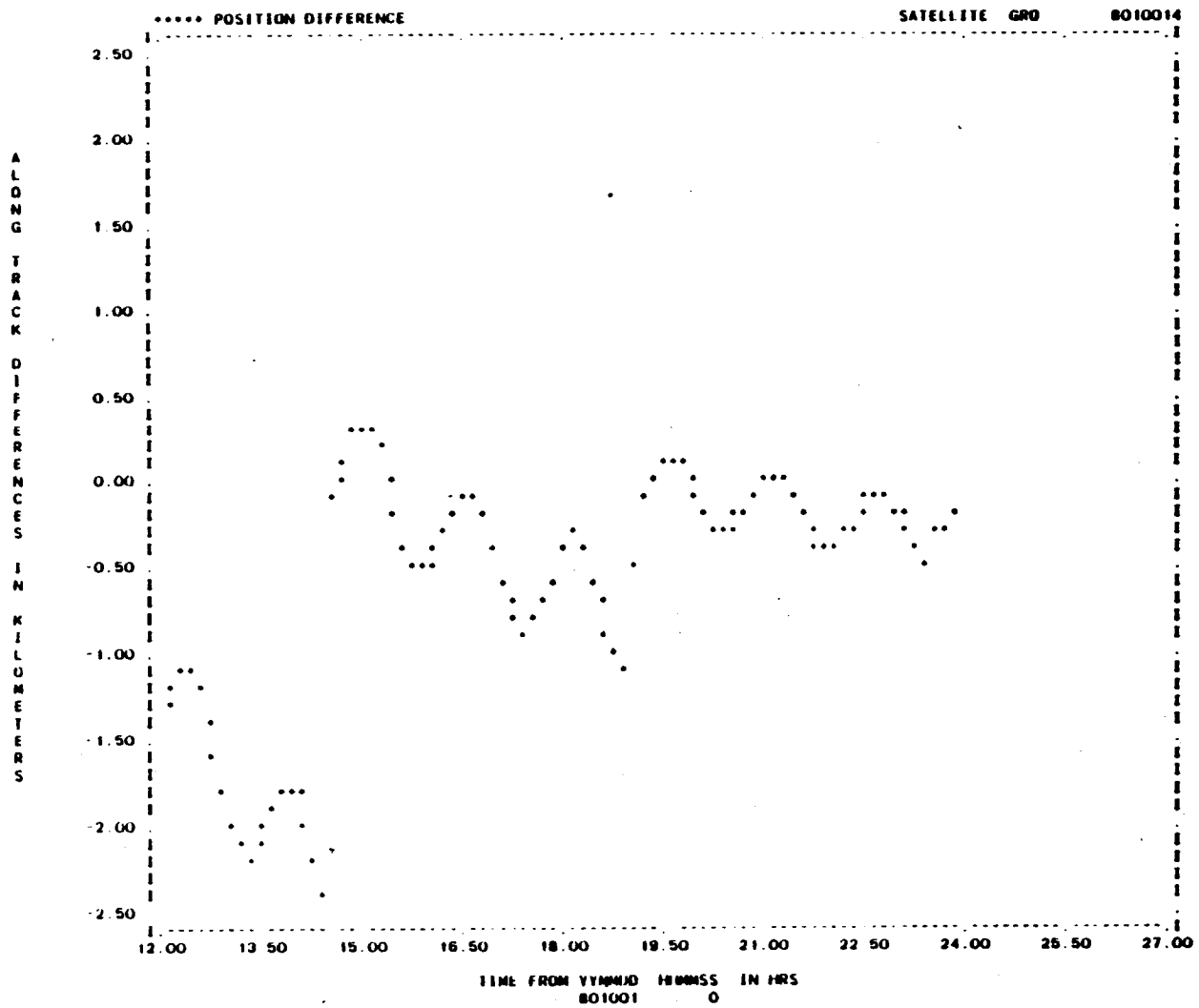

Figure B-33. Along-Track Differences for Run Q13 (2 of 2)

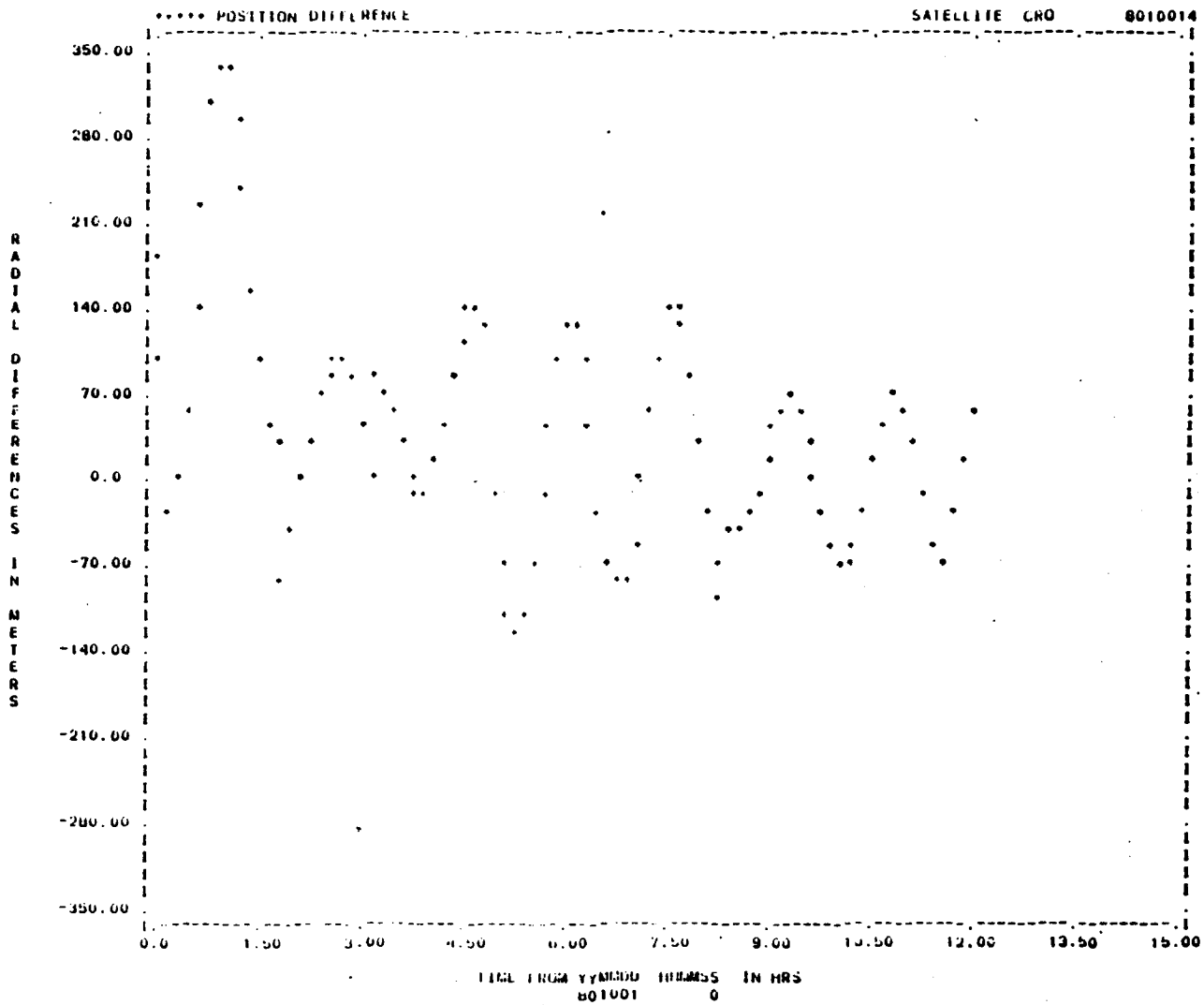

Figure B-34. Radial Differences for Run Q17 (1 of 2)

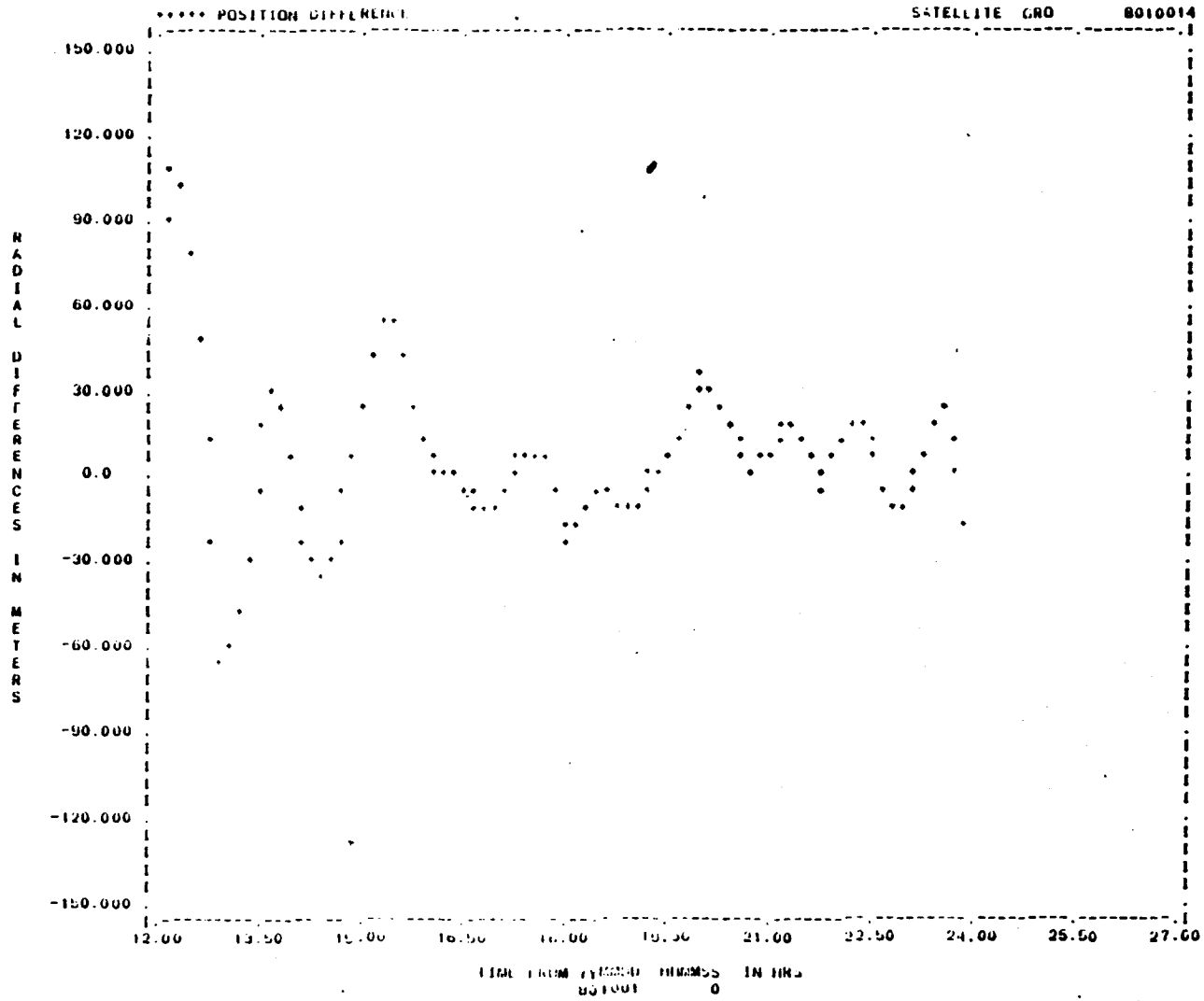

Figure B-34. Radial Differences for Run Q17 (2 of 2)

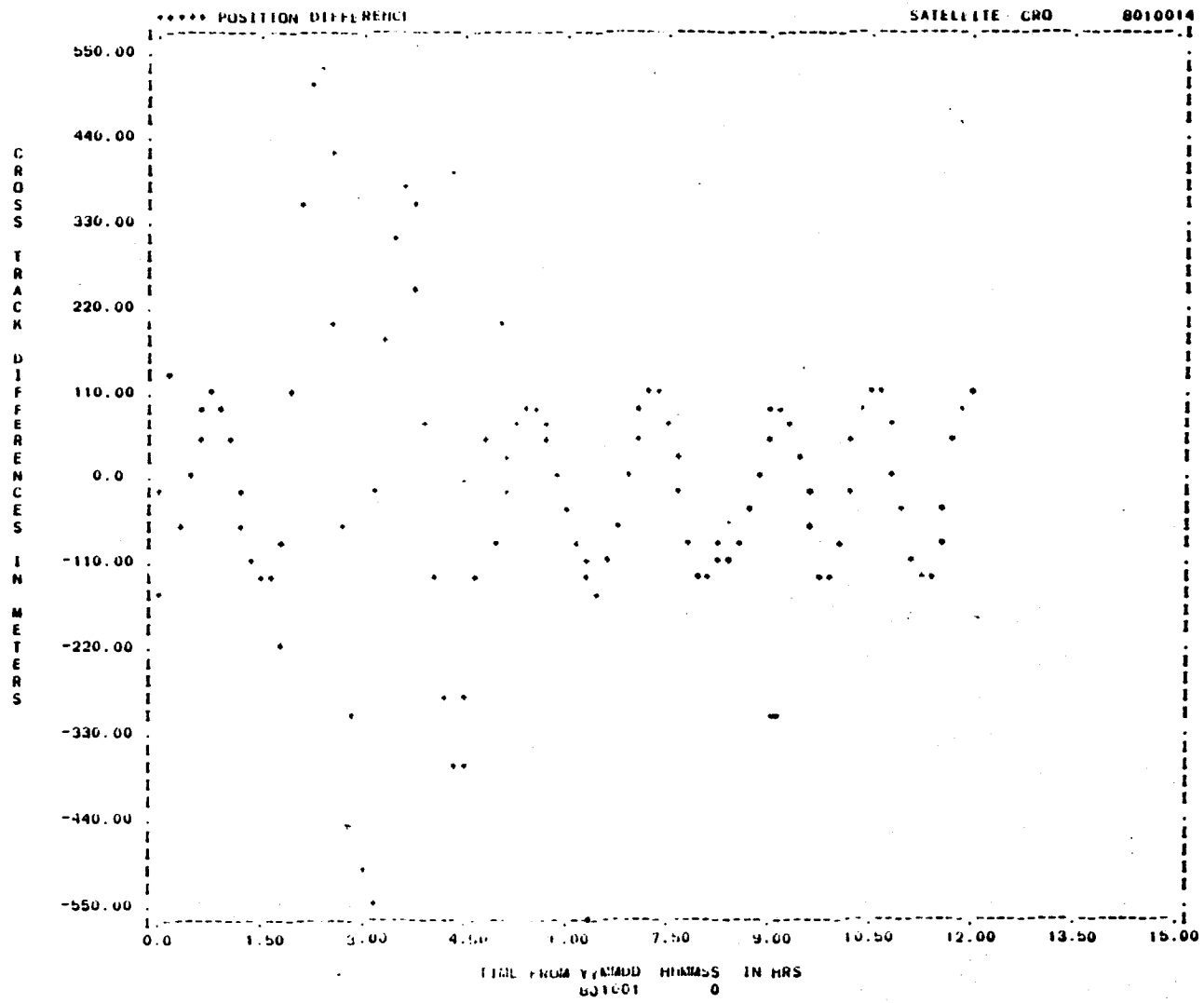

Figure B-35. Cross-Track Differences for Run Q17 (1 of 2)

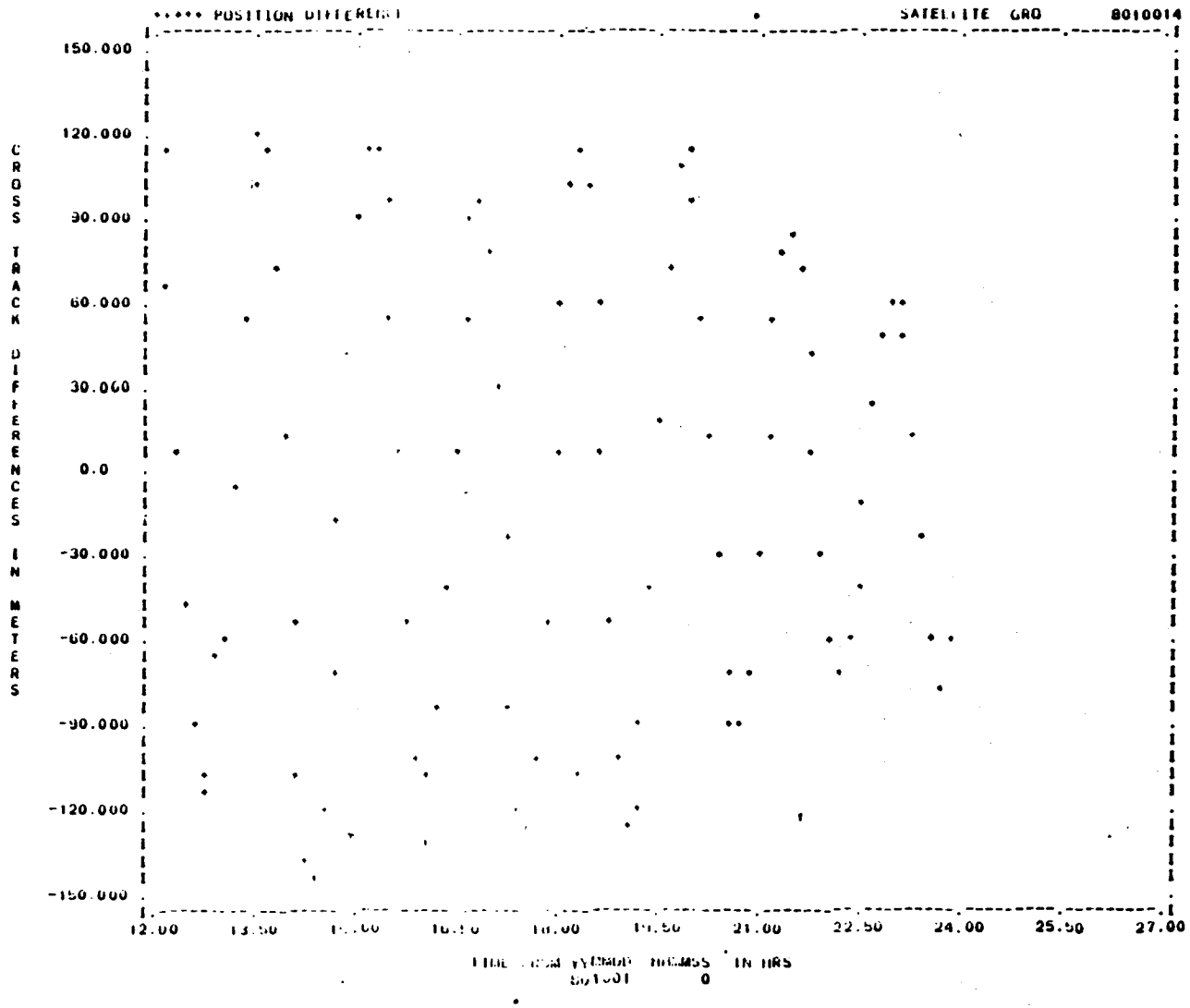

Figure B-35. Cross-Track Differences for Run Q17 (2 of 2)

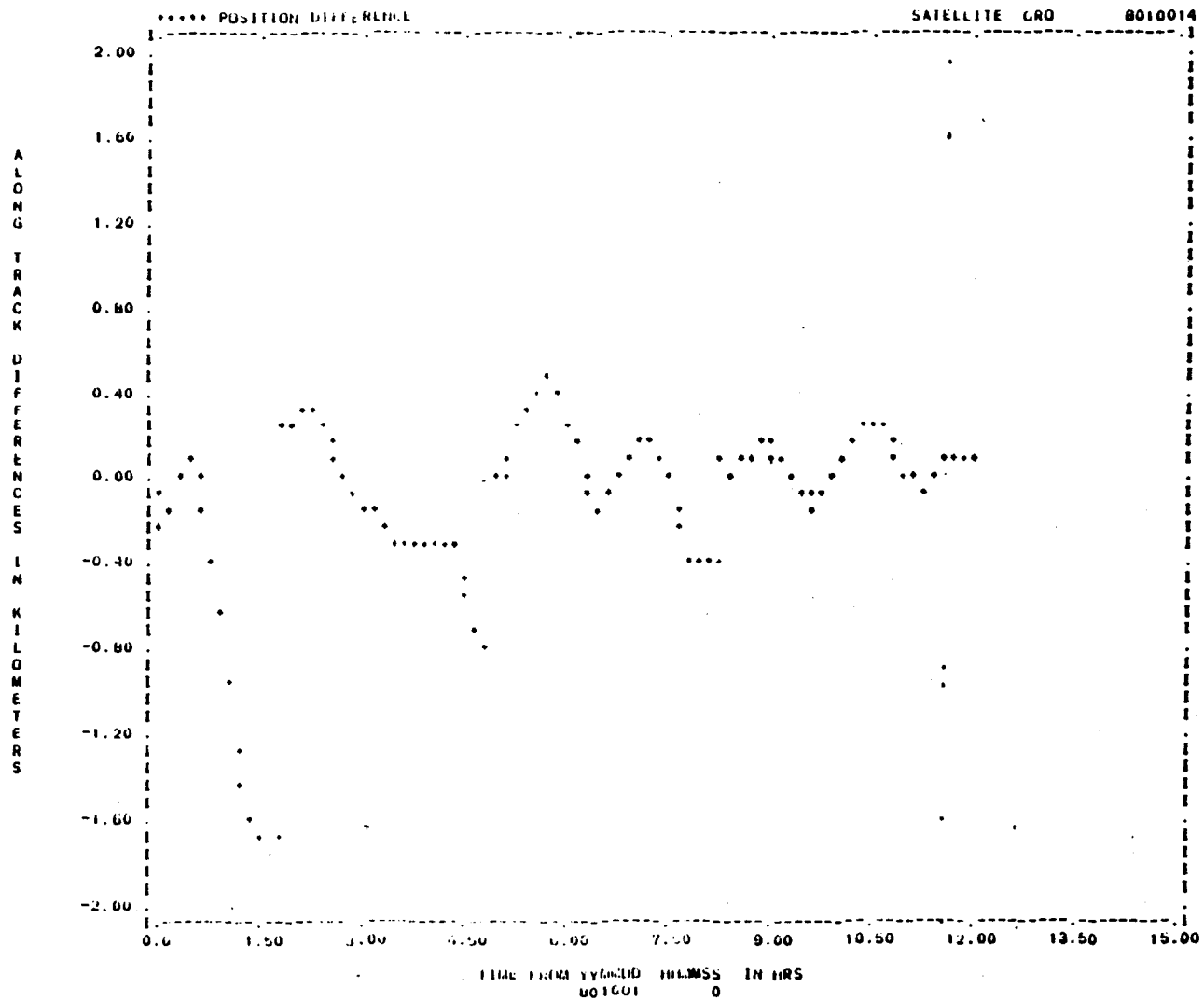

Figure B-36. Along-Track Differences for Run Q17 (1 of 2)

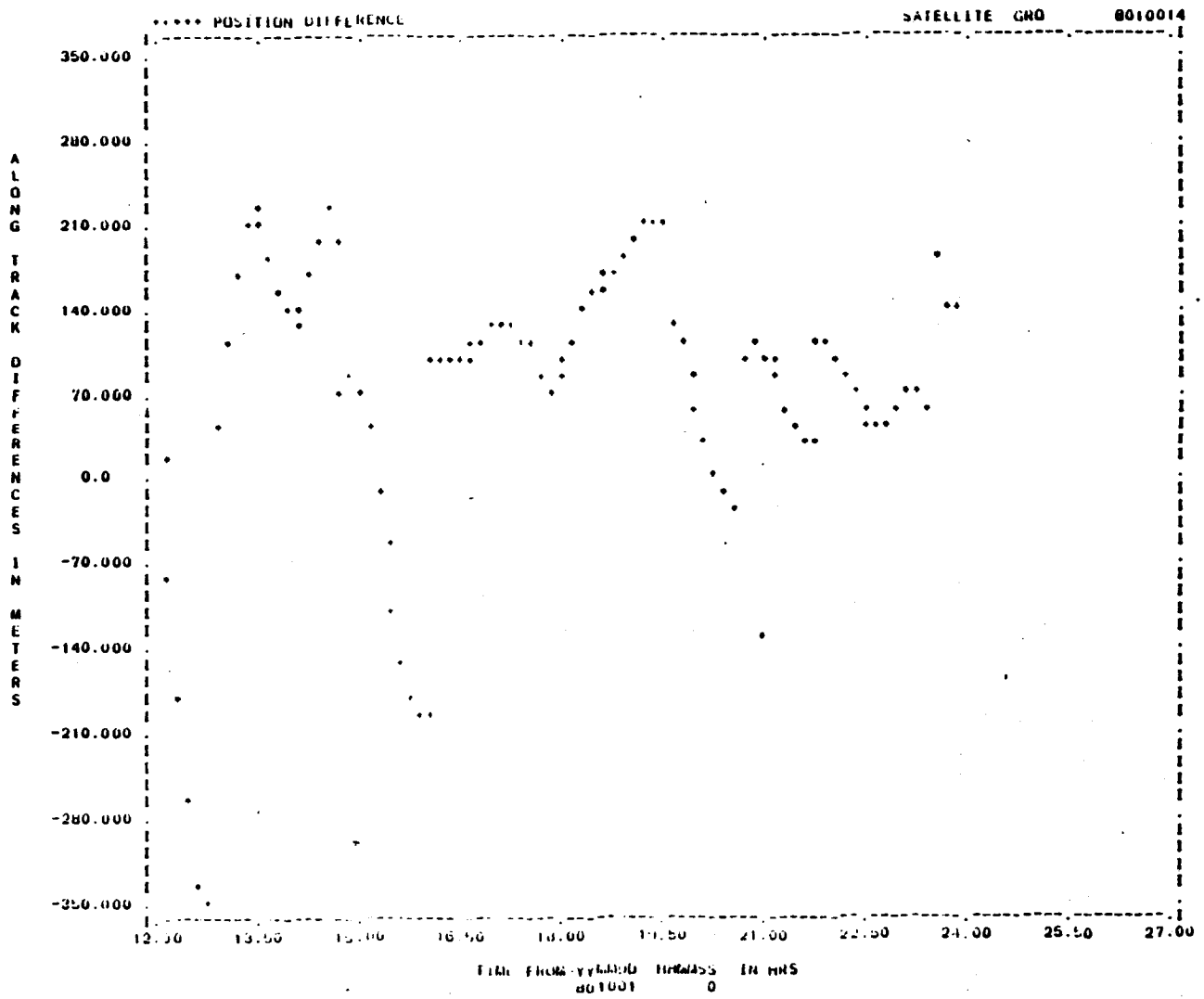

Figure B-36. Along-Track Differences for Run Q17 (2 of 2)

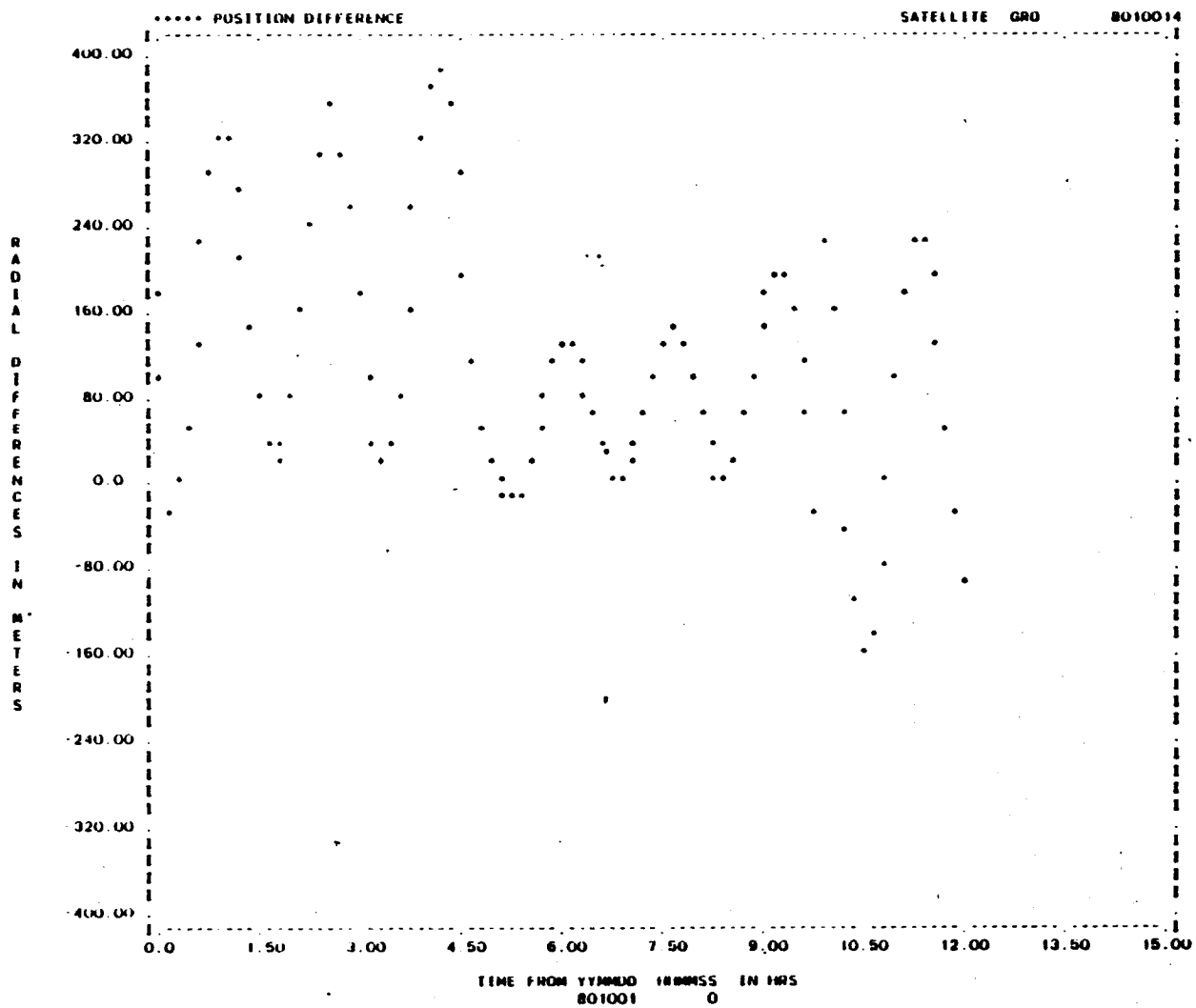

Figure B-37. Radial Differences for Run Q20 (1 of 2)

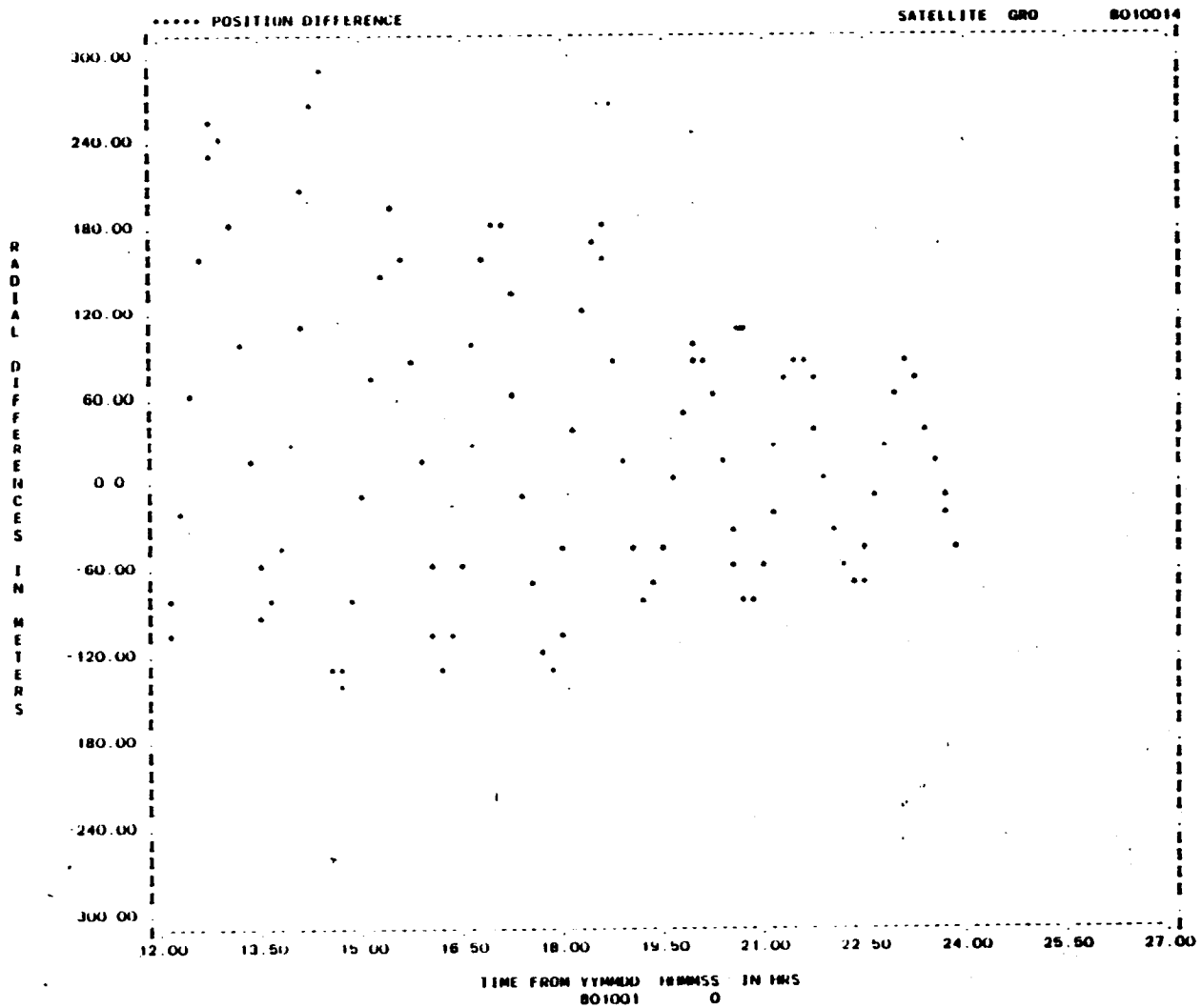

Figure B-37. Radial Differences for Run Q20 (2 of 2)

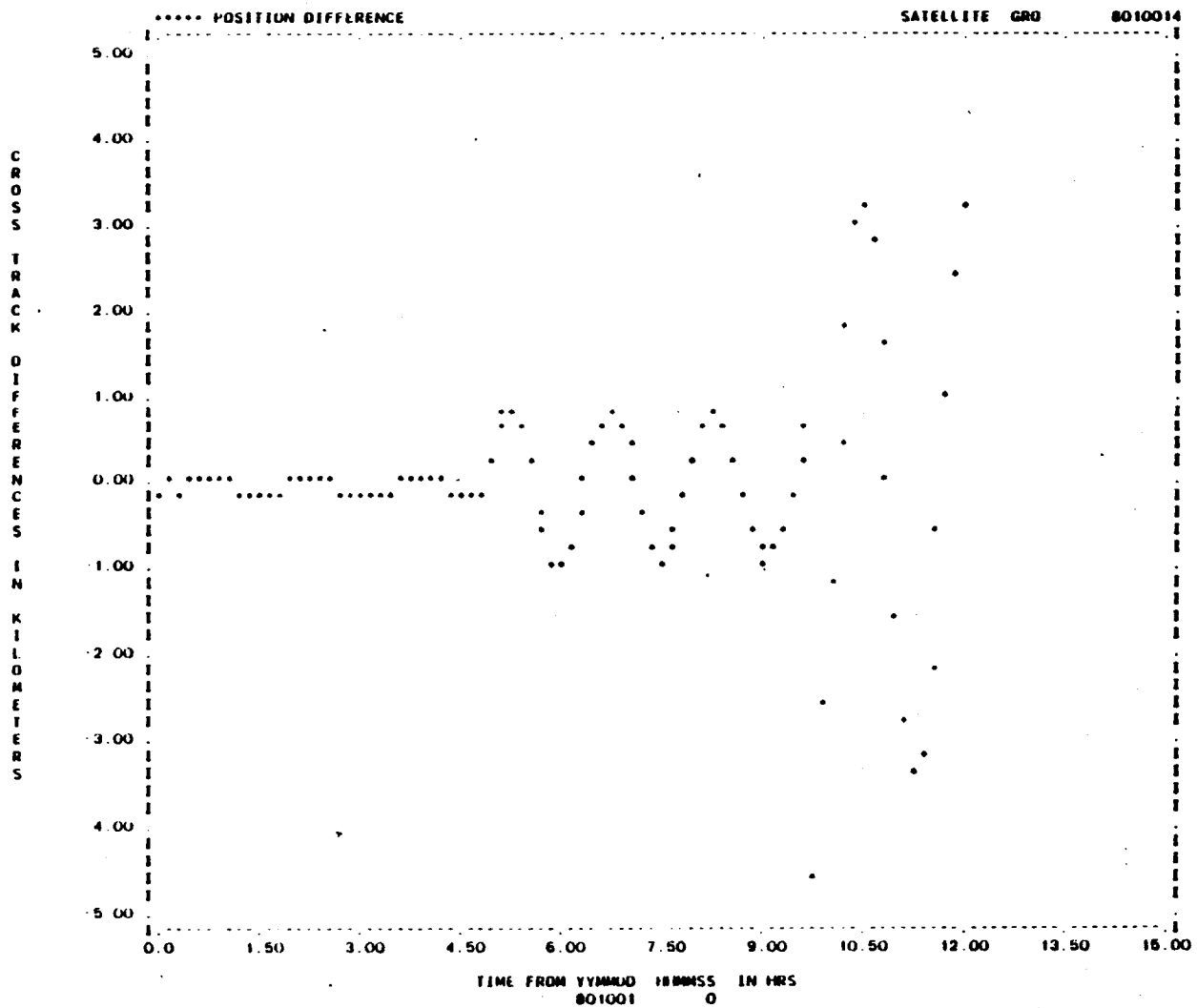

Figure B-38. Cross-Track Differences for Run Q20 (1 of 2)

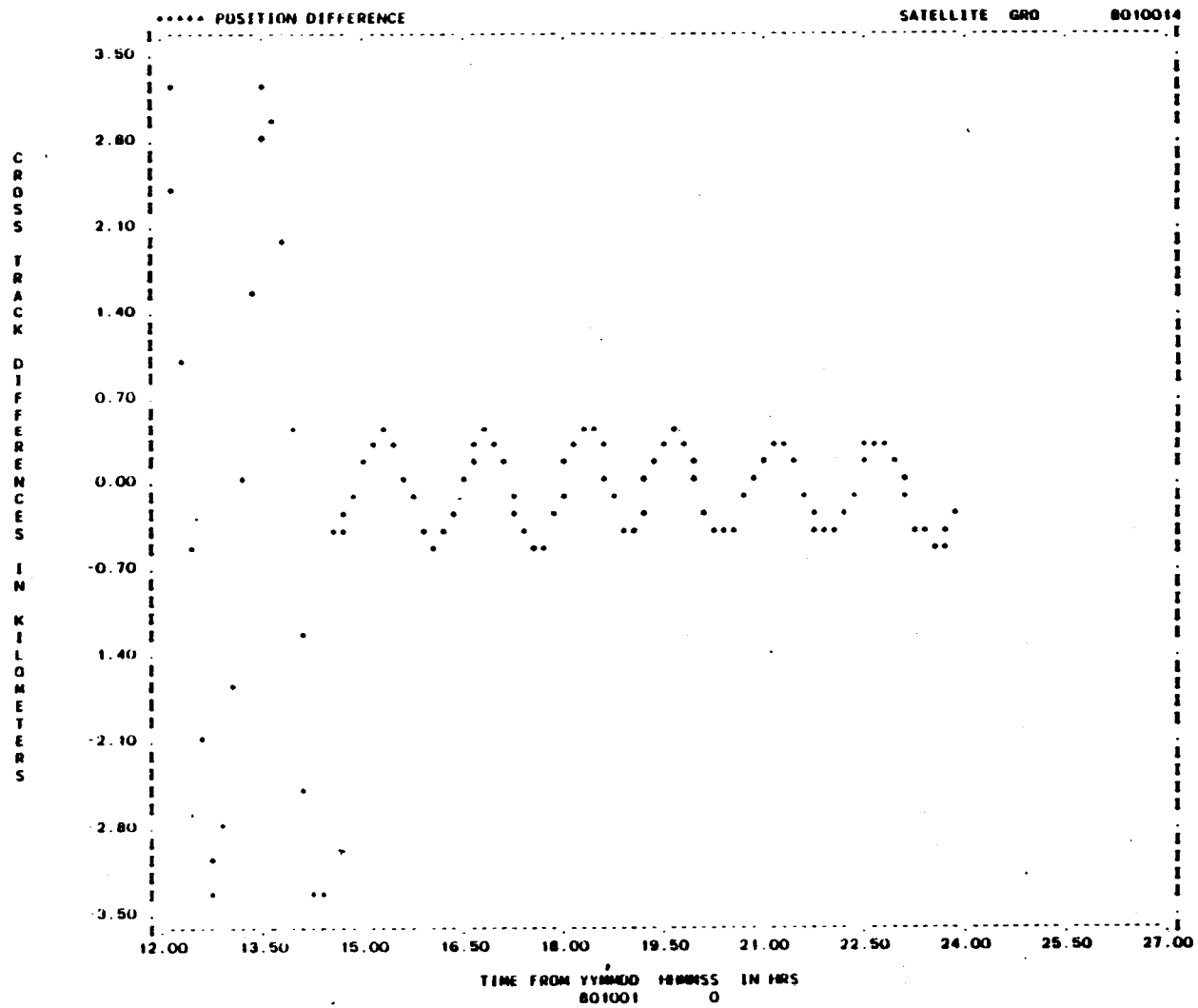

Figure B-38. Cross-Track Differences for Run Q20 (2 of 2)

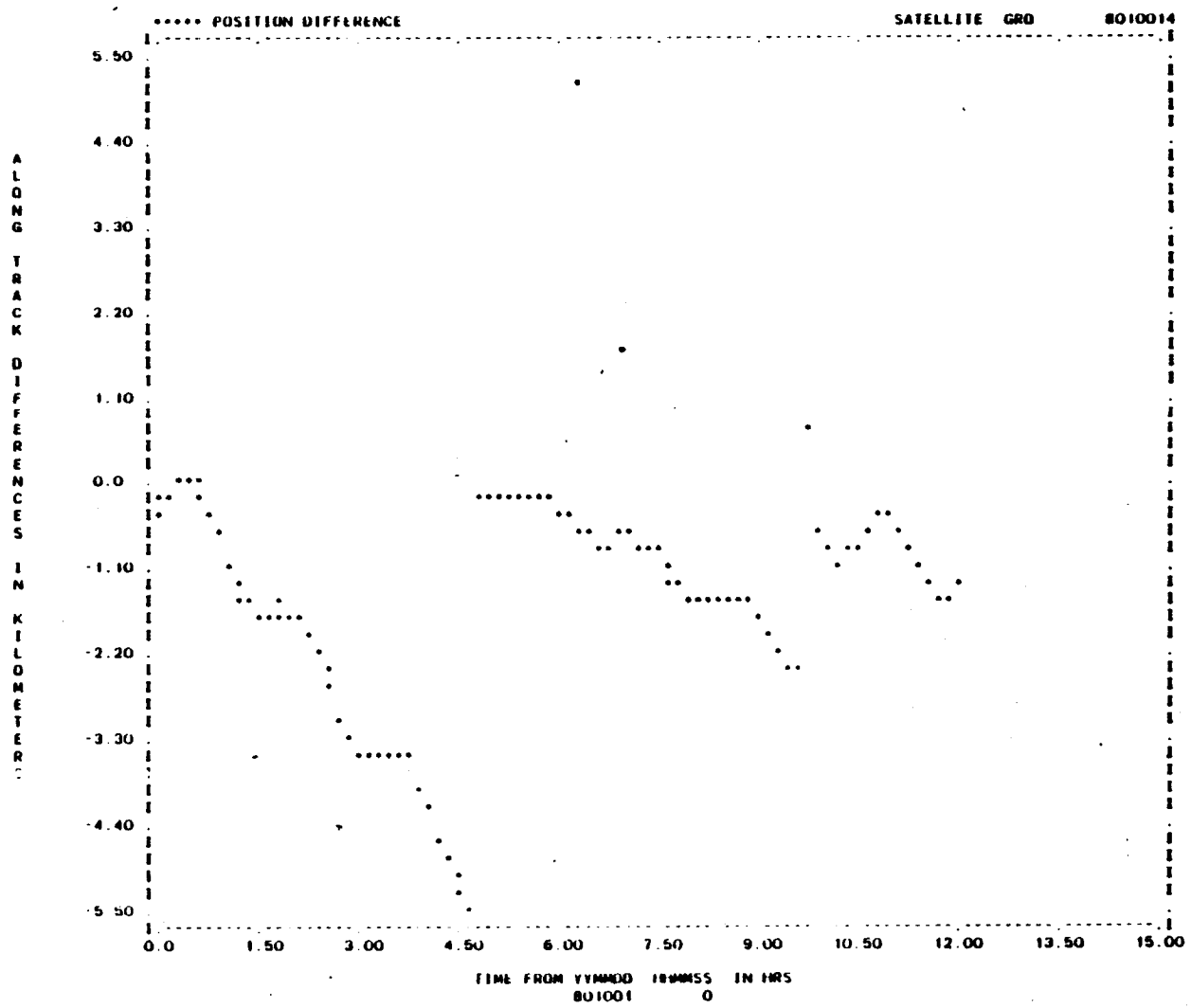

Figure B-39. Along-Track Differences for Run Q20 (1 of 2)

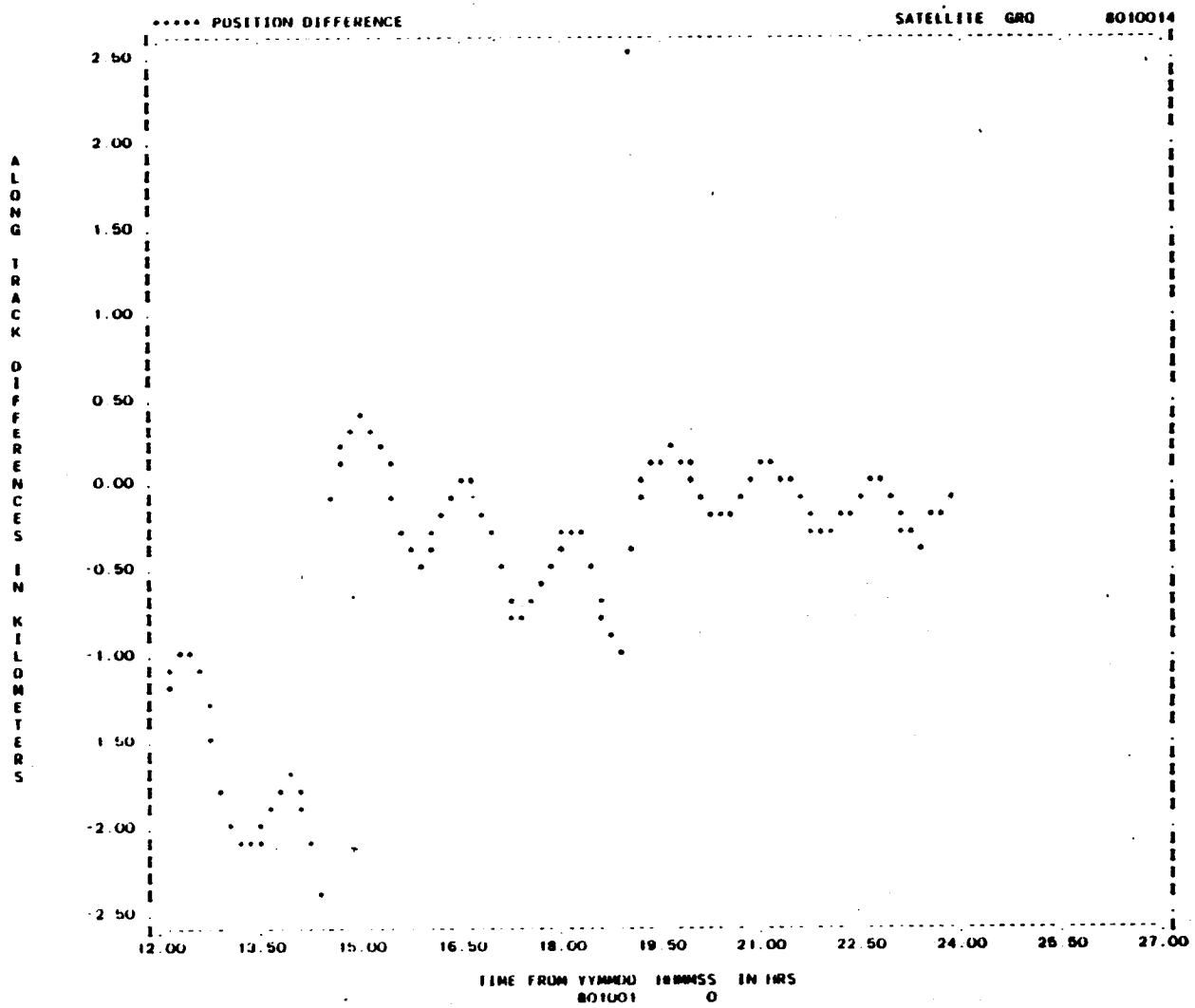

Figure B-39. Along-Track Differences for Run Q20 (2 of 2)

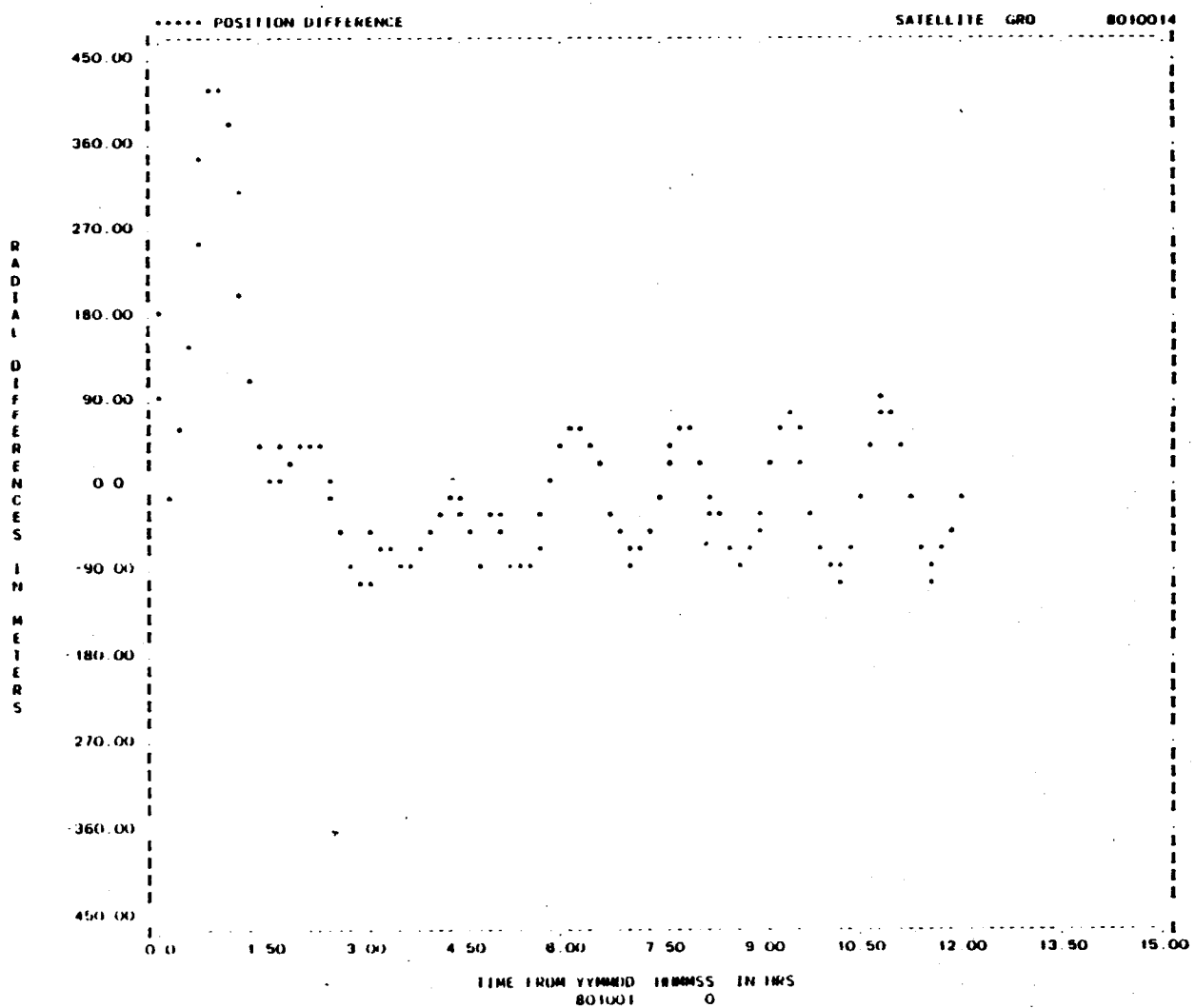

Figure B-40. Radial Differences for Run R8 (1 of 2)

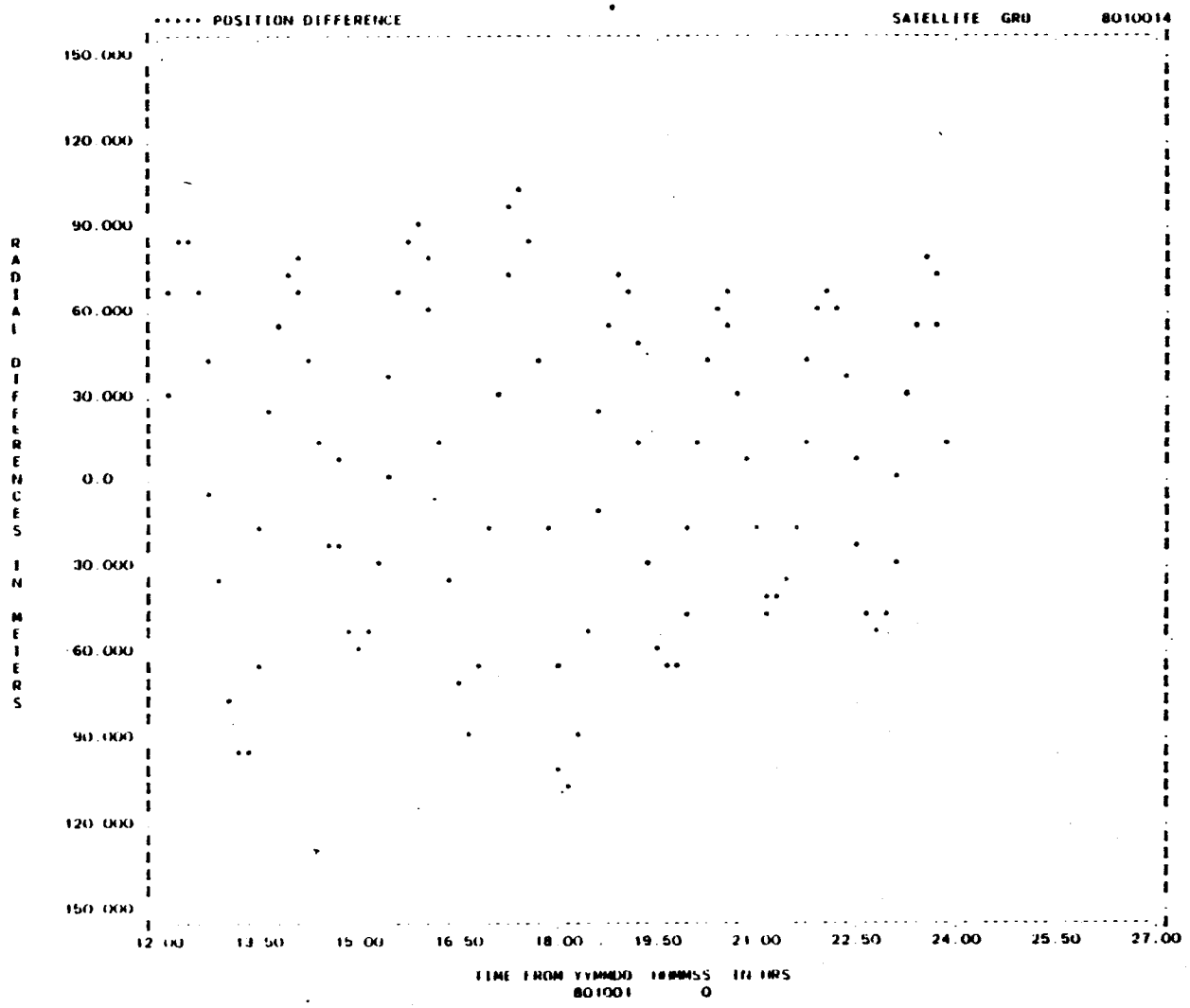

Figure B-40. Radial Differences for Run R8 (2 of 2)

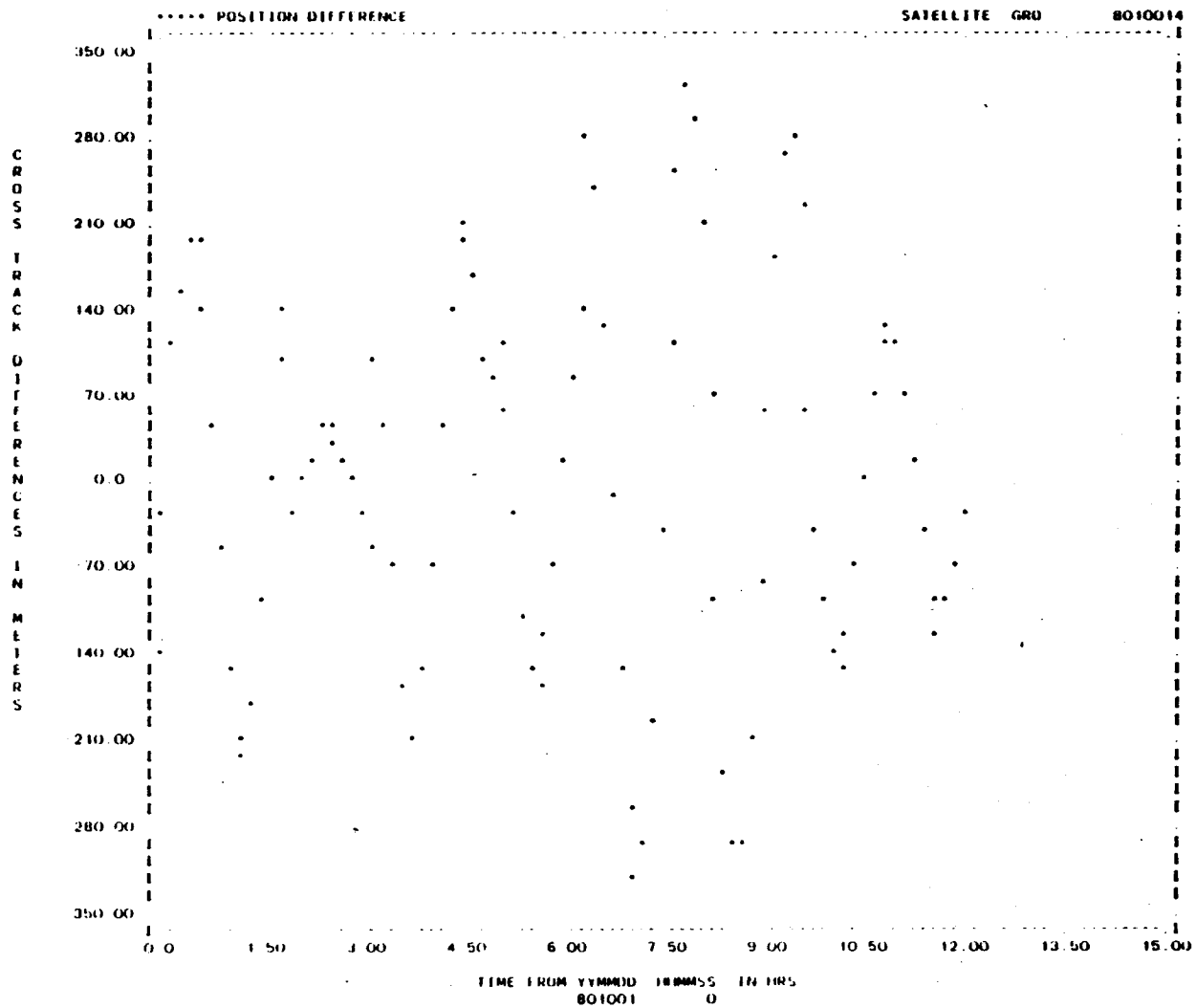

Figure B-41. Cross-Track Differences for Run R8 (1 of 2)

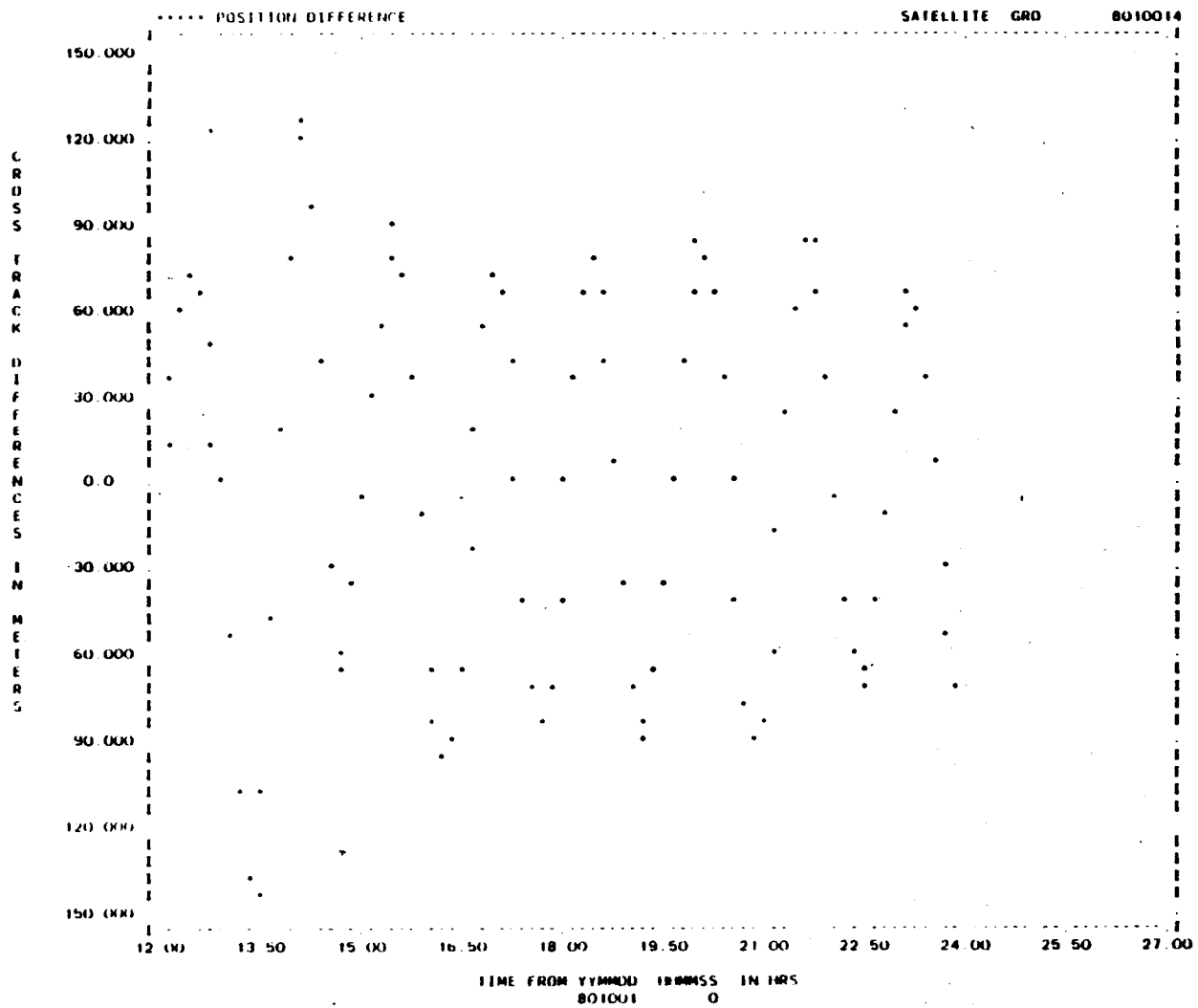

Figure B-41. Cross-Track Differences for Run R8 (2 of 2)

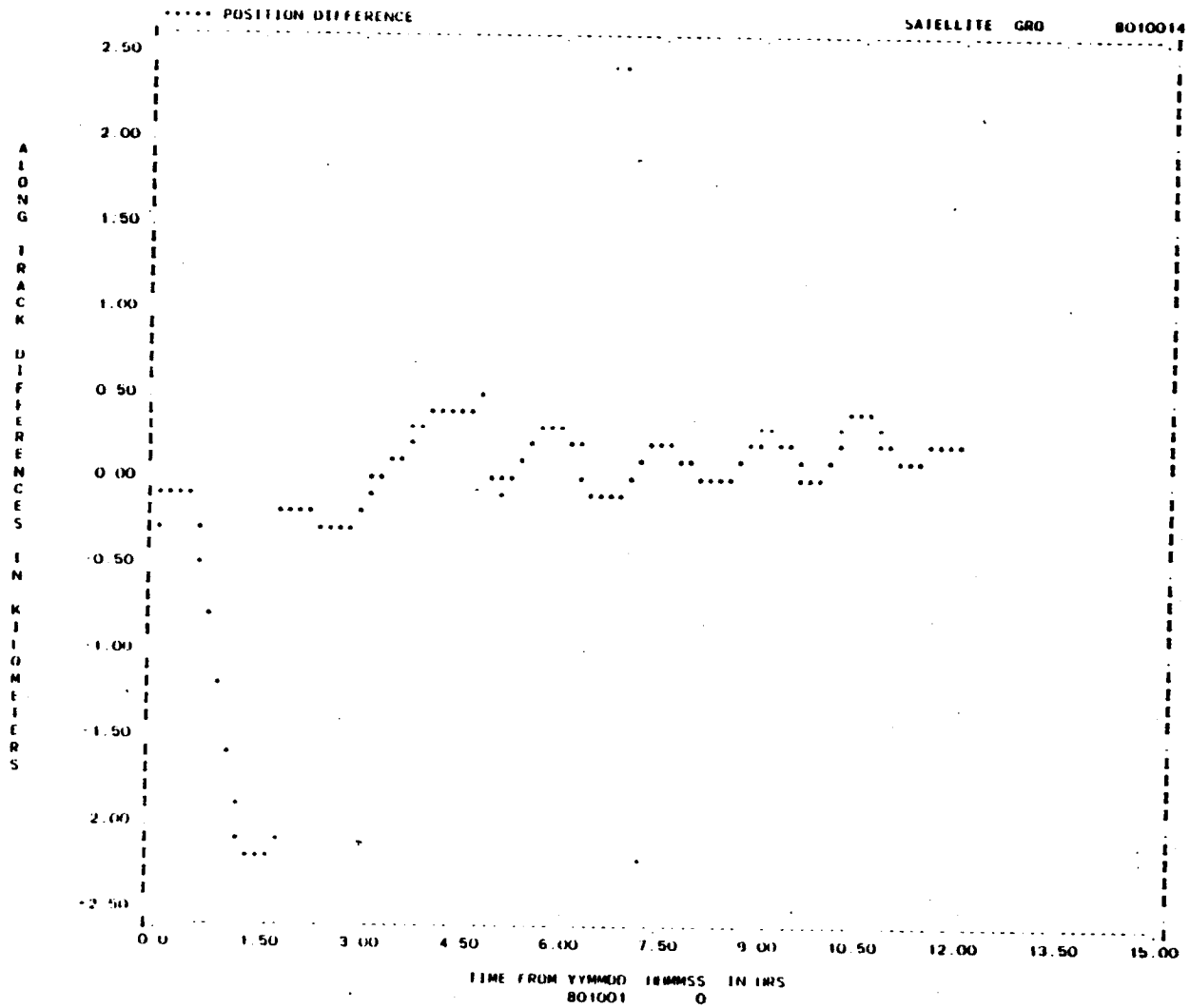

Figure B-42. Along-Track Differences for Run R8 (1 of 2)

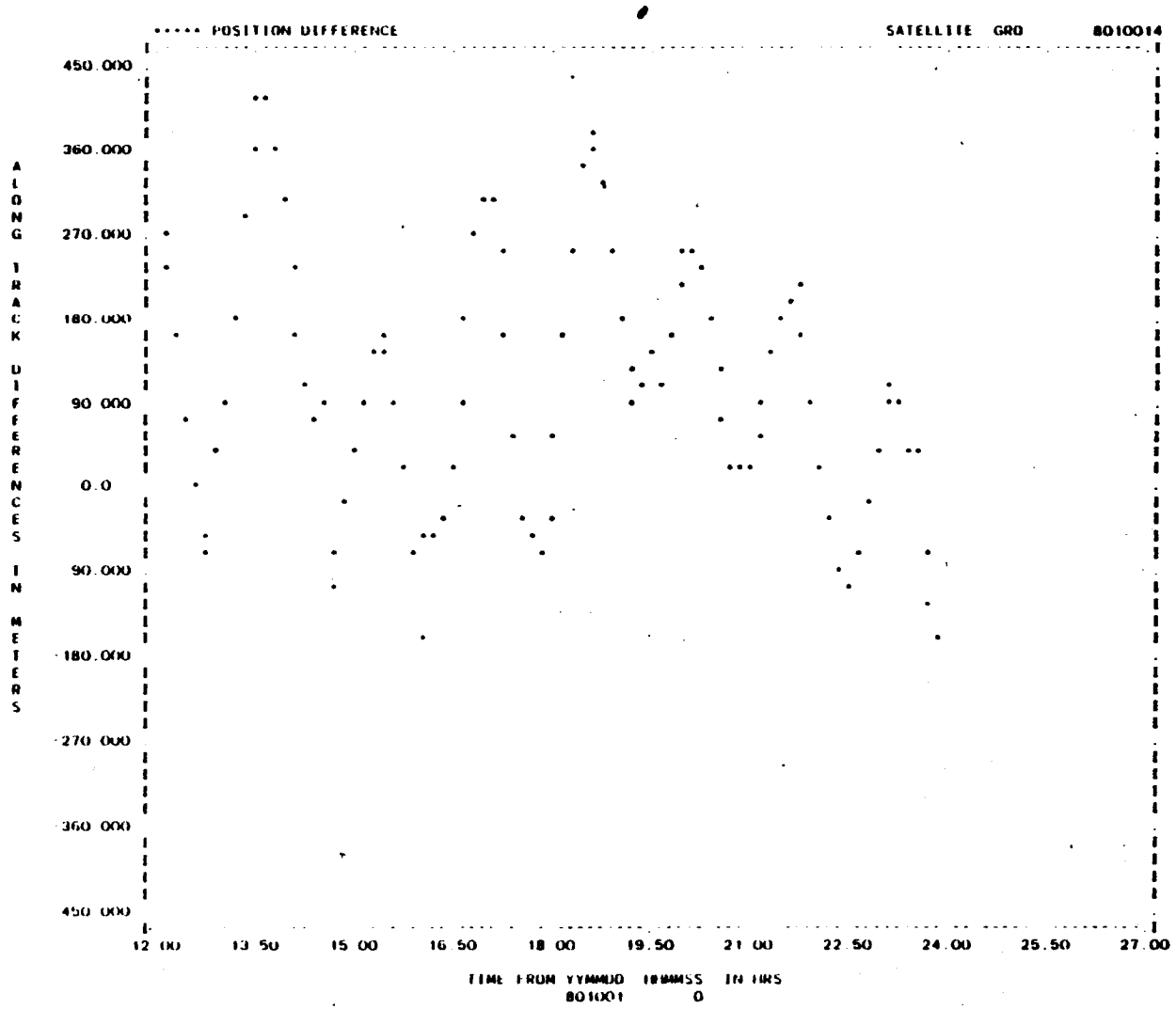

Figure B-42. Along-Track Differences for Run R8 (2 of 2)

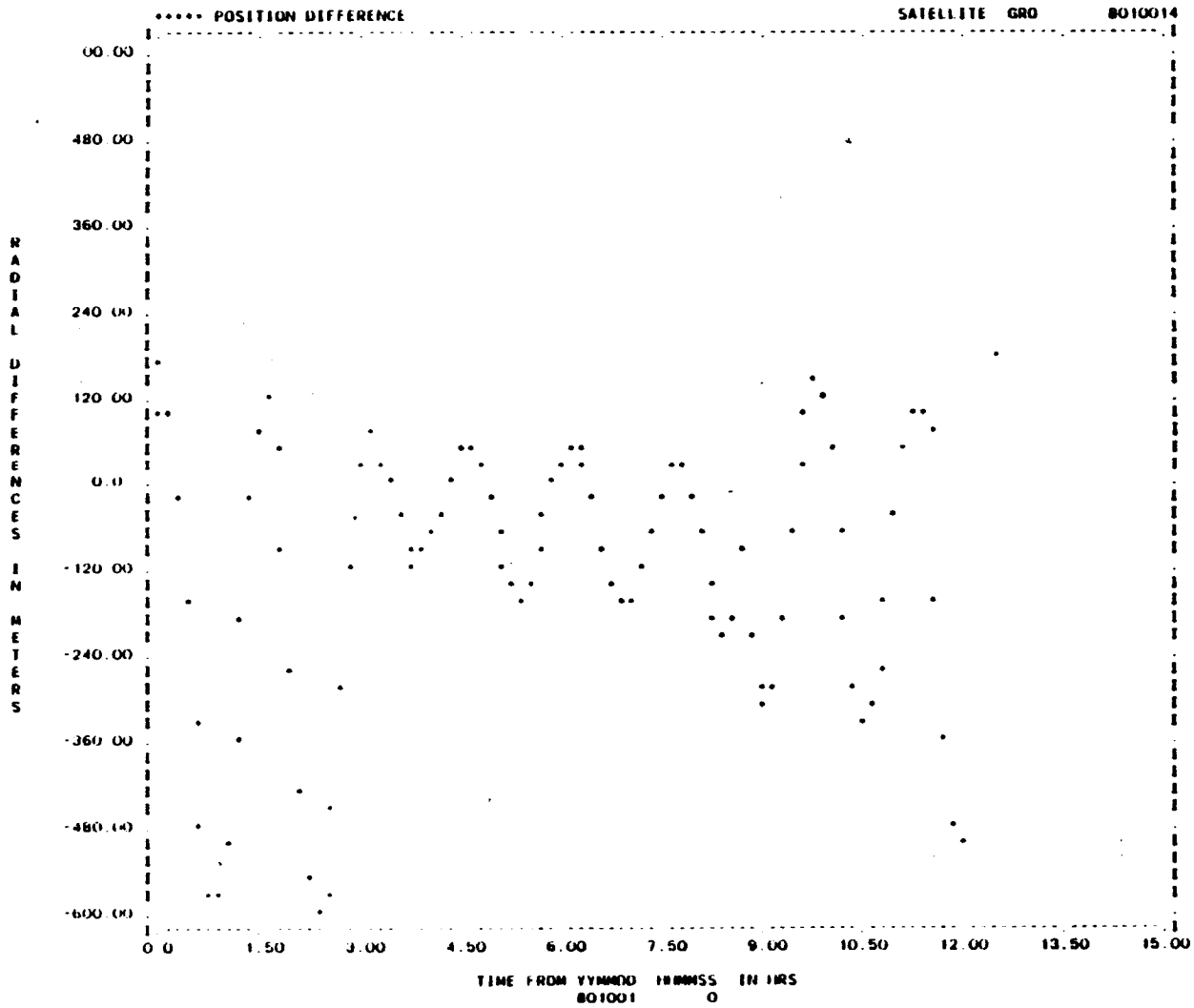

Figure B-43. Radial Differences for Run R11 (1 of 2)

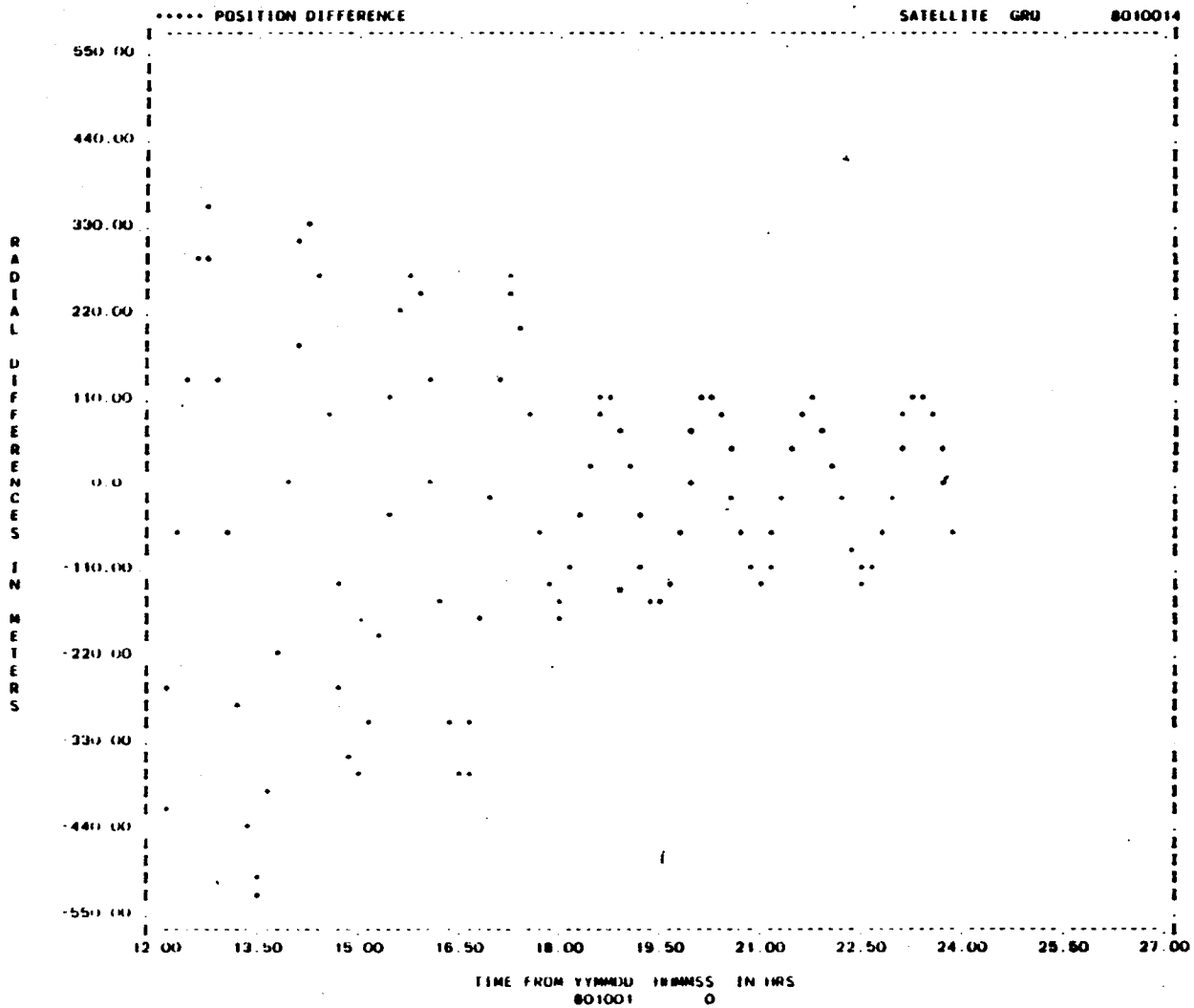

Figure B-43. Radial Differences for Run R11 (2 of 2)

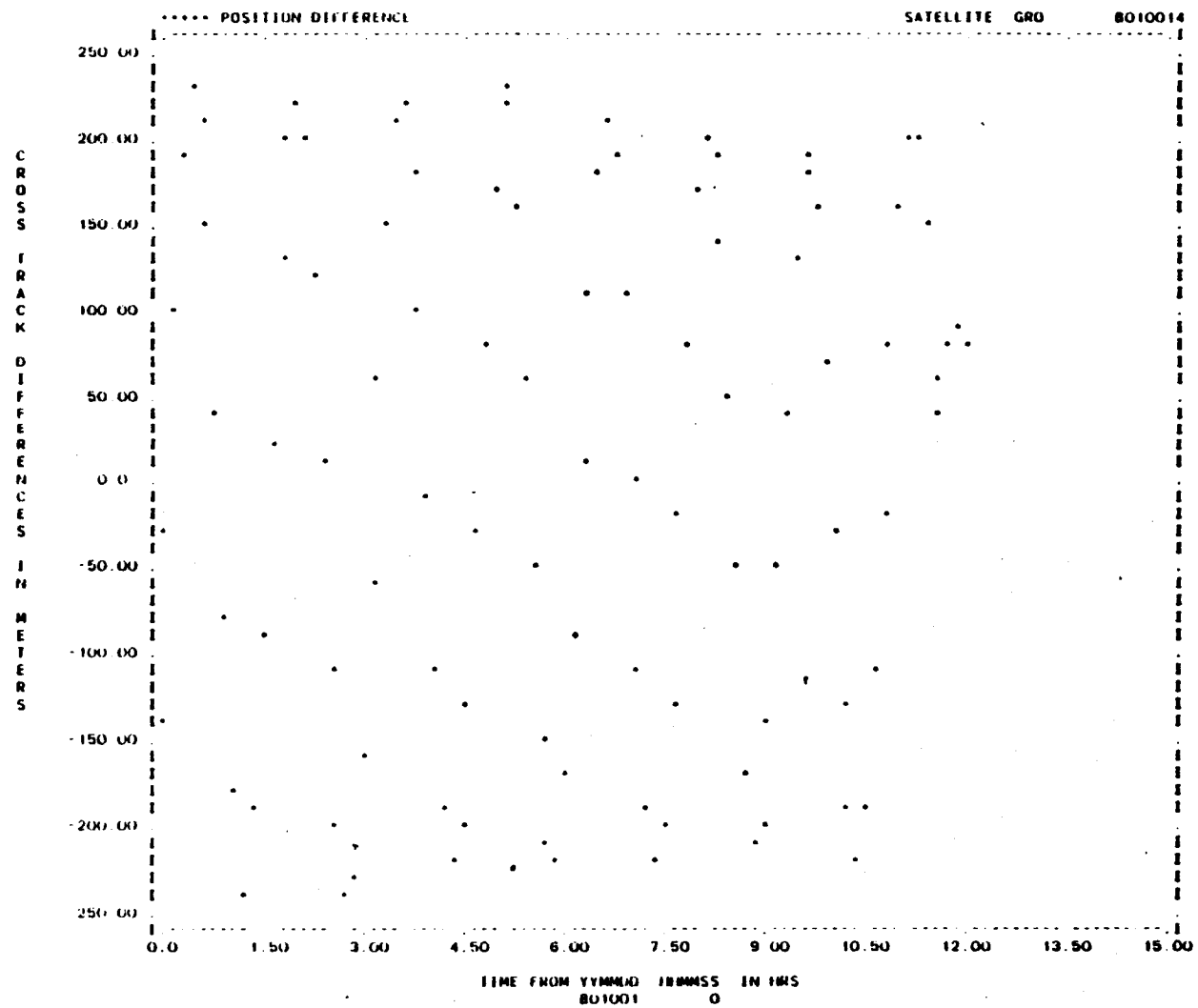

Figure B-44. Cross-Track Differences for Run R11 (1 of 2)

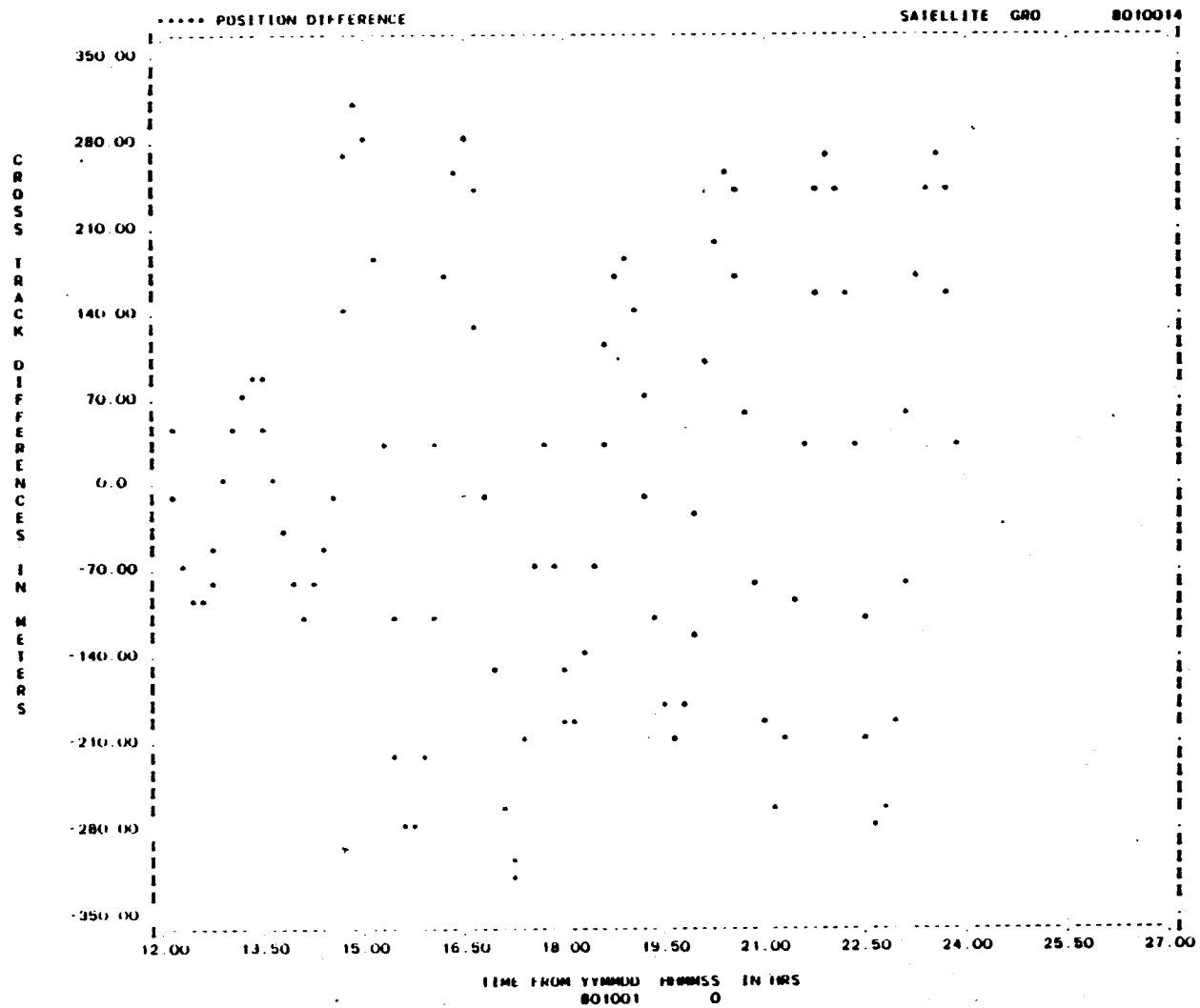

Figure B-44. Cross-Track Differences for Run R11 (2 of 2)

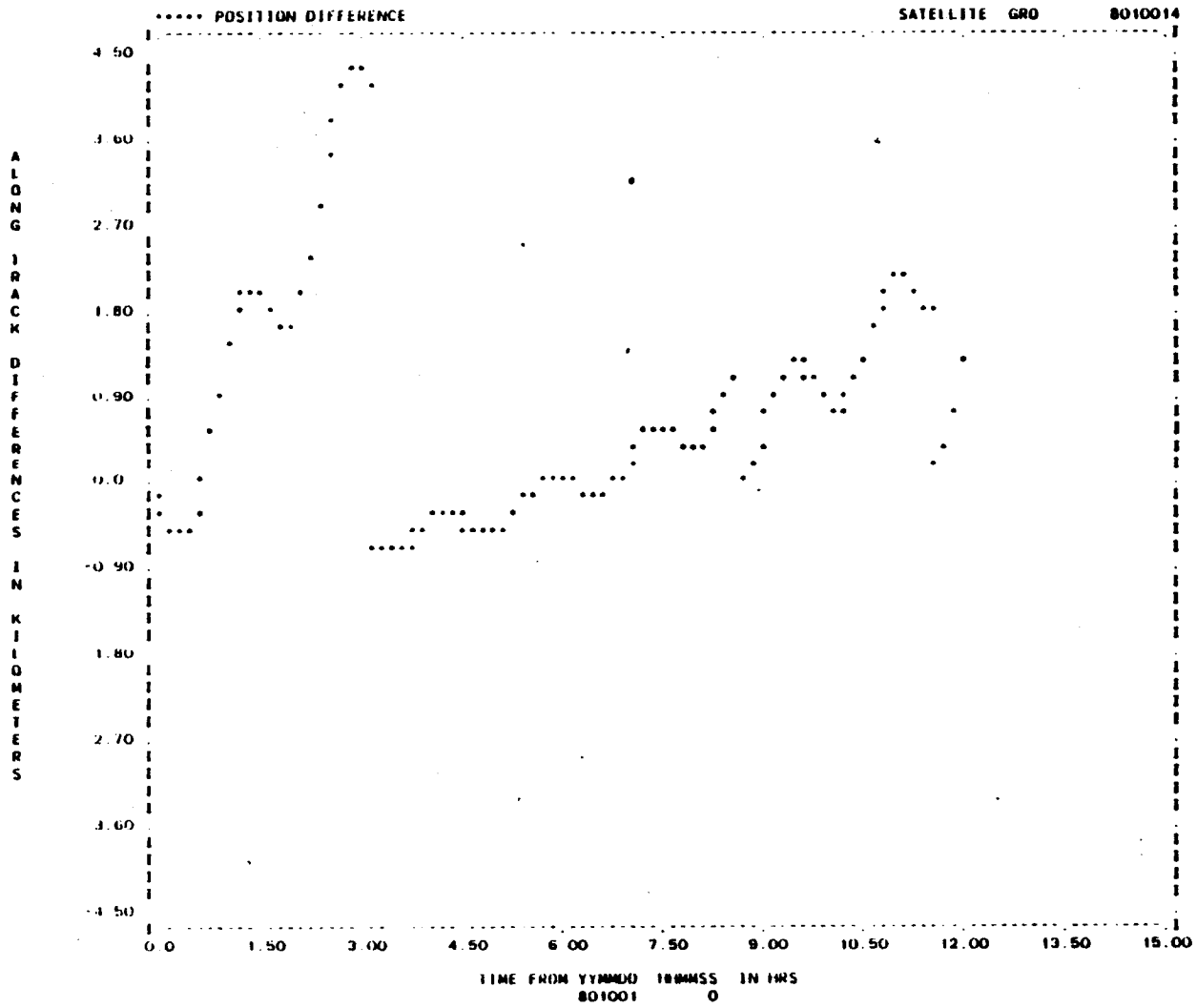

Figure B-45. Along-Track Differences for Run R11 (1 of 2)

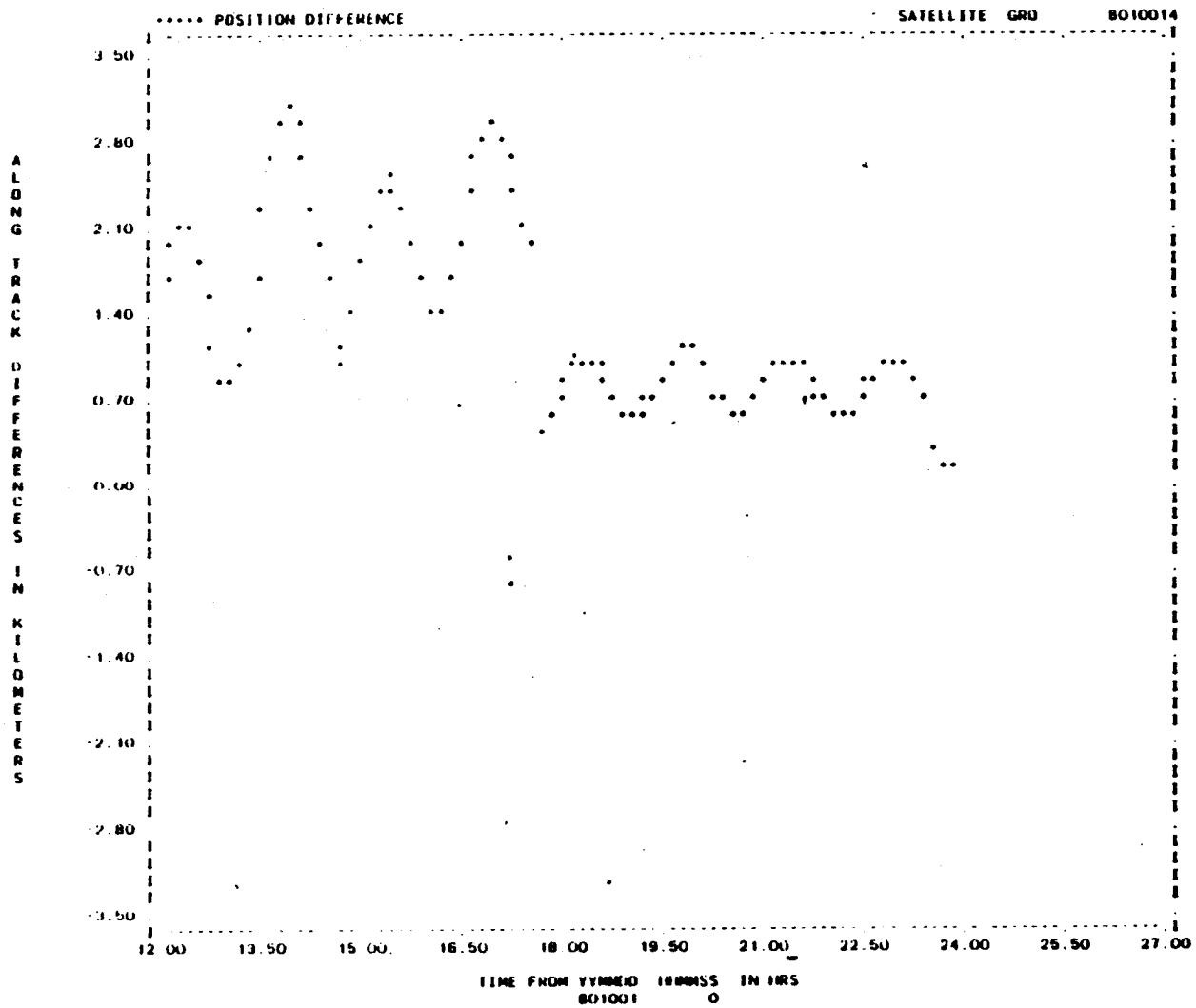

Figure B-45. Along-Track Differences for Run R11 (2 of 2)

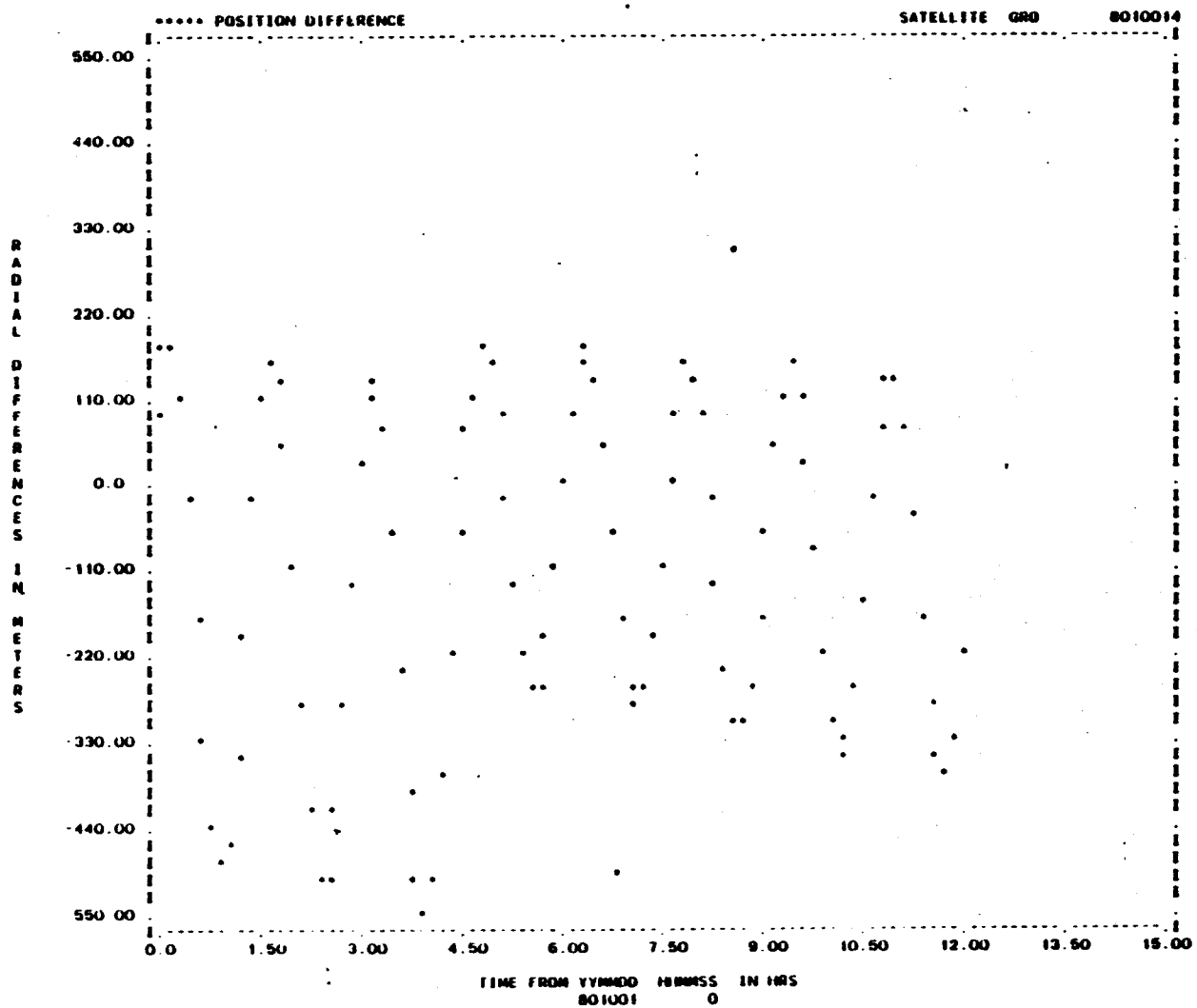

Figure B-46. Radial Differences for Run R15 (1 of 2)

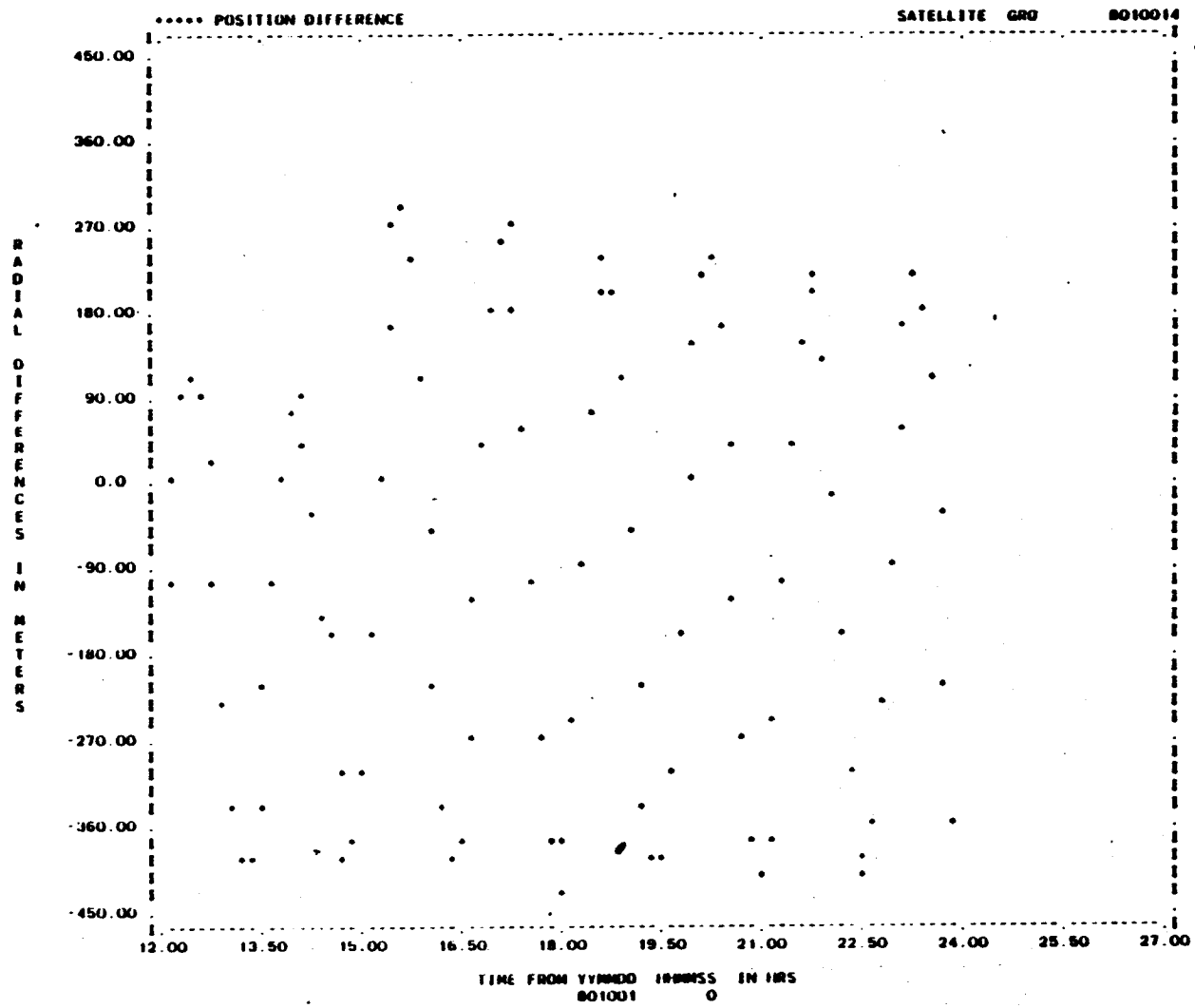

Figure B-46. Radial Differences for Run R15 (2 of 2)

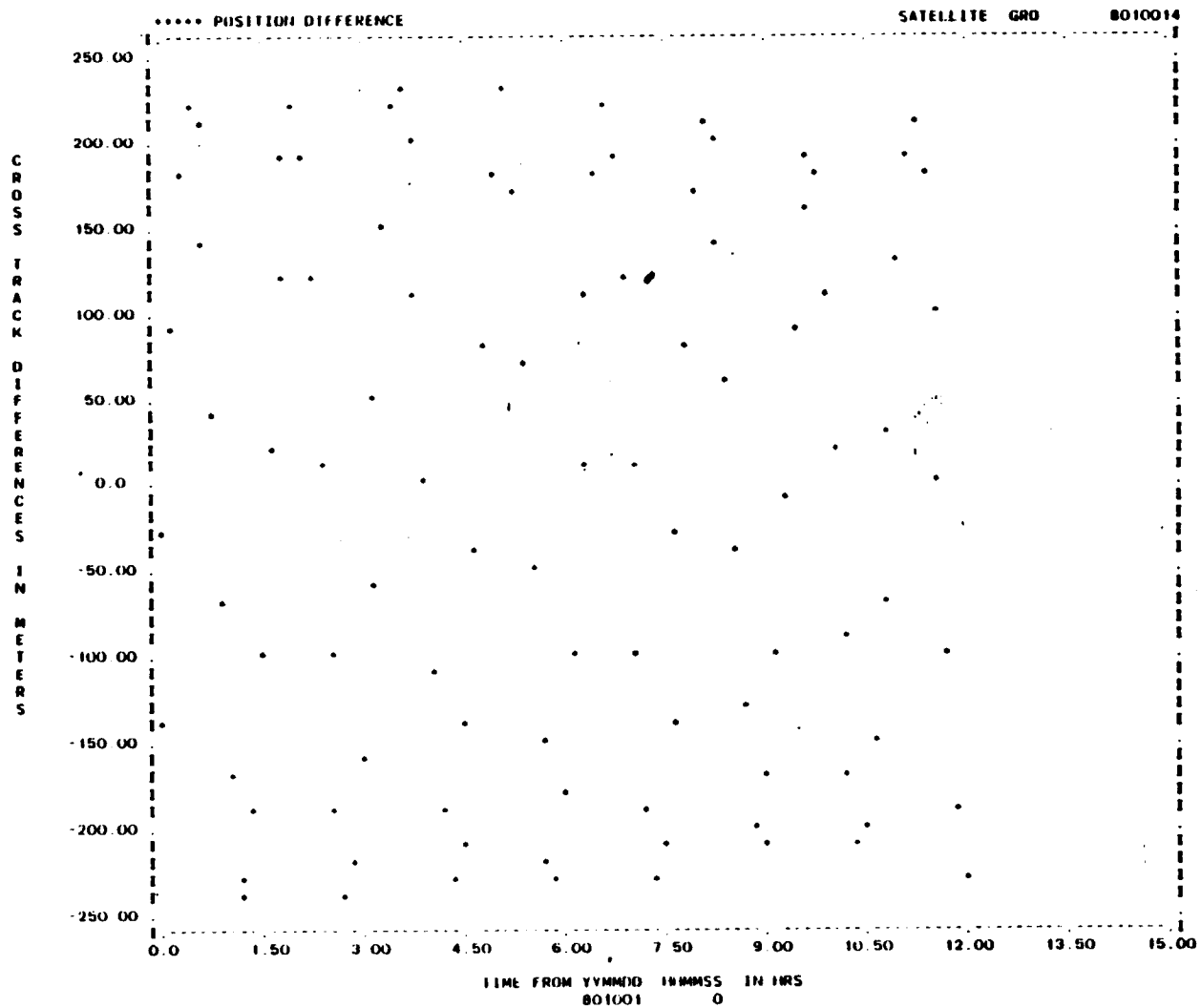

Figure B-47. Cross-Track Differences for Run R15 (1 of 2)

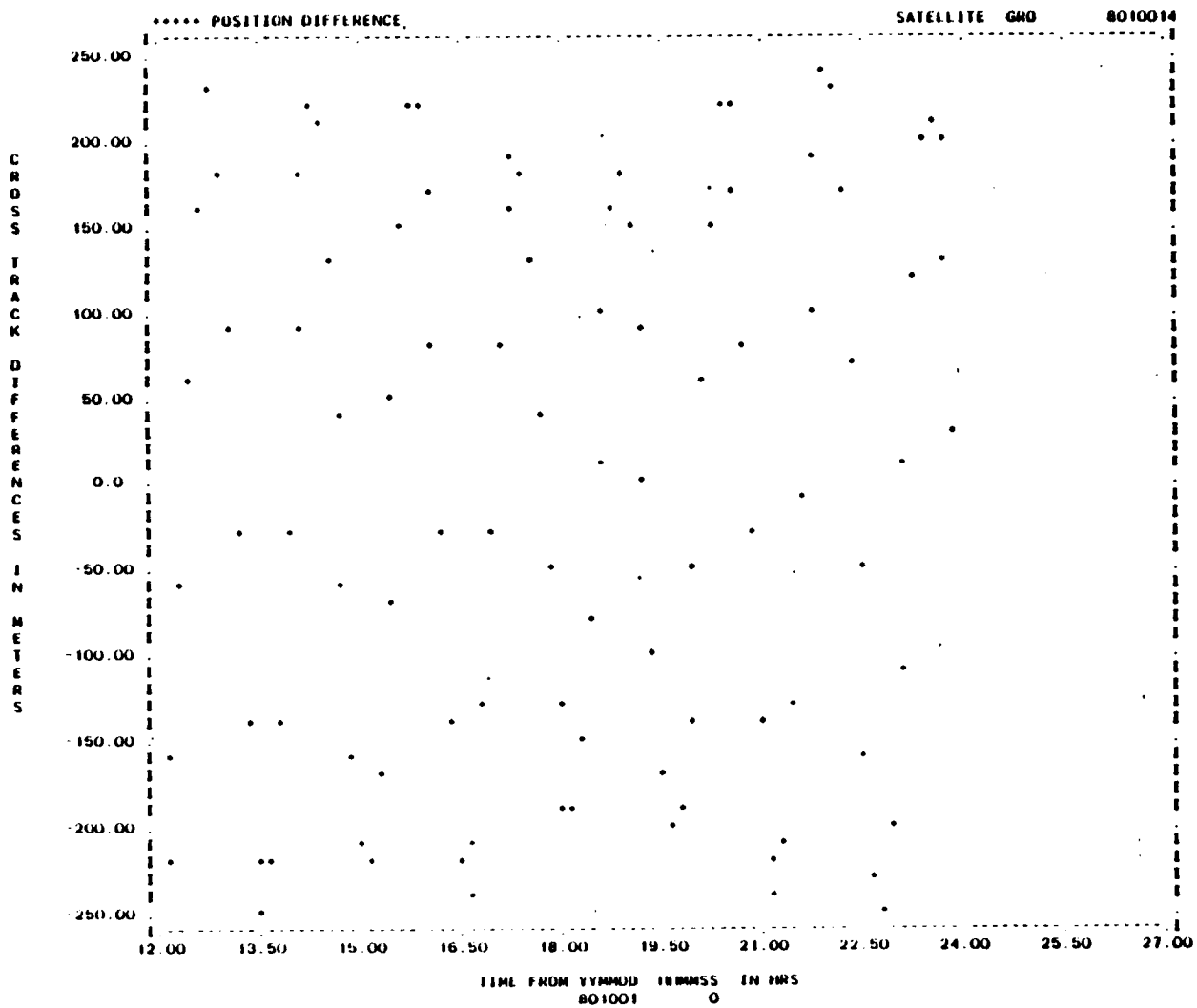

Figure B-47. Cross-Track Differences for Run R15 (2 of 2)

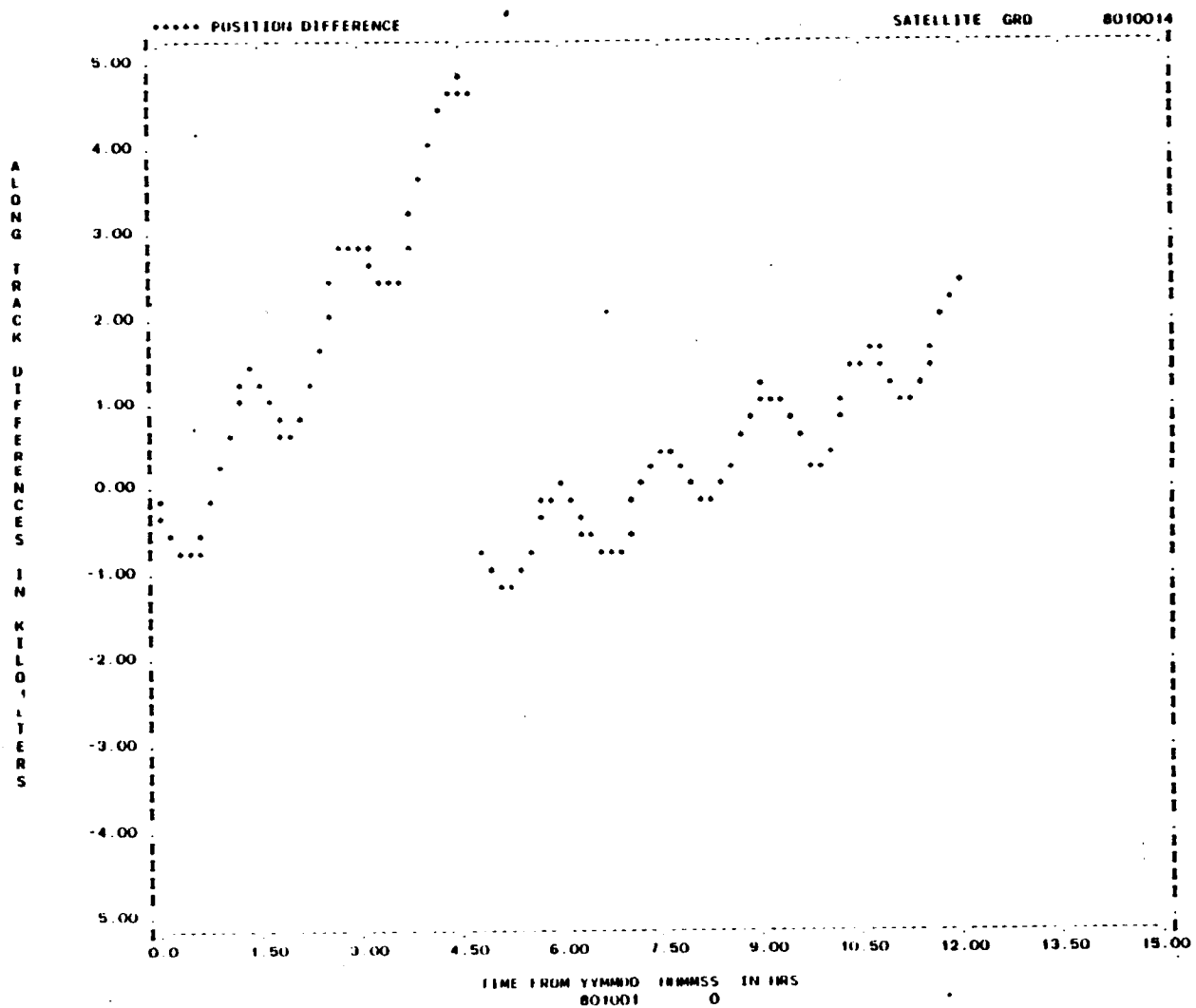

Figure B-48. Along-Track Differences for Run R15 (1 of 2)

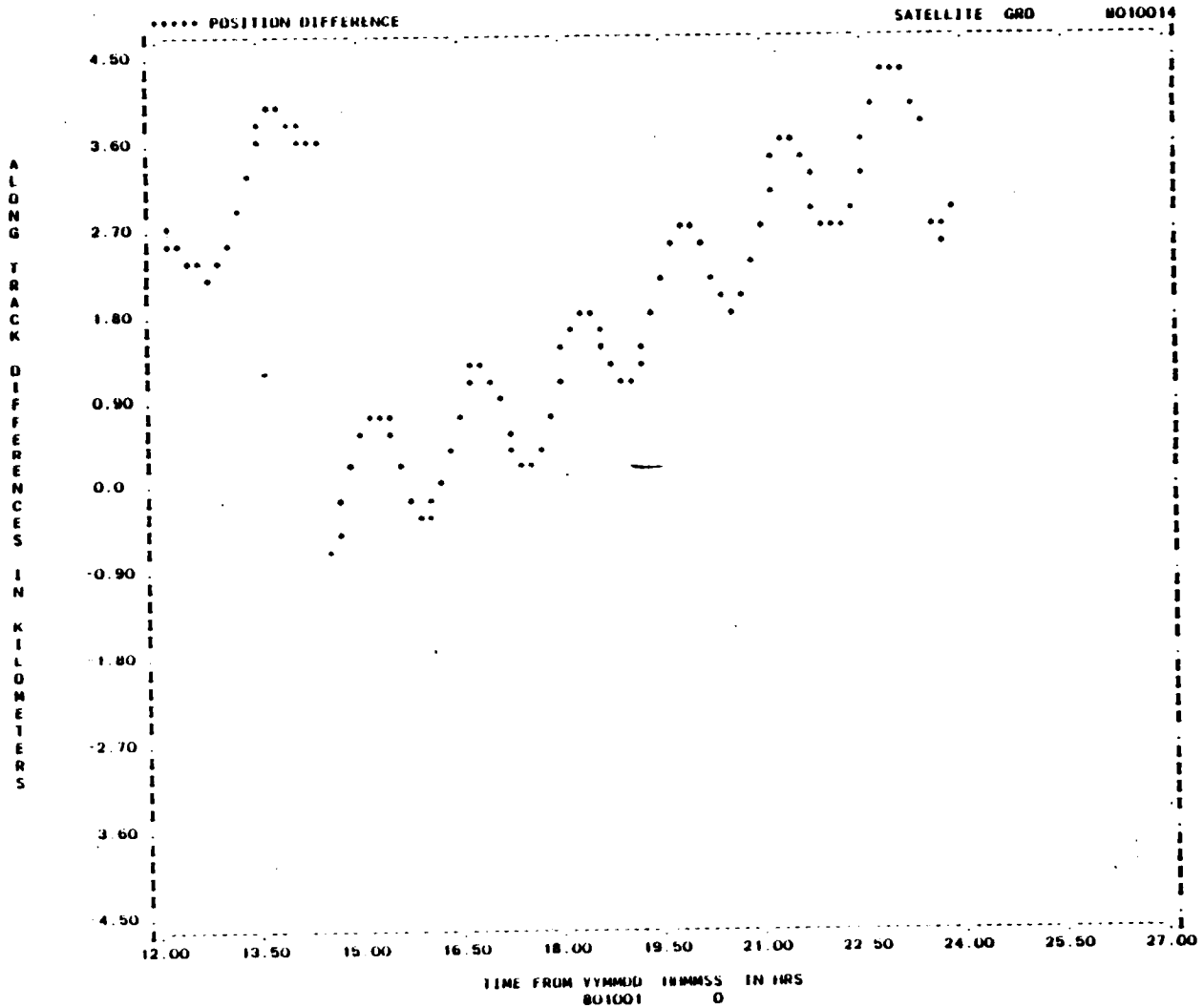

Figure B-48. Along-Track Differences for Run R15 (2 of 2)

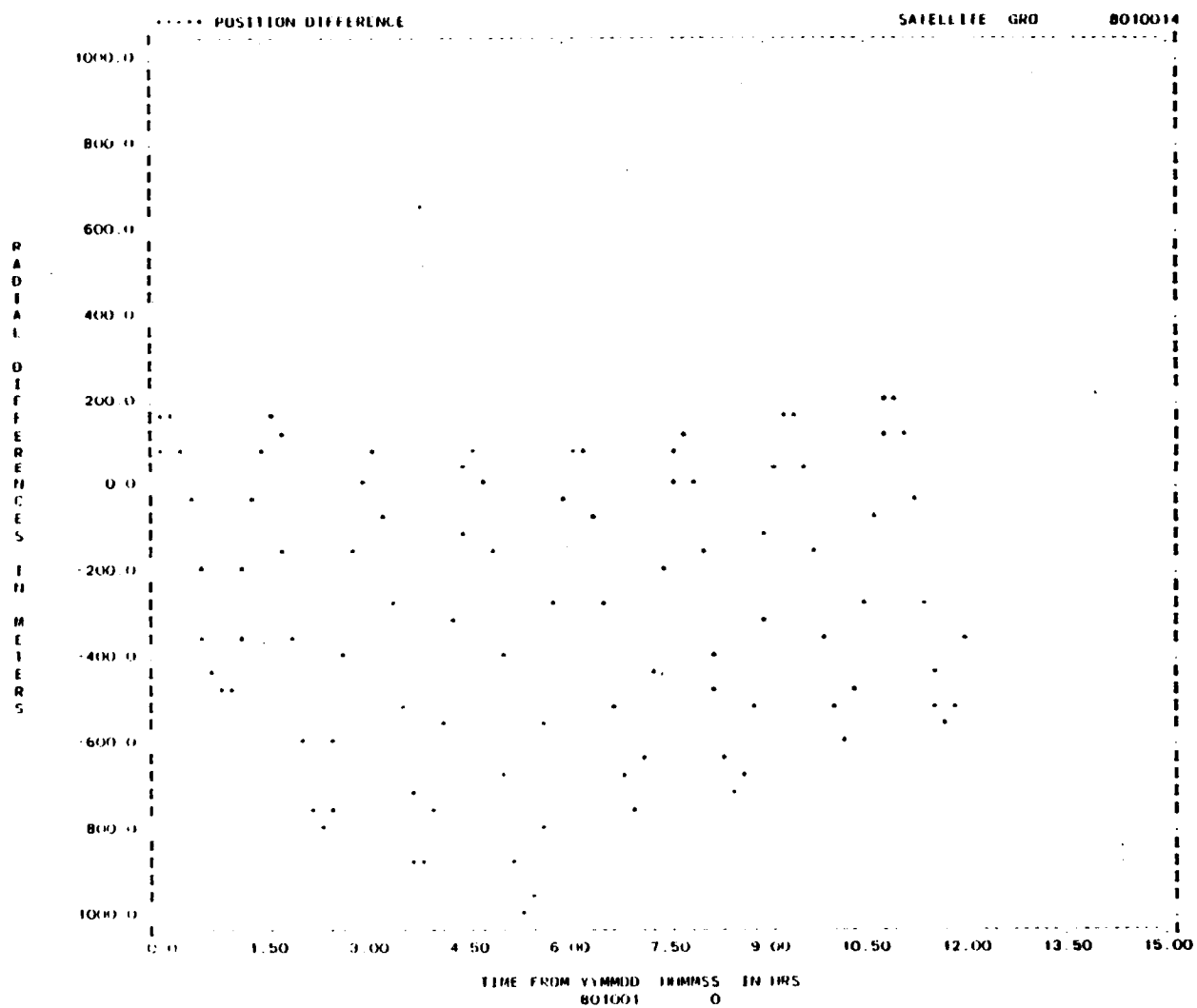

Figure B-49. Radial Differences for Run S3 (1 of 2)

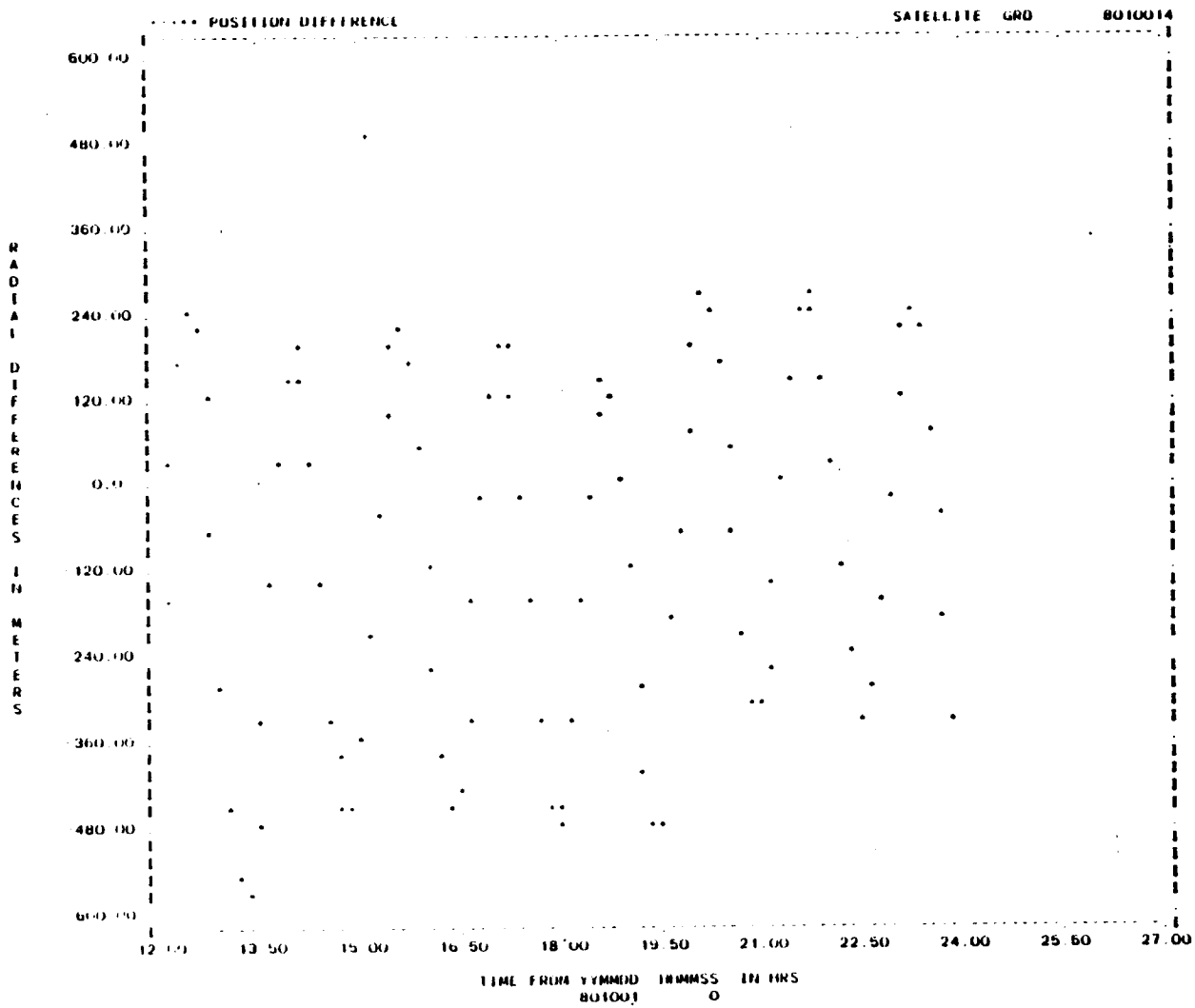

Figure B-49. Radial Differences for Run S3 (2 of 2)

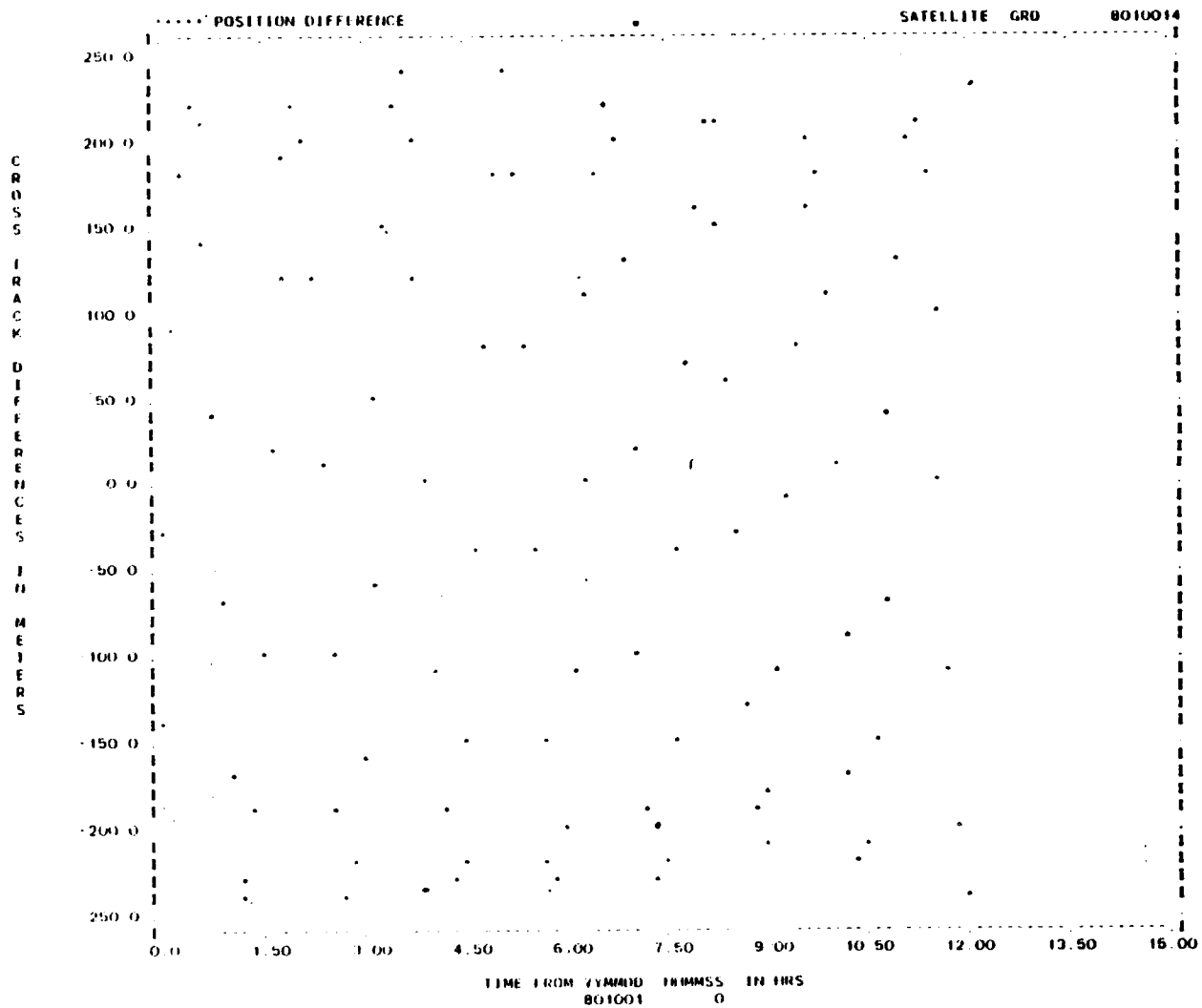

Figure B-50. Cross-Track Differences for Run S3 (1 of 2)

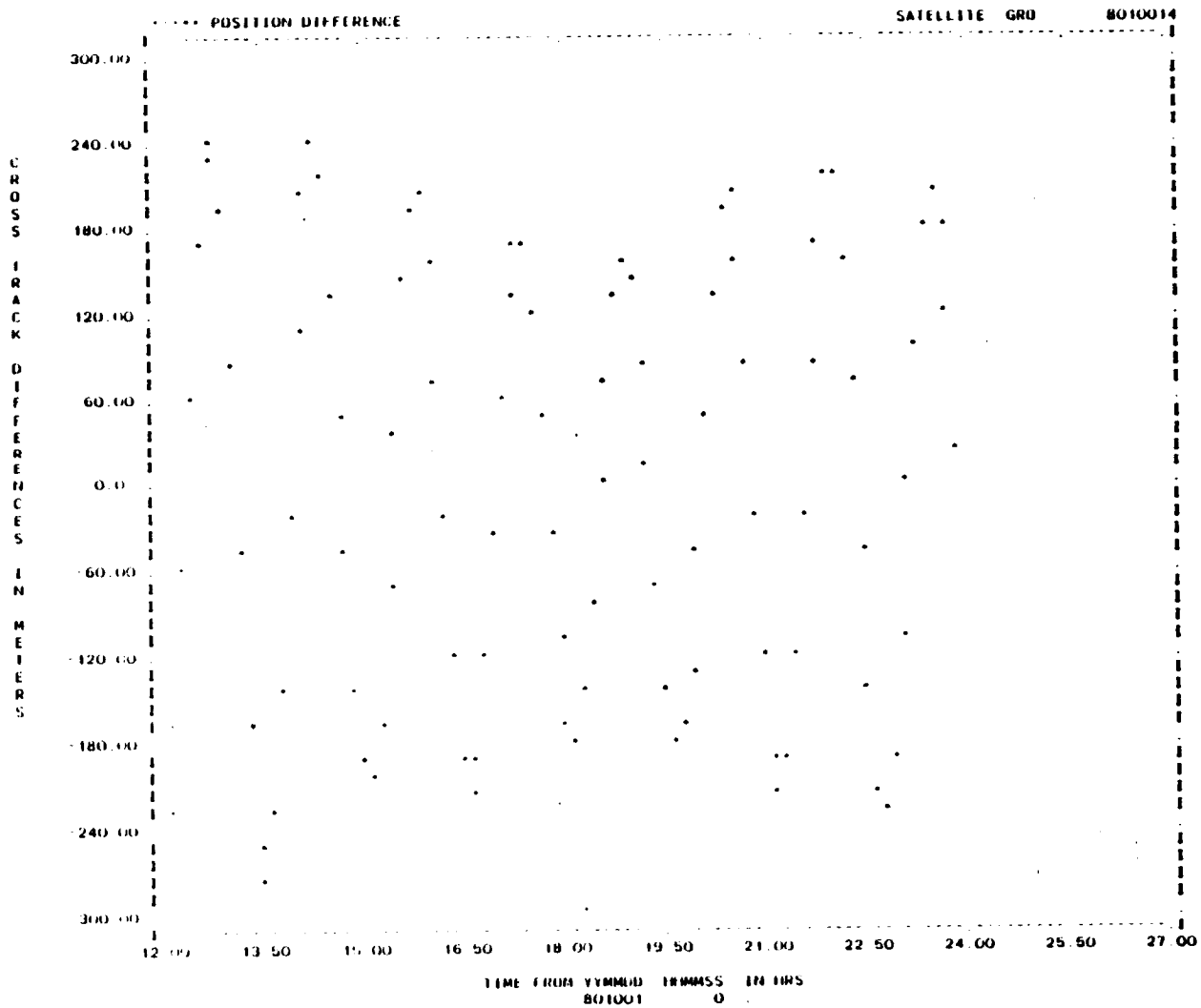

Figure B-50. Cross-Track Differences for Run S3 (2 of 2)

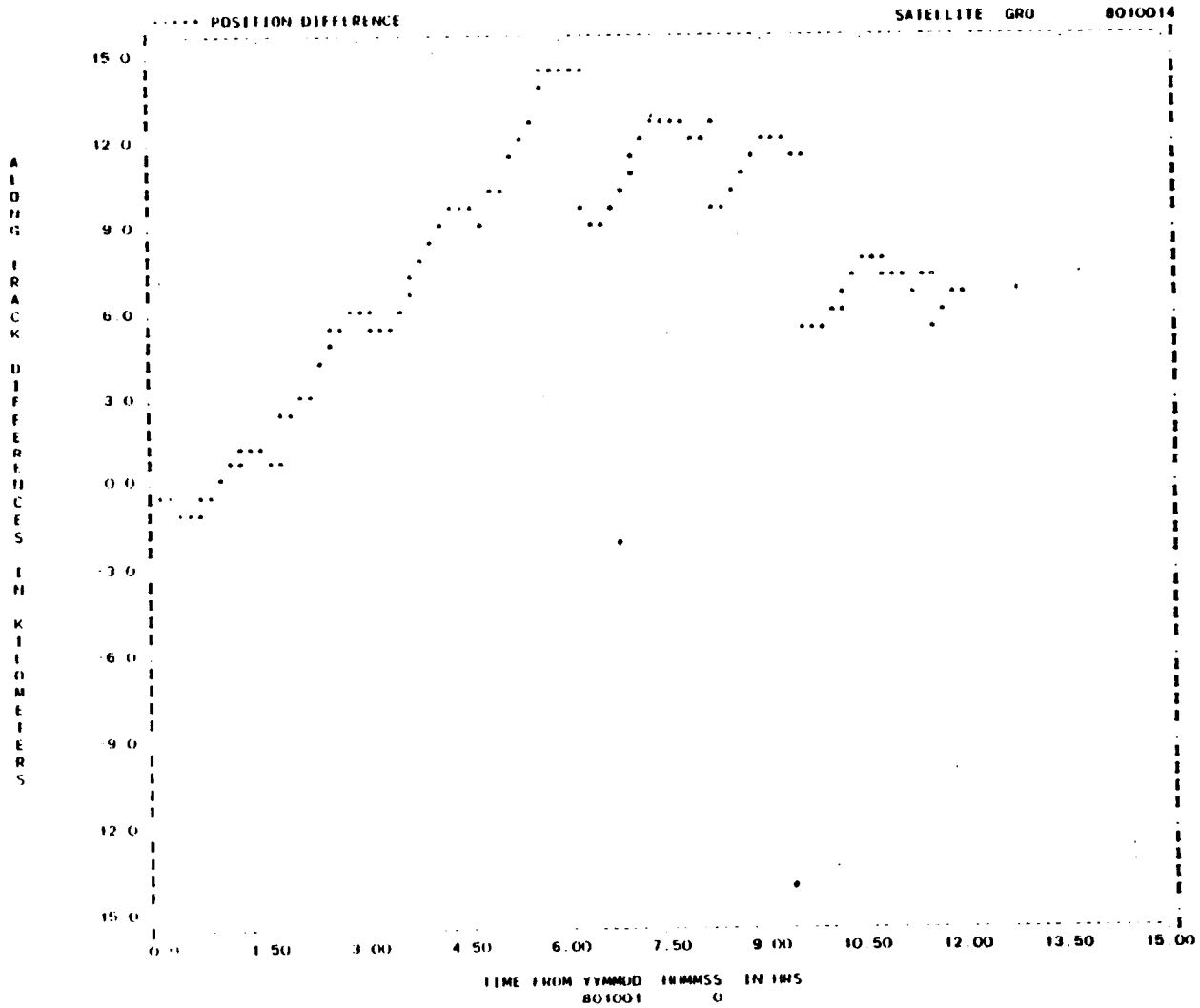

Figure B-51. Along-Track Differences for Run S3 (1 of 2)

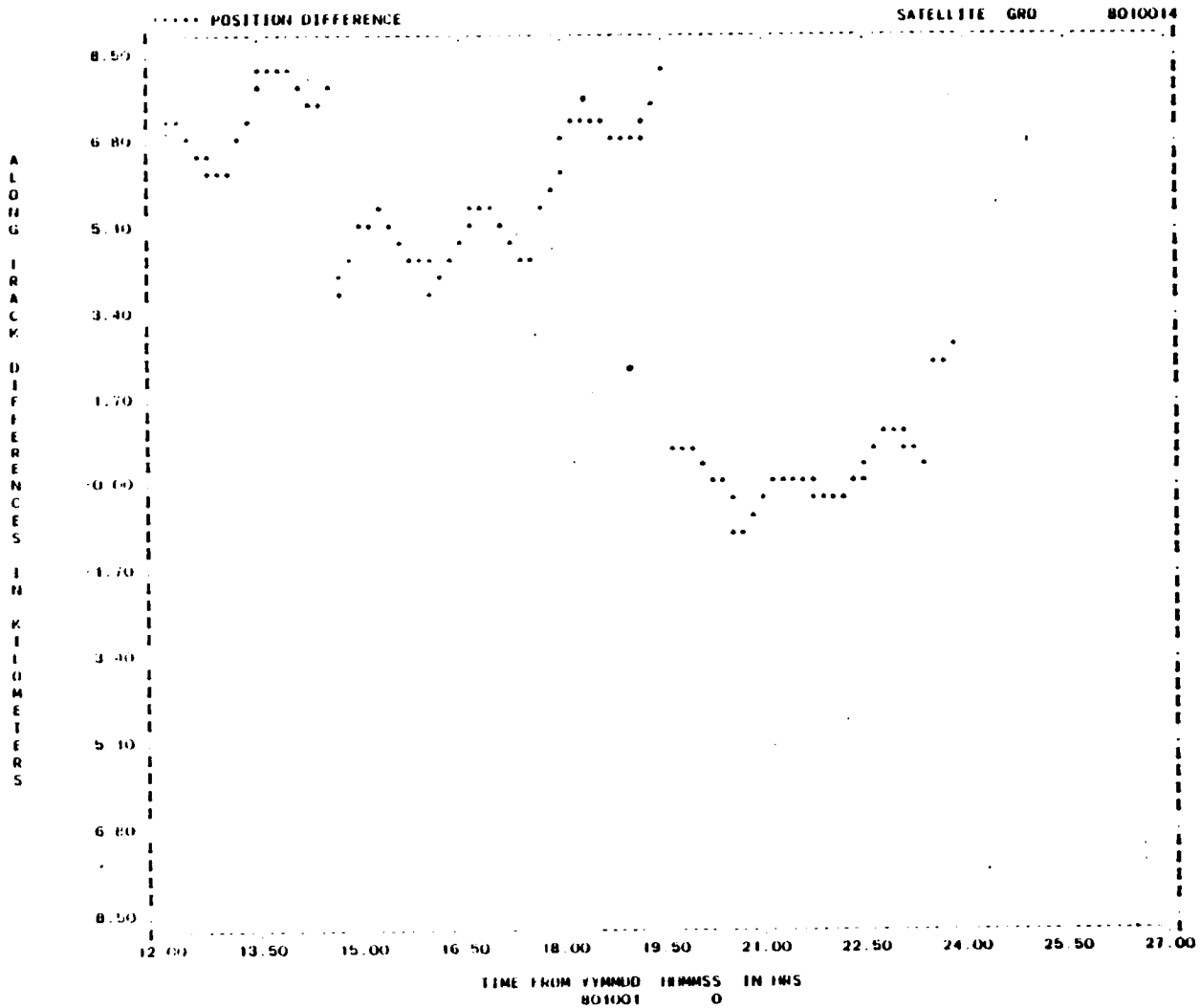

Figure B-51. Along-Track Differences for Run S3 (2 of 2)

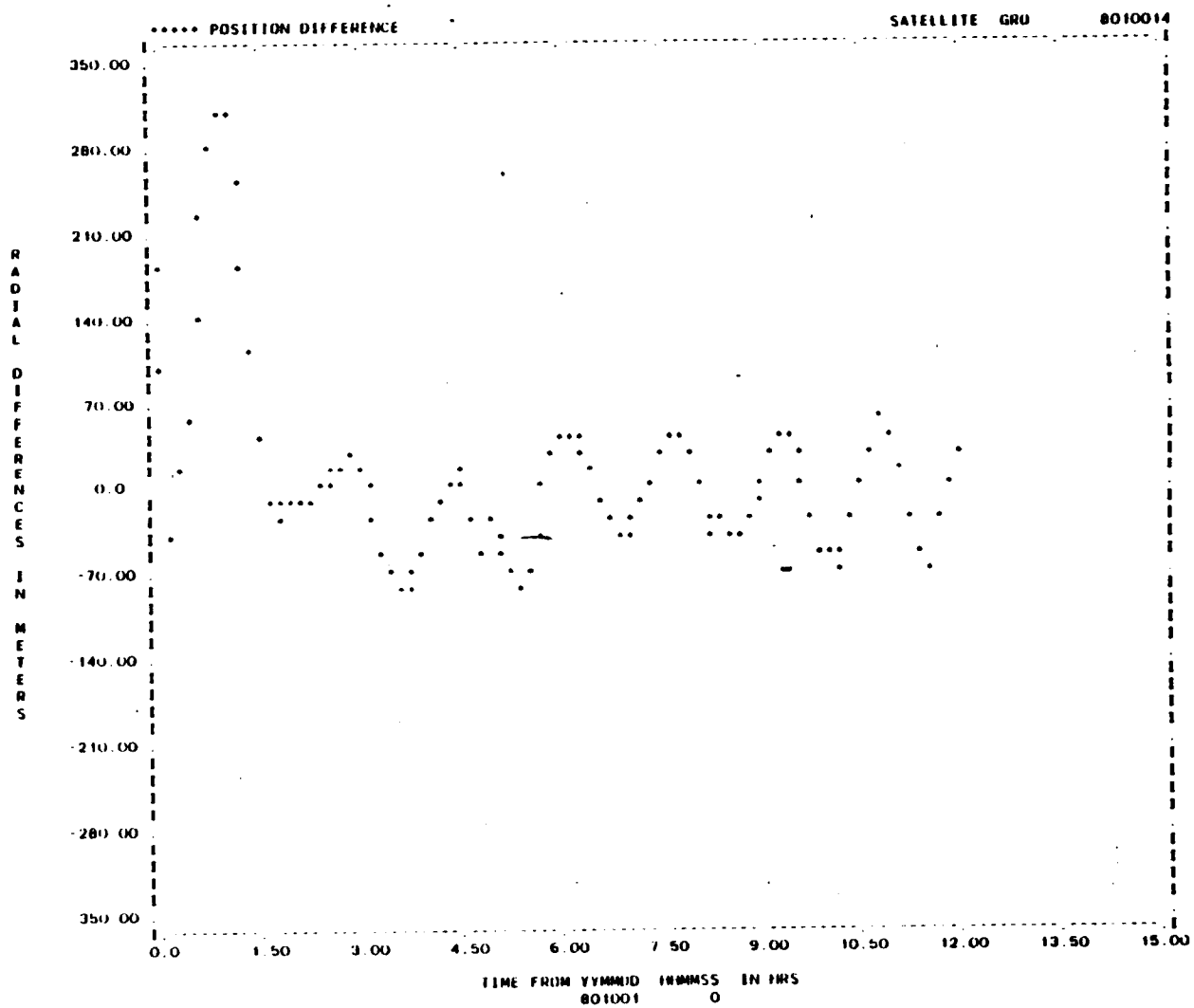

Figure B-52. Radial Differences for Run T1 (1 of 2)

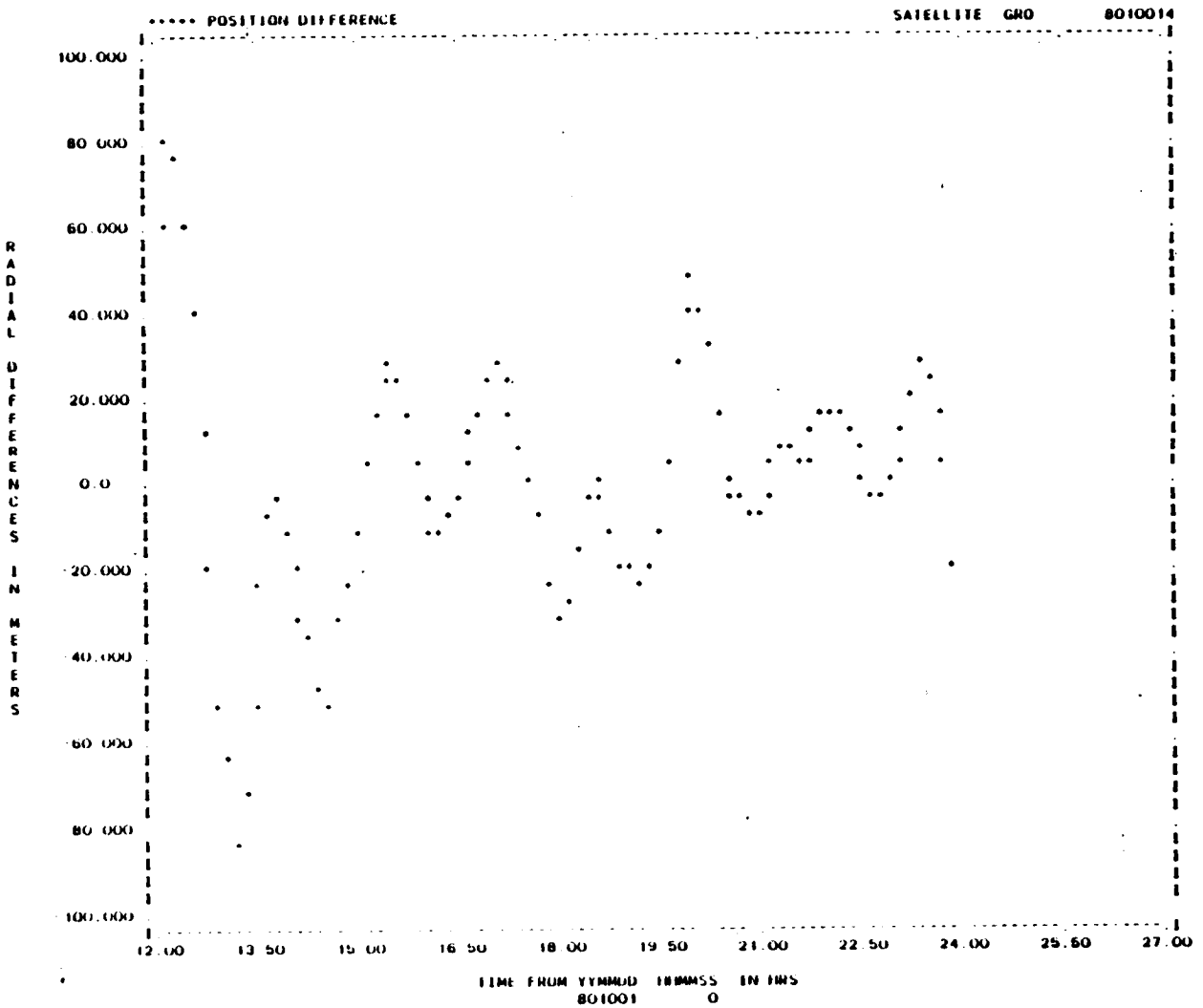

Figure B-52. Radial Differences for Run T1 (2 of 2)

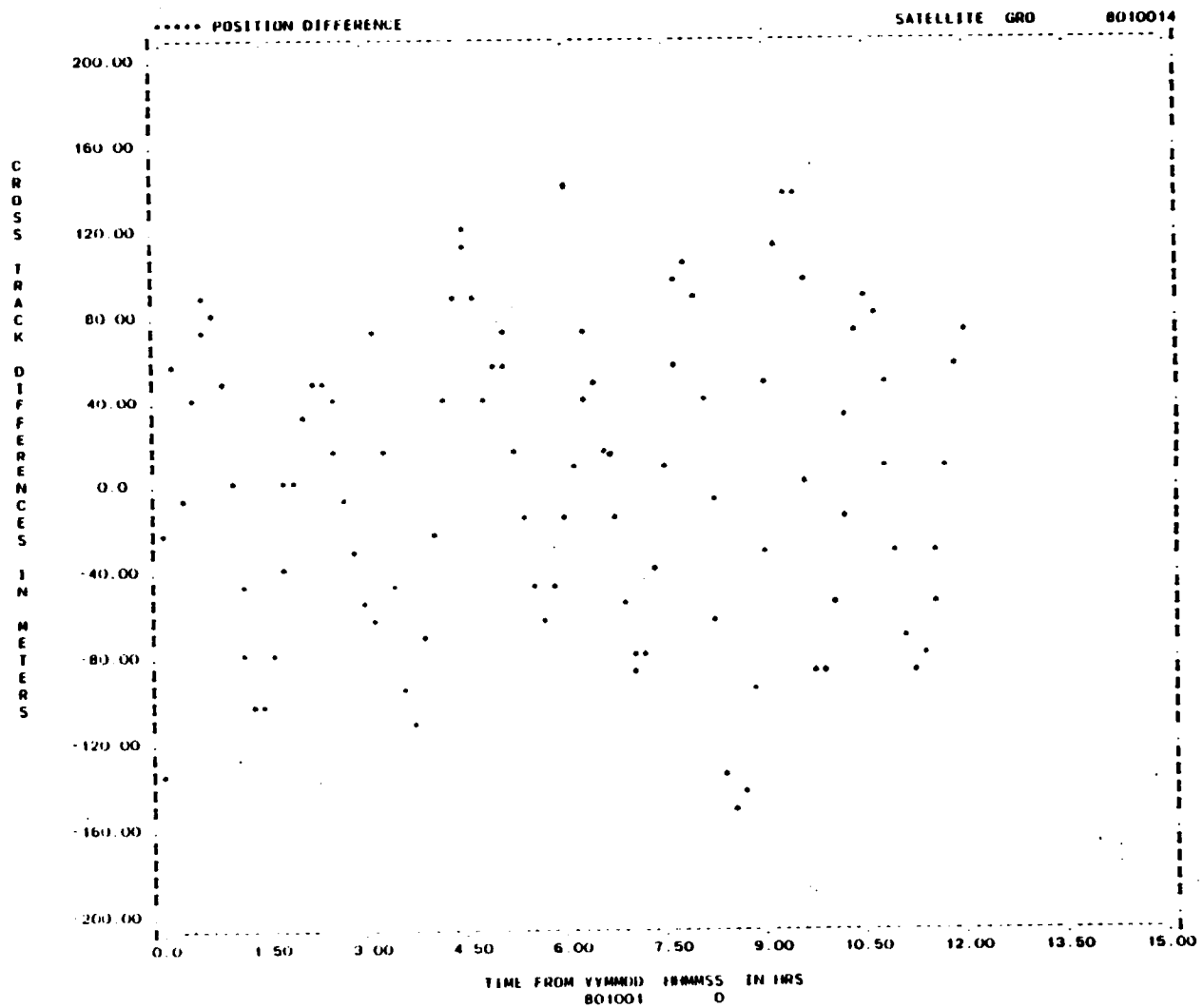

Figure B-53. Cross-Track Differences for Run T1 (1 of 2)

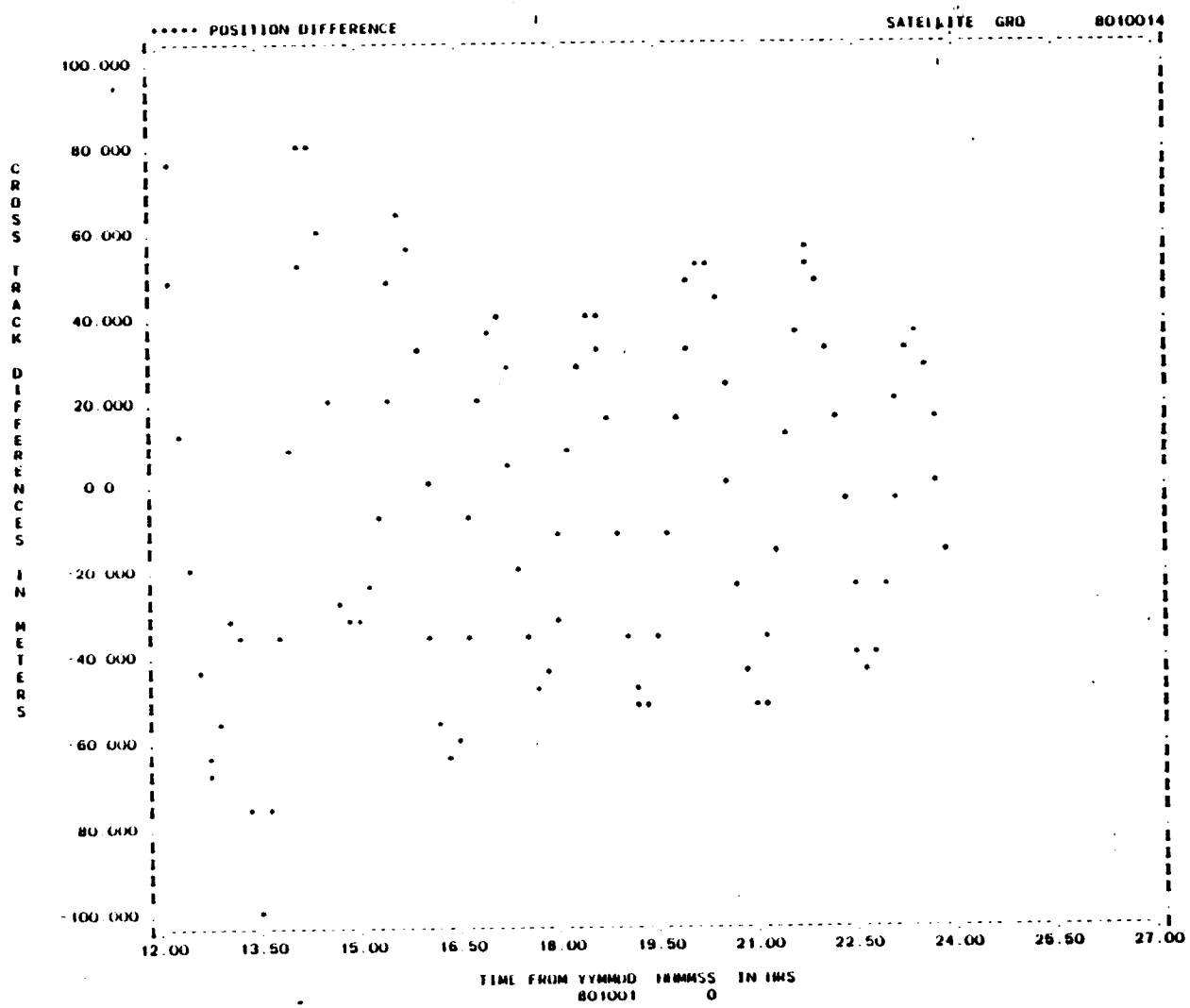

Figure B-53. Cross-Track Differences for Run T1 (2 of 2)

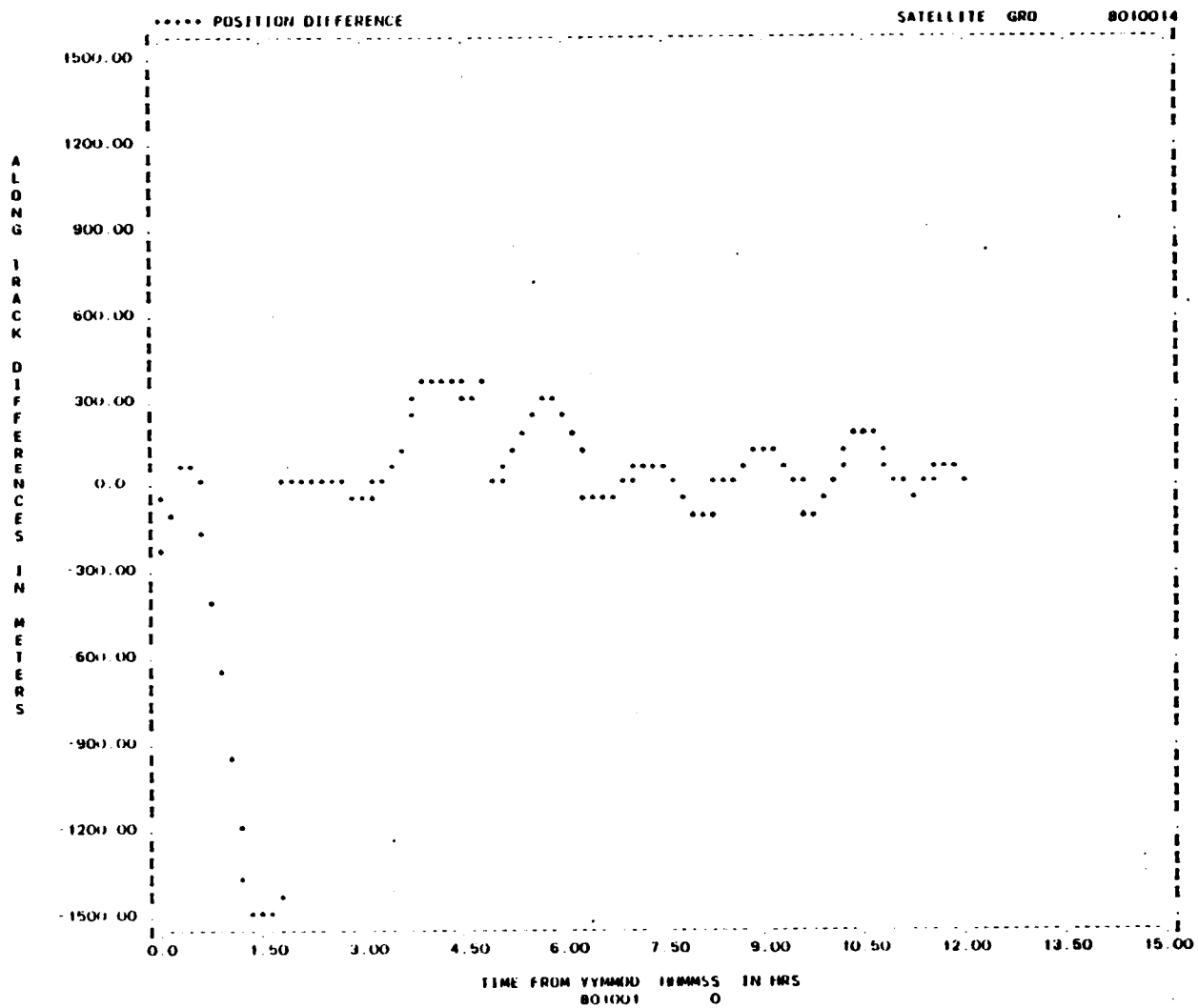

Figure B-54. Along-Track Differences for Run T1 (1 of 2)

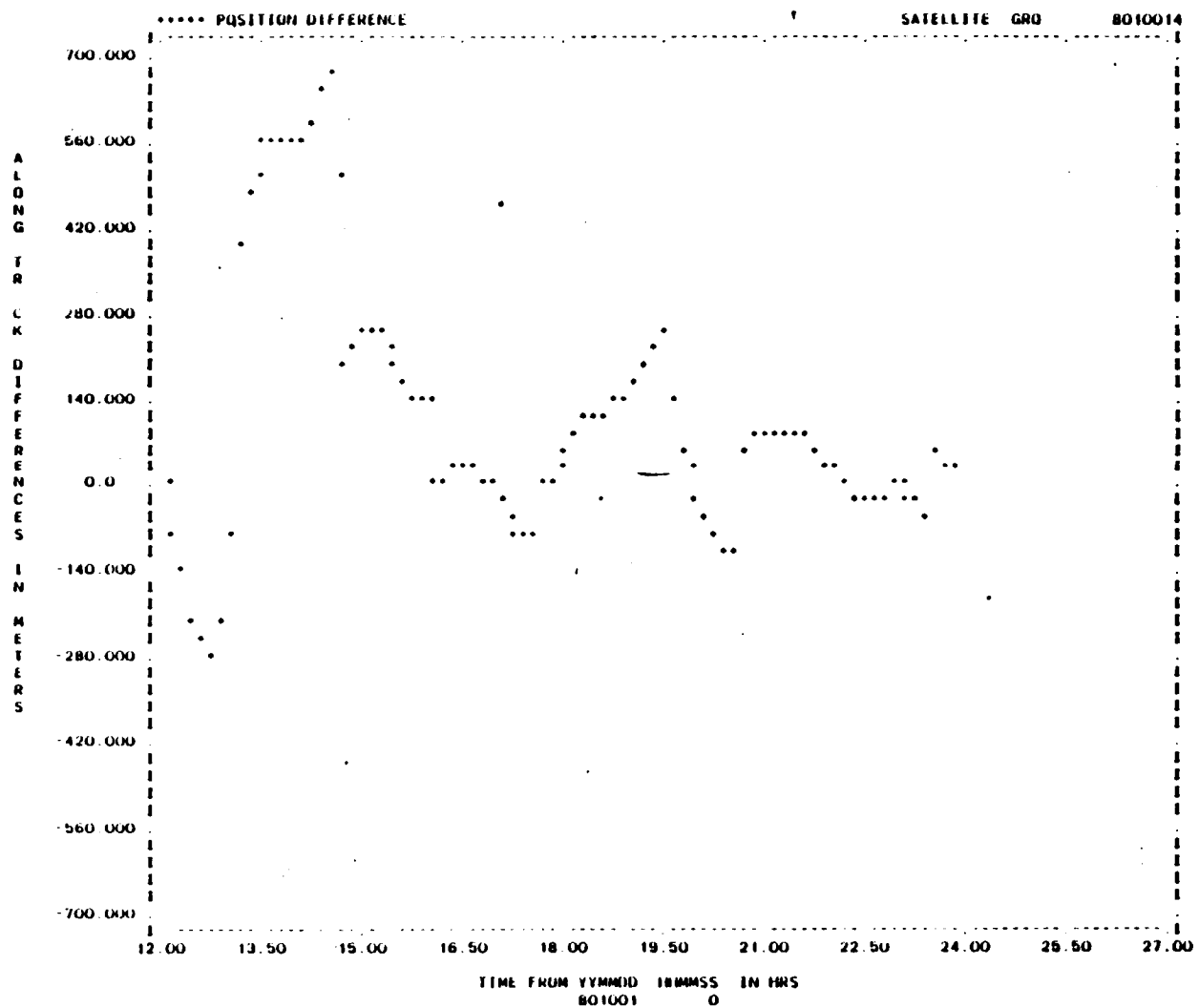

Figure B-54. Along-Track Differences for Run T1 (2 of 2)

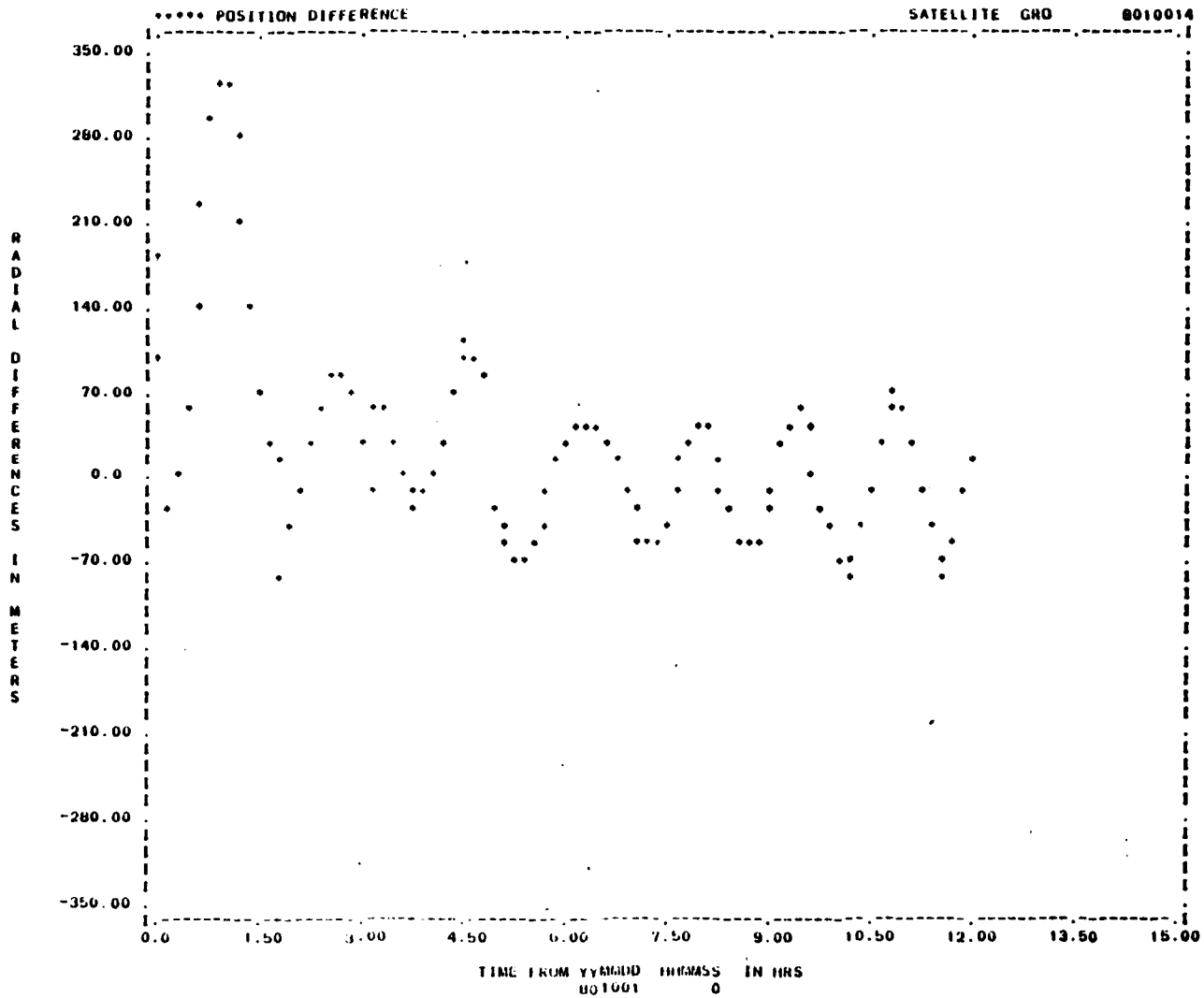

Figure B-55. Radial Differences for Run T2 (1 of 2)

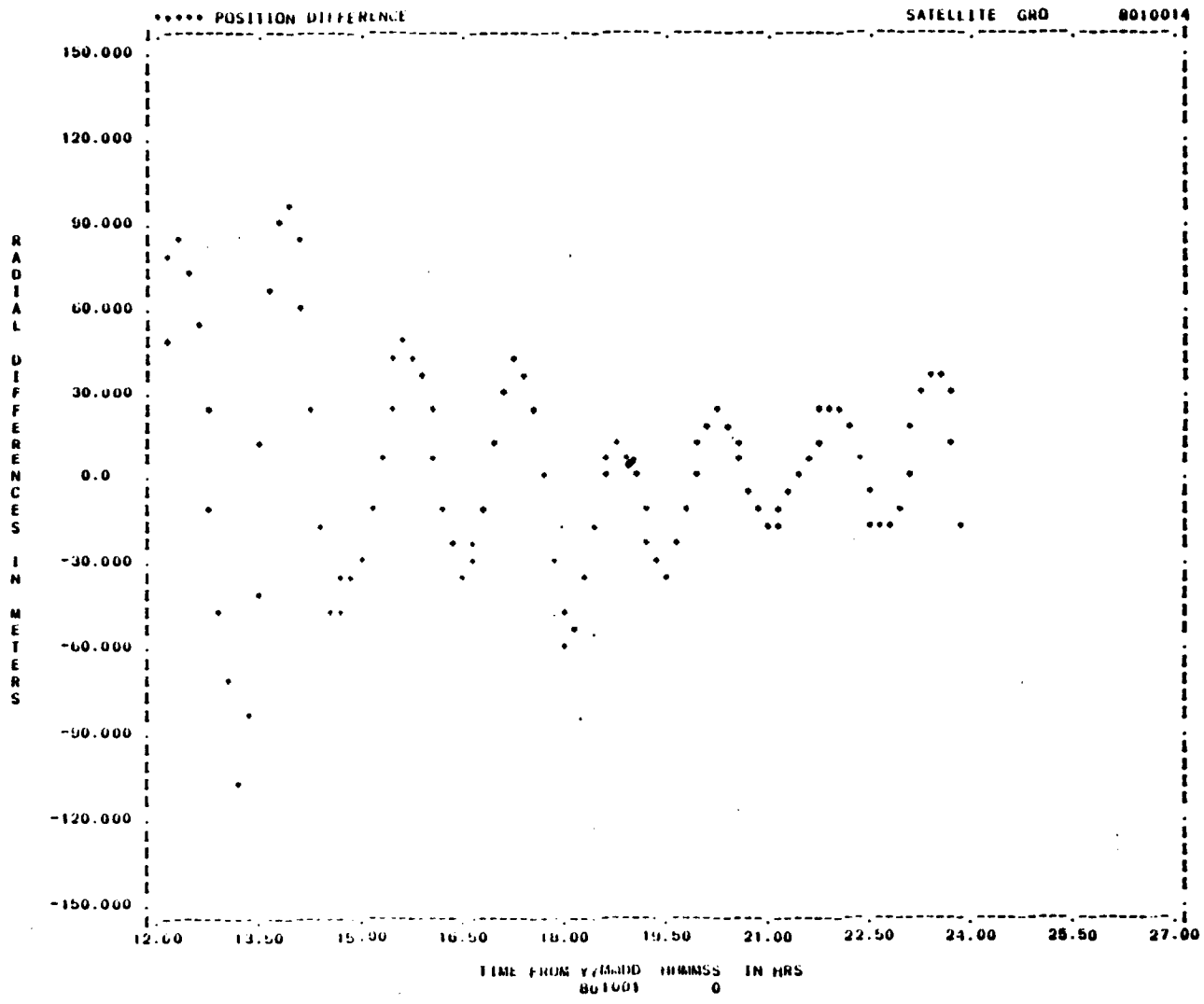

Figure B-55. Radial Differences for Run T2 (2 of 2)

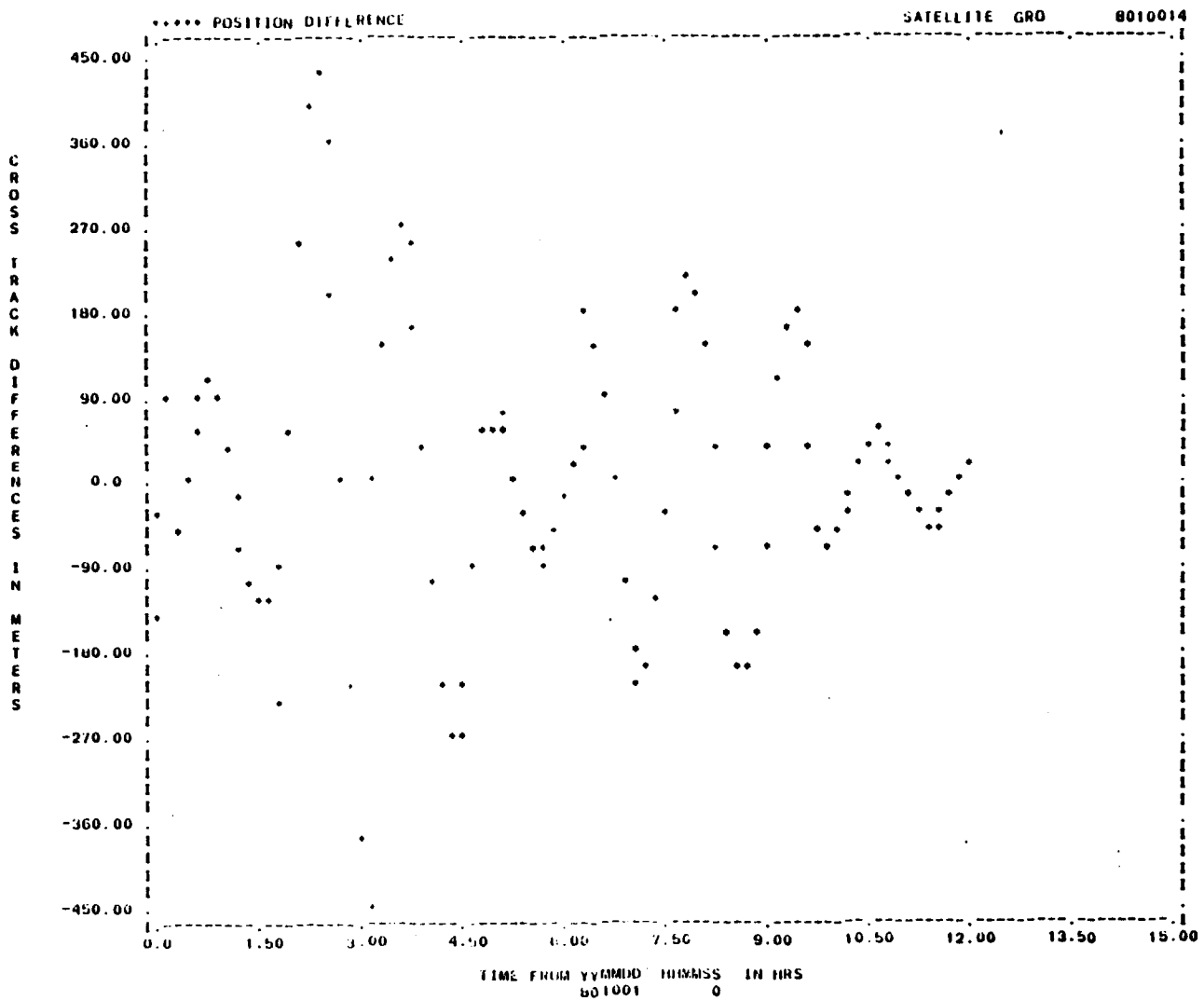

Figure B-56. Cross-Track Differences for Run T2 (1 of 2)

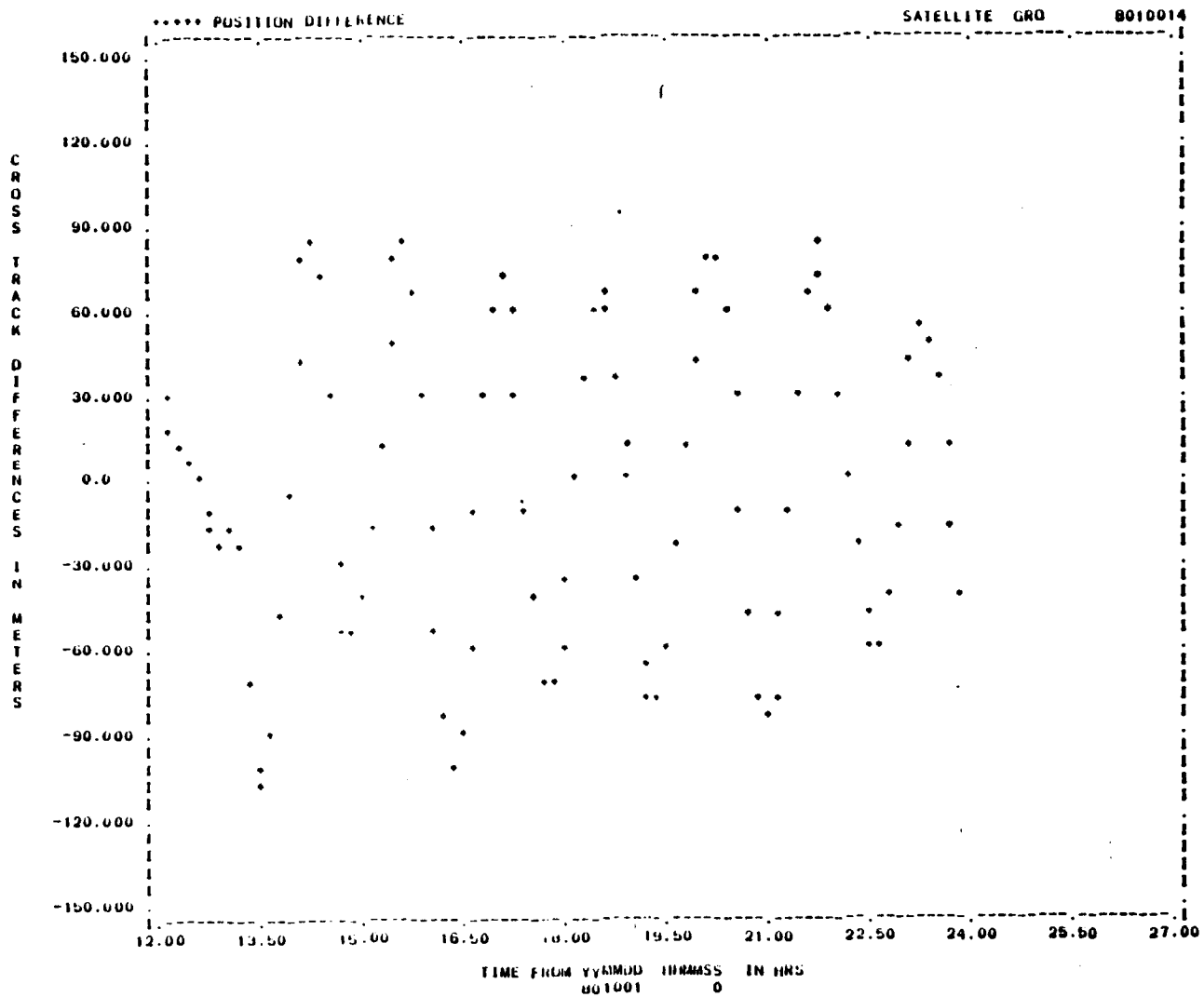

Figure B-56. Cross-Track Differences for Run T2 (2 of 2)

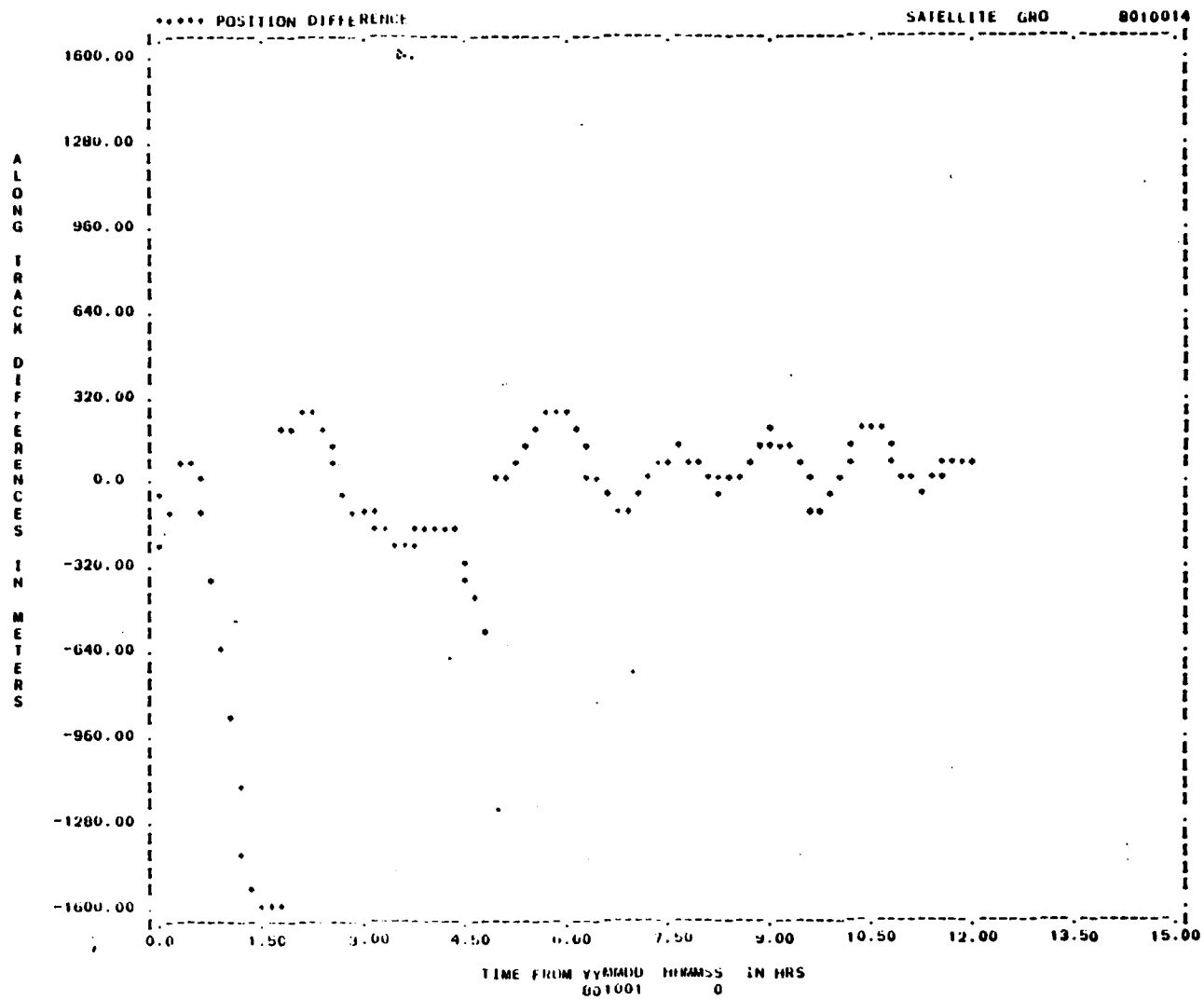

Figure B-57. Along-Track Differences for Run T2 (1 of 2)

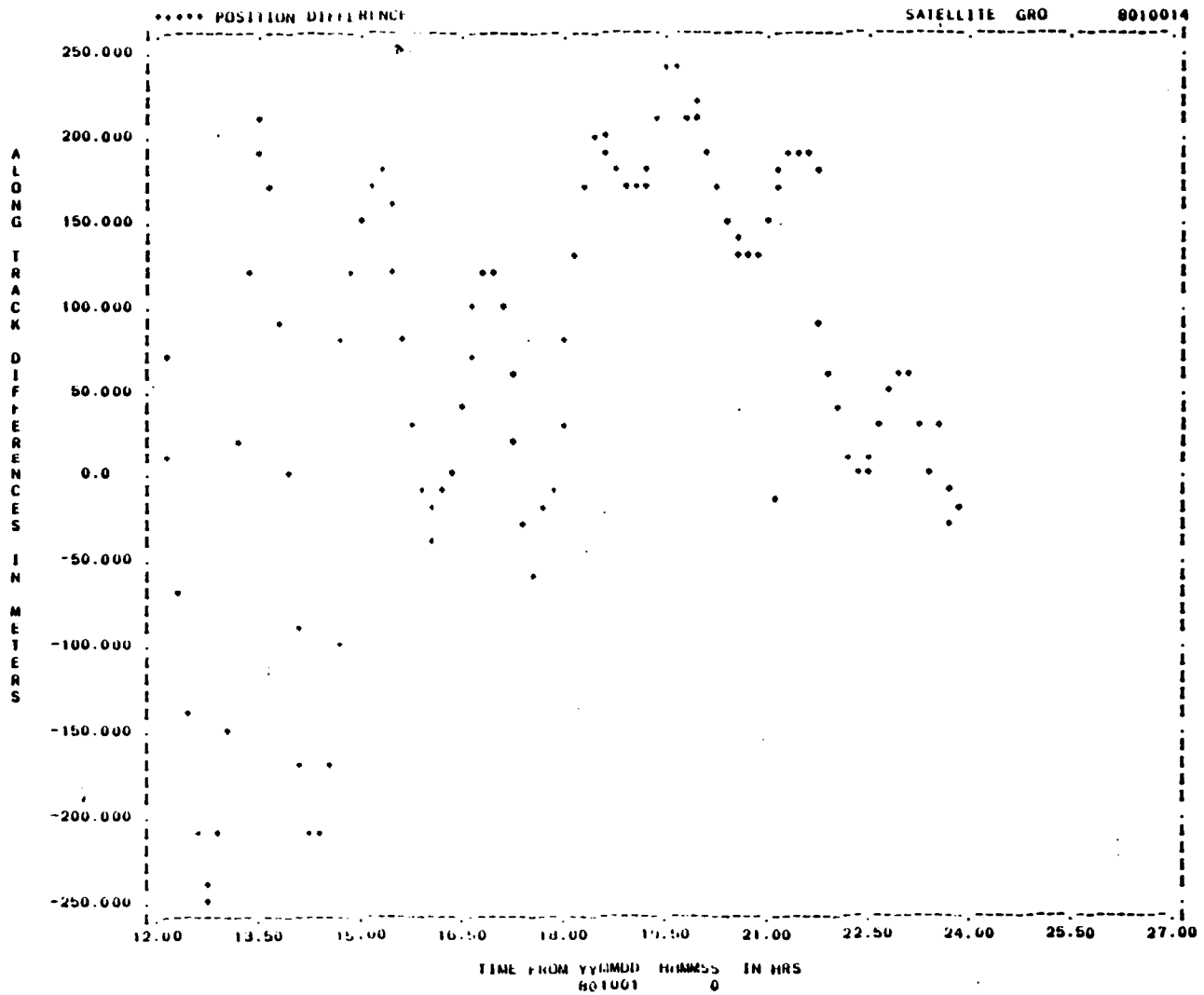

Figure B-57. Along-Track Differences for Run T2 (2 of 2)

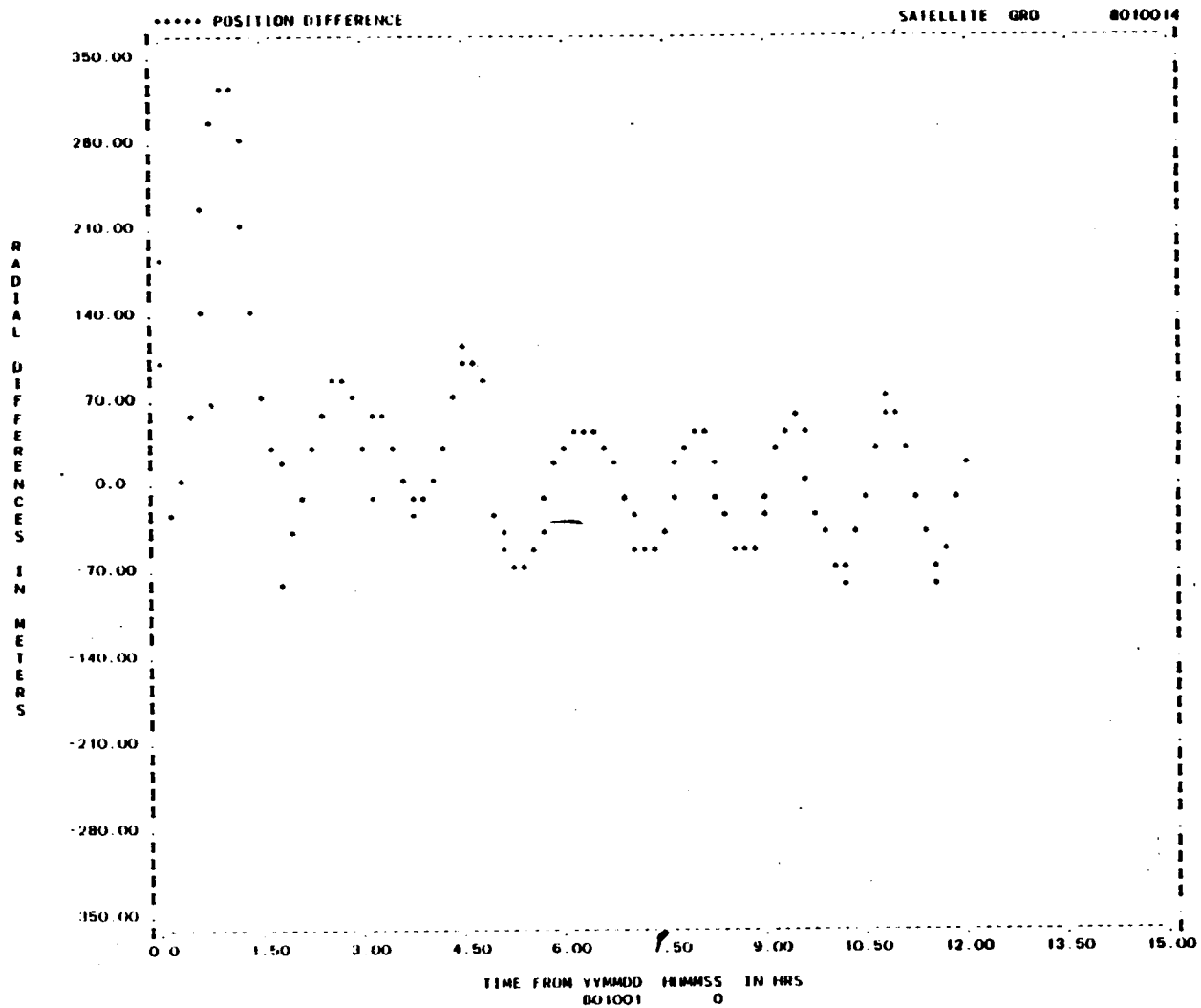

Figure B-58. Radial Differences for Run T3 (1 of 2)

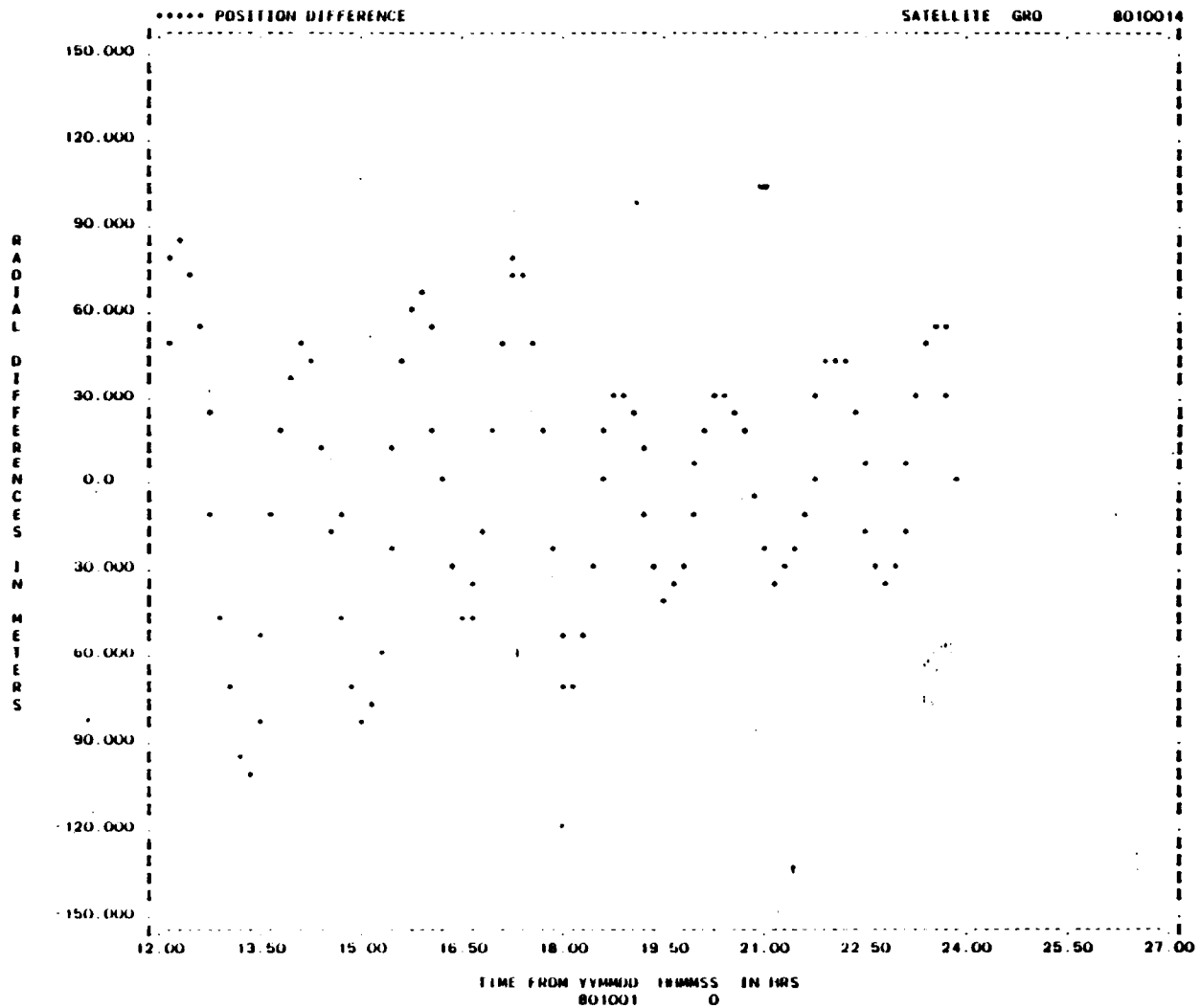

Figure B-58. Radial Differences for Run T3 (2 of 2)

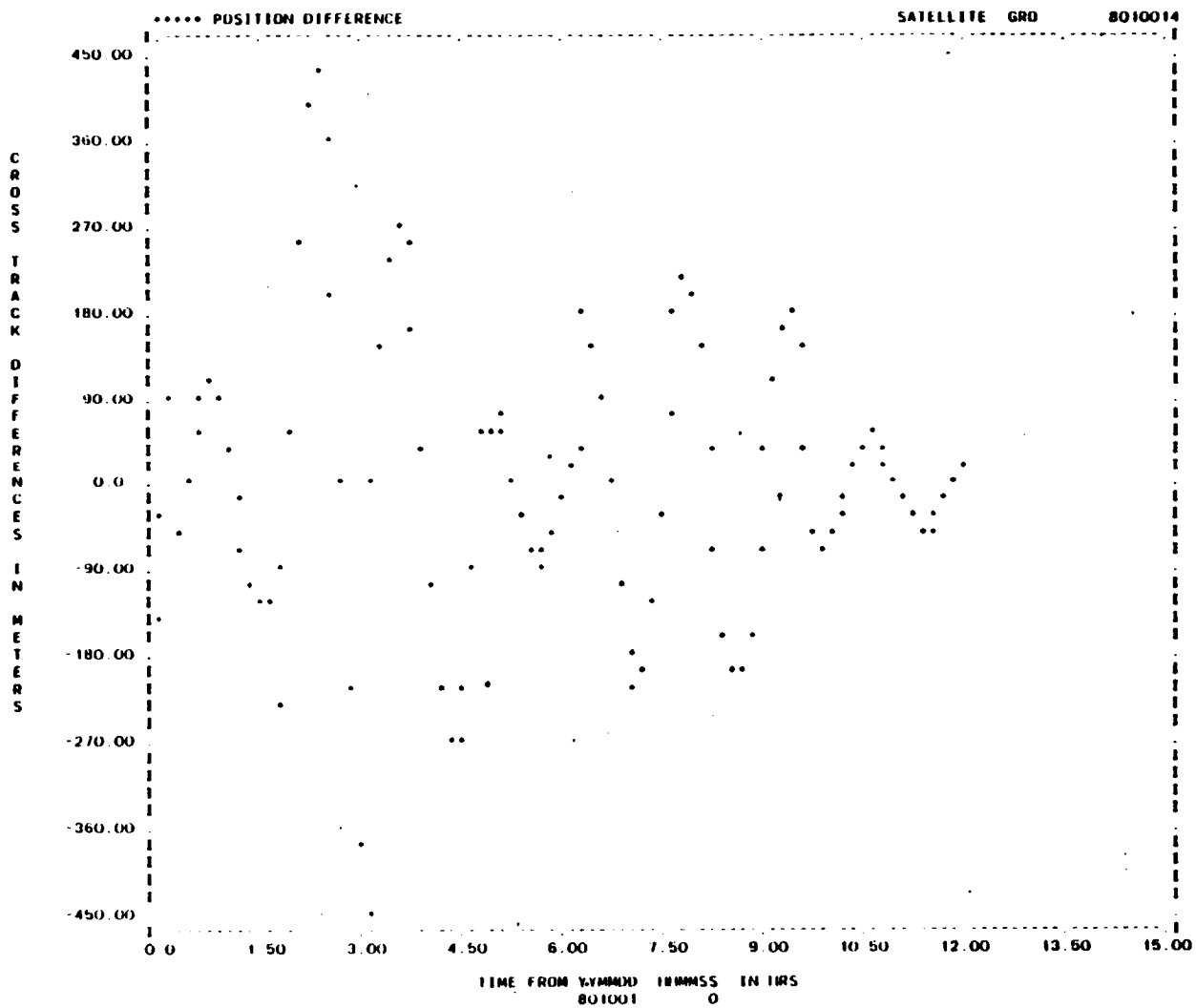

Figure B-59. Cross-Track Differences for Run T3 (1 of 2)

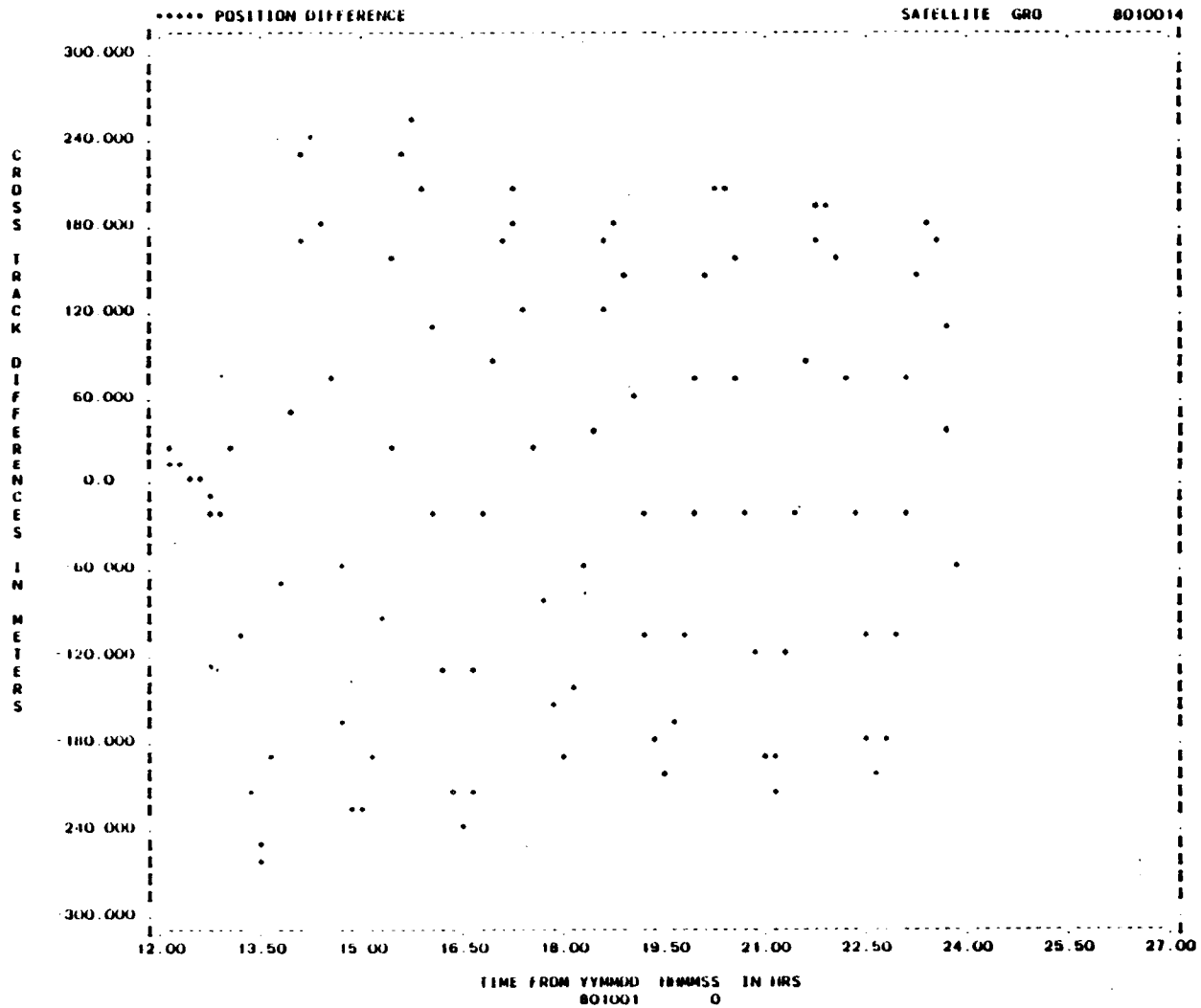

Figure B-59. Cross-Track Differences for Run T3 (2 of 2)

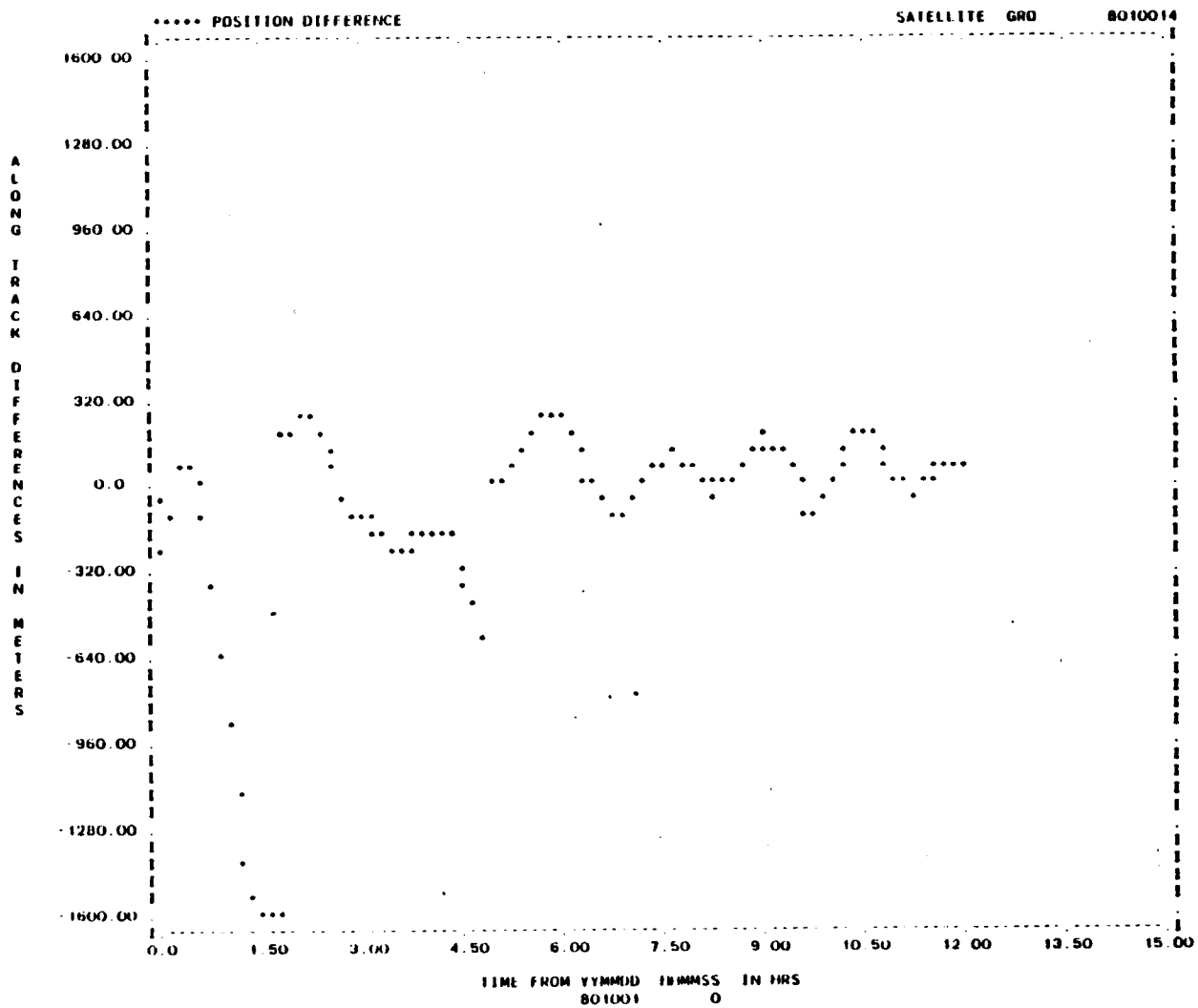

Figure B-60. Along-Track Differences for Run T3 (1 of 2)

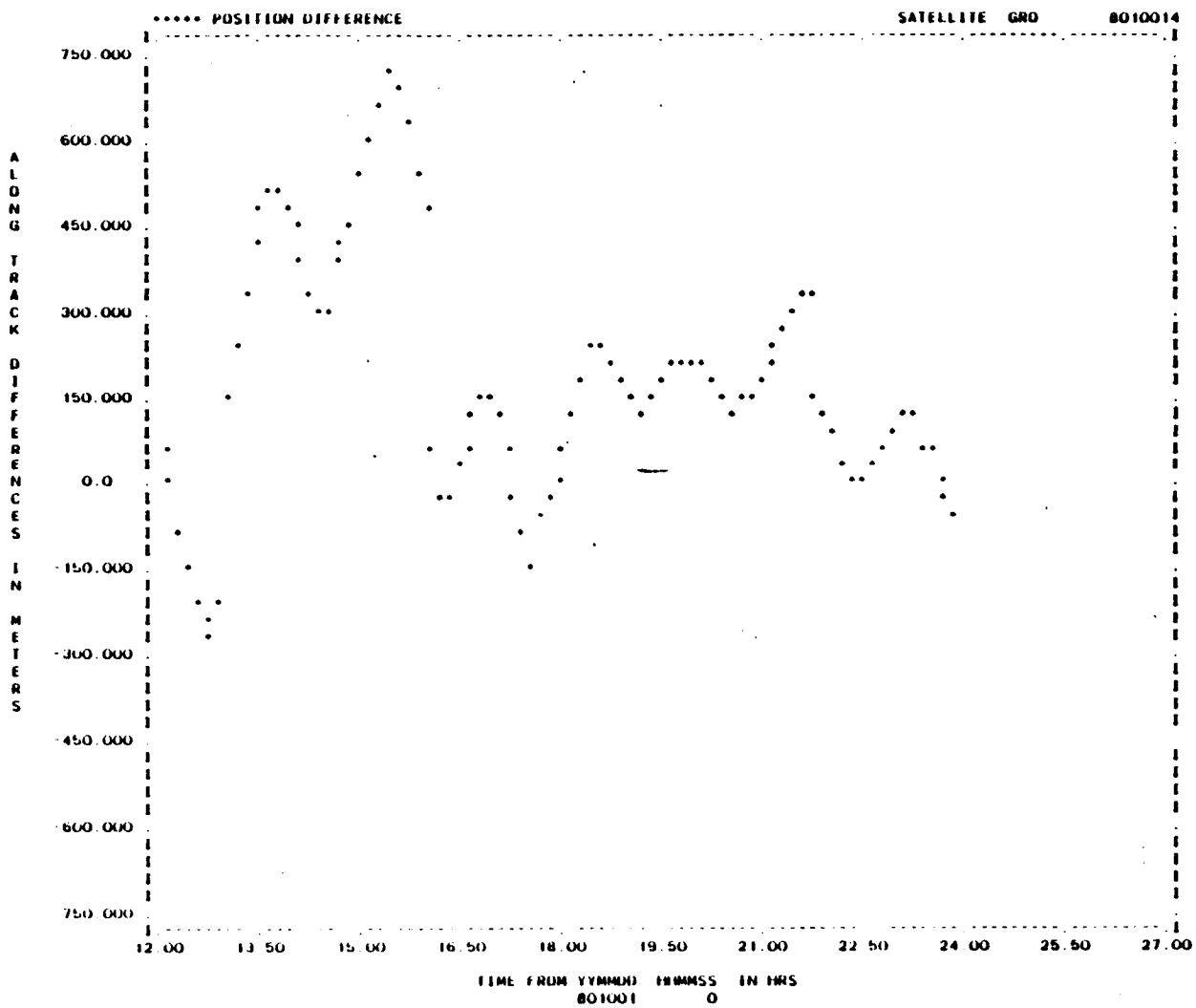

Figure B-60. Along-Track Differences for Run T3 (2 of 2)

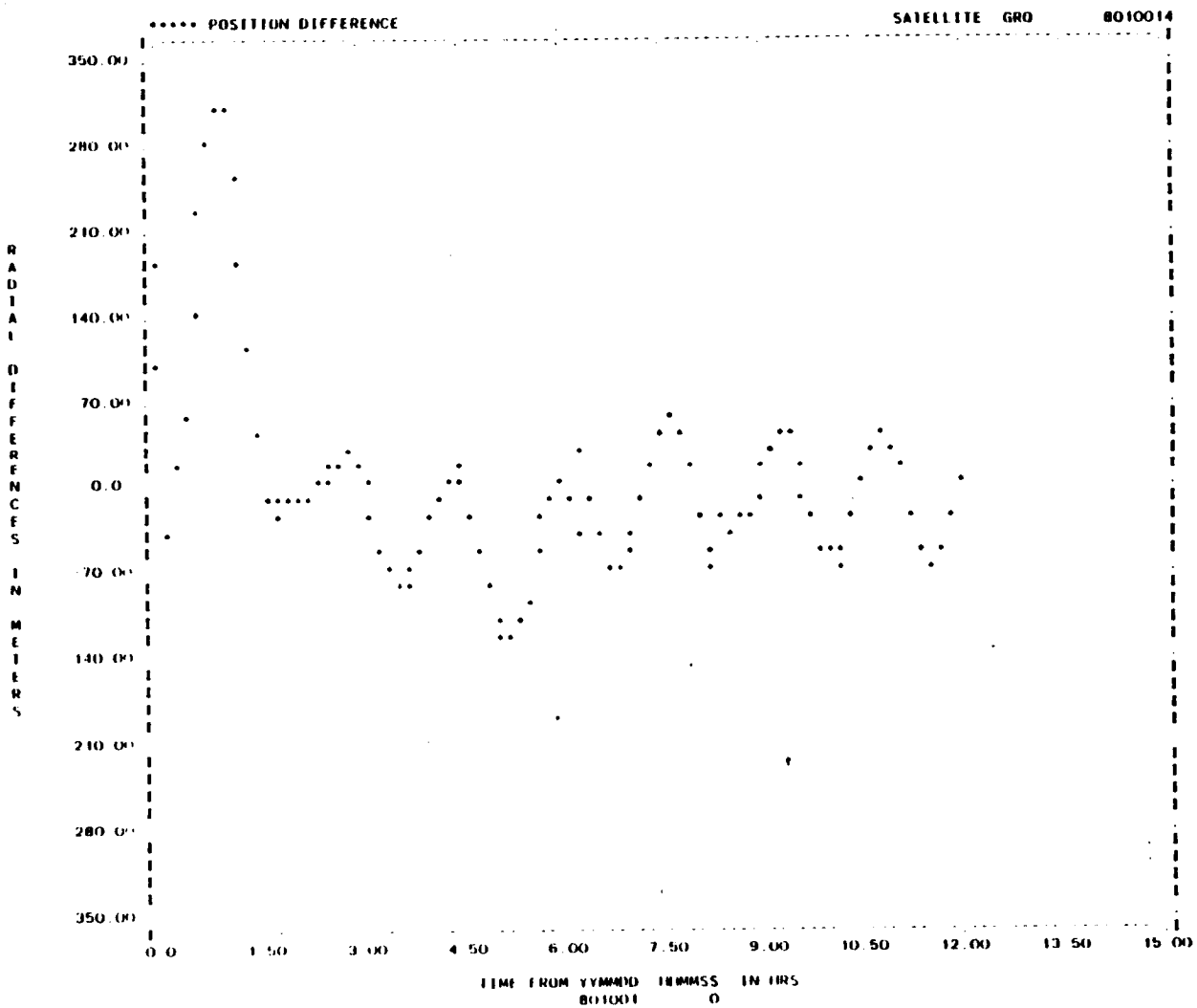

Figure B-61. Radial Differences for Run T4 (1 of 2)

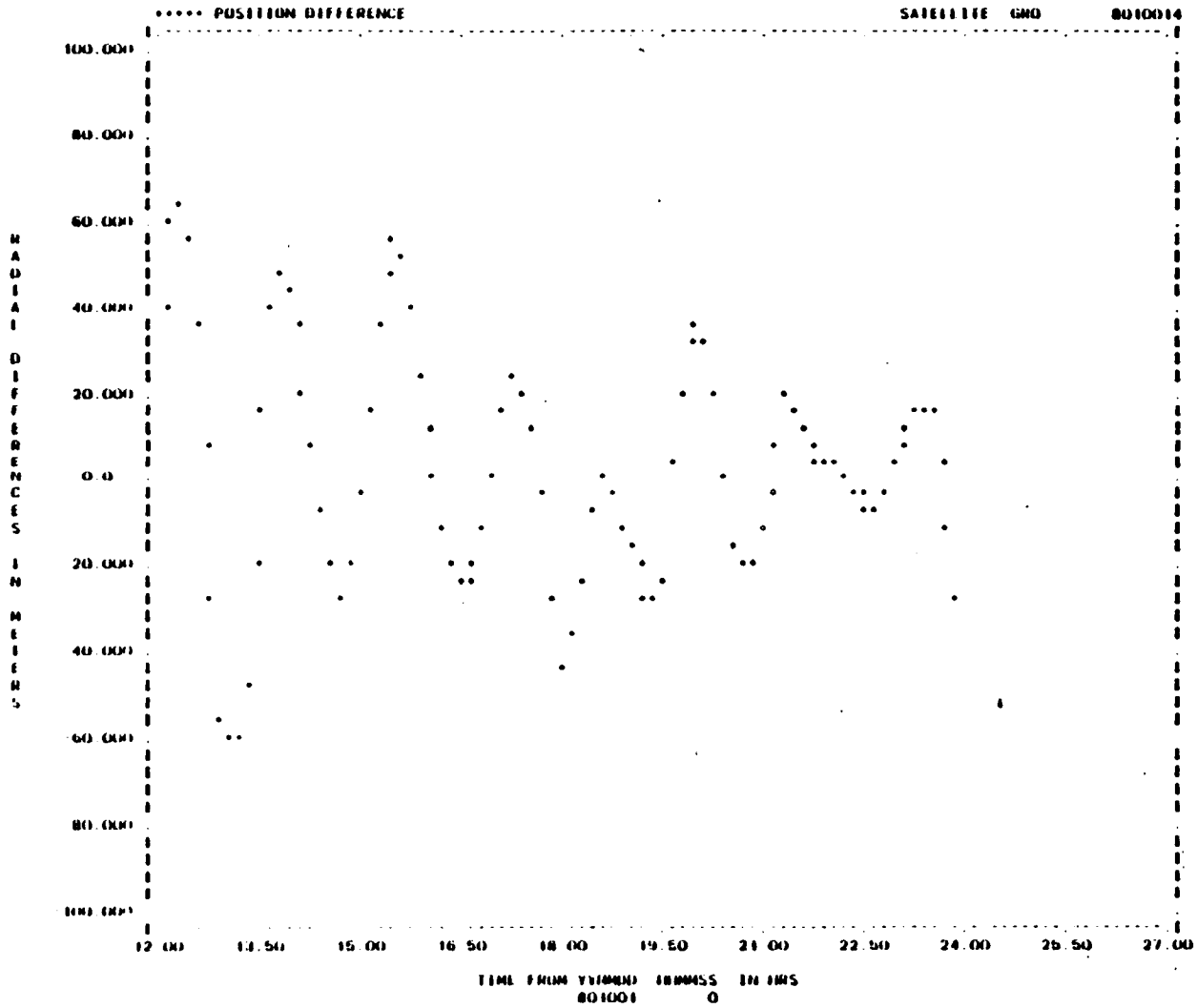

Figure B-61. Radial Differences for Run T4 (2 of 2)

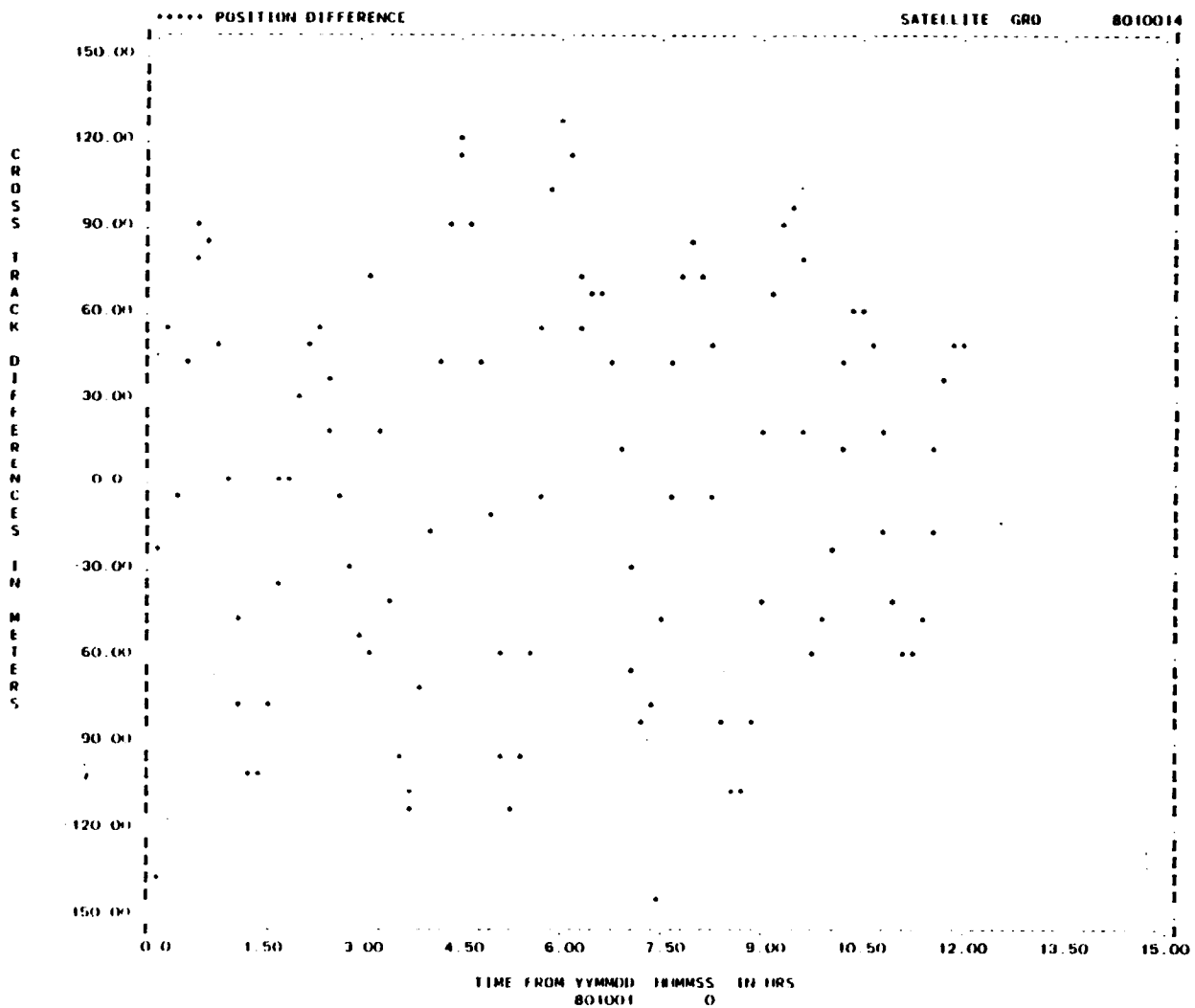

Figure B-62. Cross-Track Differences for Run T4 (1 of 2)

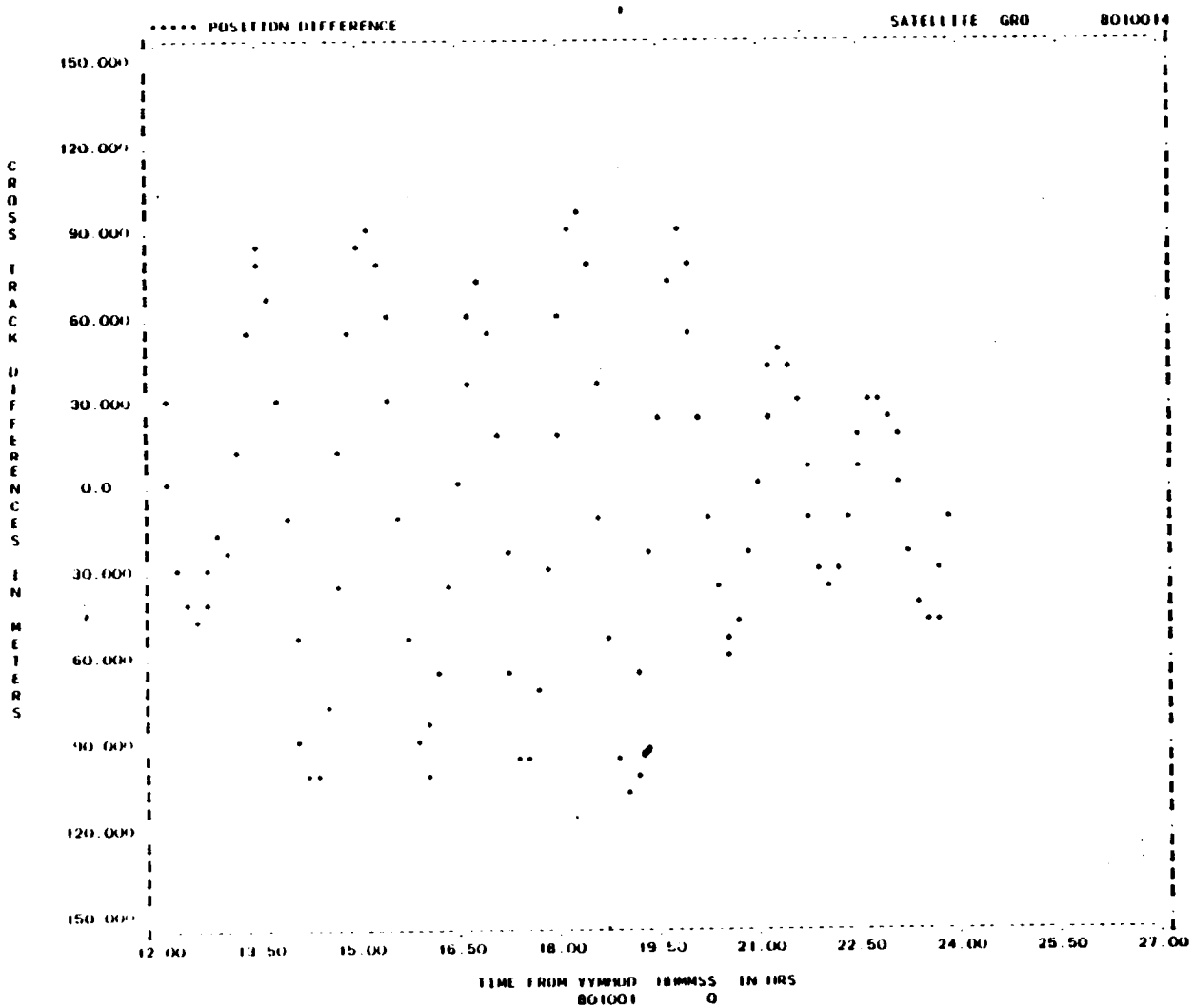

Figure B-62. Cross-Track Differences for Run T4 (2 of 2)

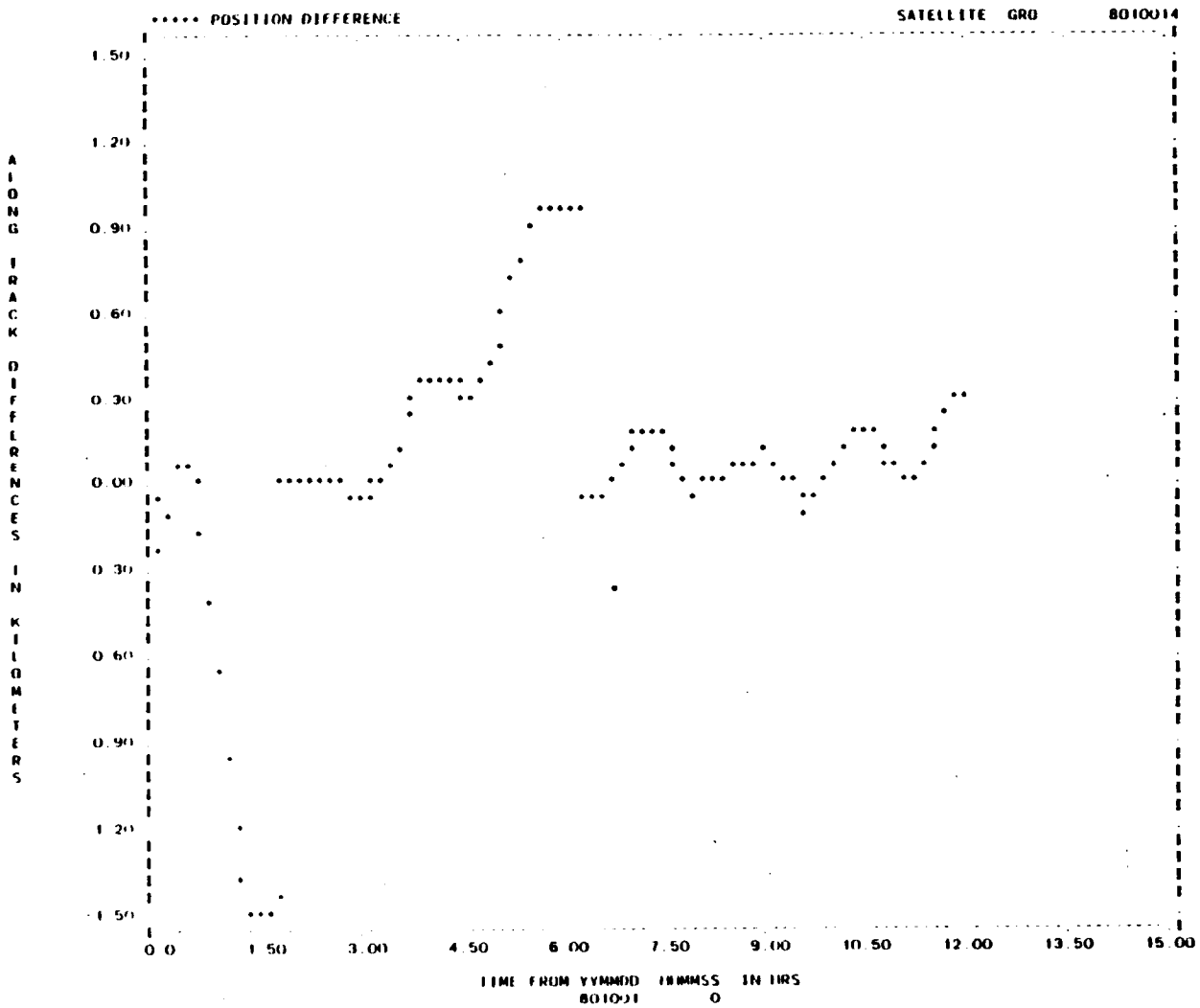

Figure B-63. Along-Track Differences for Run T4 (1 of 2)

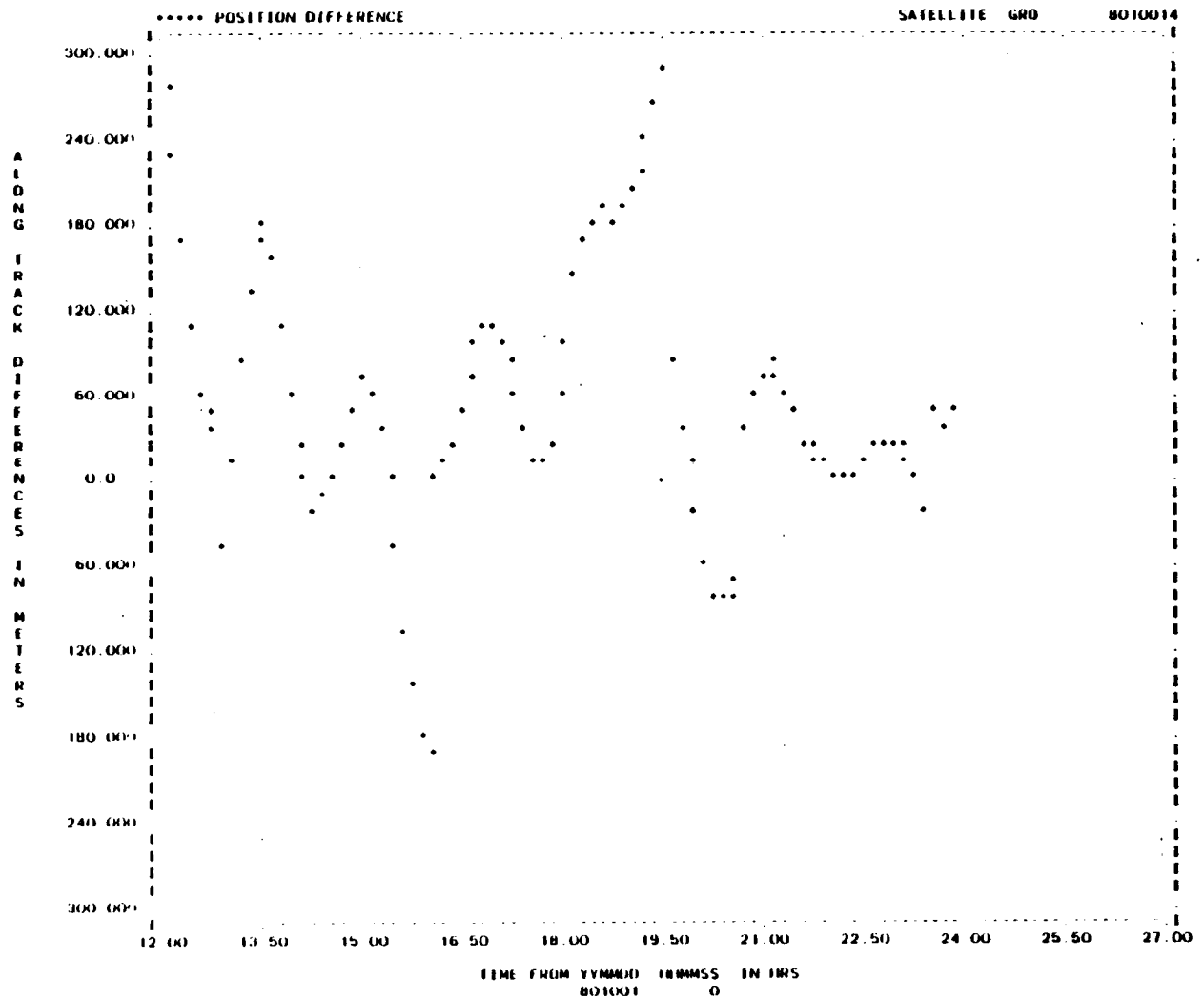

Figure B-63. Along-Track Differences for Run T4 (2 of 2)

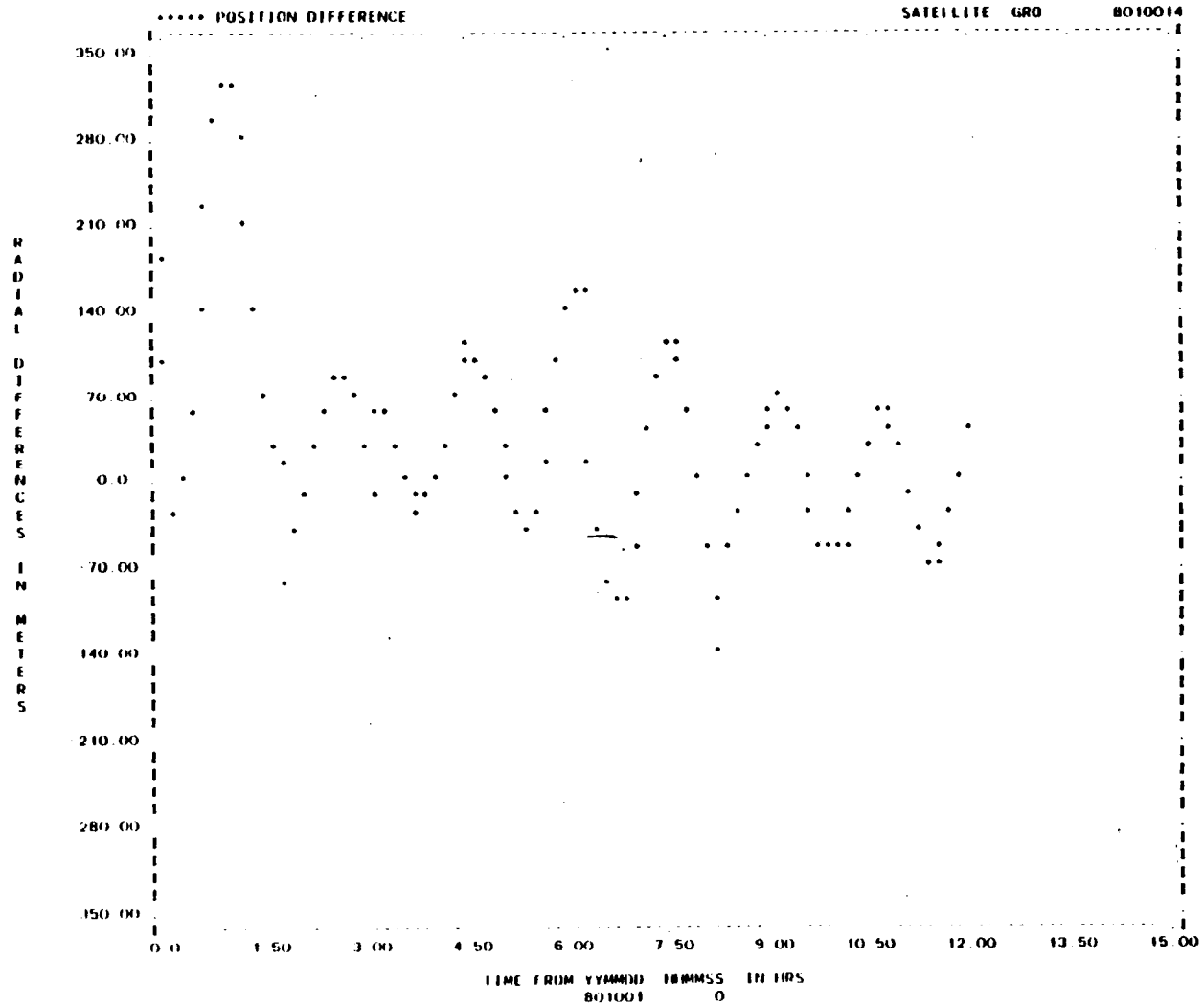

Figure B-64. Radial Differences for Run T5 (1 of 2)

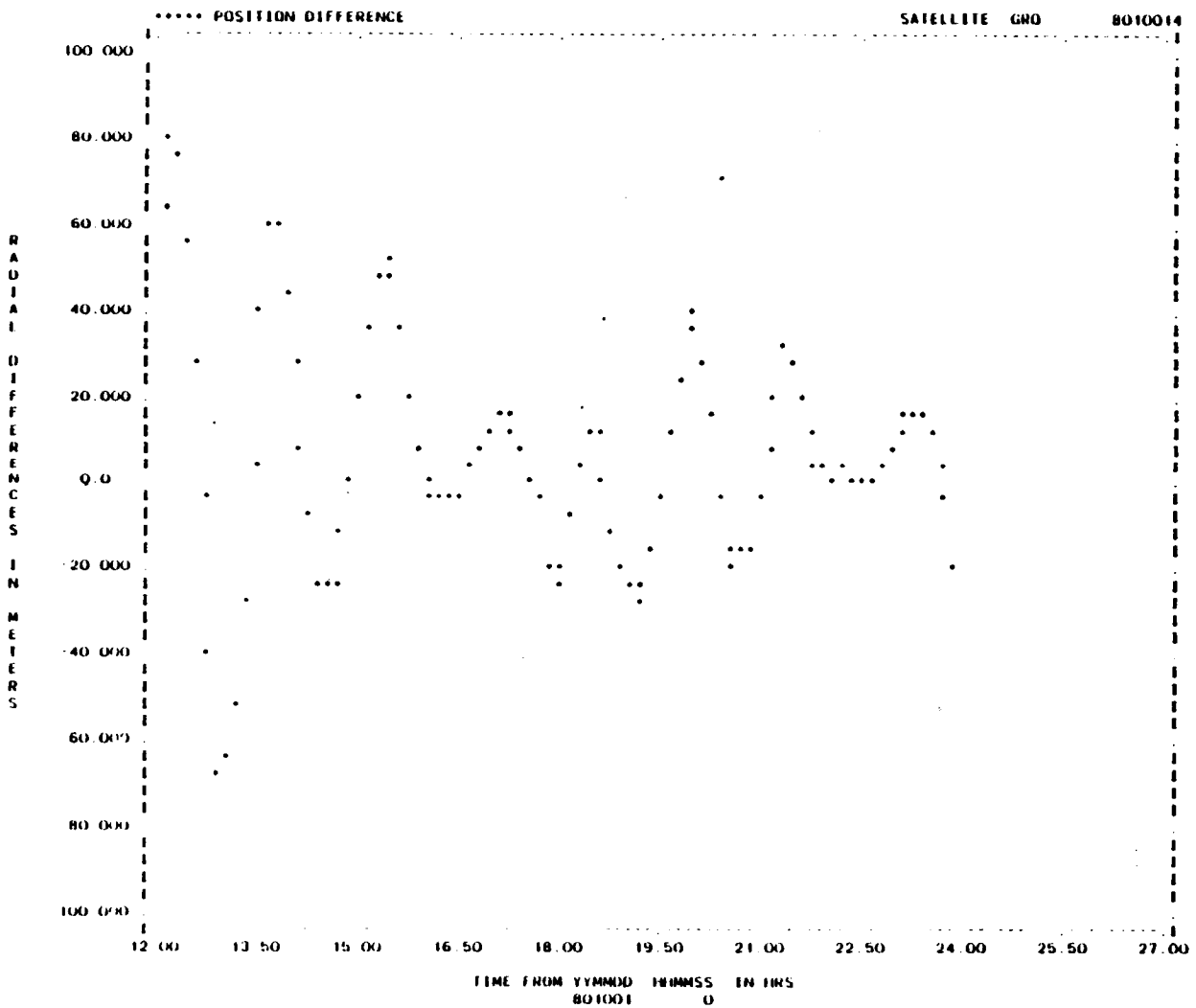

Figure B-64. Radial Differences for Run T5 (2 of 2)

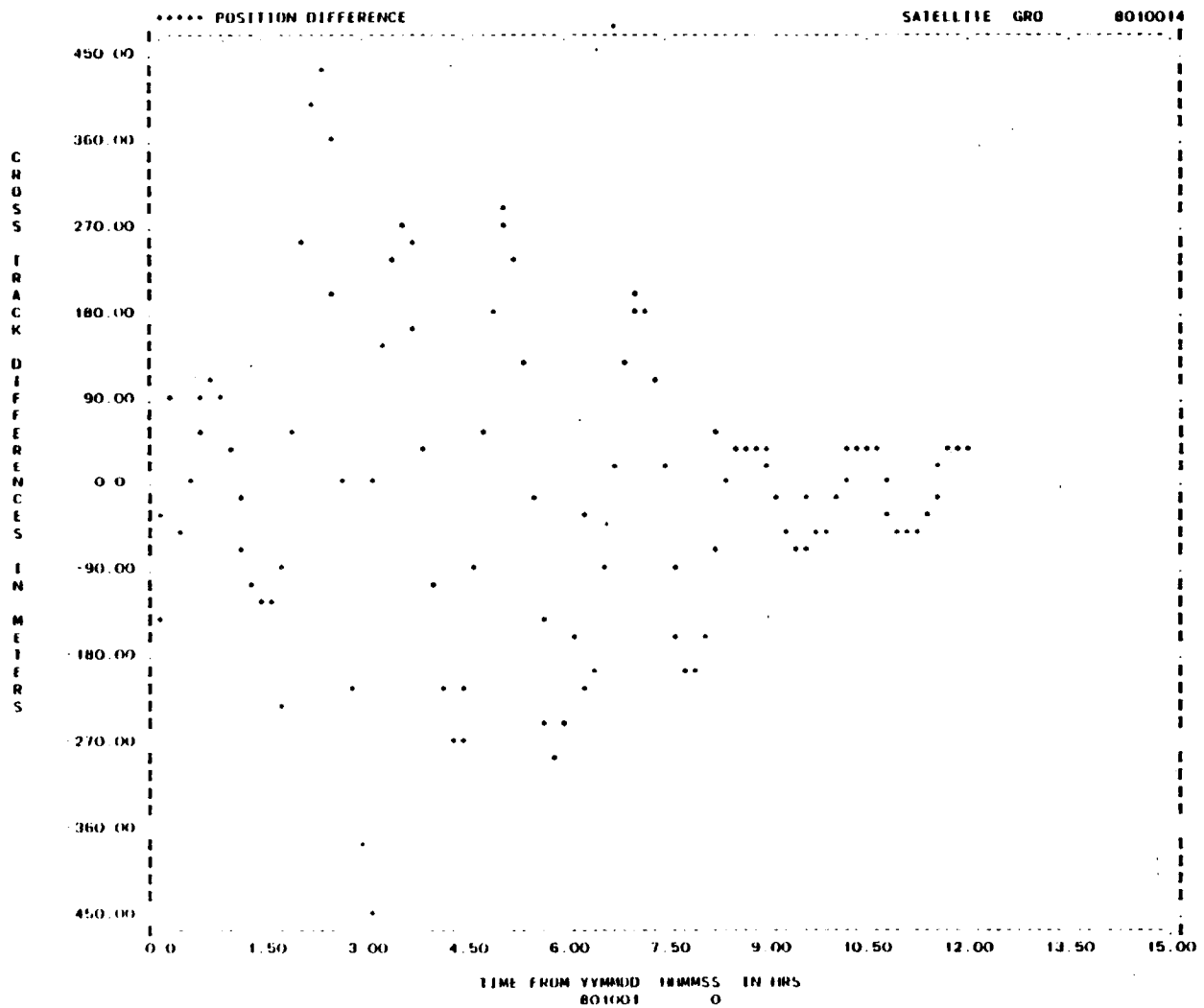

Figure B-65. Cross-Track Differences for Run T5 (1 of 2)

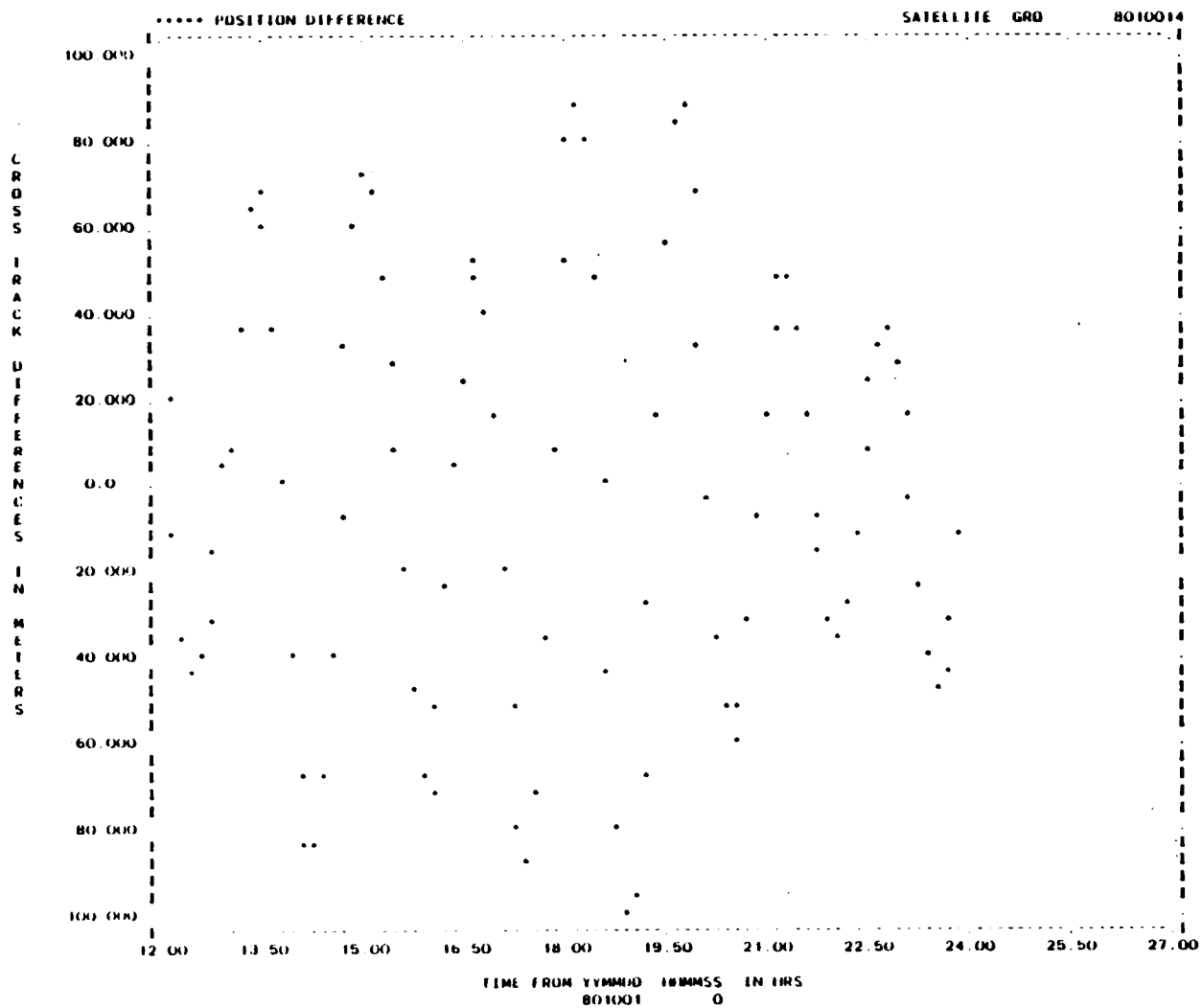

Figure B-65. Cross-Track Differences for Run T5 (2 of 2)

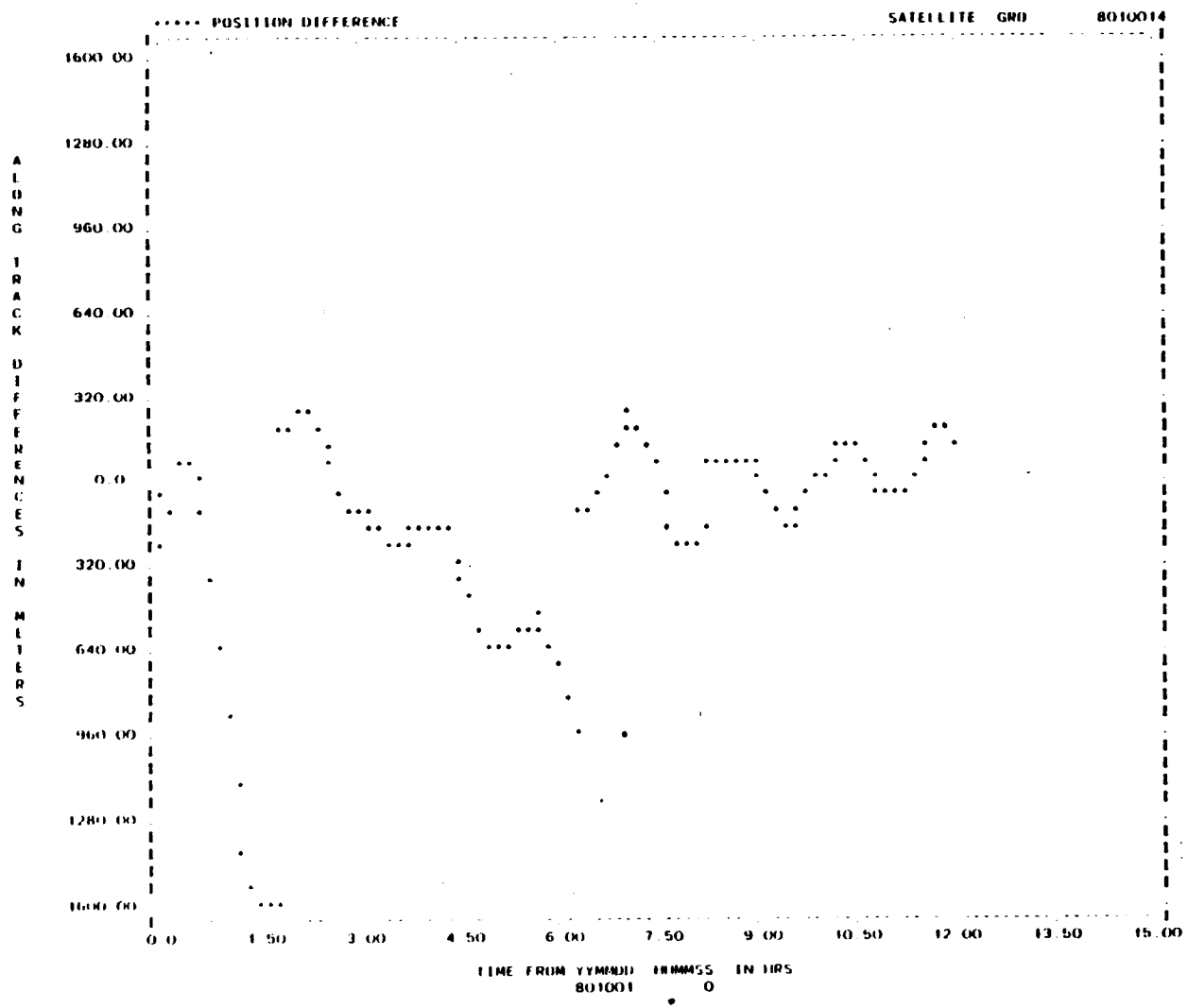

Figure B-66. Along-Track Differences for Run T5 (1 of 2)

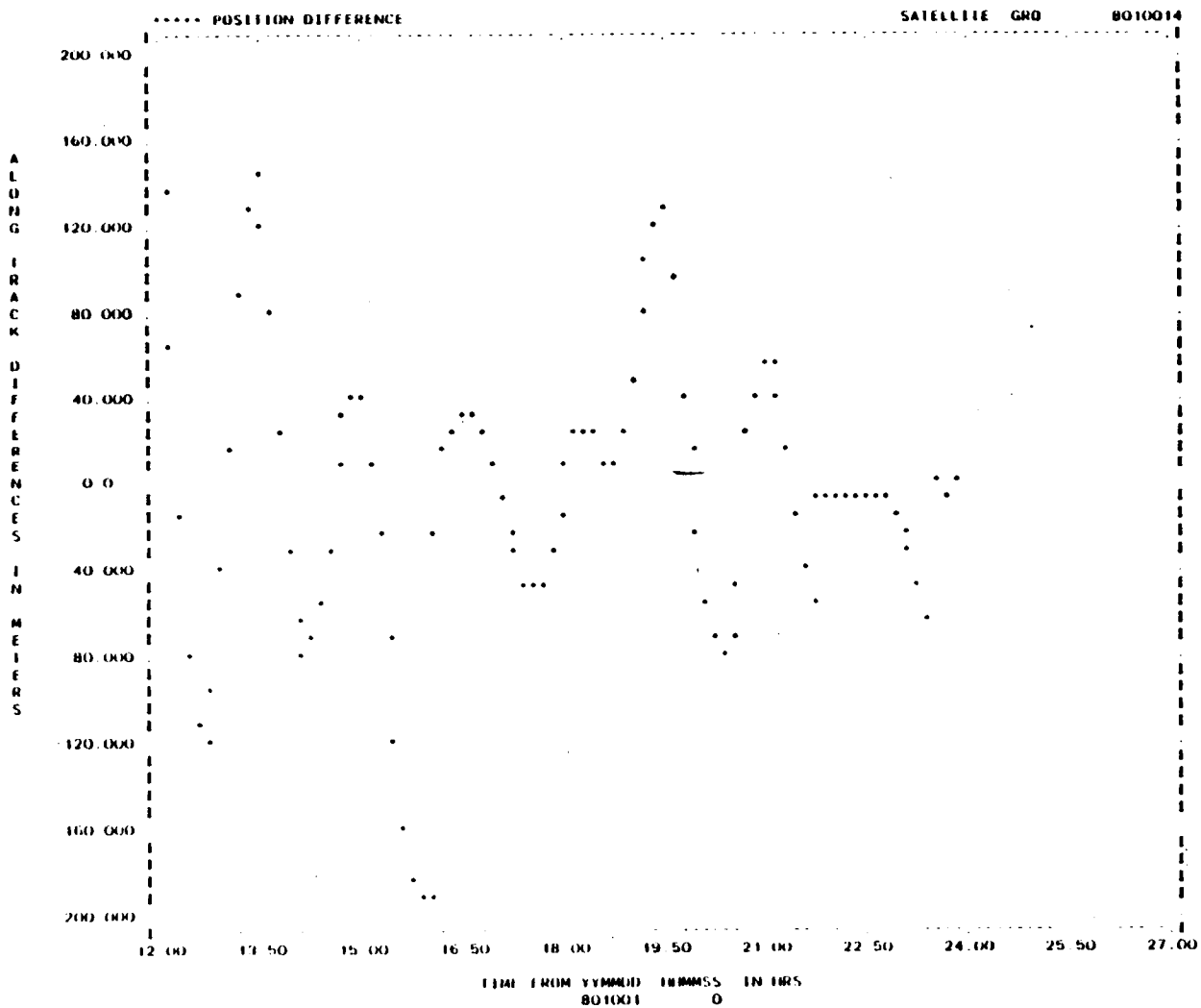

Figure B-66. Along-Track Differences for Run T5 (2 of 2)

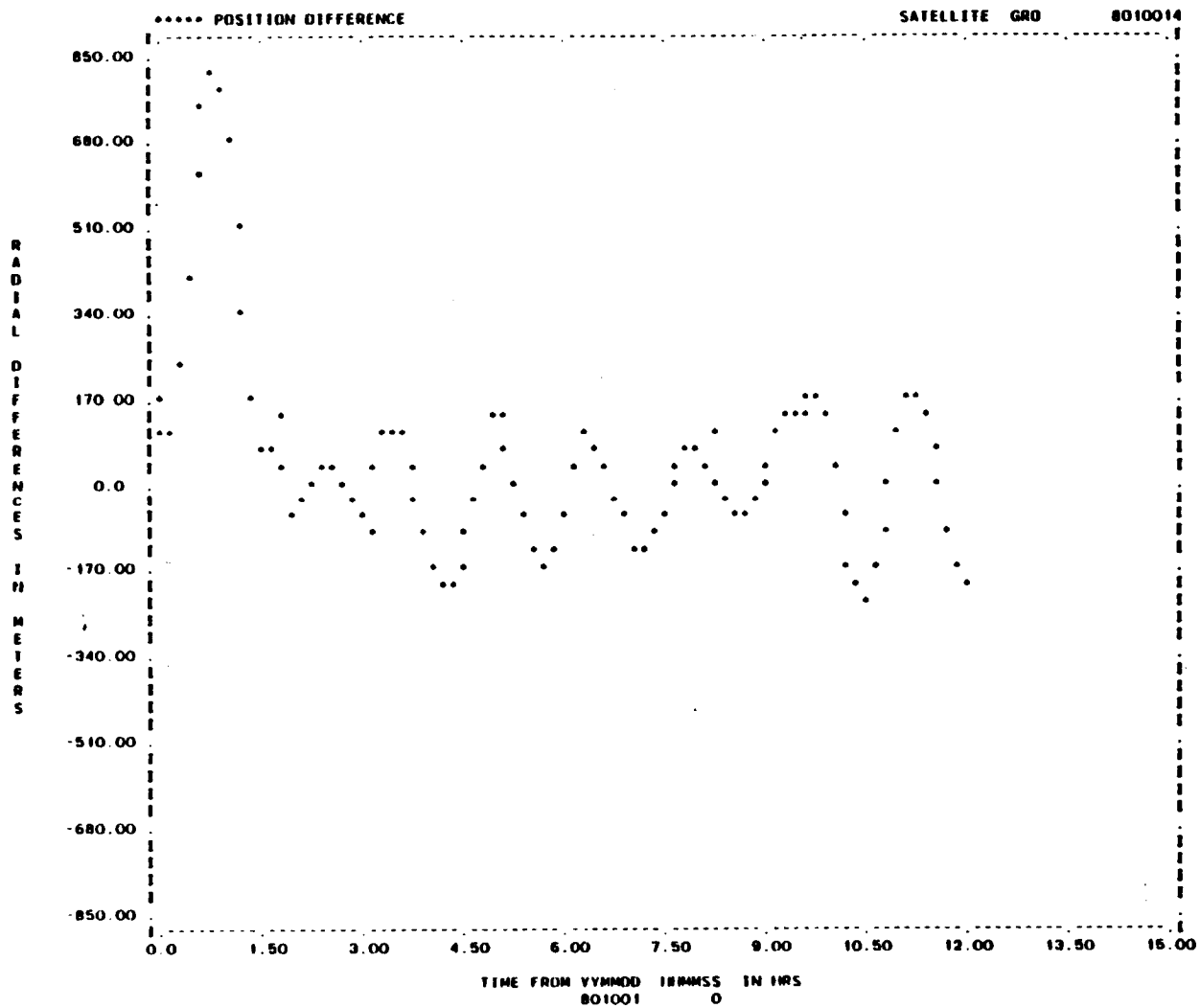

Figure B-67. Radial Differences for Run T7 (1 of 2)

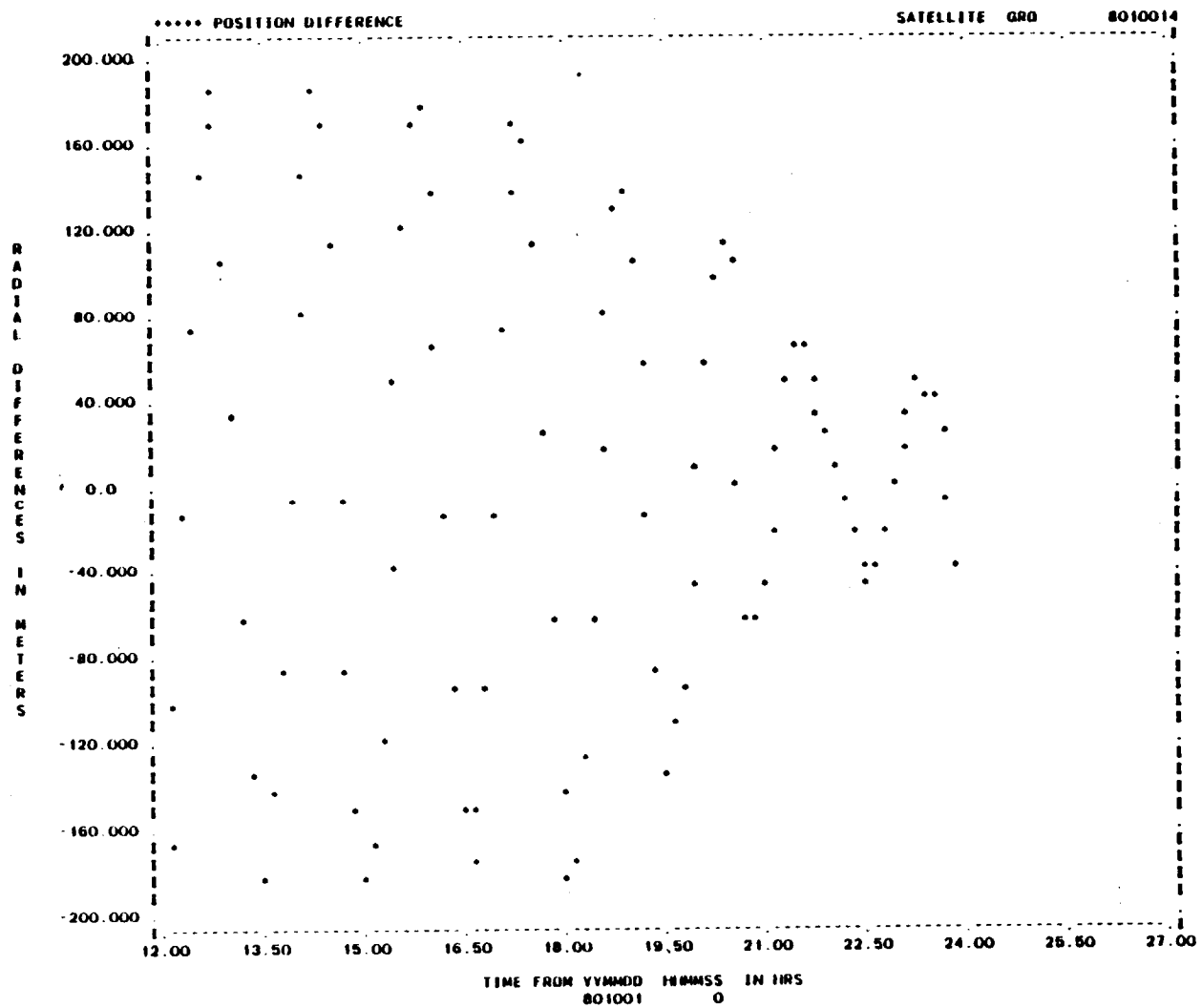

Figure B-67. Radial Differences for Run T7 (2 of 2)

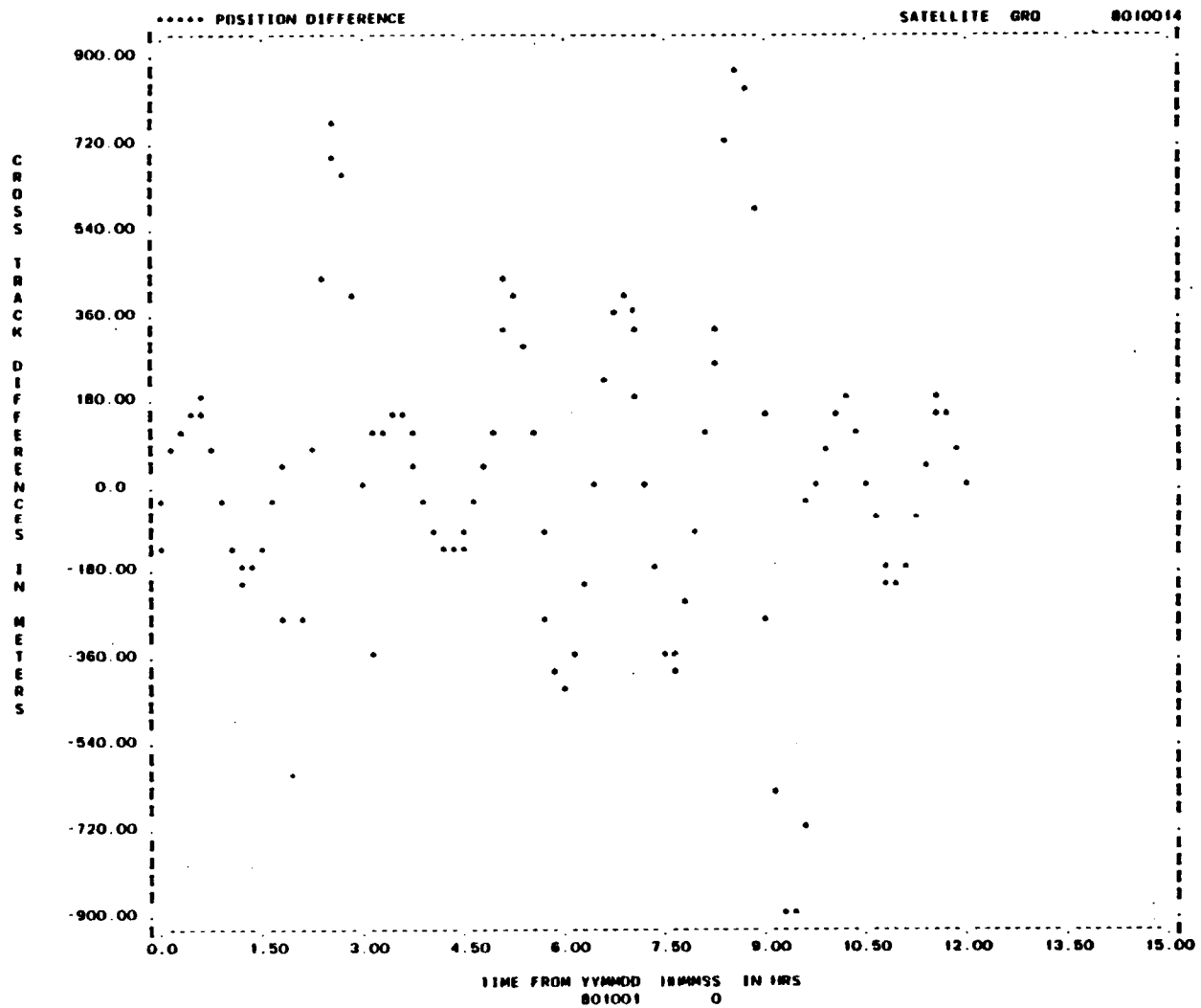

Figure B-68. Cross-Track Differences for Run T7 (1 of 2)

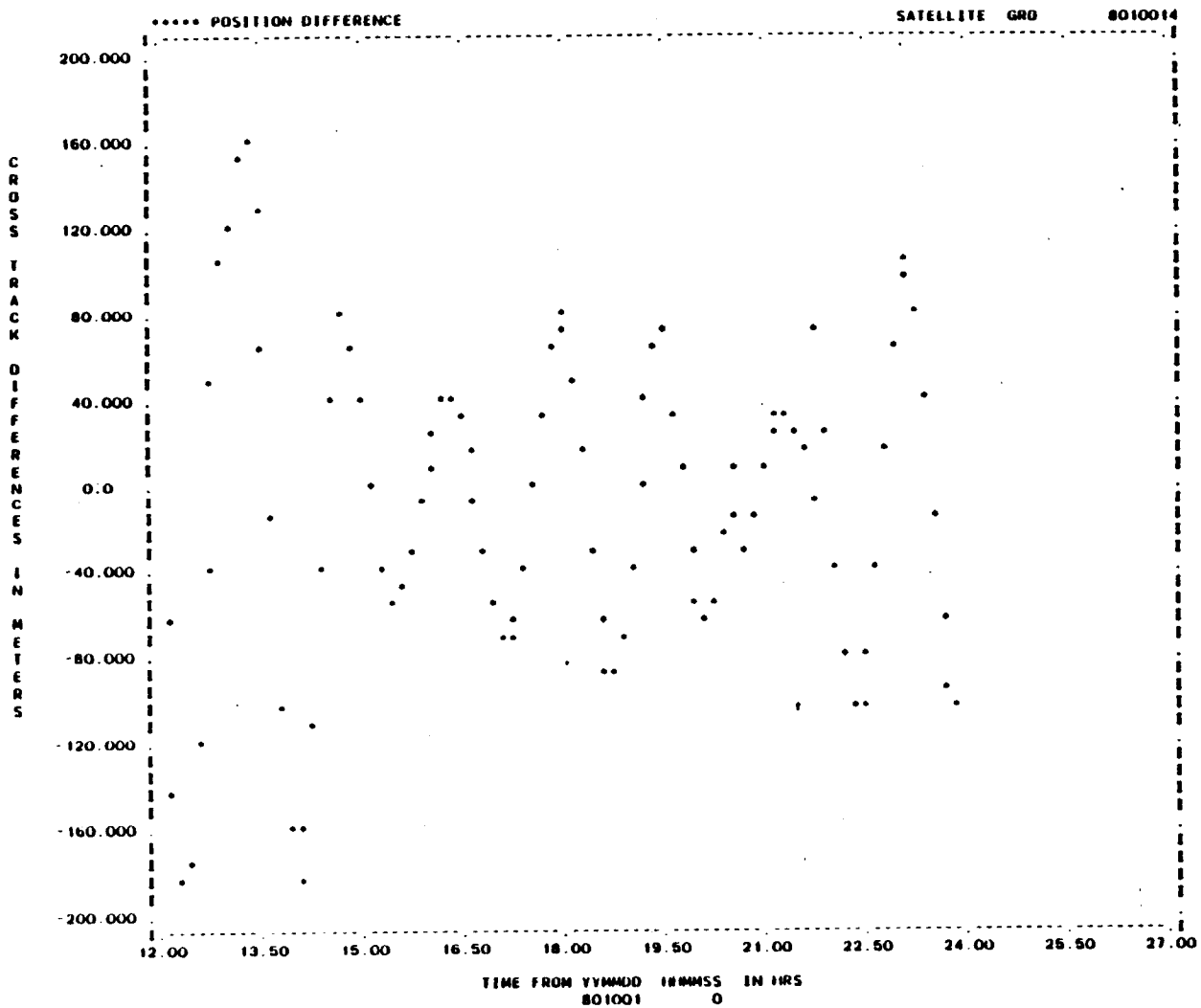

Figure B-68. Cross-Track Differences for Run T7 (2 of 2)

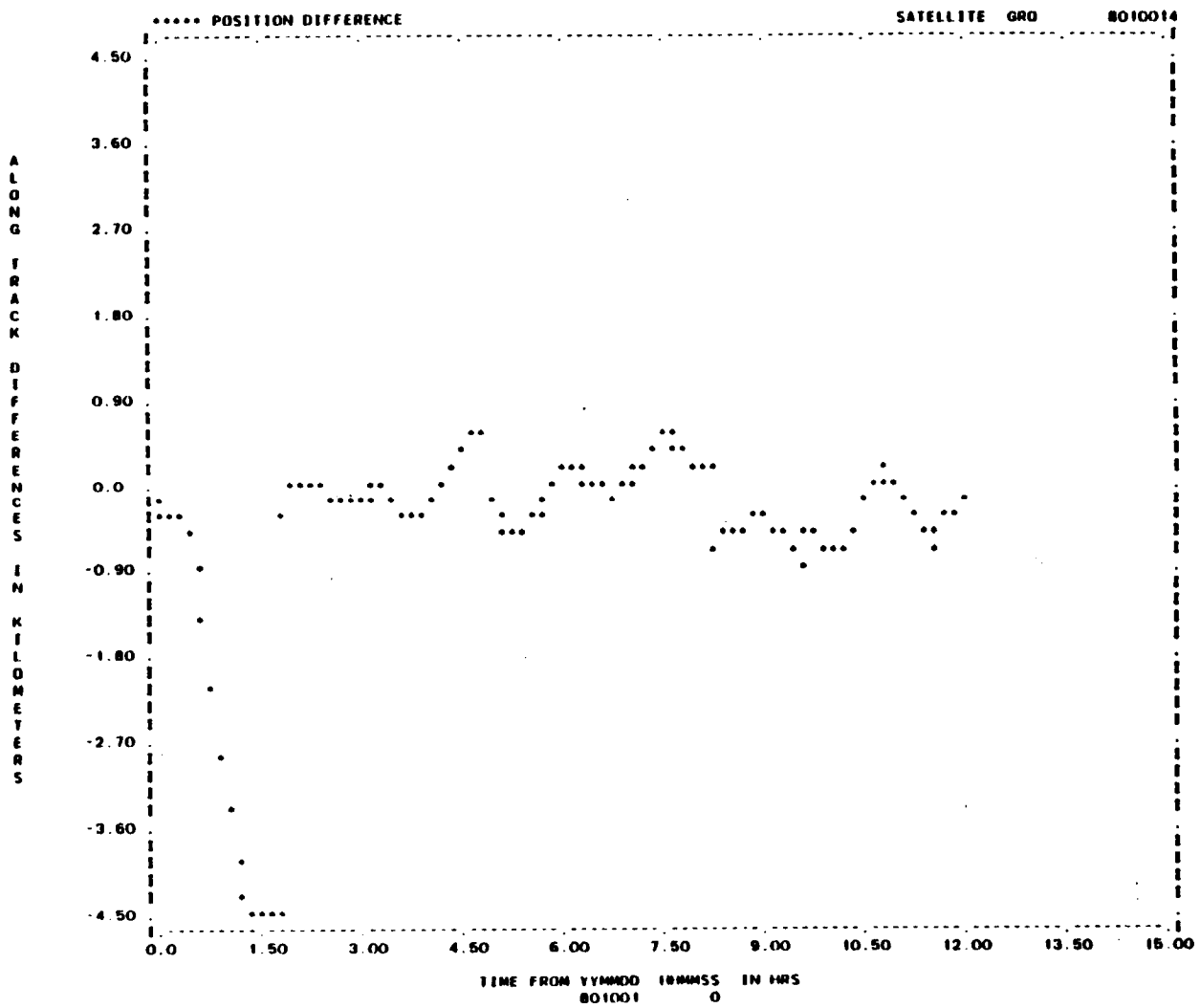

Figure B-69. Along-Track Differences for Run T7 (1 of 2)

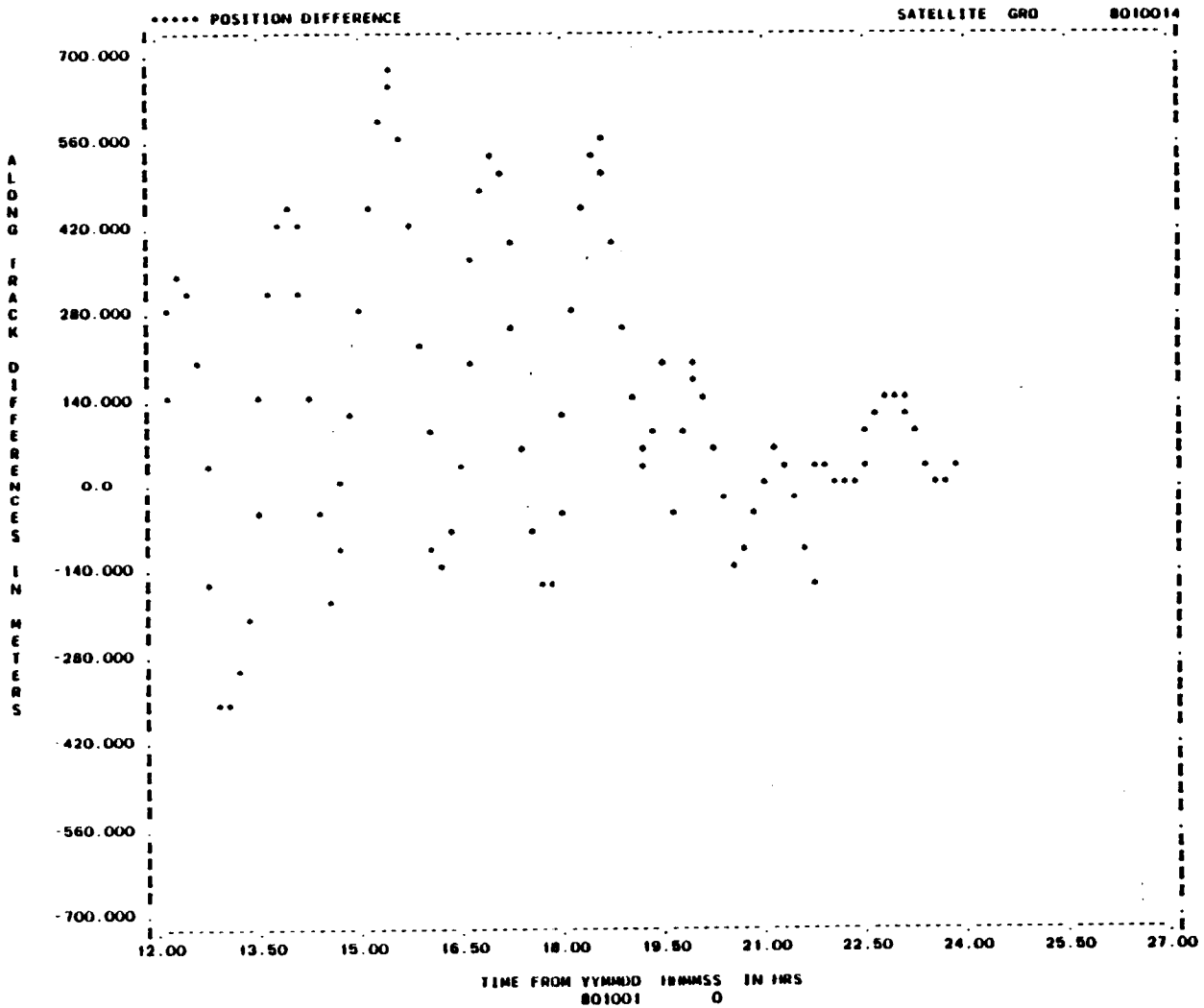

Figure B-69. Along-Track Differences for Run T7 (2 of 2)

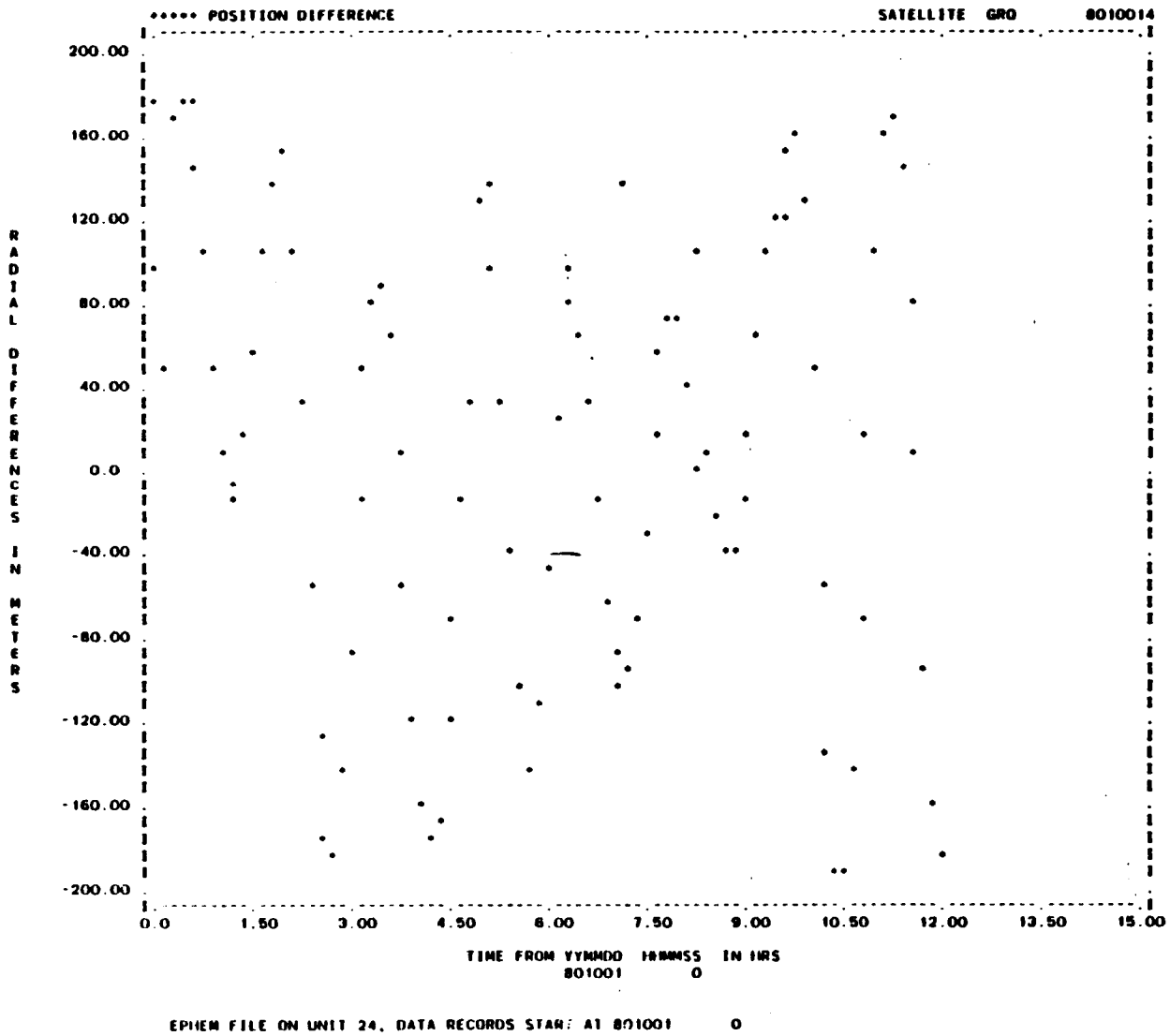

Figure B-70. Radial Differences for Run T10 (1 of 2)

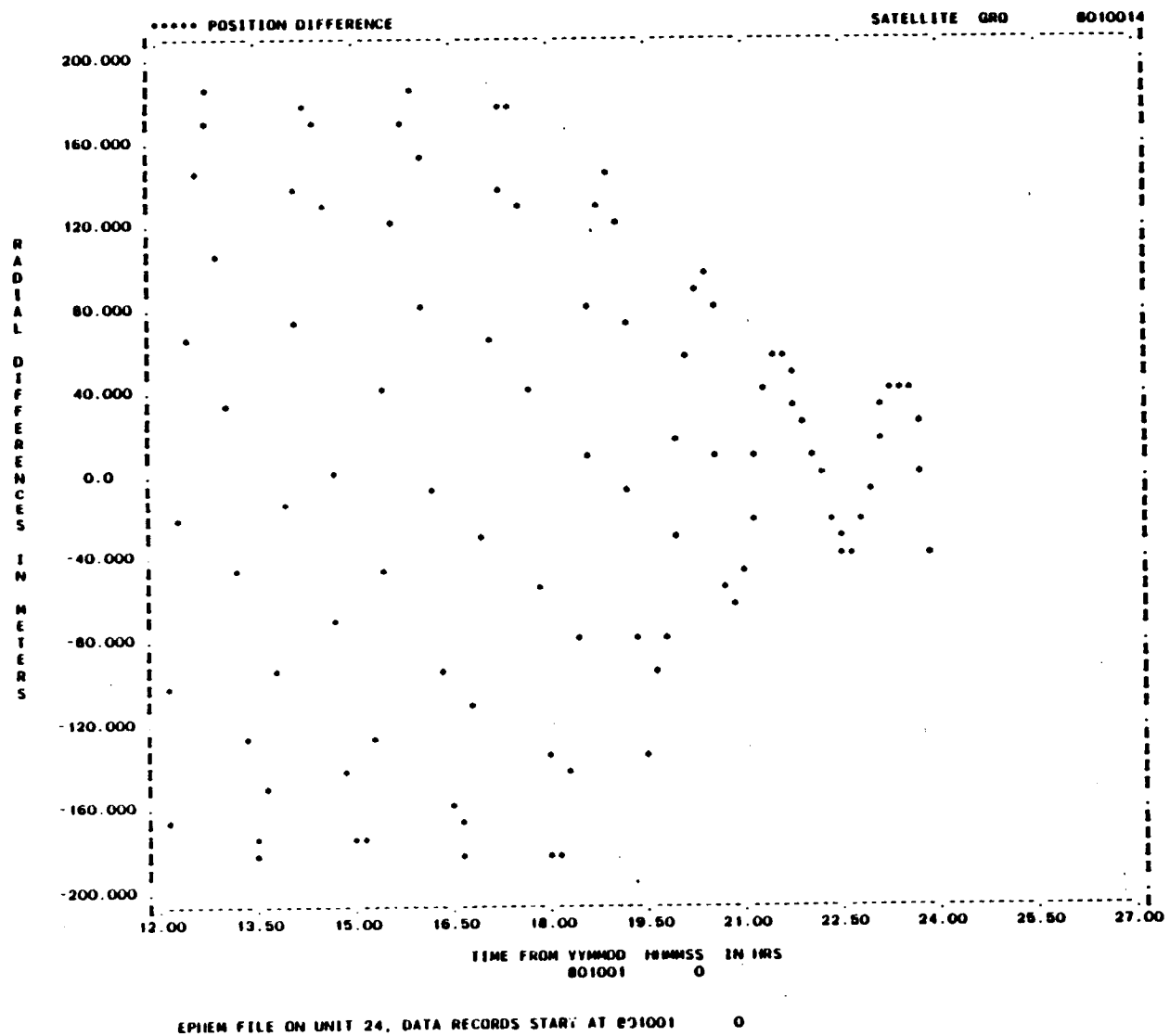

Figure B-70. Radial Differences for Run T10 (2 of 2)

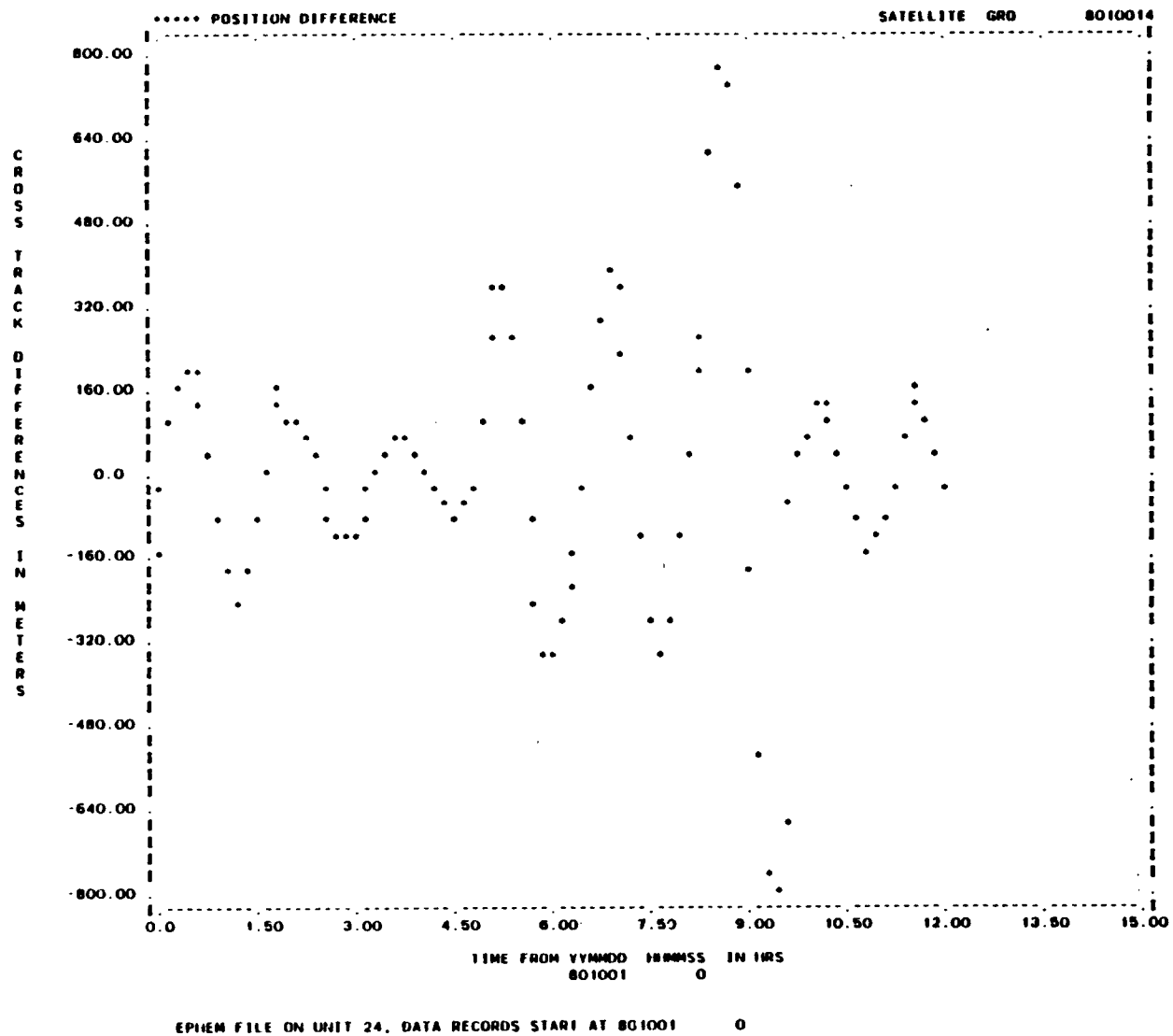

Figure B-71. Cross-Track Differences for Run T10 (1 of 2)

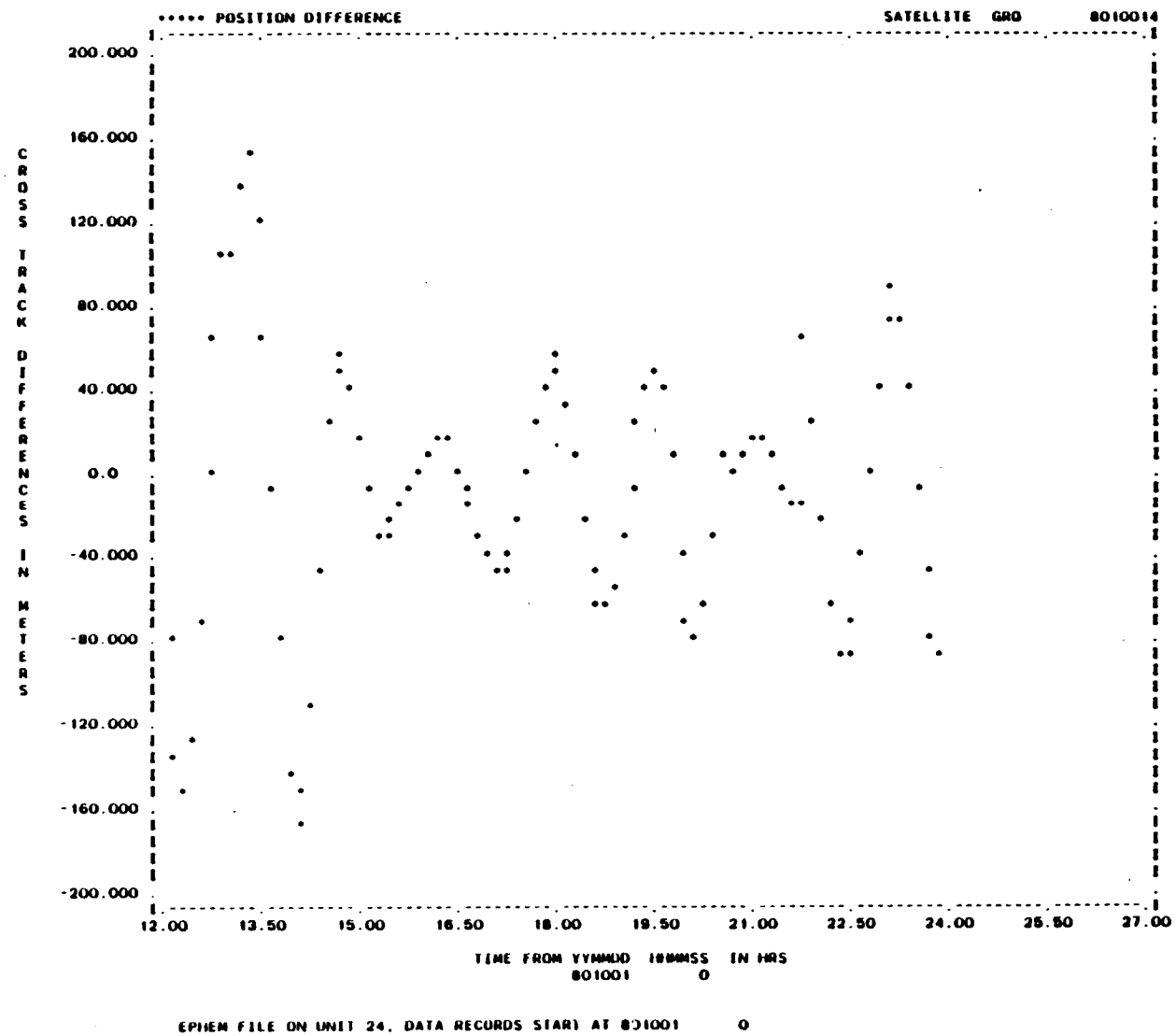

Figure B-71. Cross-Track Differences for Run T10 (2 of 2)

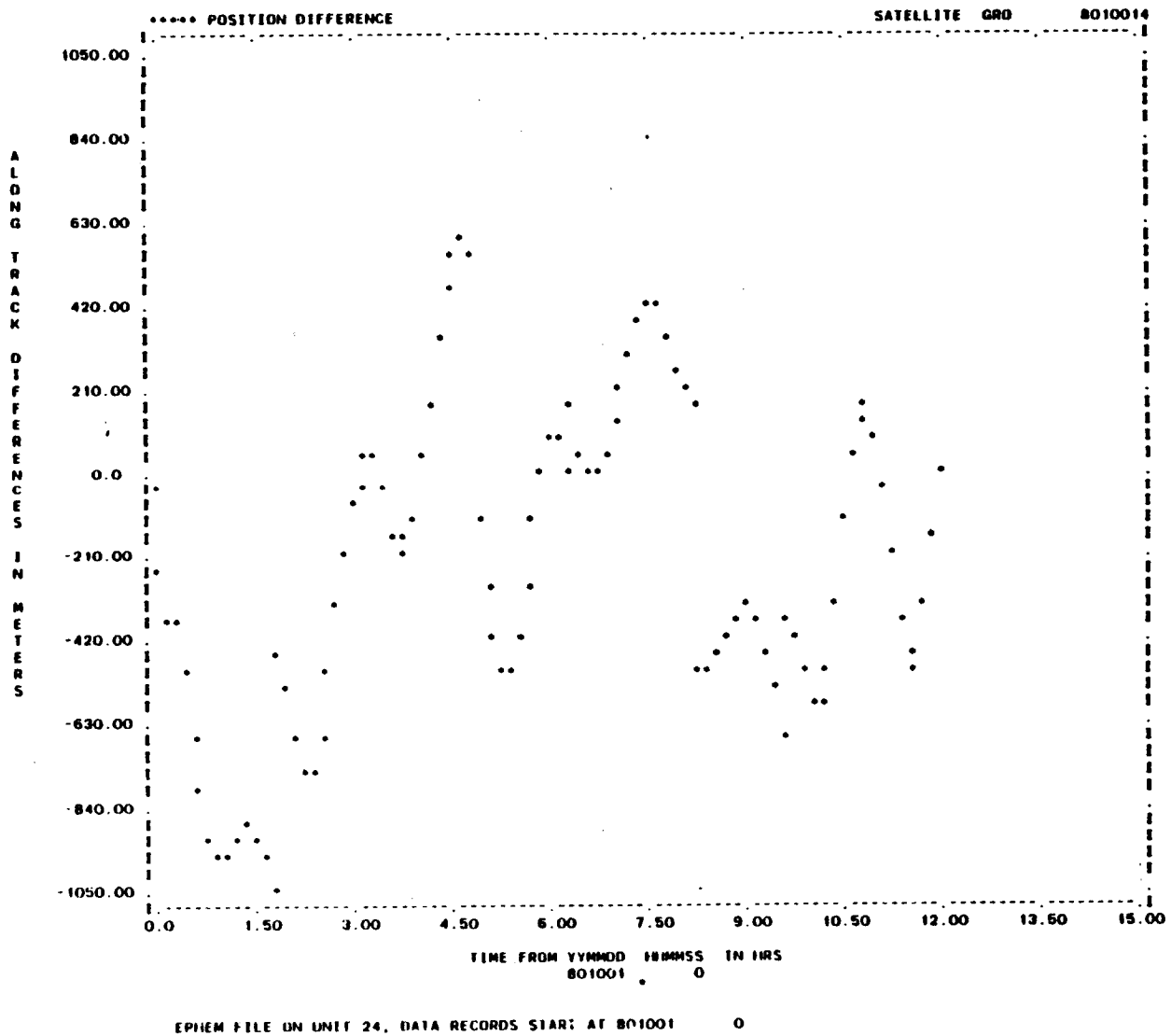

Figure B-72. Along-Track Differences for Run T10 (1 of 2)

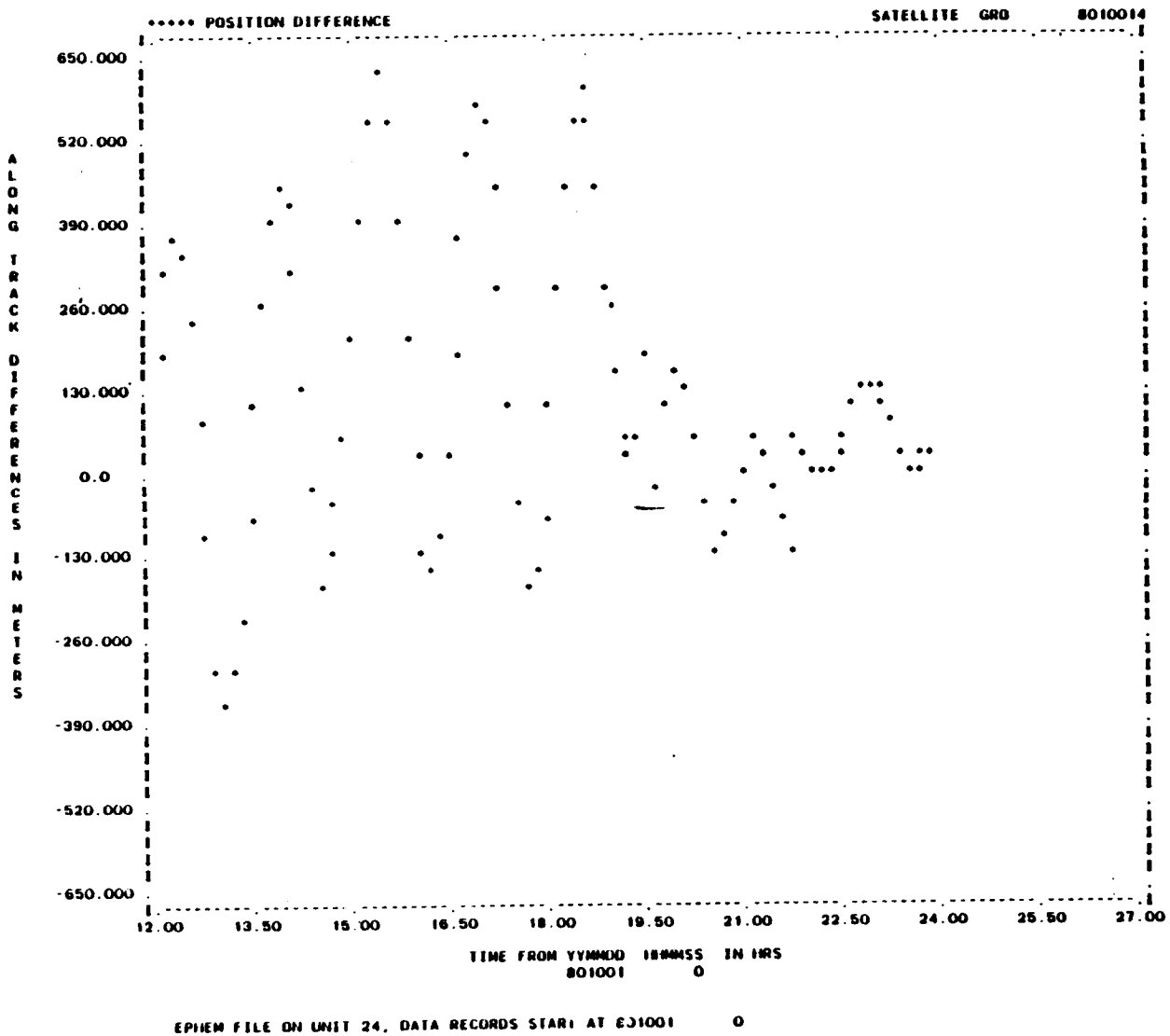

Figure B-72. Along-Track Differences for Run T10 (2 of 2)

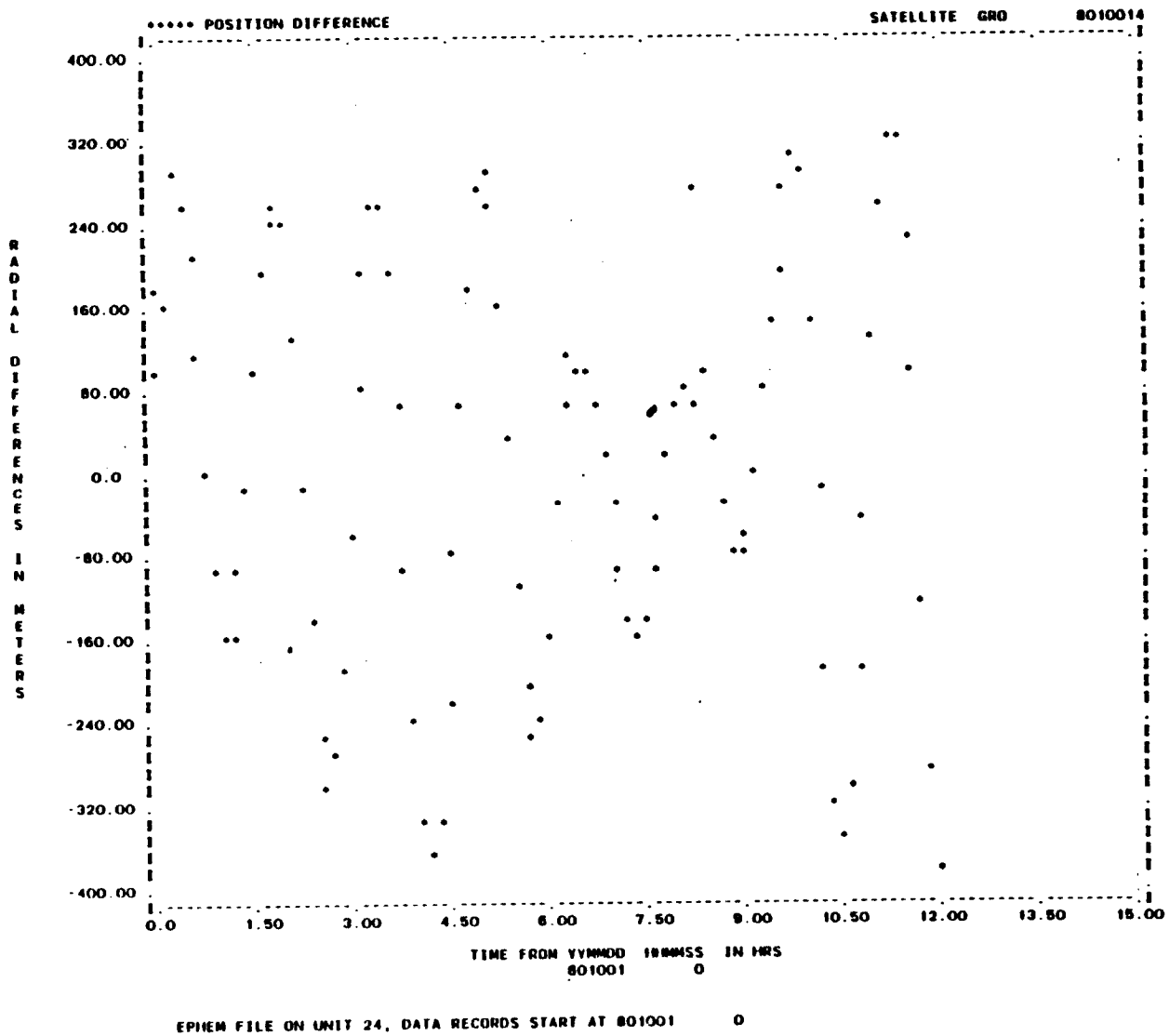

Figure B-73. Radial Differences for Run T11 (1 of 2)

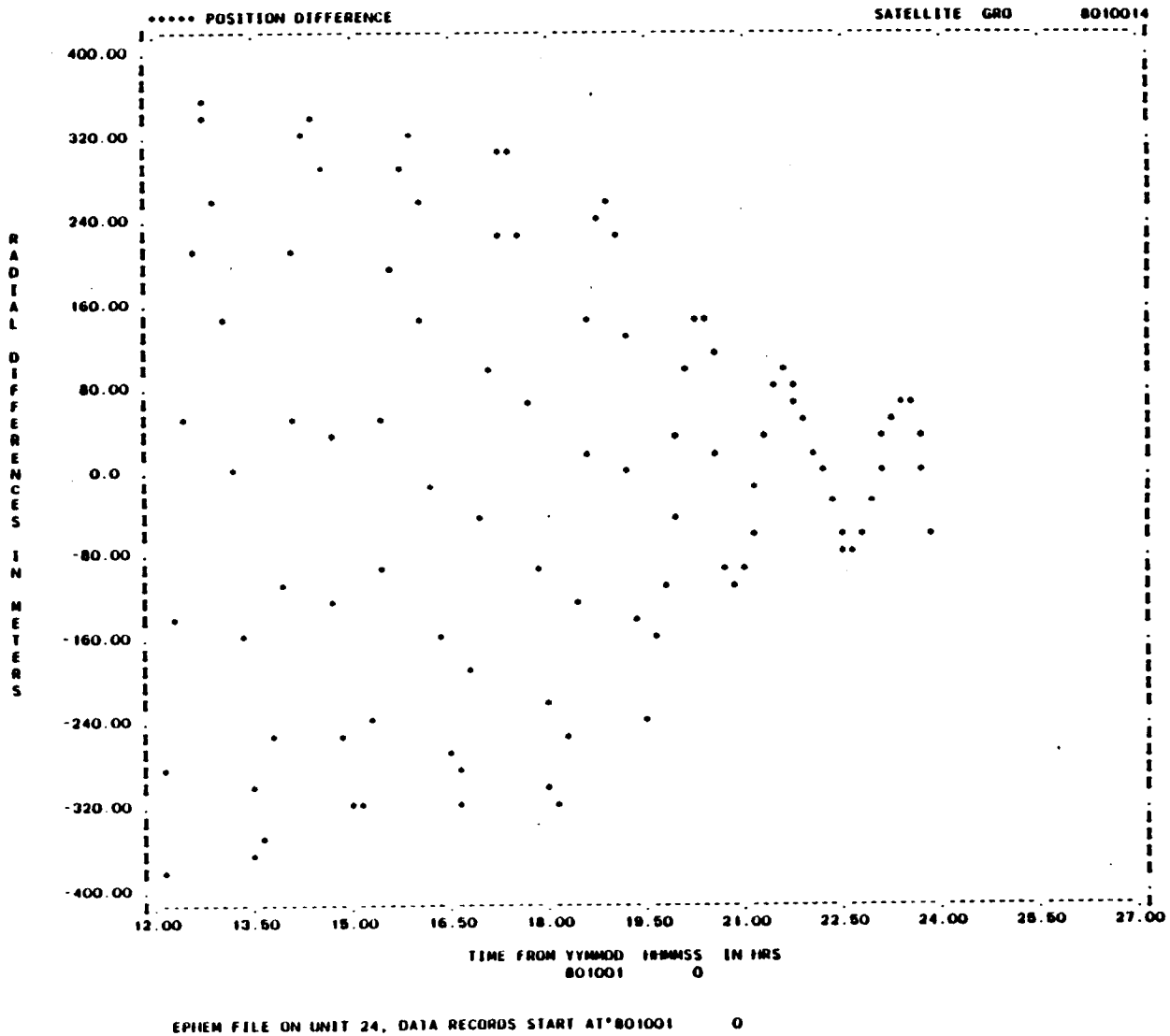

Figure B-73. Radial Differences for Run T11 (2 of 2)

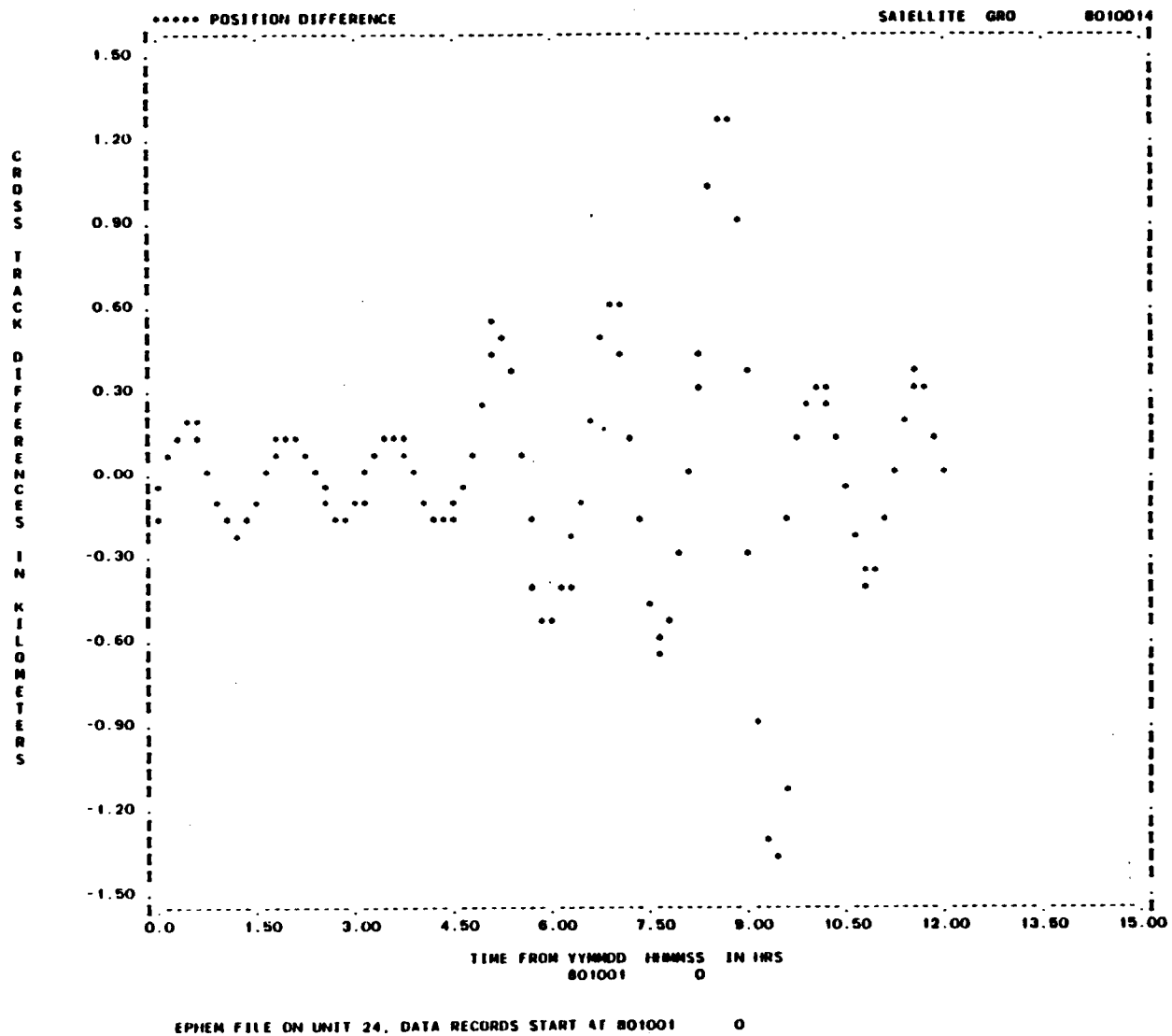

Figure B-74. Cross-Track Differences for Run T11 (1 of 2)

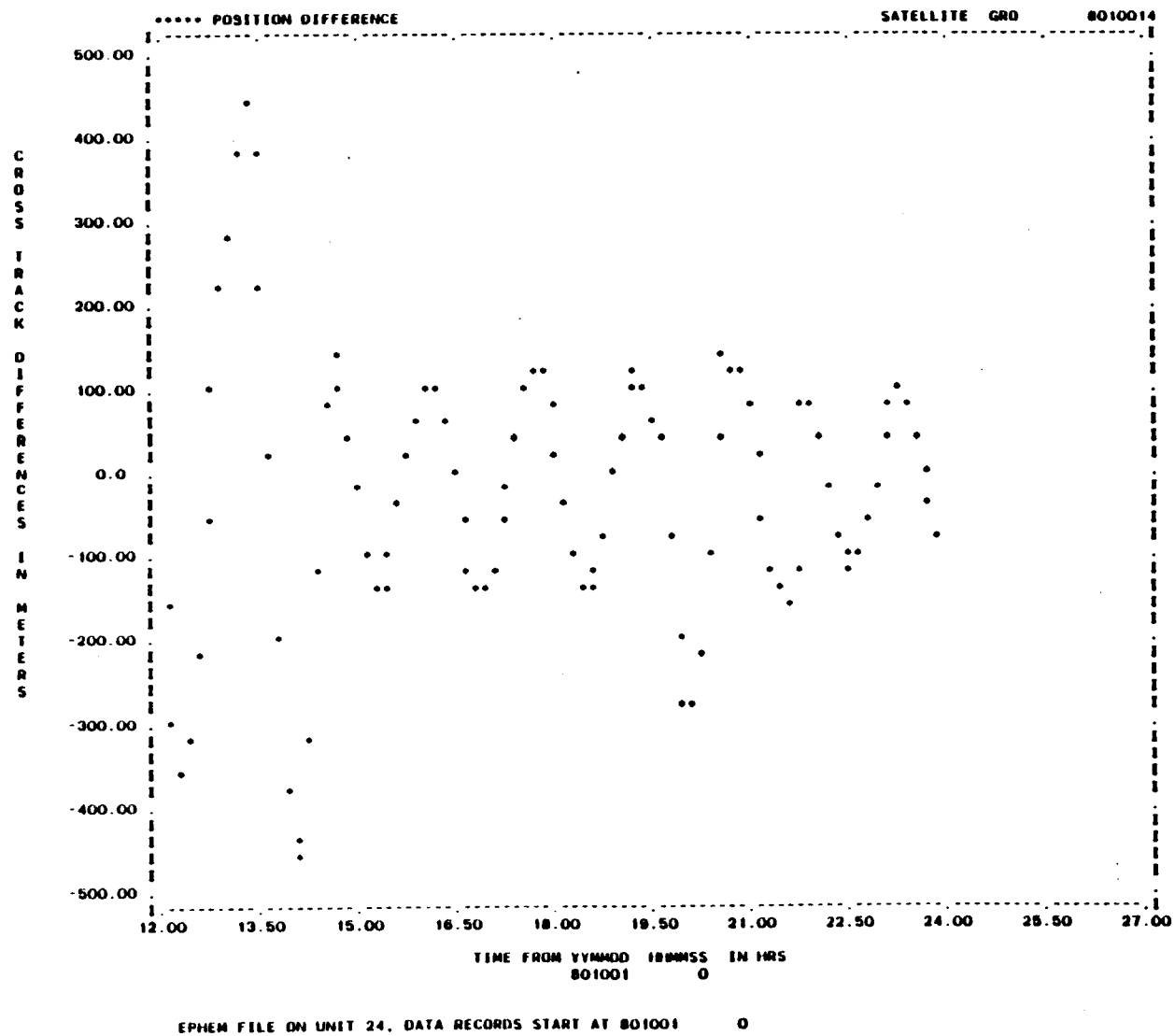

Figure B-74. Cross-Track Differences for Run T11 (2 of 2)

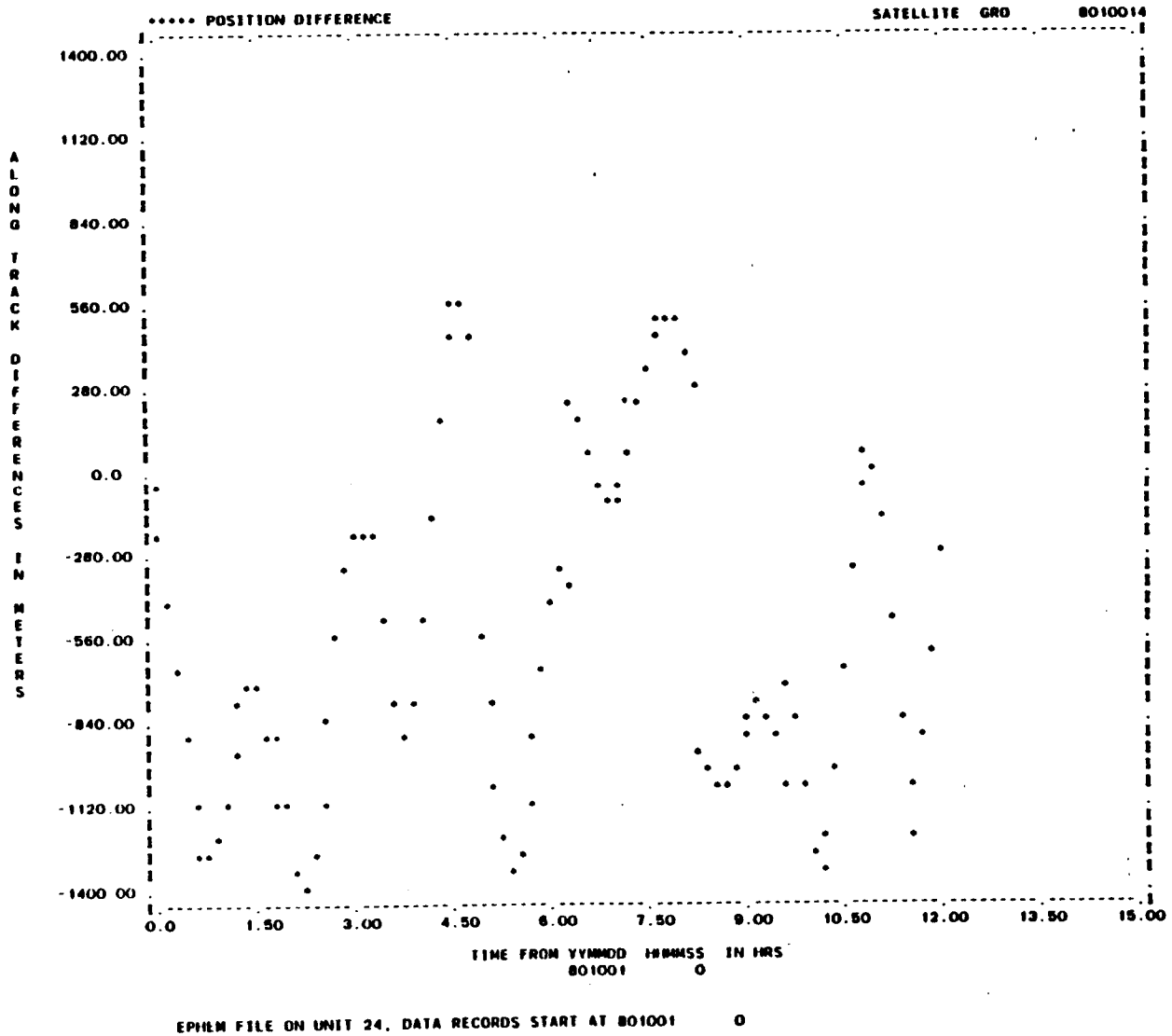

Figure B-75. Along-Track Differences for Run T11 (1 of 2)

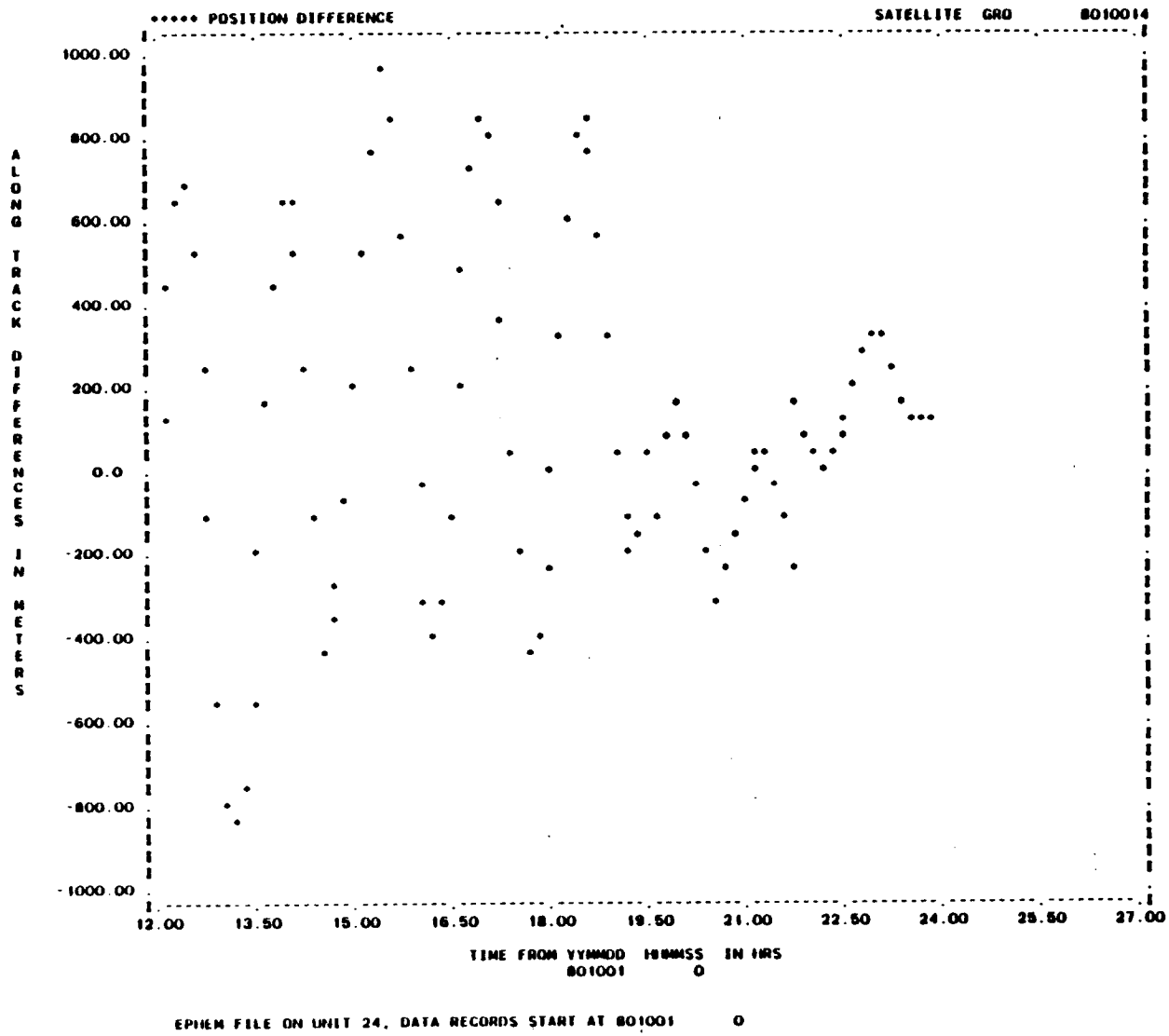

Figure B-75. Along-Track Differences for Run T11 (2 of 2)

APPENDIX C - ACCURACY OF EKF BASELINE EPHEMERIS

To assess the accuracy of the Runge-Kutta (RK) 3(4+) integrator and force models used in the R&D GTDS FILTER program, a series of Ephemeris Generation (EPHEM) and Ephemeris Comparison (COMPARE) program runs were made to compare the Landsat-D ephemeris generated in the FILTER program to the truth ephemeris generated by the Cowell integrator. Each case used the same initial state for Landsat-D and was run for a period of 12 hours. The truth model used a GEM-9 geopotential field with 15-by-15 harmonic terms, a 1964 Harris-Priester (HP) atmospheric model using a density table corresponding to a solar flux level (F) equal to 150, and a drag coefficient (C_D) equal to 2.0. The step size of the Cowell integrator was fixed at 45 seconds. The RK 3(4+) integrator was run in the variable step mode, with a tolerance of 1.0E-08. The average step taken during the 12-hour integration was 17 seconds.

Table C-1 summarizes the runs made using the RK 3(4+) integrator subjected to various force model perturbations. The reference coordinate system and the noncentral body force parameters were the same throughout all runs. The first three columns in the table specify the modeling parameters that were varied in this study. The next three columns specify the maximum radial, cross-track, and along-track ephemeris differences from the truth model, either at the 12-hour point or at the time from the starting point written below the value, whichever was greatest. The last column specifies the magnitudes of the differences in the state vector when compared to the truth ephemerides after 12 hours.

The comparison indicates that gravitational model errors and truncation of the gravity model to eighth order are

Table C-1. Runge-Kutta 3(4+) Orbit Propagator Evaluation

GRAVITY MODEL NAME/SIZE	SOLAR FLUX CONSTANT IN HP MODEL	DRAG CONSTANT, C_D	MAXIMUM EPHEMERIS ERRORS			
			$\Delta\vec{H}$	$\Delta\vec{C}$	$\Delta\vec{L}$	$\Delta\vec{R}$
GEM-9/15 x 15	150	2.0	1.5 cm	0.7 cm	29 cm	29 cm
GEM-1/15 x 15	150	2.0	39 m (@ 2.5 hr)	27 m (@ 10.8 hr)	449 m	449 m
GEM-9/8 x 8	150	2.0	40 m (@ 5 hr)	57 m (@ 9.1 hr)	388 m	388 m
GEM-1/8 x 8	150	2.0	37 m (@ 5 hr)	56 m (@ 9.1 hr)	830 m	830 m
GEM-9/15 x 15	200	2.0	6.5 m (@ 10.6 hr)	11 cm	167 m	167 m
GEM-9/15 x 15	200	2.2	7.5 m (@ 10.6 hr)	12 cm	195 m	195 m
GEM-1/8 x 8	200	2.2	39 m (@ 8.1 hr)	56 m (@ 9.1 hr)	1026 m	1026 m

7652/80

the most significant error sources, each contributing about 400 meters of error after 12 hours of prediction. An error of 50 in the solar flux number contributes about 170 meters to the final error, and an error of 10 percent in the atmospheric drag constant yields an error of about 30 meters. The error resulting from the difference in the RK and Cowell integrators is about 30 centimeters after 12 hours. Figure C-1 shows the growth in the total along-track error over 12 hours for Landsat-D. Figure C-2 shows the growth in the total along-track error for GRO, due to the mismatch in the dynamic models listed in Table 3-5 (Section 3).

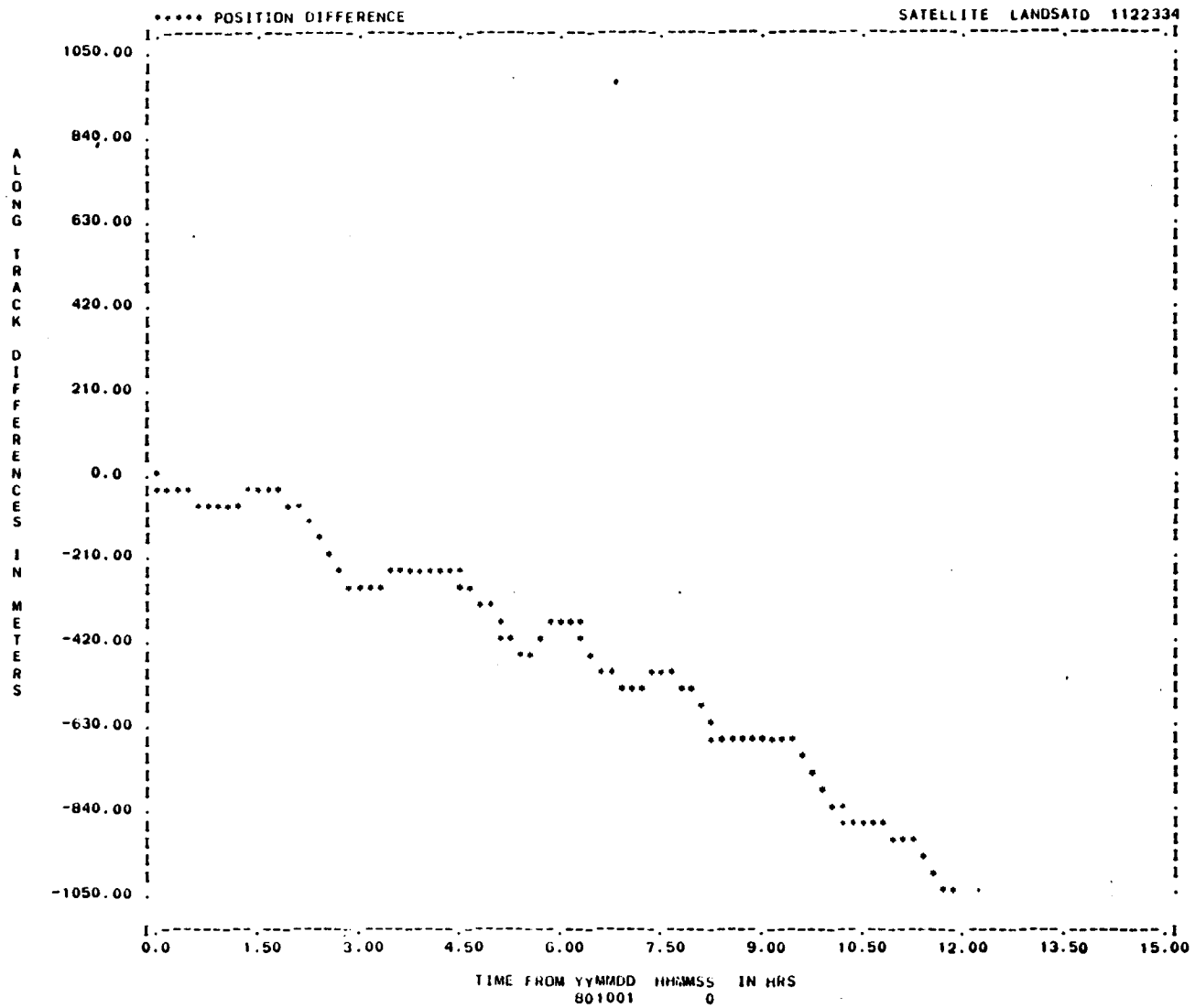

Figure C-1. Along-Track Error Over 12 Hours for Landsat-D

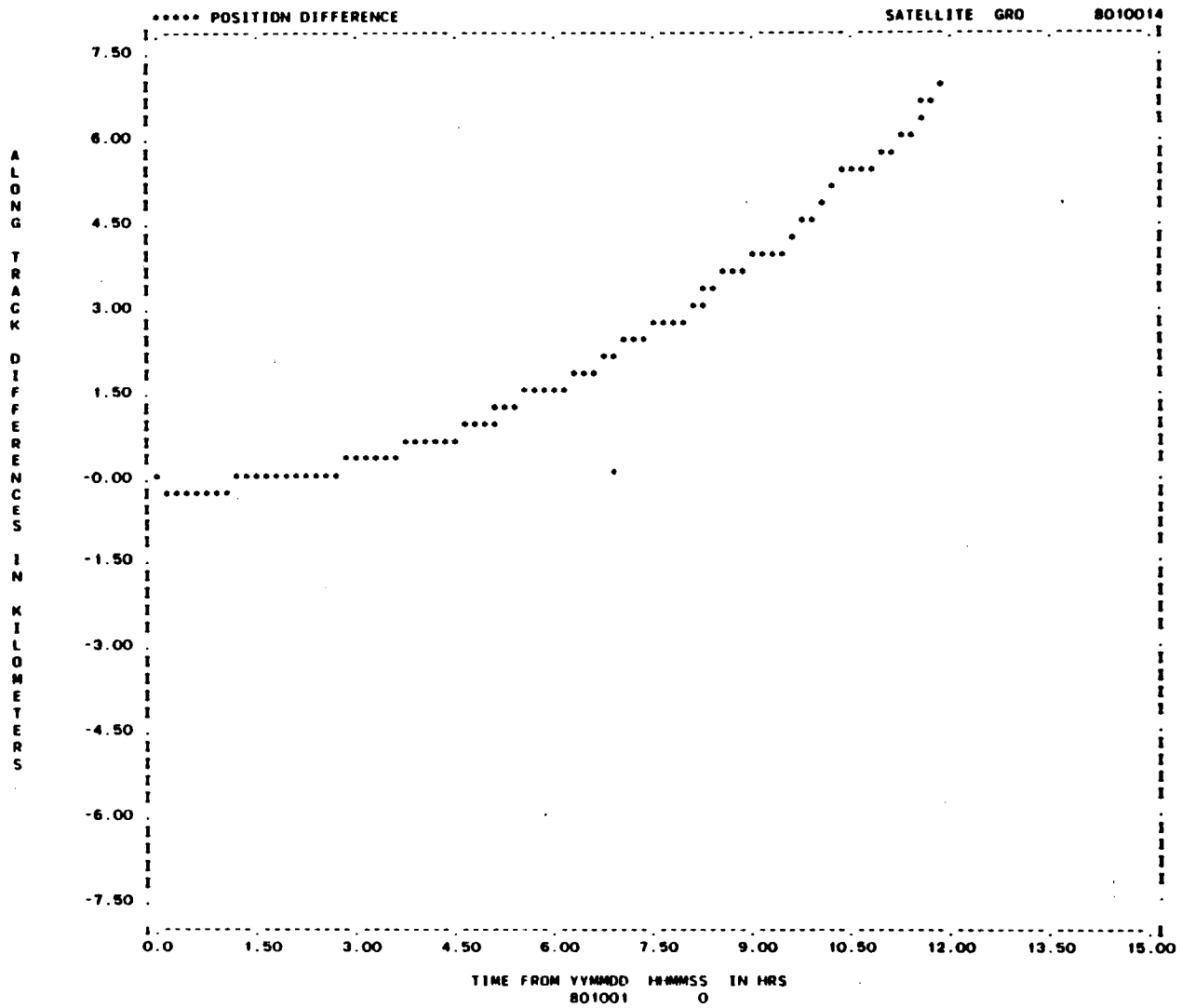

Figure C-2. Total Along-Track Error for GRO

APPENDIX D - COMPUTATION OF MEASUREMENT STANDARD DEVIATION ARISING FROM TDRS EPHEMERIS ERRORS

This appendix gives the derivation of the equations used for computation of the measurement standard deviations that were used in the EKF runs.

D.1 RANGE STANDARD DEVIATION

The range standard deviation, σ_R, is the standard deviation of the error along the line-of-sight vector from the TDRS to the spacecraft, $\vec{\ell}$. The instantaneous line-of-sight error arising from TDRS ephemeris errors is given by

$$\Delta\vec{\ell} = H_{TDRS}(t) \cos \phi(t) + [C_{TDRS}(t) + L_{TDRS}(t)] \sin \phi(t) \quad \text{(D-1)}$$

where ϕ = angle between $\vec{\ell}$ and the radius vector to the TDRS

$H_{TDRS}(t)$ = instantaneous radial ephemeris error

$C_{TDRS}(t)$ = instantaneous cross-track ephemeris error

$L_{TDRS}(t)$ = instantaneous along-track ephemeris error

The maximum value for ϕ (ϕ_{MAX}) occurs at the edge of visibility.

If the sinusoidal ephemeris error model is used, Equation (D-1) becomes

$$\Delta\vec{\ell} = [H_{TDRS} \cos \phi(t) + (C_{TDRS} + L_{TDRS}) \sin \phi(t)] \sin \frac{2\pi t}{86400} + \dot{L}_{TDRS} t \sin \phi(t) \quad \text{(D-2)}$$

where H_{TDRS}, C_{TDRS}, L_{TDRS} = amplitudes of sinusoidal terms

$\dot{L}_{TDRS}$ = along-track rate

t = time of the prediction

The standard deviation of $\Delta\vec{\ell}$ is given by

$$\sigma(\Delta\vec{\ell}) = \left\{\frac{1}{2}\left[H_{TDRS}^{2}\sigma^{2}(\cos\phi) + (C_{TDRS} + L_{TDRS})^{2}\sigma^{2}(\sin\phi)\right]^{2} + \frac{(\dot{L}_{TDRS}T)^{2}}{3}\sigma^{2}(\sin\phi)\right\}^{1/2} \tag{D-3}$$

where T is the length of the prediction.

For Landsat-D,

$$\phi_{MAX} \simeq \tan^{-1}\frac{7000}{42000} = \pm 9.5 \text{ degrees}$$

$$\cos\phi_{MAX} = 0.98$$

$$\sin\phi_{MAX} = \pm 0.16$$

$$\cos\phi_{MIN} = 1.0$$

$$\sin\phi_{MIN} = 0.0$$

Therefore,

$$\sigma^{2}(\cos\phi) = (0.99)^{2}$$

$$\sigma^{2}(\sin\phi) = \frac{(0.16)^{2}}{2} \tag{D-4}$$

Substituting into Equation (D-3) yields

$$\sigma(\Delta\vec{\ell}) \simeq \left\{\frac{1}{2}\left[H_{TDRS}^{2} + (C_{TDRS} + L_{TDRS})^{2}(0.01)\right] + \frac{(0.01)\dot{L}_{TDRS}^{2}T^{2}}{3}\right\}^{1/2} \tag{D-5}$$

The standard deviation of the range measurement is given by

$$\sigma_R = \sigma(\Delta\vec{\ell}) + \sigma_{R_{noise}}$$

For the baseline case, $\sigma_{R_{noise}} = 1$ meter, $H_{TDRS} = 35$ meters, $C_{TDRS} = 35$ meters, $L_{TDRS} = 80$ meters, $L = 250$ meters per day, and $T = 1$ day, which yields

$$\sigma_R = 29 \text{ meters} + 1 \text{ meter} = 30 \text{ meters}$$

D.2 DELTA-RANGE STANDARD DEVIATION

The contribution to the delta-range standard deviation arising from TDRS ephemeris error is given by

$$\sigma_{\Delta R} = E\left\{\left[\frac{\Delta\vec{\ell}(t) - \Delta\vec{\ell}(t - \Delta T)}{\Delta T}\right]^2\right\}^{1/2} \qquad \text{(D-6)}$$

where E signifies expected value, and $\Delta\vec{\ell}(t)$ is given by Equation (D-2).

Using the approximations

$$\sin\omega(t - \Delta T) \simeq \sin\omega(t) - (\dot{\omega}\Delta T)\cos\omega(t)$$

and

$$\cos\omega(t - \Delta T) \simeq \cos\omega(t) + (\dot{\omega}\Delta T)\sin\omega(t)$$

yields

$$\frac{\Delta\vec{\ell}(t) - \Delta\vec{\ell}(t - \Delta T)}{\Delta T} = H_{TDRS}\left[\frac{2\pi}{86400} \cos \phi(t) \cos \frac{2\pi t}{86400}\right.$$

$$\left. - \dot{\phi} \sin \phi(t) \left(\sin \frac{2\pi t}{86400} - \frac{2\pi \Delta T}{86400} \cos \frac{2\pi t}{86400}\right)\right]$$

$$+ (C_{TDRS} + L_{TDRS})\left[\frac{2\pi}{86400} \sin \phi(t) \cos \frac{2\pi t}{86400}\right.$$

$$\left. + \dot{\phi} \cos \phi(t) \left(\sin \frac{2\pi t}{86400} - \frac{2\pi \Delta T}{86400} \cos \frac{2\pi t}{86400}\right)\right]$$

$$+ \dot{L}_{TDRS} T[\dot{\phi} \cos \phi(t)] + \dot{L}_{TDRS}[\sin \phi(t)$$

$$- \dot{\phi} \Delta T \cos \phi(t)]$$

For a 7000-kilometer-altitude spacecraft such as Landsat-D or GRO,

$$\phi \simeq \frac{19 \text{ degrees}}{50 \text{ seconds}} = 0.0001 \text{ radian per second}$$

Keeping terms to one part in 10^3 yields

$$\frac{\Delta\vec{\ell}(t) - \Delta\vec{\ell}(t - \Delta T)}{\Delta T} = H_{TDRS}\left[0.00007 \cos \phi(t) \cos \frac{2\pi t}{86400}\right.$$

$$\left. - 0.0001 \sin \phi(t) \sin \frac{2\pi t}{86400}\right]$$

$$+ (C_{TDRS} + L_{TDRS})\left[0.00007 \sin \phi(t) \cos \frac{2\pi t}{86400}\right.$$

$$\left. + 0.0001 \cos \phi(t) \sin \frac{2\pi t}{86400}\right]$$

$$+ \dot{L}_{TDRS}[0.0001T \cos \phi(t) + \sin \phi(t)$$

$$- 0.001 \cos \phi(t)]$$

Taking the expected value and using Equation (D-4) yields

$$\sigma^2_{\Delta R} = H^2_{TDRS}[2.5 \times 10^{-9}]$$

$$+ (C_{TDRS} + L_{TDRS})^2(5 \times 10^{-9})$$

$$+ \dot{L}^2_{TDRS}\left[(10^{-8})\frac{T^2}{3} + 0.01\right]$$

Using a value for T of 1 day yields

$$\sigma^2_{\Delta R} = (2.5 \times 10^{-9})H^2_{TDRS} + (C_{TDRS} + L_{TDRS})^2(5 \times 10^{-9})$$

$$+ L^2_{TDRS}(25)$$

Using the nominal values of H_{TDRS} = 35 meters, C_{TDRS} = 35 meters, L_{TDRS} = 80 meters, and $\dot{L}_{TDRS}$ = 250 meters per 86,400 seconds yields $\sigma_{\Delta R}$ = 1.4 centimeters.

APPENDIX E - SAMPLE DECK SETUP

Figure E-1 presents a sample of the deck setup that was used with R&D GTDS to generate the results presented in this study. The setup given corresponds to run R7 in Table 5-3.

INPUT CARD IMAGES

```
COLUMN 1
        CONTROL    EPHEM                                                GRO        8010014
        ELEMENT1   2  2  1   6778.140          0.0017                  28.0
        ELEMENT2             0.0                0.0                     0.0
        EPOCH                801001.0           0.0
        ORBTYPE    2  1  2  45.
        OUTPUT     1  3  1   801001.0          240000.0                1800.0
        DMOPT
        WORKATM    5
        END
        OGOPT
        AUTOFORC   1  4
        MAXORDEQ   1         15.0
        MAXDEGEQ   1         15.0
        POTFIELD   1  5
        SOLRAD     1         2.0
        OUTOPT     3  1  2   801001000000.0     801001240000.0          438.0
        DRAG       1         1.0
        DRAGPAR    3  0      2.0
        SCPARAM              0.000020           1700.0
        END
        FIN
        CONTROL    EPHEM                                                GRO        8010014
        ELEMENT1   2  2  1   6778.140          0.0017                  28.0
        ELEMENT2             0.0                0.0                     0.0
        EPOCH                801001.0           0.0
        ORBTYPE    2  1  2  45.
        OUTPUT     1  3  1   801001.0          240000.0                1800.0
        DMOPT
        WORKATM    5
        END
        OGOPT
        AUTOFORC   1  4
        MAXORDEQ   1         15.0
        MAXDEGEQ   1         15.0
        POTFIELD   1  5
        SOLRAD     1         2.0
        STATEPAR   1
        STATETAB   1  2  3  4.                 5.                      6.
        OUTOPT     0  1  1   800930235500.0    801001240050.0            60.0
        OUTPART    1         1.
        DRAG       1         1.0
        DRAGPAR    3  0      2.0
        SCPARAM              0.000020           1700.0
        END
        FIN
        CONTROL    DATASIM                                              GRO        8010014
        DMOPT
        TDRID      1  2
        /GPSDATA1     1
        OBSDEV    82 83      1.0                10.0
        END
        DCOPT
        DSPEA1     6         801001.            0.0
        DSPEA2    19  1  1   801001.0           240000.0
        DSPEA3     0  1  1
        END
        GPSOPT
        TDRSSCH    1  1      801001001000.      801001001959.
        TDRSSCH    1  2      801001015000.      801001015959.
        TDRSSCH    2  1      801001031000.      801001031959.
        TDRSSCH    1  3      801001045500.      801001050459.
        TDRSSCH    2  2      801001062000.      801001062959.
        TDRSSCH    1  4      801001082000.      801001082959.
        TDRSSCH    2  3      801001094300.      801001095259.
        TDRSSCH    1  5      801001114000.      801001114959.
        TDRSSCH    2  4      801001130000.      801001130959.
        TDRSSCH    1  6      801001144000.      801001144959.
        TDRSSCH    2  5      801001161000.      801001161959.
        TDRSSCH    2  6      801001174000.      801001174959.
        TDRSSCH    1  7      801001193600.      801001194559.
        TDRSSCH    2  7      801001204000.      801001204959.
        TDRSSCH    1  8      801001215000.      801001215959.
        TDRSSCH    1  9      801001233000.      801001233959.
```

Figure E-1. Sample Deck Setup (1 of 2)

```
GPSBIAS    1  1  1   23.3
GPSCONF    6
GPSPOSER   1         35.0                35.0                80.0
GPSVELER   1         0.5                 0.5                  0.28935
GPSSEE     1  1  3   10.0                10.0
GPSSIM1    0  1  1   10.0                29.                 0.0
GPSSIM2    0  0  1   864C0.0
GPSSIM4              0.0                            2.00+ 5   0.2
END
FIN
CONTROL    FILTER                                   GRO        8010014
ELEMENT1   2  1  1   6766.72            -0.1                0.1
ELEMENT2             0.0003              6.7824              3.606
EPOCH                801001.0            0.0
ORBTYPE   10  2  2   15.0
OBSINPUT  14         801001000000.0      801001240000.0
DMOPT
TDRID      1  2
WORKATM    7
/GPSDATA1     1
OBSDEV    82 83      -40.0               10.0
END
DCOPT
CONVERG    1
EDIT                 1000000.0
PRINTOUT   1      1  1.0                 2.0
END
GPSOPT
USERBIAS   1  3  1                                1.00+ 6
GPSSIM4              0.0                          2.20+ 5   0.0
END
FILOPT
FILTER     2  1  1   1.0                           .
INPUT      1  1  1
SPNOISE   44 55 66              1.00-18            1.00-18              1.00-18
DYNOISE                         1.00-14
UCLOCKPN                                           1.00-23
END
OGOPT
AUTOFORC   2  4
POTFIELD   1  3
MAXORDEQ   1         8.0
MAXDEGEQ   1         8.0
SOLRAD     1         2.0
DRAG       1         1.0
DRAGPAR    3  0      2.2
DRAGPAR    1  1      0.0                                 1.0
COVARNC   11 22 33   0.1                 0.1                 0.1
COVARNC   44 55 66    0.000001            0.000001           0.000001
STATEPAR   1  1
OUTOPT    23  1  2   801001000000.0      801001240000.0      438.0
END
FIN
CONTROL    COMPARE                                  GRO        8010014
COMPOPT
CMPEPHEM   2202202   801001000000.0      801001240000.0      7.3
CMPPLOT   15
END
FIN
CONTROL    COMPARE                                  GRO        8010014
COMPOPT
CMPEPHEM   2202202   801001090000.0      801001120000.0      7.3
CMPPLOT   15
END
FIN
CONTROL    COMPARE                                  GRO        11223344
COMPOPT
CMPEPHEM   2202202   801001210000.0      801001240000.0      7.3
CMPPLOT   15
END
FIN
```

Figure E-1. Sample Deck Setup (2 of 2)

REFERENCES

1. Computer Sciences Corporation, Goddard Trajectory Determination System Research and Development (GTDS R&D) User's Guide (draft), August 1978

2. --, CSC/SD-79/6032, The Research and Development Goddard Trajectory Determination System (R&D GTDS) Filter Program Software Specifications and User's Guide, J. B. Dunham, December 1979

3. National Aeronautics and Space Administration, Goddard Space Flight Center, STDN Report No. 101.2, Tracking and Data Relay Satellite System User's Guide, Revision 3, January 1978

4. Computer Sciences Corporation, CSC/TM-80/6234, Onboard Orbit Determination With Tracking and Data Relay Satellite System Data, Volume II: Sliding Batch Differential Corrector (SBDC) Evaluation, K. A. Preiss and J. B. Dunham, November 1980

5. EKF comparison graphs, available from A. C. Long (Computer Sciences Corporation)